Transactions of the ASME, Journal of Heat Transfer (ISSN 0022-1481) is published monthly by The American Society of Mechanical Engineers, Three Park Avenue, New York, NY 10016. Periodicals postage paid at New York, NY and additional mailing offices. POSTMASTER: Send address changes to Transactions of the ASME, Journal of Heat Transfer, c/o THE AMERICAN SOCIETY OF MECHANICAL ENGINEERS, 22 Law Drive, Box 2300, Fairfield, NJ 07007-2300. **CHANGES OF ADDRESS** must be received at Society headquarters seven weeks before they are to be effective. Please send old label and new address.

Journal of Heat Transfer

Published Monthly by ASME

VOLUME 131 • NUMBER 7 • JULY 2009

RESEARCH PAPERS

(Contents continued on inside back cover)

This journal is printed on acid-free paper, which exceeds the ANSI Z39.48-1992 specification for permanence of paper and library materials. ♾™
♻ 85% recycled content, including 10% post-consumer fibers.

Journal of Heat Transfer Volume 131, Number 7 JULY 2009

The ASME Journal of Heat Transfer is abstracted and indexed in the following:

Applied Science and Technology Index, Chemical Abstracts, Chemical Engineering and Biotechnology Abstracts (Electronic equivalent of Process and Chemical Engineering), Civil Engineering Abstracts, Compendex (The electronic equivalent of Engineering Index), Corrosion Abstracts, Current Contents, E & P Health, Safety, and Environment, Ei EncompassLit, Engineered Materials Abstracts, Engineering Index, Enviroline (The electronic equivalent of Environment Abstracts), Environment Abstracts, Environmental Engineering Abstracts, Environmental Science and Pollution Management, Fluidex, Fuel and Energy Abstracts, Index to Scientific Reviews, INSPEC, International Building Services Abstracts, Mechanical & Transportation Engineering Abstracts, Mechanical Engineering Abstracts, METADEX (The electronic equivalent of Metals Abstracts and Alloys Index), Petroleum Abstracts, Process and Chemical Engineering, Referativnyi Zhurnal, Science Citation Index, SciSearch (The electronic equivalent of Science Citation Index), Theoretical Chemical Engineering

Spray Cooling With Ammonia on Microstructured Surfaces: Performance Enhancement and Hysteresis Effect

Huseyin Bostanci[1]
e-mail: huseyin.bostanci@rinitech.com

Daniel P. Rini
e-mail: dan@rinitech.com

Rini Technologies, Inc. (RTI),
582 South Econ Circle,
Oviedo, FL 32765

John P. Kizito
Department of Mechanical and Chemical Engineering,
North Carolina A&T State University,
Greensboro, NC 27411
e-mail: jpkizito@ncat.edu

Louis C. Chow
Department of Mechanical, Materials and Aerospace Engineering,
University of Central Florida,
Orlando, FL 32816
e-mail: lchow@mail.ucf.edu

Experiments were performed to investigate spray cooling on microstructured surfaces. Surface modification techniques were utilized to obtain microscale indentations and protrusions on the heater surfaces. A smooth surface was also tested to have baseline data for comparison. Tests were conducted in a closed loop system with ammonia using RTI's vapor atomized spray nozzles. Thick film resistors, simulating heat source, were mounted onto 1×2 cm^2 heaters, and heat fluxes up to 500 W/cm^2 (well below critical heat flux limit) were removed. Two nozzles each spraying 1 cm^2 of the heater area used 96 ml/cm^2 min (9.7 $gal/in.^2$ h) liquid and 13.8 ml/cm^2 s (11.3 $ft^3/in.^2$ h) vapor flow rate with only 48 kPa (7 psi) pressure drop. Comparison of cooling curves in the form of surface superheat ($\Delta T_{sat}=T_{surf}-T_{sat}$) versus heat flux in the heating-up and cooling-down modes (for increasing and decreasing heat flux conditions) demonstrated substantial performance enhancement for both microstructured surfaces over smooth surface. At 500 W/cm^2, the increases in the heat transfer coefficient for microstructured surfaces with protrusions and indentations were 112% and 49% over smooth surface, respectively. Moreover, results showed that smooth surface gives nearly identical cooling curves in the heating-up and cooling-down modes, while microstructured surfaces experience a hysteresis phenomenon depending on the surface roughness level and yields lower surface superheat in the cooling-down mode, compared with the heating-up mode, at a given heat flux. Microstructured surface with protrusions was further tested using two approaches to gain better understanding on hysteresis. Data indicated that microstructured surface helps retain the established three-phase contact lines, the regions where solid, liquid, and vapor phases meet, resulting in consistent cooling curve and hysteresis effect at varying heat flux conditions (as low as 25 W/cm^2 for the present work). Data also confirmed a direct connection between hysteresis and thermal history of the heater.
[DOI: 10.1115/1.3089553]

Keywords: heat transfer, thermal management, electronics cooling, two-phase, enhanced surfaces, hysteresis

1 Introduction

In light of cooling requirements of today's high heat flux generating devices, spray cooling continues to be a viable solution for a wide range of applications from electronics to laser systems to directed-energy weapons. Spray cooling has been demonstrated to remove high heat fluxes, provide uniform device temperatures, and use relatively low coolant flow rates enabling design of compact and lightweight thermal management systems.

Although a vast amount of research has been done on heat transfer enhancement in general, studies focusing on spray cooling enhancement are fairly limited. In early works, Pais et al. [1] and Sehmbey et al. [2] examined the effects of surface roughness and contact angle using water with air atomized nozzle at flow rates up to 85 ml/cm^2 min water and 400 ml/cm^2 s air and found enhancement in the heat transfer coefficient with decreasing surface roughness and increasing contact angle. They obtained heat fluxes up to 1250 W/cm^2 at 11°C surface superheat on ultrasmooth ($R_a=0.3$ μm) copper surface.

Kim et al. [3] investigated spray cooling enhancement on microporous coated surfaces using water at flow rates up to 1.5 ml/cm^2 min. The porous layer was fabricated using a mixture of methyl-ethyl-keytone (MEK), epoxy, and aluminum powder, and its maximum thickness was 500 μm. They found that the critical heat flux (CHF) increased by 50% relative to the uncoated surface. However, the highest heat flux reached was 3.2 W/cm^2 at 65°C surface superheat due to very low flow rates.

Stodke and Stephan [4] studied spray cooling on microstructured and microporous surfaces using water at 60 mbar system pressure and 85 ml/cm^2 min flow rate. Pyramidal microgrooves and micropyramids with 75 μm height increased the wetted area by a factor of 1.4. Porous layer with 100 μm thickness was very similar to that used by Kim et al. [3] and created with the same ingredients. A maximum heat flux of 97 W/cm^2 was observed for the micropyramid surface compared with 30 W/cm^2 for the flat surface, both at a surface superheat of 12°C. This enhancement was much larger than the surface area enhancement. However, microporous surface caused a significant degradation in heat transfer compared with the uncoated surface resulting in 14 W/cm^2, the maximum heat flux at 12°C superheat due to the poor thermal conductivity of the epoxy binder.

Amon et al. [5] and Hsieh and Yao [6] performed spray cooling experiments with water using 1×2 nozzle array at very low flow rates of up to 4.41 ml/cm^2 min on square microstuds with

[1]Corresponding author.

Contributed by the Heat Transfer Division of ASME for publication in the JOURNAL OF HEAT TRANSFER. Manuscript received April 1, 2008; final manuscript received December 15, 2008; published online May 5, 2009. Review conducted by Roger Schmidt. Paper presented at the 2008 ASME Heat Transfer, Fluids, Energy, Solar, and Nano Conferences (HTFESN2008), Jacksonville, FL, August 10–14, 2008.

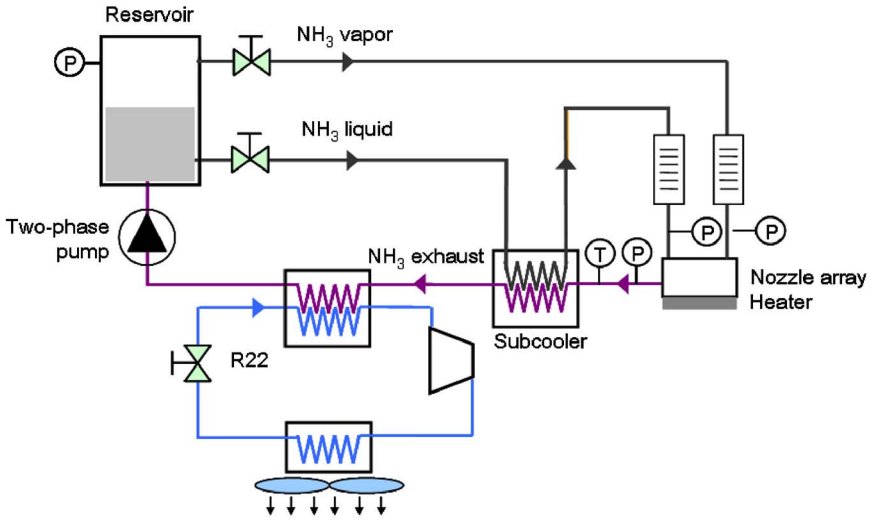

Fig. 1 Schematic of the experimental setup

160–480 μm heights. This surface texture on silicon was found to have little effect in the single phase and dry out regimes. The authors attributed the higher heat transfer observed for the micro-textured surfaces in the intermediate regimes to more effective spreading of the liquid by capillary forces. The maximum heat flux achieved was just over 50 W/cm^2 at 55°C surface superheat.

Silk et al. [7] investigated the effect of surface geometry in spray cooling with PF-5060 using 2×2 nozzle array at 96 ml/cm^2 min flow rate. They used embedded structures (dimples, pores, and tunnels) and compound extended structures (straight fins, cubic pin fins, and dimples) all in the order of 1 mm size. Of these macrostructured surfaces, straight fins and porous tunnels performed the best providing a CHF of 175 W/cm^2 for gassy conditions at surface superheats of up to 36°C and offered CHF enhancement of 62% over a flat surface.

Coursey et al. [8] recently performed spray cooling tests focusing on straight fin geometry with heights between 0.25 mm and 5 mm. They used PF-5060 at flow rates up to 62 ml/cm^2 min and found that fin heights between 1 mm and 3 mm were optimum for heat fluxes up to 124 W/cm^2 at 19°C surface superheat.

Most of the mentioned efforts [3–8] used various pressure atomized nozzles. Pais et al. [1] and Sehmbey et al. [2] employed air atomized nozzles in their tests where air flow field was thought to help thin the liquid film and maintain lower coolant partial pressures at evaporation surface eventually yielding higher heat transfer coefficients.

Besides the evaluation of heat transfer enhancement, none of the previous spray cooling research on surface effects [1–8] reported a hysteresis phenomenon, which results in lower surface superheats in cooling-down mode, compared with heating-up mode at a given heat flux. Many nucleate pool boiling literature, however, addressed hysteresis issue especially with highly wetting liquids such as R-113 and FC-72.

Bergles and Chyu [9] and Marto and Lepere [10] were among the first to mention boiling hysteresis known as "temperature excursion" or "temperature overshoot" hysteresis, which manifests itself with large temperature drops on surface when nucleation starts.

Shi et al. [11] later observed another type of boiling hysteresis and described it as "temperature deviation" hysteresis. This hysteresis caused temperature deviation between the cooling curves in the heating-up and cooling-down modes. Lower surface superheats occurred in the cooling-down mode of fully developed nucleate boiling regime and distinguished itself from the temperature overshoot hysteresis that occurs at boiling incipience.

Several mechanisms can be identified in explaining boiling hysteresis. One of these, recognized since the early works, was "vapor gathering" where nucleation site, initially flooded with highly wetting fluid, requires a large surface superheat for the first bubble departure, but retains enough vapor afterward, enabling boiling at much lower surface superheat. In other mechanisms, early growing bubbles help neighboring cavities, which retained less or no residual gas, and activate at lower surface superheats by "vapor propagation" (for nonwetting fluids) and "vapor covering" (for wetting fluids). Shi et al. [11] concluded that vapor gathering, vapor propagation, and vapor covering are the main mechanisms of temperature overshoot hysteresis, while further vapor propagation causes temperature deviation hysteresis.

Hwang and Kaviany [12], on the other hand, used microporous surfaces in their boiling tests and observed temperature deviation hysteresis with an opposite trend where cooling-down mode resulted in higher surface superheats, compared with heating-up mode, at a given heat flux. They thought that the hysteresis was caused by the trapped vapor within the porous layer, which decreases the effective conductivity.

The main objectives of the present study can be summarized as to investigate performance enhancement and hysteresis effect in spray cooling of microstructured surfaces. This work uses vapor atomized nozzles with anhydrous ammonia as coolant that would enable high heat flux devices, such as laser diodes, to operate at room temperatures. Two types of microstructured surfaces with indentations and protrusions along with a smooth surface were tested to generate cooling curves, compare their performance, and determine heat transfer enhancement. Additional experiments with one of the microstructured surfaces were performed to gain better understanding of hysteresis in spray cooling.

2 Experimental Setup and Procedure

Experiments were conducted in a closed loop spray cooling system. Figure 1 includes the schematic of the system where main components are reservoir, 1×2 nozzle array, subcooler, condenser, and pump. In this setup, the reservoir supplies ammonia liquid and vapor to the nozzle array. Liquid and vapor mixes in the atomizer nozzles, and the resulting spray cools a 1×2 cm^2 heater where heat source thick film resistors are mounted. Exhaust from 1×2 nozzle array slightly subcools the incoming liquid supply in a small heat exchanger before flowing into the larger heat exchanger to condense. Finally, RTI's two-phase pump takes the liquid and vapor ammonia and transfers it back to the reservoir, providing the pressure difference that is needed to drive ammonia in the cycle and generate the spray. A separate air-cooled R-22

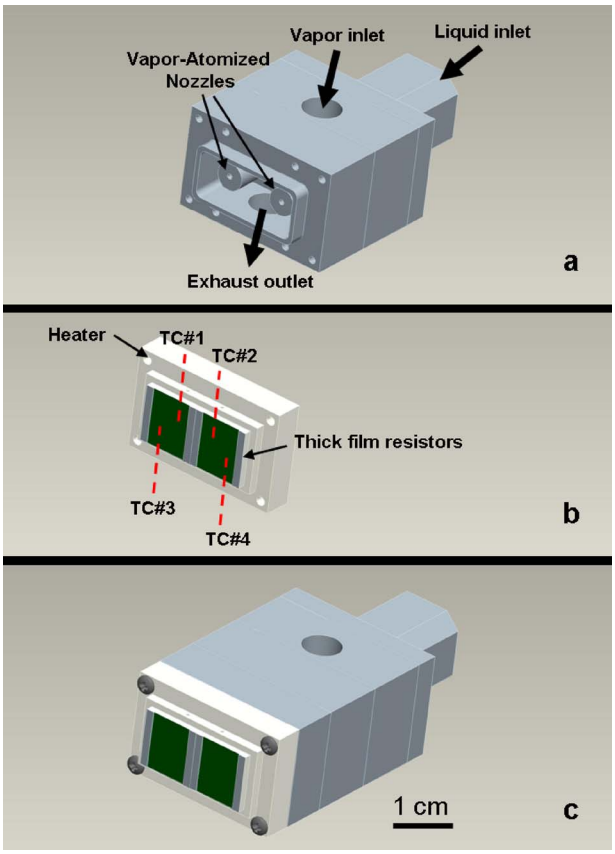

Fig. 2 RTI's 1×2 vapor atomized nozzle array (*a*), 1×2 heater (*b*), and entire nozzle array-heater assembly (*c*)

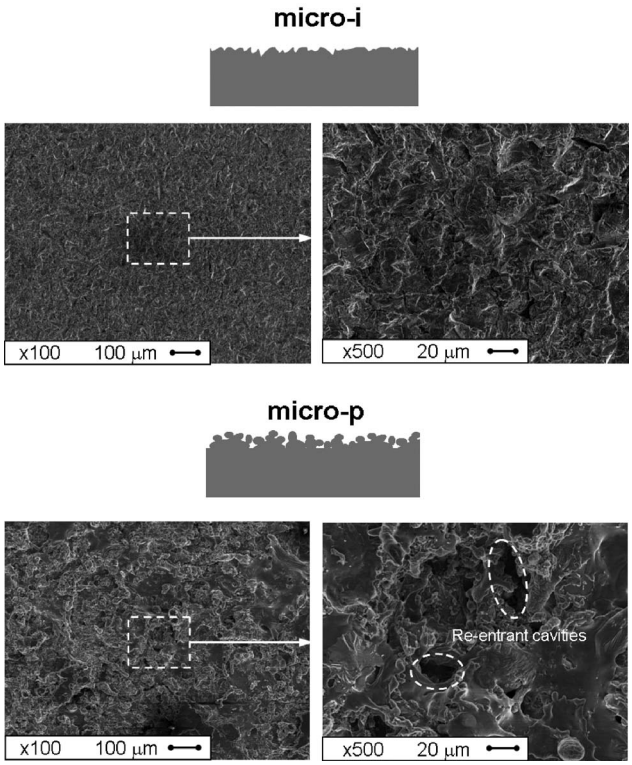

Fig. 3 Schematics and SEM images of micro-i (top) and micro-p (bottom) surfaces

cycle is employed to reject heat from the ammonia cycle to the ambient. The system allows controlling flow rates and pressures across the nozzle array and is equipped with computer controlled data acquisition system for accurate data recording.

2.1 Working Fluid. Anhydrous ammonia (Refrigerant 717) was the working fluid used in the present work. Ammonia has the second highest latent heat of vaporization after water among refrigerants (1368 kJ/kg and 2257 kJ/kg, respectively, at atmospheric pressure) that enables high heat flux removal. For applications that require low temperature device operation, ammonia becomes advantageous to water by offering lower saturation temperature at a given pressure, compared with water. Ammonia, however, is not compatible with all of the commonly used engineering materials and requires careful material selection and design.

2.2 Spray Nozzle. RTI's highly compact 1×2 vapor atomized nozzle array, shown in Fig. 2, was used in all tests. In these nozzles a fine liquid stream is injected into a high velocity vapor stream. The shear force created by the vapor stream atomizes the liquid into fine droplets that are ejected from the nozzle orifice.

2.3 Heaters and Spray Surfaces. Heaters had a 1×2 cm^2 spray surface area, and aluminum was selected as heater material due to its compatibility with ammonia. Heat source was simulated using two of 1 cm^2 thick film resistors soldered into the heater's back surface. Heat flux was determined from the total power supplied into thick film resistors per unit base area ($q''=V\cdot I/A$). The heater temperature was monitored with four type-T thermocouples embedded halfway in the heater wall and spaced equally across the 2 cm^2 area, as indicated in Fig. 2. Temperature spread resulted from four thermocouples did not exceed ±1°C at 200 W/cm^2 and ±1.5°C at 500 W/cm^2, indicating uniform cooling across the surface. Spray surface temperature was calculated by extrapolating average of four thermocouple readings through the known distance to surface and assuming steady 1D conduction through heater wall ($T_{surf}=TC_{avg}-(q''\cdot x)/k$). In practice, when thick film resistors are replaced with the actual device (such as laser diodes), temperature at the mounting surface can be estimated by starting with surface superheat, extrapolating it through the actual wall thickness, used in that particular design, and adding the saturation temperature of ammonia at the system operation pressure.

Test heaters had two types of microstructured spray surfaces, fabricated using RTI's surface modification techniques, along with a smooth one for comparison. One of the heaters had indentations with R_a of 2–2.5 μm and referred to as "micro-i" (microstructured with indentations), while the other heater had protrusions with R_a of 15.0–16.0 μm and referred to as "micro-p" (microstructured with protrusions). Heater with smooth surface had R_a of 0.3–0.5 μm. Figure 3 illustrates typical microstructured surfaces of both types and presents scanning electron microscope (SEM) images at different magnifications. In addition to its characteristic microsize protrusions, micro-p surface also offers many randomly sized re-entrant cavities with some of the large ones marked in Fig. 3.

2.4 Test Conditions and Procedure. All tests were conducted using saturated ammonia at 550–570 kPa (65–68 psig) and 7–8°C. Liquid and vapor flow rates for each nozzle were 96 ml/cm^2 min and 13.8 ml/cm^2 s, respectively, with only 48 kPa (7 psi) pressure drop across nozzle.

Since the main goals were to investigate spray cooling enhancement and hysteresis on microstructured surfaces, cooling curves (surface superheat versus heat flux) were generated in the heating-up and cooling-down modes for all the test heaters to compare their performance. In all tests, heat flux is gradually increased in steps of 25–100 W/cm^2 up to 500 W/cm^2, and the corresponding heater temperatures are recorded every 3 s over

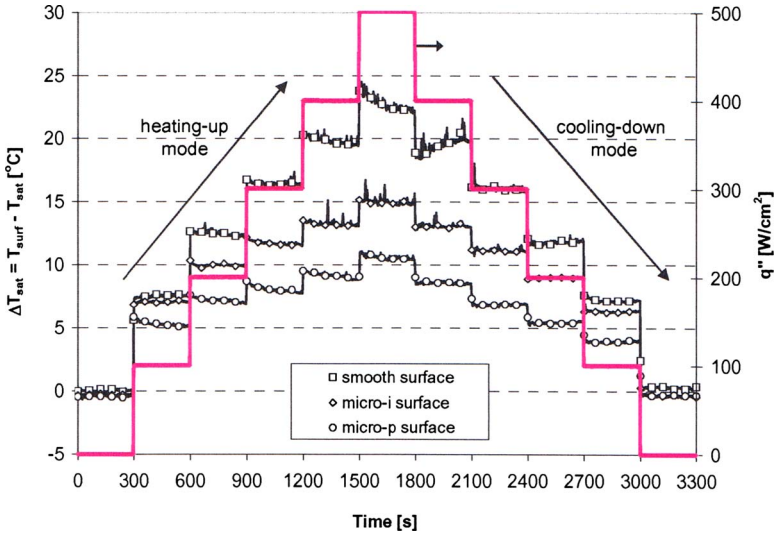

Fig. 4 Surface superheat as a function of time as heat flux changes in steps of 100 W/cm^2 every 5 min from 0 to 500 then back to 0 W/cm^2 for smooth and microstructured surfaces in heating-up and cooling-down modes

3–5 min long steps. Steady-state conditions are usually reached in approximately 3 min. When cooling curves are generated, data are time averaged over the last 30 s of each heat flux step to closely represent the steady conditions. Although 500 W/cm^2 heat flux comfortably represents most of today's high heat flux devices (such as laser diodes), this is well below the maximum heat flux that can be safely removed by the presented ammonia spray cooling system.

2.5 Uncertainty Analysis. Uncertainties were estimated mainly for heat flux and temperature measurements. Error involved in heat flux measurement (considering variations in voltage, current, and area) was $\pm 2.3\%$ at 500 W/cm^2. Error in temperature measurements from the embedded thermocouples in the heater wall (considering thermocouple and data acquisition system specifications) was calculated to be $\pm 1.0°C$. Spray surface temperature had a slightly higher uncertainty at $\pm 1.1°C$. Heat transfer coefficients included $\pm 5.5\%$, 7.7%, and 10.3% uncertainties at 500 W/cm^2 for smooth, micro-i, and micro-p surfaces, respectively. Heat loss from thick film resistors to the surroundings was negligibly small (<1 W) based on calculations considering natural convection and black body radiation from 100°C heater surface to 20°C ambient air.

3 Results and Discussion

Spray cooling data obtained from smooth, micro-i, and micro-p surfaces are presented in Fig. 4. In these tests, the heat flux was first gradually increased in steps of 100 W/cm^2 every 5 min from 0 W/cm^2 to 500 W/cm^2 (heating-up mode) and then decreased in a similar manner back to 0 W/cm^2 (cooling-down mode). Cooling curves from these three surfaces with time-averaged temperatures are plotted in Fig. 5 for an easier performance comparison. As shown, both microstructured surfaces provided significant performance enhancement over smooth surface, while micro-p surface was superior to micro-i surface. Steep changes in the cooling curves of both microstructured surfaces indicate contribution of phase-change mechanism into overall heat transfer.

Several heat transfer mechanisms were proposed earlier for the phase-change regime of spray cooling, namely, free surface

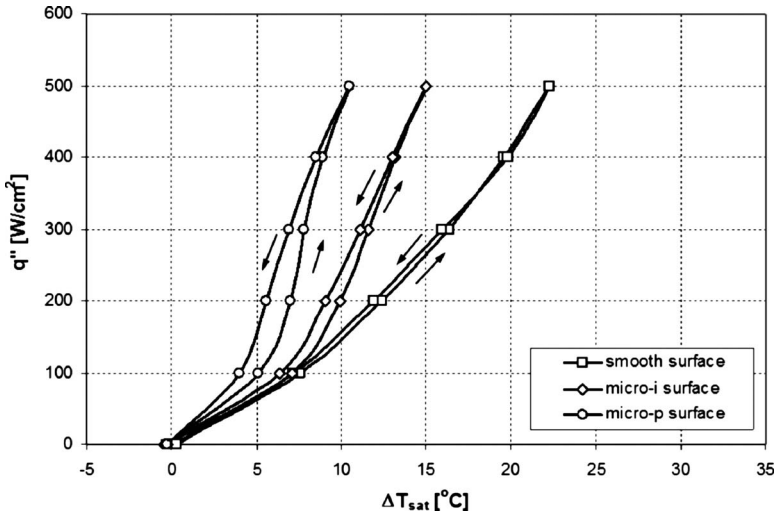

Fig. 5 Surface superheat as a function of heat flux for smooth and microstructured surfaces in heating-up and cooling-down modes

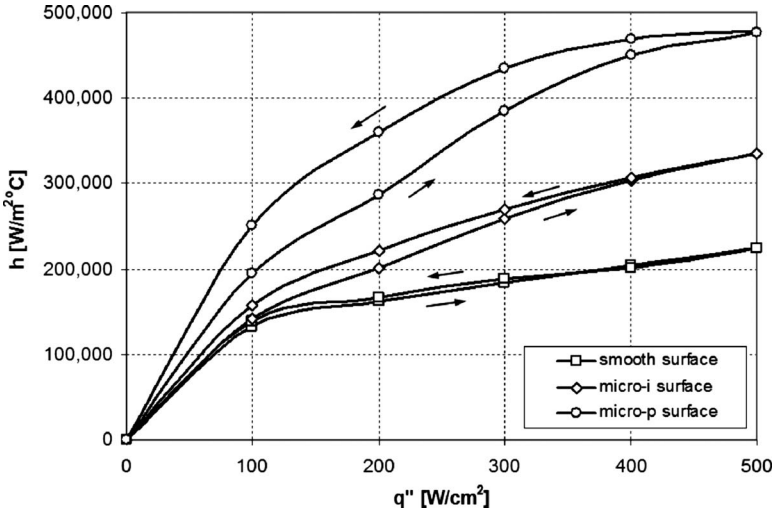

Fig. 6 Heat transfer coefficients as a function of heat flux for smooth and microstructured surfaces in heating-up and cooling-down modes

evaporation, boiling through surface and secondary nucleation, and contact line heat transfer. Pais et al. [13] suggested that free surface evaporation provides high heat transfer rates since liquid molecules from a thin liquid film can efficiently escape into vapor/ambient at the surface. As liquid film thickness decreases, heat is conducted from the hot heater surface to the liquid/vapor interface with less resistance resulting in higher cooling performance. Yang et al. [14] and Rini et al. [15] investigated boiling through surface and secondary nucleation and observed that in addition to nucleation sites on the surface cavities, many more secondary nucleation sites are generated within the liquid layer as liquid droplets from spray strike on the liquid surface and entrain vapor. Additional bubbles that grow from secondary nucleation sites can greatly enhance boiling heat transfer and increase turbulent mixing within the film promoting convection and free surface evaporation. Horacek et al. [16] obtained visualization and measurement of the three-phase contact line, the region where solid, liquid, and vapor phases meet, during spray cooling experiments on a smooth surface. They found a strong correlation between contact line length and heat flux, and concluded that phase-change contribution to heat transfer is directly proportional to contact line length. Horacek et al. [16] considered two possible mechanisms that might be responsible for heat transfer at the contact line, being either thin film heat transfer mechanism or an alternate mechanism, such as transient conduction into the liquid when it moves over hot surface as observed in pool boiling.

Based on the outlined phase-change heat transfer mechanisms, we can now examine the current results. It is obvious that all three surfaces are subjected to similar free surface evaporation and secondary nucleation mechanisms since the spray conditions are the same throughout the tests. In addition to these mechanisms, substantial heat transfer enhancement provided by microstructured surfaces can be attributed to increase in surface area and stronger contribution of other phase-change mechanisms. Both microstructured surfaces provide a spectrum of cavity sizes and thus have the potential to generate additional surface nucleation sites and increase three-phase contact line length density. Better performance of micro-p surface, compared with micro-i surface, can be explained with its complex structure that offers more surface area and re-entrant cavities, as pointed out in Fig. 3.

The heat transfer coefficients obtained from test surfaces are plotted in Fig. 6 as a function of heat flux. As seen, heat transfer coefficient continuously increased as heat flux increased and reached 224,000 $W/m^2\,°C$ for smooth, 334,000 $W/m^2\,°C$ for micro-i, and 476,000 $W/m^2\,°C$ for micro-p surfaces at 500 W/cm^2. An enhancement factor, $h/h_{\_smooth}$, is defined to normalize heat transfer coefficients of microstructured surfaces over smooth surface. Data in Fig. 7 show 1.49 times (49%) and 2.12 times (112%) improvement for micro-i and micro-p surfaces, respectively, over smooth surface at 500 W/cm^2.

Besides the significant heat transfer enhancement, microstructured surfaces also reveal a hysteresis phenomenon when cooling curves in the heating-up and cooling-down modes are compared in Fig. 5. Although smooth surface gives nearly identical cooling curves, microstructured surfaces experience lower surface superheats in the cooling-down mode at a given heat flux. This deviation in superheats is more pronounced for micro-p surface indicating hysteresis dependence on the surface roughness level. In order to gain better understanding on hysteresis effect, additional experiments were conducted with micro-p surface.

The first set of experiments considered whether the initially observed hysteresis effect (e.g., temperature deviation between heating-up and cooling-down curves) changes with varying heat flux conditions. In these tests, heat flux was first ramped up from 0 W/cm^2 to 500 W/cm^2. In the following test segments, heat flux was ramped down to gradually decreasing values and then ramped up again through several cycles to observe how hysteresis effect changes. As plotted in Fig. 8 along with corresponding surface superheat, heat flux was changed from 0 W/cm^2 to 500 W/cm^2, then back to 150 W/cm^2, then to 300 W/cm^2, back to 100 W/cm^2, then to 200 W/cm^2, back to 50 W/cm^2,

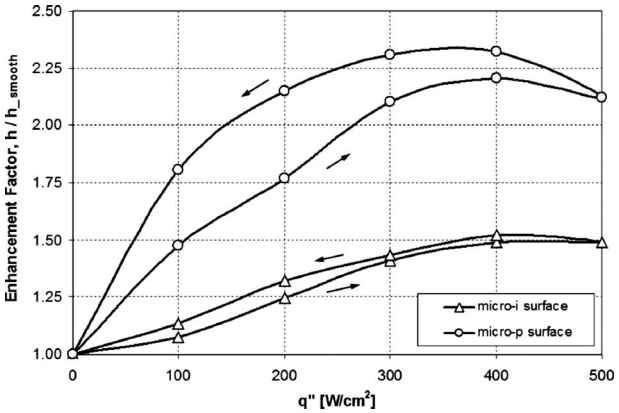

Fig. 7 Enhancement factor as a function of heat flux for smooth and microstructured surfaces in heating-up and cooling-down modes

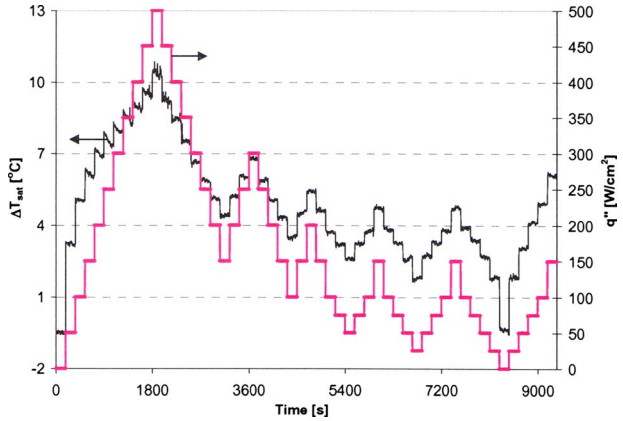

Fig. 8 Surface superheat as a function of time as heat flux changes in steps of 25–50 W/cm^2 every 3 min for micro-p surface in heating-up and cooling-down modes

and so on. All changes in heat fluxes, up or down, were in steps of 50 W/cm^2 (25 W/cm^2 for $q'' < 100$ W/cm^2) every 3 min. Change in hysteresis through the initial heating-up mode and the following test segments can easily be seen when these data are plotted in the form of cooling curves in Fig. 9. Results show that once the heater is brought to a high heat flux (and high superheat), superheat will track the same cooling curve on the left with decreasing (as low as 25 W/cm^2 for the present study) or increasing heat fluxes. However, if heat flux is reduced all the way down to zero, then superheat will follow the cooling curve on the right for heating-up mode, as can be closely seen in Fig. 10. Data therefore suggest that once the three-phase contact line is established on the surface at a certain heat flux, microstructures are able to retain vapor effectively in the cavities, and the heater can provide a consistent cooling curve and hysteresis effect at lower heat fluxes. At zero heat flux condition, microstructures cannot support the retained vapor anymore and lose the contact line length. A consecutive heat flux increase at this state is no different than initial heating-up mode where contact line is established gradually.

The second set of experiments addressed how hysteresis effect relates to thermal history of the heater. In each segment of these

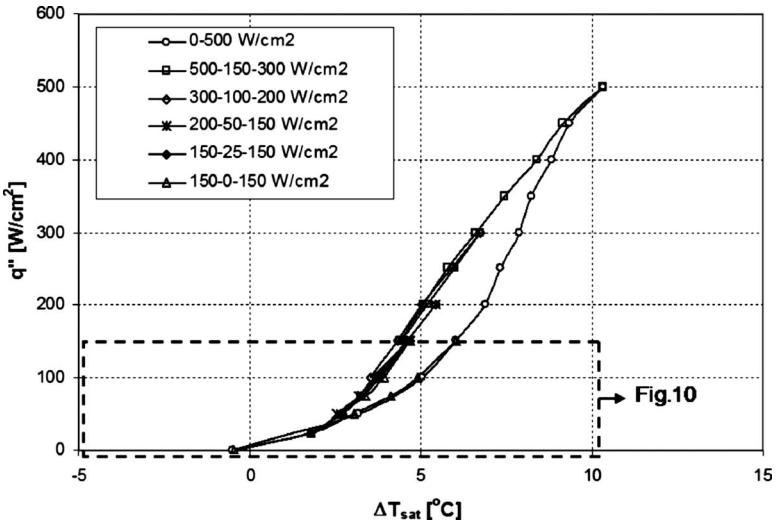

Fig. 9 Surface superheat as a function of heat flux for micro-p surface in heating-up and cooling-down modes

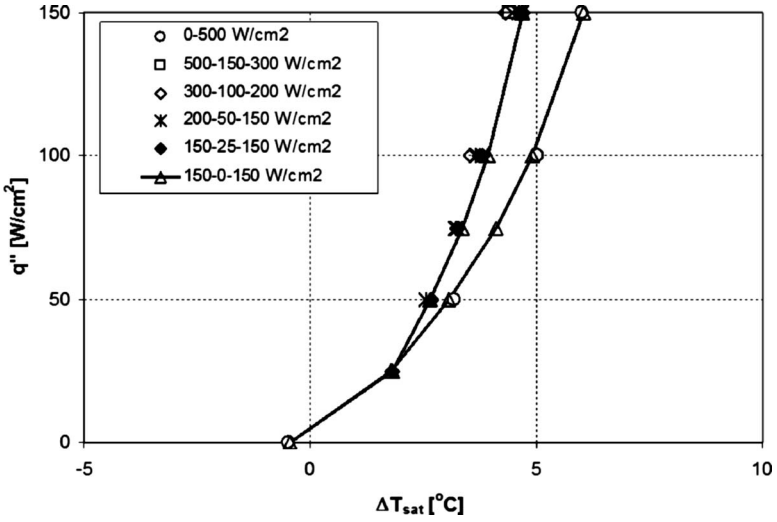

Fig. 10 Surface superheat as a function of heat flux for micro-p surface in heating-up and cooling-down modes (a close-up view of Fig. 9)

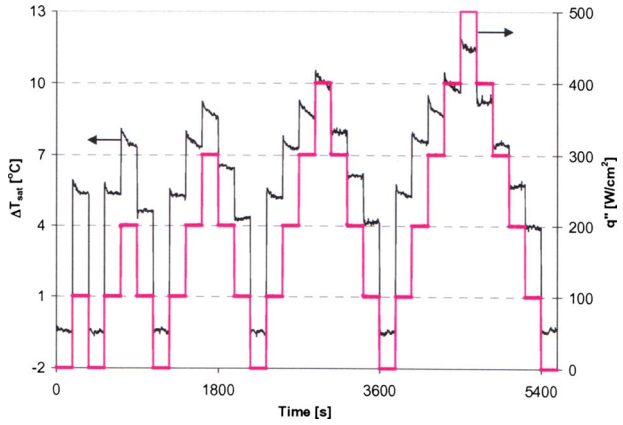

Fig. 11 Surface superheat as a function of time as heat flux changes in steps of 100 W/cm^2 every 3 min for micro-p surface in heating-up and cooling-down modes

tests, heat flux was increased up to a maximum value and then decreased down to 0 W/cm^2 each time to observe the amount of hysteresis. As seen in Fig. 11 along with corresponding surface superheat, heat flux was changed from 0 W/cm^2 to 100 W/cm^2, then back to 0 W/cm^2, then to 200 W/cm^2, back to 0 W/cm^2, then to 300 W/cm^2, back to 0 W/cm^2, and so on. All changes in heat fluxes, up or down, were in steps of 100 W/cm^2 every 3 min. The amount of hysteresis that occurred in each test segment can be better examined when cooling curves are compared in Fig. 12. Data here, and further in the close-up view in Fig. 13, clearly indicate the trend where the amount of hysteresis increases as the maximum heat flux increases from 100 W/cm^2 to 500 W/cm^2. This observation suggests that as the heat flux and surface temperature of the heater increase, the contact line length on the microstructured surface increases. If the surface can maintain some of the established contact line, as in the case of microstructured surfaces in the present study, this results in a larger hysteresis or lower superheat later at lower heat fluxes. Figure 14 reflects the change in heat transfer due to hysteresis effect quantitatively. Utilizing data from the second set of experiments, heat transfer coefficients in cooling-down mode can be normalized based on

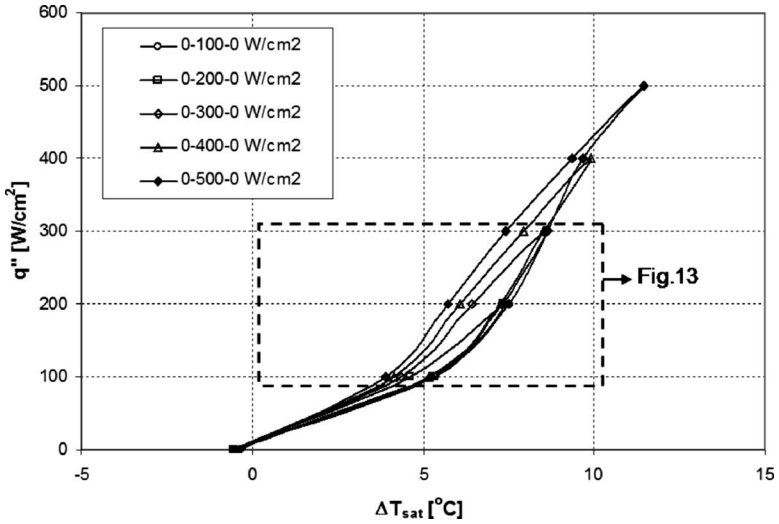

Fig. 12 Surface superheat as a function of heat flux for micro-p surface in heating-up and cooling-down modes

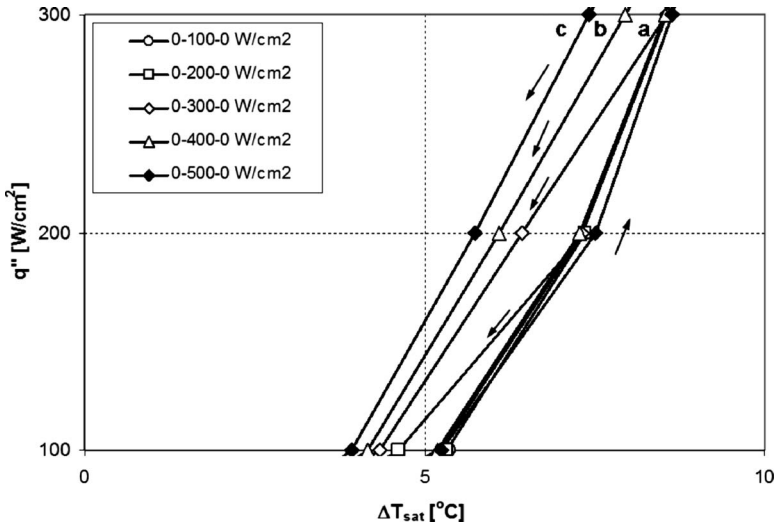

Fig. 13 Surface superheat as a function of heat flux for micro-p surface in heating-up and cooling-down modes (a close-up view of Fig. 12)

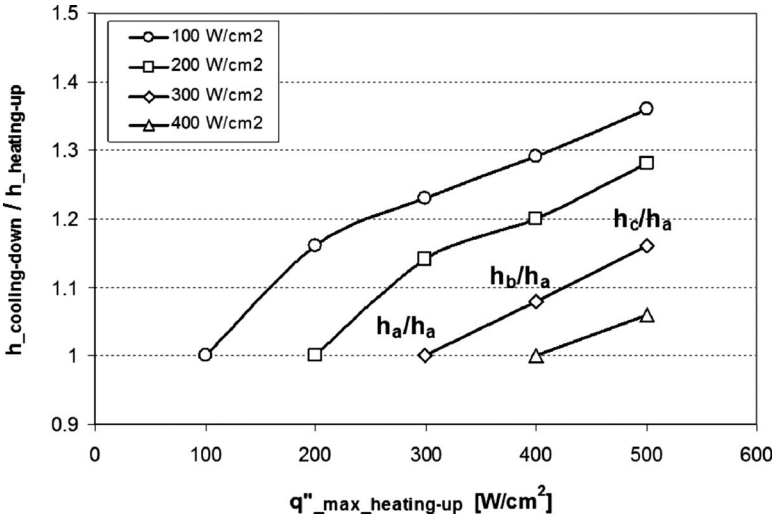

Fig. 14 Normalized heat transfer coefficients at constant heat fluxes as a function of maximum heat flux in heating-up mode indicating quantitative change in heat transfer due to hysteresis effect

those in heating-up mode. For instance, when change in heat transfer at 300 W/cm^2 is considered using normalized heat transfer coefficients of h_c/h_a, h_b/h_a, and h_a/h_a in Fig. 14, corresponding to points c, b, and a in Fig. 13, we see that the heat transfer coefficient improves at 1.08 times (8%) and 1.16 times (16%) if surface is first exposed to 400 W/cm^2 and 500 W/cm^2, respectively, and then brought back to 300 W/cm^2. Similarly, at 100 W/cm^2, the heat transfer coefficient can be increased by up to 1.36 times (36%) if surface is previously exposed to 500 W/cm^2.

Based on the findings from tests with micro-p surface, we can also explain the larger hysteresis observed with this surface in Fig. 5. Having more surface area and re-entrant cavities, micro-p surface has the potential to capture and retain more vapor and establish higher three-phase contact line density compared with micro-i surface. Therefore for the micro-p surface, the difference between the contact line lengths in the heating-up and cooling-down modes is more resulting in larger hysteresis.

4 Conclusions

An experimental spray cooling study was conducted to investigate performance enhancement and hysteresis effect on microstructured surfaces. Tests were run in a closed loop system with ammonia using RTI's vapor atomized spray nozzles. Heaters with micro-i (microstructured with indentations), micro-p (microstructured with protrusions), and smooth surfaces were tested at heat fluxes up to 500 W/cm^2. Results for both microstructured surfaces showed substantial performance enhancement resulting in heat transfer coefficients of 334,000 $W/m^2\,°C$ for micro-i and 476,000 $W/m^2\,°C$ for micro-p surfaces at 500 W/cm^2 that correspond to 112% and 49% increases over smooth surface, respectively. This performance enhancement can be attributed to an increase in surface area and stronger contribution of other phase-change mechanisms beyond the free surface evaporation and secondary nucleation mechanisms of spray cooling. Both microstructured surfaces provide a spectrum of cavity sizes and thus have the potential to generate additional surface nucleation sites and increase three-phase contact line length density. The micro-p surface's superior performance is believed to be due to its complex structure that offers more surface area and re-entrant cavities compared with the micro-i surface.

Microstructured surfaces also experienced hysteresis effect with lower surface superheats in the cooling-down mode at a given heat flux. Hysteresis effect was more pronounced for the micro-p surface, indicating its dependence on surface roughness level. Two sets of experiments were performed with the micro-p surface in order to address whether initially observed hysteresis changes with varying heat flux conditions and whether hysteresis relates to thermal history of the heater. Data suggested that once the three-phase contact line is established on the surface at a certain heat flux, microstructures retain vapor effectively in the cavities and help maintain contact line length so that the heater can provide a consistent cooling curve and hysteresis effect at varying heat fluxes (as low as 25 W/cm^2 for the present study). At 0 W/cm^2, the heater surface loses the contact line length and restores its initial state. Data also indicated that as the heat flux and surface temperature of the heater increase, the contact line length on the surface also increases proportionally. Since microstructures help sustain established contact line length, the heater surface experiences a larger hysteresis or lower superheat as it returns from a higher heat flux condition, showing a direct relation between hysteresis and thermal history of the heater.

Acknowledgment

The authors acknowledge Air Force Research Laboratory (AFRL) Propulsion Directorate and Universal Technology Corporation for their financial support.

Nomenclature

A = spray surface area, cm^2
h = heat transfer coefficient, $W/m^2\,°C$
I = current, A
k = thermal conductivity, $W/m\,°C$
q'' = heat flux, W/cm^2
T = temperature, °C
TC = thermocouple
R_a = average surface roughness, μm
V = voltage, V
x = TC to spray surface distance in heater wall, m

Subscripts

avg = average
sat = saturation
surf = surface

References

[1] Pais, M. R., Chow, L. C., and Mahefkey, E. T., 1992, "Surface Roughness and

Its Effects on the Heat Transfer Mechanism in Spray Cooling," ASME J. Heat Transfer, **114**, pp. 211–219.
[2] Sehmbey, M. S., Pais, M. R., and Chow, L. C., 1992, "Effect of Surface Material Properties and Surface Characteristics in Evaporative Spray Cooling," J. Thermophys. Heat Transfer, **6**(3), pp. 505–511.
[3] Kim, J. H., You, S. M., and Choi, U. S., 2004, "Evaporative Spray Cooling of Plain and Microporous Coated Surfaces," Int. J. Heat Mass Transfer, **47**, pp. 3307–3315.
[4] Stodke, C., and Stephan, P., 2005, "Spray Cooling Heat Transfer on Microstructured Surfaces," Sixth World Conference on Experimental Heat Transfer, Fluid Mechanics, and Thermodynamics, Matsushima, Miyagi, Japan.
[5] Amon, C., Yao, S. C., Wu, C. F., and Hsieh, C. C., 2005, "Microelectromechanical System-Based Evaporative Thermal Management of High Heat Flux Electronics," ASME J. Heat Transfer, **127**, pp. 66–75.
[6] Hsieh, C. C., and Yao, S. C., 2006, "Evaporative Heat Transfer Characteristics of a Water Spray on Micro-Structured Silicon Surfaces," Int. J. Heat Mass Transfer, **49**, pp. 962–974.
[7] Silk, E., Kim, J., and Kiger, K. T., 2006, Enhanced Surface Spray Cooling With Embedded and Compound Extended Surface Structures," *Proceedings of the ITHERM 2006*, San Diego, CA.
[8] Coursey, J., Kim, J., and Kiger, K. T., 2006, "Spray Cooling of High Aspect Ratio Open Microchannels," *Proceedings of the ITHERM 2006*, San Diego, CA.
[9] Bergles, A. E., and Chyu, M. C., 1982, "Characteristics of Nucleate Pool Boiling From Porous Metallic Coatings," ASME J. Heat Transfer, **104**, pp. 279–285.
[10] Marto, P. J., and Lepere, V. J., 1982, "Pool Boiling Heat Transfer From Enhanced Surfaces to Dielectric Fluids," ASME J. Heat Transfer, **104**, pp. 292–299.
[11] Shi, M.-H., Ma, J., and Wang, B.-X., 1993, "Analysis on Hysteresis in Nucleate Pool Boiling Heat Transfer," Int. J. Heat Mass Transfer, **36**(18), pp. 4461–4466.
[12] Hwang, G.-S., and Kaviany, M., 2006, "Critical Heat Flux in Thin, Uniform Porous Coatings," Int. J. Heat Mass Transfer, **49**, pp. 844–849.
[13] Pais, M. R., Tilton, D., Chow, L. C., and Mahefkey, E. T., 1989, "High Heat Flux, Low Superheat Evaporative Spray Cooling," *Proceedings of the 27th AIAA Aerospace Sciences Meeting*, Reno, NV.
[14] Yang, J., Chow, L. C., and Pais, M. R., 1996, "Nucleate Boiling Heat Transfer in Spray Cooling," ASME J. Heat Transfer, **118**, pp. 668–671.
[15] Rini, D. P., Chen, R. H., and Chow, L. C., 2002, "Bubble Behavior and Nucleate Boiling Heat Transfer in Saturated FC-72 Spray Cooling," ASME J. Heat Transfer, **124**, pp. 63–72.
[16] Horacek, B., Kiger, K., and Kim, J., 2005, "Single Nozzle Spray Cooling Heat Transfer Mechanisms," Int. J. Heat Mass Transfer, **48**(8), pp. 1425–1438.

An Experimental Study on the Design of Miniature Heat Sinks for Forced Convection Air Cooling

Vanessa Egan
e-mail: vanessa.egan@ul.ie

Jason Stafford
e-mail: jason.stafford@ul.ie

Pat Walsh
e-mail: pat.walsh@ul.ie

Ed Walsh
e-mail: edmond.walsh@ul.ie

Department of Mechanical and Aeronautical Engineering,
Stokes Institute,
University of Limerick,
Limerick, Ireland

An experimental study is performed on one of the smallest commercially available miniature fans, suitable for cooling portable electronic devices, used in conjunction with both finned and finless heat sinks of equal exterior dimensions. The maximum overall footprint area of the cooling solution is 534 mm^2 with a profile height of 5 mm. Previous analysis has shown that due to fan exit angle, flow does not enter the heat sinks parallel to the fins or bounding walls. This results in a nonuniform flow rate within the channels of the finned and finless heat sinks along with impingement of the flow at the entrance giving rise to large entrance pressure losses. In this paper straightening diffusers were attached at the exit of the fan, which resulted in aligning the flow entering the heat sinks with the fins and channel walls. Detailed velocity measurements were obtained using particle image velocimetry, which provided a further insight into the physics of the flow in such miniature geometries and in designing the straightening diffusers. The thermal analysis results indicate that the cooling power of the solution is increased by up to 20% through the introduction of a diffuser, hence demonstrating the need for integrated fan and heat sink design of low profile applications. [DOI: 10.1115/1.3110005]

Keywords: low profile, forced convection cooling, miniature fan

1 Introduction

The design and integration of miniature cooling solutions into today's portable electronic devices is moving to the forefront of electronics cooling research. The drive behind this research is consumer demand for smaller more powerful portable devices. As the surface area available for power dissipation reduces, along with technology advancements increasing the device's power consumption, the resulting heat fluxes are considerably elevated. At present most manufacturers rely on natural convection in conjunction with heat spreading technologies to maintain temperatures at acceptable consumer levels. However, sole use of these techniques produces increasing device case temperatures relative to increasing heat fluxes. If the envisaged trend in increasing heat fluxes continues, then natural convection and conduction technologies alone will no longer be able to maintain devices at acceptable temperatures. Hence, there is a need for research into cooling technologies that can enhance heat transfer rates combined with current natural convection and heat spreading techniques.

Forced convection cooling is the preferred "new" cooling technology among designers of portable electronic devices. This is due to a large number of factors including cost, reliability, power consumption, footprint area, and profile height. Liquid cooling [1] and heat pipe [2] technologies have proved useful methods in efficiently spreading heat from the heat source to secondary coolers; however, size restrictions in portable solutions suggest that these heat spreading techniques are currently only viable for larger scale electronics cooling. Similarly, phase change materials [3] have also been shown to enhance the heat transfer process by utilizing heat absorption, which occurs due to a change in state from solid to liquid. One concern with the single use of this technology is when the material is in a fully liquid state it can no longer prevent the temperature from rising in the device. Consequently natural convection and conduction are the methods of heat transfer after this point is reached. As an assisting cooling technology to the current heat transfer methods in portable devices, forced convective cooling may have the ability to deal with these increased thermal loads. An example of this is the unconventional design proposed by Walsh et al. [4], which gives a thermal resistance value of 4.5°C/W for a footprint area of 1200 mm^2 with a profile height of 4 mm including the fan.

Over the past few years a number of groups have initiated research to address the developing market of miniature forced convective air cooling. The first series of papers on such research examined the validity of the conventional scaling laws [5,6] as the fan scale is reduced to miniature dimensions. The authors found that at low Reynolds numbers boundary layer phenomena result in reducing the flow and elevating the power requirement above that expected by scaling. In the context of conventional fan scaling, variation in these parameters at low Reynolds numbers will undoubtedly result in greater uncertainty in the predicted performance of the fan if adhering to the scaling laws. Walsh et al. [7] also reported a scale effect that resulted in the flow rate delivered being significantly less than expected when operating at low Reynolds numbers. As miniature fans operate at low Reynolds numbers, the actual performance can be dissimilar to that which is predicted using conventional scaling laws [8]. With regard to the integration of miniature fans with heat sinks it is noted that impingement cooling emerges as one of the best methods to dissipate large heat loads over small areas, with thermal resistances as low as 1.4°C/W being reported [9,10] for pin-fin heat sinks. However, to achieve such performances, footprint areas of order 2000 mm^2 and profile heights of order 100 mm were reported. While this footprint area is relatively small, it is noted that such large profile heights would most likely deem this technology unacceptable for use in most portable electronic devices. Also, when considering miniature scale fans, the flow rates and pressure rises attainable are considerably lower than those attained in the aforementioned studies for impingement cooling. Hence in order to satisfy the constraints of low profile forced convection cooling a fan and heat sink in parallel are the most practical solutions. A recent analysis of fan and heat sink arrangement in terms of performance optimization has been carried out by Walsh et al.

Contributed by the Heat Transfer Division of ASME for publication in the JOURNAL OF HEAT TRANSFER. Manuscript received July 14, 2008; final manuscript received February 12, 2009; published online May 6, 2009. Review conducted by Roger Schmidt. Paper presented at iTherm 2008.

[11,12]. It was shown that best thermal performance was achieved when the fan exit angle is matched to the heat sink fin angle, i.e., flow enters the heat sink parallel to the fins. A recent study by Egan et al. [13] investigated the thermal performance of a miniature fan used in conjunction with a finned and finless heat sink. The overall footprint area of the solution was 456 mm^2 with a profile of 5 mm. Velocity measurements of the flow in the heat sinks showed that flow exited the fan at an angle to the heat sink walls and the fins. In the case of the finned heat sink it was seen that the flow strongly impinged on the heat sink fins at the entrance to the channels.

The primary objective is to determine the effect of straightening the flow prior to entering the heat sinks through the use of a diffuser. A number of different diffusers were manufactured to obtain the optimum design giving parallel flow at entry to the heat sink. The optimum diffuser design was determined from flow velocity measurements obtained using particle image velocimetry (PIV). Upon finding such a design the fan, diffuser, and heat sink solutions were characterized by repeating the heat transfer measurements carried out in Ref. [13]. Such results would conclusively show if the diffuser resulted in an overall enhancement of the heat transfer rate of the finned and finless solutions. Particle image velocimetry measurements of the flow in the heat sink at speeds ranging from 3000 rpm to 8000 rpm were also obtained and provide a further insight into the flow field within the heat sinks. The results of this study are valuable to designers of such cooling solutions as enhanced heat transfer rates may be obtained by simply adding a diffuser between the fan and heat sink.

2 Heat Sink and Diffuser Design

The fan tested for the current work is the Micronel U16LM-9 having a footprint area of 256 mm^2 and a profile of 5 mm (see Fig. 3). This is currently one of the smallest commercially available fans for forced convection cooling of electronics. The pressure versus flow rate characteristics are supplied by the manufacturer for a nominal speed of 6000 rpm. In designing the finned heat sink the pressure versus flow rate characteristics at a fan speed of 8000 rpm were used. The manufacturer's data were scaled using the fan scaling laws detailed in Ref. [14] and defined here in Eqs. (1) and (2).

$$Q \propto \text{rpm} \tag{1}$$

$$\text{SP} \propto \text{rpm}^2 \tag{2}$$

Figure 1(*a*) shows a schematic of the heat sink and highlights the variables that were optimized; these include the fin spacing (b) and fin thickness (t_{fin}). The former of these was optimized using Eq. (3), which was developed by Bejan [15] for flow between parallel plates using the intersection of asymptotes between a fully developed flow limit and a flat boundary layer flow limit

$$\frac{b_{\text{optimum}}}{L} = 2.73\left(\frac{\mu\alpha}{\Delta P \times L^2}\right)^{1/4} \tag{3}$$

In determining the optimum fin spacing, the pressure drop (ΔP) across the bank of channels was set equal to 6.5 Pa so that the fin spacing of the heat sink is optimized for a fan speed of 8000 rpm and should correspond to a total volumetric flow rate of approximately 2.5×10^{-4} m^3/s passing through the heat exchanger. In order to achieve this Eq. (3) requires that the fin spacing be approximately 1.1 mm. The second parameter examined is the thickness of the fins t_{fin}. This was optimized by ensuring that the fin efficiency is greater than 99% and Ellison [16] showed this to be the case when Eq. (4) is satisfied

$$t_{\text{fin}} \geq 40\bar{h}H^2/k_{\text{heat sink}} \tag{4}$$

The flow condition within the heat sink reflects an underdeveloped duct flow entrance region, which does not become fully developed until the heat sink exits. A value of 60 $W/m^2\,K$ was chosen for h in Eq. (4) based on an empirical Nusselt number relationship for this flow condition [17]. Using copper as the heat sink material, Eq. (4) reveals that the fin thickness should be at least 0.06 mm. However, the technique used to manufacture the heat sink required this dimension to be of order 0.3 mm, hence ensuring a more than adequate fin thickness. This also provided for a large tolerance if any discrepancies in the choice of h for Eq. (4) are apparent. Such discrepancies were found to have no influence on the calculated fin thickness, and hence the fin efficiency, when considering the experimental heat transfer measurements shown in Secs. 3 and 4. The result is that a finned heat sink with a maximum of six channels could be manufactured while maintaining the heat sink footprint constraints that were applied. The finless heat sink was manufactured to have the identical specifications of profile (4 mm), footprint area (200 mm^2), and external wall thickness (1 mm) and is shown in Fig. 1(*b*).

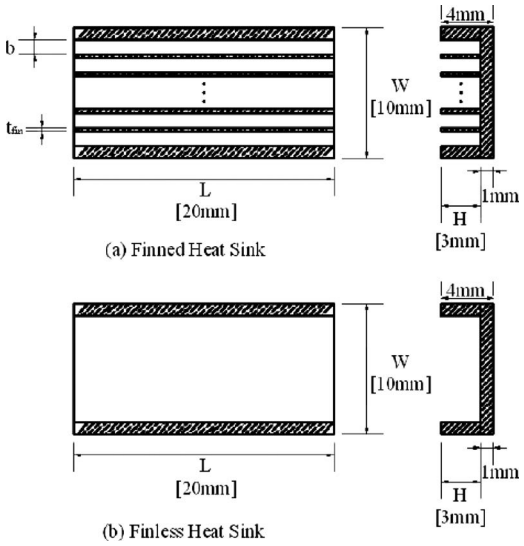

Fig. 1 Schematic of finned and finless heat sinks outlining the overall dimensions and the optimized parameters *b* and t_{fin}

As previously mentioned in order to achieve the optimum thermal performance of a fan and heat sink in parallel, flow must enter the heat sink aligned with the heat sink walls and fins [11,12]. Figure 2 is a schematic of a velocity vector diagram for a backward curved fan with a rotational speed, ω, and radial velocity, V_r. The angle of the flow exiting the fan casing can be measured using PIV and is dependent on system resistance. A high system resistance such as that created by a finned heat sink will result in

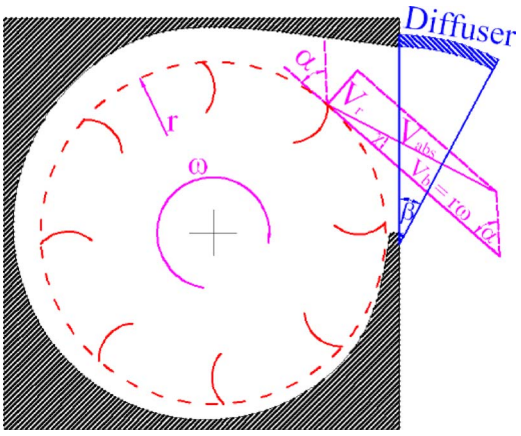

Fig. 2 Velocity triangle showing fan exit angle

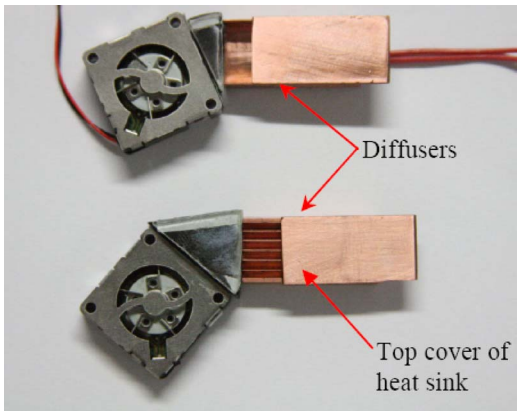

Fig. 3 Photograph of the experimental configuration employing the straightening diffusers with the finned and finless heat sinks

a lower flow rate through the fan. This in turn will result in reducing only the radial flow component and hence the angle at which fluid leaves the fan. It can be seen that high system resistances will reduce γ, while low system resistances will result in increasing this angle.

In order to align the flow exiting the fan with the heat sink walls and fins a number of diffusers with angles varying between 25 deg and 60 deg with both curved and straight walls were manufactured from polycarbonate. As discussed above, it was found that the optimum angle for flow alignment varied between the finned and the finless case. Each diffuser was tested using PIV to measure the velocity of the flow in each of the heat sinks and it was determined from the measurements that a 25 deg curved diffuser and a 50 deg straight diffuser resulted in flow alignment within the finless and finned heat sinks, respectively.

3 Experimentation

The experimental configuration shown in Fig. 3 consists of a finned and finless setup. The results presented in this paper are detailed in Table 1. The current work presents results from all four cases; however, cases 1 and 2 are detailed in Ref. [13] and encompass tests performed without a diffuser. As the thermal resistance measurement methods have been described previously [18], it has been excluded from this section.

3.1 Thermal Resistance. The experimental configuration consisted of a Micronel fan, a flow diffuser, and the optimized heat sink that was designed in Sec. 2. During experimentation the top cover of the heat sink, as shown in Fig. 3, was in position so as to create a fully closed channel. This cooling solution has a footprint area of 256 mm^2 for the fan, either 231 mm^2 or 278 mm^2 for the heat sink and diffuser and a profile of only 5 mm.

The forced convection thermal resistance is defined as

$$R_{\mathrm{th}_{\mathrm{FC}}} = \frac{(R_{\mathrm{th}_T})(R_{\mathrm{th}_{\mathrm{losses}}})}{(R_{\mathrm{th}_{\mathrm{losses}}} - R_{\mathrm{th}_T})} \tag{5}$$

The forced convective heat transfer coefficients were calculated as

$$h_{\mathrm{FC}} = \frac{1}{R_{\mathrm{th}_{\mathrm{FC}}} A_{\mathrm{conv}}} \tag{6}$$

where h is the heat transfer coefficient in W/m^2 K and A_{conv} is the convective surface area of the finned heat sink in m^2. The convective surface areas of the finned and finless heat sinks were calculated to be 0.000984 m^2 and 0.00044 m^2, respectively, with an accuracy of 1×10^{-6} m^2.

Table 1 Experimental test description

Test No.	Description
1	Finless heat, no diffuser
2	Finned heat, no diffuser
3	Finless heat, 25 deg curved diffuser
4	Finned heat, 50 deg straight diffuser

3.2 Uncertainty Analysis. An uncertainty analysis was performed [19], giving the thermal resistance an error of less than 5%. The uncertainty was greatest for natural convection and decreased with increasing fan speed. Due to a mismatch between heat source area (6×6 mm^2) and heat sink base it is possible to conclude that some form of heat spreading will be present in the heat sink base due to the change in cross-sectional area from the smaller heat source to the larger heat sink. The thin-film heater that represents the heat source is centrally positioned on the heat sink base. There is an associated resistance to this heat spreading effect that also needs to be addressed when calculating the thermal resistance of the heat sink. A maximum spreading resistance of 0.407°C/W was calculated for the range of fan speeds examined using an experimentally verified closed form study [20]. This accounts for a maximum error of 0.91% in the thermal resistance measurements presented here. Consequently, the resistance term due to heat spreading has been excluded from Eq. (5). The optical tachometer used to measure the rotational speed of the fan has a resolution of 1 rpm. However, during experimentation it was observed that the speed varied up to 50 rpm. The uncertainty in power measurements and temperature readings used to calculate thermal resistance were less than 0.1% and 0.5°C, respectively.

3.3 Velocity Measurements. The second set of experiments involved detailed velocity measurements of the flow within the channels of the heat sink. PIV was employed to obtain these velocity measurements. However, in order to obtain the optical access required for this technique, the copper top cover of the heat sink was replaced with a glass slide. Hence all PIV results were obtained without heat transfer. The following paragraphs briefly detail the principle of this technique and the setup used during experimentation [21].

PIV works on the principle of introducing seeding or tracer particles to the flow and tracking their motion over known time intervals. A water-based oil consisting of monopropalene glycols or CO_2 fog was used for the seeding, which was produced using a JEM Stage Hazer 2000. The size of seeding particles produced was approximately 10 μm diameter with a relative density of 1.05 kg/m^3 at 293 K. In order to contain the seeding particles the experimental apparatus was placed in a glass walled enclosure of dimensions 400 mm(L)$\times$250 mm(H)$\times$250 mm(W). Once the particles were released into the enclosure a laser illuminated a plane in the heat sink and the light subsequently emitted by the particles was recorded on a camera positioned perpendicular to the illuminated plane. Velocity measurements were taken for a plane at mid-depth in the heat sink channels. A schematic of the experimental setup is shown in Fig. 4.

A Nd:YAG, 532 nm, semiconductor laser was used giving a 1.5 mm thick light sheet. To measure the velocity of the particles the laser was pulsed twice with a time delay chosen so that the distance traveled by the seeding particles between images is discernible and that particles do not leave the illuminated plane within the period. Prior to experimentation, in order to calibrate the subsequent measurements, a scaling device must be inserted in the test section to obtain the correct scaling factor for the velocity measurements. This was achieved by placing a calibrated ruler in the measurement plane.

A PowerView™ Plus 2 megapixel charge-coupled-device (CCD) camera with a resolution of 1600×1200 with a 60 mm focal length lens was used to record the scattered light from the

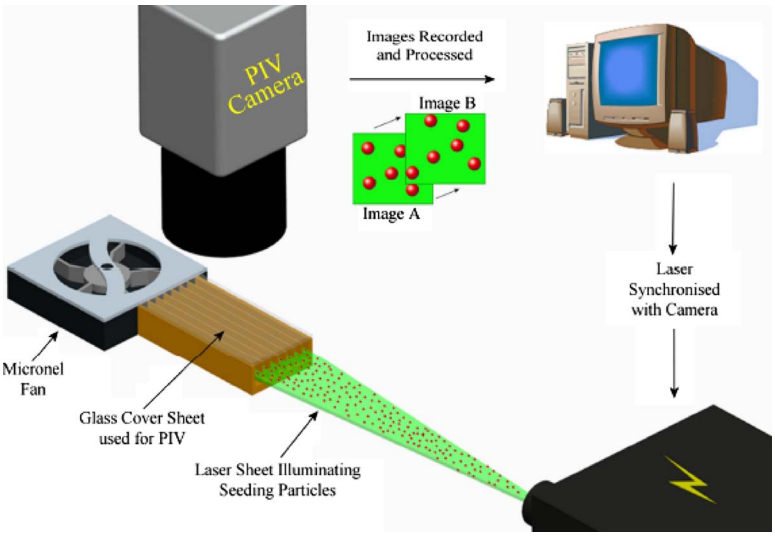

Fig. 4 PIV Experimental setup showing camera and laser positions with respect to fan and heat sink. The diffuser is inserted between the fan and heat sink.

illuminated particles and their images appear as bright spots on a dark background. A series of postprocessing steps was applied to the PIV data using TSI INSIGHT 3G software in order to remove any spurious velocity vectors that appeared due to reflections.

4 Results and Discussion

The objectives of this work are to provide optimized thermal management solutions based on previous analyses [13], using one of the smallest commercially available fans combined with finned and finless heat sink geometries. Optimization of such solutions has been considered using velocity field and thermal resistance measurements presented in this section. Velocity measurements are considered first in order to develop a suitable diffuser for each case based on design criterion previously discussed. Thermal resistance measurements, heat transfer, and flow rate results are presented following the flow field analysis, quantifying the influence of the introduction of diffusers on both heat sinks over a range of fan rotational speeds.

Figure 5 depicts the flow at the entrance region to the heat sink for both finned and finless geometries without the use of a diffuser [13]. A range of diffusers was examined for both heat sink geometries producing various heat sink to fan orientations from 25 deg to 60 deg. Therefore due to the quantity of PIV results analyzed, the quantitative data presented for this work are only considered for the diffusers, which would optimize flow alignment and distribution in both heat sink cases. Figure 6 presents a number of qualitative images of the flow distribution in the diffuser and heat sink entrance region at the medium speed of 5500 rpm. It was found that a 25 deg curved diffuser for the finless heat sink and a 50 deg straight diffuser for the finned heat sink were most beneficial. The top row of images in Fig. 6 shows the flow distribution in the finless heat sink as a result of varying diffuser angles. It is clear that as the diffuser angle is increased the flow does not become evenly distributed within the heat sink. As this pattern becomes more dominant with increased angle, it is predicted that no benefits would be achieved in flow alignment with the 60 deg diffuser. For this reason, PIV analysis was disregarded using this diffuser.

The bottom row of images in Fig. 6 describes the flow patterns when using similar diffusers with a finned geometry. The images are color contrasted to distinguish the fins (black) from their shadows in the diffuser (gray). These were unavoidably created by the laser beam used to illuminate the seeding particles within the heat sink. Consequently particle tracking was not possible in these regions of the diffuser. However, this does not affect the validity of the current work as flow structures are still visible in the diffuser, and concentration on flow characteristics within the heat sink is of

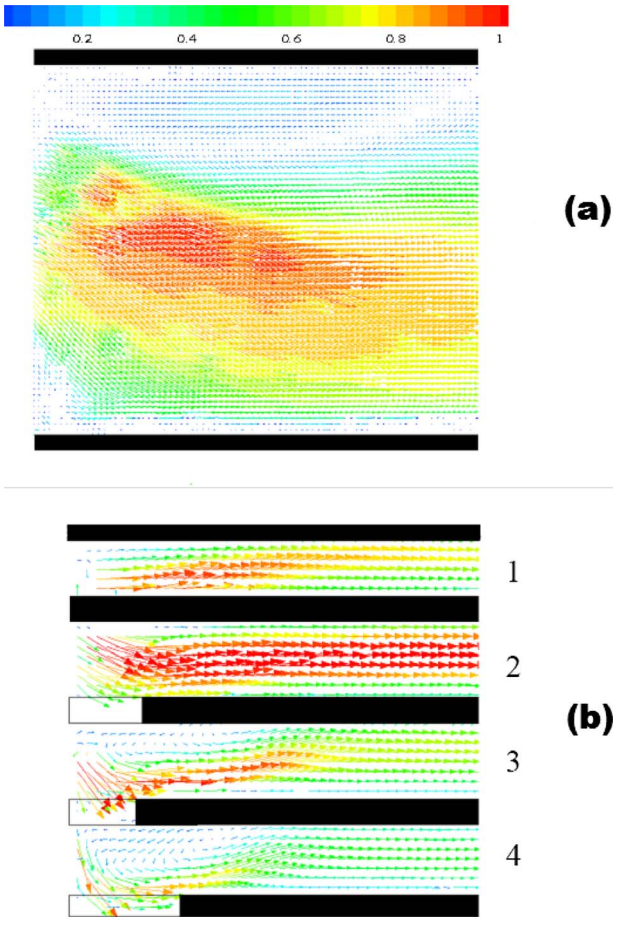

Fig. 5 Normalized PIV velocity magnitude plot, from Ref. [13], of flow in the entrance region of both finless (*a*) heat sink and channel (1–4) of finned (*b*) heat sink with no diffuser. All velocities are normalized with respect to the maximum velocity.

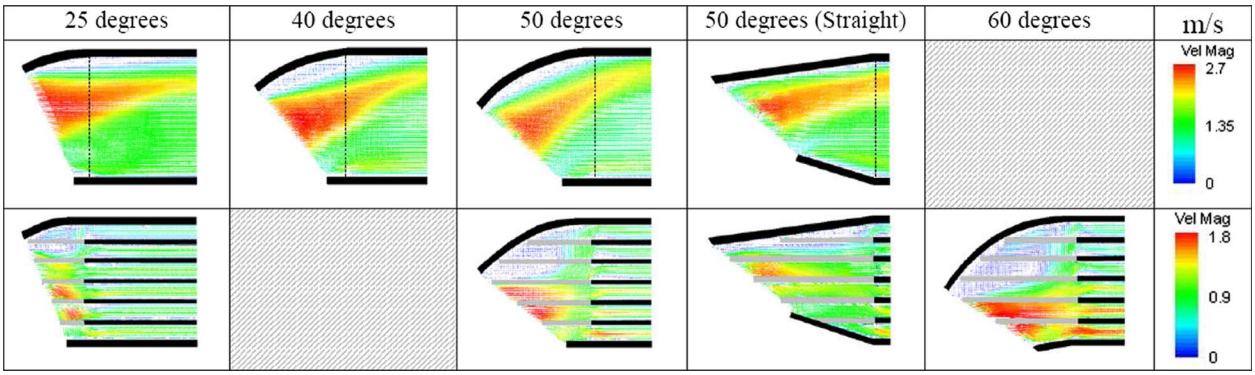

Fig. 6 PIV velocity magnitude plots depicting flow within the diffuser and heat sink entrance for both finned and finless geometries with diffuser angles of 25–60 deg

primary interest for optimizing this thermal management solution. A reduction in the angles that flow exits the fan is evident when compared with the finless images and can be attributed to the pressure rise associated with the finned geometry. At the lower angle of 25 deg the flow is relatively evenly distributed among the channels; however, this turning angle is seen to be insufficient in eliminating the impinging flow at the channel entrances against the fins, a similar effect to that shown in Fig. 5(*b*). The aim of this work is to define the influence of flow alignment with the finned geometry; hence this diffuser is unsuitable for further thermal analysis. A 50 deg curved diffuser produced an improved development in flow alignment, however, also resulted in a poor distribution across the heat sink channels. Hence, it is assumed that a 40 deg diffuser would produce a similar to worse scenario than this and was excluded from the PIV analysis. The optimum condition occurs when using a 50 deg straight diffuser, as both flow alignment and even distribution of flow are achieved. By increasing the diffuser angle to 60 deg flow alignment is apparent; however, an unbalanced distribution across the channels is noticeable. The velocity magnitude data for flow in both types of heat sink where diffusers are introduced to straighten the oncoming flow from a driving fan are presented in Fig. 7 for the finless design and Fig. 8 for the finned design.

The velocity results presented in all figures are velocity magnitudes with vector length and color varying accordingly; longer vectors represent high velocity regions. The relationship between color and velocity magnitude is indicated in the legend provided with each figure. The data presented for the current work were obtained by averaging 70 instantaneous results, each taken at a frequency of 14.5 Hz.

The PIV results for the finless heat sink and 25 deg curved diffuser are shown in Fig. 7 for a fan rotational speed of 5500 rpm. The velocity magnitude plot shown in Fig. 7 presents the fluid flow through the diffuser and heat sink, with the dashed line indicating the entrance to the heat sink from the diffuser. Considering the data presented in Figs. 7 and 5(*a*), it is possible to distinguish noticeable differences in the flow distribution due to the introduction of a diffuser. In Fig. 7 the flow is distributed relatively evenly in the channel of the finless heat sink and all other speeds examined resulted in a similar evenly distributed flow pattern. This implies that the effects of forced convection should also be relatively even across the channel section, reducing the possibility of raised temperatures in localized areas of the heat sink. However, in Fig. 5(*a*), a large region of low velocity exists near the right wall at the entrance. Hence forced convective cooling in this region will have little effect on the right wall temperature. By

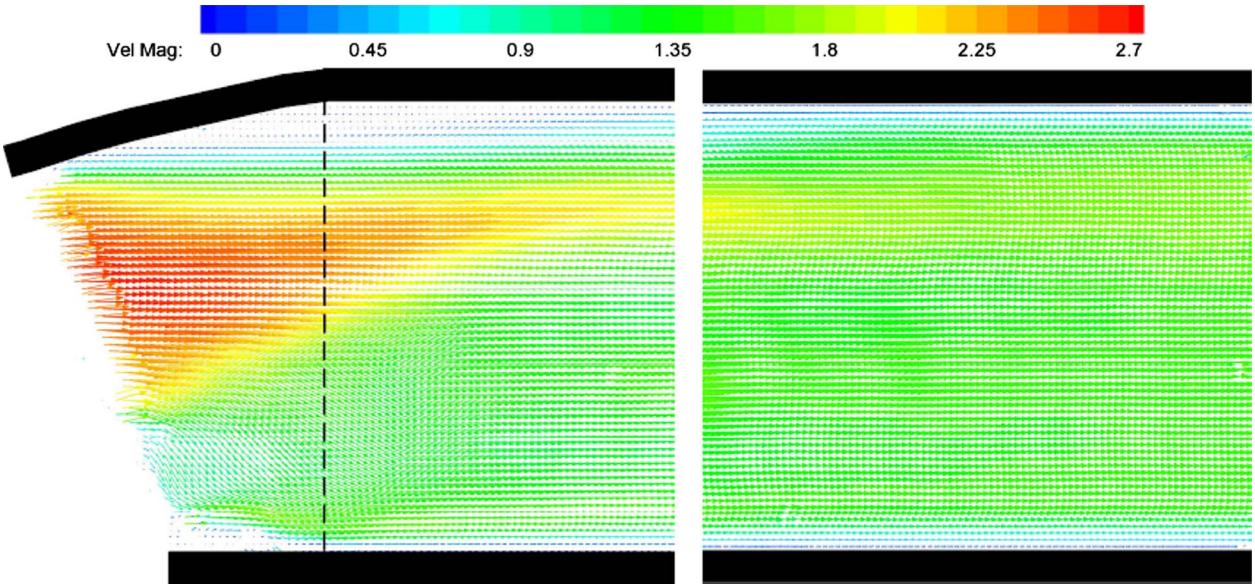

Fig. 7 PIV velocity magnitude plots depicting the flow within the diffuser and finless heat sink for a fan speed of 5500 rpm. Flow is from left to right. The respective velocity scale bar is in m/s. The dashed line represents the entrance to the heat sink from the diffuser.

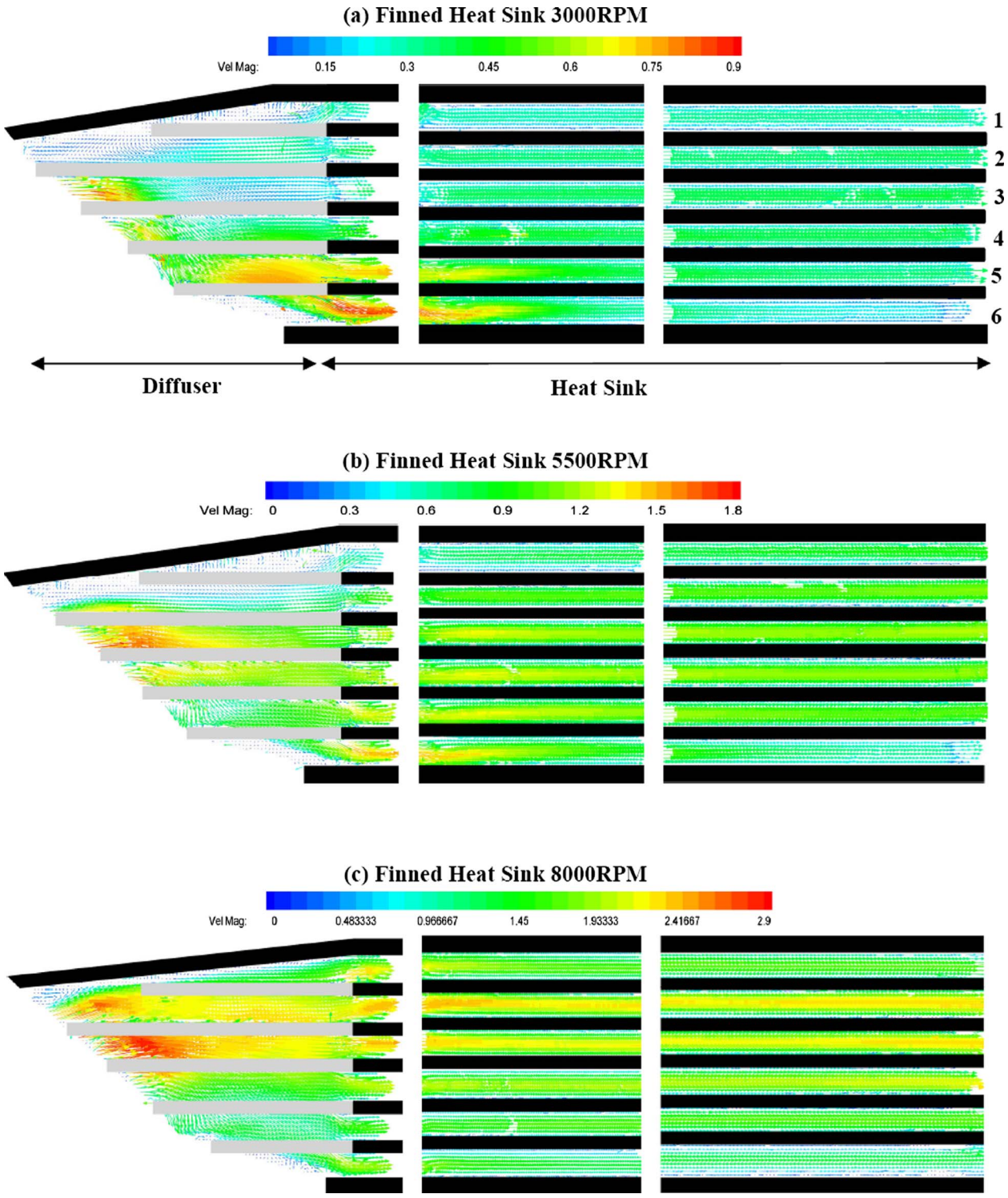

Fig. 8 PIV velocity magnitude plots of flow in finned heat sink and 50 deg straight diffuser at 3000 rpm, 5500 rpm, and 8000 rpm. Respective scale bars for velocities in m/s are given above each result. Flow is from left to right. Regions in gray are shadows from the heat sink fins, which result from the laser light entering from the right.

introducing the diffuser at the entrance to the heat sink, flow now enters the finless channel parallel to the heat sink walls, as seen from the velocity magnitude plot of Fig. 7.

The results from PIV analysis on the finned heat sink and 50 deg straight diffuser are presented in Fig. 8. The diffuser and heat sink are labeled in Fig. 8(*a*) and also color contrasted as previously mentioned. For each case considered in Fig. 8, the flow entering the heat sink shows minimal impingement on the fins as opposed to Fig. 5(*b*), where no diffuser is used at 8000 rpm. Under fully developed conditions the maximum and minimum velocities and hence flow rate are recorded in channels 3 and 6, respectively, for all three fan speeds. The percentage differences in flow rates between channels 3 and 6 for fan speeds of 3000 rpm, 5500 rpm, and 8000 rpm are 42%, 48%, and 43%, respectively. However, the standard deviation of the flow rates and velocities for all six channels is higher for a fan speed of 8000 rpm,

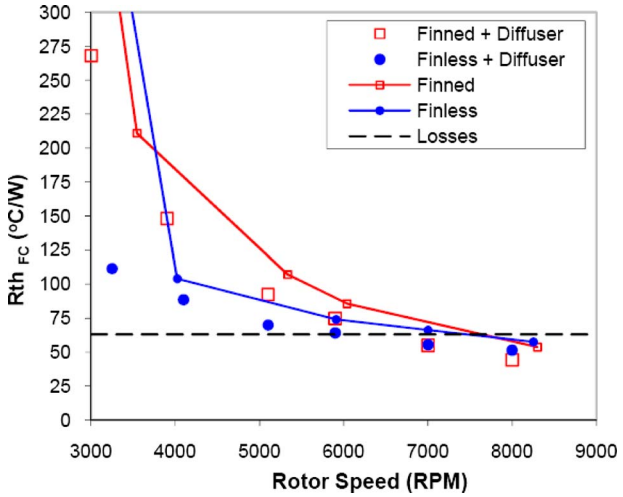

Fig. 9 Plot of forced convection thermal resistance with varying rpm. Also indicated are the effects due to secondary cooling mechanisms (losses).

suggesting that the flow distribution between channels is not as uniform at higher speeds. It can be seen from Fig. 8(*c*) that the angle of the flow entering the diffuser changes at 8000 rpm and that a longer diffuser but of the same angle may be required.

Following the selection of a diffuser for the finned and finless heat sinks using the flow field analyses discussed, the experimentation was arranged to obtain a measure of thermal resistance for a range of fan speeds from 0 rpm to 8000 rpm. The data recorded are plotted in Fig. 9. This figure, along with all subsequent figures discussed, also compares data recorded for the finned and finless cases where no diffuser was used [13]. From Fig. 9 it can be seen that a reduction in thermal resistance can be obtained through the use of a diffuser. As the rotational speed of the fan increases, the heat sink and diffuser combination clearly outperforms the heat sink without diffuser. For a finless heat sink there is a constant reduction in total thermal resistance achieved when using a diffuser between approximately 4000 rpm and 8000 rpm. Below this range of speeds, large reductions in thermal resistance are seen by using a diffuser to align the flow exiting the fan. In order to achieve a forced convective thermal resistance of lower than 115°C/W using a finned heat sink and diffuser combination, the fan must operate at a rotational speed greater than 5000 rpm. Alternatively, the use of a finless heat sink and diffuser combination produces similar thermal resistances from a fan speed of just 3000 rpm. A benefit of this is that lower operating speeds are sufficient for similar cooling effects when using the optimized finless arrangement. In terms of fan reliability, noise, and pumping power this proves highly advantageous.

For the current work these secondary cooling mechanisms were found to give a thermal resistance, $R_{\text{th-losses}}$, of 63°C/W, as shown in Fig. 9. For a fan speed of 8000 rpm, using the diffuser designed for the finned heat sink, a decrease of approximately 23% in forced convection thermal resistance is obtained. At the same operating speed, the finless heat sink and combined diffuser provide a decrease of 15.3% over a finless heat sink without diffuser. It is therefore apparent that in the case of a fan and heat sink in parallel aligning the flow with the heat sink fins produces lower thermal resistances than impinging flows [11].

At 8000 rpm the finned diffuser case results in a lower thermal resistance compared with the finless-diffuser solution. This is an expected result as the design of the finned heat sink was optimized for 8000 rpm, as discussed in Sec. 3. As previously mentioned, a difference in velocity magnitudes for both geometries can be seen in Figs. 7 and 8. This can be accredited to a higher system resistance due to the finned heat sink, which implies that higher mass flow rates are evident in the finless heat sink for each rotational speed recorded. Higher mass flow rates commonly result in increased heat transfer rates; however, Fig. 9 enforces the influence of boundary layer analysis used in the finned heat sink design, i.e., the optimum spacing of fins in a heat sink for a given pressure drop is determined based on the boundary layers merging just at the exit of the heat sink. Thermal resistance measurements for the finned case drop below that of the finless case at approximately 7500 rpm. However, the thermal resistance values for the finless-diffuser case are lower compared with finned case (test 1). Even at 8000 rpm where the forced convective thermal resistance appears to be reaching a constant value with increased rotor speed, there is a reduction of 11.3% over the forced convective thermal resistance of the finned heat sink without a diffuser. This is significant considering that the 25 deg diffuser used for the finless heat sink only increases the overall footprint area of the thermal solution by approximately 6%. It was also noted that the 50 deg diffuser used to optimize the finned heat sink increases the overall footprint area of the thermal solution by approximately 16%. This result demonstrates the need to design integrated and optimized fan and heat sink solutions for the low profile market.

Similarly for a combined fan and heat sink cooling solution, sizing issues may also be associated with the power supply necessary for operation. Considering the power requirements of a cooling solution, it is reasonable to measure shaft power supplied to the rotor when characterizing fan performance. This provides designers with power requirements for the fan alone, which may deviate considerably from the motor power required especially when considering small scale fans. The current work is not examined in this manner, as there is an enclosed motor and fan assembly designed for combined use. Power requirements are therefore presented for the motor and fan collectively. The manufacturer provides a nominal operating speed of 6000 rpm. To achieve this rotational speed, a power input of 0.163 W is required. This value increases to 0.320 W to reach an operating speed of 8000 rpm. The scale law for power consumption predicts a 1.77 factor $((8000/6000)^3)$ increase; however, the power is seen to almost double. This is due to the efficiency of the driving motor dropping off at higher speeds as bearing losses become larger. Power is therefore conserved to a greater extent when operating the cooling solution below the nominal operating speed of 6000 rpm as opposed to above this speed where power requirements rise sharply for small increases in rotational speed. Hence, depending on the level of restrictions evident with power supply choice and the thermal performance requirements, it may be beneficial to integrate a finless heat sink and diffuser design as it outperforms the finned heat sink cases below 6000 rpm, shown in Fig. 9. It is also of interest to note that this level of power consumption could be supplied by a high end mobile phone battery (Nokia BP-4L battery) for a period of 34 h of continuous use. In reality, however, the fan would only be in use while the device is in high processing mode so the actual lifetime is likely to be limited by phone functionality rather than by cooling solution.

In Fig. 10, the heat transfer coefficient is presented for forced convection cooling. Similar to the thermal resistance measurements, these data are based on the average heat transfer coefficient of the heat sink. The forced convection heat transfer coefficient for the finless cases is almost twice the average heat transfer coefficient compared with the finned cases over the rotor speeds tested. This is inversely proportional to the convective surface area of both heat sinks, as given in Eq. (6). With reference to Fig. 9, which shows thermal resistance plotted against fan speed, it is possible to conclude that in general over the range of speeds examined, the finless design will dissipate a similar and, in some cases, favorable magnitude of heat per unit of temperature compared with the finned design. The heat transfer coefficient quantifies this relative to the convective surface area of the heat sink. The finless heat sink considered here has a convective surface area of 44.7% less than the convective surface area of the finned heat

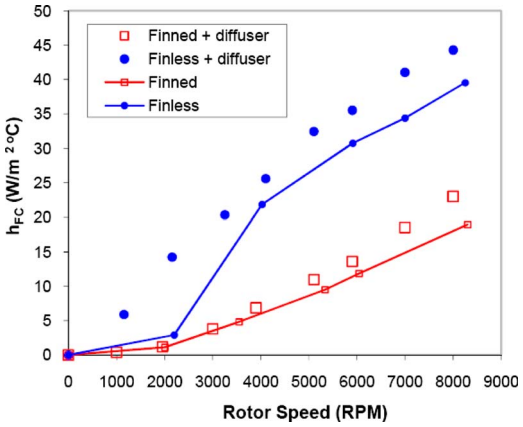

Fig. 10 The forced convection heat transfer coefficient for both finned and finless heat sinks

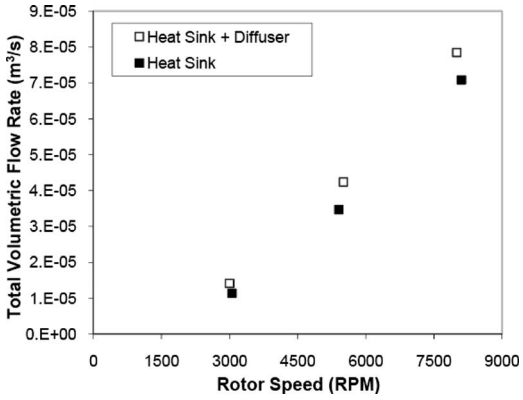

Fig. 11 Graph depicting the volumetric flow rates through heat sink measured using the PIV data presented in Fig. 8 and Ref. [13] over the three fan speeds tested

sink. It is therefore expected that the heat transfer coefficient values will be greater for the finless design as it dissipates a similar magnitude of heat using almost half the convective surface area of the finned design. Increasing rotational speed results in an increasing difference in heat transfer coefficient between heat sinks using diffusers and heat sinks without diffusers. At 8000 rpm, the finned heat sink achieves an increase of approximately 27% through the introduction of the selected diffuser. For the same rotor speed, an increase of approximately 15% is achieved for the finless heat sink using the diffuser to align the flow. This is due to the increase in flow rate and combined reduction in pressure across both heat sinks through flow alignment. The larger increase in the heat transfer coefficient for the finned heat sink with diffuser emphasizes the benefits that can be achieved in finned designs through flow alignment at this scale and possibly at larger scales. The effect of convective surface area results in a heat transfer coefficient for the finned case with diffuser to be 51% of the heat transfer coefficient for the finless case with diffuser, considered for a rotor speed of 8000 rpm.

As seen in Fig. 8 the flow within the finned heat sink channels is seen to fully develop, which makes it possible to describe the velocity profile across the entire channel cross section using the solution provided by Purday [22]. This solution describes the velocity distribution in rectangular channels of varying aspect ratios and is adapted to describe the flow in channels with an aspect ratio of $\frac{1}{3}$, such as those in the heat sink analyzed herein. The maximum velocity measured using PIV within each heat sink channel was used to yield an estimate of the corresponding flow rates in each channel. These were summed for all six channels to obtain the total volumetric flow rate passing through the system. The results are presented in Fig. 11 and compared with volumetric flow rates for the tests carried out without a diffuser [13]. It is seen that the flow rate in the finned heat sink with the diffuser attached at the entrance is on average 15% higher than just the fan and heat sink arrangement. However, the increase in volumetric flow rate at 8000 rpm is lower compared with 3000 rpm and 5500 rpm. A possible explanation for this is a higher variation in flow rate between the heat sink channels at 8000 rpm due to higher speeds affecting the flow distribution. The accuracy of the velocity measurements is due to a number of experimental factors and is estimated at 5%.

Another interesting point relating to the flow rate estimations made from the PIV data is highlighted when these measurements are compared with the fan characteristic curve provided by the fan manufacturer. It is seen that the measured flow rates are only of order 25% of the maximum attainable using such fans, subsequently verified through a flow characteristic rig [13]. This implies that the system resistance curve relating flow rate and pressure drop across the heat sink has a relatively high slope so that it intersects with the fan characteristic curve at a point that yields the low flow rates measured using the PIV data. This suggests that the pressure drop across the heat sink was larger than initially anticipated while optimizing the finned heat sink design, and due to the incorrect fan performance data provided by the manufacturer for a nominal speed of 6000 rpm. The overall effect of this is that the optimum finned heat sink design should have had slightly larger channel spacing than was used in the current study; however, it is not anticipated that this would significantly affect the optimum diffuser angle, which was highlighted from this study. In the current work, the effects of flow alignment on both designs are considered, and use of the supplied flow rate data for optimization was chosen as this is available to designers primarily.

5 Conclusions

A miniature low profile cooling solution suitable for integration into a range of portable electronics devices has been characterized through thermal resistance and velocity field measurements.

This paper presents an analysis of fan exit angle with results showing that a reduction in thermal resistance is obtained for flow entering the heat sink aligned with the fins. Flow alignment has been achieved through the introduction of a diffuser at the entrance to the heat sink.

- By accounting for fan exit angles, the thermal resistance has been reduced by up to 23% for a finned heat sink and 15% for a finless heat sink. In order to achieve these reductions the footprint area has been increased by 16% and 6%, respectively.
- A finless heat sink and diffuser outperform the conventional finned heat sink solution over a range of fan speed tested.

The experimental results show that at these low profile scales the proposed finless design outperforms the more classical finned case. The finless design also has manufacturing cost and weight benefits. Hence the results provide a basis for designers of heat sinks to address fan exit angles and finless designs.

Nomenclature

A_{conv} = convective surface area, m^2
B = fin spacing, mm
H = convective heat transfer coefficient, W/m^2 K
h_{FC} = forced convective heat transfer coefficient, W/m^2 K
$k_{heat\ sink}$ = thermal conductivity of heat sink material, W/m K
L = length of heat sink, mm
ΔP = pressure drop, Pa

Q = volumetric flow rate, m^3/s
$R_{th_{FC}}$ = thermal resistance of forced convection cooling, °C/W
$R_{th_{losses}}$ = thermal resistance of natural convection cooling, °C/W
rpm = revolutions per minute
SP = static pressure rise, Pa
t_{fin} = fin thickness, mm
W = total width of heat sink, mm

Greek Symbols

α = thermal diffusivity, m^2/s
μ = viscosity, $N\,s/m^2$

Subscripts

conv = convective
FC = forced convection

References

[1] Vogel, M. R., 1995, "Liquid Cooling Performance for 3-D Multichip Module and Miniature Heat Sink," IEEE Trans. Compon., Packag. Manuf. Technol., Part A, **18**(1), pp. 68–73.
[2] Launay, A., 2004, "Experimental Study on Silicon Micro-Heat Pipe Arrays," Appl. Therm. Eng., **24**(2–3), pp. 233–243.
[3] Tan, F. L., 2004, "Cooling of Mobile Electronic Devices Using Phase Change Materials," Appl. Therm. Eng., **24**(2–3), pp. 159–169.
[4] Walsh, E. J., Grimes, R., and Punch, J., 2007, "A Cooling Device," WO2007057871.
[5] Grimes, R., Walsh, E. J., Quin, D., and Davies, M. R. D., 2005, "Effect of Geometric Scaling on Aerodynamic Performance," AIAA J., **43**(11), pp. 2293–2298.
[6] Walsh, P., Egan, V., Grimes, R., and Walsh, E., 2009, "Profile Scaling of Miniature Centrifugal Fans," Heat Transfer Eng., **30**(1–2), pp. 130–137.
[7] Walsh, E. J., Walsh, P. A., Punch, J., and Grimes, R., "Acoustic Emissions From Active Cooling Solutions for Portable Devices," IEEE Trans. Compon. Packag. Technol., in press.
[8] Day, S. W., Lemire, P. P., Flack, R. D., and McDaniel, J. C., 2003, "Effect of Reynolds Number on Performance of a Small Centrifugal Pump," ASME Paper No. FEDSM2003-45686.
[9] Chien, H., 2001, "The Study of Micro-Fin Heat Sinks for Electronic Cooling Applications," 17th IEEE SEMI-THERM Symposium.
[10] Maveety, J. G., and Jung, H. H., 2002, "Heat Transfer From Square Pin-Fin Heat Sinks Using Air Impingement Cooling," IEEE Trans. Compon. Packag. Technol., **25**(3), pp. 459–469.
[11] Walsh, E. J., Walsh, P., Grimes, R., and Egan, V., 2008, "Thermal Management of Low Profile Electronic Equipment Using Radial Fans and Heat Sinks," ASME J. Heat Transfer, **130**(12), p. 125001.
[12] Walsh, E. J., and Grimes, R., 2007, "Low Profile Fan and Heat Sink Thermal Management Solution for Portable Electronics Applications," Int. J. Therm. Sci., **46**, pp. 1182–1190.
[13] Egan, V., Walsh, P. A., Walsh, E., and Grimes, R., "Thermal Analysis of Miniature Low Profile Heat Sinks With and Without Fins," ASME J. Electron. Packag., accepted.
[14] Bleier, F. P., 1997, *Fan Handbook: Selection, Application and Design*, McGraw-Hill, New York.
[15] Bejan, A., 2004, *Convective Heat Transfer*, Wiley, New York.
[16] Ellison, G. N., 1989, *Thermal Computations for Electronic Equipment*, Krieger, Malabar, FL.
[17] Holman, J. P., 2002, *Heat Transfer*, 9th ed., McGraw-Hill, New York.
[18] Egan, V., Walsh, P., Walsh, E., and Grimes, R., 2007, "On the Characterisation of Finned and Finless Heat Sinks for Portable Electronics," Fifth International Conference on Nanochannels, Microchannels and Minichannels, Puebla, Mexico, Jun. 18–20.
[19] Kline S. J., and McClintock F. A., 1953, "Describing Uncertainties in Single-Sample Experiments," Mech. Eng. (Am. Soc. Mech. Eng.), **75**, pp. 3–8.
[20] Song, S., Lee, S., and Au, V., 1994, "Closed-Form Equation for Thermal Constriction/Spreading Resistances With Variable Resistances Boundary Conditions," IEPS Conference.
[21] Raffel, M., 1998, *Particle Image Velocimetry: A Practical Guide*, Springer, New York.
[22] Purday, H. F. P., 1949, *An Introduction to the Mechanics of Viscous Flow (Streamline Flow)*, Dover, New York.

Subcooled Pool Boiling Experiments on Horizontal Heaters Coated With Carbon Nanotubes

V. Sathyamurthi

H-S. Ahn

D. Banerjee

S. C. Lau

Multiphase Flows and Heat Transfer Laboratory,
Department of Mechanical Engineering,
Texas A&M University,
College Station, TX 77843-3123

Pool boiling experiments were conducted with three horizontal, flat, silicon surfaces, two of which were coated with vertically aligned multiwalled carbon nanotubes (MWCNTs). The two wafers were coated with MWCNT of two different thicknesses: 9 μm (Type-A) and 25 μm (Type-B). Experiments were conducted for the nucleate boiling and film boiling regimes for saturated and subcooled conditions with liquid subcooling of 0–30°C using a dielectric fluorocarbon liquid (PF-5060) as test fluid. The pool boiling heat flux data obtained from the bare silicon test surface were used as a base line for all heat transfer comparisons. Type-B MWCNT coatings enhanced the critical heat flux (CHF) in saturated nucleate boiling by 58%. The heat flux at the Leidenfrost point was enhanced by a maximum of ~150% (i.e., 2.5 times) at 10°C subcooling. Type-A MWCNT enhanced the CHF in nucleate boiling by as much as 62%. Both Type-A MWCNT and bare silicon test surfaces showed similar heat transfer rates (within the bounds of experimental uncertainty) in film boiling. The Leidenfrost points on the boiling curve for Type-A MWCNT occurred at higher wall superheats. The percentage enhancements in the value of heat flux at the CHF condition decreased with an increase in liquid subcooling. However the enhancement in heat flux at the Leidenfrost points for the nanotube coated surfaces increased with liquid subcooling. Significantly higher bubble nucleation rates were observed for both nanotube coated surfaces. [DOI: 10.1115/1.3000595]

Keywords: pool boiling, critical heat flux, film boiling, nanotube, nanotechnology

1 Introduction

Boiling is the most efficient mode of heat transfer due to the inherent thermodynamics of the phase change phenomenon, which occurs reversibly at a constant temperature and at zero temperature gradient under uniform and infinitely slow heating. Hence, boiling is an attractive option for cooling of high heat flux devices. This work explores various potential transport mechanisms responsible for the enhancement of pool boiling heat fluxes on nanostructured surfaces using data obtained from subcooled and saturated pool boiling experiments.

Heater orientation, heater surface morphology, and thermophysical properties of the working fluid as well as the heater material, significantly alter transport mechanisms in pool boiling [1,2]. Enhancements in boiling heat transfer rates have been reported due to an increase in liquid subcooling and by employing various types of engineered microstructured surface morphologies (e.g., surface micromachined structures, graphite foams, and porous surfaces) [1,2]. Various studies reported the enhancement of pool boiling heat transfer by using newly developed materials or structures. Ramaswamy et al. [3,4] employed an enhanced structure composed of six layers of copper plates with rectangular channels machined into the substrates. This structure was used to investigate the combined effect of pressure and subcooling on the boiling performance of the enhanced structure. The authors reported that the combined effects of increasing subcooling and pressure enhanced the performance of boiling systems. They postulated that the increase in pore size and the reduction in pitch augmented the heat dissipation at wall superheats ranging from 4 K to12 K. Mudawar and Anderson [5] mounted a cylindrical pin-fin with microstructures machined into its perimeter onto an electronic chip. The critical heat flux (CHF) was enhanced in these experiments for liquid subcooling ranging from 0–35°C with FC-72 as the test fluid. Coursey et al. [6] applied graphite foams to thermal management of electronics. The foams had a porous structure consisting of interconnected graphite ligaments. The thermal conductivity of the foam was five times higher than copper. The authors claimed that the use of graphite foams as an evaporator in a thermosiphon enhanced the cooling of electronics, especially at lower chamber pressures.

Since the discovery of carbon nanotubes (CNTs) by Iijama [7] in 1991, there has been growing interest in the various applications of CNT. CNT have very broad ranges of thermal, electrical, and structural properties that may be tailored to various applications. According to Berber et al. [8], the thermal conductivity of CNT is 6600 W/m K, or about 16.5 times that of copper, at room temperature, but has a much lower value of 3000 W/m K, or about 7.6 times that of copper at 400 K. Ujereh and co-workers [9,10] reported results of their experiments on nucleate pool boiling of FC-72 on a silicon surface and on carbon nanotube coated surfaces under saturated conditions. The area of the heated surface was 12.7×12.7 mm^2. The multiwalled carbon nanotubes (MWCNTs) were synthesized using a calcined dendrimer catalyst in a plasma enhanced chemical vapor deposition (PECVD) system. The MWCNTs were 30 nm in diameter and 20–30 μm in length. The MWCNTs coated on a silicon wafer increased the CHF by 50% and enhanced the heat transfer coefficient by 400% compared with a bare silicon wafer. However, this study was restricted to nucleate boiling condition and the performance of the nanostructured surface over the film boiling regime was not reported. The authors noted that the synthesized MWCNTs did not

Contributed by the Heat Transfer Division of ASME for publication in the JOURNAL OF HEAT TRANSFER. Manuscript received November 28, 2007; final manuscript received September 9, 2008; published online April 30, 2009. Review conducted by Louis C. Burmeister. Paper presented at the 2007 ASME International Mechanical Engineering Congress (IMECE2007) Seattle, WA, November 10–16, 2007.

provide complete surface coverage. They reported no significant degradation of the MWCNT structures on the substrate as a result of the experiment.

This work is a continuation of a previous study where preliminary results for saturated pool boiling experiments on MWCNT coated heaters were reported [11]. The objective of this study was to investigate the effect of liquid subcooling on the pool boiling curve for MWCNT coated surfaces. In the present study, subcooled pool boiling experiments were performed on silicon wafers coated with MWCNTs of two different thicknesses of 9 μm and 25 μm, respectively. The boiling curves for the MWCNT coated wafers were compared with the boiling curve on an atomically smooth single crystal bare silicon wafer surface to identify the potential mechanisms responsible for heat flux enhancement (or lack of enhancement) on the MWCNT coated surfaces for the different boiling regimes.

2 Experimental Apparatus

The most significant component of the experimental apparatus was the boiling test surface. The boiling test surface consisted of one of the three silicon wafers. For each experiment, one of these wafers was fixed to the top of a copper cylinder. The surfaces of two of these silicon wafers were coated with MWCNTs of two different thicknesses: 9 μm (Type-A) and 25 μm (Type-B). The diagram of the experimental apparatus is shown in Fig. 1. Heat was supplied to the copper cylinder (diameter of 8.9 cm) from five embedded cartridge heaters. During the subcooled pool boiling experiments, the temperature of the test fluid was kept below its saturation temperature. Additional details of the experimental apparatus are also provided in Ref. [11].

A tubular heater was submerged in the test liquid. The tubular heater was used to raise and maintain the temperature of the test fluid at its saturation temperature ($\sim$56°C) in the saturated boiling experiments. For the subcooled boiling experiments, the temperature of the test fluid was kept below its saturation temperature with a coolant that was circulated from a constant temperature bath through a coiled copper heat exchanger placed just below the surface of the test fluid.

2.1 Test Surface Preparation and Characterization. For the pool boiling experiments in this study, two silicon wafers were coated with MWCNT using CVD. The MWCNT arrays had thicknesses of 9 μm and 25 μm. The details of the CVD process used in synthesis and growth of MWCNT forests were described in Ref. [12]. Vertically aligned MWCNT forests with a diameter of 8–15 nm were synthesized by passing 5 mol % C_2H_2 at 580 SCCM (SCCM denotes standard cubic centimeter per minute at STP) in helium at atmospheric pressure in a quartz tube furnace that was maintained at 680°C. A goniometer was used to measure the contact angle for PF-5060 on all the test surfaces. The contact angle for the bare surface was measured to be 10.5 deg, while for the Type-A and Type-B surfaces the contact angles were measured to be 9.6 deg and 13 deg, respectively. Thus, the test fluid PF-5060 wetted all the test surfaces very well. Contact angle measurements performed with water showed that the presence of nanotubes resulted in hydrophobic (Type-A $\sim$135 deg) and superhydrophobic (Type-B$\sim$153 deg) surfaces.

A recent study by Zhou et al. [13] showed the existence of wicking in "nanowicks" formed by mats of vertically aligned CNT on wafers. The study showed that the wicking of the liquid into the CNT mat occurred in three different flow topographies. They were: (a) corner flow (flow occurring between the edge of the CNT mat and the substrate), (b) top surface flow (flow on the CNT tips due asperities), and (c) interstitial flow (flow through the interstitial spaces between the dense CNT mats). According to this study, the surface flow was faster but less persistent than interstitial flow. Thus a liquid droplet first spread on the surface the CNT mats creating air-pockets. Subsequently, interstitial flow gradually reduced the air-pockets. The reports in the literature show that

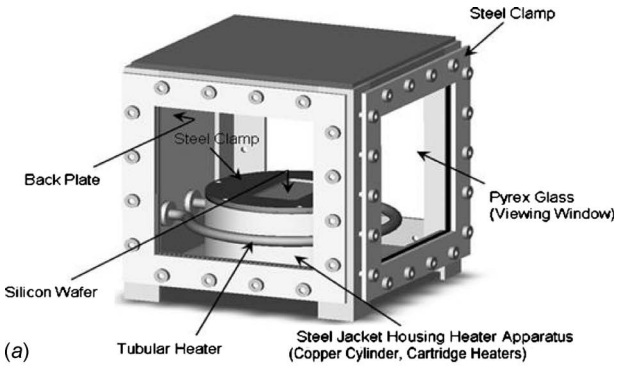

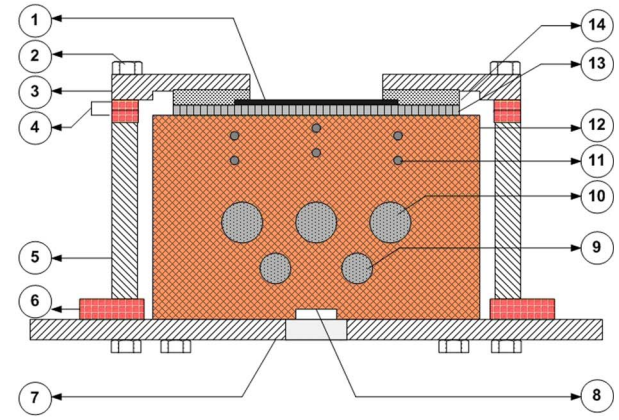

1. Test surface
2. M-4 nut
3. Steel clamp
4. Silicone rubber gaskets (1/16")
5. Steel jacket
6. Silicone rubber gasket (1/8")
7. Bottom cover plate with hole for lead wires
8. Groove for lead wires
9. 300W cartridge heater
10. 500W cartridge heater
11. K-type thermocouple
12. Copper cylinder
13. Pyrex glass wafer
14. Teflon gasket

(b)

Fig. 1 Design of experimental apparatus: (*a*) test section in viewing chamber, (*b*) schematic of the heater apparatus [11,15]

PF-5060 has a high solubility for air (50–60% by volume) [14]. Thus it is reasonable to expect that most air-pockets are eliminated when the CNT coated silicon wafers are submerged in the pool of PF-5060.

2.2 Test Section. Five cartridge heaters were inserted horizontally near the bottom of the copper cylinder, as shown in Fig. 1(*c*). A Pyrex® wafer was sandwiched between the silicon wafer and the top of the copper cylinder to minimize the electrical noise from the heaters. High thermal conductivity grease was used to minimize thermal contact resistance between surfaces at the various interfaces. Twelve K-type thermocouples were used to determine the temperature distribution in the copper cylinder. The junctions of these thermocouples were installed inside the copper cylinder at different vertical and radial positions such that they were aligned vertically. Additional thermocouples were placed in the test fluid PF-5060 to monitor the bulk temperature and the uniformity of the bulk liquid temperature. The transient signals from the thermocouples were digitized and recorded using an automated computer-controlled data acquisition system. A concentric annular stainless steel jacket with an inside diameter of 9.9 cm and a thickness of 7.6 mm was placed concentrically with the copper cylinder. The stainless steel jacket was separated from the copper cylinder by an air gap, which served as an insulation to minimize heat losses from the sides. A guard heater placed con-

centric with the steel jacket was used in the saturation experiments to maintain the bulk liquid at saturation temperature in the low heat flux regime. The silicon wafer was mounted on top of the copper cylinder and covered with an annular steel clamp fitted with a Teflon gasket (Fig. 1) to prevent any leaks. The steel clamp was seated on silicone rubber gaskets placed on top of the stainless steel jacket using M-4 nuts. Silicone rubber gaskets were also placed under the steel jacket and steel clamp to prevent leaks. The area of the test surface (silicon wafer with or without MWCNT coating) that was exposed to the test fluid during pool boiling was measured to be 5.9×3.2 cm^2 with chamfer radius of 0.3 cm.

2.3 Heat Exchanger for Subcooled Boiling Experiments. During the subcooled boiling experiments, the test fluid was maintained at a liquid subcooling of 5°C, 10°C, 20°C, or 30°C. The liquid was subcooled using a coiled copper heat exchanger. The heat exchanger coil was submerged 1.5 cm below the surface of the test fluid. The coolant within the heat exchanger was circulated using an external constant temperature bath with an electronic controller (Fig. 1(*b*)). The flow rate and the temperature of the coolant were adjusted and monitored to achieve the desired subcooling of the test fluid. During the saturated boiling experiments, the coiled copper tube heat exchanger was lifted above the surface of the test fluid.

3 Experimental Procedure

Prior to performing an experiment, one of the three test wafers was clamped on top of the copper cylinder. The viewing chamber was filled with PF-5060. The tubular heater was used to boil the test fluid for approximately 30 min at atmospheric pressure, for degassing purposes prior to each test. The power supplied to the tubular heater during degassing was ~300–500 W. It has been shown by Bhavnani et al. [14] that the percentage of dissolved air in PF-5060 does not decrease below 39% even after several days of degassing under atmospheric conditions. Hence, it is expected that the working liquid was not completely degassed under subcooled conditions since the test chamber was maintained at atmospheric pressure. The dissolved air content was not measured in this study. It can be expected however that the dissolved air content remained approximately the same after the degassing procedure prior to each run at saturated or subcooled conditions due to the fixed duration of degassing. Furthermore, completely degassed perfluorocarbon fluids are not encountered in practical phase change cooling applications. The noncondensable gases and vapor released during degassing was allowed to escape through the vent pipe, located at the back of the test section.

Some of the test fluid vapors that passed through the vent pipe during the degassing was recovered in the collection bottle by condensation for reuse. After the degassing step, the input power to the tubular heater was then adjusted to maintain the test fluid at its saturation temperature for the saturated pool boiling experiments. For a subcooled boiling experiment, the heat exchanger coil was lowered into the liquid pool prior to degassing.

The power input to the cartridge heaters was ramped in steps of 3–5 V for each data point on the boiling curve. Once steady state conditions were reached, the temperatures in the copper cylinder were recorded with the computer-controlled data acquisition system. The liquid pool temperature and ambient air temperature were also monitored with wire-bead thermocouples. The voltage and current supplied to the cartridge heaters were measured with a digital TRMS voltmeter and a digital TRMS clamp ammeter, respectively, at each steady state condition. After the CHF condition was achieved, the voltage input was increased slightly to cause transition to film boiling. To prevent burnout, the power supplied to the cartridge heaters was decreased quickly once a stably stratified vapor film covered the test surface. The system was then allowed to attain steady state. The heater voltage was decreased by 1–3 V in subsequent steps. Temperature data were recorded at each steady state condition until transition from film to nucleate boiling occurred. This procedure enabled the estimation of the minimum heat flux in film boiling (Leidenfrost point). The time interval between consecutive steady state conditions in nucleate boiling was 1–2 h. The corresponding time interval in film boiling was 2–3 h. A typical boiling experiment was 24–30 h in duration. Due to the high evaporation rates in the saturation experiments, the test fluid was replenished periodically (every 8–9 h) to maintain the fluid level at about 5 cm above the silicon wafer surface. This was done well before the next steady state condition was achieved, usually after recording the data for a previous steady state condition. Usually, this was done close to the CHF in the fully developed nucleate boiling region or in the film boiling region. The degassing procedure was not repeated, as the impact of dissolved gases in these regimes is not expected to alter the results significantly.

4 Data Reduction

The mean heat flux in the vertical direction within the copper cylinder was determined as

$$\overline{q''_{\mathrm{Cu}}} = \frac{\sum_{i=1}^{n} \frac{k_{\mathrm{Cu}} \Delta T_i}{\Delta x_i}}{n} \tag{1}$$

where k_{Cu} is the thermal conductivity of copper, and $\Delta T_i / \Delta x_i$ is the axial temperature gradient measured using vertically aligned thermocouples embedded within the copper cylinder. From the energy conservation principle, the mean heat flux on the test wafer was determined using the following relation:

$$\overline{q''_w} = \frac{\overline{q''_{\mathrm{Cu}}}}{A_w} A_{\mathrm{Cu}} \tag{2}$$

Energy conservation was checked by comparing the total power input to the cartridge heaters with the total rate of heat transfer from the boiling surface measured by the thermocouples (Eq. (2)) and was consistent. It should be noted that in the earlier study by Ahn et al. [11] the boiling curve was reported based on $\overline{q''_{\mathrm{Cu}}}$. In this study the boiling curve is reported based on $\overline{q''_w}$, which is a more consistent definition for wall heat flux.

Pool boiling experiments using thin film thermocouples (TFTs) [15] were used to obtain piecewise linear relations (lookup table) for correlating the wall temperature on the silicon surface as a function of the temperature of the copper cylinder. The lookup table was obtained for the surface temperatures in the nucleate boiling and film boiling regimes. The look up table also enabled the revision of the superheat values reported in the earlier study [11]. The uncertainty in estimating the wall temperature from the copper cylinder temperature using the lookup table is ±1°C. The uncertainty in heat flux within the copper cylinder was evaluated using the procedure of Kline and McClintock [16]. The uncertainty in surface temperature estimates on the test wafer could be from a number of sources.

1. The resolution of the data acquisition system was set by the hardware to a 16 bit accuracy, which was equivalent to an absolute error of ±0.005°C for the temperature range in this study.
2. During the experiments in this study, the standard deviation of temperature fluctuations at steady state conditions was measured to be ~±0.05°C.

Hence the total uncertainty of the temperature measurement was estimated to be ±0.055°C. Using the uncertainty values of ±1.0% for thermal conductivity for copper and of ±3.0% (machining accuracy) for the distance between two thermocouples embedded in the copper cylinder, the estimated maximum uncer-

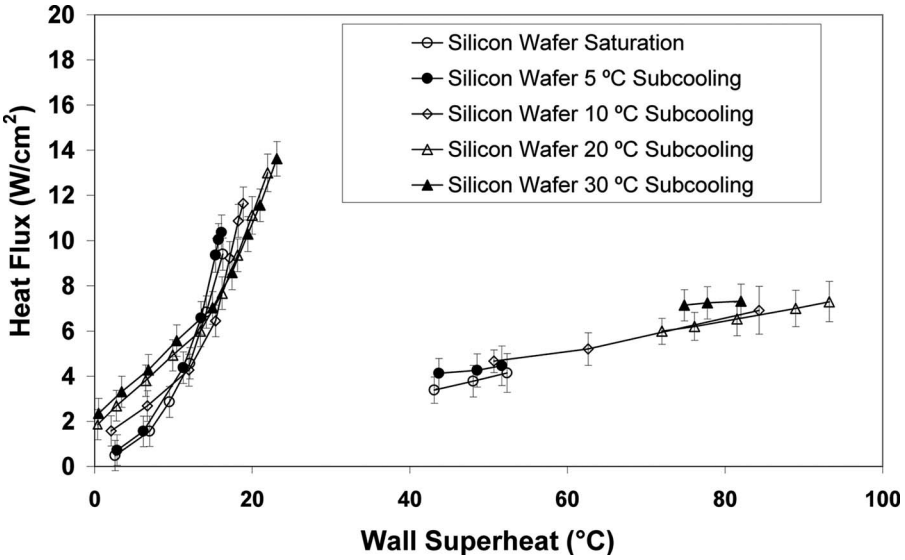

Fig. 2 Pool boiling curves for bare silicon surface at different values of liquid subcooling in nucleate and film boiling regimes

tainty of the surface heat flux near the Leidenfrost (minimum heat flux (MHF)) point was ±14%. The uncertainty was estimated to be ±6% near the CHF point.

5 Experimental Results

The pool boiling heat fluxes for the nanostructured surfaces were compared with the heat flux for an atomically smooth bare silicon wafer surface (this served as the control experiment). The experiments were repeated at least twice to ensure repeatability. An atomically smooth bare surface was chosen for the substrates as well as for the control experiments.

The rationale behind choosing silicon as a substrate was to isolate the effect of nanotubes from that of nucleating cavities on the pool boiling heat transfer rates. Variation in the number of active nucleating cavities can result in higher heat fluxes especially in the low heat flux regime. The random and nonuniform distribution of nucleating cavities that are typically encountered on commercial surfaces (e.g., copper) are difficult to characterize, and there is little control over this experimental variable for different substrates of the same material. The aim of the study was to study the effect of liquid subcooling exclusively on the efficacy of the nanostructured surfaces for enhancing heat transfer. Hence, the transport mechanisms on the nanostructures needed to be decoupled from the interferences due to random effects (i.e., random and uncontrolled distribution of nucleating cavities on the substrate). Heat fluxes in these experiments were substantially lower than those observed in commercial surfaces. Additionally, the carbon nanotubes used in this study were 9–25 μm in thickness and 8–16 nm in diameter. At these length-scales (nanometers to microns), a random uncontrolled variable such as cavity distribution can affect the interpretation of the experimental data significantly. Therefore, atomically smooth substrates were chosen for coating with carbon nanotubes.

5.1 Effect of Subcooling on Bare Silicon Surface. Control experiments performed with a bare silicon wafer provided the base line data for comparison with the heat flux data for MWCNT surfaces. The control experiments served to identify the dominant mechanisms for heat flux enhancement. Boiling inception was obtained by increasing power input to cartridge heaters. Liquid subcooling of 5°C, 10°C, 20°C, and 30°C were maintained using a copper coiled tube heat exchanger. Figure 2 shows the experimental results for a representative run on the bare silicon wafer for saturated and subcooled pool boiling.

In nucleate boiling, the heat flux increases marginally as the liquid subcooling is increased. The CHF points are obtained at wall superheats of 16.3°C, 16.1°C, 18.6°C, 21.9°C, and 23.1°C while the associated heat fluxes are 9.4 W/cm^2, 10.4 W/cm^2, 11.6 W/cm^2, 13.0 W/cm^2, and 13.6 W/cm^2 at saturation, 5°C, 10°C, 20°C, and 30°C subcooling levels, respectively. Ghiu and Joshi [17] conducted pool boiling studies on plain and enhanced copper surfaces with PF-5060 as the working fluid. The studies were carried out at saturation conditions and were restricted to the nucleate boiling regime for wall superheat values less than 29°C. In that study, the plain copper surface showed a maximum heat flux of 15.4 W/cm^2. The enhanced copper surfaces used in Ref. [17] resulted in peak transfer values from 28.9–43 W/cm^2 for different channel widths and pitch.

In the present study, it is observed that at low subcooling (5°C) the boiling curve shifts to the left compared with the saturated boiling curve. This shows that the nucleate boiling heat transfer coefficient increases with subcooling at low wall superheat. However, at high subcooling (10°C and higher) the boiling curve shifts to the right showing that there is a marginal decrease in the nucleate boiling heat transfer coefficient. This behavior is a significant departure from pool boiling curves obtained for commercial surfaces (e.g., copper) [1,2]. Stable film boiling was obtained by decreasing the power input to the heaters immediately after a rapid increase in wall temperature was detected beyond the CHF point. In film boiling, the heat flux increases marginally with subcooling for the low subcooling case of 5°C. There is a significant increase in the wall heat flux at a given wall superheat for higher liquid subcooling. The experimental results show that the Leidenfrost points shift toward higher wall superheat with an increase in subcooling. The Leidenfrost points are obtained at wall superheat of 43.1°C, 43.7°C, 50.7°C, 72°C, and 74.8°C, while the associated wall heat flux values are 3.4 W/cm^2, 4.1 W/cm^2, 4.7 W/cm^2, 6.0 W/cm^2, and 7.1 W/cm^2 for saturated, 5°C, 10°C, 20°C, and 30°C subcooled conditions, respectively.

5.2 Effect of Subcooling on Type-A MWCNT Array (9 μm Tall). Experiments for Type-A MWCNT (9 μm tall) were conducted for subcooling levels of 0–30°C. Figure 3 shows the experimental results for a representative run on the Type-A MWCNT coated wafer for saturated and subcooled pool boiling. Peak heat fluxes increased marginally with an increase in subcool-

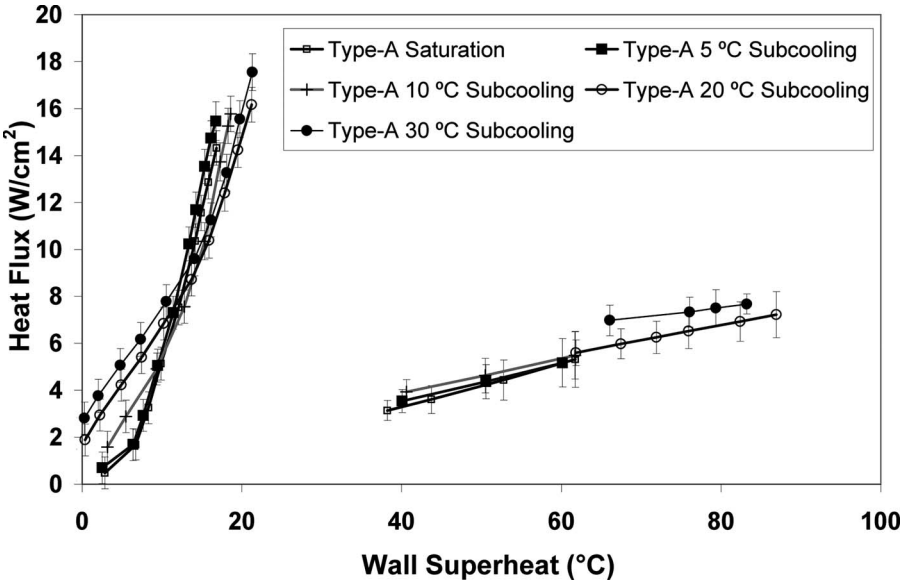

Fig. 3 Pool boiling curves for silicon surface with Type-A (9 μm tall) MWCNT, for different values of liquid subcooling in nucleate and film boiling regimes

ing. This is in contrast to the significant enhancement in heat flux observed for similar conditions on the bare silicon wafer. For liquid subcooling of 10°C, as shown in Fig. 5, the CHF condition was achieved at a higher wall superheat than 5°C subcooled and saturated conditions. Under 5°C subcooling, the CHF point was obtained at the wall superheat of 16.7°C and the associated heat flux was 15.5 W/cm^2. For the saturated condition, the wall superheat at the CHF and the associated heat flux were 16.8°C and 14.3 W/cm^2, respectively. At 20°C subcooling, peak heat flux values near the CHF was 16.2 W/cm^2 at a wall superheat of 21.2°C. It is observed that at low subcooling (5°C) the boiling curve shifts to the left compared with the saturated boiling curve. Thus, the effect of subcooling on the heat transfer coefficients for Type-A MWCNT was the same as that for a bare silicon wafer. Similar variations in heat transfer coefficients at low wall superheat were observed at low (increase in heat transfer coefficients) and high (decrease in heat transfer coefficients) levels of subcooling. In film boiling, marginal enhancements in wall heat flux values were observed as the liquid subcooling was increased for the low subcooling cases within the limits of experimental uncertainty. The Leidenfrost point was achieved at higher wall superheat as the liquid subcooling increased. A similar trend was observed for the pool boiling on silicon wafer.

5.3 Experiments Using Type-B MWCNT array (25 μm Tall). Experiments for Type-B MWCNT (25 μm tall) were conducted for subcooling levels of 0–30°C. Figure 4 shows the experimental results for a representative run on the Type-B MWCNT coated wafer for saturated and subcooled pool boiling. At 10°C subcooling, the wall heat flux near the CHF was 18.4 W/cm^2 at a wall superheat of 21.4°C. The CHF values at 5°C subcooling and saturated conditions were 16.8 W/cm^2 at a

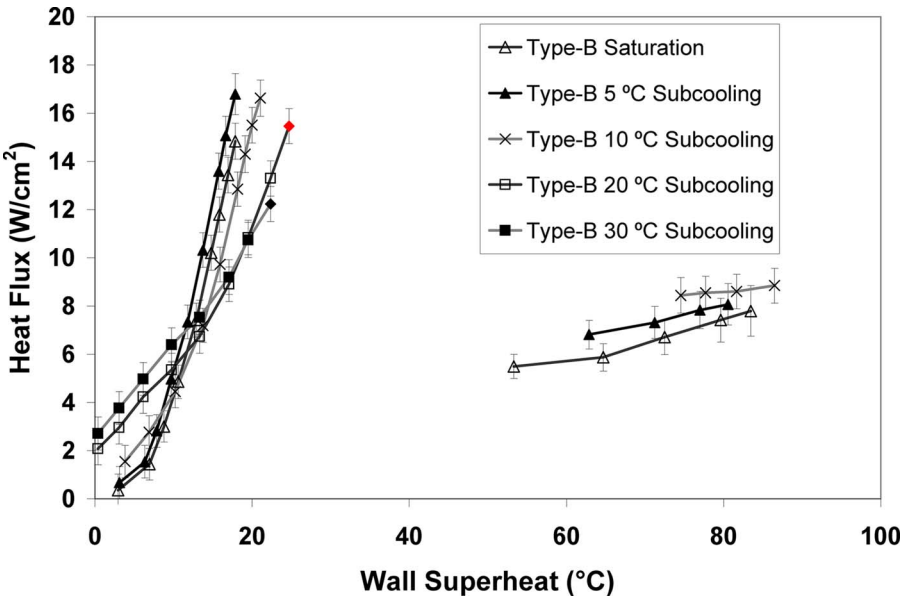

Fig. 4 Pool boiling curves for boiling on silicon surface with Type-B (25 μm tall) MWCNT, for different values of liquid subcooling in nucleate and film boiling regimes

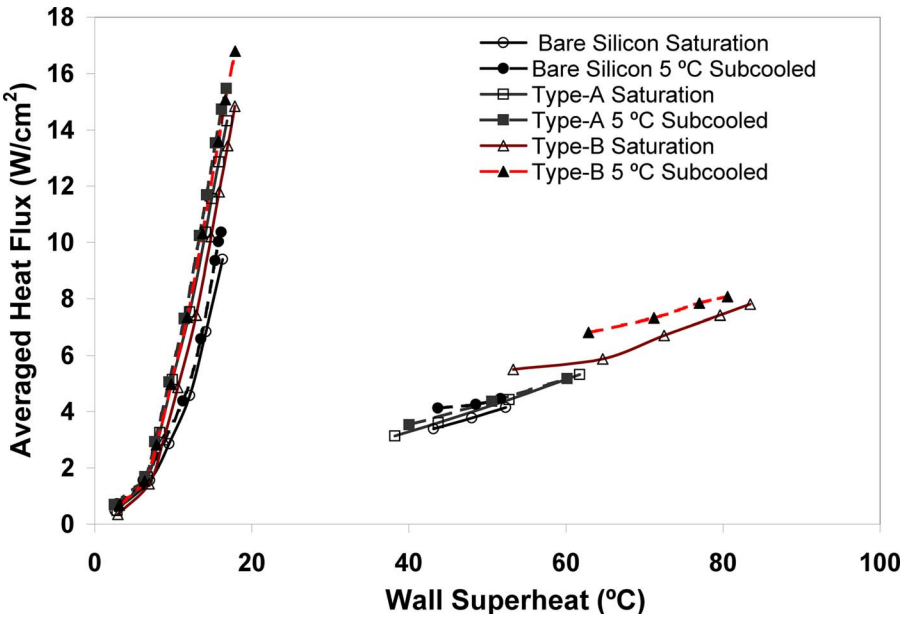

Fig. 5 Pool boiling curves for different surfaces at low values of liquid subcooling

wall superheat of 17.9°C. The CHF condition could not be sustained at 20°C and 30°C subcooling levels due to the limitations of the experimental apparatus. In these experiments before the CHF condition could be attained, the temperature within the copper cylinder exceeded 250°C—which is the maximum temperature rating for the cartridge heaters. Therefore the experiments were terminated. Hence the CHF condition and film boiling data could not be obtained for Type-B MWCNT for liquid subcooling of 20°C and 30°C. The peak heat flux values obtained in these cases are marked with a different symbol in Fig. 5. The nucleate boiling results reported in Fig. 5 are the maximum attained heat flux with the experimental apparatus used in this study.

For Type-B MWCNT, the extent of the wall superheat for the transition boiling region was much larger and more distinct than that for the bare silicon and Type-A MWCNT surfaces. This was due to significant disruption of the vapor film by the nanotubes. During transition from nucleate to film boiling, the film began forming at the edges of the test section and later spread to the center of the test section. At a wall superheat of 53.3°C under saturated boiling condition, a continuous vapor film was observed over the whole area of the exposed surface. The heat flux at the Leidenfrost point was enhanced by as much as ~150% (2.5 times) in film boiling for Type-B MWCNT compared with that for bare silicon wafer (and Type-A MWCNT).

As the liquid subcooling increased, the Leidenfrost point was observed at higher wall superheats. This was consistent with observations for the bare silicon surface (and Type-A MWCNT). The MHF points for Type-B MWCNT occurred at wall superheats of 53.3°C, 62.9°C, and 74.6°C with heat transfer rates of 5.5 W/cm^2, 6.8 W/cm^2, and 8.4 W/cm^2, respectively, under saturated, 5°C subcooled, and 10°C subcooled conditions, respectively. These heat transfer rates were substantially higher (66–150%) than corresponding values obtained for the bare silicon surface under same subcooling conditions.

5.4 Comparison of Type-A MWCNT, Type-B MWCNT, and Bare Silicon. Images of pool boiling on the bare silicon wafer, and Type-A, and Type-B MWCNT surfaces were acquired during the tests. Images were captured during the experiments in proximity to the CHF and the MHF points using a Sony Cyber-Shot DSC-P10 Digital Camera and a Canon® S3IS camera (for subcooling cases of 20°C and 30°C) under saturated and subcooled (5°C, 10°C, 20°C, and 30°C) liquid conditions. In the vicinity of the CHF points, the degree of liquid subcooling strongly influenced the bubble nucleation density, growth, and departure process. Under 10°C subcooling, no bubble columns were observed in vicinity of the CHF point probably because of the condensation effect of the subcooled liquid on the departing bubbles. In contrast, bubble columns were noticeable at the CHF for saturated pool boiling. Relatively weak bubble columns were observed for 5°C subcooled condition. A large number of small bubbles were observed to depart at high subcooling conditions close to the CHF point. By comparing the images taken under the saturated conditions, it was observed that Type-A and Type-B MWCNT surfaces displayed much more ebullient motion of the bubble columns (departing bubbles were larger in size), than for the bare silicon wafer. However, the motion of the departing bubbles during nucleate boiling for the two nanotube coated substrates (Type-A and Type-B MWCNTs) and the bare silicon surface were similar as the liquid subcooling increased. Furthermore, in all cases the MWCNT coated wafers showed a significantly larger number of bubbles departing per unit area of the wafer than the silicon wafer. Thus, the MWCNT coated wafers were observed to have higher nucleation site densities.

The degree of liquid subcooling strongly affected the shape of the departing bubbles and the texture of the stratified vapor film in the vicinity of the Leidenfrost point as it did in the proximity of the CHF point. As the liquid subcooling increased, the amount of vapor bubbles released and the size of bubbles departing from the surface decreased. For all the images, under saturation condition in the vicinity of the Leidenfrost point, a thin film was clearly observed on top of the test surface in the form of a shiny "mirror" type surface. The vapor film had a wrinkled appearance under saturation and low subcooling conditions due to "turbulent" film boiling [18]. In contrast, the subcooled cases showed a relatively smooth "laminar" film boiling. In this study, the vapor film had a wrinkled appearance under saturation and low subcooling conditions. At high subcooling levels, the vapor film had a less wrinkled appearance.

In nucleate boiling, both Type-A and Type-B MWCNT surface had higher wall heat flux values than the corresponding values for the bare silicon surface under saturated and subcooled conditions (5°C and 10°C), as shown in Figs. 5 and 6. For instance, at a given wall superheat of 10°C and under saturation condition, Type-A and Type-B MWCNT surfaces, respectively, showed

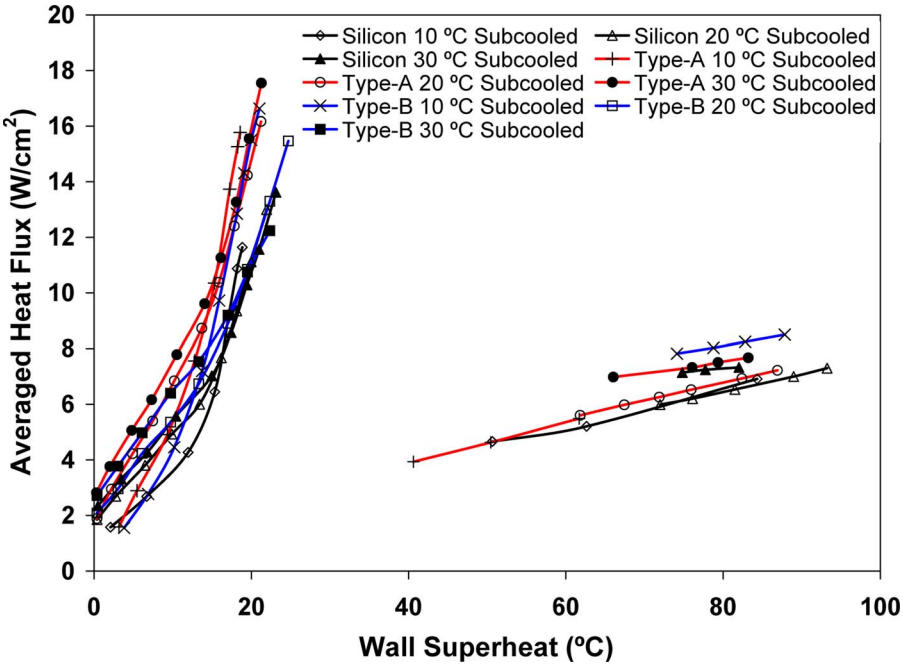

Fig. 6 Pool boiling curves for different surfaces at high values of liquid subcooling

64.6% and 33.0% higher heat fluxes than the bare silicon surface. The wall heat flux values at the CHF for Type-A and Type-B MWCNT surfaces were higher than corresponding values for the bare silicon surface under all of the liquid conditions.

For film boiling experiments under saturated and subcooled (5°C and 10°C) conditions, the wall heat fluxes for Type-B MWCNT were much higher than the corresponding values for Type-A MWCNT and the bare silicon surface. The taller MWCNT (Type-B MWCNT) structures enhanced the wall heat flux at a given wall superheat and caused the MHF point to be attained at higher wall superheat by disrupting the vapor film at the points of minimum vapor film thickness that may lead to possible collapse of the vapor film in film boiling [11,19–21]. Within the bounds of experimental uncertainty, the wall heat flux for Type-A MWCNT matched the corresponding values for the bare silicon wafer at a given superheat. Under saturated and 10°C subcooled conditions, the wall heat flux values for Type-A MWCNT were obtained as 3.1 W/cm^2 and 3.9 W/cm^2, respectively, at wall superheats of 38.2°C and 40.6°C. These were 7% and 15% lower than the corresponding values for the bare silicon wafer under the same liquid subcooling conditions.

As shown in Figs. 5 and 6, the Leidenfrost point for Type-A MWCNT was observed at a slightly lower wall superheat for saturated and subcooled conditions, compared with the bare silicon surface for the low subcooling cases. Also, at low subcooling (5°C), the Leidenfrost point shifted to lower wall superheat for bare silicon and Type-A MWCNT. The wall heat flux values in vicinity of the CHF and the MHF points are summarized in Table 1.

Figure 7 provides a schematic showing the potential disruption of the vapor film by Type-B MWCNT while Type-A MWCNT is not able to disrupt the vapor film. Hence the heat flux from Type-A MWCNT matches that of the bare silicon surface (within the bounds of measurement uncertainty), while Type-B MWCNT results in higher wall heat flux. Further explanation is provided in Sec. 5.

The effect of Type-A MWCNT array on the wall heat flux is compared with that of Type-B MWCNT array and bare silicon wafer in Figs. 6 and 7 for low and high subcooling levels, respectively. In nucleate boiling, under saturated condition, the wall heat flux values for Type-A MWCNT were higher than the corresponding values for Type-B MWCNT under fully developed nucleate boiling conditions. In the fully developed nucleate boiling region, Type-A MWCNT yielded much higher wall heat flux values than the corresponding values for the bare silicon wafer at a given wall superheat. For the saturated condition, the wall superheat at the CHF point and the associated heat flux were 16.8°C and 14.3 W/cm^2, respectively, for Type-A MWCNT. This wall heat flux value was 52.5% higher than the corresponding CHF value for the bare silicon surface. Type-B MWCNT had higher CHF values under saturated and 5°C subcooled conditions, respectively, than Type-A MWCNT. The associated wall superheat values for Type-B MWCNT were also slightly higher than the corresponding values for Type-A MWCNT under both saturated and 5°C subcooled conditions. Under 5°C subcooled conditions, Type-A MWCNT enhanced heat flux near the CHF by 49.3% compared with the bare silicon wafer (control experiment). The CHF values for Type-B MWCNT under saturated and 10°C subcooled conditions were 58% higher for the former and 19–58% higher for the latter when compared with corresponding values for the bare silicon wafer at same level of subcooling.

6 Discussion

The effect of MWCNT on pool boiling can be summarized to be due to the following.

1. The higher "effective" wall thermal conductivity due to the presence of MWCNT, which can enhance the spatial size of the wall temperature fluctuations or "cold-spots."
2. The thickness of the "hairlike" MWCNT vertical protrusions (which can disrupt the hydrodynamic instabilities, e.g., by disrupting the microlayer region in nucleate boiling and the "continuous" vapor film in film boiling). This can also lead to enhanced transient heat transfer (compared with bare silicon surface) by increasing the frequency and magnitude of the cyclical liquid-solid contacts.

The experimental results are consistent with numerical models reported in the literature. Previous numerical and experimental results by Banerjee and Dhir [19,20] and Banerjee et al. [21] have shown that the dynamic value of the minimum vapor film thickness for film boiling of PF-5060 is approximately 15–20 μm.

Table 1 Comparison of CHF and MHF values from the pool boiling experiments

Substrate	Bulk liquid subcooling (°C)	CHF		MHF	
		T_{sup} (°C)	Q(W/cm^2)	T_{sup} (°C)	Q(W/cm^2)
	Saturated	16.3	9.4	43.1	3.4
	5	16.1	10.4	43.7	4.1
	10	18.9	11.6	50.7	4.7
	20	21.9	13.0	72.0	6.0
	30	23.1	13.6	74.8	7.1
Bare					
	Saturated	16.8	14.3	38.2	3.1
	5	16.7	15.5	40.0	3.5
	10	18.6	15.8	40.6	3.9
	20	21.2	16.2	61.8	5.6
	30	21.3	17.5	66.0	7.0
Type-A					
	Saturated	17.8	14.8	53.3	5.5
	5	17.9	16.8	62.9	6.8
	10	21.4	18.4	74.6	8.4
	20	(24.7)[a]	(15.5)[a]	-	-
Type-B	30	(22.4)[a]	(12.2)[a]	-	-

[a]The maximum values obtained from the experiments are reported since critical heat flux condition could not be attained in the experiments.

The authors had discussed that surface roughness (or for example artificially engineered surface micro/nanostructures) greater than 20 μm could disrupt the vapor films at the points of minimum vapor film thickness leading to possible collapse of film boiling.

Comparing the results of Type-A and Type-B MWCNT surface, it is observed that for Type-B (25 μm tall) the film boiling is enhanced considerably more than for Type-A (9 μm thickness). This shows that an MWCNT surface with thickness greater than 20 μm possibly disrupts the vapor film. Therefore, MWCNT surface with thickness greater than 20 μm have better efficacy in enhancing heat transfer in film boiling. The effect of subcooling on heat flux enhancement is therefore more pronounced for Type-B MWCNT than for Type-A MWCNT. This mechanism is schematically demonstrated in Fig. 1.

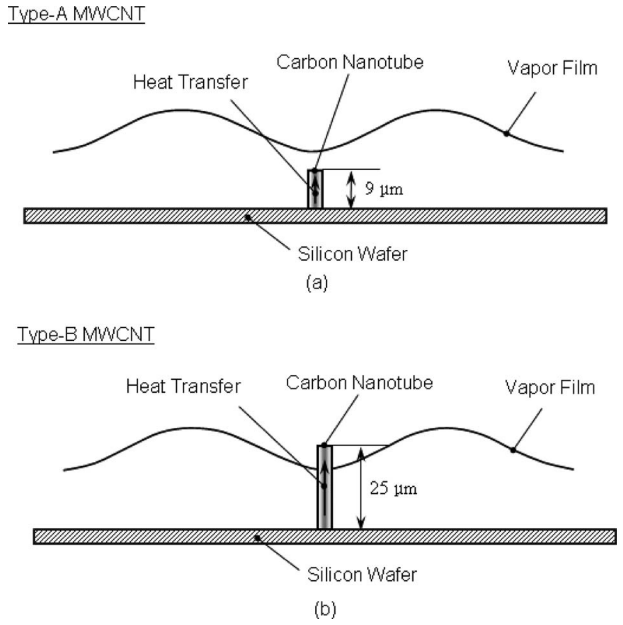

Fig. 7 Schematic of the heat transfer mechanism for carbon nanotubes in film boiling: (*a*) Type-A (9 μm thickness), and (*b*) Type-B (25 μm thickness) MWCNT

The study of Banerjee et al. [19–21] also demonstrated the existence of cold-spots in film boiling. Cold-spots are regions of lower surface temperature than the surrounding. The study by Banerjee et al. [19–21] showed that cold-spots serve as focused conduits for heat transfer in film boiling. The location of the cold-spots coincided with the location of the minimum vapor film thickness (showing that these are coupled thermal-hydrodynamic phenomena). The width of the cold-spots was a function of the wall thermal conductivity (or more specifically the thermal diffusivity of the wall material). It is expected that similar "cold spot" regions develop during nucleate boiling in the "microlayer region" on the wall. By analogy, it would be expected that the size (or width) of the cold-spots under the microlayer would be dictated by the wall thermophysical properties.

Since MWCNT structures have higher thermal conductivity than the silicon substrate, the size of the cold-spots is bigger for surfaces coated with MWCNT than for the bare silicon wafer. Hence the efficacy of the cold-spots is enhanced due to the presence of the MWCNT structures. MWCNT structures that disrupt the vapor film at the minimum vapor film thickness (or location of the cold-spots) would enhance the liquid-solid contacts and cause transient quenching of the heater surface with further augmentation of heat transfer in film boiling. Hence, Type-B MWCNT surface causes heat transfer augmentation in film boiling while heat transfer augmentation is not observed during the film boiling experiments for Type-A MWCNT surface.

From Fig. 5 it is observed that there is marginal enhancement in film boiling heat transfer ($\sim$20%) at a liquid subcooling of 5°C for the bare silicon wafer. At liquid subcoolings of 10°C, 20°C, and 30°C, the film boiling heat fluxes are enhanced by $\sim$25%, $\sim$80%, and $\sim$125%, respectively, for both bare silicon and Type-A MWCNT. The heat flux is marginally higher for Type-A MWCNT than for bare silicon in the film boiling regime at subcooling of 30°C and is similar to the heat flux values for Type-B MWCNT in subcooled film boiling at low levels of subcooling, within the bounds of the measurement uncertainty. This is consistent with numerical predictions in the literature. Numerical studies reported by Banerjee and Dhir [19,20] show that the minimum value of the dynamic vapor film thickness decreases with an increase in subcooling. Banerjee and Dhir [19,20] predicted that for subcooling of 10°C the minimum vapor film thickness is greater than 15 μm for film boiling. Hence, at subcooling greater than

10°C vapor film thickness is expected to be lower than 15 μm. The experimental results show that at subcooling exceeding 10°C, the heat flux is enhanced by 80–115%, possibly due to a decrease in the minimum thickness of the dynamic vapor film and consequently by the spontaneous disruption of the vapor film (similar to Fig. 7) by the MWCNT.

In contrast, there is low sensitivity of heat transfer augmentation to the thickness of the MWCNT surface in nucleate boiling. For a wall superheat of 10°C at high subcooling levels of 20°C and 30°C, heat fluxes are enhanced for Type-A MWCNT by 35.8% and 36.9%, respectively, and for Type-B by 10.1% and 14%, respectively, compared with the bare silicon wafer at the same levels of subcooling.

This shows that the enhancement in CHF decreased for the MWCNT coated surfaces with an increase in subcooling (when compared with the corresponding heat flux values on the bare silicon substrate). This is potentially due to the different configurations of vapor column formation at CHF for the nanotube coated surfaces compared with the bare surface (as described above). At low subcooling and saturated pool boiling the bubble size was bigger and had bigger vapor columns. Enhanced heat transfer through the microlayer potentially contributed to the higher bubble departure frequency. However, at higher subcooling, the bubble departure process was similar for nanostructured surfaces and smooth (bare) surfaces. The reason for higher heat flux at high subcooling for the nanotube coated surfaces is potentially due to the higher nucleation site densities.

This is because in nucleate boiling and at the CHF, the size and distribution of the nucleation sites is expected to be the limiting variable rather than the thickness of the surface structures. The thickness of the MWCNT in these experiments is greater than the thickness of the microlayer [2]. The thickness of the microlayer is estimated to be in the range of 10–100 nm [1,2]. Therefore, both types of MWCNT are able to disrupt the microlayer resulting in enhanced liquid-solid contact and, consequently, enabling similar heat flux enhancements at comparable wall superheat values at low subcooling levels. Alternately, the thickness of the microlayer can also be enhanced by capillary wicking due to the presence of the MWCNT "forests" which are 8–16 nm in diameter and of comparable pitch. Such a high spatial density of hairlike protrusion can provide enough capillary pressure to increase the thickness of the microlayer (estimated to be by as much as 100%) and therefore provide additional surface area for heat transfer. Hence the interfacial thermal resistance (or Kapitza resistance [2]) can be significantly reduced due to the presence of the MWCNT.

A potential mechanism for the delayed occurrence of CHF at higher superheats could be through the suppression of "mushroom" type of bubbles or enhanced formation of vapor stems that trap superheated liquids at CHF (e.g., Ref. [22]). This can occur due to the hair-like protrusion of the MWCNT into the mushroom type bubble or through formation of additional vapor stems due to presence of MWCNT on the surface. Also, an anomalous behavior is noted at low subcooling where the CHF is enhanced and occurs at lower wall superheat. This is in contrast to the behavior at high subcooling where the CHF is measured to be enhanced and to occur at high wall superheats. This behavior recurred for both nanotube coated surfaces and the MWCNT coated surfaces. Additional investigations are needed to conclusively verify the mechanisms responsible for extending the wall superheat required for CHF for boiling on nanostructured surfaces and to understand the effect of the thickness of the nanostructures on CHF.

7 Conclusions

Boiling experiments were conducted using PF-5060 as the test fluid on silicon wafer substrates. The experiments were conducted with a bare silicon wafer and two silicon wafers containing a uniform layer of vertically aligned MWCNT of two different thicknesses, respectively (Type-A: 9 μm and Type-B: 25 μm).

(1) In the nucleate boiling regime, the enhancement heat flux is weakly dependent on the thickness of the MWCNT.
(2) The heat flux enhancement for nanotube coated substrates decreases with an increase in subcooling. This is potentially due to a change in the morphology of the bubble departure process with an increase in subcooling.
(3) The nucleation site density increases on the nanotube coated surfaces compared with the bare substrate.
(4) In nucleate boiling, MWCNT coated substrates (both 9 μm and 25 μm thickness) yield higher wall heat fluxes under saturated and subcooled conditions compared with a bare silicon surface. The Type-B MWCNT array augments CHF by ~62% compared with a bare silicon surface under saturated and 10°C subcooling, respectively.
5) Wall heat flux values near the CHF for Type-B MWCNT exceed those for Type-A MWCNT under saturated condition.
(6) In the film boiling regime, the heat flux is sensitive to the thickness of the MWCNT coating. For Type-B MWCNT (25 μm thickness) the wall heat flux values are enhanced under saturated (~62%), 5°C subcooling (~62–124%), 10°C subcooling conditions (~66–148%), compared with control experiments performed on a bare silicon surface. However, for Type-A MWCNT (9 μm thickness) the wall heat flux values are similar to the corresponding values for the bare silicon surface during film boiling, for low subcooling. At high subcooling, the film boiling heat flux values are enhanced significantly and by similar magnitudes for both bare silicon and Type-A MWCNT coated heaters. This is consistent with the dynamic models for film boiling reported in the literature.
(7) Type-B MWCNT coated substrate is more sensitive to subcooling compared with Type-A MWCNT and a bare silicon wafer in the film boiling regime.

Acknowledgment

The authors gratefully acknowledge the support for this study from the Texas Engineering Experimentation Station (TEES), and the Mechanical Engineering Department new faculty startup grant that was awarded in January 2005. The authors gratefully acknowledge the help of Dr. Ray Baughman, Dr. M. Zhang, and Dr. S. Fang, at University of Texas at Dallas, for their help in synthesizing the MWCNT. The authors acknowledge the help of Mr. S. Shriraman (Graduate Student, Texas A&M University) for his help with obtaining the contact angle measurements. The authors also acknowledge the help of Mr. J. Howson, Dr. A. Mukhopadhyay, and Dr. A Bhasin from the Texas Transportation Institute at Texas A&M University for their help with training and accessing the goniometer instrument. Work was performed, in part, at the Microelectronics Research Center at UT Austin of National Nanofabrication Infrastructure Network supported by National Science Foundation under Award No. 0335765.

During this study, V.S., H-S.A., and D.B. were partially supported through various other research programs: National Science Foundation (CBET Grant No. 0630703), seedling grant from Defense Advanced Project Agency (DARPA-MTO), Micro/Nano-Fluidics Fundamental Focus Center (DARPA-MF3) through the University of California at Irvine, New Investigations Program (NIP 2005) of the Texas Space Grants Consortium (TSGC), Office of Naval Research (ONR), Air Force Office of Scientific Research (AFOSR) through the American Society for Engineering Education (ASEE) Summer Faculty Fellowship (SFFP) Program at the Air Force Research Laboratory (AFRL), Army Research Office (ARO) SBIR Phase II subcontract through Lynntech Inc., and the National Science Foundation (NSF) SBIR Phase I through NanoMEMS Research LLC.

Nomenclature

A = area (m^2)
g = acceleration due to gravity (m/s^2)
k = thermal conductivity ($W/m\,K$)
n = total number of pairs of vertically aligned thermocouples
q = average wall heat transfer in the axial direction (W)
$\overline{q''}$ = mean heat flux (W/m^2)
T = temperature (°C)
ΔT_i = temperature gradient between two vertically aligned thermocouples (°C)
ΔT = temperature gradient between top of the copper cylinder and the test surface (°C)
Δx_i = distance between the two vertically aligned thermocouples (m)
ω = relative uncertainty

Subscripts

Cu = copper cylinder
j, k = thermocouple position in a vertically aligned plane
sat = saturation condition
sup = wall superheat
v = vapor property
w = wall (boiling surface)

References

[1] Dhir, V. K., 1998, "Boiling Heat Transfer," Annu. Rev. Fluid Mech., **30**, pp. 365–401.
[2] Carey, V. P., 1992, *Liquid-Vapor Phase-Change Phenomena*, Taylor & Francis, London.
[3] Ramaswamy, C., Joshi, Y. K., Nakayama, W., and Johnson, W. B., 2000, "Combined Effects of Subcooling and Operating Pressure on the Performance of a Thermo-Siphon," IEEE Trans. Compon. Packag. Technol., **23**(1), pp. 61–69.
[4] Ramaswamy, C., Joshi, Y., Nakayama, W., and Johnson, W. B., 2003, "Effects of Varying Geometrical Parameters on Boiling From Microfabricated Enhanced Structures," ASME J. Heat Transfer, **125**, pp. 103–109.
[5] Mudawar, I., and Anderson, T. M., 1993, "Optimization of Enhanced Surfaces for High Flux Chip Cooling," J. Electron. Packag., **115**, pp. 89–100.
[6] Coursey, J., Roh, H. K., Kim, J. H., and Boudreaux, P. J., 2002, "Graphite Foam Thermosyphon Evaporator Performance," *Proceedings of the ASME IMECE2002*, New Orleans.
[7] Iijima, S., 1991, "Helical Microtubules of Graphitic Carbon," Nature (London), **354**, pp. 56–58.
[8] Berber, S., Kwon, Y. K., and Tomanek, D., 2000, "Unusually High Thermal Conductivity of Carbon Nanotubes," Phys. Rev. Lett., **84**, pp. 4613–4616.
[9] Ujereh, S., Mudawar, I., Amama, P. B., Fisher, T., and Qu, W., 2005, "Enhanced Pool Boiling Using Carbon Nanotube Surface on a Silicon Surface," ASME Paper No. IMECE2005-80065.
[10] Ujereh, S., Fisher, T., and Mudawar, I., 2007, "Effects of Carbon Nanotube Arrays on Nucleate Pool Boiling," Int. J. Heat Mass Transfer, **50**(19-20), pp. 4023–4038.
[11] Ahn, H.-S., Sinha, N., Banerjee, D., Zhang, M., Feng, S., and Baughman, R., 2006, "Pool Boiling Experiments on Multi-Walled Carbon Nanotube Forests (MWCNT)," ASME J. Heat Transfer, **128**, pp. 1335–1342.
[12] Zhang, M., Atkinson, K. R., and Baughman, R., 2004, "Multifunctional Carbon Nanotube Yarns by Downsizing an Ancient Technology," Science, **306**, pp. 1358–1361.
[13] Zhou, J. J., Noca, F., and Gharib, M., 2006, "Flow Conveying and Diagnosis With Carbon Nanotube Arrays," Nanotechnology, **17**, pp. 4845–4853.
[14] Bhavnani, S., Fournelle, G., and Jaeger, R. C., 2000, "Immersion-Cooled Heat Sinks for Electronics: Insight From High-Speed Photography," *Proceedings of the Seventh Intersociety Conference on Thermal and Thermomechanical Phenomena in Electronic Systems*, Vol. 2, pp. 310–311.
[15] Ahn, H. S., Sathyamurthi, V., Sinha, N., Lau, S., and Banerjee, D., 2005, "Boiling Experiments on Vertically Aligned Carbon Nanotubes and Using Surface Micromachined Thin Film Thermocouple (TFT)," *Proceedings of the Ninth AIAA/ASME Thermophysics and Heat Transfer Conference*, San Francisco, CA, June 5–8.
[16] Kline, S. J., and McClintock, F. A., 1953, "Describing Uncertainties in Single-Sample Experiments," Mech. Eng. (Am. Soc. Mech. Eng.), **75**, pp. 3–8.
[17] Ghiu, C.-D., and Joshi, Y., 2005, "Boiling Performance of Single-Layered Enhanced Structures," ASME J. Heat Transfer, **127**, pp. 675–683.
[18] Chang, Y. P., 1959, "Wave Theory of Heat Transfer in Film Boiling," ASME J. Heat Transfer, **81**, pp. 1–12.
[19] Banerjee, D., and Dhir, V. K., 2001, "Study of Subcooled Film Boiling on a Horizontal Disc: Part 1 Analysis," ASME J. Heat Transfer, **123**, pp. 271–284.
[20] Banerjee, D., and Dhir, V. K., 2001, "Study of Subcooled Film Boiling on a Horizontal Disc: Part 2 Experiments," ASME J. Heat Transfer, **123**, pp. 285–293.
[21] Banerjee, D., Son, G., and Dhir, V. K., 1996, "Conjugate Thermal and Hydrodynamic Analysis of Saturated Film Boiling From a Horizontal Surface," ASME HTD **334** (Part 3), pp. 57–64.
[22] Gaertner, R. F., 1963, "Distribution of Active Sites in the Nucleate Boiling of Liquids," Chemical Engineering Progress Symposium Series, Vol. 59, pp. 52–61.

Specific Heat Measurement of Three Nanofluids and Development of New Correlations

Ravikanth S. Vajjha

Debendra K. Das[1]
e-mail: ffdkd@uaf.edu

Department of Mechanical Engineering,
University of Alaska Fairbanks,
Fairbanks, AK 99775

This paper presents the specific heat measurements of three nanofluids containing aluminum oxide, zinc oxide, and silicon dioxide nanoparticles. The first two are dispersed in a base fluid of 60:40 by mass of ethylene glycol and water (60:40 EG/W) and the last one in deionized water. Measurements were conducted over a temperature range of 315–363 K, which is the normal range of operation of automobile coolants and building heating fluids in cold regions. The nanoparticle volumetric concentrations tested were up to 10%. The measured values were compared with existing equations for the specific heat of nanofluids. A close agreement with the experimental data was not observed. Therefore, a new general correlation was developed for the specific heat as functions of particle volumetric concentration, temperature, and the specific heat of both the particle and the base fluid from the present set of measurements. The correlation predicts the specific heat values of each nanofluid within an average error of about 2.7%.
[DOI: 10.1115/1.3090813]

Keywords: nanofluids, specific heat, two-phase mixture, concentration dependence, temperature dependence

1 Introduction

Nanofluids are a new class of heat transfer fluids containing dispersion of nanometer-sized particles (less than 100 nm) in conventional fluids. They have gained significant importance in the past decade due to their enhanced heat transfer capabilities. Eastman et al. [1] proved from their experiments that a mere 0.3 vol % of copper nanoparticles, having a mean diameter of less than 10 nm dispersed in ethylene glycol, can enhance the thermal conductivity by 40% over the base fluid. From the experimental findings of Xuan and Li [2], the Nusselt number increases by 40% over the base fluid for a 2% volumetric concentration of copper nanoparticles in water. This encouraging finding has motivated the scientific communities to explore the thermophysical properties of nanofluids, which influences strongly the heat transfer characteristics.

In the cold regions of the world, like Alaska, Canada, and the circumpolar countries, the heat transfer fluids used in automobiles, heat exchangers in industrial plants, and in building heating systems encounter subzero temperatures. Therefore, it is a common practice to use ethylene glycol or propylene glycol mixed with water in different proportions as a heat transfer fluid whose properties are given in the handbook of American Society of Heating, Refrigerating and Air-Conditioning Engineers (ASHRAE) [3]. Generally, ethylene glycol has a better heat transfer performance than propylene glycol, except for its toxicity. A mixture of 60% ethylene glycol and 40% water (60:40 EG/W) by mass is commonly used. Replacing the conventional heat transfer fluids with nanofluids will make systems more efficient. However, to evaluate the thermal performance of nanofluids, their thermophysical properties must be determined. The objective of the present study is to experimentally determine the specific heat of nanofluids, which represents the heat carrying capacity, and then compare the results with available theory.

The experiments were conducted for nanoparticles suspended in two different base fluids. The aluminum oxide (Al_2O_3) and zinc oxide (ZnO) nanoparticles were suspended in a base fluid of 60:40 EG/W mixture, and the silicon dioxide (SiO_2) nanoparticles were suspended in water. Very few experimental studies are available in the literature on the measurements of specific heat of nanofluids. Zhou and Ni [4] presented the measurements of the specific heat of water-based Al_2O_3 nanofluid as a function of concentration at one temperature, 33°C. However, their experiments are limited to only one nanofluid in one type of base fluid, and no correlation has been derived. Namburu et al. [5] presented specific heat measurements of SiO_2 in the 60:40 EG/W base fluid. Their data are also limited to one nanofluid, showing a plot of specific heat as a function of volumetric concentration at a fixed temperature. Therefore, in order to analyze the specific heat data of nanofluids more extensively, comprehensive measurements of three different nanofluids were carried out.

The samples of Al_2O_3, ZnO, and SiO_2 nanofluids tested had average particle sizes of 44 nm, 77 nm, and 20 nm, respectively. These nanofluids were obtained from the manufacturer Alfa Aesar [6] as high concentration (up to 50% by mass) dispersion in water and subsequently different proportions of 60:40 EG/W were added to prepare nanofluid samples of different volumetric concentrations of up to 10%. In making nanofluids, manufacturers use the surfactants to stabilize the dispersion of nanoparticles, which will affect the specific heat of the nanofluid. A variety of surfactants are used by different manufacturers. The information on the surfactant was not available from Alfa Aesar. The experiments of Hong and Marquis [7] show that a surfactant of 1% by weight yielded a good dispersion quality. Their nanofluid in ethylene glycol and water solution gave a dispersion stability of more than 1 month with an ultrasonication time of only 20 min. For such small percentage of surfactant, the effect on the specific heat may not be considerable. However, this is an important area to research by conducting measurements with different surfactants with various weight percentages.

Measured data of specific heat were compared with available theoretical equations, and close agreement was not observed. Therefore, new correlations were developed as a function of sev-

[1]Corresponding author.

Contributed by the Heat Transfer Division of ASME for publication in the JOURNAL OF HEAT TRANSFER. Manuscript received May 31, 2008; final manuscript received December 23, 2008; published online May 6, 2009. Review conducted by Patrick E. Phelan.

eral variables that are physically pertinent. These correlations will be useful in computing accurately the specific heat of nanofluids.

2 Theory

Recent research on nanofluids by Pak and Cho [8] and Maiga et al. [9] has shown that, for low volumetric particle concentrations, the convective heat transfer coefficient of nanofluids can be expressed by modifying the constants of the conventional correlations for laminar and turbulent flows developed for single-phase fluids. However, the proper thermophysical properties of nanofluids must be employed. These properties should be for a two-phase mixture of liquid and solid. A well-known correlation proposed by Dittus and Boelter [10] for convective heat transfer under turbulent flow condition is

$$\mathrm{Nu} = C\ \mathrm{Re}^a\ \mathrm{Pr}^b \tag{1}$$

In the above equation the Nusselt number ($\mathrm{Nu}=hd/k$) expresses the heat transfer coefficient h in a tube of diameter d for a fluid of thermal conductivity k. The Reynolds number ($\mathrm{Re}=Vd\rho/\mu$) of a fluid flow depends on the average velocity V, density ρ, and dynamic viscosity μ. The Prandtl number ($\mathrm{Pr}=C_p\mu/k$) is a function of specific heat C_p. All thermophysical properties including C_p depend on the nanofluid temperature and the nanoparticle volumetric concentration. Due to this dependence of the Prandtl number on the specific heat C_p of the fluid, the specific heat must be known accurately for evaluating the heat transfer coefficient of nanofluids.

For a single-phase fluid, Dittus and Boelter [10] specified $C=0.023$, $a=0.8$, and $b=0.4$ for a fluid being heated. For nanofluids, Pak and Cho [8] empirically derived $C=0.021$, $a=0.8$, and $b=0.5$ by performing experiments on γ-Al_2O_3 and TiO_2 nanofluids. Maiga et al. [9] proposed $C=0.086$, $a=0.55$, and $b=0.5$ from their numerical simulations under constant heat flux boundary conditions. Therefore, it is evident that correlations for a single-phase fluid can be extended to nanofluids. Notice from Eq. (1) that for the same Reynolds number and Prandtl number of different fluids, the Nusselt number remains unchanged. However, because the thermal conductivity k of nanofluids is higher than the base fluid, the heat transfer coefficient h becomes higher, providing the superior heat transfer performance of nanofluids. Equation (1) is a simple form of the convective flow equation, and nanofluids may involve dependence of other parameters such as the particle Peclet number, as presented by Xuan and Li [2].

Furthermore, for evaluation of the total heat transfer rate $\dot{q}$ from one fluid to another in a heat exchanger, such as in automobile radiators or building heating coils, the appropriate equation from Bejan [11] is

$$\dot{q} = \dot{m}C_p(T_i - T_o) \tag{2}$$

In Eq. (2) $\dot{m}$ is the mass flow rate of the fluid inside the flow passage, and T_i and T_o are the inlet and outlet temperatures of the fluid when the fluid transfers $\dot{q}$ amount of heat to the air surrounding it. Because specific heat directly affects the heat transfer $\dot{q}$, it must be known precisely. Another important parameter in heat transfer is thermal diffusivity $\alpha_{nf}=k_{nf}/(\rho_{nf}C_{pnf})$, which is dependent on the specific heat. This characteristic determines how fast heat will diffuse through the nanofluid such as the flow of heat from automobile engine cylinders to the coolant. Therefore, it is crucial to have accurate correlation for evaluating the specific heat of various nanofluids. Due to the aforementioned reasons, we have focused our attention on developing new correlations to determine the specific heat of nanofluids accurately in this paper.

2.1 Specific Heat Equations. With solid particles dispersed in a liquid, the equation of the specific heat for the two-phase mixture will be a function of the particle concentration. Such a correlation for nanofluids was presented by Pak and Cho [8], taking the idea from the liquid-particle mixture theory.

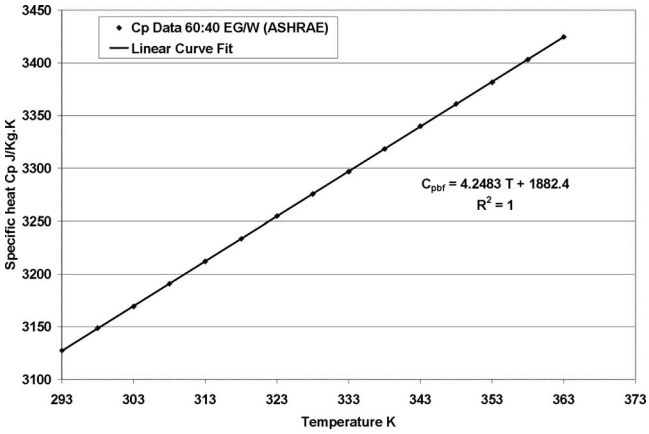

Fig. 1 Development of a curve-fit equation for the specific heat of the base fluid (60:40 EG/W) from ASHRAE [3] data

$$C_{pnf} = \phi C_{ps} + (1 - \phi)C_{pbf} \tag{3}$$

where C_{pnf} is the specific heat of the nanofluid, C_{ps} is the specific heat of the solid nanoparticle, ϕ is the particle volumetric concentration, and C_{pbf} is the specific heat of the base fluid.

Subsequently Xuan and Roetzel [12] modified this correlation by assuming thermal equilibrium between the nanoscale solid particles and the liquid phase by rewriting the above equation to include the density.

$$C_{pnf} = \frac{\phi\rho_s C_{ps} + (1 - \phi)\rho_{bf}C_{pbf}}{\rho_{nf}} \tag{4}$$

where ρ_s is the density of the solid nanoparticle, ρ_{bf} is the density of the base fluid, and ρ_{nf} is the density of the nanofluid. The product of density and specific heat is the volumetric heat capacity of each constituent and that of the nanofluid.

Both the Pak and Cho equation (Eq. (3)) and the Xuan and Roetzel equation (Eq. (4)) require the specific heat of a base fluid to calculate the specific heat of a nanofluid. In our experiments, one of the base fluids was 60:40 EG/W. The specific heat data of the base fluid were obtained from ASHRAE [3] and was plotted in Fig. 1 to develop a curve-fit relation over the temperature range at which the experiments were conducted. The data fit nicely with a coefficient of determination $R^2=1$ by a linear curve-fit.

$$C_{pbf} = 4.2483T + 1882.4 \tag{5}$$

where C_{pbf} is in J/kg K and 293 K $< T <$ 363 K.

Additionally, Eq. (4) requires an expression for the density of base fluid to calculate the specific heat of nanofluids. In Fig. 2 the curve-fit polynomial for the density of base fluid, 60:40 EG/W from ASHRAE [3] data, has been developed.

$$\rho_{bf} = -0.0024T^2 + 0.963T + 1009.8, \quad R^2 = 1 \tag{6}$$

where density is in kg/m^3 and 293 K $< T <$ 363 K.

Table 1 gives the density and specific heat of the nanoparticles used in the present research. The density values of all nanoparticles are provided by the manufacturer, Alfa Aesar [6]. The specific heats of Al_2O_3 and SiO_2 nanoparticles are taken from Ref. [13] and that of ZnO is taken from Ref. [14].

3 Experimental Setup and Procedure

The experimental setup for measuring the specific heat of any liquid is shown in Fig. 3. The apparatus consists of a 7.6 cm (3 in.) inside diameter and 16.76 cm (6.6 in.) long acrylonitrile butadiene styrene (ABS) container. This low thermal conductivity and low diffusivity material is selected to minimize heat flow from the fluid into the container wall and to ensure that the major portion of heat goes into the fluid to increase its temperature. The apparatus

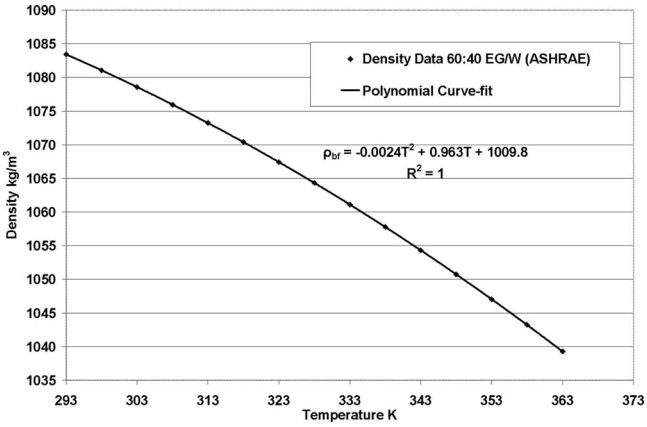

Fig. 2 Development of curve-fit relation for the density of base fluid (60:40 EG/W) from ASHRAE [3] data

is designed to hold about 0.66 l of liquid. The nanofluids are heated from about 315 to 363 K by using an electrical immersion heater, as shown in Fig. 3. Six copper-Constantan thermocouples are placed in the apparatus. Four thermocouples are placed within the liquid volume; one at the top, one at the bottom, and two in the middle (one on the heating coil). The average of the four temperatures in the liquid is taken as the mean temperature. One thermocouple is placed on the outer surface of the container and one at the midpoint of the insulation. These thermocouples are connected to a data logger that records the temperature data at every 15 s interval. The container is insulated by two layers of insulation. The inner layer is 6.35 cm (2.5 in.) thick fiber glass insulation surrounding the container that fits the contour of the cylindrical container. The outer layer consists of 10 cm (4 in.) thick extruded polystyrene board insulation. This arrangement minimizes the heat flow away from the fluid. A Variac is used to supply constant wattage to the immersion heater, and the power input into the nanofluid is monitored by a power meter.

The thermal energy supplied to the electrical heater heats the nanofluid, heating coil, container, and the insulation. Each of these components was weighed carefully in a mass balance. A small amount of heat is also transmitted to the environment through the insulation. The specific heat of a nanofluid was calculated from the following equation:

Table 1 Properties of nanoparticles

Type of nanoparticle	Density of particle (kg/m^3)	Specific heat of particle (J/kg K)
Al_2O_3 (44 nm)	3600	765
SiO_2 (20 nm)	2220	745
ZnO (77 nm)	5600	514

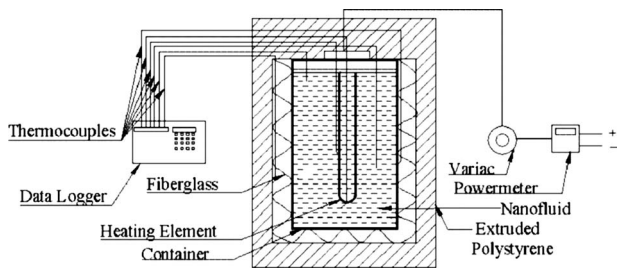

Fig. 3 Experimental setup for specific heat measurement of nanofluids

$$C_{pnf} = \frac{\dot{Q}\Delta t - m_C C_{PC}\Delta T_C - m_{CO} C_{PCO}\Delta T_{CO} - m_{IN} C_{PIN}\Delta T_{IN} - \dot{q}_L \Delta t}{m_{nf}\Delta T_{nf}} \tag{7}$$

where $\dot{Q}$ is the heat applied to the electrical heater in watts determined from the power meter. The time interval Δt is measured by the data logger (s), ΔT is the temperature rise (K), m is the mass (kg), C_P is the specific heat (J/kg K), and $\dot{q}_L$ is the heat transfer to the environment (W). The subscripts C represents the container, CO the heating coil, and IN the insulation. The masses of the container, coil, and insulation are measured individually by an electronic mass balance. The specific heat of container (ABS plastic) is taken from a handbook, and the specific heats of the coil and insulations are taken from Ref. [13]. The temperature change ΔT is recorded at every 15 s interval. The surface temperatures of the insulations and their dimensions are measured at the same time interval. The thermal conductivities of insulations are taken from Ref. [13]. Using these data the heat transfer to the environment through the insulation is calculated from the heat conduction equation.

4 Results and Discussions

4.1 Uncertainty of Experimental Data. From Eq. (7), the uncertainty in the specific heat measurement can be determined from the standard approach presented by Coleman and Steele [15]. The parameters we measured were the rate of heat input to the nanofluid, the temperature, and the mass of several objects and dimensions of insulations.

$$\frac{\delta C_{pnf}}{C_{pnf}} = \left[\left(\frac{\delta \dot{Q}}{\dot{Q}}\right)^2 + \left(\frac{\delta m_c}{m_c}\right)^2 + \left(\frac{\delta \Delta T_C}{\Delta T_C}\right)^2 + \left(\frac{\delta m_{CO}}{m_{CO}}\right)^2 + \left(\frac{\delta \Delta T_{CO}}{\Delta T_{CO}}\right)^2 + \left(\frac{\delta m_{IN}}{m_{IN}}\right)^2 + \left(\frac{\delta \Delta T_{IN}}{\Delta T_{IN}}\right)^2 + \left(\frac{\delta \dot{q}_L}{\dot{q}_L}\right)^2 + \left(\frac{\delta m_{nf}}{m_{nf}}\right)^2 + \left(\frac{\delta \Delta T_{nf}}{\Delta T_{nf}}\right)^2 \right]^{1/2} \tag{8}$$

Specific heats of the container, heating element, and insulations were directly read from tabulated values in books and were not measured quantities in this experiment. The data acquisition system was capable of sampling temperatures at intervals of microseconds. Therefore, the uncertainty in Δt of 15 s was considered negligible. For the power meter, $(\delta \dot{Q}/\dot{Q})$ is about 1%. For the electronic precision mass balance, $(\delta m/m)$ is about 0.5%. The uncertainty in measurements of temperature for copper-Constantan thermocouple used in this apparatus is $\pm 0.5°$C between $-100°$C and $400°$C. Therefore, at the mean temperature of $50°$C within the range of measurements, $(\delta T/T) = 1\%$. The uncertainty in calculating the heat loss through the insulation can be expressed as

$$\frac{\delta \dot{q}_L}{\dot{q}_L} = \left[\left(\frac{\delta A}{A}\right)^2 + \left(\frac{\delta T_C}{T_C}\right)^2 + \left(\frac{\delta T_O}{T_O}\right)^2 + \left(\frac{\delta X_1}{X_1}\right)^2 + \left(\frac{\delta X_2}{X_2}\right)^2 \right]^{1/2} \tag{9}$$

where X_1 and X_2 are thicknesses of insulations, and T_C and T_O are the surface temperatures of insulations. The thermal conductivities of insulations were taken from Ref. [13]. The uncertainty in length measurement $\delta L/L$ by the modern metrological gauge is about 0.5%. The area A is proportional to the square of the length dimension L, so the uncertainty in area measurement is $\delta A/A = [(2(\delta L/L))^2]^{1/2}$. Using the above numbers $\delta \dot{q}_L/\dot{q}_L = 1.87\%$. Finally combining all the uncertainties together in Eq. (8) the uncertainty in measurement of the specific heat of nanofluid is $(\delta C_{pnf}/C_{pnf}) = 3.1\%$.

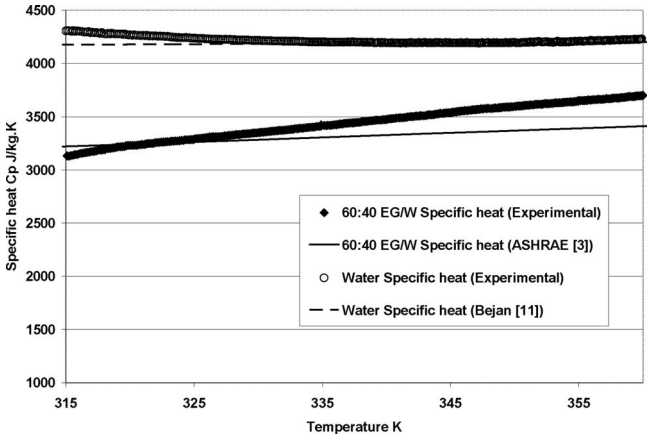

Fig. 4 Comparison of measured values of the specific heat of two base fluids, 60:40 EG/W and water, with the ASHRAE [3] and Bejan [11] data, respectively

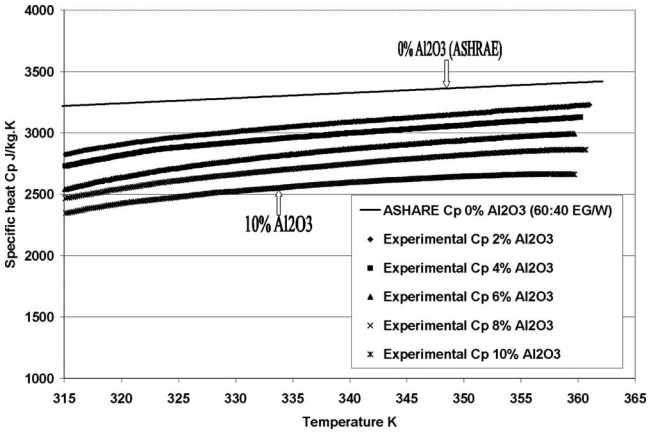

Fig. 5 Measured specific heat values for different concentrations of the Al_2O_3 nanofluid in a base fluid of 60:40 EG/W

4.2 Benchmark Test Cases. Before measuring the specific heat of any nanofluid with this apparatus, benchmark tests were conducted with the two base fluids, 60:40 EG/W and deionized water whose specific heats are accurately known from the ASHRAE [3] handbook and Bejan [11], respectively. A mass of about 0.7 kg of base fluid was introduced into the container for the specific heat measurement. A constant heat rate of 40 W was supplied to the heating element to increase the temperature of water to 363 K. The temperature change was recorded at every 15 s interval.

The results of these measurements and the data from ASHRAE [3] and Bejan [11] are presented in Fig. 4 over a temperature range of 315–363 K. Since we have measured data at every 15 s, the data points are numerous. Therefore, the experimental results appear as a continuous line in Fig. 4. A good agreement is observed between the current measurements and the published data. The maximum error between the measurement and ASHRAE data for 60:40 EG/W is about 7.0%, and an average error of 4% is observed. A maximum error of about 3.1% and an average error of 1.9% are observed between the measurement and the data of Bejan for water.

4.3 Al_2O_3 Nanofluid. After verifying the accuracy of the apparatus and the measurement procedure by comparing the measured specific heat values of the base fluid, comprehensive measurements of specific heat were conducted for the Al_2O_3 nanofluid, with particle volumetric concentrations of 2%, 4%, 6%, 8%, and 10% dispersed in the base fluid of 60:40 EG/W. Figure 5 presents the data for Al_2O_3 nanofluid. It is observed that the specific heat of this nanofluid decreases with an increase in the volume concentration. Furthermore, like many single-phase liquids, the specific heat of this nanofluid also increases with temperature.

From the data, subsequently empirical correlations were developed. Yaws [16] presented the specific heat correlations of many liquids in the cubic polynomial form, as shown in Eq. (10).

$$C_{pnf} = A_i + B_i T + C_i T^2 + D_i T^3 \tag{10}$$

where $i = 1-5$ is the number of concentrations.

Following that approach we developed correlations for the Al_2O_3 nanofluid in the same form. For each concentration in Fig. 5, a cubic polynomial in the form of Eq. (10) was developed with a coefficient of determination $R^2 = 0.99$. Next, all these coefficients A, B, C, and D were curve fitted against the five concentrations. It was found that only a fourth order polynomial (Eq. (11)) could give a good coefficient of determination $R^2 \geq 0.99$.

$$A_i = a_1\phi^4 + a_2\phi^3 + a_3\phi^2 + a_4\phi + a_5 \tag{11}$$

Similarly, three other fourth order polynomials are necessary for B_i, C_i, and D_i. Das [17] presented a complete set of polynomials and the resulting correlation for the Al_2O_3 nanofluid in the form C_{pnf} (T, ϕ). However, these polynomials are highly oscillatory showing high and low peaks. Although the above approach mathematically includes the dependence of both temperature and concentration, calculating the specific heat at intermediate values of ϕ and T may yield highly off results. Moreover, this equation is applicable to only Al_2O_3 nanoparticles suspended in a base fluid of 60:40 EG/W mixture, so similar tedious polynomials have to be developed for other nanofluids. Therefore, this approach was discarded, and an attempt was made to develop a simpler and more general correlation. The development of this new correlation, which includes the dependence of temperature, concentration, and specific heat of both the nanoparticles and the base fluid used in the nanofluids, is described in Sec. 4.8.

4.4 Volumetric Heat Capacity. The volumetric heat capacity $(C_{pvnf} = \rho_{nf} C_{pnf})$ of a nanofluid is the quantity of heat required to raise the temperature of a unit volume of nanofluid by 1°C. It is of interest to determine how this heat capacity is affected by the presence of nanoparticles in a liquid. Figure 6 presents the volumetric heat capacity of an Al_2O_3 nanofluid at three different temperatures, 310 K, 340 K, and 360 K, as a function of particle volumetric concentration. It is observed that the volumetric heat capacity calculated from the experimental specific heat values and

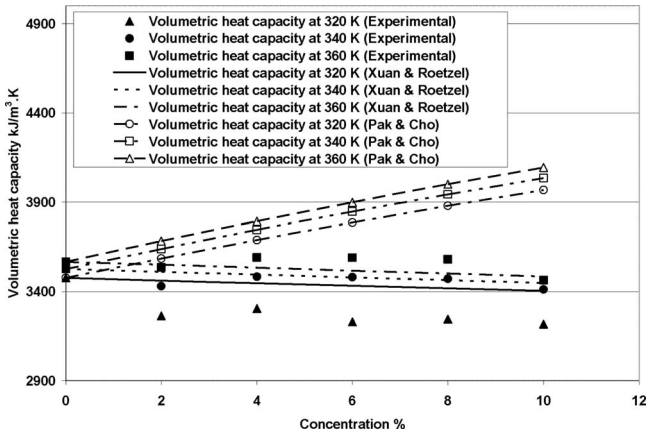

Fig. 6 Variation in volumetric heat capacity of the Al_2O_3 nanofluid with concentration at three different temperatures

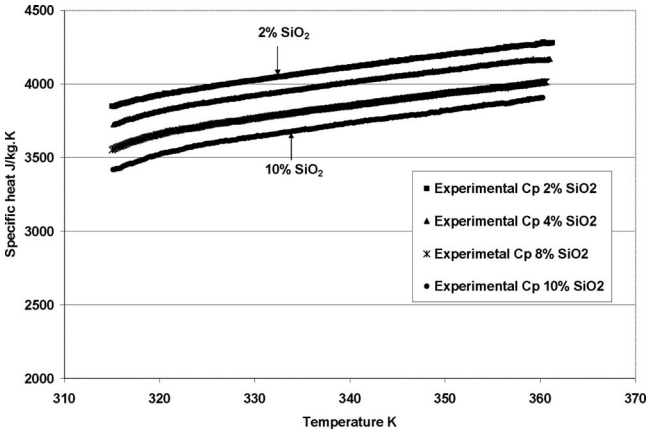

Fig. 7 Variation in the specific heat of SiO_2 nanofluid of different volumetric concentrations with temperature

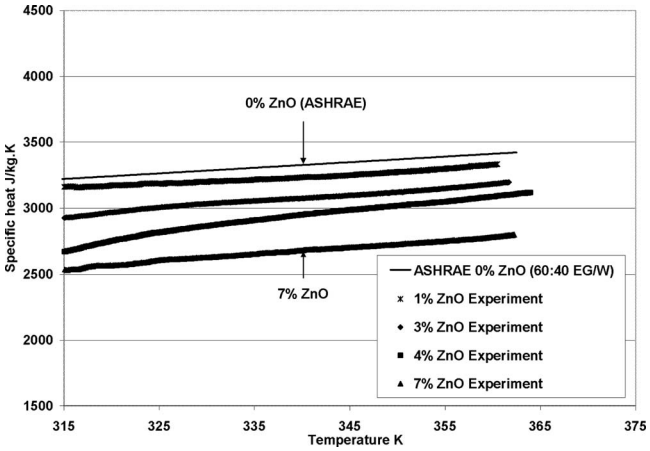

Fig. 8 Variation in the specific heat with temperature for a ZnO nanofluid at different particle volume concentrations

from the Xuan and Roetzel [12] correlation remains nearly constant with a variation in concentration. The density of the nanofluid increases, and the mass-based specific heat decreases with an increase in concentration. The product of these two opposite changes nullifies the effect of concentration variation on the volumetric heat capacity, making it a constant. It is also observed from Fig. 6 that the volumetric heat capacity calculated from the Pak and Cho [8] correlation increases with the increase in concentration. This is because the Pak and Cho correlation overpredicts the specific heat value when compared with the experimental data.

The heat transfer rate in a heat exchanger is $\dot{q}=\dot{V}C_{pv}\Delta T$. A constant volumetric heat capacity indicates that no extra volumetric flow rate $\dot{V}$ will be necessary in a heat exchanger when replacing the conventional fluid with nanofluid for the same amount of heat transfer rate $\dot{q}$ under a similar temperature change ΔT of the fluid. The volumetric heat capacity increases with an increase in temperature. From Fig. 6 we notice that, for a temperature increase of 12%, the volumetric heat capacity of the experimental data increases by 8%. Therefore, the use of nanofluid is more beneficial at higher temperatures.

4.5 SiO_2 Nanofluid. Figure 7 displays the measured specific heat values of the SiO_2 nanofluid varying in particle volumetric concentration from 2% to 10%. In order to include the effect of a different base fluid on the specific heat of a nanofluid, this experiment was conducted with water as the base fluid. The results in Fig. 7 show that the specific heat of this nanofluid increases moderately with an increase in temperature. However, the specific heat decreases substantially with an increase in particle volumetric concentration.

4.6 ZnO Nanofluid. Figure 8 presents the experimental values of the specific heat of the ZnO nanofluid. The base fluid in this experiment was 60:40 EG/W. The specific heat results show similar trends, as shown by the prior two nanofluids, namely, an increase in the specific heat with an increase in temperature and a decrease in the specific heat with an increase in particle volumetric concentration.

4.7 Comparison With Existing Correlations. A major objective of the present study was to verify if Eq. (3), given by Pak and Cho [8], and Eq. (4), given by Xuan and Roetzel [12], match the measured specific heat values accurately. Figure 9 shows the comparison between the experimental and the theoretical specific heat values for a 7% volumetric concentration of the ZnO nanofluid. An overprediction of about 17% by the Pak and Cho equation is observed. The error with the Xuan and Roetzel equation increases with the temperature, reaching a maximum value of 9.5% at 363 K. It appears that these equations do not represent the specific heat of a nanofluid properly. The conventional formula, Eq. (4), is based on the thermal equilibrium between the nanoparticles and the liquid phase. We believe that the solid phase particles and the liquid phase are not in thermal equilibrium. Due to their higher thermal diffusivity, the nanoparticles absorb heat faster than the base fluid and attain a higher temperature than the base fluid. The situation deviates more and more from the thermal equilibrium when the temperature increases with the addition of more heat. Due to a higher temperature rise of particles, an energy balance yields a higher specific heat value for the nanofluid. This conjecture is confirmed by comparing the present experimental specific heat values with Eq. (4), as observed in Fig. 9. The percentage deviation increases with the increase in temperature. It is also clear that the deviation will increase with an increase in the particle volumetric concentration. Furthermore, Eq. (4) does not have the temperature as a variable exclusively. The temperature effect is accounted for mildly via the base fluid, which is not adequate. Therefore, it is imperative that a new correlation is developed as function of particle and fluid specific heats, concentration, and temperature for accurate calculation of the specific heat of nanofluids.

4.8 General Correlation for Three Nanofluids. Finally, from the measured data of three nanofluids in two base fluids, a general correlation was developed for the specific heat. It is well known that the specific heat should be dependent on temperature, particle volumetric concentration, and specific heat of the nano-

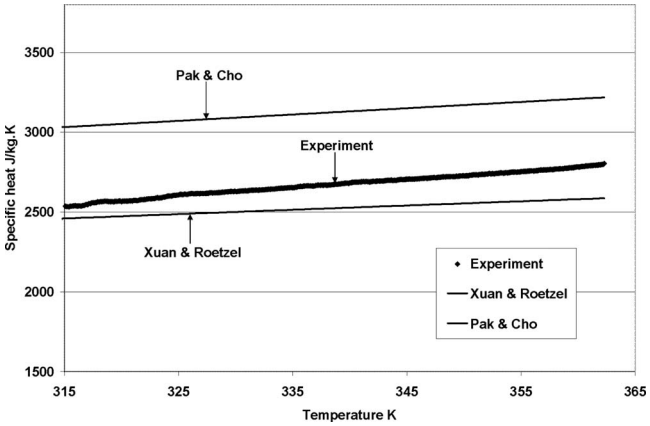

Fig. 9 Comparison of the experimental specific heat values with the Pak and Cho equation (Eq. (3)) and the Xuan and Roetzel equation (Eq. (4)) for a 7% ZnO nanofluid

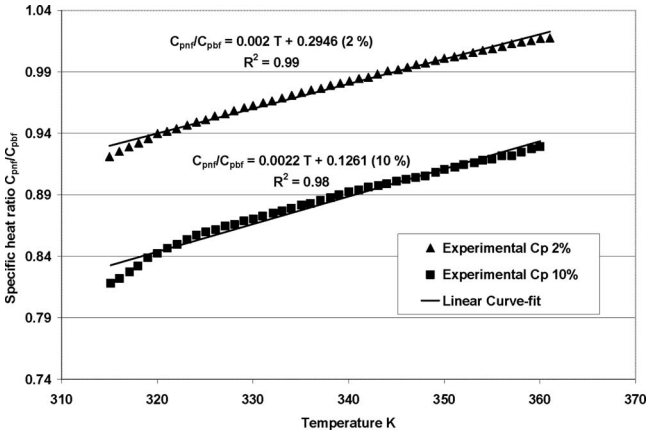

Fig. 10 Variation in the specific heat ratio of the Al_2O_3 nanofluid with temperature for two particle volumetric concentrations

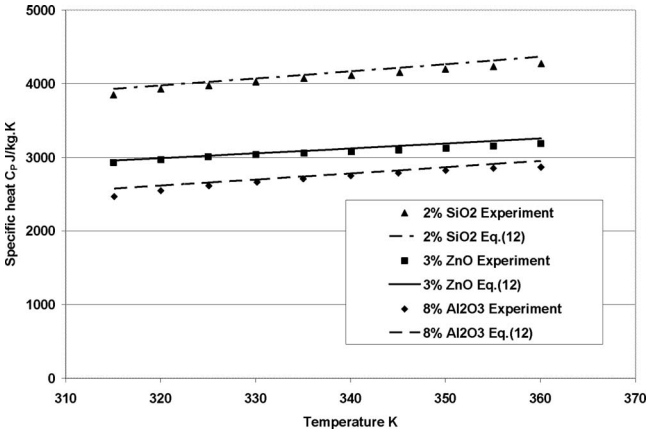

Fig. 11 Comparison of the experimental specific heat values of 2% SiO_2, 3% ZnO, and 8% Al_2O_3 with the present correlation presented as Eq. (12)

particle and the base fluid. The correlation was developed as a specific heat ratio (C_{pnf}/C_{pbf}) of the nanofluid to the base fluid so that it can be used for different base fluids. First the specific heat ratio was plotted against temperature for two different particle volume concentrations to determine the nature of variation in the specific heat ratio with temperature and concentration. Figure 10 presents the variation in the Al_2O_3 nanofluid with temperature for two particle volumetric concentrations. From this figure, one can observe that the specific heat ratio of the nanofluid is a linear function of temperature within the range of the experiment and is inversely proportional to the concentration of the nanofluid.

With these observations, a new correlation was derived using the statistical software of Silva and Silva [18]. The equation that best fits the experimental data of all three nanofluids prepared from two kinds of base fluids is given as Eq. (12).

$$\frac{C_{pnf}}{C_{pbf}} = \frac{\left((A^*T) + B^*\left(\frac{C_{ps}}{C_{pbf}}\right)\right)}{(C+\phi)} \tag{12}$$

The curve-fit coefficients for each nanofluid are tabulated in Table 2. This equation is applicable over the temperature range of $315\ \text{K} < T < 363\ \text{K}$ for volumetric concentrations ranging from $0 < \phi \leq 0.1$ for Al_2O_3 and SiO_2 nanofluids and $0 < \phi \leq 0.07$ for ZnO nanofluid.

In order to demonstrate the accuracy of Eq. (12), three arbitrary particle volumetric concentrations were chosen for three nanofluids. They are 2% SiO_2, 3% ZnO, and 8% Al_2O_3. The results of calculations using Eq. (12) and the experimental data of specific heat are presented in Fig. 11. An excellent agreement between the new correlation and experimental data is observed.

5 Conclusions

The specific heat values of an EG/W mixture (60:40 by mass) without any nanoparticle suspension obtained from the experiments show good agreement with those of the ASHRAE [3] data, validating the accuracy of experimental setup and procedure. Measurements show that the specific heat value decreases as the volumetric concentration of nanoparticles increases. This decrease is compatible with the lower specific heat of particles being added to the base fluid. The specific heat increases with an increase in temperature. Existing equations do not predict the specific heat of nanofluids accurately. Therefore, a general specific heat correlation, developed from the experimental data of Al_2O_3, SiO_2, and ZnO nanofluids, takes into account particle volume concentration, temperature, and specific heat of both the particles and that of the base fluid. These data include two different base fluids: (i) water and (ii) 60:40 EG/W. This new correlation is applicable for concentrations up to 10% for Al_2O_3 and SiO_2 nanofluids, and up to 7% for a ZnO nanofluid, within the temperature range of 315–363 K. A fair estimate of specific heats of other nanofluids, for which no correlation exists, can be made from this general equation. Future measurements of other nanofluids should establish the universality of this correlation or any refinement.

Table 2 Curve-fit coefficients for different nanofluids

Nanofluid	*A*	*B*	*C*	Max. error (%)	Avg. absolute error (%)
Al_2O_3	0.0008911	0.5179	0.4250	5	2.28
SiO_2	0.001769	1.1937	0.8021	3.1	1.5
ZnO	0.0004604	0.9855	0.299	4.4	2.7

Acknowledgment

Financial assistance from the Department of Mechanical Engineering at the University of Alaska Fairbanks is gratefully acknowledged. Additional support has been provided by Alaska EPSCoR, with funding from the National Science Foundation Award No. 0701898 and the state of Alaska.

References

[1] Eastman, J. A., Choi, S. U. S., Li, S., Yu, W., and Thompson, L. J., 2001, "Anomalously Increased Effective Thermal Conductivities of Ethylene Glycol-Based Nanofluids Containing Copper Nanoparticles," Appl. Phys. Lett., **78**, pp. 718–720.
[2] Xuan, Y., and Li, Q., 2003, "Investigation on Convective Heat Transfer and Flow Features of Nanofluids," ASME J. Heat Transfer, **125**, pp. 151–155.
[3] ASHRAE, 2005, *ASHRAE Handbook: Fundamentals*, American Society of Heating, Refrigerating and Air-Conditioning Engineers Inc., Atlanta, GA.
[4] Zhou, S., and Ni, R., 2008, "Measurement of the Specific Heat Capacity of Water-Based Al_2O_3 Nanofluid," Appl. Phys. Lett., **92**, p. 093123.
[5] Namburu, P. K., Kulkarni, D. P., Dandekar, A., and Das, D. K., 2007, "Experimental Investigation of Viscosity and Specific Heat of Silicon Dioxide Nanofluids," Micro & Nano Letters, **2**(3), pp. 67–71.
[6] Alfa Aesar, 2007, URL: http://www.alfaaesar.com.
[7] Hong, H., and Marquis, F. D. S., 2007, "Carbon Nanoparticle-Containing Hydrophilic Nanofluid," U.S. Patent Application No. 2007/0158610 A1, pending.
[8] Pak, B. C., and Cho, Y. I., 1998, "Hydrodynamic and Heat Transfer Study of Dispersed Fluids With Submicron Metallic Oxide Particles," Exp. Heat Transfer, **11**, pp. 151–170.
[9] Maiga, S. B., Nguyen, C. T., Galanis, N., Roy, G., Mare, T., and Coqueux, M., 2006, "Heat Transfer Enhancement in Turbulent Tube Flow Using Al_2O_3 Nanoparticle Suspension," Int. J. Numer. Methods Heat Fluid Flow, **16**, pp. 275–292.
[10] Dittus, P. W., and Boelter, L. M. K., 1985, "Heat Transfer in Automobile Radiators of the Tubular Type," Int. Commun. Heat Mass Transfer, **12**, pp. 3–22.

[11] Bejan, A., 1993, *Heat Transfer*, 2nd ed., Wiley, New York.
[12] Xuan, Y., and Roetzel, W., 2000, "Conceptions for Heat Transfer Correlations of Nanofluids," Int. J. Heat Mass Transfer, **43**, pp. 3701–3707.
[13] Incropera, F. P., and DeWitt, D. P., 1996, *Introduction to Heat Transfer*, 3rd ed., Wiley, New York.
[14] Adachi, S., 2004, *Handbook on Physical Properties of Semiconductors*, Vol. 3, Springer-Verlag, Berlin, p. 68.
[15] Coleman, H. W., and Steele, W. G., 1999, *Experimentation and Uncertainty Analysis for Engineers*, 2nd ed., Wiley, New York.
[16] Yaws, C. L., 1977, *Physical Properties—A Guide to the Physical, Thermodynamic and Transport Property Data of Industrially Important Chemical Compounds*, McGraw-Hill, New York.
[17] Das, D. K., 2008, "Specific Heat Measurement of Different Nanofluids and Their Influence on Heat Transfer," *Proceedings: Institution of Engineers (India), 49th Session Technical Annual*, Orissa State Center, India, pp. 1–8.
[18] Silva, W. P., and Silva, C. M. D. P. S., 2008, "LAB Fit Curve Fitting Software (Nonlinear Regression and Treatment of Data Program) V 7.2.42 (1999-2008)," available from worldwide web: www.labfit.net.

M. Ferraiuolo
Junior Researcher
e-mail: m.ferraiuolo@cira.it

A. Riccio
Senior Researcher
e-mail: a.riccio@cira.it

Laboratory of Computational Mechanics,
CIRA-Italian Aerospace Research Centre,
via Maiorise snc,
Capua, 81043, Italy

M. Gigliotti
Associate Professor
University of Poitiers,
Laboratoire de Mécanique et Physique des Matériaux (LMPM),
Ecole Nationale Supérieure de Mécanique et Aérotechnique (ENSMA),
1 Avenue Ader,
86961 Chasseneuil-Futuroscope, France
e-mail: marco.gigliotti@lmpm.ensma.fr

D. Tescione
Senior Researcher
Laboratory of Computational Mechanics,
CIRA-Italian Aerospace Research Centre,
via Maiorise snc,
Capua, 81043, Italy
e-mail: d.tescione@cira.it

R. Gardi
System Engineer
e-mail: r.gardi@cira.it

G. Marino
Project Manager
e-mail: g.marino@cira.it

Space Programs Office,
CIRA-Italian Aerospace Research Centre,
via Maiorise snc,
Capua, 81043, Italy

Thermostructural Design of a Flying Winglet Experimental Structure for the EXPERT Re-entry Test

Within the framework of the European Experimental Re-entry Test Bed (EXPERT) Program, aimed at improving the understanding of physical phenomena occurring during the return of space vehicles from space to earth, the design of a flying winged experimental payload has been performed in order to assess the thermomechanical behavior and resistance of ultrahigh temperature ceramics (UHTC) in real flight aerothermal environment. The EXPERT flying winglet article is intended to reproduce such conditions. Particular interest covers the design of the interfaces between the UHTC winglet and the EXPERT capsule thermal protection systems since thermal stresses arise during the re-entry phase. The fixation of the winglet to the capsule is achieved by means of dedicated bolts that must tolerate mechanical loads occurring at the first stages of the flight, that is, lift-off, ascent, and separation stages. The thermostructural design is performed by employing ANSYS/Workbench finite element commercial code; simulations take into account transient thermostructural loading conditions, the elastic-fragile behavior of the ceramic materials, and the temperature dependent elastic-plastic behavior of the capsule thermal protection systems. In the postprocessing phase, UHTC critical areas have been identified by following two different approaches. The first approach is deterministic and consists in applying a maximum stress criterion, the stress at a node is compared with the temperature dependent strength at that node. The second approach, which is commonly employed for elastic-fragile materials, is probabilistic and consists in applying a Weibull-like failure criterion. Thermal and structural analyses simulating the re-entry phase have demonstrated that the maximum stresses and temperatures evaluated do not exceed their corresponding limits. Then, a configuration respecting all the requirements of the design has been identified, and its thermal and mechanical performances are discussed in detail. [DOI: 10.1115/1.3109242]

Keywords: winglet, thermostructural analyses, ultra high temperature ceramics, hot structures

1 Introduction

Aircraft structures designed for supersonic flights are subjected to aerodynamic heating caused by the air in the boundary layer being progressively slowed down. This process generates heat and consequently all the external surfaces on the aircraft are heated. This in turn leads to nonuniform transient temperatures that produce thermal stresses and deformations. Likewise, spacecraft structures are subjected to aerodynamic heating during launch and re-entry phases of their operations, in addition to solar radiation while operating in space [1].

The design of structures for winged flight vehicles that fly through the Earth's atmosphere poses several challenges to structural designers. First of all, the selection of materials and design structures that can withstand the aerothermal loads of high speed flight. These loads are applied on the external surfaces of the flight vehicle and consist of pressure, skin friction (shearing stresses), and aerodynamic heating (heat flux). Pressure and skin friction have important roles in aerodynamic lift and drag, while aerodynamic heating is the predominant structural load [2,3].

Aerodynamic heating induces elevated temperatures that can affect the structural behavior in the following two ways.

1. Elevated temperatures degrade the material's ability to withstand loads since elastic properties, such as Young's modulus, are significantly reduced. Moreover, allowable stresses are reduced.
2. Thermal stresses are generated by the restrained local or global thermal expansions/contractions.

The development of future low risk re-entry vehicles is strongly linked to the capability of employing reusable sharp hot structures. This choice is driven by the need to improve safety and to

Contributed by the Heat Transfer Division of ASME for publication in the JOURNAL OF HEAT TRANSFER. Manuscript received May 20, 2008; final manuscript received February 6, 2009; published online May 5, 2009. Review conducted by Ben Q. Li.

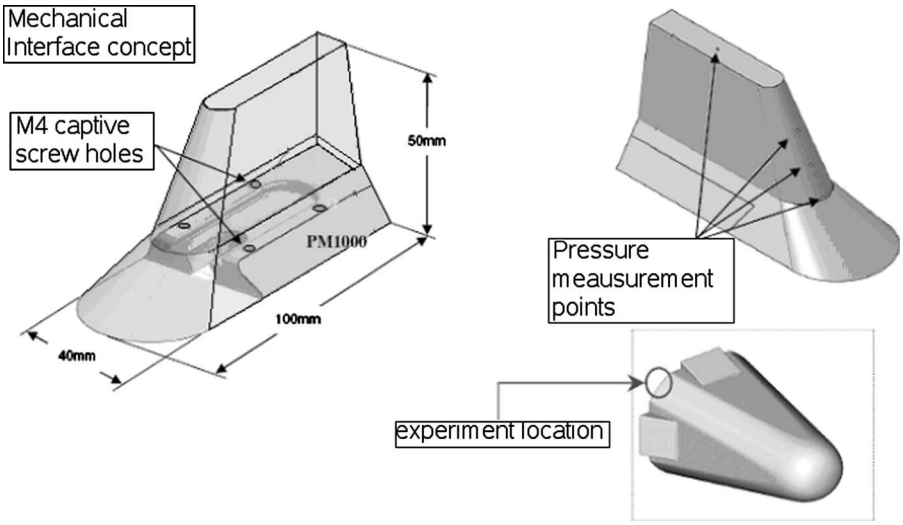

Fig. 1 Winglet connection with PM1000 support interface and winglet location on the EXPERT capsule

allow typical aircraft maneuverability. The sharp hot structures (SHS) technology consists of adopting ultra high temperature ceramics (UHTC) that are characterized by high thermal, mechanical, and chemical properties [4–6].

Unlike classic thermal protection systems (TPSs), hot structures have both thermal and structural functions; they work well at elevated temperatures, near the radiation equilibrium condition where aerodynamic heating is entirely radiated to the external space and no thermal energy is transferred in the internal structure of the re-entry vehicle [7].

The idea is to adopt this technology for critical areas of the vehicle such as nose cap and wing leading edge. During hypersonic flight, significantly higher heating occurs on a sharp structural component compared with a blunt one [8]; this is due to the well-known functional dependence of the stagnation point heat flux on the inverse of the square root of the curvature radius. Therefore, to use a sharp configuration, new materials capable of withstanding the high temperatures must be developed. The high temperatures and the high thermal gradients can induce in sharp hot structures relevant thermal stresses.

The European Experimental Re-entry Test Bed (EXPERT) is an in-flight research program, with the objective to improve the understanding of critical aerothermodynamics phenomena, such as transition, catalysis, blackout, real gas effects, and shock wave boundary layer interactions, associated with flap efficiency and heating. It includes multiple Space Launch Vehicle VOLNA flights on generic configurations. At present two ballistic flights (5 km/s and 6 km/s) are planned [9].

In the frame of the EXPERT Program, the Italian Aerospace Research Centre (CIRA) is developing a scientific payload, which will be mounted on the EXPERT capsule, devoted to the in-flight testing of an innovative class of high temperature materials that can be considered as potential candidate materials for new concepts of hot structures.

The objective of the technical activities is the design, manufacturing and testing of a structural subcomponent represented by a small winglet made of ultra high temperature ceramics. The UHTC chosen for the experiment is a dense (more than 5 kg/dm^3) ZrB_2-SiC composite ceramic, which can withstand temperatures higher than 2500°C.

The winglet-shaped test article chosen for such application is designed in order to achieve significant temperatures at its tip during the re-entry phase and in order to prevent unacceptable heating at the interface with the EXPERT capsule.

Since the payload is far from the stagnation point in a zone where heat fluxes are relatively low, the winglet shape is conceived in such a way to provoke local perturbations of the heat fluxes around it and to engender critical conditions for the materials under test. These perturbations should not influence critically the EXPERT capsule TPS. The payload/capsule interface design should be aimed at the minimization of the thermal stresses [10,11] caused by the difference in terms of thermal expansion coefficient and Young's modulus between the ceramic and the metallic parts. The design drivers can be summarized in the following lines.

1. The winglet has to be shaped in order to generate high thermal fluxes at its tip.
2. Temperatures on thermal protection systems should remain lower than their limits.
3. Mechanical interfaces have to be designed in order to prevent the failure of the payload, since the difference between the coefficient of thermal expansion of the materials in contact is relevant.
4. The payload weight must not modify the aerodynamics of the capsule.
5. A potential failure of the payload must not compromise the integrity of the capsule.

Moreover, the article has to resist the remarkable accelerations encountered during the capsule mission [12].

Figure 1 shows the winglet external shape (maximum burden) and its aerodynamic configuration. The ceramic part of the winglet is mounted on the EXPERT capsule TPS through a PM1000 support/interface. It should be remarked that the nature of the contacts at the interfaces between ceramic and metallic parts presents several uncertainties. In fact, they cannot be attached (glued or bolted, for instance) because of the relevant difference in terms of coefficients of thermal expansion and the poor fracture toughness of the ceramic-based material with respect to the metallic one. As a consequence the connection should be done only by means of dedicated interfaces. These are opportunely shaped in order to eliminate rigid body motion and, at the same time, to avoid rigid constraint [13–15] leading to excessive thermal stresses.

Therefore since gaps are expected to establish at such interfaces, they should be considered in the numerical models in order to realistically simulate the behavior of the connection.

In general, the independent variables in the thermal stress calculations are the modulus of elasticity, the coefficient of thermal

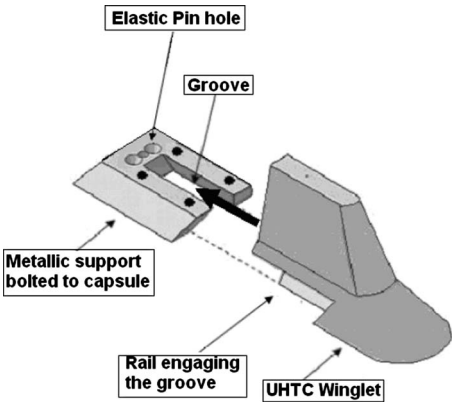

Fig. 2 Assembling scheme

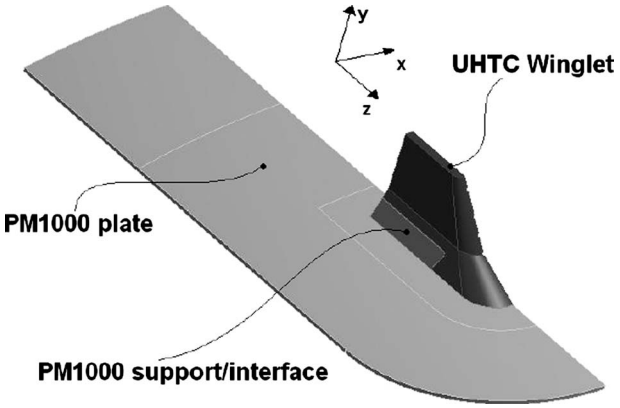

Fig. 3 Geometry of the model considered for finite element analyses

expansion, and the temperature differential. When a bar is prevented from growing by infinitely rigid external restraint, a stress σ of magnitude $E\alpha\Delta T$ will be generated (E is the Young Modulus, α is the coefficient of thermal expansion, and ΔT is the temperature difference); to compute realistic restraints and thermal stresses, a fourth variable must be added to the thermal stress equation, which is a restraining factor K

$$\sigma = KE\alpha\Delta T \tag{1}$$

In such a way the deflections caused by the applied thermal load will reduce the stress in the thermally strained member by a factor K by allowing some thermal expansion. Then, the thermal stress in a structural member will be a maximum corresponding to $K=1$ for a fully restrained member and will be nonexistent ($K=0$) for an unrestrained member. This simple explanation of thermal stresses is fundamental to understanding thermal-structural design [16,17]. Actually, thermal stresses may be categorized as stresses caused either by external restraints or stresses caused by internal restraints. The stresses in the second category are the results of regions of the structure having different temperatures, different stiffnesses, or different thermal expansion coefficients. Under these conditions the member may restrain itself, thus producing thermal stresses.

Then, it is necessary to design interfaces where K values are as small as possible.

One of the main aims of the present paper is to assess the performance of winglet/PM1000 interfaces and the capabilities to simulate them. Particular attention has been paid to the contact surface modeling, which is the most challenging problem in the finite element simulation of the thermomechanical behavior of hot structures.

The thermal and structural analyses performed take also into account the postyield hardening capabilities of the PM1000 metallic based material, the elastic-fragile behavior of the ZrB_2-SiC composite ceramic and their corresponding thermal and mechanical temperature dependent properties.

Figures 1 and 2 illustrate how the UHTC winglet is connected with the PM1000 support and the winglet location on the EXPERT capsule.

The assembling scheme of the ceramic winglet with the metallic support is shown in Fig. 2. An elastic pin, which has not been considered for finite element analyses, is mounted on the PM1000 support in order to avoid the disassembling of the payload.

Half Winglet has been considered for finite element analyses because of the load and geometry symmetry with respect to the yz plane (see Fig. 3).

2 Computational Fluid Dynamics Analyses

Three dimensions computations have been performed by using the CIRA code H3NS. It is a structured multiblock finite volume solver that allows for the treatment of a wide range of compressible fluid dynamic problems and has been widely validated. The fluids treated as a mixture of perfect gases in the case of thermochemical nonequilibrium flows. The chemical model for air is due to Park and is characterized by 17 reactions among five species (O, N, NO, O_2, and N_2), neglecting the presence of inert gas in the air (e.g., Ar). The energy exchange between vibrational and translational modes is modeled with the classical Landau–Teller nonequilibrium equation, with average relaxation times taken from the Millikan–White theory modified by Park. For what concerns transport coefficients, the viscosity of the single species is evaluated by a fit of collision integrals calculated by Yun and Mason, the thermal conductivity is calculated by means of the Eucken law; the viscosity and thermal conductivity of the gas mixture are then calculated by using the semi-empirical Wilke formulas. The diffusion of the multicomponent gas is computed through a sum rule of the binary diffusivities of each couple of species (from the tabulated collision integrals of Yun and Mason). For what concerns turbulent modeling, two-equation k-ε (with and without compressibility effects) models are available.

With respect to the numerical formulation, the conservation equations, in integral form, are discretized by means of a finite volume cell centered technique. Inviscid fluxes are computed with a flux difference splitting method, and second order formulation is obtained by using an essentially nonoscillatory (ENO)-like reconstruction of interface values. Viscous fluxes are computed with a classical centered scheme. Time integration is performed by employing an explicit multistage Runge–Kutta algorithm coupled with an implicit evaluation of the chemical and vibrational source terms.

The winglet will fly along a 5 km/s entry trajectory. The maximum heat flux conditions along the reentry have been used for the three-dimensional CFD computations of the aerodynamic field around the winglet.

Laminar to turbulent boundary-layer transition is considered one of the most critical aerothermodynamic phenomena due to the associated local temperature peaks and drag increase; unfortunately it is not yet fully understood from a physical point of view and hypersonic transition prediction based on ground test extrapolation-to-flight is not reliable. In fact, chemistry effects are difficult to simulate in ground facilities, and cold hypersonic facilities are affected by external disturbances (wind tunnel related), which constitute dominant sources of perturbations for transition triggering. Thus, only flight experiments with well-characterized disturbances (triggering transition where required) may provide essential information to be coupled with ground facilities data and numerical simulation results.

With regard to catalicity, since the uncertainty in the available experimental data, compared with literature models, is very high,

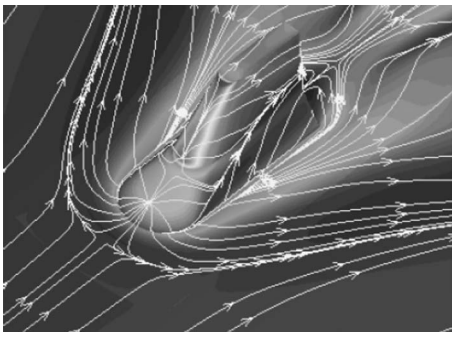

Fig. 4 Air flow direction around the winglet

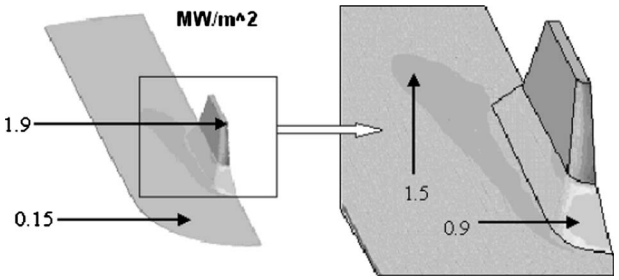

Fig. 6 Heat flux distribution at $t=115$ s

the most critical condition for the PM1000 plate has been considered, which are noncatalytic winglet and fully catalytic PM1000 plate [18].

The air flow direction in the proximity of the winglet is illustrated in Fig. 4.

3 Thermostructural Analysis

The present paragraph describes the finite element model adopted for the thermal and the structural analyses.

Aerodynamic heat fluxes, calculated by means of CFD analyses illustrated in the previous paragraph, have been employed as inputs for the thermostructural analyses.

Thermal fluxes applied on the finite element model are evaluated by means of the following equation:

$$\dot{Q} = h(H_0 - c_p T_w) \tag{2}$$

where

- h is the convection coefficient evaluated by CFD analysts
- H_0 is the total enthalpy
- c_p is the specific heat
- T_w is the wall temperature

T_w is updated at every time step starting from 300 K, which is the initial temperature of the body.

The calculated heat fluxes are multiplied by a safety factor equal to 1.2 (this value has been evaluated by aerothermodynamic analysts in order to take into account the possible laminar to turbulent boundary-layer transition which cannot be predicted [19]).

The heat flux distribution on the external surface of the body has been estimated according to the approach described below.

At first the diagram of the heat fluxes at the stagnation point versus time was traced (see Fig. 5). Then the time instant (t^*) corresponding to the maximum heat flux (q^*) was individuated.

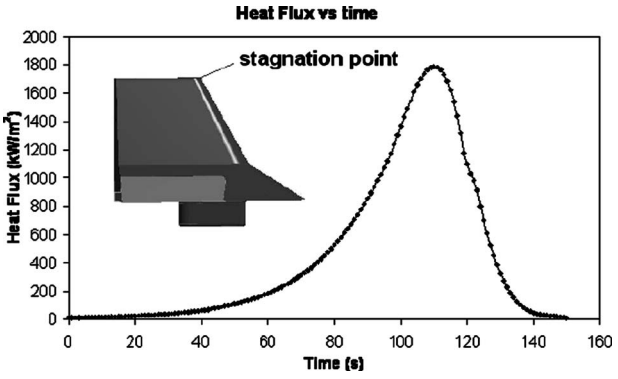

Fig. 5 Heat flux variation with time for the stagnation point

Successively, knowing the heat flux at each point of the body at t^*, a scale factor, defined as the ratio between the considered heat flux value and q^*, can be calculated for every point.

Finally, the scale factors have been used to obtain the heat flux of every point at every time instant.

All the thermostructural analyses have been performed by employing the commercial code ANSYS [20]. In the preprocessor phase, computer aided three dimensional interactive appplication (CATIA) [21] models have been imported into the ANSYS Workbench tool.

Figure 5 describes heat flux variation with time for the stagnation point during the re-entry phase. The maximum heat flux value is almost 1900 W/m^2.

The stagnation point is located on the winglet tip; a flow reattachment occurs on the PM1000 plate near the UHTC winglet. To be more precise, the hypersonic flow separates at the winglet tip and reattaches downstream provoking heat flux peaks on the PM1000 plate (Fig. 6 illustrates the heat flux distribution at $t=115$ s, when the maximum heat flux for the stagnation point is detected; a zoom of the reattachment area is also illustrated).

The half structure has been modeled because of the load and geometry symmetry along the longitudinal axis of the winglet/plate. The model includes part of the metallic EXPERT capsule TPS base plate.

The analyses have been performed in a sequential way, considering a thermostructural uncoupled approach. As a first step, the unsteady temperatures have been evaluated by performing nonlinear transient thermal analyses. The following boundary conditions for the thermal analyses have been employed:

1. transient thermal fluxes (from CFD calculations) applied at the exposed external surfaces
2. radiation conditions applied at all the external surfaces
3. adiabatic conditions on the symmetry plane and on PM1000 plate internal surface

Winglet and plate emissivity have been, respectively, set equal to 0.66 and 0.7.

Radiation conditions have been simulated by employing the ANSYS AUX12 radiation matrix method: This method works for generalized radiation problems involving two or more surfaces receiving and emitting radiation [22]. The method consists in generating a matrix of form factors (view factors) between radiating surfaces (or between a radiating surface and the ambient) and using the matrix as a superelement in the thermal analysis. Hidden or partially hidden surfaces can be included, as well as a space node that can absorb radiation energy [23,24].

With regard to the structural analyses, temperatures evaluated in the previous transient thermal analysis have been applied as body force load on the finite element structural model. Static structural analyses have been performed at specified time instants (where higher temperatures occur).

Symmetry conditions have been applied on the symmetry plane, the plate has been assumed to be simply supported. The rear line of the plate has been fixed to prevent the system rigid

Table 1 Thermal conductivity, specific heat, thermal expansion coefficient, Young's modulus, and tensile strength for the PM1000

Temperature (K)	Thermal conductivity (W/m K)	Specific heat (J/kg K)	Thermal expansion coefficient (1/K)	Young modulus (GPa)	Tensile strength (MPa)
300	12	450	1.3×10^{-5}	190	490
700	22	590	1.6×10^{-5}	160	380
1100	32	730	1.9×10^{-5}	130	230
2000	50	950	2.5×10^{-5}	50	55

body motion. On the contrary, the UHTC part has been connected to the PM1000 support/interface and to the PM1000 plate by means of friction contacts only.

A sensitivity analysis has been performed in order to select the optimum mesh in terms of shape and number of elements. Two elements in the PM100 plate thickness have been considered.

The discretized domain has around 150,000 nodes. Three-dimensional "20 node thermal solid" and "10 node tetrahedral thermal solid" have been employed for the thermal analysis; "20 node structural solid" and "10 node tetrahedral structural solid" elements have been chosen for the structural analyses. Interfaces are modeled by using CONTA174/TARGE170 "8 node surface to surface contact" elements.

The materials employed are as follows:

1. ZrB_2-SiC UHTC ceramic winglet
2. PM1000 interfaces (support+bolts)

The elastic-plastic behavior of the PM1000 material has been modeled in ANSYS by means of the bilinear kinematic hardening law; it considers two linear stress-strain relationships characterized by two different slopes up to and beyond the yield stress limit. Moreover, the bilinear kinematic hardening option assumes that the total stress range is equal to twice the yield stress [25].

PM1000 thermal and mechanical properties variations with temperature are shown in Table 1.

Density and Poisson's modulus have been considered constant with temperature; their values together with the temperature limit use are summarized in Table 2.

Table 3 represents tensile strength, thermal conductivity, specific heat, and thermal expansion variations with temperature for the UHTC.

Table 2 Density, Poisson's modulus, and temperature limit used for the PM1000

Density (kg/m^3)	Poisson's modulus	Temperature limit (K)
8240	0.3	1600

Table 3 Thermal conductivity, specific heat, thermal expansion coefficient, Young's modulus, and tensile strength for the UHTC

Temperature (K)	Thermal conductivity (W/m K)	Specific heat (J/kg K)	Thermal expansion coefficient (1/K)	Tensile strength (MPa)
300	62	470	6×10^{-6}	490
700	64	680	6.1×10^{-6}	560
1100	65	710	6.7×10^{-6}	610
2000	66	800	7.1×10^{-6}	100

Table 4 Density, Poisson's modulus, Young's modulus, and temperature limit used for the UHTC

Density (kg/m^3)	Poisson's modulus	Young's modulus (GPa)	Temperature limit (K)	Compressive strength (MPa)
5610	0.14	480	2300	300

Density, Poisson's modulus, Young's modulus, temperature limit use, and compressive strength for the UHTC have been considered constant with temperature; their values are summarized in Table 4.

Since no literature data concerning friction factor values between ceramic and metallic surfaces are available, a sensitivity analysis has been performed in order to evaluate the influence of the friction factor values on the stress fields. Three friction coefficients (FCs) have been considered as follows:

1. FC=0.1
2. FC=0.3
3. FC=0.5

The analyses performed have demonstrated that the FC=0.3 condition is the most critical for the structure. Then a friction factor equal to 0.3 has been chosen to model friction between UHTC winglet and PM1000.

An asymmetric "pure penalty method" has been used for modeling bonded contacts, while "augmented Lagrange method" has been chosen for frictional contact surfaces [26]. The latter is more suitable for complex geometries in "sliding contact" conditions, where it is fundamental to obtain accurate results. Both of these are penalty-based contact formulations, where a finite amount of penetration between the contact surfaces is required in order to maintain equilibrium and to compute the contact normal force.

Then

$$F_{\text{normal}} = k_{\text{normal}} x_{\text{penetration}} \tag{3}$$

where F_{normal} is the contact force in the normal direction, k_{normal} is the normal stiffness, and $x_{\text{penetration}}$ is the penetration. According to this method, the higher the contact stiffness k_{normal}, the lower the penetration $x_{\text{penetration}}$ However, as long as $x_{\text{penetration}}$ is small or negligible, the solution results will be accurate. The main difference between the pure penalty method and the augmented Lagrange method is that the latter augments the contact force (pressure) calculations.

For pure penalty,

$$F_{\text{normal}} = k_{\text{normal}} x_{\text{penetration}} \tag{4}$$

For augmented Lagrange,

$$F_{\text{normal}} = k_{\text{normal}} x_{\text{penetration}} + \lambda \tag{5}$$

Because of the extra term λ, the augmented Lagrange method is less sensitive to the magnitude of the contact stiffness k_{normal}.

In general, problems involving contact mechanics are highly nonlinear and are usually affected by convergence issues, related to excessive values of the contact initial gap or penetration. Both the augmented Lagrange method and the pure penalty method are capable of handling initial nonzero gaps or penetrations, however threshold values (depending on the problem at hand) cannot be trespassed. Moreover, cases involving large gaps and surfaces bonded together can result in fictitious moments being transmitted across the boundaries. Ways to circumvent convergence problems may consist in using "weak springs" of opportune stiffness within the contact mechanics. However, excessive spring stiffness values may lead to fictitious contact forces and unphysical results.

In the pos-processing phase, UHTC critical areas have been identified by following two different approaches. The first ap-

Table 5 Maximum UHTC failure index (*FI*) values and Weibull probability of failure (F_w) at $t=75$ s, 100 s, and 115 s, respectively

Time (s)	Max UHTC *FI*	UHTC F_w ($V_0=50$ mm^2)	UHTC F_w ($V_0=480$ mm^2)
75	0.15	0.46×10^{-3}	0.47×10^{-4}
100	0.51	0.77×10^{-5}	0.81×10^{-6}
115	1.20	0.23×10^{-2}	0.24×10^{-3}

proach is deterministic and consists in applying a maximum stress criterion, the stress at a node is compared with the temperature dependent strength at that node, that is

$$FI = \frac{S_{\text{node}} \cdot SF}{S_{\max}(T)} \tag{6}$$

In Eq. (6) *FI* is the failure index, S_{node} is the stress at a certain node, $S_{\max}(T)$ is the temperature dependent strength at that node, and *SF* is the safety factor, which is equal to 1.4. This value has been required by the EXPERT Program design team for all the payloads mounted on the re-entry capsule.

Obviously, according to this criterion, failure occurs when $FI>1$.

The second approach, which is commonly employed for elastic-fragile materials, is probabilistic and consists in applying a Weibull-like failure criterion, for which the probability of failure F_w $(0<F_w<1)$ for a stressed material is given by Eq. (7)

$$F_w = 1 - \exp\left(\sum_{i=1}^{N}\left(\frac{S_i}{S_{\max}(T)}\right)^m \frac{V_i}{V_0}\right) \tag{7}$$

where V_i is the volume of a stressed element, V_0 is a reference volume, m is the Weibull modulus, S_i is the element stress, and N is the total number of elements. In the present case V_0 equals the volume of the samples employed for experimental strength assessment [27].

4 Results and Discussion of the Results

This paragraph illustrates the results of the thermomechanical analyses performed on the finite element model described in Sec. 3.

The maximum UHTC temperature value (about 2200 K) is reached at the stagnation point where the highest heat fluxes are encountered (see also Fig. 5).

The time instant at which the stagnation point reaches its highest value matches with the time instant at which maximum heat flux is encountered in the same point.

The PM1000 component temperature continues to increase even after the maximum heat flux instant (115 s); this is due to the heat flowing from the winglet. The maximum temperature values are detected where the flow reattachment occurs.

The thermal analysis demonstrates that

1. the 1600 K temperature limit for the PM1000 is never exceeded
2. the maximum UHTC temperature is 2238K; this value does not exceed the ZrB2-SiC temperature limit use, which is 2288 K (multiple use temperature limit)

Table 5 shows maximum UHTC failure index (*FI*) and Weibull probability of failure F_w evaluated at $t=75$ s, 100 s,, and 115 s. The most critical condition, $FI=1.2$, is attained at 115 s, when the UHTC reaches its maximum temperature. According to the deterministic analysis, the allowable values are exceeded. However, that critical *FI* values are attained in a very small area in correspondence of stress concentrators. Truly, a high percentage of the UHTC volume is considerably understressed with failure index values well below 0.3: This can be appreciated by the probabilistic analysis, which takes into explicit account not only the values of stress but also the volume of the stressed parts.

Two values of reference volume V_0 are employed for estimating F_w: they refer to two different test campaigns carried out on two similar UHTC materials. It can be seen that in the worst case, $V_0=50$ mm^2, F_w does not exceed 0.25% (see Table 5). According to the Weibull analysis, the occurrence of failure is a quite remote event.

The maximum failure index value is detected near the interface with PM1000, which is characterized by a significantly greater coefficient of thermal expansion (see Table 1). Then, the PM1000 support pulls against the UHTC winglet provoking high stresses at the interface.

5 Summary and Conclusions

A thermostructural design has been performed on a winglet that will be mounted on the EXPERT capsule for atmospheric re-entry experiments.

The winglet is made of ZrB_2-SiC, an ultra high temperature ceramic, and is connected with a PM1000 support by means of a PM1000 support interface to accommodate thermal stresses arising during the re-entry phase of the capsule; the PM1000 support, in turn, is connected with the capsule thermal protection systems by means of PM1000 bolts. The main difficulty has been met in the design of the interfaces between the UHTC and the metallic structure where it is important to alleviate thermal stresses and, at the same time, to assure that the connection is still working at elevated temperature. Thermal stresses have been minimized by decreasing the internal restraints and, then, the restraining factor *K*. In the finite element simulation phase, particular attention has been paid to the model discretization; in fact, for complex interface geometries the mesh of contact regions should be very fine. In addition, a different contact algorithm is chosen (augmented Lagrangian) for frictional contact surfaces in order to perform static nonlinear analyses without convergence solution problems.

Elastic-plastic behavior of the PM1000 plate has been taken into account in the finite element model in order to obtain accurate results: when the PM1000 behavior becomes plastic, stresses distribute over a greater volume. As a consequence peak stress values will decrease.

A statistical approach for the prediction of failure of the UHTC component has been employed. In fact, the strength of ceramic materials can unpredictably change from component to component even if a set of nominally identical specimens are tested under the same conditions. Therefore, the strength of a brittle material is not a deterministic variable and has to be described in terms of statistical distributions. According to the Weibull statistical distribution, the greater the volume of the stressed material, the higher the probability of failure.

Finally, the strengths of the thermal and structural analyses performed are elastic-plastic behavior of the PM1000, accurate contact modeling, and statistical approach for the evaluation of critical areas. The weaknesses are those related to the finite element discretization of the model and to the uncertainties associated with CFD analyses, the material properties, and the friction coefficients between contact surfaces.

The finite element analyses simulating the re-entry phase have demonstrated that the maximum stresses and temperatures evaluated do not exceed their corresponding limits. As a result, the conceived support/interface could be used for future applications where critical thermal stresses arise, since two or more structures made of different materials (then different coefficients of thermal expansion) are connected. Moreover ultra high temperature ceramics could be used as hot structures, that is, they are able to tolerate thermal stresses at very high temperatures. That kind of materials could be employed in the critical areas of the re-entry vehicles where high heat fluxes are encountered.

The presented hot structure, before being tested in flight, will be tested in the Plasma wind tunnel facility, where the illustrated thermostructural results will be compared with test results. The validation of the numerical models employed for the winglet design is fundamental to verify the thermal and structural assumptions considered and, then, to improve thermostructural design and analysis capabilities.

References

[1] Thornton Earl, A., 1996, *Thermal Structures for Aerospace Applications* (AIAA Series), 2nd ed., AIAA, Reston, VA, pp. 103–118.

[2] Kelly, H. N., Rummler, D. R., and Jackson, R., 1983, "Research in Structures and Materials for Future Space Transportation Systems—An Overview," J. Spacecr. Rockets, **20**, pp. 89–96.

[3] Shih, P. K., Prunty, J., and Mueller, R. N., 1988, "Thermostructural Concepts for Hypervelocity Vehicles," AIAA Paper No. 88–2295.

[4] Marino, G., 2003, "New Materials and Related Fabrication Processes for Hot Structures on RLV's," 54th International Astronautical Congress of the International Astronautical Federation, the International Academy of Astronautics, and the International Institute of Space Law, Bremen, Sep. 29, Paper No. IAC-03-I.3.01.

[5] Scatteia, L., Riccio, A., Rufolo, G., De Filippis, F., Del Vecchio, A., and Marino, G., 2005, "PRORA-USV SHS: Ultra High Temperature Ceramic Materials for Sharp Hot Structures," AIAA/CIRA 13th International Space Planes and Hypersonics Systems and Technologies Conference, Capua, Italy, May 16–20.

[6] Russo, G., 2001, "The PRORA-USV Programme," Fourth European Symposium on Aerothermodynamics for Space Vehicles, CIRA, Capua, Italy, pp. 37–48, Paper No. ESA-SP-487.

[7] Glass, D., 2008, "CMC-Based Hot Structures," First Workshop on Science and Technology of UHTC-Based Hot Structures, CIRA, Capua, Italy, Oct. 28–29.

[8] Ferraiuolo, M., Riccio, A., Tescione, D., and Gigliotti, M., 2008, "A Fast Procedure for Optimizing Thermal Protection Systems for Re-Entry Vehicles," J. Br. Interplanet. Soc., **61**, pp. 478–486.

[9] Muylaert, J., Cipollini, F., Walpot, L., and Ottens, H., 2007, "Flight Experiments for Hypersonic Vehicle Development Expert," Research and Technology Organization.

[10] Daryabeigi, K., 2002, "Thermal Analysis and Design Optimization of Multilayer Insulation for Re-Entry Aerodynamic Heating," J. Spacecr. Rockets, **39**(4) pp. 509–514.

[11] Poteet, C., Abu-Khajeel, H., and Hsu, S.-Y., 2004, "Preliminary Thermal-Mechanical Sizing of a Metallic Thermal Protection System," J. Spacecr. Rockets, **41**(2), pp. 173–182.

[12] Juvinall, R. C., and Marshek, K. M., 2002, "Fundamentals of Component Machine Design," 2nd ed., Wiley, New York, pp. 363–374.

[13] Tamma, K. K., and Thornton E. A., 1987, "Re-Entry Thermal/Structural Finite-Element Modeling/Analysis of Shuttle Wing Configurations," J. Spacecr. Rockets, **24**(2), pp. 101–108.

[14] Scotti, J. S., Clay, C., and Rezin, M., 2003, "Structures and Material Technologies for Extreme Environments Applied to Reusable Launch Vehicles," AIAA Paper No. AIAA-2003-2697.

[15] Tachibana, Y., and Iyoku, T., 2004, "Structural Design of High Temperature Metallic Components," Nucl. Eng. Des., **233**, pp. 261–272.

[16] Taylor, A. H., and Jackson, L. R., 1977, "Heat-Sink Structural Design Concepts for a Hypersonic Research Airplane," AIAA Paper No. 77-392.

[17] Thornton, E. A., and Dechaumphaij, P., 1986, "Coupled Flow, Thermal, and Structural Analysis of Aerodynamically Heated Panels," Progress Report No. 0021-8669.

[18] Di Benedetto, S., Marini, M., and Gardi, R., 2007, "CFD Analysis of the EXPERT Winglet in Plasma Wind Tunnel conditions," West-East High Speed Flow Field Conference, Moscow, Russia, Nov. 19–22.

[19] Di Clemente, M., 2006, "Numerical Prediction of Aerothermodynamic Effects on a Reentry Vehicle Body Flap Configuration," 57th International Astronautical Congress, Valencia, Spain, Oct. 2–6.

[20] ANSYS® and ANSYS Workbench® Reference Documentation, Version 10.0.

[21] CATIAV Reference User Manual.

[22] Liu, L. H., and Liu, L. J., 2007, "Discontinuous Finite Element Approach for Coupled Radiative Transfer Equation," ASME J. Heat Transfer, **129**(8), pp. 1069–1074.

[23] Zhao J. M., and Liu L. H., 2007, "Spectral Element Approach for Coupled Radiative and Conductive Heat Transfer in Semitransparent Medium," ASME J. Heat Transfer, **129**(10), pp. 1417–1424.

[24] Mazumder, S., 2005, "A New Numerical Procedure for Coupling Radiation in Participating Media With Other Modes of Heat Transfer," ASME J. Heat Transfer, **127**(9), pp. 1037–1045.

[25] Keppas, L. K., Anifantis, N. K., Katsareas, D. E., and Youtsos, A. G., 2006, *Residual Stress and Its Effects on Fatigue and Fracture*, Springer, the Netherlands.

[26] Ferraiuolo, M., Riccio, A., Tescione, D., Gardi, R., and Marino, G., 2008, "Contact Sensitivity Analysis of a Coupling Pin for the Nose Cap of a Launch Reentry Vehicle," J. Br. Interplanet. Soc., **61**, pp. 14–19.

[27] Vittal, S., and Hajela, P., 2003, "Probabilistic Design Using Empirical Distributions," AIAA Paper No. AIAA-2003-1658.

Turbulent Forced Convection in a Plane Asymmetric Diffuser: Effect of Diffuser Angle

H. Lan

B. F. Armaly

J. A. Drallmeier

Department of Mechanical and Aerospace Engineering,
Missouri University of Science and Technology,
Rolla, MO 65401

A simulation of two-dimensional turbulent forced convection in a plane asymmetric diffuser with an expansion ratio of 4.7 is performed, and the effect of the diffuser angle on the flow and heat transfer is reported. This geometry is common in many heat exchanging devices, and the turbulent convective heat transfer in it has not been examined. The momentum transport in this geometry, however, has received significant attention already, and the studies show that the results from the $\overline{v^2}$-f type turbulence models provide better agreement with measured velocity distributions than that from the k-ε or k-ω turbulence models. In addition, the $\overline{v^2}$-f type turbulence models have been shown to provide good heat transfer results for separated and reattached flows. The k-ε-ζ ($\overline{v^2}$-f type) turbulence model is used in this study due to its improved numerical robustness, and the FLUENT-CFD code is used as the simulation platform. User defined functions for the k-ε-ζ turbulence model were developed and incorporated into the FLUENT-CFD code, and that process is validated by simulating the flow and the heat transfer in typical benchmark problems and comparing these results with available measurements. This new capability is used to study the effect of the diffuser angle on forced convection in an asymmetric diffuser, and the results show that the angle influences significantly both the flow and the thermal field. The increase in that angle increases the size of the recirculation flow region and enhances the rate of the heat transfer. [DOI: 10.1115/1.2977545]

Keywords: k-ε-ζ turbulence model, separated flow, diffuser, forced convection

Introduction

Flow separation and reattachment that develop due to changes in geometry occur in many heat exchanging devices. The heat transfer rate varies greatly in the separated and reattached regions of the flow, and the need to accurately simulate such behavior in 2D and 3D turbulent flows has attracted a great deal of interest. Studies on turbulent separating/reattaching flow have been conducted extensively during the past decades, and the flow in 2D plane asymmetric diffuser has been investigated both experimentally and numerically [1–8]. Obi et al. [1] and Buice and Eaton [2,3] reported velocity measurements in a 10 deg diffuser. These measurements have been used as a benchmark for validating and improving turbulence models. Makiola and Ruck [4] reported velocity measurements in diffusers with diffuser angles varying from 10 deg to 90 deg and observed that a decrease in diffuser angle decreases the size of the recirculation flow region and reduces the magnitude of the streamwise velocity inside that region. Iaccarino [5] examined the flow in a 10 deg diffuser using different commercial CFD codes and compared the performance of a low-Reynolds number k-ε turbulence model with that of the $\overline{v^2}$-f turbulence model [9]. He concluded that the low-Reynolds number k-ε turbulence model could not predict the recirculation flow region that was measured in this specific geometry, but the $\overline{v^2}$-f turbulence model provided results that compared well with measured values. Kaltenbach et al. [6] examined the flow in the same geometry (10 deg diffuser) using large-eddy simulation (LES) and reported that the mean flow, pressure coefficient, and skin friction are in excellent agreement with measurements, but the agreement with velocity fluctuations and wall shear stress is less satisfactory. Apsley and Leschziner [7] also examined the flow in this geometry using both linear and nonlinear eddy-viscosity turbulence models, as well as differential stress turbulence models, and they concluded that nonlinear models could not produce the measured results in the reversed flow region. From the performance of the differential stress turbulence model, they concluded that the pressure-strain interaction is a crucially important element that influences the predictive performance, and the wall-normal Reynolds stresses are highly sensitive to this interaction.

The results from the above studies indicate that the $\overline{v^2}$-f turbulence model [9] predicts separated/reattached flows with reasonable accuracy and can be used with a moderate computational cost. The model introduces two additional transport equations to the standard k-ε turbulence model, where one is for the wall-normal Reynolds stress component $\overline{v^2}$ and the other is for the elliptic relaxation function (f) that is related to the pressure-strain interaction. The $(\overline{v^2})^{1/2}$ is demonstrated to be a more appropriate velocity scale in turbulent transport toward a wall than the $k^{1/2}$ that is normally used as the velocity scale in the k-ε turbulence model since the former is a measure of turbulence anisotropy [10]. The elliptic relaxation function f accounts for the wall blocking effect on the Reynolds stress [11]. Durbin [9] obtained good agreement between predicted and measured velocities using the $\overline{v^2}$-f turbulence model for flows with massive separation, smooth separation, and unsteady vortex shedding [10]. However, it has been reported that this turbulence model is subject to some numerical difficulties, and various modified versions were proposed [11–14] to alleviate these difficulties. Hanjalic et al. [14] proposed some modifications to this model in order to make it more robust and less sensitive to near-wall grid clustering, and this modified model is used in this study and is identified as the k-ε-ζ turbulence model in this manuscript. User defined functions (UDFs) is developed for incorporating this turbulence model into the FLUENT-CFD code, and this code is used as the simulation platform in this study.

Contributed by the Heat Transfer Division of ASME for publication in the JOURNAL OF HEAT TRANSFER. Manuscript received January 2, 2008; final manuscript received April 25, 2008; published online May 13, 2009. Review conducted by Gautam Biswas. Paper presented at the 2007 ASME International Mechanical Engineering Congress (IMECE2007), Seattle, WA, November 10–16, 2007.

The first objective of this study is to incorporate the k-ε-ζ turbulence model into the FLUENT-CFD code in order to improve its predicting capabilities of turbulent convection in separated and reattached flows. The developed UDF for this turbulence model and its inclusion in the FLUENT-CFD code will be validated by simulating several benchmark cases and comparing the simulated results with published data. This CFD code is used extensively as a simulation tool for two- and three-dimensional flows in complex geometries due to its capabilities for solving different types of flows with various choices of built-in models and various built-in grid generating schemes. In addition it is well documented and is relatively easy to be used. So the inclusion of an improved turbulence model in such an extensively used simulation tool can be beneficial to some users. The second objective of this study is to simulate the effect of the diffuser angle on the turbulent forced convection (heat transfer) in 2D asymmetric plane diffusers with a fixed expansion ratio using the above developed capability. To the authors' knowledge, detailed measurements or predictions of turbulent forced convection (heat transfer) in this geometry have not appeared in the literature, and these two objectives motivated the current study.

Model Description

The k-ε-ζ turbulence model is a modified version of the original $\overline{v^2}$-f model where the $\overline{v^2}$ equation is replaced by an equation for $\zeta=\overline{v^2}/k$, the ratio of wall-normal Reynolds stress to turbulent kinetic energy. It has been shown that the new equation for ζ is more robust numerically than the $\overline{v^2}$ equation [14] so that the numerical stability of the model is greatly improved. A quasilinear pressure-strain model is also applied in the f equation with additional improvements for nonequilibrium wall-bounded flows [14]. The governing equations for turbulent forced convection, together with the k-ε-ζ turbulence model and the corresponding boundary conditions, are listed below:

$$\frac{\partial \rho U_i}{\partial x_i} = 0 \tag{1}$$

$$\frac{\partial}{\partial x_j}(\rho U_i U_j) = -\frac{\partial p}{\partial x_i} + \frac{\partial}{\partial x_j}\left[(\mu+\mu_t)\left(\frac{\partial U_i}{\partial x_j}+\frac{\partial U_j}{\partial x_i}\right)\right] \tag{2}$$

$$\frac{\partial}{\partial x_j}(\rho U_j \bar{T}) = \frac{\partial}{\partial x_j}\left(\left(\frac{\mu}{\mathrm{Pr}}+\frac{\mu_t}{\mathrm{Pr}_t}\right)\frac{\partial \bar{T}}{\partial x_j}\right) \tag{3}$$

$$\frac{\partial}{\partial x_j}(\rho U_j k) = \frac{\partial}{\partial x_j}\left[\left(\mu+\frac{\mu_t}{\sigma_k}\right)\frac{\partial k}{\partial x_j}\right] + G_k - \rho\varepsilon \tag{4}$$

$$\frac{\partial}{\partial x_j}(\rho U_j \varepsilon) = \frac{\partial}{\partial x_j}\left[\left(\mu+\frac{\mu_t}{\sigma_\varepsilon}\right)\frac{\partial \varepsilon}{\partial x_j}\right] + \frac{C_{\varepsilon 1}G_k - C_{\varepsilon 2}\rho\varepsilon}{T} \tag{5}$$

$$\frac{\partial}{\partial x_j}(\rho U_j \zeta) = \frac{\partial}{\partial x_j}\left[\left(\mu+\frac{\mu_t}{\sigma_\zeta}\right)\frac{\partial \zeta}{\partial x_j}\right] + \rho f - \frac{\zeta G_k}{k} \tag{6}$$

$$L^2\nabla^2 f - f - \frac{1}{T}\left(c_1 + c_2\frac{G_k}{\rho\varepsilon}\right)\left(\zeta - \frac{2}{3}\right) = 0 \tag{7}$$

where

$$\mu_t = C_\mu \zeta k T \tag{8}$$

$$G_k = \mu_t\left(\frac{\partial U_i}{\partial x_j}+\frac{\partial U_j}{\partial x_i}\right)\frac{\partial U_i}{\partial x_j} \tag{9}$$

$$T = \max\left[\min\left(\frac{k}{\varepsilon}, \frac{0.6}{\sqrt{3}C_\mu \bar{S}\zeta}\right), C_T\left(\frac{\nu}{\varepsilon}\right)^{0.5}\right] \tag{10}$$

Table 1 Coefficients in the k-ε-ζ turbulence model

C_μ	$C_{\varepsilon 2}$	c_1	c_2	σ_k	σ_ε	σ_ζ	C_T	C_L	C_η
0.22	1.9	0.4	0.65	1.0	1.3	1.2	6.0	0.36	85

$$L = C_L \max\left[\min\left(\frac{k^{1.5}}{\varepsilon}, \frac{k^{0.5}}{\sqrt{3}C_\mu \bar{S}\zeta}\right), C_\eta\left(\frac{\nu^3}{\varepsilon}\right)^{0.25}\right] \tag{11}$$

$$\bar{S} = \sqrt{2S_{ij}S_{ij}} \tag{12}$$

$$S_{ij} = \frac{1}{2}\left(\frac{\partial U_i}{\partial x_j}+\frac{\partial U_j}{\partial x_i}\right) \tag{13}$$

where T and L are the turbulent time scale and the turbulent length scale, respectively. All other variables go to zero when the wall is approached except for ε and f,

$$\varepsilon_w = \lim_{y\to 0}\frac{2\nu k}{y^2} \tag{14}$$

$$f_w = \lim_{y\to 0}\frac{-2\nu\zeta}{y^2} \tag{15}$$

The values of the above model constant coefficients are listed in Table 1 and the nonconstant coefficient $C_{\varepsilon 1}$ has the following expression:

$$C_{\varepsilon 1} = 1.4(1.0 + 0.012/\zeta) \tag{16}$$

UDFs were developed and utilized for solving the four turbulence model equations (Eqs. (4)–(7)) together with the other governing equations for the flow and thermal fields using the FLUENT-CFD solver. The use of the developed UDF for this turbulence model with the FLUENT-CFD solver in simulating the flow and the heat transfer for several benchmark problems (i.e., for channel flow, for convection adjacent to a backward-facing step, and for normally impinging jet flow on a heated flat plate and flow in a plane asymmetric 10 deg diffuser) produced results that compared well with measured data. A constant Prandtl number of 0.9 was used in the solution of the energy equation for all these problems.

Although the source term in Eq. (4) is theoretically exact, some treatment is needed in the numerical realization stage of the simulation. The turbulent dissipation rate, ε, which appears as a source term in that equation, is numerically realized by $\varepsilon_{i,j}^n = k_{i,j}^n / T_{i,j}^{n-1}$ instead of using its value as $\varepsilon_{i,j}^n = \varepsilon_{i,j}^{n-1}$ from the last iteration. Using the former numerical expression in the simulation produces heat transfer results that agree better with measurements compared to using the latter one. The use of either one of these expressions, however, produces similar flow results. This treatment is similar to the one that has been utilized in the process of deriving Eq. (5) from the ε equation that appears in the standard k-ε turbulence model.

The governing equations are solved by a segregated solver using the FLUENT-CFD code, and the SIMPLEC algorithm is used to deal with the coupling between the flow field and the pressure fields. The PRESTO! scheme is used for the pressure correction equation, and the QUICK scheme is used for all the other equations. A grid-independent solution was obtained for each of the benchmark cases that were tested.

Validation of the Developed UDF for the Turbulence Model

The developed UDF code is tested and validated by simulating four benchmark problems and by comparing the simulated results with available benchmark data. Properties for the air that are used in the numerical validation are evaluated at a temperature of 293 K and are equivalent to density $\rho = 1.225\ \mathrm{kg/m^3}$, molecular

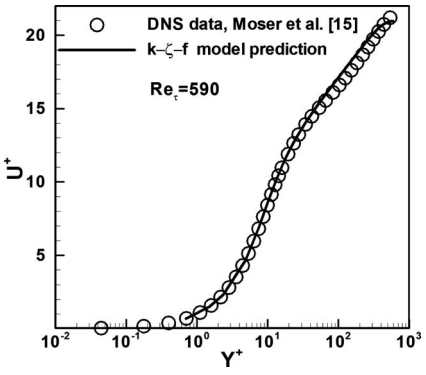

Fig. 1 Fully developed velocity distribution in the channel flow at Re$_\tau$=590

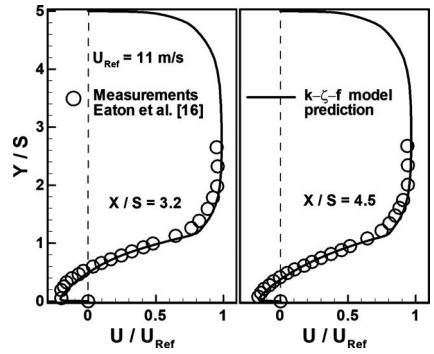

Fig. 3 Mean stream velocity distribution in the recirculation region

viscosity $\mu=1.81\times10^{-5}$ kg/m s, specific heat capacity $C_p=1005$ J/kg k, and thermal conductivity $\lambda=0.0242$ W/m k.

The first benchmark problem is a two-dimensional fully developed channel flow with a Reynolds number of 590 ($Re_\tau=590$), which is based on friction velocity and half channel height [15]. In the current study, a duct height of 1.5 cm and bulk air velocity of 22 m/s are used for generating a Reynolds number of $Re_\tau=590$. The nondimensional velocity distribution and turbulence scalar (k and ζ) distributions versus the nondimensional wall coordinate in a fully developed flow regime are presented in Figs. 1 and 2, respectively. It is shown that the simulated results for both time-averaged mean velocity and turbulent quantities generated from using the k-ε-ζ turbulence model compare very well with the corresponding direct numerical simulation (DNS) data.

The second benchmark problem is the turbulent forced convection adjacent to a 2D backward-facing step. Vogel and Eaton [16] measured both the flow and the heat transfer in this geometry (step height of $S=3.79$ cm and expansion ratio of 1.25) for a Reynolds number of 28,000 (based on the step height and an inlet free stream velocity of 11 m/s). The inlet air flow is isothermal and with a developing boundary layer thickness of 1.1S. The measured reattachment length, X_r, is reported in Ref. [16] as $X_r=6.7S$, and the simulated value while using the k-ε-ζ turbulence model is $X_r=7.1S$ (a simulated reattachment length of 26.9 cm or a difference of less than 6% from the measured value). The simulated reattachment lengths using the Abe–Kondoh–Nagano (AKN) low-Reynolds number k-ε turbulence model and using the k-ω shear stress transport (SST) turbulence model (two built-in turbulence models in the FLUENT-CFD code [17]) are 5.4S and 6.5S, respectively. The comparison of the simulated mean velocity distribution with measured values inside the recirculation flow region is presented in Fig. 3, and all the velocities in this figure are normalized by a reference velocity of $U_{ref}=11$ m/s. It can be seen from the figure that the simulated velocity distribution compares well with measurements.

Heat transfer measurements in the same backward-facing step geometry using the same flow conditions as stated in the above paragraph were also reported in Ref. [16]. The experimental thermal boundary conditions consist of a uniform heat flux supplied on the stepped wall (downstream from the sudden expansion) at a rate of 270 W/m^2, while all the other walls are insulated. Measured and simulated results for the Stanton number on the downstream stepped wall are presented and compared in Fig. 4. The simulated results from using two other turbulence models (AKN low-Re k-ε and the k-ω SST) are also shown in that figure for comparison. The Stanton number resulting from using the AKN low-Reynolds number turbulence model is more than 30% higher than the measured values in the recirculation flow region, while the simulated results using the k-ε-ζ turbulence model provide good agreement with the measured values. The use of the k-ω SST turbulence model generates heat transfer results that are also in good agreement with measured values for this geometry, but, as will be shown later, this model cannot predict other benchmark problems very well.

The third benchmark problem is a normally impinging circular jet air flow on a heated flat plate [18], for which measurements are available in the ERCOFTAC database. The Reynolds number is 23,000 based on the upstream bulk velocity and a nozzle diameter of $D=2.6$ cm. The height of the jet discharging above the plate is two times the nozzle diameter (D), and the discharged air flow is fully developed and isothermal. The air jet flow impinges normally on a flat plate that is heated by a uniform heat flux (q_w) of 300 W/m^2. Further details about this impinging jet air flow can be found in the work of Baughn and Shimizu [18]. A comparison

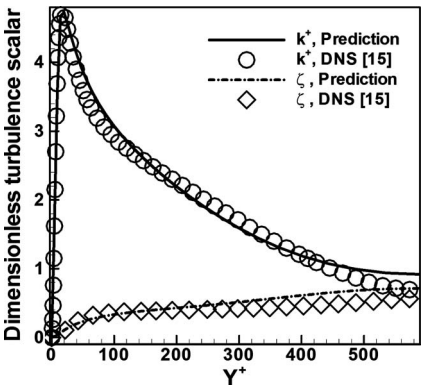

Fig. 2 Turbulence scalar distribution in the channel flow at Re$_\tau$=590

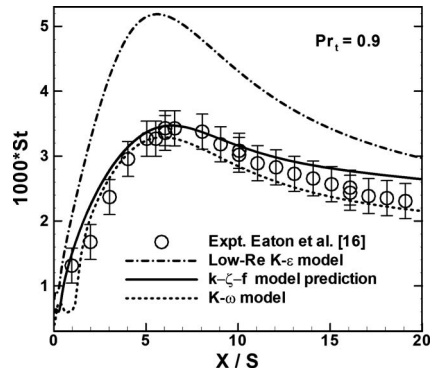

Fig. 4 Stanton number comparison for the heated wall in the backward-facing step flow

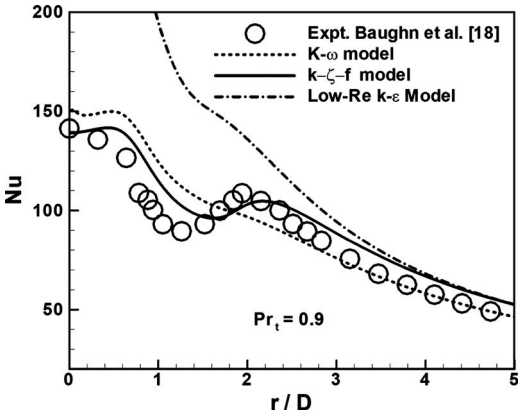

Fig. 5 Nusselt number comparison for the normally impinged jet flow on a flat plate

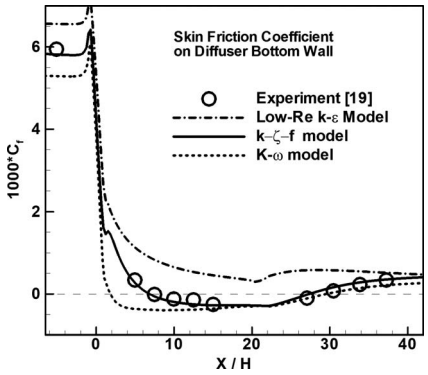

Fig. 7 Skin friction coefficient comparison for a 10 deg diffuser

between the measured and simulated results for the Nusselt number on the heated plate is presented in Fig. 5. The AKN low-Reynolds number k-ε turbulence model fails to simulate the magnitude of the measured heat transfer rate in the stagnation flow region, and the k-ω SST turbulence model fails to simulate the measured behavior in the same region. The k-ε-ζ turbulence model shows significant improvement in simulating the behavior and the magnitude of the heat transfer in the stagnation flow region.

The fourth benchmark problem that is used to validate the developed UDF code is the 2D flow in a plane asymmetric 10 deg diffuser having an expansion ratio of 4.7. Flow measurements (for mean velocity and skin friction coefficient) in this geometry were reported by Buice and Eaton [3,19]. The measurements are reported for a Reynolds number of 20,000 based on the upstream channel height ($H=1.5$ cm) and the upstream bulk velocity of 20 m/s [3]. Isothermal air flow with a fully developed velocity distribution in the upstream duct is introduced at the inlet of the diffuser. Comparisons between measured and simulated results are presented in Fig. 6 for the mean velocity distribution and in Fig. 7 for the distribution of the skin friction coefficient. Results from using the AKN low-Reynolds number k-ε turbulence model for simulating this flow are also presented in Fig. 6 and show that this turbulence model fails to develop any recirculation flow region in this small diffuser angle geometry. The k-ω SST turbulence model simulates reasonably well the reattachment point for this flow, but it fails in simulating accurately the flow separation point in this diffuser, as shown in Fig. 7. The k-ε-ζ turbulence model, however, generates results that provide good agreements with measurements.

The good agreements between measured and simulated results for the above four benchmark problems validate the developed UDF for the k-ε-ζ turbulence model and the process of its inclusion in the FLUENT-CFD code. The results also show that this turbulence model offers significant improvement over the commonly used turbulence models that are presently included in the FLUENT-CFD code.

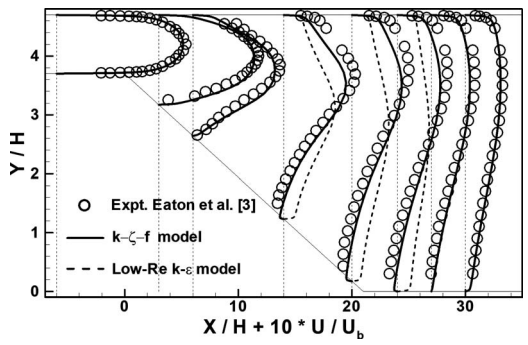

Fig. 6 Mean stream velocity comparison in a 10 deg diffuser

Problem Statement and Its Simulation

The two-dimensional asymmetric diffuser geometry that is used in this study has an upstream duct height of $H=1.5$ cm and a downstream duct height of $h=4.7H$, thus resulting in an expansion ratio of 4.7 and a step height of 5.55 cm. Isothermal (at a temperature of 293 K) and fully developed turbulent air flows are introduced into the diffuser with a bulk streamwise velocity of $U_b=20$ m/s, resulting in a Reynolds number $\mathrm{Re}_H=20{,}000$ (based on the upstream duct height and upstream bulk velocity, U_b). The upstream bulk velocity is chosen as a reference velocity, $U_{\mathrm{ref}}=U_b=20$ m/s in this study. This geometry and flow conditions are similar to those used in the experiment by Buice and Eaton [19], where the diffuser angle was fixed at 10 deg. In this study, however, the diffuser angle will be varied between 6.5 deg and 90 deg while keeping the expansion ratio fixed at 4.7 in order to examine the effect of the diffuser angle on the heat convection. A uniform and constant heat flux of $q_w=200$ W/m^2 is supplied to the bottom wall of the diffuser (starting from the first intersection corner of the diffuser) while treating all the other walls as adiabatic surfaces, as shown in Fig. 8.

The computational domain that is used in this study is 0.045 m long upstream and 1.8 m long downstream from the first sharp corner of the diffuser, i.e., $-3 \leq X/H \leq 120$. Using a longer downstream length of $150H$ did not change the reattachment length or the bottom wall temperature distribution. The origin of the x-coordinate axis for the simulation is taken at the first corner of the diffuser (that is the intersection of the upstream duct with the inclined wall of a diffuser), and the bottom wall of the diffuser is the beginning of the y-coordinate, as shown in the schematic of the diffuser geometry and the computational domain in Fig. 8. The velocity distribution from a fully developed turbulent air flow in a duct (duct height of $H=1.5$ cm and bulk streamwise velocity of

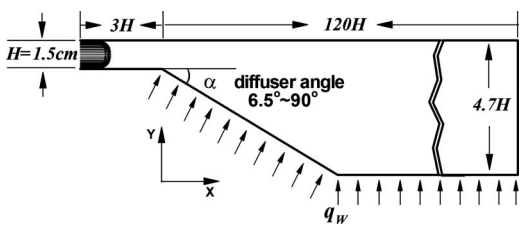

Fig. 8 Schematic of the asymmetric diffuser and the computational domain

Table 2 Grid independence study for the 30 deg diffuser angle case

Grid points ($X \times Y$)	Y_p^+	X_s/H	X_r/H
180×60	6.0	0	30.43
280×60	6.0	0	30.67
280×100	3.21	0	30.86
280×120	1.54	0	30.95
280×140	0.93	0	31.0

20 m/s) and a uniform temperature of 293 K are used as the inlet boundary conditions for the diffusers and are imposed at the inlet plane of $X/H=-3$. A pressure-outlet boundary condition is used at the diffuser's exit plane of $X/H=120$. A nonuniform structured computational grid is used in the simulation with a finer grid near the solid walls and in the regions where high velocity or temperature gradients occur. The grid density in the wall-normal direction is much more critical than the streamwise grid density for an accurate simulation. For example, for the diffuser with a diffuser angle of 30 deg, a difference of less than 1% in the reattachment length resulted from a simulation that uses a computational grid of 180×60 points ($X \times Y$) as compared to the simulation that uses a computational grid of 280×60 points. A grid-independent simulation was checked and verified for each individual diffuser, and a sample of such study for the 30 deg diffuser is shown in Table 2. All the results presented in this study were generated from simulations with fine grids in which the resulting y^+ for the first near-wall grid points are always less than unity.

Due to the large range of the diffuser's angles that are considered in this study, different types of a nonuniform structured grid distribution are used for simulating the flow and the heat transfer in these diffusers. A body-fitted type of a nonuniform structured grid distribution is used when the diffuser angle is equal to, or smaller than, 30 deg. For diffusers with a diffuser angle of 60 deg or larger, the nonuniform structured grid is generated zone by zone after partitioning the simulation domain into several zones, and in each zone quasiquadrilateral cells are generated. Typical grid styles and distributions for the two cases that are discussed above are shown in Figs. 9 and 10.

For grid consideration, the computational cell skewness value (defined as the difference between the shape of a cell and the shape of an equilateral cell of equivalent volume [17]) is a measure of grid quality, and it is recommended that it should be kept at a value of less than 0.8 (in the range of 0–1, where 0 means perfect cell) for generating good simulation results [17]. By using the grid generation strategy that was described above, the skewness value for diffusers with a diffuser angle of $\alpha \leqslant 30$ deg is smaller than 0.26, and that for diffusers with a diffuser angle of $\alpha \geqslant 60$ deg is smaller than 0.35. Nonuniform but unstructured grid distributions (triangular cells are used in the expansion region) with smaller skewness values were tested for both the 30 deg and

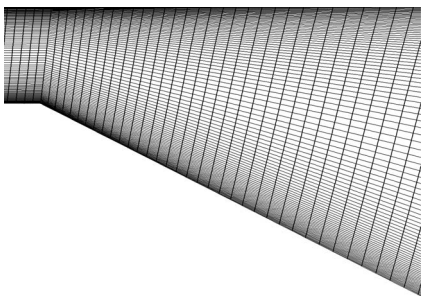

Fig. 9 Body-fitted grid for diffuser angles smaller than (including) 30 deg

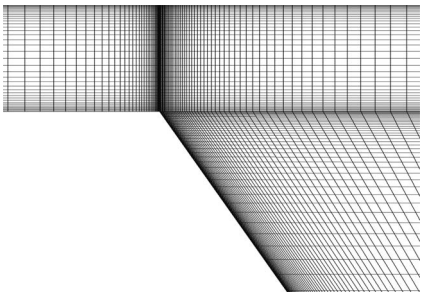

Fig. 10 Quasiquadrilateral grid for diffuser angles greater than (including) 60 deg

the 60 deg diffusers, and these produced the same results as the ones generated by using the nonuniform structured grid distributions that are shown in Figs. 9 and 10. For that reason, the nonuniform structured grid distribution was used in generating all the results that are presented in this study. The computation is considered as converged when the residuals for velocity and temperature are smaller than 10^{-8} and the residuals for all other variables are smaller than 10^{-6}, and all the presented results are from converged solutions.

Results and Discussion

Simulated streamlines are presented in Fig. 11 to illustrate the effect of the diffuser angle on the general flow behavior. The expected primary recirculation flow region develops downstream from the first sharp corner, and an increase in the diffuser angle results in a larger recirculation flow region and, consequently, a larger reattachment length. For the backward-facing step geometry (diffuser angle of 90 deg), a very small recirculation flow region appears to develop at the bottom corner of the step with an opposite recirculation flow direction than the one in the primary recirculation flow region, but such region is not observed in diffusers with smaller diffuser angles. In diffusers with diffuser angles less than 30 deg, flow separation does not start at the first corner of the diffuser but further downstream along the inclined step wall. The results in Fig. 11 also show that a recirculation flow region does not develop in diffusers with diffuser angles equal to, or smaller than, 6.5 deg. The flow separation and reattachment locations for the different diffusers are listed in Table 3. The results show that the separation and reattachment points do not change appreciably for the cases when the diffuser angle varies from 30 deg to 90 deg, but significant changes in these locations develop when the diffuser angle is below 30 deg. The magnitude

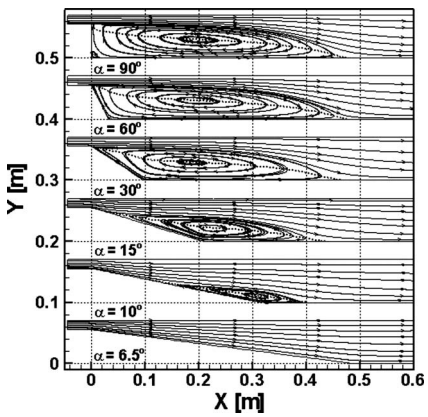

Fig. 11 Streamlines in diffusers with different diffusers

Table 3 Separation and reattachment points for different diffusers

Diffuser angle (deg)	X_s/H	X_r/H	$(X_r-X_s)/H$
6.5	NA	NA	NA
10	7.07	27.33	20.16
15	1.33	28.89	27.56
30	0	31.0	31.0
60	0	31.66	31.66
90	0	31.82	31.82

of the velocities that develop in the recirculation flow region increases as the diffuser angle increases, and this is responsible for the increase in the heat transfer.

The effect of the diffuser angle on the air temperature distribution is presented in Fig. 12 through plots of temperature contours. A local hot region develops near the second corner of the diffuser due to relatively low convective velocities in that region of the flow, and the maximum air temperature that develops in the region increases as the diffuser angle increases. The thickness of the heated fluid layer that develops above the bottom heated wall also increases as the diffuser angle increases.

The effect of the diffuser angle on the streamwise wall temperature distribution for the heated bottom wall is presented in Fig. 13, and the small arrow symbols in this figure identify the locations of the second corner in each diffuser. Significant changes in the wall temperature develop in the first half of the recirculation flow regions when the diffuser angle varies between 30 deg to 90 deg. It is interesting to note that in that range of diffuser angles the flow separation and the reattachment locations do not change appreciably but the wall temperature does. The peak in these distributions occurs in the neighborhood of the second corner of each specific diffuser and the magnitude of that peak increases as the diffuser angle increases. However, in the fully developed regime, the wall temperature is higher when the diffuser angle is smaller; i.e., a smaller diffuser angle corresponds to worse cooling of the heated wall by the inlet fluid in the fully developed flow region. The peak that develops in the wall temperature distribution for a diffuser angle of 90 deg is 337.5 K, but it is not shown in Fig. 13 in order to enhance the visibility of the other peaks that are presented in the figure.

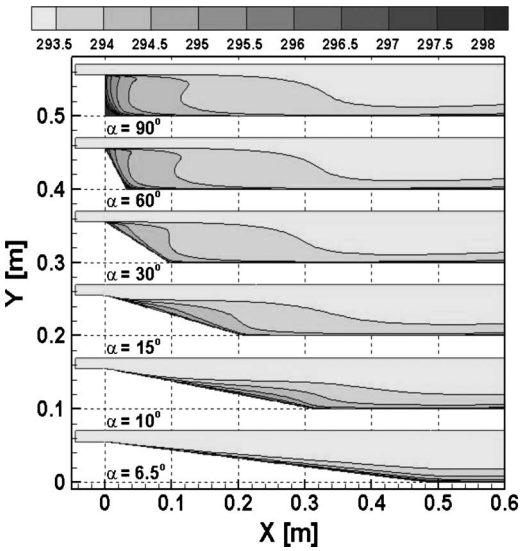

Fig. 12 Temperature contours in diffusers with different diffusers

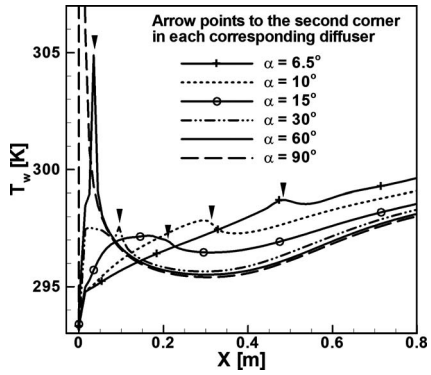

Fig. 13 Temperature along the heated wall in different diffusers

The effect of the diffuser angle on the streamwise distribution of the bulk air temperature is presented in Fig. 14. The bulk air temperature and the peak exhibited in its distribution increase with increasing diffuser angle. The increase in bulk air temperature with increasing diffuser angle is due to the increase in the heated wall surface area. The bulk air temperature for the smallest diffuser angle of 6.5 deg exhibits no peaks since no flow recirculation is developed in the diffuser, and its behavior is similar to a flow in a straight duct. The fully developed flow region in each diffuser can be identified by the region where the slope is starting to be constant in these distributions, i.e., similar to a fully developed bulk air temperature distribution in a straight duct with the same thermal boundary conditions.

The effect of the diffuser angle on the streamwise distribution of the Stanton number (based on the bulk temperature) is presented in Fig. 15 (the distributions for the 60 deg and 90 deg diffusers are not easily differentiable from each other in the fully developed regime). A higher diffuser angle produces a higher heat transfer rate, and this is due to the effect of a larger recirculation flow region and stronger interactions between the fluid and the heated wall inside this region. The region that is in the neighborhood of the second corner of the diffuser corresponds to a region with the local minimum Stanton number, i.e., a location with a relatively low local convective heat transfer rate. After this minimum value, the Stanton number starts to increase to a peak in a location upstream of the reattachment point. This peak is higher and moves upstream as the diffuser angle increases. The distance between the reattachment point and the location where the Stanton number is a maximum increases with increasing diffuser angle. The Stanton number starts to decrease after its peak along the streamwise direction and approaches asymptotically its fully developed flow behavior as in a duct with a constant cross-sectional area.

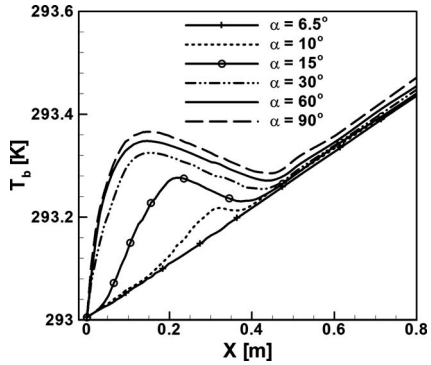

Fig. 14 Streamwise distribution of bulk temperature in different diffusers

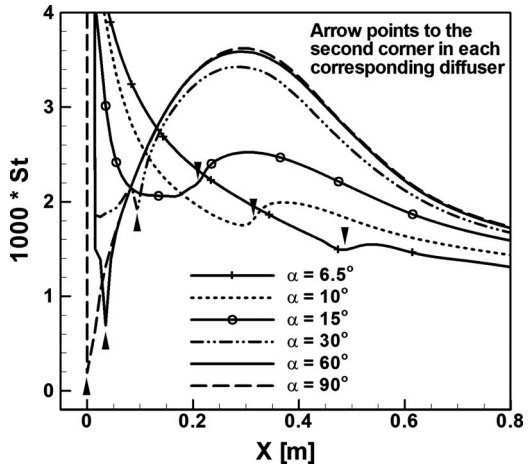

Fig. 15 Stanton number distribution along the heated wall in different diffusers

Conclusions

UDFs for the k-ε-ζ turbulence model have been developed and incorporated into the FLUENT-CFD code for the purpose of examining the effect of an asymmetric diffuser angle on forced convection. The developed UDF code was validated by simulating four benchmark problems that included both turbulent flow and heat transfer measurements and by comparing the simulated results with published data. Very good agreements between simulated results and measurements were obtained for these benchmark problems. The results generated by using this turbulence model compare better with benchmark data than the ones that are generated by using commonly used turbulence models that are presently included in the FLUENT-CFD code. The simulated results for the asymmetric diffuser indicate that most of the characteristics increase as the diffuser angle increases, such as the size of the recirculation flow region, the reattachment length, the maximum wall temperature, the bulk air temperature and its peak, and the maximum Stanton number. When the diffuser angle is smaller than 30 deg, flow separation does not start at the first corner of the diffuser but further downstream along the diffuser's inclined wall. A recirculation flow region does not develop when the diffuser angle is equal to, or smaller than, 6.5 deg. The increase in the diffuser angle also results in the increasing magnitude of reversed flow velocities in the recirculation flow region, and this enhances the heat transfer rate. The distance between the reattachment point and the location where the Stanton number is a maximum increases with increasing diffuser angle. The developed UDF code for the k-ε-ζ turbulence model could be used to predict turbulent heat transfer in other geometries with separated and reattached flows with reasonable accuracy, and it offers some improvements to the capabilities of the FLUENT-CFD code.

Acknowledgment

This work was supported in part by DOE Basic Energy Sciences Grant No. DE-FG02-03ER46067 and by NSF Grant No. CTS-0352135. The authors gratefully acknowledge Dr. Popovac (Delft University of Technology) for his kind help and advice.

Nomenclature

C_f = skin friction coefficient, $C_f = \mu(du/dy)_w/(0.5\rho u_b^2)$
C_p = thermal specific heat ($J\,kg^{-1}\,K^{-1}$)
D = nozzle diameter (m)
f = elliptic relaxation function
G_k = turbulent kinetic energy production (times density) ($kg\,m^{-1}\,s^{-3}$)
H = upstream channel height in diffuser geometry (m)
k = turbulent kinetic energy ($m^2\,s^{-2}$)
k^+ = nondimensional turbulent kinetic energy, $k^+ = k/u_\tau^2$
L = turbulent length scale (m)
Nu = Nusselt number, $\mathrm{Nu} = q_w D/\lambda(\bar{T}_w - \bar{T}_{in})$
Pr_t = turbulent Prandtl number
q_w = heat flux ($W\,m^{-2}$)
r = radius from the jet impingement center point (m)
Re_τ = Reynolds number based on friction velocity and half channel height for two-dimensional channel flow, $\mathrm{Re}_\tau = u_\tau \delta/\nu$
S = step height (m)
$\bar{S}$ = strain rate magnitude (s^{-1})
S_{ij} = strain rate tensor (s^{-1})
St = Stanton number, $\mathrm{St} = q_w/[\rho U_{ref} C_p(\bar{T}_w - \bar{T}_b)]$ (in the second test case of convection in 2D backward-facing step, $\mathrm{St} = q_w/[\rho U_{ref} C_p(\bar{T}_w - \bar{T}_{in})]$)
T = turbulent time scale (s)
$\bar{T}$ = temperature (K)
$\bar{T}_b$ = bulk average temperature, $\bar{T}_b = \int \rho u \bar{T} dy / \int \rho u dy$ (K)
U_b = bulk average velocity ($m\,s^{-1}$)
U_i = velocity component ($m\,s^{-1}$)
U_{ref} = reference velocity ($m\,s^{-1}$)
u_τ = friction velocity, $u_\tau = \sqrt{\tau_w/\rho}$ ($m\,s^{-1}$)
$\overline{v^2}$ = wall-normal Reynolds stress component ($m^2\,s^{-2}$)
x_i = coordinate vector component (m)
X_r = reattachment point (m)
X_s = separation point (m)
y^+ = nondimensional distance from the wall, $y^+ = y u_\tau/\nu$, y is the distance from the wall

Greek Symbols

α = diffuser angle (deg)
δ = half channel height (for two-dimensional channel flow) (m)
ε = turbulent dissipation rate ($m^2\,s^{-3}$)
λ = thermal conductivity ($W\,m^{-1}K^{-1}$)
μ_t = turbulence viscosity ($kg\,m^{-1}\,s^{-1}$)
ν = kinematic viscosity ($m^2\,s^{-1}$)
ρ = density ($kg\,m^{-3}$)
τ_w = wall shear stress, $\tau_w = \rho\nu(dU/dy)_w$ ($kg\,m^{-1}\,s^{-2}$)
ζ = $\overline{v^2}/k$

Subscripts

in = inlet of the computational domain
w = wall
p = first near-wall point

References

[1] Obi, S., Aoki, K., and Masuda, S., 1993, "Experimental and Computational Study of Separating Flow in an Asymmetric Plane Diffuser," *Ninth Symposium in Turbulent Shear Flows*, Kyoto, Japan, Aug. 16–19, pp. 305-1–305-4.
[2] Buice, C., and Eaton, J., 1996, "Experimental Investigation of Flow Through an Asymmetric Plane Diffuser," Annual Research Briefs, Center of Turbulence Research, Stanford University, pp. 243–248.
[3] Buice, C., and Eaton, J., 2000, "Experimental Investigation of Flow Through an Asymmetric Plane Diffuser," ASME J. Fluids Eng., **122**, pp. 433–435.
[4] Makiola, B., and Ruck, B., 1990, "Experimental Investigation of a Single-sided Backward-Facing Step Flow With Inclined Step Geometries," *Engineering Turbulence Modeling and Experiments*, Elsevier, New York, pp. 487–497.

[5] Iaccarino, G., 2001, "Predictions of a Turbulent Separated Flow Using Commercial CFD Codes," ASME J. Fluids Eng., **123**, pp. 819–828.
[6] Kaltenbach, H., Fatica, M., Mittal, R., Lund, T., and Moin, P., 1999, "Study of Flow in a Plane Asymmetric Diffuser Using Large-Eddy Simulation," J. Fluid Mech., **390**, pp. 151–185.
[7] Apsley, D., and Leschziner, M., 1999, "Advanced Turbulence Modeling of Separated Flow in a Diffuser," Flow, Turbul. Combust., **63**, pp. 81–112.
[8] Lien, F., and Kalitzin, G., 2001, "Computations of Transonic Flow With the $\overline{v^2}$-f Turbulence Model," Int. J. Heat Fluid Flow, **22**, pp. 53–61.
[9] Durbin, P., 1991, "Near-Wall Turbulence Closure Modeling Without Damping Functions," Theor. Comput. Fluid Dyn., **3**, pp. 1–13.
[10] Durbin, P., 1995, "Separated Flow Computations With the $k-\varepsilon-\overline{v^2}$ Model," AIAA J., **33**(4), pp. 659–664.
[11] Laurence, D., Uribe, J., and Utyuzhnikov, S., 2004, "A Robust Formulation of the $\overline{v^2}$-f Model," Flow, Turbul. Combust., **73**, pp. 169–185.
[12] Lien, F., and Durbin, P., 1996, "Non-Linear $k-\varepsilon-\overline{v^2}$ Modeling With Application to High-Lift," *Proceedings of 1996 Summer Programme*, Centre for Turbulence Research, Stanford University, pp. 5–22.
[13] Davidson, L., Nielsen, P., and Sveningsson, A., 2003, "Modifications of the $\overline{v^2}$-f Model for Computing the Flow in a 3D Wall Jet," *Turbulence Heat and Mass Transfer 4*, K. Hanjalic, Y. Nagano, and M. J. Tummers, eds., Begell House, Inc., New York, pp. 577–584.
[14] Hanjalic, K., Popovac, M., and Hadziabdic, M., 2004, "A Robust Near-wall Elliptic-Relaxation Eddy-Viscosity Turbulence Model for CFD," Int. J. Heat Fluid Flow, **25**, pp. 1047–1051.
[15] Moser, R., Kim, J., and Mansour, N., 1999, "Direct Numerical Simulation of Turbulent Channel Flow Up to Re_τ=590," Phys. Fluids, **11**, pp. 943–945.
[16] Vogel, J., and Eaton, J., 1984, "Heat Transfer and Fluid Mechanics Measurements in the Turbulent Reattaching Flow Behind a Backward-Facing Step," Stanford University, Report No. MD-44.
[17] FLUENT 6.2 User's Guide, Fluent Inc., 2005.
[18] Baughn, J., and Shimizu, S., 1989, "Heat Transfer Measurements From a Surface With Uniform Heat Flux and an Impinging Jet," ASME J. Heat Transfer, **111**, pp. 1096–1098.
[19] Buice, C., and Eaton, J., 1997, "Experimental and Computational Study of Turbulent Separating Flow in an Asymmetric Plane Diffuser," Thermosciences Division, Department of Mechanical Engineering, Stanford University, CA, Report No. TSD-107.

Heat Transfer and Pressure Drop Correlations for Square Channels With 45 Deg Ribs at High Reynolds Numbers

Akhilesh P. Rallabandi

Huitao Yang

Je-Chin Han
e-mail: jc-han@tamu.edu

Department of Mechanical Engineering,
Turbine Heat Transfer Laboratory,
Texas A&M University,
College Station, TX 77843-3123

Systematic experiments are conducted to measure heat transfer enhancement and pressure loss characteristics on a square channel (simulating a gas turbine blade cooling passage) with two opposite surfaces roughened by 45 deg parallel ribs. Copper plates fitted with a silicone heater and instrumented with thermocouples are used to measure regionally averaged local heat transfer coefficients. Reynolds numbers studied in the channel range from 30,000 to 400,000. The rib height (e) to hydraulic diameter (D) ratio ranges from 0.1 to 0.18. The rib spacing (p) to height ratio (p/e) ranges from 5 to 10. Results show higher heat transfer coefficients at smaller values of p/e and larger values of e/D, though at the cost of higher friction losses. Results also indicate that the thermal performance of the ribbed channel falls with increasing Reynolds numbers. Correlations predicting Nusselt number (Nu) and friction factor ($\bar{f}$) as a function of p/e, e/D, and Re are developed. Also developed are correlations for R and G (friction and heat transfer roughness functions, respectively) as a function of the roughness Reynolds number (e^+), p/e, and e/D. [DOI: 10.1115/1.3090818]

1 Introduction

Cooling gas turbine vanes and blades let the engine operate at a higher temperature and therefore, at a higher efficiency. Modern engines incorporate a lot of external and internal cooling technologies. Film cooling is used on the surface of the blade, pin-fin cooling is used inside the trailing edge, impingement cooling is used inside the leading edge, and rib-turbulated cooling is used in the central body of the blade.

In a gas turbine engine, a small percentage of the air passing though the compressor is ducted such that it bypasses the combustion chamber and flows through a channel within the blade acting as a coolant. A common technique used to enhance heat transferred from the hot blade to the coolant air is rib-turbulated cooling—where the flow inside the channel is tripped by a series of ribs—inducing turbulence and therefore increasing the heat transfer. However, this obstructed turbulent flow inevitably incurs a large pressure drop (owing to increased form drag due to the ribs). The designer must therefore keep both heat transfer and pressure drop in mind before selecting a channel. Of late, rib-turbulated cooling has also being used in solar air heaters [1].

Scaled down experiments (preserving the Reynolds number within the incompressible flow regime) are key to analyzing the various parameters that effect rib-turbulated cooling. Experiments are typically run at and around room temperature and at much lower pressures than those encountered in gas turbines. The results are presented in an appropriate nondimensional form and can be scaled up and down by the designer.

When the spacing between two consecutive ribs (p) is very large in comparison with the height of the rib (e), the heat transfer enhancement and friction factor penalty tend to be small, since the channel has very few ribs. Taller ribs tend to increase the heat transfer coefficient (at the cost of incurring a larger pressure drop). Most of the literature focuses on lower blockage ratios ($e/D < 0.2$). High blockage channels have been investigated by Taslim and Lengkong [2] and more recently by Bailey and Bunker [3].

Instead of using ribs perpendicular to the flow to trip the flow, it has been found that using ribs inclined to the flow is more beneficial from both heat transfer and friction factor (pressure drop) perspectives. This is because secondary flows developing along the turbulators introduce a "secondary" swirl within the channel, which improves the heat transfer coefficient. Investigations into the structure of the secondary flow have been performed in the literature [4–6].

Further derivatives of the inclined rib concept (the crossed ribs, the V-shaped rib, inverted V-shaped rib, the broken parallel rib, the V-shaped broken ribs, delta and wedge shaped ribs, etc.) have been studied by Lau et al. [7] and Han et al. [8,9]. V-shaped ribs are shown to enhance heat transfer over parallel ribs at lower friction factors than comparable parallel ribs. The broken V-shaped ribs are found to enhance heat transfer further at a comparable pressure drop.

At lower Reynolds numbers in the ribbed channel, both the friction factor and average "fully developed" Nusselt number are found to be relatively low. The typical friction factor ($\bar{f}$) tends to attenuate to a constant value as the Reynolds number is increased. The Nusselt number shows a monotonically increasing trend with the Reynolds number.

When these parameters are compared with a those of a smooth channel, (f_0 and Nu_0), the $\bar{f}/f_0$ ratio tends to increase with Re, since f_0 tends to fall with Re, as is documented in classic experiments conducted by Moody [10]. Though the heat transfer coefficient increases in absolute value with an increase in Re, the enhancement ratio over a corresponding smooth channel tends to decrease with an increase in Reynolds number. It is well established that the thermal performance (F) of the channel, defined as $F=(\mathrm{Nu}/\mathrm{Nu}_0)/(\bar{f}/f_0)^{1/3}$, tends to fall with increasing Re.

There are many studies available in literature, which consider channels of varying aspect ratios from $W/H=\frac{1}{4}$ to $W/H=4$. Though the ribbed-side heat transfer augmentation is of the same order in all cases, the friction factor is much higher for channels

Contributed by the Heat Transfer Division of ASME for publication in the JOURNAL OF HEAT TRANSFER. Manuscript received June 23, 2008; final manuscript received November 25, 2008; published online May 14, 2009. Review conducted by Frank Cunha.

with wider aspect ratios [11]. Studies by Taslim et al. [12] have focused on cooling passages embedded in the leading edge of the blade. Zhang et al. [13] performed studies on a ribbed triangular channel.

Turbine blades are typically manufactured by casting—which results in fillets at the edges of ribs in the internal passages. Investigations [14] have been conducted on the influence of the profile on the heat transfer coefficients and friction factor. It is found to reduce the pressure drop penalty without adversely affecting the heat transfer—a beneficial effect.

From the above discussion it is evident that the heat transfer coefficient and the friction factors depend on a variety of parameters. Dipprey and Sabersky [15] detailed a method to analyze the pressure drop and heat transfer in a rough duct using nondimensional parameters based on the turbulent boundary layer law-of-the-wall. Han et al. [16–21] adapted these parameters to rib-roughened channels. This correlation has been applied to various rib configurations (V-shaped, V-shaped broken etc.) [8,9] and aspect ratios [18–21].

Early experiments were conducted based on the thin-foil heater method, where a "center-line" heat transfer coefficient was determined by placing thermocouples on the centerline of the channel [18,20]. More recently, the copper plate method (in which each wall of the channel is divided into multiple regions comprising one high conductivity copper plate each) has been employed [8]. Local heat transfer coefficients have been also measured by naphthalene sublimation [22], liquid crystals [23], and IR thermography. These local measurement techniques indicate clearly the various regions of flow separation and reattachment and zones of high heat transfer and low heat transfer. Computational methods [24], as of late, have started lending further insights into secondary flow structures.

The current study focuses on land based power generation turbines, where internal passage Reynolds numbers are very high (100,000–500,000). Almost all studies in open literature focus on Reynolds numbers lower than 100,000. Here, Reynolds numbers ranging from 30,000 to 400,000 with blockage ratios (e/D) ranging from 10% to 18% and spacing ratios (p/e) ranging from 5 to 10 are studied. The correlation by Han et al. [18–20] is modified to fit into the parameter range investigated; a new correlation to predict Nu and $\bar{f}$ for the parameter range investigated is presented. The copper plate technique is used to obtain regionally averaged heat transfer coefficients.

2 Test Section and Experimental Procedure

Air at high pressure is ducted in from three Ingersoll Rand oil free compressors operating at a pressure of 820 kPa (120 psi). This air enters the flow loop shown in Fig. 1(a). The flow rate of air is metered using a 50.8 mm (2 in.) diameter orifice plate flow meter. This metering is performed by measuring pressures immediately upstream of the orifice plate and across the orifice plate (using digital and inclined manometers, respectively). The air enters a plenum downstream of the orifice flow meter. The test section is placed immediately downstream of the plenum, such that the flow experiences a sudden contraction (8:1) before entering the instrumented test section. This contraction induces an aerodynamic and thermal "developing" region in the channel before a "fully developed" state is obtained. This is arbitrary to simulate the entrance geometry of blade internal cooling.

The test section utilized is detailed in Fig. 1. It has a square cross section of 101.6×101.6 mm^2 ($4'' \times 4''$). Each of the four walls is subdivided into ten sequential streamwise regions, comprising of one copper plate each. Regions are separated by rubber gaskets to inhibit thermal conduction. Angled (45 deg) ribs are attached in a nonstaggered parallel pattern on the front and back surfaces only. The top and bottom surfaces are left smooth. Ribs used are made of copper and attached to the copper plates using a 0.05 mm thick double sided tape (to ensure uniform thermal contact). They are reinforced on either side using small pieces of foil tape. Some ribs do cross over from one region to the next region—and might create a conductive path for heat to flow from one region to another. This effect is neglected in data reduction—and might lead to minor errors in computing local heat transfer coefficients. This is not expected to affect the average heat transfer coefficient (used in the correlation), computed by averaging the fully developed regions, depicted in Fig. 2(a).

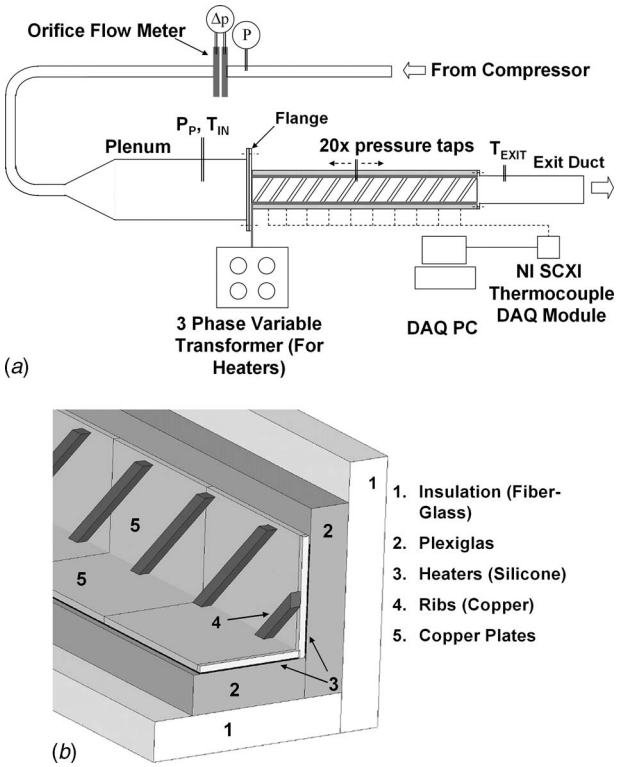

Fig. 1 (a) Schematic of experimental setup, indicating flow meter, plenum, test section, and temperature measurement system and (b) detailed view of instrumented test section

Four silicone heaters (manufactured by Watlow Inc.) are glued to the back of each surface (top, front, bottom, and back). The power input can be varied by controlling four separate single phase transformers and can be measured by measuring the voltage applied to the heater by a digital multimeter.

Each plate is instrumented with T type copper-constantan thermocouples, the front (ribbed) and top (smooth) copper plates have four thermocouples each, while the back (ribbed) and the bottom (smooth) plates have one thermocouple each. The thermocouples are buried inside a 0.4 mm (1/64 in.) diameter hole drilled on the plate and held in place by using an epoxy resin. These thermocouples are connected to a National Instruments SCXI 1000 Chassis via the NI SCXI 1303 terminal block. The temperatures are measured using the NI LABVIEW program. Thermocouples in the plenum and in the exit duct are connected to a digital thermometer.

Each of the ten top plates has two pressure taps, located at 25% and 75% of its length. Static pressure is measured using either an inclined manometer or a digital manometer, depending on its value.

The test section is installed in a 4 cm (1.5 in.) thick Plexiglas housing. Further insulation is provided (while running the heat transfer tests) by encapsulating the entire test section in a thick layer of fiber-glass. Figure 1(b) shows a cross-sectional illustration of the test section. Heat losses still incurred are calibrated for by running a heat loss test with all the insulation in place. Fur-

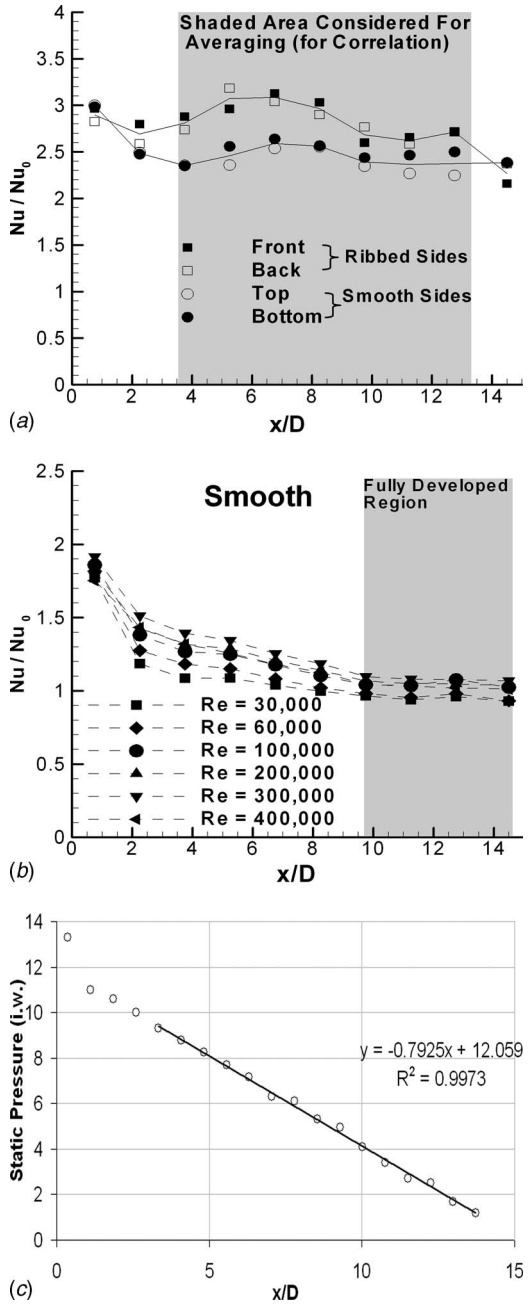

Fig. 2 (*a*) Values of Nu considered for averaging ($x/D>4$) for a ribbed channel (here shown on a typical Nu/Nu_0 profile) and (*b*) normalized Nusselt number ratios for a smooth channel. Ratio approaches 1 in the highlighted fully developed region and (*c*) friction factor derived by fitting straight line to measured static pressure profile for $x/D>4$ for a ribbed channel.

thermore, during the heat loss test, the test section is filled with fiber-glass in order to prevent heat leakage into the test section.

An exit duct downstream of the instrumented channel is provided to ensure thermal and hydraulic fully developed conditions are retained as the flow exits the channel.

Various cases tested and rib configurations are summarized in Table 1.

3 Data Reduction

The Reynolds number is computed using the expression

Table 1 Total to projected area ratio for all tests

	$p/e=5$	$p/e=7.5$	$p/e=10$
$e/D=0.1$	1.57	1.37	1.28
$e/D=0.15$	1.57	1.37	1.28
$e/D=0.18$	1.57	1.37	1.28

$$\mathrm{Re} = \frac{\rho u D}{\mu} \tag{1}$$

where u is the velocity in the test section, which is computed from the mass flow rate calculated from the orifice plate flow meter

$$u = \frac{\dot{m}}{\rho H^2} \tag{2}$$

Since the power supply to the heater is controlled by a single phase transformer, the heat flux through each plate can be calculated. The heat flux through each plate is maintained constant in the experiment, and the temperatures are measured by the thermocouple embedded in the copper plates.

The heat transfer coefficient, h is estimated (based on Newton's law of cooling) as

$$h = \frac{q - q_{\mathrm{loss}}}{A_P(T - T_b)} \tag{3}$$

The heat transfer coefficient in this study is based on the plate area (projected area) and not on the total area. Results are interconvertible and can be obtained by multiplying the area ratio for each case. The conversion factors are detailed in Table 1. From the table, it might seem counterintuitive that the area enhancement ratio for different values of e/D is identical—and that $A_{\mathrm{total}}/A_{\mathrm{projected}}$ is only a function p/e. This is because, for a constant p/e, as e/D increases, though the surface area of increased by each rib increases, the total number of ribs decreases. This ensures that the area ratio does not depend on e/D.

The heat loss is calibrated based on a heat loss test. The test section (with all insulation in place and its interior filled with fiber-glass as mentioned earlier) is heated until a steady state temperature is reached. The heat supplied at steady state is equal to the heat leakage through the external insulation. This test is conducted for two steady state temperatures, corresponding to the lowest and highest temperatures expected in the experiment. A heat loss correlation is then derived for each copper plate—and this correlation is used to compute the heat loss (q_{loss})—which is used in Eq. (3). For the ribbed channel, typical heat loss values are to the tune of 3–5% of the total heat supplied.

T_b is the local "bulk-mean" temperature, computed by interpolating the exit and inlet temperatures. Computing the exit temperature using an energy balance yields at most a 10% discrepancy over the measured temperatures.

The Nusselt number is defined as

$$\mathrm{Nu} = \frac{hD}{k_{\mathrm{air}}} \tag{4}$$

The average fully developed average Nusselt number for all ribbed cases is computed by considering the region highlighted in Fig. 2(*a*) for all ribbed cases. Figure 2(*b*) indicates the corresponding area considered for averaging smooth channel heat transfer data.

The friction factor used here is the Moody factor, defined for a pipe

$$\bar{f} = \frac{D}{2\rho u^2}\left|\frac{dP}{dx}\right| \tag{5}$$

The parameter dP/dx in this study is the slope of the least-squares-best-fit line graph in the region shown in Fig. 2(*c*), a

negative quantity. Static pressures are measured along a smooth surface.

The Prandtl number has the conventional definition

$$\mathrm{Pr} = \left(\frac{\mu c_p}{k}\right)_{\mathrm{air}} \approx 0.7 \tag{6}$$

The Stanton number is defined as

$$\mathrm{St} = \frac{\mathrm{Nu}}{\mathrm{Re\ Pr}} \tag{7}$$

The smooth channel correlations of Dittus–Boelter and Moody are utilized for normalizing the ribbed channel data, as is conventional in literature. The classical Dittus–Boelter correlation is

$$\mathrm{Nu}_0 = 0.023\ \mathrm{Re}^{0.8}\ \mathrm{Pr}^{0.4} \tag{8}$$

The Swamee–Jain approximation to the Colebrook correlation (for turbulent flow in a smooth pipe) is

$$f_0 = 0.331/\left(\ln\left(\frac{5.74}{\mathrm{Re}^{0.9}}\right)\right)^2 \tag{9}$$

Also computed is a "heat transfer performance" (F), a metric indicating the economic viability of the cooling scheme

$$F = \frac{\dfrac{\mathrm{Nu}}{\mathrm{Nu}_0}}{\left(\dfrac{\bar{f}}{f_0}\right)^{1/3}} \tag{10}$$

Dipprey and Sabersky [15] used the turbulent universal logarithmic boundary layer expressions to arrive at pertinent nondimensional groups (e^+, R, and G), which can correlate rough channel experimental data. Han and Park [20] used similar nondimensional groups (assuming rib roughness to be similar to sand-grain roughness) to correlate ribbed channel experimental data—with excellent agreement. Roughness parameters, as adapted by Han and Park [20], are computed as follows.

The parameter e^+ is the roughness Reynolds number. It is defined as

$$e^+ = \frac{e}{D}\mathrm{Re}\left(\frac{f}{2}\right)^{1/2} \tag{11}$$

The friction roughness function, R is defined as

$$R(e^+) = \left(\frac{2}{f}\right)^{1/2} + 2.5\ln\left(\frac{2e}{D}\frac{2W}{W+H}\right) + 2.5 \tag{12}$$

The heat transfer roughness function, G is defined as

$$G(e^+,\mathrm{Pr}) = R(e^+) + \frac{\dfrac{f}{2\ \mathrm{St}_r} - 1}{\left(\dfrac{f}{2}\right)^{1/2}} \tag{13}$$

where St_r is the averaged Stanton number corresponding to the ribbed sides only, and f is the equivalent four sided ribbed channel friction factor, computed from the two-sided ribbed case ($\bar{f}$) as follows:

$$f = \bar{f} + \frac{H}{W}(\bar{f} - f_0) \tag{14}$$

4 Results and Discussion

4.1 Heat Transfer Correlation. Figure 2(b) shows heat transfer (Nusselt number) results for the smooth case, normalized with the Dittus–Boelter correlation. ($\mathrm{Nu}/\mathrm{Nu}_0$). This ratio exceeds 1 significantly at low values of x/D, as would be expected of a developing turbulent flow in a pipe. At larger values of x/D, it is seen to attenuate to 1, validating the heat transfer measurements. The Nusselt numbers in the developed region are averaged and plotted against the Reynolds number in Fig. 3(a)—as a baseline for comparisons with ribbed heat transfer results.

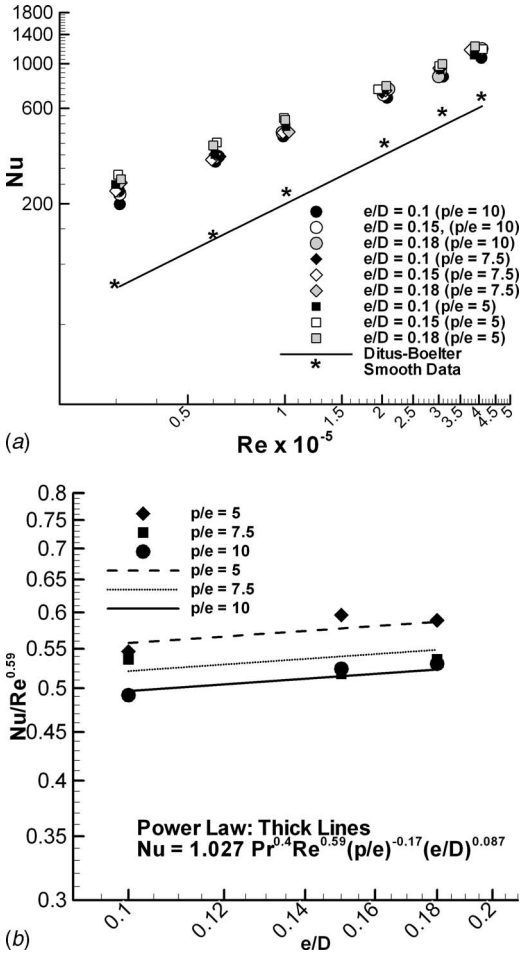

Fig. 3 (*a*) Fully developed ribbed-side average Nusselt numbers obtained in various test cases and (*b*) correlation for average Nu as a function of Re, rib height (*e*/*D*), and spacing (*p*/*e*)

Figures 4–6 depict the variation in the normalized Nusselt number ($\mathrm{Nu}/\mathrm{Nu}_0$) with x/D for various ribbed configurations. The shape of the curves is qualitatively similar to results reported by Han et al. [8] for 45 deg ribs—with a local maxima located at intermediate values of x/D. This local maxima is a signature of the secondary flow induced by inclined ribs. Ribs placed at 90 deg to the flow do not display this behavior. Another trend evident from these figures is that the $\mathrm{Nu}/\mathrm{Nu}_0$ strictly falls with increasing Re—which is also consistent with literature [20].

Significant enhancements of the heat transfer coefficient on the smooth side are also observed at high Reynolds numbers and at high values of e/D. This could be attributed to the secondary flow traveling along the rib "impinging" onto the smooth surface—and also to the high turbulence levels induced by the ribs. Figures 4–6 indicate that the enhancements on the smooth side are often comparable to those on the rough side.

The rib spacing (p/e) also has a decreasing monotonic relationship with the Nusselt number (i.e., as the spacing between two consecutive ribs increases, the Nusselt number decreases). This can be attributed to two reasons. First, the heat transfer interface area between the flow and the test section increases as ribs (which are thermally active, since they are made of copper) are placed more densely within the channel. This would result in a higher

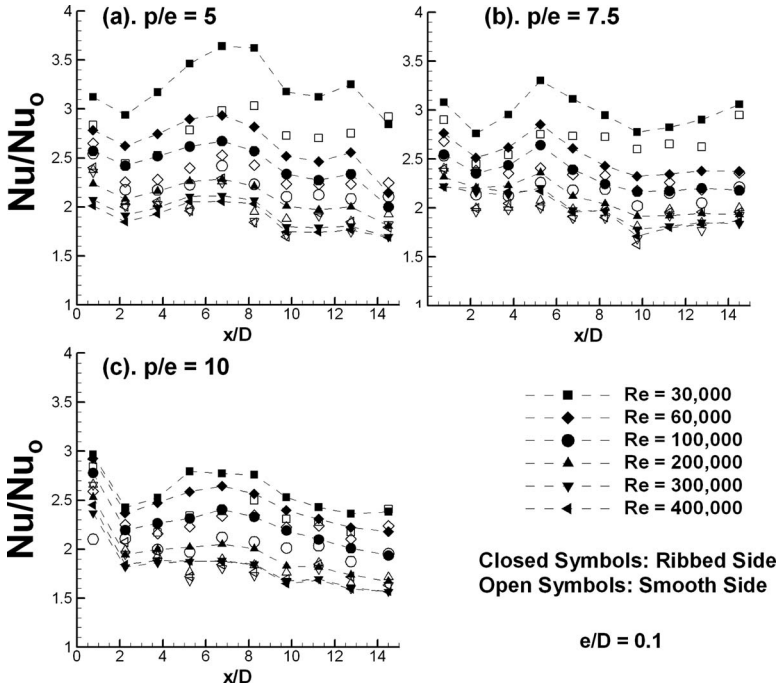

Fig. 4 Nusselt number ratios plotted along the channel for $e/D=0.1$: (*a*) $p/e=5$, (*b*) $p/e=7.5$, and (*c*) $p/e=10$

heat transfer coefficient based on projected area for the same heat transfer coefficient based on total area. Second, a larger number of ribs (smaller p/e) could induce greater secondary flow—and greater turbulence. This effect is schematically explained in Fig. 7(*a*), which compares three separate p/e ratios for a single e/D (0.1). The size of the recirculation zone downstream of the rib in each case remains the same, as does the reattachment (high heat transfer) zone. The boundary layer then starts to develop (reducing local heat transfer as it becomes thicker) until it is tripped by the next rib. This further reduces the heat transfer coefficient for larger values of p/e (as there is more distance between two consecutive ribs). The combined effect is evident in Figs. 3–6.

The rib height has an increasing monotonic relationship with the Nusselt number. This effect can be attributed to the obstruction to the flow, which enhances the secondary flow—and therefore heat transfer—as is demonstrated by Figs. 3–6. The recirculation

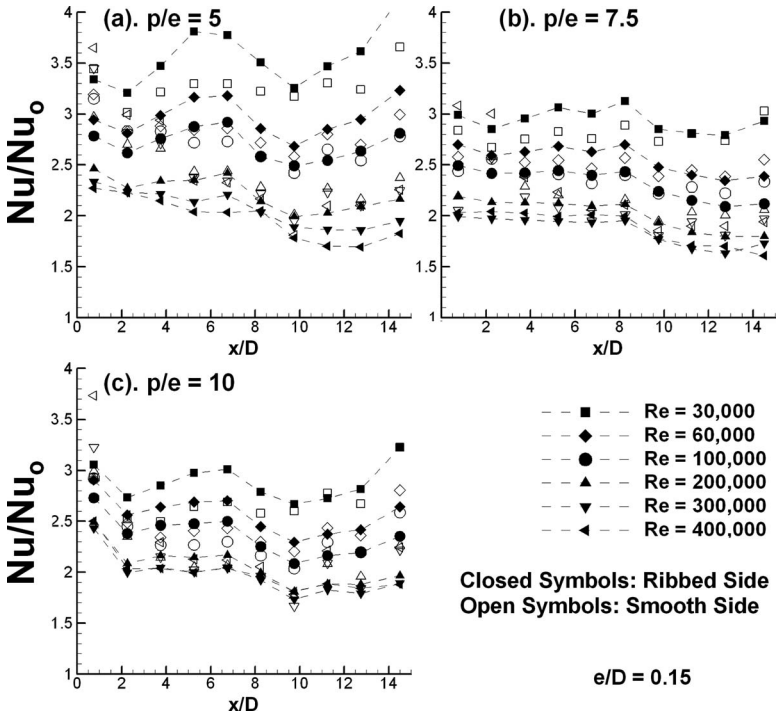

Fig. 5 Nusselt number ratios plotted along the channel for $e/D=0.15$: (*a*) $p/e=5$, (*b*) $p/e=7.5$, and (*c*) $p/e=10$

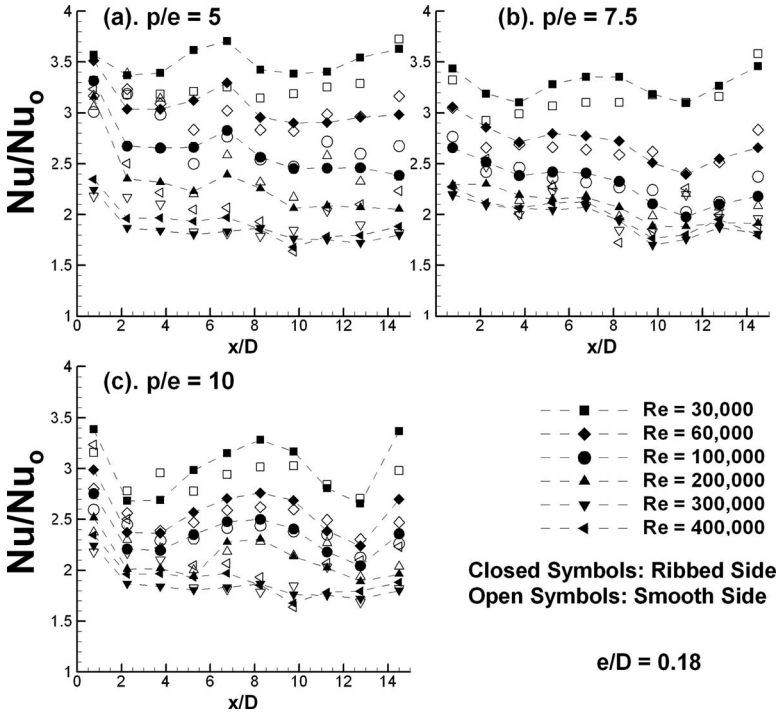

Fig. 6 Nusselt number ratios plotted along the channel for $e/D=0.18$: (*a*) $p/e=5$, (*b*) $p/e=7.5$, and (*c*) $p/e=10$

zone, the reattachment zone, and the developing boundary layer region all increase in size as e increases (Fig. 7(*a*)). Heat transfer increases significantly in the separation and reattachment zones due to the increased rib height. This results in an overall increase in heat transfer. An increase in rib height does not result in an increase in total area available for heat transfer for a given p/e, as is demonstrated in Table 1.

For the range of parameters (p/e and e/D) studied, Fig. 3(*a*) indicates that the ribbed-side averaged Nu values, when plotted on a log-log scale against Re, all seem to be linear (with the same slope). This indicates that the relationship between Nu and Re is amenable to correlation by a power law with a parameter independent exponent. A correlation is developed by computing a least-squares best fit for the parameter range studied in the experiment.

$$\mathrm{Nu} = 1.027\ \mathrm{Pr}^{0.4}\ \mathrm{Re}^{0.59}\left(\frac{p}{e}\right)^{-0.17}\left(\frac{e}{D}\right)^{0.09}$$

$$30{,}000 < \mathrm{Re} < 400{,}000, 5 < \frac{p}{e} < 10, 0.1 < \frac{e}{D} < 0.2 \quad (15)$$

This correlation has a maximum deviation of $\sim 7\%$.

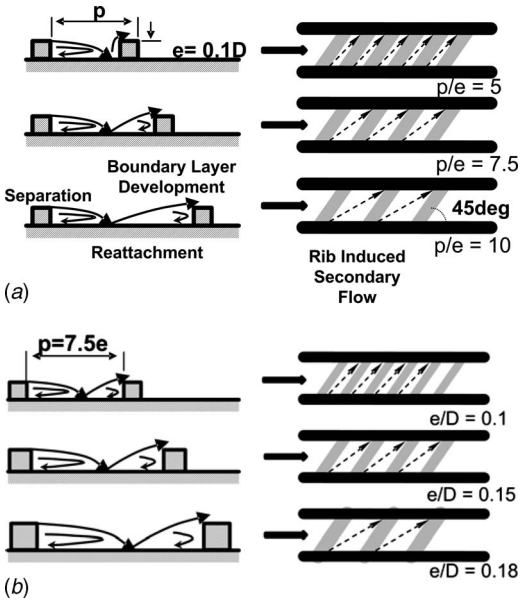

Fig. 7 (*a*) Schematic of flow over inclined ribs indicating the effect of rib spacing for constant rib height and (*b*) schematic of flow over inclined ribs indicating effect of rib height (for constant p/e)

4.2 Friction Factor Correlation. Increasing the number of ribs and height of the ribs (decreasing p/e and increasing e/D) has a beneficial impact on the heat transfer coefficient by tripping the flow, increasing turbulence, and inducing secondary swirls. This increase comes at a price: higher friction losses. A designer, therefore, needs friction data to complement heat transfer data.

Friction factors in a smooth pipe are due to skin friction only, and have a tendency to reduce with Re [10]. However, when ribs are introduced, the regime shifts from a purely skin friction case to a case dominated by form drag due to the ribs. The flow encounters obstructions (ribs) and forms separation zones immediately downstream of the ribs, which induces drag on the test section, and therefore a pressure drop in the flow. Ribs also trip the boundary layer—necessitating the development of a new boundary layer after the flow reattaches. This results in thinner boundary layers between the ribs and, therefore, higher friction factors.

There is consensus in literature that the friction factor for a ribbed channel remains largely independent of Re, beyond a certain Re. The measurements (Fig. 8(*a*)) indicate that there is no dependence of $\bar{f}$ on Re. However, $\bar{f}/f_0$ increases with Re, since f_0 falls with Re.

Clearly, the greater the obstruction (larger e/D) or the larger the number of ribs (lower p/e), the greater the disturbance to the flow,

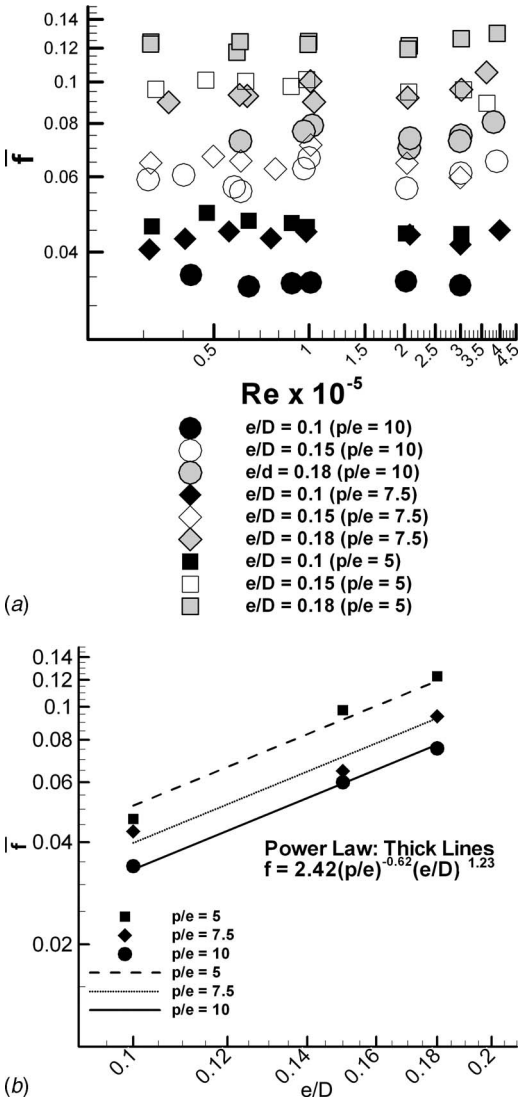

Fig. 8 (*a*) Friction factors for various test cases and (*b*) correlation for friction factor as a function of *e*/*D* and *p*/*e*

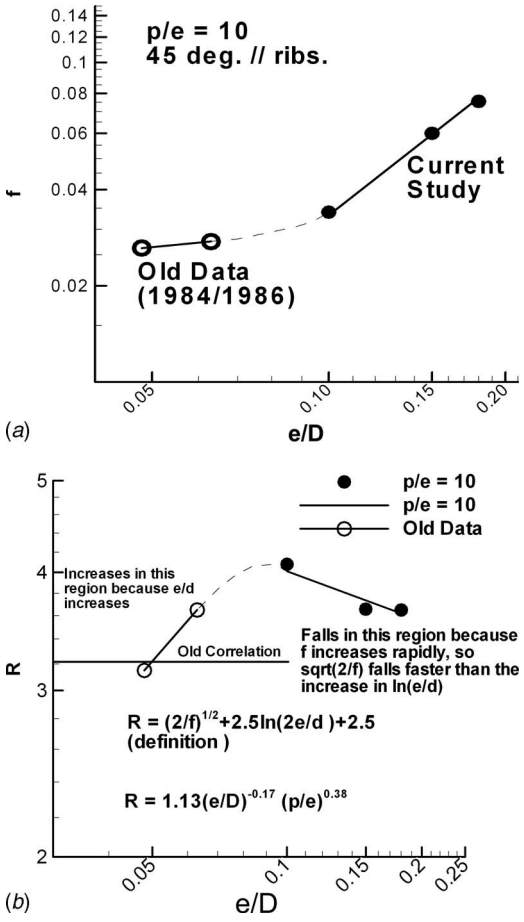

Fig. 9 (*a*) Comparison of current friction factor with raw data from Refs. [20,21] and (*b*) comparison of current friction roughness (*R*) with correlation published earlier [20,21]

and the greater is the friction factor. This is seen in Figs. 8(*a*) and 8(*b*).

This relationship is summarized by the correlation

$$\bar{f} = 2.46\left(\frac{p}{e}\right)^{-0..62}\left(\frac{e}{D}\right)^{1.23}$$

$$30{,}000 < \mathrm{Re}, 5 < \frac{p}{e} < 10, 0.1 < \frac{e}{D} < 0.2 \qquad (16)$$

This correlation has a maximum deviation of 8%.

Figure 9(*a*) shows comparisons with earlier studies for $p/e = 10$. At low values of e/D (old tests), the exponent of the $\bar{f}$ versus e/D correlation seems a lot lower than at higher values of e/D. This could be because of increased form drag owing to increased blockage by the ribs.

4.3 Thermal Performance. Figure 10(*a*) compares the ribbed-side-average heat transfer enhancement ($\mathrm{Nu}/\mathrm{Nu}_0$) on the ordinate with ($\bar{f}/f_0$) on the abscissa. This graph shows the deterioration in performance (decreasing $\mathrm{Nu}/\mathrm{Nu}_0$ and increasing in $\bar{f}/f_0$) as Re increases.

The thermal performance, F, is proportional to the heat transfer enhancement ($\mathrm{Nu}/\mathrm{Nu}_0$) and is inversely related the friction factor ratio, $\bar{f}/f_0$. Since $\mathrm{Nu}/\mathrm{Nu}_0$ for a given configuration tends to fall with increasing Re and $\bar{f}/f_0$ tends to increase with increasing Re, F decreases with increasing Re. The measured dependence of F on Re is shown in Fig. 10(*b*).

The shortest rib ($e/D=0.1$) case has the best thermal performance, whereas the $e/D=0.18$ case has the worst performance. This can also be appreciated from Fig. 10(*a*), which shows that by increasing e/D from 0.1 to 0.18, one increases Nu only by ~30%, whereas one increases the corresponding friction factor by ~400%!

The thermal performance exceeds unity only when Re $<100{,}000$, indicating possible issues with economic viability at higher values of Re. However, when the application demands the removal of a large amount of heat, the turbine designer must be prepared for a disproportionately large pressure drop penalty—as lower Reynolds numbers would result in lower Nusselt numbers (in absolute value)—and would not satisfy the purpose of removing a large amount of heat.

4.4 Generalized Correlation. The parameters G and R (heat transfer and friction roughness, respectively) have been used in literature to absorb the effect of rib height (e/D) and Reynolds number (Re) into one variable. G and R have been correlated with $e+$ (a nondimensional roughness Reynolds number) and p/e. Expressions of the form $R=C_1(p/e)^m$ and $G=C_2(p/e)^m(e+)^n$ have been utilized to accurately correlate experimental data.

But in our case, Fig. 9(*a*) indicates a change in slope (in the

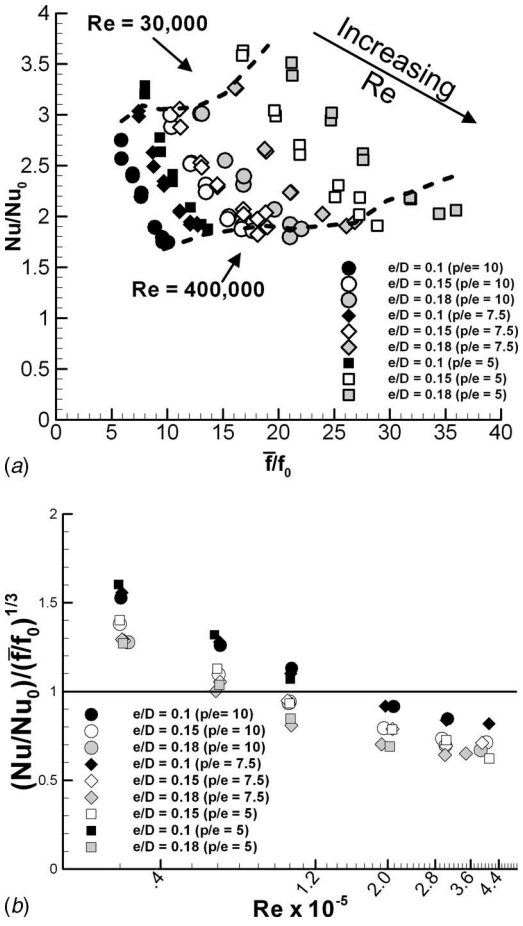

Fig. 10 (*a*) Ribbed side average Nusselt number enhancement ratio (compared with a smooth channel) plotted against friction factor penalty ratio for all cases and (*b*) thermal performance for all experimental cases. Performance is below 1 for most cases with Reynolds number exceeding 100,000, indicating a significant pressure loss penalty.

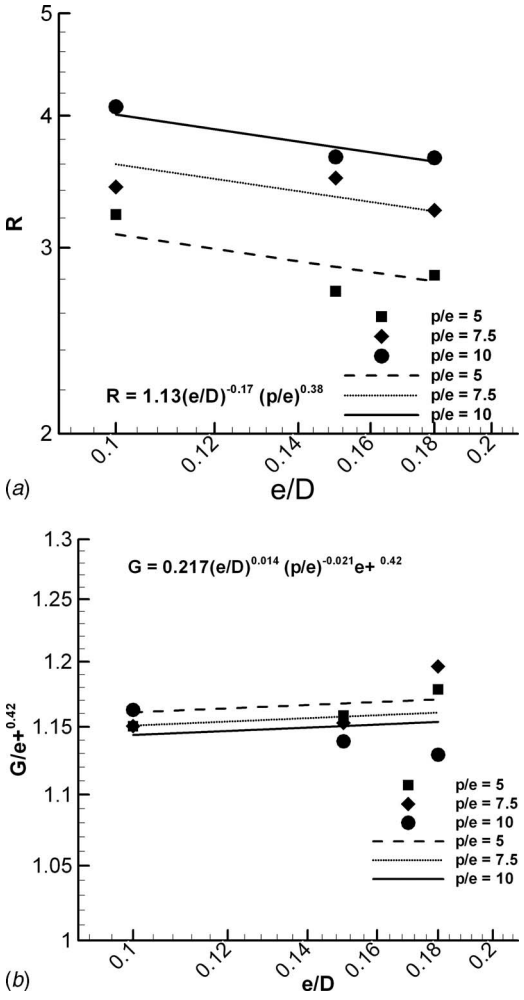

Fig. 11 Correlations for *R* and *G* as a function of *e*/*D* and *p*/*e*

log-log plot) in $\bar{f}$ versus e/D. Since $\bar{f}$ starts increasing at a much higher rate, corresponding values of R start falling faster, as can be seen in Fig. 9(*b*). Therefore, variations in e/D will have to be factored in explicitly in the correlation, as shown in Fig. 11(*a*). The heat transfer roughness (G), on the other hand, does not vary much with e/D or p/e (Figs. 12(*b*) and 11(*b*)). The following correlations are proposed (extending work done by Han et al. [22]):

$$R = 1.13\left(\frac{e}{D}\right)^{-0.17}\left(\frac{p}{e}\right)^{0.38} \tag{17}$$

$$G = 1.24\left(\frac{e}{D}\right)^{0.014}\left(\frac{p}{e}\right)^{-0.02}(e^{+})^{0.42} \tag{18}$$

Figures 12 and 11 indicate that the correlations for R and G do not agree with the earlier published correlations. This discrepancy can be attributed to the vastly disjoint nature of the parameter space considered—the older study [20] considers $0.048 < e/D < 0.078$ and $10 < p/e < 20$, and $\mathrm{Re} < 70{,}000$, whereas the current study's parameter range is summarized in Table 1. The current study explores a range of e/D, which is considerably larger than that in Ref. [20]. The turbulent boundary layer universal logarithmic velocity profile assumption is valid when the surface roughness is relatively small. Larger rib thickness could invalidate this assumption owing to greater form drag caused by flow separating and reattaching due to the rib in comparison of with the skin friction. This causes a dependence of R and G on e/D, as well as on e^{+}. In addition, the current study focuses entirely on 45 deg parallel ribs in a square channel; the older studies also consider channels with various aspect ratios and various rib angles. And also, the data in literature [20,21] have been obtained using center-line thermocouples embedded on a foil heater; current data have been obtained using copper plates to regionally average heat transfer coefficients.

5 Error Analysis

The Kline–McLintock [25] scheme has been used to estimate the experimental uncertainty. The maximum experimental uncertainty in measuring the Reynolds number is estimated to be 3%, and the maximum experimental uncertainty in the Nusselt number (which corresponds with the lowest temperature difference between the plate and the bulk-mean temperature) is estimated to be 5%. The uncertainty of the friction factor is estimated to be 7%.

6 Conclusions

Detailed regionally averaged heat transfer (Nusselt number) enhancement ratio profiles have been presented for both ribbed and smooth surfaces for the parameter range $5 < p/e < 10$, $0.1 < e/D < 0.18$, and $30{,}000 < \mathrm{Re} < 400{,}000$.

In general, greater heat transfer enhancements (compared with a smooth channel) were observed at larger blockage ratios and at smaller rib-rib spacings. These high heat transfer enhancements

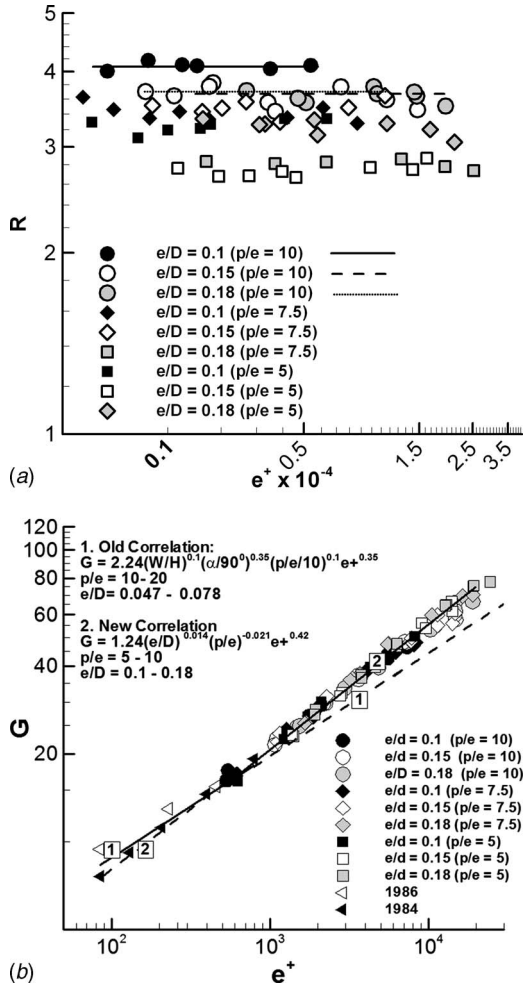

Fig. 12 (*a*) Variation in friction roughness (*R*) with roughness Reynolds number (e^+) and (*b*) heat transfer roughness parameter *G* from current study plotted against roughness Reynolds number e^+, compared with data from Refs. [20,21]

were accompanied by large pressure drop penalties (when compared with a smooth channel), resulting in a lower thermal performance.

At higher values of e/D and Re, the smooth surface also displayed high Nu enhancement.

Nusselt number enhancement ratio falls with an increase in Re, whereas friction factor ratio increases with an increase in Re, for smooth and ribbed surfaces.

The heat transfer performance is found to be below unity for cases with large Reynolds number and large values of e/D.

A power law correlation is presented for friction factor and Nusselt number for the range studied.

A correlation is proposed based on the parameters, R and G described in Ref. [20] for the range explored in this study.

Further studies could focus on extending the correlation to cover the influence of aspect ratio, different rib angles, and profiled ribs. V-shaped and broken V-shaped ribs can also be tested at high Reynolds numbers. Studies could also attempt to find local heat transfer coefficients (perhaps using IR or liquid crystal thermography).

Acknowledgment

This work has been supported through the Marcus Easterling Endowment fund. Special acknowledgment is due to the late Dr. Huitao Yang who designed and fabricated the test section. We also thank Dr. Dong-Ho Rhee and Diganta Narzary for their help in solving various experimental issues.

Nomenclature

- c_p = specific heat
- D = hydraulic diameter
- e = rib height
- e^+ = roughness Reynolds number, defined in Eq. (11)
- $\bar{f}$ = measured friction factor (Moody)
- f = equivalent friction factor for channel with four rib-roughened walls, Eq. (14)
- f_o = friction factor corresponding to smooth channel flow (Moody), Eq. (9)
- F = thermal Performance, defined in Eq. (10)
- G = nondimensional heat transfer roughness function, defined in Eq. (13)
- H = height of channel
- K = thermal conductivity
- Nu = Nusselt number
- Nu_0 = Nusselt number corresponding to smooth channel flow (Dittus–Boelter)
- p = spacing between consecutive ribs, defined in Fig. 7(*b*)
- Pr = Prandtl number
- R = Nondimensional friction roughness function, defined in Eq. (12)
- Re = Reynolds number
- St = Stanton number
- W = width of channel (=H in this case)
- μ = dynamic viscosity
- ρ = density

References

[1] Ebrahim Momin, A. M., Saini, J. S., and Solanki, S. C., 2002, "Heat Transfer and Friction in Solar Air Heater With V-Shaped Rib Roughness on Absorber Plate," Int. J. Heat Mass Transfer, **45**(16), pp. 3383–3396.
[2] Taslim, M. E., and Lengkong, A., 1998, "45 deg Staggered Rib Heat Transfer Coefficient Measurements in a Square Channel," ASME J. Turbomach., **120**(3), pp. 571–580.
[3] Bailey, J. C., and Bunker, R. S., 2003, "Heat Transfer and Friction in Channels With Very High Blockage 45° Staggered Turbulators," ASME Paper No. GT2003-38611.
[4] Kiml, R., Mochizuki, S., and Murata, A., 2001, "Effects of Rib Arrangements on Heat Transfer and Flow Behavior in a Rectangular Rib-Roughened Passage: Application to Cooling of Gas Turbine Blade Trailing Edge," ASME J. Heat Transfer, **123**, pp. 675–681.
[5] Casarsa, L., Cakan, M., and Arts, T., 2002, "Characterization of the Velocity and Heat Transfer Fields in an Internal Cooling Channel With High Blockage Ratio," ASME Paper No. GT-2002-30207.
[6] Rau, G., Çakan, M., Moeller, D., and Arts, T., 1998, "The Effect of Periodic Ribs on Local Aerodynamic and Heat Transfer Performance of a Straight Cooling Channel," ASME J. Turbomach., **120**(2), pp. 368–375.
[7] Lau, S. C., Kukreja, R. T., and McMillin, R. D., 1991, "Effects of V-Shaped Rib Arrays on Turbulent Heat Transfer and Friction of Fully Developed Flow in a Square Channel," Int. J. Heat Mass Transfer, **34**(7), pp. 1605–1616.
[8] Han, J. C., Zhang, Y. M., and Lee, C. P., 1991, "Augmented Heat Transfer in Square Channel With Parallel Crossed and V-Shaped Angled Ribs," ASME J. Heat Transfer, **113**, pp. 590–598.
[9] Han, J. C., Huang, J. J., and Lee, C. P., 1993, "Augmented Heat Transfer in Square Channels With Wedge-Shaped and Delta-Shaped Turbulence Promoters," J. Enhanced Heat Transfer, **1**(1), pp. 37–52.
[10] Moody, L. F., 1944, "Friction Factors for Pipe Flow," Trans. ASME, **66**, pp. 671–684.
[11] Park, J. S., Han, J. C., Ou, S., and Boyle, R. J., 1992, "Heat Transfer Performance Comparisons of Five Different Rectangular Channels With Parallel Angled Ribs," Int. J. Heat Mass Transfer, **35**(11), pp. 2891–2903.
[12] Taslim, M. E., Li, T., and Spring, S. D., 1997, "Measurements of Heat Transfer Coefficients and Friction Factors in Rib Roughened Channels Simulating Leading Edge Cavities of a Modern Turbine Blade," ASME J. Turbomach., **119**, pp. 601–609.
[13] Zhang, Y. M., Gu, W. Z., and Han, J. C., 1994, "Augmented Heat Transfer in Triangular Ducts With Full and Partial Ribbed Walls," AIAA J., **8**(3), pp 574–579.
[14] Taslim, M. E., and Spring, S. D., 1994, "Effects of Turbulator Profile and

Spacing on Heat Transfer and Friction in a Channel," J. Thermophys. Heat Transfer, **8**(3), pp. 555–562.
[15] Dipprey, D. F., and Sabersky, R. H., 1963, "Heat and Momentum Transfer in Smooth and Rough Tube at Various Prandtl Numbers," Int. J. Heat Mass Transfer, **6**, pp. 329–353.
[16] Han, J. C., Glicksman, L. R., and Rosenhow, W. M., 1978, "An Investigation of Heat Transfer and Friction for Rib-Roughened Surfaces," Int. J. Heat Mass Transfer, **21**, pp. 1143–1156.
[17] Han, J. C., 1984, "Heat Transfer and Friction in Channels With Two Opposite Rib-Roughened Walls," ASME J. Heat Transfer, **106**, pp. 774–781.
[18] Han, J. C., 1988, "Heat Transfer and Friction Characteristics in Rectangular Channel With Rib Turbulators," ASME J. Heat Transfer, **110**, pp. 321–328.
[19] Han, J. C., and Park, J. S., 1988, "Developing Heat Transfer in Rectangular Channels With Rib Turbulators," Int. J. Heat Mass Transfer, **31**(1), pp. 183–195.
[20] Han, J. C., and Park, J. S., 1986, "Measurement of Heat Transfer and Pressure Drop in Rectangular Channels With Turbulence Promoters," NASA Report No. 4015.
[21] Han, J. C., Park, J. S., and Lei, C. K., 1984, "Heat Transfer and Pressure Drop in Blade Cooling Channels With Turbulence Promoters," NASA Report No. 3837.
[22] Han, J. C., Chandra, P. R., and Lau, S. C., 1988, "Local Heat/Mass Transfer Distributions Around Sharp 180 deg Turns in Two-Pass Smooth and Rib-Roughened Channels," ASME J. Heat Transfer, **110**, pp. 91–98.
[23] Ekkad, S. V., and Han, J. C., 1997, "Detailed Heat Transfer Distributions in Two-Pass Square Channels With Rib Turbulators," Int. J. Heat Mass Transfer, **40**(11), pp. 2525–2537.
[24] Su, G., Chen, H. C., Han, J. C., and Heidman, J. D., 2004, "Computation of Flow and Heat Transfer in Tow-Pass Rotating Rectangular Channels (AR =1:1,AR=1:2,AR=1:4) With 45-deg Angled Ribs by a Reynolds Stress Turbulence Model," ASME Paper No. GT2004-53662.
[25] Kline, S. J., and McLintock, F. A., 1953, "Describing Uncertainties in Single-Sample Experiments," Mech. Eng. (Am. Soc. Mech. Eng.), **75**(1), pp. 3–8.

Investigation of Plate Falling Film Absorber With Film-Inverting Configuration

X.-Y. Cui
e-mail: xiaoyu_cui@usst.edu.cn

J.-Z. Shi

C. Tan

Z.-P. Xu

Institute of Thermal Engineering,
University of Shanghai for Science and Technology,
Shanghai 200093, China

The performance enhancement of absorbers is closely related to the investment costs of absorption cooling systems. In this paper, a new film-inverting design for plate falling film absorber is proposed. The absorber consists of consecutive inclined plates. The absorbent solution is distributed at the top of the first plate and forms a liquid film falling down along the plate. Meanwhile, the falling film absorbs the water vapor generated by the evaporator. At the bottom of this plate, the film is guided to the next one and at the same time the film is inverted and its inner side to the vapor is exposed. In this way, the absorption process can be enhanced. A mathematical model is developed for the simulation of heat and mass transfer in this new type of absorbers and is solved numerically. The experiments were carried out under different conditions and the influences of absorption pressure, solution flow rate, solution inlet temperature, and cooling water on the absorption process were investigated experimentally. Comparisons show a good consistency between the experiment and numerical results. [DOI: 10.1115/1.3089550]

Keywords: heat and mass transfer, absorber, falling film absorption, film-inverting, lithium bromide aqueous, absorption cooling

1 Introduction

The absorber is usually the largest and most expensive component in an absorption cooling system. Its characteristics have direct effect on the performance of the whole system. The applications of technology on heat and mass transfer enhancement on such equipment have been widely studied. The conventional absorbers usually consist of a bundle of horizontal falling film tubes. In recent years, plate heat exchangers and plate-fin heat exchangers have also been used due to their compactness and high efficiency in heat and mass transfer. To improve the performance of absorbers, different surface structures such as fins, grooves, and protrusions have been applied to the external surfaces of the absorbers. According to the early researches [1–7], it is known that the plate absorbers and the plate-fin absorbers are more compact and efficient.

In 2003, Islam et al. [8] investigated a tubular falling film absorber with film-inverting configuration shown in Fig. 1. Under each tube (except the lowest one), there is a film guide plate to invert the film. This film-inverting technology differs from the previous modifications that enhance heat and mass transfer mainly through fluid mixing. The experiment results show the obvious improvements on heat and mass transfer in the absorber. The maximum increase in vapor absorption rate of about 100% is obtained with the film-inverting design compared with conventional absorbers. However, additional guide plates are needed, which increase the pressure drop and make the configuration more complicated.

In the present work, the film-inverting technology is introduced into a falling film plate absorber. The plate falling film absorber with the film-inverting technology has two advantages: First, the length of the plates can be adjusted conveniently to maximize the absorption effect; second, no additional guide plates are needed. An experimental setup was built and the absorption performances under different operation conditions were measured. Numerical calculations also have been carried out on the falling film, and the results have been compared with that from the experiments.

2 Plate Falling Film Absorber With Film-Inverting Configuration

The process for plate falling film absorption can be described briefly as follows: The absorbent solution falls down along the tilted plate due to gravity in the form of film. The plates are cooled by the coolant flowing through the channels inside the plate. The vapor condenses on the outside surface (vapor-liquid interface) of the liquid film flowing along the plates and is absorbed into the film. The released heat is transferred to the plate by heat convection and is removed by the coolant flowing inside the plates. The temperature and concentration differences between the film inside (plate-liquid interface) and the film outside (vapor-liquid interface) form a gradient of the temperature and concentration across the film section, respectively, which causes heat and mass transfer through the film [9].

The plate falling film absorber with film-inverting configuration consists of several tilted plates, as is shown in Fig. 2. The absorbent solution is distributed at the top of the first plate and forms a liquid film falling down along the plate. While falling, the liquid film absorbs the water vapor, and the concentration gradient of the solution at the vapor interface decreases. At the bottom of this plate, the film is guided to the next one and at the same time the film is inverted and its inner side to the vapor is exposed. Because this newly exposed liquid layer has higher LiBr concentration, the absorption process is thus enhanced. With a similar manner, the film comes to the third and fourth plates, and so on. From plate to plate, the film will be inverted again and again and exposes its "fresh" side to the water vapor, and thus the absorption process can be enhanced.

3 Mathematical Model and Numerical Solution

The absorption process is a complicated process in which heat and mass transfer are coupled with each other. Water vapor will at first condense at the vapor-film interface and then diffuse into the film. Since the thickness of the falling film is very small, the boundary theory can be applied, and the governing equations de-

Contributed by the Heat Transfer Division of ASME for publication in the JOURNAL OF HEAT TRANSFER. Manuscript received March 25, 2008; final manuscript received December 17, 2008; published online May 1, 2009. Review conducted by Louis C. Chow.

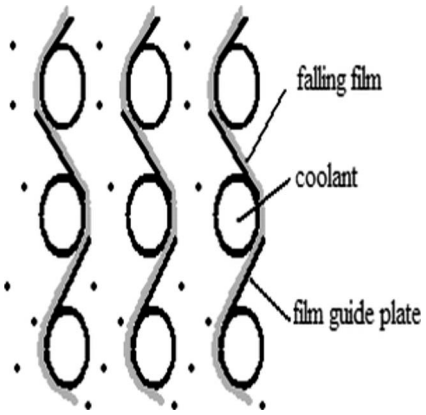

Fig. 1 Schematic of the tubular falling film with the film-inverting configuration

scribing the heat and mass transfer in the vertical falling film absorption are two dimensional. Figure 3 is the illustration of the falling film absorption process. To simplify the problem, the following assumptions are made.

1. Vapor is a single component and is still, and the temperature is uniform within the vapor.
2. The vapor-liquid interface is in phase equilibrium, and no viscous stress.

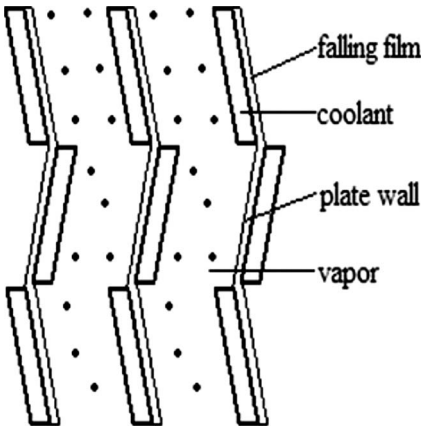

Fig. 2 Schematic of the plate falling film absorber with the film-inverting configuration

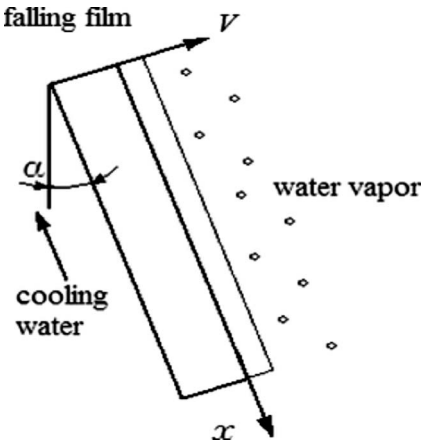

Fig. 3 Falling film absorption process

3. The solution is incompressible Newtonian fluid, with constant physical properties. The density variation with the concentration is negligible.
4. The falling film flow is laminar. The plate surface is smooth.
5. The diffusion along the film falling direction can be neglected. The absorption heat is released at the vapor interface.

The governing equation system can be written as follows:

$$\frac{\partial u}{\partial x} + \frac{\partial v}{\partial y} = 0 \tag{1}$$

$$u\frac{\partial u}{\partial x} + v\frac{\partial u}{\partial y} = v\frac{\partial^2 u}{\partial y^2} + g\cos\alpha \tag{2}$$

$$u\frac{\partial T}{\partial x} + v\frac{\partial T}{\partial y} = a\frac{\partial^2 T}{\partial y^2} \tag{3}$$

$$u\frac{\partial c}{\partial x} + v\frac{\partial c}{\partial y} = D\frac{\partial^2 c}{\partial y^2} \tag{4}$$

in which the concentration is defined as

$$c = c_{\mathrm{LiBr}} = \frac{m_{\mathrm{LiBr}}}{m_{\mathrm{water}} + m_{\mathrm{LiBr}}} \tag{5}$$

Obviously, we have

$$c_{\mathrm{water}} = 1 - c_{\mathrm{LiBr}} \tag{6}$$

For boundary conditions,

$$x = 0: \quad u = u(y), \quad v = v(y), \quad T = T(y), \quad c = c(y) \tag{7}$$

$$y = 0: \quad u = v = 0, \quad \frac{\partial c}{\partial y} = 0, \quad T = T_{\mathrm{wall}}(x) \tag{8}$$

$$y = \delta: \quad \frac{\partial u}{\partial y} = 0, \quad v = \frac{D}{c}\frac{\partial c}{\partial y}, \quad -\lambda\frac{\partial t}{\partial y} = \frac{\rho D}{c}\frac{\partial c}{\partial y}H, \quad f(c,p,T) = 0 \tag{9}$$

in which the temperature of the plate wall $T_{\mathrm{wall}}(x)$ was measured in the experiment; $(\rho D/c)(\partial c/\partial y)$ is the vapor mass flux absorbed at the vapor-liquid interface, H is the absorption heat, and $f(c,p,T)=0$ is the phase equilibrium relationship at the interface.

Equations (1)–(7) are valid in the plate region. For the liquid flows in the gap between the two consecutive plates, we can set $\alpha=0$ in the above governing equations, and consider that at both sides of the film there is vapor absorbed into the film. Then the boundary conditions become

$$x = 0 \quad : u = u(y), \quad v = v(y), \quad T = T(y), \quad c = c(y) \tag{10}$$

$$y = 0 \quad \text{and} \quad \delta: \quad \frac{\partial u}{\partial y} = 0, \quad v = \frac{D}{c}\frac{\partial c}{\partial y}, \quad -\lambda\frac{\partial T}{\partial y} = \frac{\rho D}{c}\frac{\partial c}{\partial y}H, \quad f(c,p,T) = 0 \tag{11}$$

in which $u(y)$, $v(y)$, $T(y)$, and $c(y)$ are their outlet values of the previous plate region.

To reduce the variables in the above equations, the stream function $\Psi = \int_0^y u dy$ is introduced. We further define three dimensionless parameters: $\omega = (\Psi - \Psi_i)/(\Psi_e - \Psi_i)$, $\theta = x/L$, and $\bar{u} = u/u_0$, in which Ψ_i and Ψ_e are the values of the steam function at the wall and at the vapor-liquid interface, respectively, L is the plate length, and u_0 is the uniform inlet velocity of the first plate. Then the governing equations could be transformed into $\theta-\omega$ domain as

Table 1 Details of Φ, $\bar{D}_\Phi$, and $\bar{S}_\Phi$ in the governing equations

Φ	$\bar{D}_\Phi$	$\bar{S}_\Phi$
$\bar{u}$	$16\ \mathrm{Re}_L/\mathrm{Re}^2$	$g\bar{u}L\cos\alpha/u_0^2$
T	$16\ \mathrm{Re}_L/\mathrm{Re}^2\ \mathrm{Pr}$	0
c	$16\ \mathrm{Re}_L/\mathrm{Re}^2\ \mathrm{Sc}$	0

$$\frac{\partial\Phi}{\partial\theta}+b''\omega\frac{\partial\Phi}{\partial\omega}=\bar{D}_\Phi\frac{\partial}{\partial\omega}\left(\bar{u}\frac{\partial\Phi}{\partial\omega}\right)+\bar{S}_\Phi$$

in which $b''=(16R_{eL}/R_e^2)(\bar{u}/S_c)(1/c)(\partial c/\partial w)_{w=1}$. Φ is a general variable and can be $\bar{u}$, T, and c, respectively, as shown in Table 1. The diffusion coefficient and source term for velocity, temperature, and concentration equation are also listed in Table 1.

The boundary conditions are transformed correspondingly as follows:

(a) Plate region

$$\theta=0{:}\bar{u}=\bar{u}(\omega),\quad T=T(\omega),\quad c=c(\omega) \tag{12}$$

$$\omega=0{:}\bar{u}=0,\quad T=T_{\mathrm{wall}}(\theta),\quad \frac{\partial c}{\partial\omega}=0 \tag{13}$$

$$\omega=1{:}\frac{\partial\bar{u}}{\partial\omega}=0,\quad -\lambda\frac{\partial c}{\partial\omega}=\frac{\rho D}{c}\frac{\partial c}{\partial\omega}H,\quad f(c,p,T)=0 \tag{14}$$

(b) (b) Gap region

$$\theta=0{:}\quad \bar{u}=\bar{u}(\omega),\quad T=T(\omega),\quad c=c(\omega) \tag{15}$$

$$\omega=0\quad\text{and}\quad 1{:}\frac{\partial\bar{u}}{\partial\omega}=0,\quad -\lambda\frac{\partial c}{\partial\omega}=\frac{\rho D}{c}\frac{\partial c}{\partial\omega}H,\quad f(c,p,T)=0 \tag{16}$$

The general governing equation system can be solved numerically by the use of the control volume method. The central difference scheme is applied to the diffusion term. The convection term is discretized with the upwind scheme and backward difference scheme. The discretized equations can be calculated using the tridiagonal matrix algorithm (TDMA). The computation steps for the plate region are as follows.

(a) Begin the calculation from the front of the first plate at $\theta=\Delta\theta$.
(b) Assume an initial value of the vapor mass flux $\Omega'=-(\rho D/c\,\partial c/\partial y)_{y=\delta}$ at θ.
(c) Calculate the dimensionless velocity distribution $\bar{u}(\theta,\omega)$ at θ according to its upwind values of $\bar{u}(\theta-\Delta\theta,\omega)$.
(d) Use the assumed value of Ω in the boundary condition $\lambda\,\partial T/\partial y=\Omega' H$ at $\omega=1$ and the calculated $\bar{u}(\theta,\omega)$ to calculate the temperature distribution $T(\theta,\omega)$ at θ according to the known values of $T(\theta-\Delta\theta,\omega)$.
(e) Use the calculated value of $T(\theta,1)$ to calculate the boundary value of the concentration $c(\theta,1)$ according to the phase equilibrium relationship $f[c(\theta,1),p,T(\theta,1)]=0$.
(f) Use the calculated values of $\bar{u}(\theta,\omega)$ and $c(\theta,1)$ to calculate the concentration distribution $c(\theta,\omega)$ at θ according to the known values of $c(\theta-\Delta\theta,\omega)$.
(g) Verify the mass flux $\Omega=-(\rho D/c\,\partial c/\partial y)_{y=\delta}$ according to the calculated $c(\theta,\omega)$.
(h) If $|\Omega-\Omega'/\Omega|\le\varepsilon$ (e.g., $\varepsilon=10^{-4}$), the computation for velocity, temperature, and concentration at location θ is considered to be convergent. Otherwise, set $\Omega=\Omega+\xi(\Omega'-\Omega)$ and repeat Steps (d)–(h), where ξ is the relax factor
(i) Move to the next location $\theta+\Delta\theta$, and repeat Steps (b)–(i) until $\theta=1$.

The computation steps for the gap region are similar to those for the plate region.

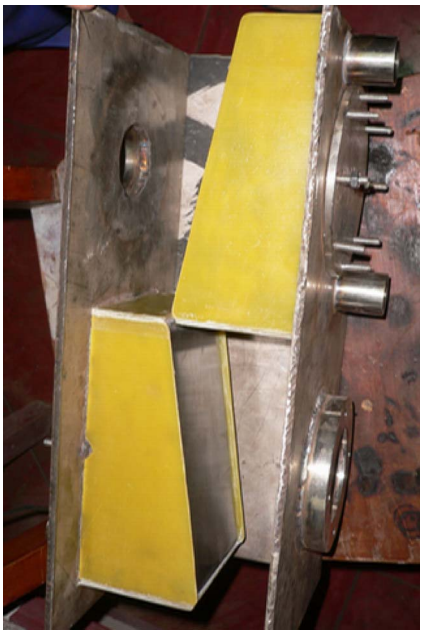

Fig. 4 Film-inverting configuration in experimental absorber

4 Experimental Setup and Procedure

A prototype of the absorber with one film inversion is shown in Fig. 4. The dense solution first flows to a tank that is located at the top of the absorber. The solution in tank overflows and flows down along the two consecutive inclined plates with an angle of 15 deg but inclined to the opposite direction. The arrangement of the two plates allows the film to be inverted successfully. The two plates have the same size with 0.2 m in length and 0.1 m in width. Through glass the falling film could be observed. The water vapor flows into the absorption chamber from the top through a pipe. The cooling water flows upward in the opposite direction of the film at the other side of the plate. The dense solution is diluted by absorbing the vapor in the chamber when falling down. After the absorption is completed, the diluted solution leaves the absorber from its bottom. The absorber is wrapped up with thermally insulating material.

The system adopted in the experiment is an open system, as is shown in Fig. 5. The setup consists of the falling film absorber with film inversion, a pressure stabilization cylinder, a liquid container, a receiving tank, an evaporator, a condenser, a water-cooling system, a measurement system, and a data acquisition system. A photo of the system is shown in Fig. 6.

First, the lithium bromide solution is heated by an electric heater in the receiving tank. The generated vapor is condensed after entering into the condenser. Through measuring the condensed water, the concentration of the solution in the evaporator can be controlled. When the concentration of the solution meets the requirements for the experiment, the generation process is completed. After the solution is cooled down to a certain temperature in the air, all of the solution is pumped to the liquid container, from where the solution in the pressure stabilization cylinder comes and the level of the solution in the pressure stabilization

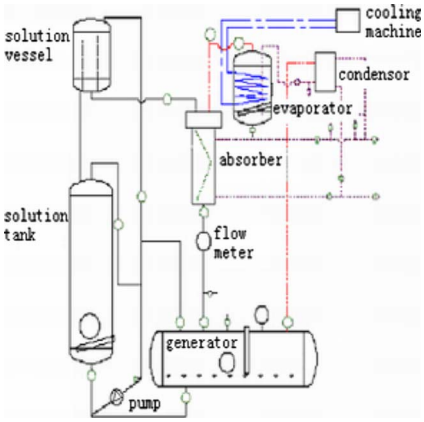

Fig. 5 The schematic of the experimental setup

cylinder is maintained. The pure water in the evaporator is cooled down by the coiled evaporation tubes of the refrigerator. Through adjusting the inlet solution flow rate, cooling water flow rate, temperature, and the electrical heater in the evaporator to control the vapor pressure in the absorber, the absorption process can be operated.

The temperature is measured using copper Constantan thermal coupler. And the measurement of solution flow rate is done by calibrated graduated cylinder, while the cooling water flow rate is measured by weighing method. The sample of the solution is collected through a valve. The specific gravity of the solution is measured by liquid specific gravity balance. The concentration of the solution is obtained from its temperature and gravity. Absolute pressure transducer is used to measure the absorption pressure. There are round glass windows installed on the evaporator, liquid container, and receiving tank to monitor the liquid levels.

The experiment and its measured data can be verified through the thermal balance calculation with the measured solution temperature and concentration at the inlet and outlet of the absorber, solution flow rate, cooling water temperature at the inlet and outlet, cooling water flow rate, and vapor pressure. The heat transfer coefficient and absorption rate, which are indicators of the heat and mass transfer characteristics, can also be obtained through calculations with these measured data.

Fig. 6 Experiment setup

There are several factors that affect the film absorption. Among them, the main factors are the flow rate, inlet temperature, inlet concentration of the solution, absorption pressure, and plate wall cooling conditions. Changing one of those factors, it will change the heat and mass transfer, as well as the absorption rate. The response relationship indicates the absorption characteristics with those factors. Here the absorption rate and convective heat transfer coefficient are used to represent the absorption characteristics.

For the absorption rate,

$$m = \frac{G_s}{A} \times \left(1 - \frac{c_{\text{out}}}{c_{\text{in}}}\right) \tag{17}$$

For the convection heat transfer coefficient at solution side

$$h = Q/(A\Delta T_m) \tag{18}$$

$$\Delta T_m = \frac{(T_{\text{in}} - T_{\text{wall}}) - (T_{\text{out}} - T_{\text{wall}})}{\ln \dfrac{T_{\text{in}} - T_{\text{wall}}}{T_{\text{out}} - T_{\text{wall}}}} \tag{19}$$

where ΔT_m is the mean logarithmic temperature difference of the plate and film.

5 Comparison of Experiment and Numerical Results

Plate falling film absorber with film-inverting configuration is made of stainless steel. The absorber contains two parts: The upper one is the overflow channel, and the lower is separated into two sections by falling film plates. One section, wedged shape cavity, is full of cooling water, and the other is the absorption space. There are two inclined plates (falling film plates) of 0.1 m width, 0.2 m height, and 4 mm thickness. Both the inclined angles are set to 15 deg from vertical direction to guarantee the successful inversion of film from the upper plate to the lower one, shown in Fig. 4. Each plate has six thermocouples set in the channels grooving at the cooling side, to measure the temperature distribution in each plate.

Solution flow was measured by the calibrated decanter at the inlet and outlet of the absorber, and the error is 1 ml. Temperature is measured by thermocouple, and the error is $\pm 0.1°$C. Concentration is calculated based on specific gravity and temperature, and the absolute error is less than 0.1%. The specific gravity is measured with hydrometer. Absorption pressure is measured by pressure transmitter, ranged from 0 kPa to 2510 kPa and precise class 0.15.

The comparisons between experiment and numerical results when absorber pressure, film flow rate, solution inlet temperature, or cooling water flow rate changes are shown from Figs. 7–10.

Figure 7 shows that the absorption pressure has a significant effect on the absorption process. As the absorption pressure goes up from 0.90 kPa to 1.75 kPa, the outlet concentration reduces from 0.589 to 0.579, and the absorption rate is almost doubled, increased from 0.0065 $\text{kg/m}^2\,\text{s}$ to 0.0125 $\text{kg/m}^2\,\text{s}$. The heat transfer coefficient at the solution side increases from 3015.5 $\text{W/m}^2\,\text{K}$ to 4752.4 $\text{W/m}^2\,\text{K}$. This enhancement is caused by an increase in water mass flux at the vapor-liquid interface.

The effect of the film flow rate on the absorption performance is shown in Fig. 8. As the flow rate of the solution film increases, the Reynolds number increases from 45.2 to 188.3, and the heat transfer coefficient increases from 2105.3 $\text{W/m}^2\,\text{K}$ to 3075.5 $\text{W/m}^2\,\text{K}$. However, the absorption rate decreases since the duration time of the solution in the absorber is reduced. The absorption rate decreases from 0.0092 $\text{kg/m}^2\,\text{s}$ to 0.0071 $\text{kg/m}^2\,\text{s}$.

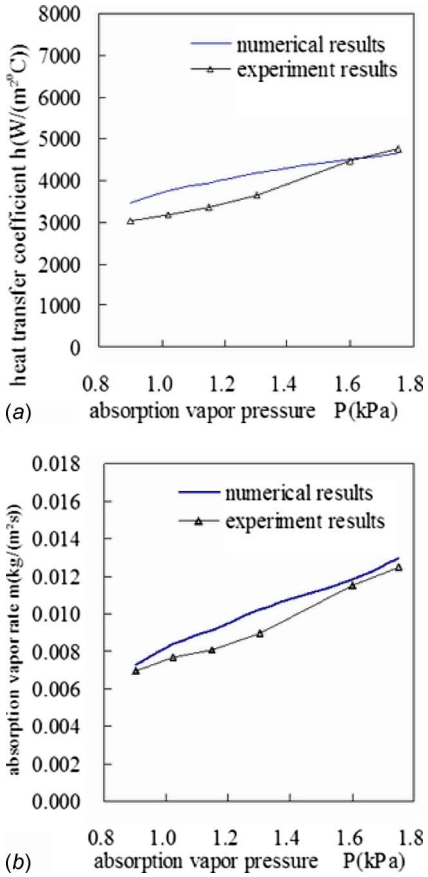

Fig. 7 The effect of absorption pressure on absorption characteristics (Re=59.3, c_{in}=0.606, T_{in}=41.5°C, G_w=0.018 kg/s): (*a*) convection heat transfer coefficient and (*b*) absorption rate

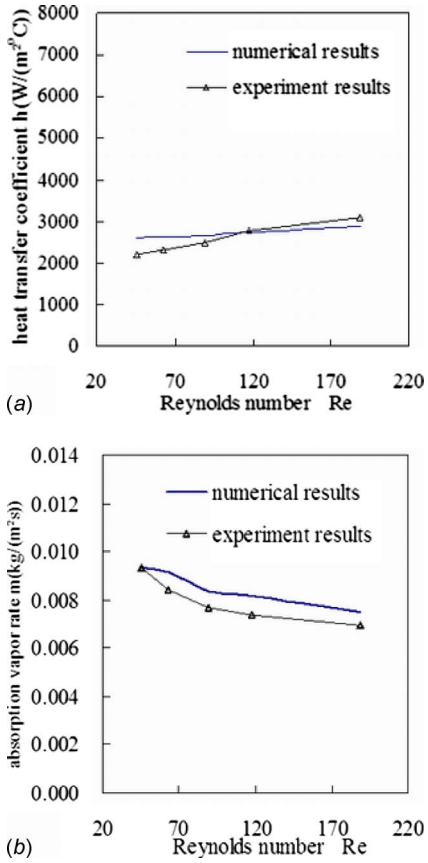

Fig. 8 Effect of film flow rate on absorption characteristics (c_{in}=0.60, p=1020 Pa, T_{in}=44.7°C, G_w=0.020 kg/s): (*a*) convection heat transfer coefficient and (*b*) absorption rate

Experiments have shown a few situations. One is the quality of the falling film. When the flow rate is small (Re < 20), the film cannot cover the plates completely. The quality of the falling film is sure to weaken the absorption.

The increase in solution temperature would yield a decrease in absorption rate. As is shown in Fig. 9, when the inlet solution temperature increases from 40.2°C to 43.9°C, the driving force for absorption decreases a little. As a result, the absorption rate decreases from 0.0064 kg/m^2 s to 0.0055 kg/m^2 s. However, the temperature difference between the solution and cooling water increases due to a decrease in heat transfer coefficient from 3105.7 W/m^2 °C to 2252.4 W/m^2 °C. The change in the heat transfer coefficient and absorption rate with the inlet solution temperature is relatively flat, which indicates that the inlet solution temperature has less significant effect on the absorption characteristics.

Figure 10 illustrates the effect of the plate temperature on the absorption performance. When the flow rate of cooling water increases, the cooling condition becomes better and the wall plate temperature decreases. So the liquid film temperature is lowered, which will enhance the vapor absorption. The absorption rate increases accordingly from 0.0065 kg/m^2 s to 0.0084 kg/m^2 s. The heat transfer coefficient decreases by a little, from 3251.6 W/m^2 °C to 2511.2 W/m^2 °C.

The above figures also show relative consistency between the experiment data and the calculation results. The maximum relative error is 18.5%, which is the one set of heat transfer coefficient between the experiment and numerical calculation, and the maximum relative error for thermal balance relative error is 27.5%. The difference is within acceptable range. The conditions used in the experiment absorber are typical conditions of absorbers being operated in the industrial lithium bromide absorption refrigeration system. It can be seen that most of the convective heat transfer coefficients are from 2500 W/m^2 °C to 3200 W/m^2 °C, which is twice as large as that of the traditional shell and tube falling film absorber.

6 Calculation Results and Analysis

Computation has been further done for lithium bromide aqueous solution absorption process, using the following conditions: an inlet concentration of 0.60, an inlet temperature of 40°C, an inlet Reynolds number of 30, a plate wall temperature of 30°C, and a vapor pressure of 1020 Pa.

Figure 11 shows the temperature and concentration distributions at different cross sections in a film falling along a 0.6 m vertical plate. From the two figures, it can be seen that the heat transfers more rapidly than the mass does within the liquid film. The film temperature decreases quickly because of the cooled plate wall; the T of lower cross section is lower than the inlet solution T. Only the T of the higher section is higher than inlet T; for instance, only the calculated solution temperature at $y/\delta > 0.8$ exceeds 40°C in Fig. 11. This tendency is caused by the release of absorption heat on the interface. But it takes more time for the water condensed from the vapor at the vapor-liquid interface to be diffused to the area near the plate wall in the film. Hence, film inversion exposes the film with the high concentration side to the vapor, which enhances the absorption.

Figure 12 is the comparison of the temperature and concentration at the vapor-liquid interface between the configuration with one film inversion and that without film inversion. It shows that just after the film is inverted, the concentration at the vapor-liquid

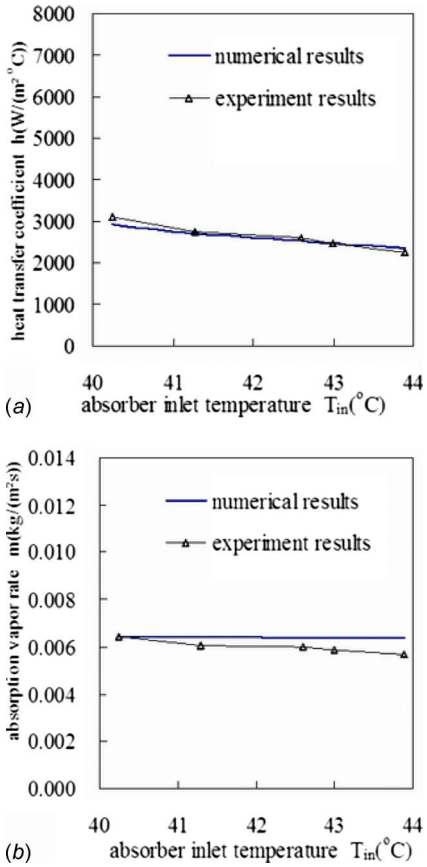

Fig. 9 Effect of solution inlet temperature on absorption characteristics (Re=50.3, c_{in}=0.60, p=1020 Pa, G_w=0.017 kg/s): (*a*) convection heat transfer coefficient and (*b*) sbsorption rate

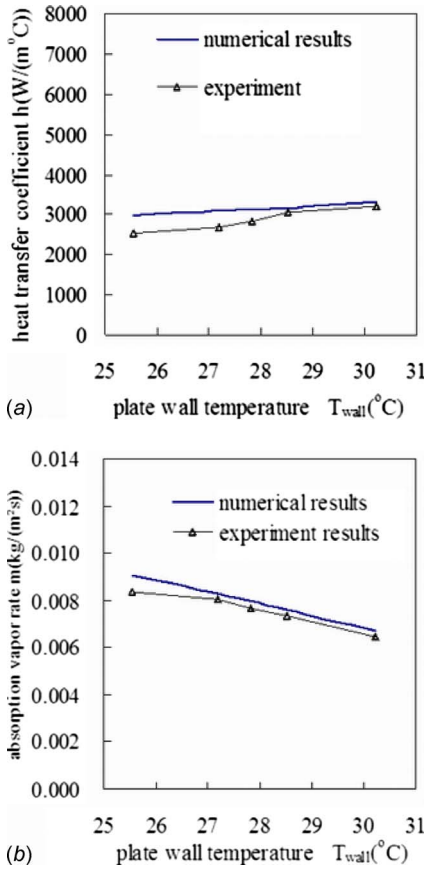

Fig. 10 Effect of cooling conditions on absorption characteristics (Re=56.9, c_{in}=0.592, T_{in}=38.7 °C, p=1020 Pa, G_w=0.017 kg/s): (*a*) convection heat transfer coefficient and (*b*) absorption rate versus plate wall temperature

interface changes to 0.60 instantly, and then decreases as vapor is absorbed into the film through the interface. Meanwhile only one temperature data at X=0.29 m are clearly low (=30°C) in comparison with the other data, because after the film inversion, the original wall-side film inverts to the vapor with low temperature (=wall temperature=30°C). Then the temperature increased abruptly as well when the film is inverted due to more heat released at the interface. The comparison of the absorption rate between film inversion and without film inversion is shown in Fig. 13. For the configuration without film inversion, the absorption rate decreases as the film falls along the plate. For the configuration with film inversion, the absorption rate jumps up when the film is inverted and the average absorption rate is greater than that of the configuration without film inversion.

Figure 14 shows the temperature and concentration distributions at the front, middle, and end of the second plate, respectively, after the film inverted. The total length of both plates is 0.6 m. Around the inlet area, the velocity of the liquid close to the wall reduced rapidly due to the solid wall of the plate. Some of the liquid moves outward the plate. Transverse flow exists at that area, which enhances the heat and mass transfer. For the liquid close to the vapor-liquid interface, it has low velocity. The lithium bromide concentration decreases quickly, which causes the temperature to increase. Also the velocity increases quickly for there is little viscous force from the still vapor. Just a few millimeters, the temperature of the liquid close to the plate at the inlet changes from high to low and that close to the vapor-liquid interface changes from low to high. The lithium bromide concentration shows different distributions that are high at the center and low at the two sides of the film. The results indicate slow mass diffusion in the film. The shape of the concentration distribution does not change even at the end of plate.

The effect of plate angle on the absorption for film-inverting configuration has been numerically investigated as well. The total plate length is 0.6 m and the film is inverted once at half length. Figure 15 shows the changes in the outlet temperature means and concentration means with the two plate angles. The first plate angle signed as α, and the second as β. When the plates are vertically placed, the outlet temperature mean and concentration mean are the lowest and the absorption is the best among different plate angles. When both plate angles are less than 10 deg, the differences among the temperature and concentration means are small. When the plate angles increase, although the film falls down more slowly, and it takes more time for the flow to pass along the plates, the film becomes thicker, which weakens the heat and mass transfer process. And as a result, the outlet temperature and concentration increase. When the angles of both plates are large, the plate angles have more effects on outlet concentration than that on outlet temperature. And the angle of the second plate has more effects on the outlet temperature and concentration than that of the first plate.

When the total film length is set, the outlet temperature and concentration means with different film-inverting times have been shown in Figs. 16 and 17.

From Fig. 16, the outlet mean temperature for one film inversion is higher than that without film inversion, while the outlet mean temperature for two and more film inversions is lower than that without film inversion. This could be explained as follows: Although the heat transfer is enhanced by the film inversion, the

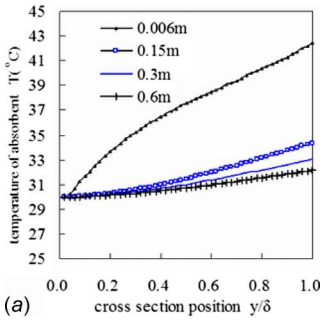

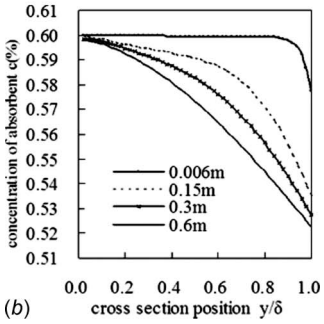

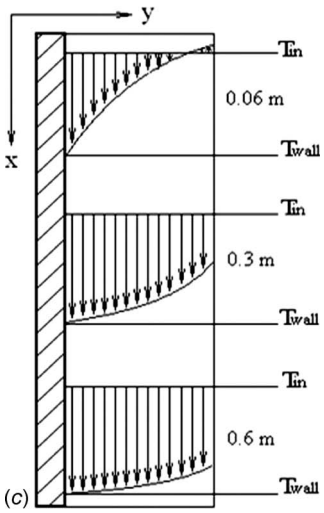

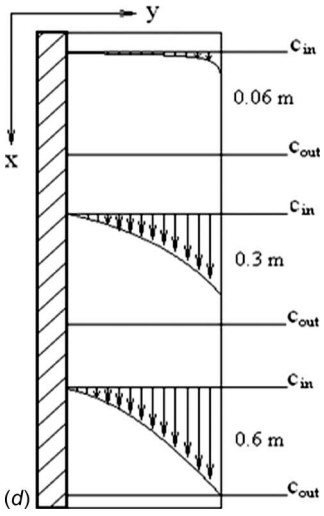

Fig. 11 Temperature and concentration distribution of different film section for vertical plate falling film absorber: (*a*) temperature distribution, (*b*) concentration distribution, (*c*) *T* distribution of different film sections, and (*d*) *C* distribution of different film section

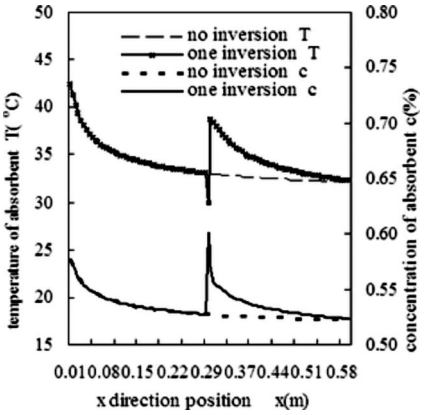

Fig. 12 Interface temperature and concentration with and without film inversion

film inversion also enhances the vapor absorption process and more vapor is condensed into water and absorbed into the film. More heat is released into the film. This absorption enhancement is more significant for one film inversion, as shown in Fig. 17. As a result, the outlet mean temperature for one film inversion is higher than that without film inversion.

As is shown in Fig. 17, the outlet mean concentration decreases as the inverting time increases, which indicates that the absorption process is enhanced with the film inversion. However, from economic viewpoint, it is not that the more the film inverted, the better. The first inversion has the best effect. From the second film inversion and so on, the inlet concentration has a distribution that is high in the middle and low at two ends, and the effect of the inversion on the absorption is less than that of the first inversion. As an example, with one film inversion, the absorption rate calculated in this paper is increased by 92.5%, but with the second inversion, the absorption rate is increased only by 0.3% compared with that for one inversion.

In the case that the whole falling film length is specified, different combinations of first and second plate lengths have different effects on the absorption rate. Figures 18 and 19 show the outlet mean temperature and mean concentration change with the first plate length, while the whole plate is set to be 0.6 m for one-time film inversion.

As shown in Fig. 18, there is an optimal length for the first plate to obtain the best mass transfer in the absorption process. If the first plate is too short, the difference of the concentration at the two sides of the film is not large enough, which reduces the film-inverting effect. On the contrary, if the first plate is too long, the difference of the concentration at the two sides of the film is large

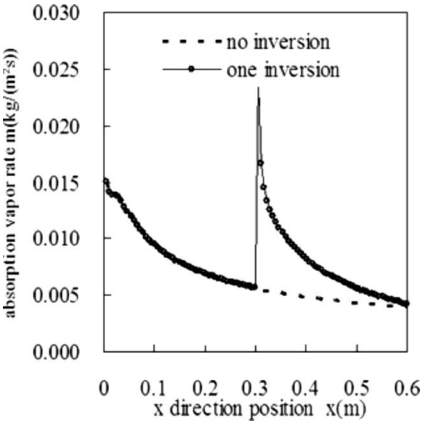

Fig. 13 Absorption rate with and without film inversion

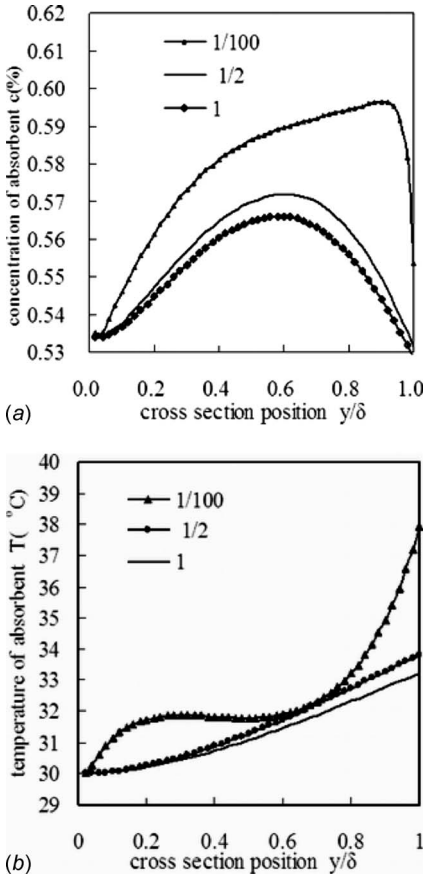

Fig. 14 Temperature and concentration distribution on the second plate with film inverted

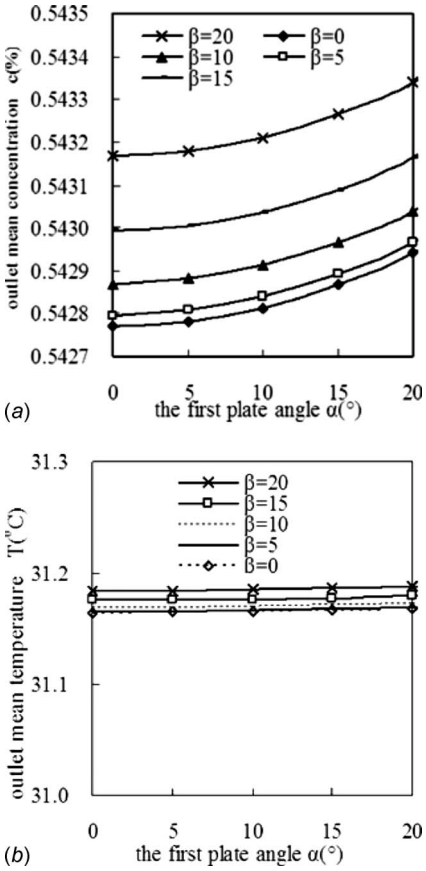

Fig. 15 Outlet mean temperature and concentration versus first and second plate angles for configuration with film inversion, 0.3 m each for the first and second plates. (*a*) outlet mean concentration and (*b*) outlet mean temperature

enough. However, a longer length of the first plate means a shorter length of the second plate and there will not be enough length for the absorption at the second plate. The outlet temperature mean is affected by film inversion, plate wall cooling, and the heat released at the vapor-liquid interface. Although the heat is transferred faster than the mass, and it is enhanced by the film inversion, the heat transfer is slower than the heat release at the vapor-liquid interface and the outlet temperature mean changes with the first plate length, as shown in Fig. 18. For the case of film absorption calculated in this paper, the best first plate length is 0.17 m, while the second is 0.43 m in terms of the mass transfer.

In the case of configuration design, it is possible to obtain the optimized configuration through the calculation of the mathematical model. For the conditions given in this paper, if 0.56 of outlet concentration is required, the plate length needs to be 0.6 m with no film inversion. However, we adopt one time film inversion and use the following steps to optimize the whole plate length.

a. Set the length of the first plate.
b. Give the second plate a heuristic length and do the calculation.
c. Change the length of the second plate and repeat Step b until the outlet concentration reaches its target value (=0.56).
d. Search the optimal length of the first plate by repeating Steps b and c so that the total plate length reaches its minimum.

By the method, the plate length is optimized, the total plate length only needs to be 0.32 m, and the first plate length is 0.14 m. This example shows that after the optimization the total plate length can be reduced by 0.28 m, which could reduce a lot of the volume of the absorber.

7 Conclusions

A new configuration that incorporates film inversion in the plate falling film absorber was proposed. The new configuration has a higher absorption rate, which can reduce the size of the absorber. Both detailed experiment and detailed numerical study on the absorption process with this new configuration were carried out.

For the numerical simulation, a mathematical model for the heat and mass transfer within the plate falling film with film inversion was proposed. The numerical calculation approach also has been developed using the control volume method.

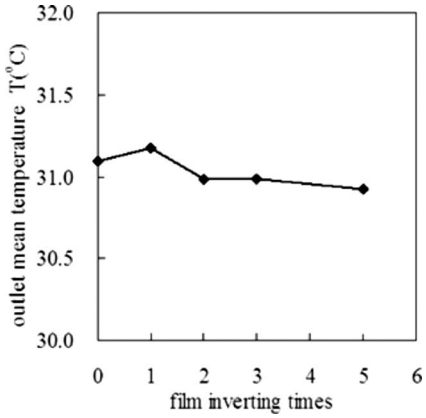

Fig. 16 Outlet mean temperature versus film-inverting times

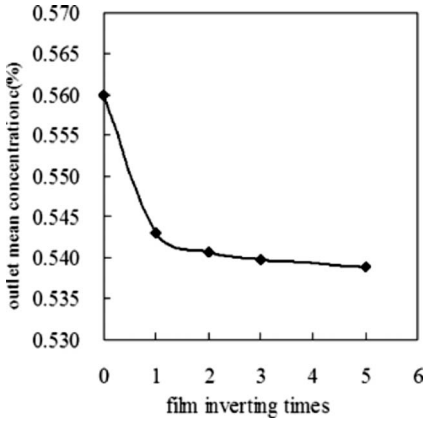

Fig. 17 Outlet mean concentration versus film-inverting times

A plate falling film prototype with film inversion has been built and experiment tests have been done on the absorption characteristics with different absorption pressures, solution flow rates, and solution inlet temperatures.

Comparisons between the experiment data and the numerical results show that the numerical results are in consistency with the experiment results. The differences between them are not large and within acceptable range from engineering viewpoint. The numerical results show that film inversion enhances the absorption so that the absorber size can be reduced. The times of film inversion, plate lengths, and inclined plate angles all have effect on the absorption process.

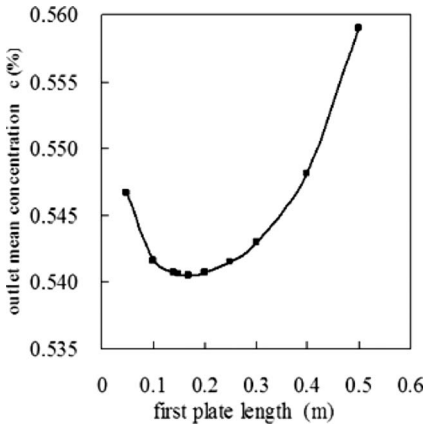

Fig. 18 Outlet concentration mean changes with first plate length

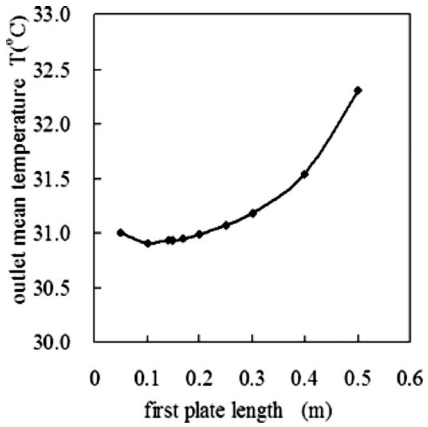

Fig. 19 Outlet temperature mean changes with first plate length

Acknowledgment

This paper is supported by the National Natural Science Foundation of China (Project No. 50576056) and the Shanghai Leading Academic Discipline Project (Project No. S30503).

Nomenclature

a = absorbent thermal diffusivity (m^2/s)
A = absorption area (m^2)
c = concentration of LiBr (kg/kg)
D = mass diffusivity (m^2/s)
g = gravity acceleration (m/s^2)
G = mass flow rate (kg/s)
h = heat transfer coefficient ($W/m^2°C$)
H = absorption heat (J)
L = plate length (m)
m = absorption vapor rate (kg/m^2 s)
M = absorbent flow rate (kg/s)
Q = heat load (J)
P = absorption vapor pressure (Pa)
Pr = Prandtl number
Re = Reynolds number
Sc = Schmidt number
T = temperature (°C)
u = x-velocity (m/s)
v = y-velocity (m/s)

Greek Symbols

α = the plate angle, the first plate angle (deg)
β = the inverted plate angle (deg)
ρ = absorbent density (kg/m^3)
λ = absorbent thermal conductivity (W/m^2 s)
δ = film thickness (m)
Ω = vapor mass rate (kg/m^2 s)
Ψ = stream function (m^2/s)
ν = solution kinematical viscosity (m^2/s)

Subscripts

out = absorber outlet
in = absorber inlet
w = water
wall = plate wall
s = solution

References

[1] Shitara, A., and Nishiyama, N., 1995, "Study on Transfer of Plate-Fin Type Generator for Absorption Machines," *Proceedings of the 19th International Congress of Refrigeration*, Hague, Vol. IIIa. B1, pp. 184–191.

[2] Bassols, J., Langreck, R., Schneider, R., Kuckelkorn, B., and Veelken, H., 1995, "Absorption Cooling Machine Based on Compact Plate-Fin Heat Exchangers," *Proceedings of the 19th International Congress of Refrigeration*, Hague, Vol. IIIa. B2, pp. 240–245.

[3] Flamensbeck, M., Summerer, F., Riesch, P., and Ziegler, G. A., 1998, "Cost Effective Absorption Chiller With Plate Heat Exchangers Using Water and Hydroxides," Appl. Therm. Eng., **18**(6), pp. 413–425.

[4] Setterwall, F., Glebov, D., and Wilkensten, B., 2001, "Low Temperature Driven Absorption Chiller," *Proceedings of the Second International Heat Powered Cycles Conference*, Paris, France, September, pp. 349–353.

[5] Reay, D. A., 2002, "Compact Heat Exchangers, Enhancement and Heat Pumps," Int. J. Refrig., **25**, pp. 460–470.

[6] Chen, Y. P., and Li, Y. B., 2002, "Experimental Study of Double Dimensional Cross Wave Surface Plate Lithium Bromide Aqueous Falling Film Absorber," *Proceedings of the Annual Conference on Heat and Mass Transfer*, Chinese Engineering Thermophysics Committee, Shanghai, pp. 921–924, in Chinese.

[7] Cheng, Z. M., Cui, X. Y., and Li, M. L., 2003, "Structure and Performance Study of Lithium Bromide Absorption Refrigerator Based on Plate Fin Heat Exchanger," *Proceedings of the International Conference on Energy and the Environment*, Shanghai, pp. 922–924.

[8] Islam, M. R., Wijeysundera, N. E., and Ho, J. C., 2003, "Performance Study of a Falling-Film Absorber With a Film-Inverting Configuration," Int. J. Refrig., **26**, pp. 909–917.

[9] Killion, J. D., and Garimella, S. A., 2001, "Critical Review of Models of Coupled Heat and Mass Transfer in Falling Film Absorption," Int. J. Refrig., **24**, pp. 755–797.

Model of Radiation and Heat Transfer in Laser-Powder Interaction Zone at Selective Laser Melting

A. V. Gusarov

I. Yadroitsev

Ph. Bertrand

I. Smurov

DIPI Laboratory,
Ecole Nationale d'Ingénieurs de Saint-Etienne (ENISE),
58 rue Jean Parot,
Saint-Etienne 42023, France

A model for coupled radiation transfer and thermal diffusion is proposed, which provides a local temperature field. Single-line scanning of a laser beam over a thin layer of metallic powder placed on a dense substrate of the same material is studied. Both the laser beam diameter and the layer thickness are about 50 μm. The typical scanning velocity is in the range of 10–20 cm/s. An effective volumetric heat source is estimated from laser radiation scattering and absorption in a powder layer. A strong difference in thermal conductivity between the powder bed and dense material is taken into account. The above conditions correspond to the technology of selective laser melting that is applied to build objects of complicated shape from metallic powder. Complete remelting of the powder in the scanned zone and its good adhesion to the substrate ensure fabrication of functional parts with mechanical properties close to the ones of the wrought material. Experiments with single-line melting indicate that an interval of scanning velocities exists, where the remelted tracks are uniform. The tracks become "broken" if the scanning velocity is outside this interval. This is extremely undesirable and referred to as the "balling" effect. The size and the shape of the melt pool and the surface of the metallurgical contact of the remelted material to the substrate are analyzed in relation to the scanning velocity. The modeling results are compared with experimental observation of laser tracks. The experimentally found balling effect at scanning velocities above ~20 cm/s can be explained by the Plateau–Rayleigh capillary instability of the melt pool. Two factors destabilize the process with increasing the scanning velocity: increasing the length-to-width ratio of the melt pool and decreasing the width of its contact with the substrate. [DOI: 10.1115/1.3109245]

Keywords: powder bed, absorbing scattering medium, melt pool, capillary instability

1 Introduction

The process of selective laser melting (SLM) is a technique of direct manufacturing from metallic powder. Its principal difference from conventional powder metallurgy processes is local heating and binding of powder by a scanning laser beam. Rapid manufacturing [1] of complex parts (see examples in Fig. 1(*a*)) is assured by this method. The SLM includes scattering and absorption of laser radiation in the powder, heat conduction, melting and coalescence of powder particles, formation of the melt pool, and its solidification. Figure 1(*b*) shows a typical scheme of layer-by-layer SLM fabrication. A SLM machine comprises of a fabrication plate (1) with two holes to which two containers are attached. A roller (2) delivers powder from the left container and deposits a thin powder layer in the right container (I). The thickness of the layer (about 50 μm [2]) is controlled by pistons moving up (3) and down (4). The deposited layer is scanned by a laser beam (5), which ensures local melting and binding to the previously fabricated layer (II). A part of a complex shape can be obtained in the right container after multiple deposition-scanning cycles (III). The complete remelting of the powder in the scanning zone is shown in Fig. 1(*c*), and its good adhesion to the substrate ensures obtaining functional parts with high mechanical properties [2,3]. The process of SLM is sensitive to a number of parameters such as the powder layer thickness, the power and the diameter of the laser beam, and the scanning speed.

Numerical simulation of heat transfer in the laser-powder interaction zone is applied to optimize the process parameters [4–9]. The thermal model by Bugeda et al. [5] simulates a laser beam moving along a straight line over the surface of a semi-infinite powder bed. The initial state of the material is uniform loose powder. Laser heating provokes coalescence of powder particles, which changes the effective thermal conductivity. Therefore, the equation of thermal diffusion is coupled with an equation of powder consolidation kinetics. The mechanism of consolidation by viscous flow driven by surface tension is studied in Ref. [5]. An Arrhenius-type dependence of viscosity versus temperature is employed, which can be applied to amorphous polymer powders. An improved kinetic equation is developed in Ref. [6] for crystalline polymers. A similar model of thermal diffusion coupled with consolidation kinetics proposed by Tolochko et al. [7] is adapted for metallic powders and takes into account the solid-state sintering controlled by diffusion below the melting point and instantaneous consolidation at melting. The above models neglect mass flow due to shrinkage at powder consolidation. A numerical approach to take the shrinkage into account is proposed in Ref. [8]. However, the shrinkage produces a nonflat top surface of the melt pool and provokes significant surface tension forces, whose influence on the free surface has not been rigorously calculated.

Models in Refs. [9–11] concern not only the laser-powder interaction zone but also the temperature distribution in the whole powder bed scanned by laser, which can be useful to calculate

Contributed by the Heat Transfer Division of ASME for publication in the JOURNAL OF HEAT TRANSFER. Manuscript received April 15, 2008; final manuscript received January 28, 2009; published online May 1, 2009. Review conducted by Ben Q. Li.

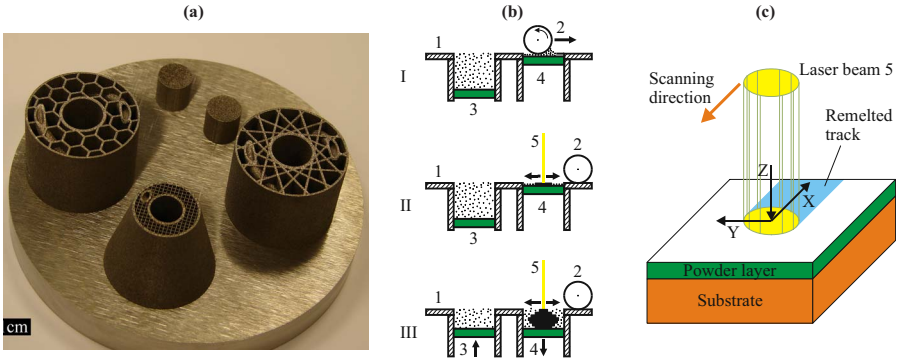

Fig. 1 Selective laser melting. (*a*) Fabricated parts. (*b*) Scheme of the process: (I) deposition of a powder layer, (II) scanning of the first layer, and (III) layer-by-layer fabrication. and (*c*) Detailed view of the laser-powder interaction zone: (1) fabrication plate, (2) roller, (3) powder delivery piston, (4) fabrication piston, and (5) laser beam.

residual thermal stresses [9]. Several consecutive laser scans along parallel lines on the surface of a semi-infinite powder bed are simulated. Such complicated geometry necessitates increased spatial resolution in calculations, and so these models are simplified relative to the detailed models of the interaction zone [5–8]. Thus, consolidation kinetics is simplified in Refs. [9–11], and models in Refs. [9,10] apply to the top powder layer and are essentially two dimensional.

The half-infinite powder bed was the target in the models of the interaction zone [5–7], while the complex target consisting of a powder layer on the top of a half-infinite solid was studied in recent works [8,12]. In the layer-by-layer technology, the solid substrate originates from the previously bound powder layers. Its thermal influence can be significant because of much higher thermal conductivity. In addition, this approach allows to consider the principal question about the binding between layers.

The conventional scheme where the laser beam directly strikes a continuous melt pool and the moving pool absorbs the loose powder is used in the model in Ref. [8], while the laser beam directly interacts with powder in the model in Ref. [12]. These two approaches can be distinguished as the model of immediate consolidation of powder after melting [8] and the model of slow consolidation [12]. The first approach is well known and approved, for example, at laser cladding. However, the hypothesis of immediate consolidation is not evident at SLM because the process parameters are considerably different, for example, the laser beam is one to two orders of magnitude thinner. Indeed, the experimentally measured time of coalescence of two 100–150 μm particles was in the range from several milliseconds to several tens of milliseconds [13], while the time of laser beam passage is of the order of a fraction of millisecond in the SLM machine [3]. Another reason to apply the model of slow consolidation, where the processes of radiation transfer and shrinkage are essentially separated in space is the experimentally observed detachment of the remelted material from the loose powder [3] (see also the discussion in Sec. 4).

This work concerns modeling the laser-powder interaction zone based on the assumption of slow consolidation and aims to clarify physical processes at SLM. A single-line scan on a layer of unconsolidated powder is studied, as shown in Fig. 1(*c*). The substrate is implied to be solid and thermally thick. The model includes laser radiation transfer described in Sec. 2 and conductive heat transfer described in Sec. 3.

2 Radiation Transfer

The freshly deposited powder is not mechanically compressed in the SLM machine in order to not destroy the underlying consolidated part. Therefore, it has as high porosity as freely poured powder, which is in the range 40–60% for typical metallic powders employed in SLM [14]. Laser radiation penetrates into powder through pores to a depth of several particle diameters because of multiple reflections [15]. This is comparable with the powder layer thickness. Thus, laser energy is deposited not on the surface but in the bulk of the powder layer. The objective of this section is to estimate the parameters of the volumetric heat source due to laser radiation absorption, which is necessary for further heat transfer calculations.

Figure 2 shows the model of radiation transfer, where the powder layer of thickness L is uniformly irradiated at normal incidence with power density Q_0. The collimated incident beam is scattered inside the powder and gives rise to radiation propagating in all directions, which is characterized by its angular intensity $I(z,\theta)$ at depth z and polar angle θ. The radiation intensity is defined in the ordinary way as the energy flux through the unit surface of the plane parallel to the substrate at depth z (see Fig. 2) transferred by rays within a small solid angle about direction θ divided by this solid angle and by cos θ [16]. Assuming a large area being irradiated that contains a great number of structural features, powder can be considered as a homogeneous absorbing scattering medium, and the radiation transfer equation (RTE) can be employed [17] as

$$\mu\frac{\partial I(z,\mu)}{\partial z}=\beta\left\{\frac{\omega}{2}\int_{-1}^{1}I(z,\mu')P(\mu',\mu)d\mu'-I(z,\mu)\right\} \quad (1)$$

where $\mu=\cos\theta$, β is the extinction coefficient, ω is the scattering albedo, and $P(\mu',\mu)$ is the scattering phase function. In the case of opaque powder particles, the effective values of the extinction coefficient and albedo are [17]

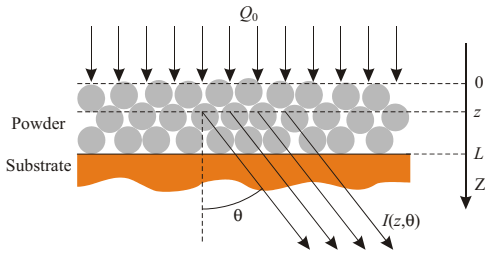

Fig. 2 Laser radiation transfer in a powder layer on a substrate: (Q_0) incident power density, (z) depth, (L) layer thickness, (θ) radiation propagation angle, and ($I(z,\theta)$) radiation intensity

$$\beta = S/4 \quad \text{and} \quad \omega = \rho \tag{2}$$

where S is the specific powder surface per unit pore volume, and ρ is the hemispherical reflectivity of the powder material in the dense form. The scattering phase function can be obtained from the directional reflectivity of the powder material [17]. In the case of spherical metallic particles, the specular reflection law with constant directional reflectivity can be applied [16,17], which gives isotropic scattering

$$P(\mu', \mu) = 1 \tag{3}$$

The boundary condition on the powder surface $z=0$ specifies normally-collimated incident radiation

$$I(0, \mu) = \frac{Q_0}{2\pi}\delta(\mu - 1) \quad \text{at} \quad \mu > 0 \tag{4}$$

where δ is the Dirac delta function. The specular reflection with reflectivity ρ is assumed on substrate surface $z=L$ as

$$I(L, \mu) = \rho I(L, -\mu) \quad \text{at} \quad \mu < 0 \tag{5}$$

The radiation intensity I splits into two collimated terms and a diffused one [17]:

$$I(z, \mu) = \frac{Q_+(z)}{2\pi}\delta(\mu - 1) + \frac{Q_-(z)}{2\pi}\delta(\mu + 1) + F(z, \mu) \tag{6}$$

where Q_+ and Q_- are the power densities of the forward and backward, respectively. Collimated radiation originated from the incident laser radiation and its reflection by the substrate and F is the intensity of the diffuse component originated from (multiple) scattering of the collimated components. The substitution of Eq. (6) into RTE (1) and boundary conditions (4) and (5) gives a separate problem for the collimated components [17]

$$\frac{dQ_+}{dz} = -\beta Q_+, \quad \frac{dQ_-}{dz} = \beta Q_-, \quad Q_+(0) = Q_0, \quad Q_-(L) = \rho Q_+(L) \tag{7}$$

with the solution

$$Q_+ = Q_0 e^{-\xi} \quad \text{and} \quad Q_- = \rho Q_0 e^{\xi - 2\lambda} \tag{8}$$

where $\xi = \beta z$ is the dimensionless coordinate and $\lambda = \beta L$ is the optical thickness, as well as the boundary problem for the RTE describing the diffuse radiation [17]

$$\mu\frac{\partial F(z, \mu)}{\partial z} = \frac{\beta\omega}{4\pi}\{Q_+(z)P(1, \mu) + Q_-(z)P(-1, \mu)\} + \beta\left\{\frac{\omega}{2}\int_{-1}^{1} F(z, \mu')P(\mu', \mu)d\mu' - F(z, \mu)\right\} \tag{9}$$

$$F(0, \mu) = 0 \quad \text{at} \quad \mu > 0 \quad \text{and} \quad F(L, \mu) = \rho F(L, -\mu) \quad \text{at} \quad \mu < 0 \tag{10}$$

In the framework of the two-flux method, an approximate solution of Eqs. (9) and (10) is looking for

$$F(z, \mu) = F_+(z)h(\mu) + F_-(z)[1 - h(\mu)] \tag{11}$$

where h is the step Heaviside function. The substitution of Eq. (11) into Eq. (9) and integration over intervals $0 < \mu < 1$ and $-1 < \mu < 0$ gives two moment equations for dimensionless coefficients $f_\pm = 2\pi F_\pm / Q_0$ [17] as

$$\pm\frac{1}{2}\frac{df_\pm}{d\xi} = \frac{\rho}{2}(q_+ + q_- + f_+ + f_-) - f_\pm \tag{12}$$

where dimensionless functions $q_+ Q_+ / Q_0 = e^{-\xi}$ and $q_- = Q_- / Q_0 = \rho e^{\xi - 2\lambda}$ are introduced and relations (2) and (3) are taken into account. Boundary conditions for $f_\pm$ follow from Eq. (10) as

$$f_+(0) = 0 \quad \text{and} \quad f_-(\lambda) = \rho f_+(\lambda) \tag{13}$$

The general solution of Eq. (12) is

$$f_+ + f_- = C_1 e^{-2a\xi} + C_2 e^{2a\xi} - \frac{4\rho(e^{-\xi} + \rho e^{\xi - 2\lambda})}{4\rho - 3} \tag{14}$$

$$f_+ - f_- = aC_1 e^{-2a\xi} - aC_2 e^{2a\xi} - \frac{2\rho(e^{-\xi} - \rho e^{\xi - 2\lambda})}{4\rho - 3} \tag{15}$$

where $a = \sqrt{1 - \rho}$. Arbitrary constants C_1 and C_2 are found from boundary conditions (13)

$$C_1 = 2\rho\frac{(1 - a)(1 - \rho^2)e^{-\lambda} - [1 + a - \rho(1 - a)]e^{2a\lambda}(3 + \rho e^{-2\lambda})}{(4\rho - 3)D} \tag{16}$$

$$C_2 = 2\rho\frac{[1 - a - \rho(1 + a)]e^{-2a\lambda}(3 + \rho e^{-2\lambda}) - (1 + a)(1 - \rho^2)e^{-\lambda}}{(4\rho - 3)D} \tag{17}$$

$$D = (1 - a)[1 - a - \rho(1 + a)]e^{-2a\lambda} - (1 + a)[1 + a - \rho(1 - a)]e^{2a\lambda} \tag{18}$$

Net radiative energy flux density is calculated by definition in Ref. [16] as

$$Q = 2\pi\int_{-1}^{1} I\mu d\mu = \pi(F_+ - F_-) + Q_+ - Q_- \tag{19}$$

where Eqs. (6) and (11) are taken into account in the right hand side. In the dimensionless form

$$q = \frac{Q}{Q_0} = \frac{f_+ - f_-}{2} + q_+ - q_- = \frac{\rho a}{(4\rho - 3)D}\{(1 - \rho^2)e^{-\lambda}[(1 - a)e^{-2a\xi} + (1 + a)e^{2a\xi}] - (3 + \rho e^{-2\lambda}) \times \{[1 + a - \rho(1 - a)]e^{2a(\lambda - \xi)} + [1 - a - \rho(1 + a)]e^{2a(\xi - \lambda)}\}\} - \frac{3(1 - \rho)(e^{-\xi} - \rho e^{\xi - 2\lambda})}{4\rho - 3} \tag{20}$$

Absorptivity of the system powder-substrate defined as the fraction of the incident radiation passed the powder surface, is estimated as

$$A = q(0) = \frac{\rho a}{(4\rho - 3)D}\{2(1 - \rho^2)e^{-\lambda} - (3 + \rho e^{-2\lambda}) \times \{[1 + a - \rho(1 - a)]e^{2a\lambda} + [1 - a - \rho(1 + a)]e^{-2a\lambda}\}\} - \frac{3(1 - \rho)(1 - \rho e^{-2\lambda})}{4\rho - 3} \tag{21}$$

The fraction of incident radiation absorbed by the substrate is

$$A_s = q(\lambda) = \frac{\rho a}{(4\rho - 3)D}\{(1 - \rho^2)e^{-\lambda}[(1 - a)e^{-2a\lambda} + (1 + a)e^{2a\lambda}] - 2(1 - \rho)(3 + \rho e^{-2\lambda})\} - \frac{3(1 - \rho)^2 e^{-\lambda}}{4\rho - 3} \tag{22}$$

The volumetric heat source due to radiation absorption is

$$U = -\frac{dQ}{dz} = -\beta Q_0\frac{dq}{d\xi} \tag{23}$$

3 Conductive Heat Transfer

In the moving coordinate system shown in Fig. 1(*c*), the heat conduction equation is

$$\frac{\partial H}{\partial t} - v\frac{\partial H}{\partial x} = \frac{\partial}{\partial x}\left(k\frac{\partial T}{\partial x}\right) + \frac{\partial}{\partial y}\left(k\frac{\partial T}{\partial y}\right) + \frac{\partial}{\partial z}\left(k\frac{\partial T}{\partial z}\right) + U \quad (24)$$

where volumetric enthalpy H is related with temperature T by the thermal equation of state

$$T = \begin{cases} H/C_s, & H \le C_s T_m \\ T_m, & C_s T_m < H < C_s T_m + H_m \\ T_m + (H - C_s T_m - H_m)/C_l, & H \ge C_s T_m + H_m \end{cases} \quad (25)$$

where C_s and C_l are the specific heats in solid and liquid phases, respectively, T_m is the melting point, H_m is the latent heat of melting, t is the time, v is the scanning velocity, k is the thermal conductivity, and U is the volumetric heat source given by Eq. (23). The power density in the laser beam of full radius R is approximated by a bell-like radial distribution

$$Q_0 = Q_m\left(1 - \frac{r}{R}\right)^2\left(a + \frac{r}{R}\right)^2, \quad 0 < r < R \quad (26)$$

with $r^2 = x^2 + y^2$ and maximum Q_m related to total laser power

$$W = 2\pi\int_0^R Q_0(r) r dr = \frac{\pi}{3}R^2 Q_m \quad (27)$$

Thermal conductivity of metallic powder k_p is about 100 times less than that of dense material k_d [14]. To take into account this difference, phase function ϕ is introduced, which is equal to 0 in the powder phase and 1 in the dense phase. The thermal conductivity is specified as

$$k = k_p + (k_d - k_p)\phi \quad (28)$$

The phase function is initially set to 0 in the powder layer and 1 in the substrate. It is also set to 1 if the temperature T exceeds the melting point T_m, which means consolidation of powder. Outside the melting zone, the evolution of the phase function is calculated from the transport equation

$$\frac{\partial \phi}{\partial t} - v\frac{\partial \phi}{\partial x} = 0 \quad (29)$$

Equation (29) applied outside the melting front is independent of heat transfer equation (24). The phase function ϕ depends on temperature through its boundary condition at the melting front, where ϕ is assigned the value of 1. This equation is introduced to trace the points of powder where the temperature has ever been above the melting temperature, and therefore the matter tends to change from the dispersed state to the dense state.

Equations (24) and (29) are numerically solved in the rectangular computation domain $\{x = -X^-, \ldots, X^+; y = 0, \ldots, Y; z = 0, \ldots, Z\}$ with faces $x = -X^-$, $x = X^+$, $y = Y$, and $z = Z$ far from the origin not to influence the laser-matter interaction zone. The boundary conditions of isolated walls are used at the faces of the domain for Eq. (24)

$$\frac{\partial H}{\partial \mathbf{n}} = 0 \quad (30)$$

where $\mathbf{n}$ is the normal to the corresponding face. This condition also assures the mirror symmetry against plane $y = 0$. Equation (29) requires a boundary condition at face $x = -X^-$ as

$$\phi = \begin{cases} 0, & z < L \\ 1, & z \ge L \end{cases} \quad (31)$$

where L is the thickness of the powder layer, and a boundary condition at the melting front

$$\phi = 1 \quad (32)$$

which is applied in the three-dimensional domain where $T \ge T_m$ in the numerical procedure but changes nothing downstream the melting front.

The computational domain is divided into $N_x \times N_y \times N_z$ rectangular cells with the sizes of $\Delta x = (X^- + X^+)/N_x$, $\Delta y = Y/N_y$, and $\Delta z = Z/N_z$ and the centers at $x_i = -X^- + \Delta x/2 + i\Delta x$, $y_j = \Delta y/2 + j\Delta y$, and $z_l = \Delta z/2 + l\Delta z$, with integers $i = 0, \ldots, N_x - 1$, $j = 0, \ldots, N_y - 1$, and $l = 0, \ldots, N_z - 1$. The typical parameters are $N_x \times N_y \times N_z = 240 \times 80 \times 80$ and $\Delta x = \Delta y = \Delta z = 2.5$ μm. The convergence of the numerical scheme was checked by calculating the same problem at the grid with the number of cells reduced by a factor of 2 in each dimension, and no significant differences in results were obtained.

The heat transfer equation (24) is approximated by the following explicit conservative finite-difference scheme with second order accuracy in space and first order accuracy in time

$$\begin{aligned} &\frac{H_{ijl}(t + \Delta t) - H_{ijl}(t)}{\Delta t} - v\frac{H_{i+1/2,jl}(t) - H_{i-1/2,jl}(t)}{\Delta x} \\ &= \frac{1}{\Delta x}\left[\frac{k(T_{i+1,jl}) + k(T_{ijl})}{2}\frac{T_{i+1,jl}(t) - T_{ijl}(t)}{\Delta x} \right. \\ &\quad \left. - \frac{k(T_{ijl}) + k(T_{i-1,jl})}{2}\frac{T_{ijl}(t) - T_{i-1,jl}(t)}{\Delta x}\right] \\ &\quad + \frac{1}{\Delta y}\left[\frac{k(T_{i,j+1,l}) + k(T_{ijl})}{2}\frac{T_{i,j+1,l}(t) - T_{ijl}(t)}{\Delta y} \right. \\ &\quad \left. - \frac{k(T_{ijl}) + k(T_{i,j-1,l})}{2}\frac{T_{ijl}(t) - T_{i,j-1,l}(t)}{\Delta y}\right] \\ &\quad + \frac{1}{\Delta z}\left[\frac{k(T_{ij,l+1}) + k(T_{ijl})}{2}\frac{T_{ij,l+1}(t) - T_{ijl}(t)}{\Delta z} \right. \\ &\quad \left. - \frac{k(T_{ijl}) + k(T_{ij,l-1})}{2}\frac{T_{ijl}(t) - T_{ij,l-1}(t)}{\Delta z}\right] \end{aligned} \quad (33)$$

where Δt is the time increment, the grid function H_{ijl} is defined as the cell average, and T_{ijl} is calculated by the thermal equation of state (25). The advection equation (29) is approximated as

$$\frac{\varphi_{ijl}(t + \Delta t) - \varphi_{ijl}(t)}{\Delta t} = v\frac{\varphi_{i+1/2,jl}(t) - \varphi_{i-1/2,jl}(t)}{\Delta x} \quad (34)$$

The grid functions H_{ijl} and ϕ_{ijl} are defined as the cell averages, T_{ijl} is calculated by the thermal equation of state (25), and the half-integer values $H_{i+1/2,jl}$ and $\phi_{i+1/2,jl}$ are estimated from the corresponding integer values by the "minmod" slope limiter method [18] to obtain a nonoscillatory second order approximation of the advection terms.

The time step Δt is restricted by the stability conditions for the explicit schemes

$$\Delta t < \frac{\Delta x^2}{8a}, \quad \Delta t < v\Delta x \quad (35)$$

where Δx is the minimum cell size and a the maximum thermal diffusivity. The typical value of Δt is of the order of 10^{-7} s.

4 Thermal and Optical Properties

Calculations are made for stainless steel type 316L with a melting point $T_m = 1700$ K, a latent heat of melting $H_m = 2.18$ GJ/m^3, and specific heats of $C_s = 4.25$ MJ/m^3 K in solid and $C_l = 5.95$ MJ/m^3 K in liquid phases. Thermal conductivity of this alloy considerably increases with temperature above the room temperature. The temperature range near the melting point and above is the most important for the studied problem where there

are no reliable experimental data, so that a constant value of $k_d = 20$ W/m K is accepted, which is obtained by extrapolation to the melting point.

The effective thermal conductivity of loose metallic powders is controlled by gas in the pores [14]. Therefore, it is essentially independent of material but depends on the size and morphology of the particles and the void fraction, as well as on the thermal conductivity of the gas. For 10–50 μm powders, the effective thermal conductivity is typically from 0.1 to 0.2 W/m K in air at room temperature [14]. The thermal conductivity of gas increases approximately as square root of temperature, so that a value around $k_p = 0.3$ W/m K is expected near the melting point. This value is still much less than the thermal conductivity of solid, so that the modeling results are not expected to be sensitive to the thermal conductivity of powder. The above constant value at the melting point is used in calculations. The thermal dependence is neglected. The contribution of radiative heat transfer to the thermal conductivity k_r can be estimated as [19]

$$k_r = \frac{16l}{3}\sigma T^3 \tag{36}$$

where l is Rosseland's path and σ is the Stephan–Boltzmann constant. The value of l is around the grain size in the powder bed. The typical values of $l = 20$ μm and $T = 2000$ K result in $k_r = 0.05$ W/m K. This is much less than k_p, and so the radiative heat transfer is neglected in the model.

The optical properties are estimated for the laser wavelength of 1.075 μm. The hemispherical reflectivity of pure iron $\rho = 0.7$ is accepted for steel 316L. This is consistent with experimental data for powders of this steel [17,20] obtained at the room temperature. The temperature dependence is neglected because of lack of data. The extinction coefficient β of loose powders was measured in Ref. [21], where a strong dependence on the size and the morphology of particles was reported. It can be estimated by Eq. (2). Assuming that the powder bed consists of spherical particles of diameter D distributed in space with number density n, this equation gives

$$\beta = \frac{1}{4}\frac{\pi D^2 n}{1 - \pi D^3 n/6} = \frac{3}{2}\frac{1-\varepsilon}{\varepsilon}\frac{1}{D} \tag{37}$$

where porosity $\varepsilon = 1 - \pi D^3 n/6$ is defined. The optical thickness

$$\lambda = \beta L = \frac{3}{2}\frac{1-\varepsilon}{\varepsilon}\frac{L}{D} \tag{38}$$

is proportional to the number of monolayers (L/D). For typical parameters of $D = 20$ μm and $L = 50$ μm ($L/D = 2.5$ monolayers), the optical thickness is estimated as $\lambda = 3.75$ for porosity $\varepsilon = 1/2$ and $\lambda = 1.875$ for $\varepsilon = 2/3$.

5 Estimation of Laser Energy Deposition

Figure 3 shows the depth profiles of radiative energy flux and volumetric heat source in the powder layer calculated by Eqs. (20) and (23), respectively. Vertical line on the right of each curve corresponds to the substrate surface. Approximately linear decrease in the flux at low optical thickness ($\lambda = 1$ in Fig. 3(*a*)) evolves into approximately exponential decay with increasing the optical thickness ($\lambda = 4$ in Fig. 3(*a*)). The corresponding energy deposition distributions (Fig. 3(*b*)) are proportional to the derivative of the flux. They change from a roughly uniform distribution over the powder layer at $\lambda = 1$ to an approximately exponential function at $\lambda = 4$. The deviation from the exponential Beer–Lambert–Bouguer law is due to the radiation scattering in the powder.

The fraction of incident laser radiation absorbed by the substrate A_s decreases with the optical thickness of the powder layer (lower curve in Fig. 4, calculated by Eq. (22)), while the fraction absorbed in the powder $A - A_s$ increases (middle curve) so that the total absorptivity A considerably increases (upper curve, calculated by Eq. (21)) relative to the absorptivity of dense material $1 - \rho = 0.3$.

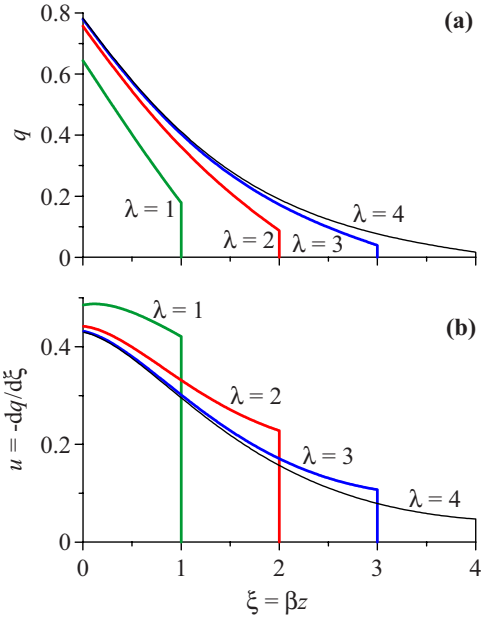

Fig. 3 (*a*) Dimensionless radiative flux $q = Q/Q_0$ and (*b*) volumetric heat source $u = UI(\beta Q_0)$ in the powder layer versus dimensionless depth ξ for various values of optical depth λ at the reflectivity of dense material $\rho = 0.7$

Figure 5 shows the radial profiles of power density Q_0 in the incident laser beam, which are employed for the calculations. They are specified according to Eqs. (26) and (27) by total beam

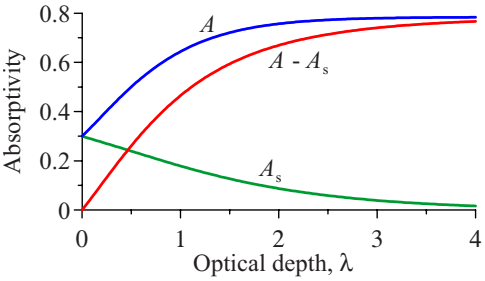

Fig. 4 Total absorptivity of the system powder-substrate A and fractions of the incident laser radiation absorbed by the surface of the substrate A_s and in the powder $A - A_s$ versus optical depth of the powder layer λ at the reflectivity of dense material $\rho = 0.7$

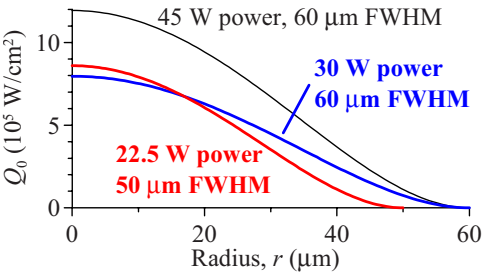

Fig. 5 Radial profiles of power density in the incident laser beam employed for the calculations. The total beam power and the FWHM are specified for each curve.

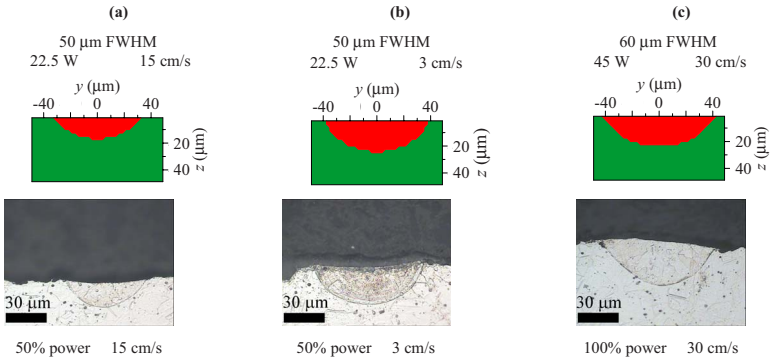

Fig. 6 Cross-sections of laser tracks on the stainless steel substrate without powder: calculated phase diagrams (upper row) and experimental micrographs (lower row)

power W and full radius R, which is approximately equal to the full width of the beam at half maximum (FWHM).

6 Results and Discussion

The experimental results are obtained with SLM machine "Phenix Systems" employing 1.075 μm laser of 50 W nominal power and 70 μm nominal beam diameter. Taking into account absorption by the optical system, the maximum laser power is estimated as 45 W. The pumping power of the laser can be reduced producing laser radiation of reduced power, which is measured in fractions of the maximum power.

To validate the model, heat transfer in the substrate without powder is modeled first. Figure 6 compares experimental cross section micrographs (on the bottom) with the calculated projections of the melt pool on the plane perpendicular to the scanning direction (on the top). The absorbed fraction of laser energy $1-\rho=0.3$ used in calculations is expected to be the most uncertain model parameter because it is estimated from the reflectivity ρ measured at the room temperature, while the absorptivity of metals generally tends to increase with temperature. Another questionable point of the model is the negligence of the Marangoni convection in the melt pool. Both the increase in absorptivity with temperature and the convection enlarge the melt pool. The observed agreement between the experiment and the model shown in Fig. 6 indicates that the absorptivity does not significantly increase with temperature and the contribution of the Marangoni convection to heat transfer is low.

The diameter of the laser beam is evaluated by its traces at reduced laser power. The full diameter estimated from such experiments is around 100 μm. However, a slow dependence on the laser power is possible. Therefore, two values of FWHM diameter of 50 μm and 60 μm were tested in the calculations. The difference was not principal. However, the shape of the experimental melt pool is reproduced better by 50 μm FWHM at 50% power (22.5 W) and by 60 μm FWHM at 100% power (45 W).

Figure 7 presents the typical modeling results for a 50 μm powder layer on a substrate. The isotherms in diagrams (c) and (d) show the melting point $T_m=1700$ K. The level in diagram (e) is the powder-substrate interface. The incident laser power of 30 W chosen for this calculation is less than the maximum of 45 W to take into account heat losses by evaporation. According to the preliminary calculations, the beam of 45 W incident power considerably overheats the powder layer above the boiling point because of low thermal conductivity of powder. Indeed, while no evaporation is experimentally observed from the noncovered substrate, the traces of evaporation as ejection of droplets are noticed

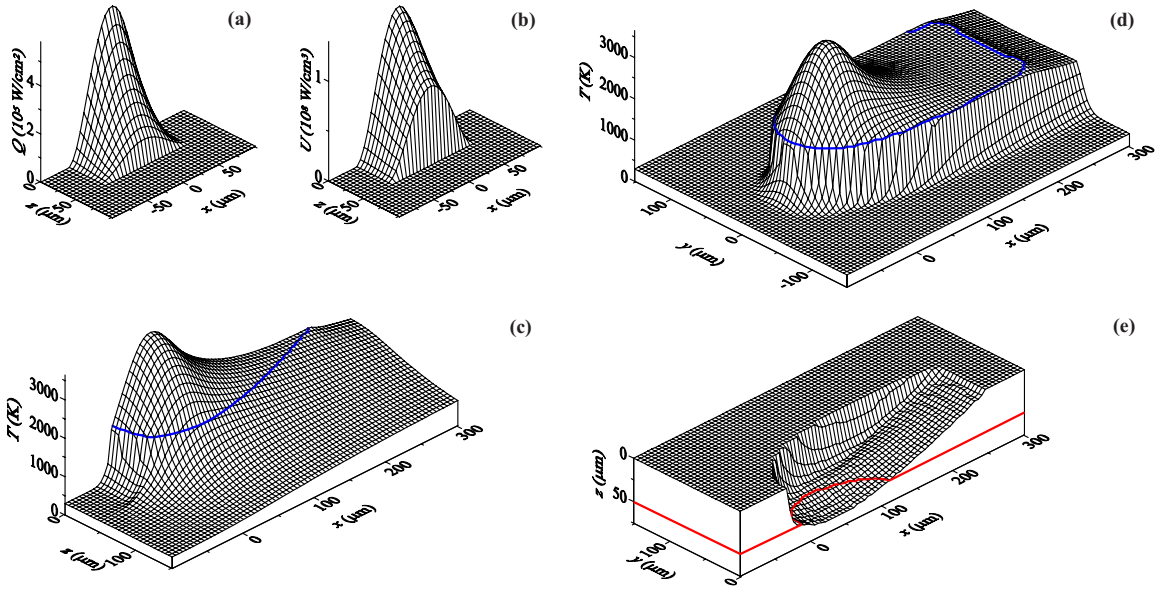

Fig. 7 Laser beam scanning of a 50 μm powder layer with optical thickness $\lambda=2$ at the incident laser power of 30 W, the laser beam FWHM of 60 μm, and the scanning velocity of 20 cm/s. Distributions at the symmetry plane $y=0$: (*a*) normal component of net laser radiation flux density Q, (*b*) volumetric heat source due to absorption of laser radiation U, (*c*) temperature T, (*d*) temperature T at the top powder surface $z=0$, and (*e*) melt pool shape.

for the sandwich powder/substrate [3]. The fraction of the evaporated material is experimentally estimated to be low. Nevertheless, the evaporation can contribute to the energy balance of the process.

Two principal effects of evaporation are expected. First, the hot vapor and the droplets shield the target from the incident laser radiation so that the beam intensity at the target surface is reduced. Second, the thermal energy released after the laser beam absorption is partly spent to evaporation and taken away with vapor. These complex processes are taken into account by reducing the incident laser power. The value of 30 W is found to result in reasonable maximum temperatures around the boiling point. The same effective incident laser power of 30 W is applied to all the calculations made for the powder/substrate system.

The net laser energy flux density Q (Fig. 7(*a*)) and volumetric heat source U (Fig. 7(*b*)) are estimated by Eqs. (20), (23), and (26). The value of Q at the top powder surface $z=0$ gives total power density absorbed by the system powder layer substrate. It is less than the corresponding incident power density given by the blue curve in Fig. 5. The value of Q at the powder-substrate interface $z=50$ μm gives power density absorbed by the surface of the substrate, which is considerably less than the incident one. The volumetric deposition of laser energy decreases with the depth according to Fig. 7(*b*) but is important until the bottom of the powder layer.

The influence of the scanning velocity v on conductive heat transfer is estimated by the Peclet number $\mathrm{Pe}=vR/\chi$ with thermal diffusivity χ. The thermal diffusivity of the dense solid phase is estimated as 4.7 mm^2/s from the parameters listed in Sec. 4, while the value of 0.07 mm^2/s is obtained for the powder. For the example shown in Fig. 7, these two different diffusivities give the Peclet number of $\sim$2.6 in the dense material and $\sim$170 in the powder. In the center of the melt pool, where the Peclet number is about unity, the influence of the scanning is small and the temperature distribution is approximately symmetric about axis (OZ) because the laser beam is axially symmetric. However, the temperature maximum is slightly shifted relative at the center of the laser beam. This is clearer in Fig. 8(*d*), where the projection of the laser beam on the surface is shown by a broken-line circle. At the periphery of the melt pool and especially near the powder phase, the Peclet number is large, so that the scanning considerably violates the axial symmetry. Therefore, the melt pool is highly stretched along the scanning direction (see Fig. 7(*e*)).

The sharp edge in the temperature distribution of Fig. 7(*d*) at the powder-liquid boundary (front boundary of the melt pool) appears due to a high difference in thermal conductivity. The similar edge at the rear boundary of the melt pool is due to liberation of the latent heat at solidification.

Figure 8 presents the experimental top view of the remelted tracks (a) and their cross section micrographs (b), as well as the calculated temperature distribution on the top powder surface (d) and phase distribution in the cross-section (c) at various scanning velocities. The zones of the remelted material (center), loose powder (top sides), and the substrate (bottom) are distinguished by contrast in Fig. 8(*c*). The experiments are made at the incident laser power of $\sim$45 W and $\sim$60 μm FWHM. To take into account heat losses by evaporation, the reduced effective laser power of 30 W is used for the calculations as explained above. The thickness of the powder layer is fixed to $L=50$ μm. However, its optical thickness λ depends on the porosity, which is not controlled in the experiments. Therefore, calculations are made at two values of $\lambda=2$ and 3.

The maximum surface temperature (see Fig. 8(*d*)) considerably exceeds the boiling point of $\sim$3200 K, especially at lower scanning velocity. This is consistent with the experimentally observed intensive evaporation. The maximum temperature could be less if the radiative thermal conductivity proportional to T^3 according to Eq. (29) were taken into account. The volumetric heat source U in Eq. (24) is evaluated by the one-dimensional radiation transfer model. Application of this model for the present problem where the laser beam width (60 μm) is comparable with the characteristic depth (50 μm) overestimates U in the center, so that the temperature maximum is expected to be overestimated too. The boiling point isotherm at $T=1700$ K (bold curves in Fig. 8(*d*)) gives the top contour of the melt pool. The melt pool becomes longer and narrower with increasing the scanning velocity. Its top surface slightly increases with the optical thickness λ because of redistribution of the heat source U, more energy is deposited near the surface.

The calculated shape of the remelted zone (Fig. 8(*c*)) is quite different from the experimentally observed one (Fig. 8(*b*)) and indicates melt flow not taken into account by the model. This flow is expected to be driven by the surface tension force. Indeed, the initially molten powder is attached to the substrate in the central part of the melt pool, while its lateral parts do not contact with the substrate (see Fig. 8(*c*)). Therefore, the sides completely detach from the substrate and the nonmelted powder to form a rounded free surface, as shown in Fig. 8(*b*), which reduces the surface energy. The melt deformation is schematically shown in Fig. 9. This mechanism explains the bright zones at the sides of the remelted cylinders on the top view (a), which are interpreted as the substrate surface became visible because the powder above it is consumed. Comparison between Figs. 8(*a*) and 8(*d*) indicates that the width of the powder-consumed band approximately corresponds to the calculated maximum width of the melt pool. This suggests that the melt flow is weak in the forward half of the pool ($x<100$ μm), so that the heat transfer model gives the correct value of its maximum width. On the contrary, a strong melt flow is expected in the backward half ($x>100$ μm), where the results given by the model are rough.

The surface tension-driven flow is supposed to be negligible in the central bottom part of the melt pool, so that the shape of the remelted zone of the substrate is correctly estimated by the model (compare Figs. 8(*b*) and 8(*c*)). In particular, the width of the contact between the remelted powder and the substrate is quite correct. This is confirmed by Fig. 10, where the two characteristic dimensions of the remelted track are plotted as functions of the scanning velocity. The calculated width of the powder-consumed band is defined as the maximum width of the melt pool and taken from Figs. 8(*c*) and 8(*d*). The calculated width of the contact is defined as the maximum width of the melt pool at the substrate surface ($z=50$ μm) and taken from Fig. 8(*c*). The corresponding experimental values are taken from Figs. 8(*a*) and 8(*b*). Comparison between calculations for $\lambda=2$ and $\lambda=3$ indicates that these two dimensions are not sensitive to the optical thickness λ. Both the width of the powder-consumed band and the width of the contact decrease with the scanning velocity v, as shown in Fig. 10. Experimental contact width becomes noisy above $v=14$ cm/s. At such high scanning velocities, the process becomes unstable, and the remelted cylinder tends to break into separate droplets (see Fig. 8(*a*) for $v=20$ and 24 cm/s). For example, the cross section micrograph shown in Fig. 8(*b*) for $v=20$ cm/s is likely to pass across such a droplet. Therefore, the remelted zone is considerably larger than in the neighbor micrographs. The width of the contact with the substrate considerably varies along the track at high v. This produces the experimental uncertainty and the discrepancy with the calculations shown in Fig. 10.

Fragmentation of the remelted tracks at SLM is a well-known drawback of the technique referred to as the "balling" effect [22]. An interval of the scanning velocity where the SLM process is stable was shown to exist for the conditions similar to those tested in this work [3,23]. The "balling" effect appears both at the lower and the upper bounds of this interval. It is explained by a capillary instability of the melt pool at high length-to-width ratios when it fragments with reducing the surface energy [23]. The fragmentation shown on the right of Fig. 8(*a*) concerns the upper stability limit at $v\sim20$ cm/s. According to the micrographs in Fig. 8(*b*),

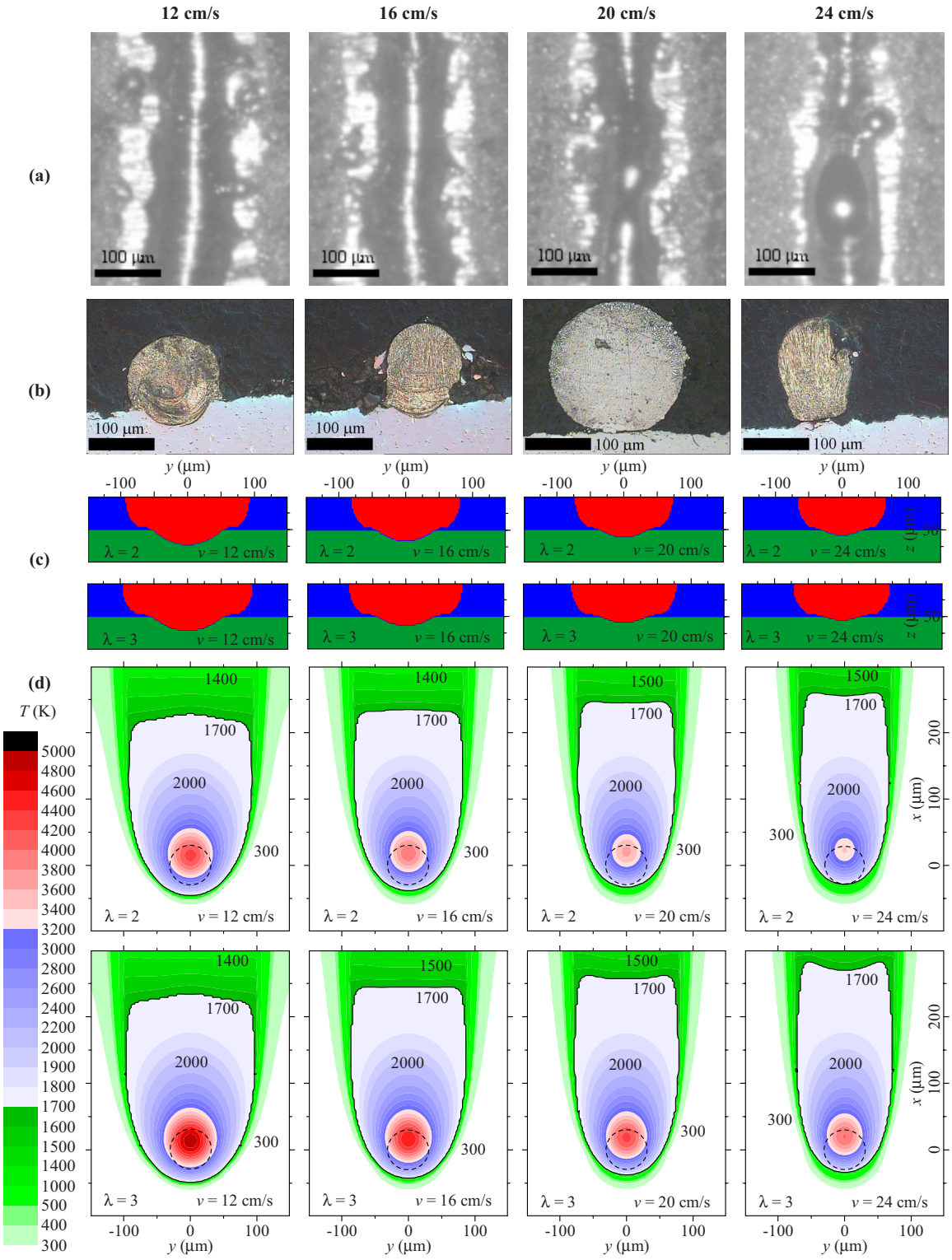

Fig. 8 Comparison between experiments ((*a*) and (*b*)) and calculations ((*c*) and (*d*)) at various scanning velocities (marked on the top of each column): (*a*) top view of remelted tracks; (*b*) cross section micrographs; (*c*) calculated phase distribution in cross-section with the substrate on the bottom, the powder on the sides, and the remelted zone in the center; and (*d*) surface temperature distribution. The broken-line circles on diagrams (*d*) are projections of the laser beam.

the contact between the remelted powder and the substrate tends to vanish at $v > 20$ cm/s. While the calculated contact width at this velocity is still about 60 μm, the modeling indicates that this parameter is the most sensitive to v and decreases fast. Therefore, the upper stability limit can also be related to the loss of the contact between the molten powder and the substrate.

As shown in Fig. 8(*d*), the length of the melt pool at the stability limit $v = 20$ cm/s is about 300 μm and its width about

Fig. 9 Qualitative evolution of phase distribution in the cross-section of a track with the substrate on the bottom, the powder on the sides, and the melt in the center: (*a*) just melted and (*b*) after minimizing the melt surface

150 μm. The height is equal to the powder layer thickness $L = 50$ μm. According to the above discussion, the surface tension transforms this liquid volume to a shape similar to a circular cylinder with the length of 300 μm and the diameter about 100 μm estimated from volume conservation. The circumference of this cylinder is about its length, which is the limit of the Plateau–Rayleigh capillary instability of a liquid cylinder [24]: The cylinder breaks into two droplets if the length exceeds the circumference. The ratio of the length to the circumference would be greater than unity if the radial shrinkage due to gas ejection from pores were taken into account. Thus, the Plateau–Rayleigh instability can explain the balling effect at $v = 20$ cm/s. When the scanning velocity v decreases, the length of the melt pool decreases and its width increases (see Fig. 8(*d*)), so that the Rayleigh ratio of length-to-circumference decreases, which should stabilize the melt pool. However, the crucial stabilizing factor could be the contact between the melt cylinder and the substrate, which disappears at $v \sim 20$ cm/s and increases fast with decreasing the velocity. To break into droplets, the melt should be detached from the substrate between the droplets, which creates additional free surface. This explains the stabilizing effect of the contact.

7 Conclusion

The proposed model of laser beam interaction with the powder bed at SLM consists in coupled radiation and heat transfer in a thin powder layer deposited on a dense substrate. At the studied layer thickness of ~ 50 μm and grain size of ~ 20 μm, laser radiation can penetrate into powder by an open pore system until the substrate and create a volumetric heat source. The melt pool formed around the laser beam contacts the substrate by its central part only. Such a complex shape of the melt surface can produce its deformation driven by surface tension. The lateral parts of the melt pool are expected to detach from the neighbor powder to form a rounded free surface with reduced surface energy. Thus, a cylinderlike remelted volume attached to the substrate is formed in the middle of a considerably larger powder-consumed band. The widths of the powder-consumed band and the contact between the remelted material and the substrate can be estimated by the thermal model neglecting melt flow. The balling effect at high scanning velocities (above ~ 20 cm/s for the present conditions) can be explained by the Plateau–Rayleigh capillary instability of a liquid cylinder. Two factors destabilize the process with increasing the scanning velocity: increasing the length-to-circumference ratio and decreasing the width of the contact with the substrate. The modeling results can be used to predict whether the balling effect is expected.

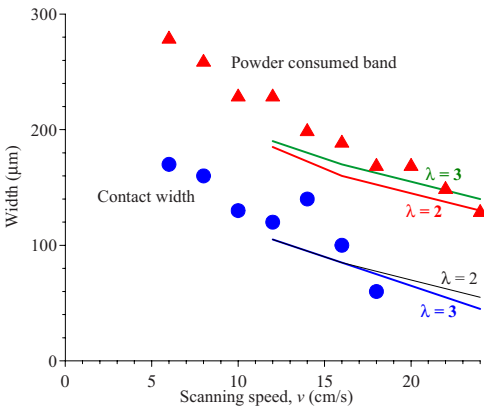

Fig. 10 Widths of the powder-consumed band and the contact of the remelted material with the substrate versus the scanning velocity: experiments (points) and calculations (lines) at two values of the optical thickness, $\lambda = 2$ and $\lambda = 3$

Acknowledgment

The authors would like to thank Direction Générale des Entreprises, Conseil Général de la Loire, and Saint-Etienne Métropole for their financial support of the "MULTIMAT" Project, within the Competitiveness Cluster ViaMéca, and also to CETIM Foundation for its financial support of the "Multimatérial and Multifunctional Products" Project.

References

[1] Santos, E. C., Shiomi, M., Osakada, K., and Laoui, T., 2006, "Rapid Manufacturing of Metal Components by Laser Forming," Int. J. Mach. Tools Manuf., **46**, pp. 1459–1468.
[2] Yadroitsev, I., Bertrand, Ph., Laget, B., and Smurov, I., 2007, "Application of Laser Assisted Technologies for Fabrication of Functionally Graded Coatings and Objects for the International Thermonuclear Experimental Reactor Components," J. Nucl. Mater., **362**, pp. 189–196.
[3] Yadroitsev, I., Bertrand, Ph., and Smurov, I., 2007, "Parametric Analysis of the Selective Laser Melting Process," Appl. Surf. Sci., **253**, pp. 8064–8069.
[4] Choi, J., Han, L., and Hua, Y., 2005, "Modeling and Experiments of Laser Cladding With Droplet Injection," ASME J. Heat Transfer, **127**, pp. 978–986.
[5] Bugeda, G., Cervera, M., and Lombera, G., 1999, "Numerical Prediction of Temperature and Density Distributions in Selective Laser Sintering Processes," Rapid Prototyping J., **5**, pp. 21–26.
[6] Tontowi, A. E., and Childs, T. H. C., 2001, "Density Prediction of Crystalline Polymer Sintered Parts at Various Powder Bed Temperatures," Rapid Prototyping J., **7**, pp. 180–184.
[7] Tolochko, N. K., Arshinov, M. K., Gusarov, A. V., Titov, V. I., Laoui, T., and Froyen, L., 2003, "Mechanisms of Selective Laser Sintering and Heat Transfer in Ti powder," Rapid Prototyping J., **9**, pp. 314–326.
[8] Xiao, B., and Zhang, Y., 2008, "Numerical Simulation of Direct Metal Laser Sintering of Single-Component Powder on Top of Sintered Layers," ASME J. Manuf. Sci. Eng., **130**, p. 041002.
[9] Matsumoto, M., Shiomi, M., Osakada, K., and Abe, F., 2002, "Finite Element Analysis of Single Layer Forming on Metallic Powder Bed in Rapid Prototyping by Selective Laser Processing," Int. J. Mach. Tools Manuf., **42**, pp. 61–67.
[10] Patil, R. B., and Yadava, V., 2007, "Finite Element Analysis of Temperature Distribution in Single Metallic Powder Layer During Metal Laser Sintering," Int. J. Mach. Tools Manuf., **47**, pp. 1069–1080.
[11] Kolossov, S., Boillat, E., Glardon, R., Fisher, P., and Locher, M., 2004, "3D FE Simulation for Temperature Evolution in the Selective Laser Sintering Process," Int. J. Mach. Tools Manuf., **44**, pp. 117–123.
[12] Gusarov, A. V., Yadroitsev, I., Bertrand, Ph., and Smurov, I., 2007, "Heat Transfer Modeling and Stability Analysis of Selective Laser Melting," Appl. Surf. Sci., **254**, pp. 975–979.
[13] Klocke, F., and Wagner, C., 2003, "Coalescence Behaviour of Two Metallic Particles as Base Mechanism of Selective Laser Sintering," CIRP Ann., **52**, pp. 177–180.
[14] Rombouts, M., Froyen, L., Gusarov, A. V., Bentefour, E. H., and Glorieux, C., 2005, "Photopyroelectric Measurement of Thermal Conductivity of Metallic Powders," J. Appl. Phys., **97**, p. 024905.
[15] Wang, X. C., Laoui, T., Bonse, J., Kruth, J. P., Lauwers, B., and Froyen, L., 2002, "Direct Selective Laser Sintering of Hard Metal Powders: Experimental Study and Simulation," Int. J. Adv. Manuf. Technol., **19**, pp. 351–357.
[16] Siegel, R., and Howell, J. R., 1981, *Thermal Radiation Heat Transfer*, Hemisphere, New York.
[17] Gusarov, A. V., and Kruth, J.-P., 2005, "Modelling of Radiation Transfer in Metallic Powders at Laser Treatment," Int. J. Heat Mass Transfer, **48**, pp.

3423–3434.
[18] Leveque, R. J., 1992, *Numerical Methods for Conservation Laws*, Birkhauser Verlag, Berlin.
[19] Zel'dovich, Y. B., and Raiser, Y. P., 1967, *Physics of Shock Waves and High-Temperature Hydrodynamic Phenomena*, Academic, New York.
[20] Gusarov, A. V., Bentefour, E. H., Rombouts, M., Froyen, L., Glorieux, C., and Kruth, J.-P., 2006, "Normal-Directional and Normal-Hemispherical Reflectances of Micron- and Submicron-Sized Powder Beds at 633 and 790 nm," J. Appl. Phys., **99**, p. 113528.
[21] Rombouts, M., Froyen, L., Gusarov, A. V., Bentefour, E. H., and Glorieux, C., 2005, "Light Extinction in Metallic Powder Beds: Correlation With Powder Structure," J. Appl. Phys., **98**, p. 013533.
[22] Morgan, R., Sutcliffe, C. J., and O'Neill, W., 2001, "Experimental Investigation of Nanosecond Pulsed Nd:YAG Laser Re-Melted Pre-Placed Powder Beds," Rapid Prototyping J., **7**, pp. 159–172.
[23] Kruth, J. P., Froyen, L., Van Vaerenbergh, J., Mercelis, P., Rombouts, M., and Lauwers, B., 2004, "Selective Laser Melting of Iron-Based Powder," J. Mater. Process. Technol., **149**, pp. 616–622.
[24] Chandrasekhar, S., 1961, *Hydrodynamic and Hydromagnetic Stability*, Clarendon, Oxford.

Transport Processes Governing the Drawing of a Hollow Optical Fiber

Jing Yang

Yogesh Jaluria

Department of Mechanical and Aerospace Engineering,
Rutgers, State University of New Jersey,
98 Brett Road,
Piscataway, NJ 08854

This paper presents a mathematical model to simulate the silica hollow optical fiber-drawing process. Two neck-down profiles, which represent the inner and outer surfaces of the hollow fiber, are generated by using an iterative numerical scheme. The zonal method is applied to calculate the radiative transport within the glass. The effects of variable properties for air are investigated and results indicate that these can be neglected for simulating the draw process under typical draw conditions. Inclusion of buoyancy in the flow is also studied and it is found that the flow can be significantly affected due to buoyancy. The validation of the model is carried out by comparing the results with those obtained by using the optical thick method as well as those for a solid-core fiber. The effects of drawing parameters such as the temperature of the furnace, feeding speed, and drawing speed on the temperature and velocity distributions and on the draw tension are studied. It is found that the geometry and qualities of the final hollow optical fiber are highly dependent on the drawing parameters, especially the drawing temperature and the feeding speed. [DOI: 10.1115/1.3090809]

1 Introduction

In the past few years, an important new class of optical fiber, hollow or microstructure fiber, has emerged. Hollow optical fibers have many advantages over the conventional solid-core optical fibers. These include high laser power thresholds, low insertion loss, no end reflection, ruggedness, and small beam divergence. Due to the presence of air core, microstructure fibers can achieve a low attenuation through structural design rather than high-transparency material selection and can be used to provide infrared laser beam and the high-power delivery. Microstructure optical fibers are widely used for medical applications, sensor technology, diagnostics, and CO_2 and Er:YAG (yttrium aluminum garnet) laser delivery, besides traditional telecommunications [1–3].

Hollow optical fibers are fabricated by drawing a macroscopic hollow preform (typically a few centimeters in outer diameter) down into a fiber (typically 125 μm in outer diameter) in a conventional fiber-drawing tower. The preform is fed into the drawing furnace by a feeding mechanism, heated up to the softening temperature, which is about 1900 K for silica, mostly through radiation heat transfer from the furnace surface, and drawn down at a chosen draw speed to obtain a fiber by drawing the softened material. Following the drawing furnace, the fiber is monitored to adjust its diameter and then cooled in an accelerated cooling section and coated by a polymer in a coating applicator. The process of hollow fiber drawing in a furnace is investigated. The drawing of hollow fibers in the furnace is a very complicated process, which involves a combination of conduction, natural and forced convections, and radiation transport. The perform narrows down sharply in the furnace and yields the "neck-down region," which consists of two neck-down profiles in hollow fiber drawing. The geometry of the final hollow fiber is determined by the two neck-down profiles, which strongly depend on the fiber-drawing conditions, namely, the speed of the preform, the drawing speed, the temperature distribution at the furnace wall, draw tension, material, and preform geometry. The geometry of the final fiber plays an important role in the optical characteristics and performance of the fiber. The wall thickness of the fiber is designed to get low signal loss over a target wavelength region. The presence of a large air core is needed in the hollow fiber for high-power laser delivery. It is desirable to avoid the air core from closing completely during the process, which may occur under certain drawing conditions.

The study of the optical fiber-drawing process has been of considerable interest since the late 1960s. There are a number of papers concerning numerical and theoretical models of solid-core optical fiber drawing. For example, Paek and Runk [4] presented a physical model for the neck-down profile and temperature distribution using a one-dimensional analysis. Myers [5] developed a one-dimensional model for unsteady glass flow. Lee and coworkers [6–18] developed more comprehensive models to investigate the complete thermal transport and the resulting neck-down profile in furnace drawing. Recently Chen and Jaluria [19] developed a model to study the effect of core-cladding structure in the drawing process. Few investigations on hollow fiber drawing have been carried out. Fitt et al. [20,21] are among the few researchers who investigated and modeled this process. They proposed a theoretical framework to simulate the fabrication of small-scale hollow glass capillaries. Sarboh et al. [22] developed a mathematical model for the drawing process of glass capillary tubes by studying three basic zones—the heating zone, the drawing zone, and the cooling zone—separately. A numerical study on collapse prediction during hollow optical fiber drawing was carried out by Chakravarthy and Chiu [23].

In this paper, a numerical model with the zonal method for radiation analysis is developed to investigate the hollow fiber-drawing process. The effects of buoyancy and variable properties for air on the simulation of silica hollow fiber-drawing process can be neglected as indicated by the results from this model. Comparisons between the zonal method and the optically thick method are carried out. The results from these two methods are similar. The temperature along the outer surface obtained from the optically thick method is higher than that from the zonal method because radiation can be transmitted directly through the medium in the zonal method but not in the optically thick method. The

Contributed by the Heat Transfer Division of ASME for publication in the JOURNAL OF HEAT TRANSFER. Manuscript received June 3, 2008; final manuscript received October 28, 2008; published online May 12, 2009. Review conducted by Ben Q. Li. Paper presented at the ASME 2008 Summer Heat Transfer Conference (HT2008), Jacksonville, FL, August 10–14, 2008.

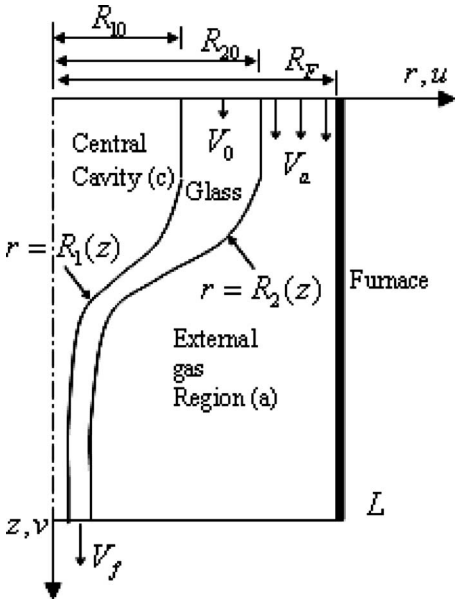

Fig. 1 Schematic of the hollow fiber-drawing process

results are also in agreement with those in literature on solid-core fiber drawing. The effects of drawing parameters on the transport processes and on draw tension are determined.

2 Mathematical Modeling

The geometry and coordinate system for the neck-down region in the furnace are shown in Fig. 1. The flow in the furnace is separated into the three regions of the central cavity, the glass layer and the external gas region by two neck-down profiles $r=R_1$ and $r=R_2$. The typical outer diameter of the preform $2R_{20}$ is about 5.0 cm and the typical outer diameter of the final fiber is about 125 μm. Thus, the preform diameter is reduced by about two orders of magnitude during the drawing process. A conjugate problem, involving the gas flow in the central cavity, the flow of glass, and the forced convection flow of aiding purge external gas, is considered. Conduction, convection, and radiation heat transfer mechanisms are involved in the model.

Laminar flow is taken in the glass due to its high viscosity. Also, the typically low velocities of the gas flow employed in practice can be assumed to result in laminar flow. The flows of glass and internal and external gases in cylindrical furnace are all taken as incompressible and axisymmetric. Then, the full governing equations for gas and glass for variable properties are written as follows [9,16].

For continuity equation,

$$\frac{\partial v}{\partial z}+\frac{1}{r}\frac{\partial (ru)}{\partial r}=0 \tag{1}$$

For z-momentum equation,

$$\rho\left(\frac{\partial v}{\partial t}+u\frac{\partial v}{\partial r}+v\frac{\partial v}{\partial z}\right)=-\frac{\partial p}{\partial z}+\left(\frac{1}{r}\frac{\partial}{\partial r}\left(\mu\left(\frac{\partial v}{\partial r}+\frac{\partial u}{\partial z}\right)\right)\right)+2\frac{\partial}{\partial z}\left(\mu\frac{\partial v}{\partial z}\right)-g\beta(T-T_{\mathrm{ref}}) \tag{2}$$

For r-momentum equation,

$$\rho\left(\frac{\partial u}{\partial t}+u\frac{\partial u}{\partial r}+v\frac{\partial u}{\partial z}\right)=-\frac{\partial p}{\partial r}+\left(\frac{2}{r}\frac{\partial}{\partial r}\left(\mu r\frac{\partial u}{\partial r}\right)\right)+\frac{\partial}{\partial z}\left(\mu\left(\frac{\partial v}{\partial r}+\frac{\partial u}{\partial z}\right)\right) \tag{3}$$

For energy equation,

$$\rho C_p\left(\frac{\partial T}{\partial t}+u\frac{\partial T}{\partial r}+v\frac{\partial T}{\partial z}\right)=\frac{1}{r}\frac{\partial}{\partial r}\left(rK\frac{\partial T}{\partial r}\right)+\frac{\partial}{\partial z}\left(K\frac{\partial T}{\partial z}\right)+\Phi+S_r \tag{4}$$

where Φ is the viscous dissipation term and S_r is the radiation source term. Φ is only kept for the glass flow due to the high viscosity of glass. Here,

$$\Phi=\mu\left(2\left[\left(\frac{\partial u}{\partial r}\right)^2+\left(\frac{u}{r}\right)^2+\left(\frac{\partial v}{\partial z}\right)^2\right]+\left(\frac{\partial v}{\partial r}+\frac{\partial u}{\partial z}\right)^2\right)$$

The Boussinesq approximations are used for the buoyancy effects [24]. Since the flows in three regions are all taken as axisymmetric, a vorticity-streamfunction approach is advantageous to use for solving this problem.

A coordinate transformation is employed to convert the three regions into simpler cylindrical or annular regions. The transformed coordinate systems for the three regions are given as follows.

In the central cavity,

$$\eta=\frac{r}{R_1(z)},\quad \beta=\frac{z}{L} \tag{5}$$

In the glass fiber,

$$\eta=\frac{r-R_1(z)}{R_2(z)-R_1(z)},\quad \beta=\frac{z}{L} \tag{6}$$

In the external gas region,

$$\eta=\frac{R_F-r}{R_F-R_2(z)},\quad \beta=\frac{z}{L} \tag{7}$$

At the top of the preform, uniform velocity and temperature are assumed. At the fiber exit, axial diffusion is neglected. At the furnace wall, the temperature distribution is taken as specified. Along the axis, symmetry is employed. Along the interfaces ($r=R_1$ and $r=R_2$), the streamfunction values are set equal to constant values and a force balance and continuity of velocity, temperature, and heat flux are applied. A correction scheme for the neck-down profiles in hollow fiber drawing is employed. The two neck-down profiles of the hollow fiber are determined based on the balance of the surface forces and mass conservation. Since the variation of pressure in the radial direction is quite small, which is proved by the analysis of Fitt et al. [20], radially lumped pressure is employed in the correction scheme. A one-dimensional lumped axial velocity assumption is reasonable for the correction scheme, as noted by earlier studies on the velocity distribution [4]. For further details, see Ref. [13].

Draw tension plays an important role in the characteristics and geometry of the final hollow fiber due to generation of microcracks and weak spots, and can be controlled during drawing process. Draw tension applied at the end of fiber is balanced with several forces, which are the viscous, surface tension, gravity, inertia, and shear forces. Details on these forces and how they are formulated are given in references given earlier for solid-core fibers. These are extended to hollow fibers by considering the two free surfaces and the force balance is used to determine the surface profiles. Gravitational and viscous forces dominate in most cases, but surface tension effects become important as the hole becomes smaller during the draw process. The last one is exerted by the internal and external gases. Since the gas viscosity is small, compared with the viscosity of glass, the shear force due to internal and external gases can be ignored [25]. As given by Manfre [26], the draw tension F_T for hollow fiber drawing can be expressed as

$$F_T = F_\mu + F_\zeta + F_I - F_g = 3\pi\mu(R_2^2 - R_1^2)\frac{\partial v}{\partial z} + 2\pi(\zeta R_2^2 H_2 + \zeta R_1^2 H_1)$$
$$+ \pi\rho\int_z^L (R_2^2 - R_1^2) v\frac{\partial v}{\partial z}dz - \pi\rho g\int_z^L (R_2^2 - R_1^2)dz \quad (8)$$

where F_μ is the force due to glass viscous stress, F_ζ is the force due to surface tension at the two neck-down profiles, F_I is the force due to inertia, and F_g is the force due to gravity.

A nonuniform grid scheme similar to the one developed by Lee [6] is applied for the present study. A 369×41 grid is used in the central cavity, a 369×21 grid is used in the fiber, and a 369×61 grid is used in the external gas. The governing transport equations are solved using a false transient scheme. The equations are discretized using second-order central differencing. The streamfunction, vorticity, and energy equations are solved using an alternating direction implicit (ADI) approach by alternating traverses in the z and r directions, respectively. For any given neck-down profiles, the above false transient iterative procedure is carried out for about 2000 steps to save computational time, which has been found adequate for the radius correction [13]. Then the neck-down profiles are modified by the numerical corrective procedure. For further details on the numerical scheme, see Ref. [13].

3 Radiation Model

The zonal method is applied to model the radiative transport within the glass [27,28]. The preform is discretized into axisymmetric volume ring elements, as well as surface elements, and the transport rates between these are calculated. The assumptions made in the zonal method are the following.

(1) The furnace is considered to be a gray and diffuse surface, with an emissivity of 0.75 [29]. The inner and outer surfaces of hollow fiber are modeled as diffuse spectral surfaces.

(2) Glass is assumed to be a semitransparent and nonscattering participating medium with banded absorption coefficients. Myers' two-band model [5] is applied, which is expressed as

$$a = 4.0\ \text{cm}^{-1} \quad \text{for} \quad 3.0\ \mu\text{m} \le \lambda < 4.8\ \mu\text{m}$$
$$a = 150.0\ \text{cm}^{-1} \quad \text{for} \quad 4.8\ \mu\text{m} \le \lambda < 8.0\ \mu\text{m} \quad (9)$$

The refractive index is assumed constant at 1.42. The hemispherical total transmissivities and reflectivities are [30]

$$\rho^{1,c} = \rho^{2,o} = 0.08, \quad \tau^{1,c} = \tau^{2,o} = 0.92, \quad \rho^{1,g} = \rho^{2,g} = 0.54,$$
$$\text{and} \quad \tau^{1,g} = \tau^{2,g} = 0.46$$

(3) The top and bottom openings of purge gas and central cavity are approximated as black surfaces at ambient temperature. The top and bottom ends of hollow fiber are assumed to be black surfaces.

The discretization scheme used for zonal method is similar to that used by Yin and Jaluria [15]. The radiative source term can be obtained by considering three enclosures in furnace shown in Fig. 2. One is the outer purge gas enclosure composed of the furnace surface, the outer neck-down profile of the hollow fiber, and the top and bottom openings of the purge gas. The other is the glass layer enclosure composed of the inner and outer neck-down profiles and the top and bottom ends of the hollow fiber. The last one is the central cavity enclosure, which consists of the inner neck-down profile and the top and bottom openings of the central cavity. Superscripts o, g, and c denote these three enclosures, respectively, in the radiative energy equations. Superscript 1 denotes the interface between the hollow fiber and the central cavity and the interface between the hollow fiber and the purge gas is denoted with superscript 2. The subscript l denotes the lth absorbing band. The radiative energy equations, in terms of radiosity and irradiation for each absorption band, are given in earlier papers [31,32].

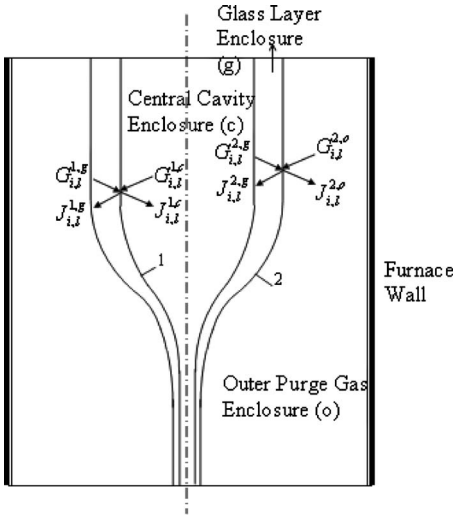

Fig. 2 Schematic for the zonal method

The irradiation and radiosity equations are solved by using Gauss–Seidel iteration with a convergence criterion of 10^{-5}. In order to save computational time, a 30×5 coarse grid developed by Yin and co-workers [14,15] is used for radiation. But this coarse grid size is verified to be fine enough to produce grid-independent results. Also, validation studies, as outlined later, are used to ensure that the grid employed is satisfactory. The radiative source terms obtained from the coarse grid are interpolated into the finer grid by using a bilinear interpolation algorithm. A parallel computer code, with message-passing interface (MPI), is developed for the computation of the direct exchange areas. On a 128-processor dedicated parallel machine, the CPU time is typically of the order of a few hours, depending on the starting values. For further details, see Refs. [31,32].

4 Results and Discussions

4.1 Thermal Transport in the Furnace. The drawing conditions for a typical drawing process are shown in Table 1. The glass properties taken from Fleming [25] are functions of the temperature. The properties of the gas are assumed to be constant at a reference temperature of 1000 K. The furnace temperature profile is shown in Fig. 3. This profile is based on actual measurements on a draw tower at Rutgers University and has been used in earlier studies of solid-core fiber drawing. Pressurization of the gas in the core and the effect of buoyancy are initially neglected. The profile

Table 1 Drawing parameters for a typical case

Furnace diameter	Furnace length	Preform's inner diameter	Preform's outer diameter	Feeding speed	Drawing speed	Inlet velocity of the purge gas
7 cm	30 cm	2.5 cm	5 cm	3.75 mm/min	10 m/s	0.1 m/s

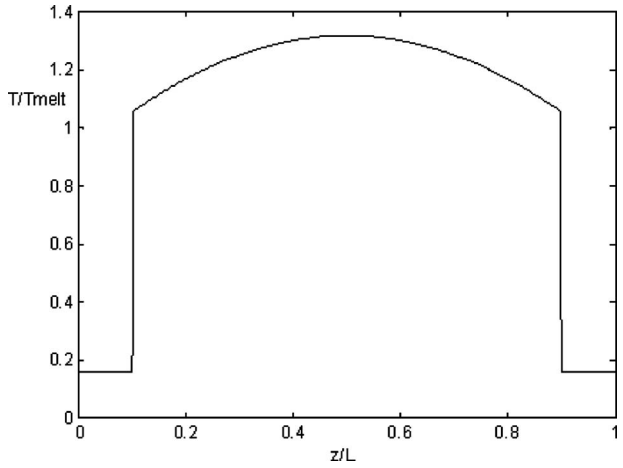

Fig. 3 Furnace temperature profile

correction scheme is applied to get the final converged neck-down profiles. The results in terms of streamlines and isotherms for a typical case are shown in Fig. 4. The thicker black lines in Fig. 4 present the two neck-down profiles. The values of the isotherms are the nondimensional temperature, with the softening temperature of silica glass 1900 K as the characteristic temperature. It is clear that the flow and temperature distributions in the hollow fiber drawing are similar to those in the solid-core fiber drawing. In the central cavity, air flows down and leaves the bottom boundary due to the fiber viscous drag, and the temperature distribution is determined by thermal diffusion.

4.2 The Effects of Buoyancy and Variable Properties. The previous results on heat transport in hollow optical fiber drawing have ignored the effects of temperature dependent gas properties and buoyancy. However, silica optical fiber is drawn over a large temperature range, where the properties of air change substantially. In order to investigate the effect of variable properties and buoyancy, cases with constant properties, variable properties, and buoyancy effects included are compared. The variable properties for air can be computed using the state equation of an ideal gas and power law correlations [32], respectively, which are expressed as follows:

$$\frac{\rho}{\rho_{\text{ref}}} = \frac{T_{\text{ref}}}{T}$$

$$\frac{C}{C_{\text{ref}}} = \left(\frac{T}{T_{\text{ref}}}\right)^{0.104}, \quad \frac{\mu}{\mu_{\text{ref}}} = \left(\frac{T}{T_{\text{ref}}}\right)^{0.65}, \quad \frac{K}{K_{\text{ref}}} = \left(\frac{T}{T_{\text{ref}}}\right)^{0.79} \tag{10}$$

The Boussinesq approximations are used for the buoyancy effects. Figure 5 shows the contours of the streamfunction and temperature for the case with the buoyancy effects. Streamlines in the central cavity are quite different from that shown in Fig. 4. At the top boundary, gas is driven down by the moving fiber due to the no-slip condition. Then it flows up near the center line because of the presence of the lower circulation, which arises due to the buoyancy effects. However, the thermal field in the central cavity is similar to that without buoyancy effect included. Conduction is still the dominating heat transfer method, compared with free convection, in the central cavity. In the purge gas region, there arises a circulation near the furnace wall due to buoyancy effects, which

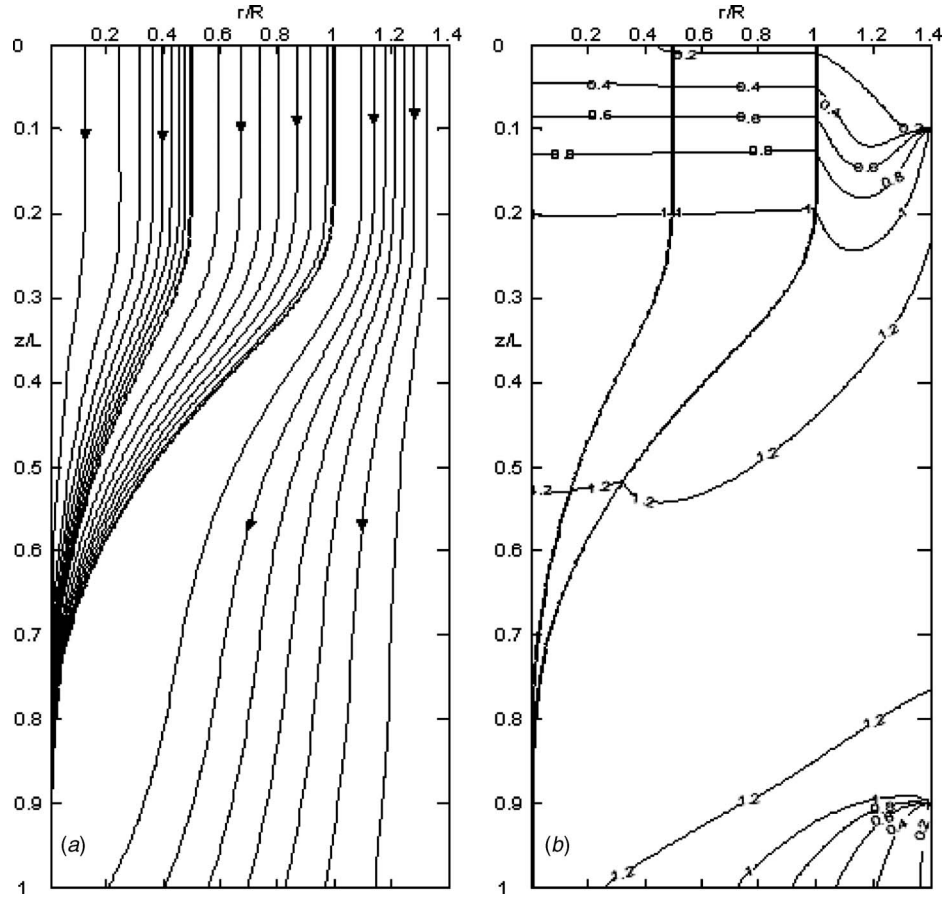

Fig. 4 Streamlines and isotherms for a typical case without buoyancy effects

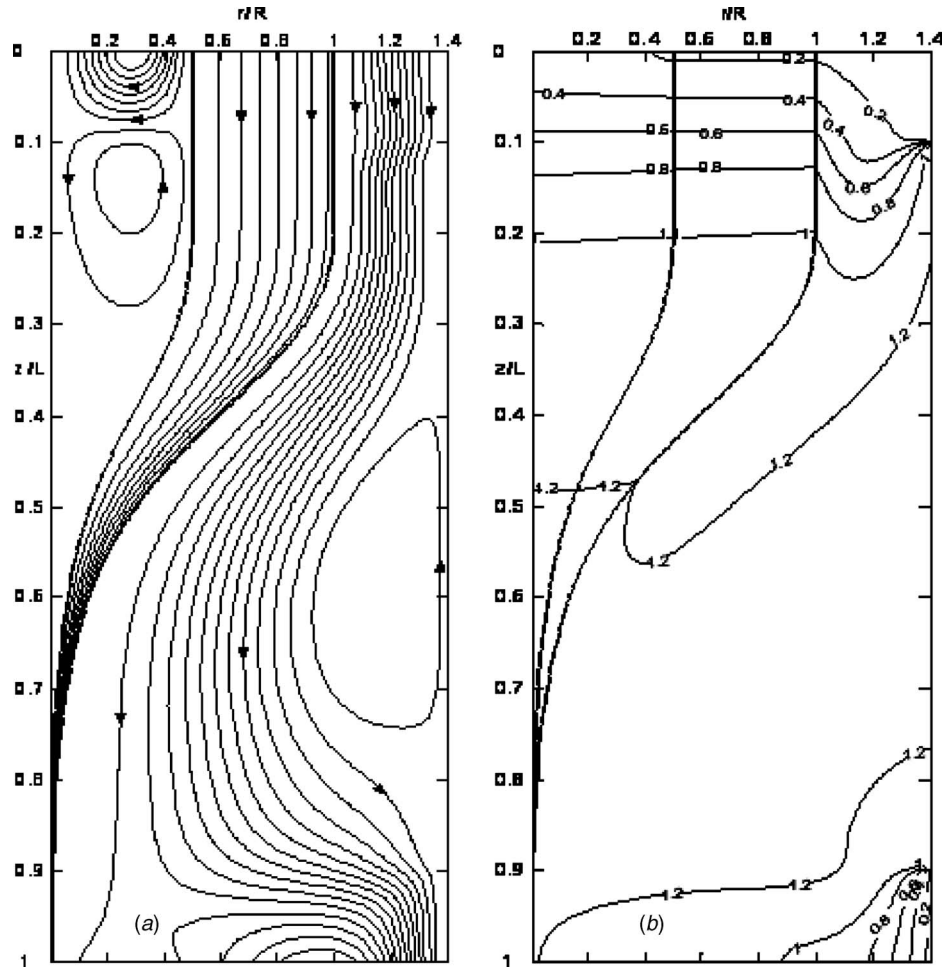

Fig. 5 Streamlines and isotherms for a typical case with buoyancy effects included

cause minor differences in the temperature contours. Property changes in glass have also been considered here, as done in earlier studies, using the available property data, as mentioned before.

The geometry and the quality of the hollow optical fiber depend on the neck-down profiles and the temperature distribution along the fiber. Hence, in order to investigate the effect of variable properties for gas and buoyancy, it is important to compare the two neck-down profiles and the temperature distributions along the fiber. Figures 6 and 7 show the temperature distributions along the outside preform and neck-down profiles for these three cases. The results are very close. It is seen that the effects of variable properties for gas and buoyancy can be neglected when the hollow optical fiber-drawing process is simulated to predict the geometry and quality of the hollow optical fiber.

4.3 Validation. Comparison between the zonal method and the optically thick method is carried out. Unless otherwise mentioned, the drawing parameters are the same as the typical case. The furnace temperature profile is assumed to be parabolic with a maximum value of 2500 K in the middle and a minimum of 2000 K at both ends. The temperature distribution and heat flux along the outer surface obtained from these two methods are shown in Figs. 8 and 9. The optically thick method assumes that all the radiation is absorbed at the surface and then reradiated as a diffusion process due to absorption over a very short optical distance [27]. So there is no radiation that is transmitted directly through the medium. But the zonal method allows it. This explains why the temperature at the outer surface obtained from the optically thick method is higher than that from the zonal method. The heat flux along the outer surface from the zonal method is higher than that from the optically thick method. This is due to the lower temperature distribution along the outer surface from the zonal method. The neck-down profiles obtained from these two methods, shown in Fig. 10, are similar in form. But there are significant differences in the actual approach to the final diameter, with the

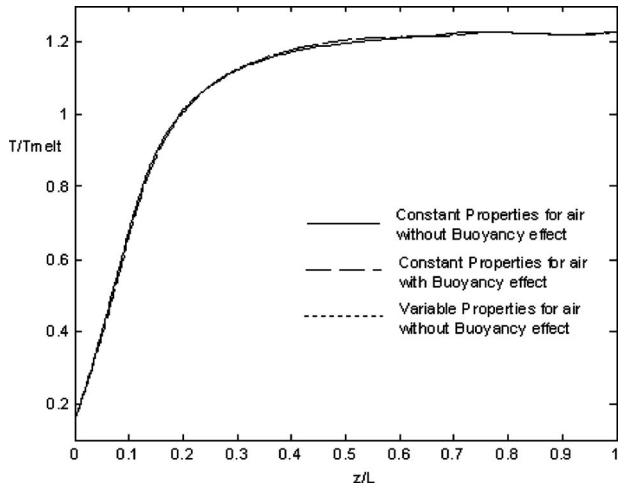

Fig. 6 Temperature distributions along the axis for cases with constant properties, variable properties, and with buoyancy effects included

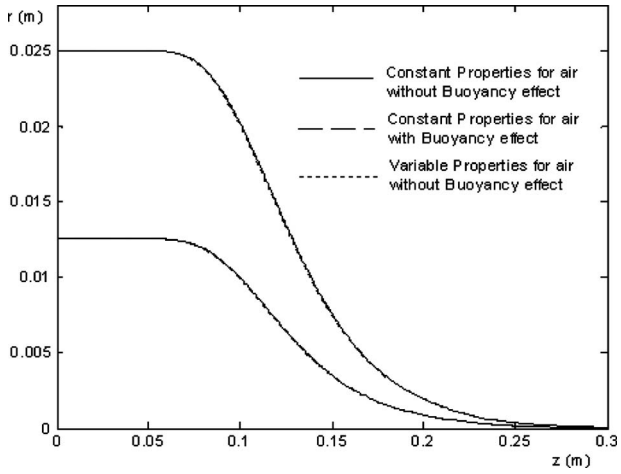

Fig. 7 Neck-down profiles for cases with constant properties, variable properties, and with buoyancy effects included

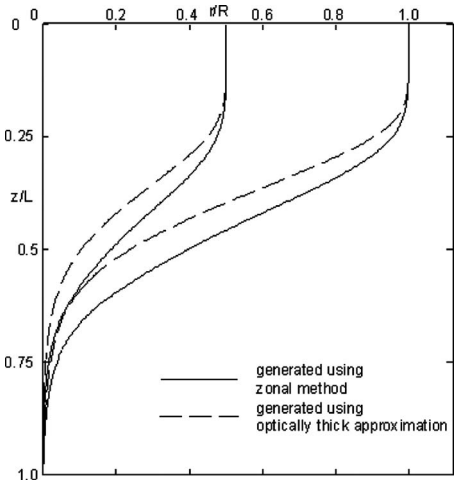

Fig. 10 Neck-down profiles for the hollow fiber drawing generated by using the zonal method and the optically thick method

zonal method showing a much more gradual variation in the profile due to absorption within the glass. This also results in differences in the velocity and temperature distributions. The neck-down region of the profiles obtained from the optically thick method begins earlier than that from the zonal method, since the temperature at the outer surface computed from the optically thick method is slightly higher than that from the zonal method, as seen in Fig. 8. The zonal method is more accurate than the optically thick method, particularly in hollow fiber drawing because of the air core. The results were also compared with those for solid-core optical fiber drawing. It was found that as the diameter of the central air core was reduced, the results approached those for the solid-core case, as expected.

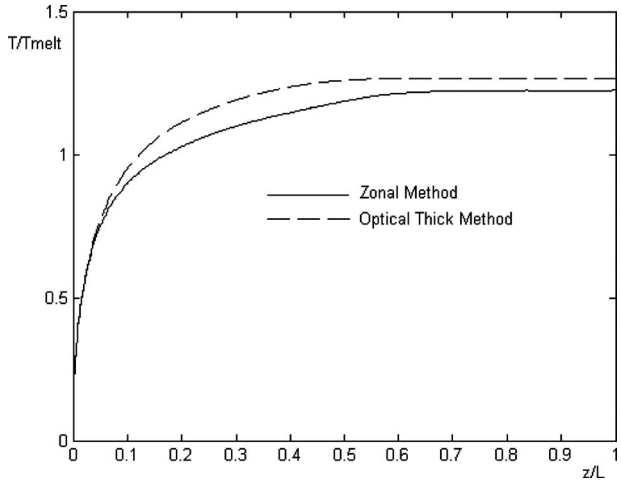

Fig. 8 Temperature distributions at the outer surface computed by using the zonal method and the optically thick method

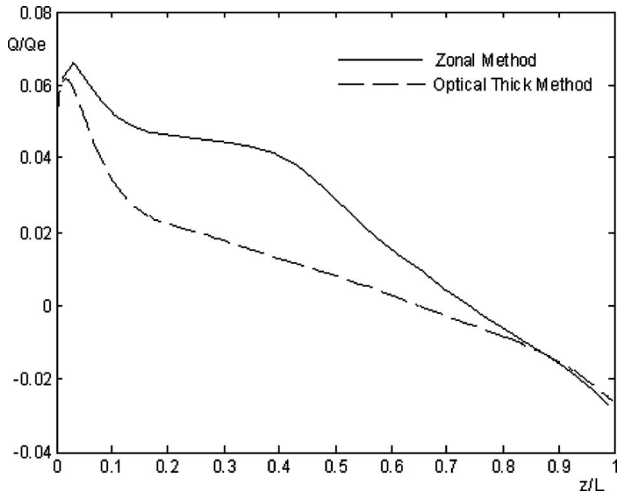

Fig. 9 Heat flux along the outer surface computed by using the zonal method and the optically thick method

4.4 Drawing Parameters. Several drawing parameters are varied to study their effects on the geometry of the final hollow fiber. The temperature distribution at the furnace wall is assumed to be a parabolic profile, with the maximum in the middle and minimum at the two ends. The difference between maximum and minimum temperatures is fixed at 500 K. The maximum temperature of the parabolic distribution is referred to as the drawing temperature. The default drawing temperature is 2500 K. The other parameters are the same as the typical case.

The hollow optical fiber-drawing process is not geometry preserving. Some collapse may occur from the initial preform radius ratio, which means the ratio of the radius of the inner profile to that of the outer profile R_1/R_2 is variable along the axis. Here, a collapse ratio C is defined to describe the collapse process as

$$C(z) = 1 - \frac{R_1(z)/R_2(z)}{R_{10}/R_{20}} \tag{11}$$

Thus, $C=0$ when the radius ratio of the final fiber equals the initial radius ratio, and $C=1$ when the central cavity is closed.

Figure 11 shows the variation of the collapse ratio of the final hollow fiber with the drawing temperature for different drawing speeds. It is seen that the collapse ratio increases with an increase in the drawing temperature and with a decrease in the drawing speed. The collapse ratio increases five times at a drawing speed of 10 m/s when the drawing temperature increases from 2500 K to 2700 K, but decreases only about 2% at a drawing temperature of 2500 K when the draw speed goes up from 10 m/s to 20 m/s. Therefore, the drawing temperature affects the collapse ratio very significantly while the influence of the drawing speed is quite small.

These changes in the collapse ratio can be explained by considering the time spent by the preform/fiber in the drawing furnace. The total time of preform/fiber in the furnace, which depends on the preform feeding speed and the drawing speed, is the sum of the time to heat the preform up and the time for the preform/fiber

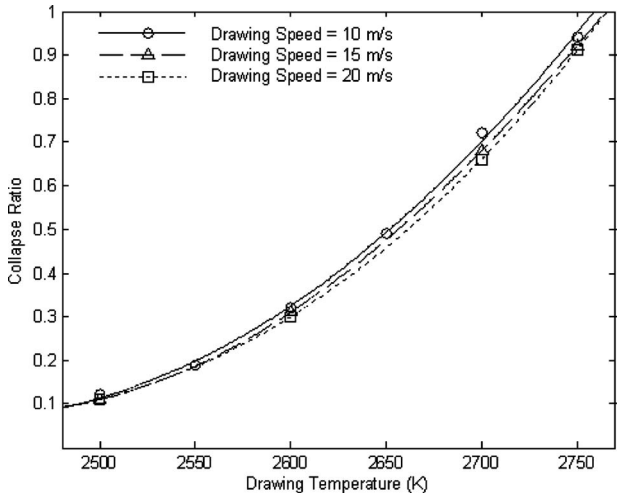

Fig. 11 Variation of the collapse ratio with the drawing temperature for different drawing speeds

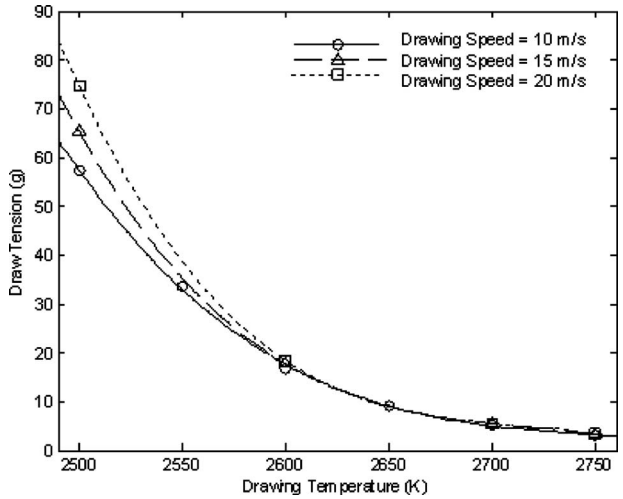

Fig. 12 Variation of the draw tension with the drawing temperature for different drawing speeds

to deform. At the same preform feeding and drawing speeds, the total time of preform/fiber in the furnace is almost constant. The time to heat the preform is shorter at higher furnace temperatures, which implies that the time for collapse increases. Therefore, the collapse ratio increases at a higher furnace temperature. When the drawing speed or the preform feeding speed decreases, the total time of preform/fiber in the furnace will increase. The collapse ratio increases since the time to heat the preform is nearly the same for different drawing speeds or preform feeding speeds at the same drawing temperature. Since the drawing speed is much greater than the preform feeding speed, the collapse time is more sensitive to the preform feeding speed than the drawing speed. So the collapse ratio is more sensitive to the preform feeding speed than the drawing speed. Though exact data are not available for a direct comparison of the collapse ratio results, these trends have been observed in other investigations and are physically realistic.

These results suggest that increasing the drawing speed or the preform feeding speed or decreasing the furnace temperature can avoid the central cavity from collapsing. Since the geometry of the final hollow fiber depends on the collapse ratio, the drawing temperature and the preform feeding speed, which are the dominating factors in the collapse of central cavity, can be used to control the geometry of the final hollow fiber.

4.5 Draw Tension. Draw tension is crucial to fiber quality and process feasibility. Higher draw tension can lead to viscous rupture of the fiber. So the effects of the drawing parameters, i.e., the drawing temperature, the preform feeding speed, the drawing speed, and initial radius ratio, on the draw tension are investigated. Figure 12 shows the variation of the draw tension with the drawing temperature for different drawing speeds. The variation of the draw tension with the preform feeding speed is shown in Fig. 13. It is clear that the draw tension increases with a decrease in the drawing temperature and an increase in the drawing speed and the preform feeding speed. These phenomena can be explained by the temperature of the fiber in the drawing furnace. Higher drawing furnace temperature, lower drawing speed, or lower preform feeding speed can cause higher temperature of the fiber. Higher temperature of the fiber decreases the viscous force dramatically because glass viscosity decreases exponentially with an increase in temperature [2].

The effects of the drawing parameters on the draw tension are considered to obtain the sensitivity of the draw tension to these parameters. The draw tension increases about 20 times for 10 m/s drawing speed when the drawing temperature decreases less than 10% from 2750 K to 2500 K. A 50% increase in the drawing speed from 10 m/s to 15 m/s increases the draw tension by only about 15% at the 2500 K drawing temperature. A 50% increase in the preform feeding speed, from 3.0 mm/min to 4.5 mm/min, increases the draw tension by 60% at the 2500 K drawing temperature. So the drawing temperature is the most dominating factor in determining the draw tension. The draw tension is more sensitive to the preform feeding speed than the drawing speed. The sensitivities of the draw tension to the drawing temperature, the drawing speed, and the preform feeding speed are the same as those of the collapse ratio.

The draw tensions with different preform radius ratios are shown in Fig. 14. It is seen that the draw tension increases about two times when the preform radius ratio decreases from 0.6 to 0.3. This phenomenon is attributed to the variation of viscosity and the cross-sectional area of the fiber. It is known that the temperature of the preform/fiber in the drawing furnace increases with an increase in the initial radius ratio. Higher temperature of the fiber will decrease the viscous force, which is dominating to the draw tension, due to the reduced viscosity. In addition, higher preform radius ratio means a smaller cross-sectional areas of the fiber. The smaller cross-sectional area of the fiber leads to lower draw tension. Therefore, the preform radius ratio is another important factor in the draw tension, besides the drawing temperature and the preform feeding speed.

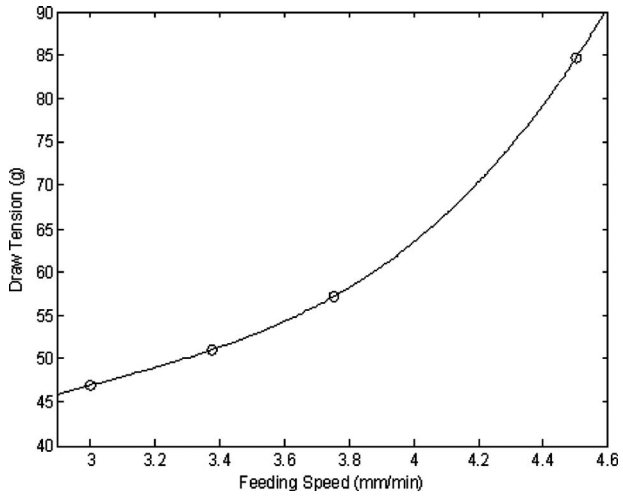

Fig. 13 Variation of the draw tension with the feeding speed

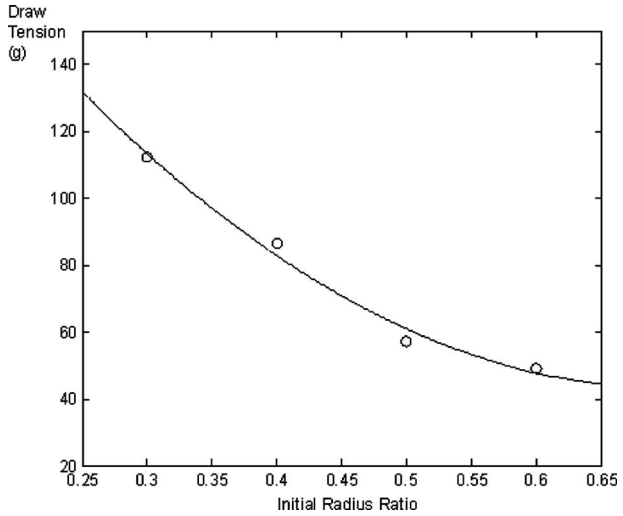

Fig. 14 Variation of the draw tension with the preform radius ratio

5 Conclusions

A numerical model, with the generation of the two neck-down profiles, has been presented for the hollow optical fiber-drawing process in this paper. The effects of variable properties of air and buoyancy are investigated first. The results show that these effects in the model can be neglected. The radiative transport within glass is solved by the zonal method, which is more accurate than the optically thick method in hollow optical fiber drawing. Comparison between the zonal method and the optically thick method is carried out for the validation.

The geometry and quality of the final hollow fiber, namely, the collapse ratio and the draw tension, are studied. The collapse ratio of the final hollow fiber increases when the drawing or feeding speed decreases or the furnace temperature increases. So a faster drawing or feeding speed or lower furnace temperature can avoid the collapse of the central cavity. The draw tension is dependent on the drawing parameters and the preform geometry. The numerical results show that a faster drawing or feeding speed or lower furnace temperature or lower preform radius ratio can increase the draw tension. Through the study of sensitivity of drawing parameters, the drawing temperature and the feeding speed are found to be very important factors to the geometry of the final hollow fiber and the draw tension. The preform radius ratio also plays an important role in the draw tension.

Acknowledgment

The authors acknowledge the financial support provided by the National Science Foundation and the discussions with Professor C.E. Polymeropoulos and Professor J. Harrington, as well as the help of Dr. Chunming Chen in developing the computer model.

Nomenclature

a = absorption coefficient
C = collapse ratio
C_p = specific heat at constant pressure
D = diameter
F_{i-j} = view factor between surface ring elements i and j
$\underline{G}$ = irradiation
$\overline{G_jG_i}$ = direct exchange area between volume ring element i and volume ring element j
$\overline{G_jS_i}$ = direct exchange area between surface ring element i and volume ring element j
g = acceleration due to gravity
J = radiosity
K = thermal conductivity
L = furnace length
n = refractive index
N_s = number of discretized surface zones
N_g = number of discretized volume zones
p = pressure
Q = heat flux
r = radial coordinate
$R_1(z)$ = profile radius of the core
$R_2(z)$ = profile radius of the outer surface of fiber/perform
R_F = radius of the furnace
$\underline{S_r}$ = radiation source term
$\overline{S_jS_i}$ = direct exchange area between surface ring elements i and j
T = temperature
T_{melt} = softening temperature
t = time
u = radial velocity component
v = axial velocity component
z = axial coordinate

Greek Symbols

β = dimensionless axial coordinate
ε = emissivity
ζ = surface tension
η = dimensionless radial coordinate
λ = wavelength
μ = dynamic viscosity
ν = kinematic viscosity
τ = transmissivity
ρ = reflectivity; density
σ = Stefan–Boltzmann constant
Φ = viscous dissipation term

Subscripts

0 = preform inlet conditions
c = centerline
F = furnace
f = fiber
ref = reference conditions
λ = absorbing band

Superscripts

1 = interface between glass layer and central cavity
2 = interface between glass layer and outer purge gas
c = outer purge gas enclosure
g = glass layer enclosure

References

[1] Cregan, R. F., Mangan, B. J., Knight, J. C., Birks, T. A., Russell, P. S. J., Roberts, P. J., and Allan, D. C., 1999, "Single Mode Photonic Band Gap Guidance of Light in Air," Science, **285**, pp. 1537–1539.
[2] Monro, T. M., Belardi, W., Furusawa, K., Baggett, J. C., Broderick, N. G. R., and Richardson, D. J., 2001, "Sensing With Microstructured Optical Fibres," Meas. Sci. Technol., **12**, pp. 854–858.
[3] van Eijkelenborg, M. A., Argyros, A., Barton, G., Bassett, I. M., Fellew, M., Henry, G., Issa, N. A., Large, M. C. J., Manos, S., Padden, W., Poladian, L., and Zagari, J., 2003, "Recent Progress in Microstructured Polymer Optical Fibre Fabrication and Characterisation," Opt. Fiber Technol., **9**, pp. 199–209.
[4] Paek, U. C., and Runk, R. B., 1978, "Physical Behavior of the Neck-Down Region During Furnace Drawing of Silica Fibers," J. Appl. Phys., **49**(8), pp. 4417–4422.
[5] Myers, M. R., 1989, "A Model for Unsteady Analysis of Perform Drawing," AIChE J., **35**, pp. 592–602.
[6] Lee, S. H.-K., 1993, "Numerical Investigation on the Neck-Down Region of a Furnace Drawn Optical Fiber," Ph.D. thesis, Rutgers University, New Brunswick, NJ.
[7] Lee, S. H.-K., and Jaluria, Y., 1995, "The Effects of Geometry and Temperature Variations on the Radiative Transport During Optical Fiber Drawing," J. Mater. Process. Manuf. Sci., **3**, pp. 317–331.

[8] Lee, S. H.-K., and Jaluria, Y., 1995, "Effects of Streamwise Convergence in Radius on the Laminar Forced Convection in Axisymmetric Ducts," Numer. Heat Transfer, Part A, **28**, pp. 19–38.
[9] Lee, S. H.-K., and Jaluria, Y., 1996, "Effects of Variable Properties and Viscous Dissipation During Optical Fiber Drawing," ASME J. Heat Transfer, **118**, pp. 350–358.
[10] Choudhury, S. R., 1995, "Thermal Transport in the Optical Fiber Drawing Process," Ph.D. thesis, Rutgers University, New Brunswick, NJ.
[11] Choudhury, S. R., and Jaluria, Y., 1998, "Thermal Transport Due to Material and Gas Flow in a Furnace for Drawing an Optical Fiber," J. Mater. Res., **13**(2), pp. 494–503.
[12] Choudhury, S. R., and Jaluria, Y., 1998, "Practical Aspects in the Drawing of an Optical Fiber," J. Mater. Res., **13**(2), pp. 483–493.
[13] Choudhury, S. R., Jaluria, Y., and Lee, S. H.-K., 1999, "Generation of the Neck-Down Profile for Furnace Drawing of Optical Fiber," Numer. Heat Transfer, Part A, **35**, pp. 1–24.
[14] Yin, Z. L., 1997, "Numerical Investigation of Thermal Transport in Optical Fiber Drawing Processes," Ph.D. thesis, Rutgers University, New Brunswick, NJ.
[15] Yin, Z. L., and Jaluria, Y., 1997, "Zonal Method to Model Radiative Transport in an Optical Fiber Drawing Furnace," ASME J. Heat Transfer, **119**(3), pp. 597–603.
[16] Yin, Z. L., and Jaluria, Y., 1998, "Thermal Transport and Flow in High-Speed Optical Fiber Drawing," ASME Trans. J. Heat Transfer, **120**, pp. 916–930.
[17] Cheng, X., and Jaluria, Y., 2002, "Effect of Draw Furnace Geometry on High-Speed Optical Fiber Manufacturing," Numer. Heat Transfer, Part A, **41**, pp. 757–781.
[18] Cheng, X., and Jaluria, Y., 2004, "Feasibility of High Speed Furnace Drawing of Optical Fibers," ASME J. Heat Transfer, **126**, pp. 852–857.
[19] Chen, C., and Jaluria, Y., 2004, "Numerical Simulation of Transport in Optical Fiber Drawing With Core-Cladding Structure," ASME Heat Transfer/Fluids Engineering Summer Conference, Charlotte, NC.
[20] Fitt, A. D., Furusawa, K., Monro, T. M., and Please, C. P., 2001, "Modeling the Fabrication of Hollow Fibers: Capillary Drawing," J. Lightwave Technol., **19**(12), pp. 1924–1931.
[21] Fitt, A. D., Furusawa, K., Monro, T. M., Please, C. P., and Richardson, D. J., 2002, "The Mathematical Modelling of Capillary Drawing for Holey Fibre Manufacture," J. Eng. Math., **43**, pp. 201–227.
[22] Sarboh, S. D., Milinkovic, S. A., and Debeljkovic, D. L. J., 1998, "Mathematical Model of the Glass Capillary Tube Drawing Process," Glass Technol., **39**(2), pp. 53–67.
[23] Chakravarthy, S. S., and Chiu, W. K. S., 2005, "Collapse Prediction During Hollow Optical Fiber Fabrication," ASME Summer Heat Transfer Conference, San Francisco, CA.
[24] Gebhart, B., Jaluria, Y., Mahajan, R. L., and Sammakia, B., 1988, *Buoyancy-Induced Flows and Transport*, Hemisphere, Washington, DC.
[25] Fleming, J. D., 1964, "Fused Silica Manual," U.S. Atomic Energy Commission, Report No. B-153.
[26] Manfre, G., 1969, "Forces Acting in the Continuous Drawing of Glass Fibers," Glass Technol., **10**, pp. 99–106.
[27] Siegel, R., and Howell, J., 2001, *Thermal Radiation Heat Transfer*, Taylor and Francis, London.
[28] Scholze, H., 1990, *Glass, Nature, Structure, and Properties*, translated by M. J. Lakin, Springer-Verlag, New York, pp. 271–272.
[29] Gubareff, G. G., and Janssen, J. E., and Torborg, R. H., 1960, *Thermal Radiation Properties Survey*, Honeywell Research Center, Minneapolis, MN.
[30] Siegel, R., and Spuckler, C. M., 1992, "Effect of Index of Refraction on Radiation Characteristics in a Heated Absorbing, Emitting and Scattering Layer," ASME J. Heat Transfer, **114**, pp. 781–784.
[31] Chen, C., and Jaluria, Y., 2007, "Numerical Simulation of Transport in Optical Fiber Drawing With Core-Cladding Structure," ASME J. Heat Transfer, **129**, pp. 559–567.
[32] Chen, C., 2007, "Transport Processes in Drawing of Optical Fibers With Core-Cladding Structure," Ph.D. thesis, Rutgers University, New Brunswick, NJ.

C. S. Yang
Department of Computer Science and Information Engineering,
Far East University,
Hsin-Shih, Tainan County 744, Taiwan

D. Z. Jeng
Aeronautics Research Laboratory,
Chung-Shan Institute of Science and Technology,
Taichung, Taiwan

K. A. Yih

C. Gau[1]
e-mail: gauc@mail.ncku.edu.tw

Win Aung

Institute of Aeronautics and Astronautics and
Center for Micro/Nano Science and Technology,
National Cheng Kung University,
Tainan 70101, Taiwan

Numerical and Analytical Study of Reversed Flow and Heat Transfer in a Heated Vertical Duct

Both analytical and numerical calculations are performed to study the buoyancy effect on the reversed flow structure and heat transfer processes in a finite vertical duct with a height to spacing ratio of 12. One of the walls is heated uniformly and the opposite wall is adiabatic. Uniform air flow is assumed to enter the duct. In the ranges of the buoyancy parameter of interest here for both assisted and opposed convection, a reversed flow, which can be observed to initiate in the downstream close to the exit, propagates upstream as Gr/Re^2 increases. The increase in the Reynolds number has the effect of pushing the reversed flow downstream. Simple analytical models are developed to predict the penetration depth of the reversed flow for both assisted and opposed convection. The models can accurately predict the penetration depth when the transport process inside the channel is dominated by natural convection. Local and average Nusselt numbers at different buoyancy parameters are presented. Comparison with the experimental data published previously was also made and discussed. Good agreement confirms many of the numerical predictions despite simplifications of the numerical process made, such as two-dimensional and laminar flow assumptions. [DOI: 10.1115/1.3109998]

Keywords: mixed convection in vertical channel, flow reversal, penetration depth, heat transfer correlations

1 Introduction

Combined free and forced convection flow in a vertical channel with asymmetric wall temperature or heat flux conditions has been studied extensively in the past. This configuration is relevant to the application of solar energy collector, the modeling of heat exchangers in industry, and the cooling processes in nuclear reactors and modern electronic system. In the vertical channel, buoyancy effects can become significant and distort the velocity and the temperature profiles of the flow. The assisting buoyancy can increase the heat transfer, while the opposing buoyancy decreases. Eventually, flow reversal may occur when the temperature difference or the buoyancy force inside the channel is sufficiently large. Flow reversals may play an important role that affects the stability and the structure of the entire channel flow, the pressure drop, the wall friction, and the heat transfer along the wall [1–3].

A limited number of experiments have been performed to indicate that assisted or opposed buoyancy can have a significant effect on the flow and heat transfer in the tube [4–10] and in the vertical parallel plate duct [11,12]. A clear indication of recirculating flow, which can significantly affect the heat transfer is found in Refs. [8–10]. In a heated vertical parallel plate channel for both assisted and opposed convection, flow reversal and its structure have been clearly visualized [13–15]. For opposed convection, a thin layer of reversed flow occurs along the heated wall, and can significantly enhance the heat transfer. For assisted convection, the reversed flow forms a V-shaped recirculating flow along the adiabatic wall, and has only a slight effect on the heat transfer. At high buoyancy, however, due to the counter flow motion and the mixing between the mainstream and the reversed flow, the reversed flow may render the flow in its vicinity highly unstable and give rise to transition to turbulent flow. It should be noted that all the flow and heat transfer results obtained have included the effect of freestream turbulence intensity of the entrance air. The turbulence intensity of the entrance air is generated by the current wind tunnel system and is not very high. However, it is difficult to differentiate the effect of turbulence intensity from the effects of the reversed flow and buoyancy. To provide flow and heat transfer information without the influence of turbulence, one needs to use numerical calculations.

In the numerical aspect, the boundary layer equations have been used to solve the mixed convection in the upstream region of vertical channels where flow reversal does not occur [16,17]. Since these equations neglect the streamwise diffusion terms and are parabolic in nature, a marching solution procedure can be used. In the downstream region where flow reversal occurs, however, solutions could not be obtained. Ingham et al. [18,19] employed the FLARE approximation in the numerical procedure, which allows the marching to be continued in the region where flow reversal occurs. The solution thus obtained can be iterated upon using a method similar to that employed by Williams [20]. The same numerical procedure was adopted to solve mixed convection of three-dimensional developing flow in a vertical rectangular duct [21] when the Reynolds and the Peclet numbers are relatively large. For a relatively low Reynolds or Peclet number flow, as is considered here, the streamwise diffusion terms have to be included in the governing equations. With the inclusion of the streamwise diffusion terms, Naito and Nagano [22,23] solved the vorticity transport and stream function equations for mixed convection in the entrance region between inclined parallel plates maintained at different temperatures. The local Nusselt number, the skin friction coefficient, and the criteria for the occurrence of flow reversal are reported. For vertical parallel plate channel, the same set of equations were solved by da Silva et al. [24] with a hybrid numerical analytical method, which combines the analytical formalism of the classical integral transform method and the error controlled numerical solution of ordinary differential systems. An analysis for fully developed laminar mixed convection in vertical channel and the conditions for onset of flow reversal are also provided [25]. For the stability of laminar-turbulent transition

[1]Corresponding author.

Contributed by the Heat Transfer Division of ASME for publication in the JOURNAL OF HEAT TRANSFER. Manuscript received June 21, 2008; final manuscript received February 3, 2009; published online May 5, 2009. Review conducted by Gautam Biswas.

analysis, Chen and Chung [26] adopted stability analysis and found that the thermal-buoyant instability is the dominant type for buoyancy assisted flow. However, information on the propagation of the reversed flow structure and its effect on the heat transfer are lacking.

The current work aims at numerically solving the coupled momentum and energy equations that include the streamwise diffusion terms for mixed convection in a finite vertical duct. The duct and the experimental conditions are identical to those described in Refs. [13–15] for the case of parallel plate channel. The purpose of the present work is to eliminate the effect of freestream turbulence on the flow and heat transfer results, especially when flow reversal occurs, for buoyancy assisted and opposed convection. The current work focuses only on the case when the flow is laminar and for the low ranges of both Re and Gr/Re^2. The effects of both the buoyancy parameter Gr/Re^2 and the Reynolds number on the occurrence and propagation of the reversed flow and the heat transfer are presented. Simple models used to predict the penetration depths of the reversed flow for both assisted and opposed convection are developed. Comparison of the penetration depth between the model prediction and numerical results is made. Correlations of the average Nusselt number in terms of the buoyancy parameter are also made. In addition, all the computational results are compared with the experimental data published in Refs. [13–15] for the case of the parallel plate channel.

2 Mathematical Formulation

Since the duct considered corresponds exactly to the one employed in the experiments [13–15] for the case of parallel plate channel, the left wall is heated uniformly, while the right wall is adiabatic. The inlet air has both uniform velocity and temperature profiles. The flow inside the duct can be assumed as laminar and two-dimensional. Since the experimental observation in the previous work [13–15] indicates that the mixed convection flow may not be steady, the unsteady motion of the fluid is included in the current calculation. All the fluid properties are assumed to be constant, except for density variations in the buoyancy term. With the assumption of the Boussinesq approximation, the nondimensional form of the conservation equations for a two-dimensional laminar, mixed convection in a vertical duct may be written as

$$\frac{\partial U}{\partial X}+\frac{\partial V}{\partial Y}=0 \tag{1}$$

$$\frac{\partial U}{\partial \tau}+U\frac{\partial U}{\partial X}+V\frac{\partial V}{\partial Y}=-\frac{\partial P}{\partial X}+\frac{1}{\mathrm{Re}}\left(\frac{\partial^2 U}{\partial X^2}+\frac{\partial^2 U}{\partial Y^2}\right)+\frac{\mathrm{Gr}}{\mathrm{Re}^2}\theta \tag{2}$$

$$\frac{\partial V}{\partial \tau}+U\frac{\partial V}{\partial X}+V\frac{\partial V}{\partial Y}=-\frac{\partial P}{\partial Y}+\frac{1}{\mathrm{Re}}\left(\frac{\partial^2 V}{\partial X^2}+\frac{\partial^2 V}{\partial Y^2}\right) \tag{3}$$

$$\frac{\partial \theta}{\partial \tau}+U\frac{\partial \theta}{\partial X}+V\frac{\partial \theta}{\partial Y}=\frac{1}{\mathrm{Re}\ \mathrm{Pr}}\left(\frac{\partial^2 \theta}{\partial X^2}+\frac{\partial^2 \theta}{\partial Y^2}\right) \tag{4}$$

Since the velocity inside the duct is relatively low, both the viscous dissipation and the pressure work in Eq. (4) are negligible. In the above equations, all the variables have been nondimensionalized using the dimensionless parameters defined as follows

$$X=x/D_h,\quad Y=y/D_h$$

$$U=u/u_o,\quad V=v/u_o$$

$$\mathrm{P}=p/(\rho u_o^2),\quad \theta=(T-T_o)/(qD_h/k)$$

$$\mathrm{Re}=u_oD_h/\nu,\quad \mathrm{Gr}=g\beta qD_h^4/(k\nu^2)$$

$$\mathrm{Pr}=\nu/\alpha,\quad \tau=u_ot/D_h \tag{5}$$

However, different sets of dimensionless parameters were adopted to nondimensionalize the governing equations of the system [16–19]. In their reports, instead of Gr/Re^2, the parameter Gr/Re was obtained in the buoyancy force term of the momentum equation. In this report, however, it is more convenient to choose Gr/Re^2 for the presentation of calculated results. It is noted that Eqs. (1)–(4) are coupled and need to be solved simultaneously at each time step.

The boundary conditions are defined as follows:

$$Y=0.0:\quad U=0,\quad V=0,\quad \frac{\partial \theta}{\partial Y}=-1 \tag{6a}$$

$$Y=0.5:\quad U=0,\quad V=0,\quad \frac{\partial \theta}{\partial Y}=0 \tag{6b}$$

$$X=0.0:\quad U=1,\quad V=0,\quad \theta=0 \tag{6c}$$

at the exit where $X=6.0$ and both the velocity and the temperature distribution are not known.

Using the method of two-point extrapolation, the results calculated in the interior are used to find the ones at the boundary. In addition, by using the conservation of mass, i.e., the mass flow rate at the inlet equals to that at the outlet, the U-velocity at the exit can be corrected right before the next iteration. The correction factor C can be calculated by the following equation

$$C=\int_{\mathrm{in}} U dY \Big/ \int_{\mathrm{out}} U dY \tag{7}$$

when the calculated velocity field converges at each time step, the value of C approaches unity. Therefore, the correction factor can be used as an indication of the convergence of solution at each time step.

3 Numerical Procedure

Fully implicit finite-difference equations are obtained by integrating the conservation equations (1)–(4) over the control volume about a grid point and over a time step. The principle of the implicit scheme is that the new value of the physical quantity around each control volume is calculated from the old value within this control volume. Therefore, a new value of the physical quantity prevails over the entire time step. Numerical solutions for the pressure and the temperature equations are calculated at the main grid, while the velocity is obtained at a staggered grid. To solve the discretized equations, the semi-implicit method for pressure-linked equations (SIMPLE) algorithm is used [27]. The computation is performed in 128×32 uniform grid lines; however, a much larger number of grid points have been used to check and confirm that the current solution obtained does not depend on the number of grid points selected. The criterion of convergence at each time step is based on the mass residual that is less than 1.0×10^{-6}.

4 Results and Discussion

4.1 Streamlines and Isotherms. To check the accuracy of the current numerical scheme, the predictions of velocity and temperature distributions are compared with the results of Aung and Worku [17]. The agreement found is very good. During the transient calculation of the flow, however, the oscillation or unsteady motion of the fluid has not been found. A steady state solution can be obtained when both Re and Gr/Re^2 are not very large. It is surmised that to model the fluid oscillations observed in the previous experiments, it would be necessary to account for the transition process and the turbulent motion of the fluid. This is beyond the scope of the current study. Therefore, we focus on the steady state results.

Figures 1 and 2 show the effect of Re and Gr/Re^2 on the flow structure and isotherm for assisted convection, while Figs. 3 and 4 present the results for opposed convection. For assisted convection with $Re=200$ or 400, the increase in Gr/Re^2 (i.e., when natu-

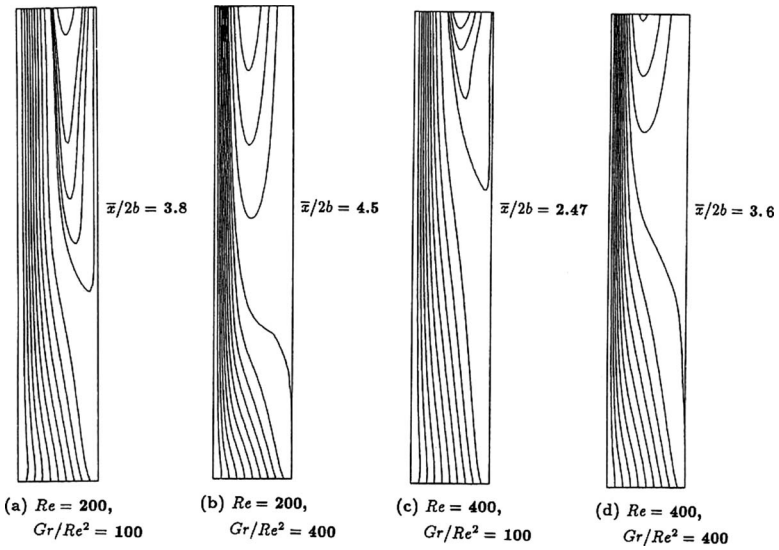

Fig. 1 Streamline plots for assisted convection with (*a*) Re=200, Gr/Re^2 =100, (*b*) Re=200, Gr/Re^2=400, (*c*) Re=400, Gr/Re^2=100, and (*d*) Re=400, Gr/Re^2=400

ral convection effect becomes more significant) can make a deeper penetration of the reversed flow and a wider recirculating region, as shown in Fig. 1. For $Gr/Re^2=100$ or 400, however, the increase in Re (i.e., when forced convection effect becomes more significant) can push the reversed flow downstream, as shown in Fig. 1. For a sufficiently high value of Re, flow reversal will not occur. The above results are similar to the trends found in the experiments [14]. However, the increase in Re makes the recirculating region more narrow at downstream location, as shown in Figs. 1(*b*) and 1(*d*). This result is contrary to the finding in the experiment [14]. This difference can be attributed to the relatively low buoyancy parameter used in the numerical calculation, while in the experiment the buoyancy parameter imposed is relatively high and the flow in the downstream may have become turbulent.

For opposed convection with Re=600 or 200, the increase in Gr/Re^2 causes the occurrence of flow reversal, as shown in Figs. 3(*b*) and 3(*d*). For $Gr/Re^2=-3$, however, the increase in Re also has an effect to cause the reversed flow to occur. This finding is contradictory to the result for assisted convection. This is due to the fact that the reversed flow is driven primarily by the opposed buoyancy (Gr), which, to maintain a constant value for Gr/Re^2, can increase quadratically as Re increases. Therefore, the result of increasing Re is overruled by that of increasing Gr. However, a quantitative comparison between the prediction and the data could not be made. This is due to the fact that both Gr/Re^2 and Re

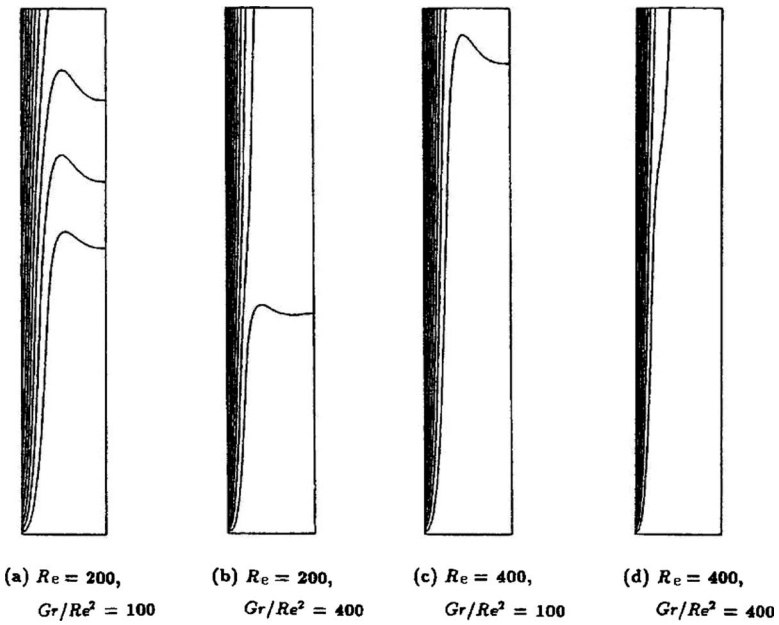

Fig. 2 Isotherms for assisted convection with (*a*) Re=200, Gr/Re^2=100, (*b*) Re=200, Gr/Re^2=400, (*c*) Re=400, Gr/Re^2=100, and (*d*) Re=400, Gr/Re^2 =400

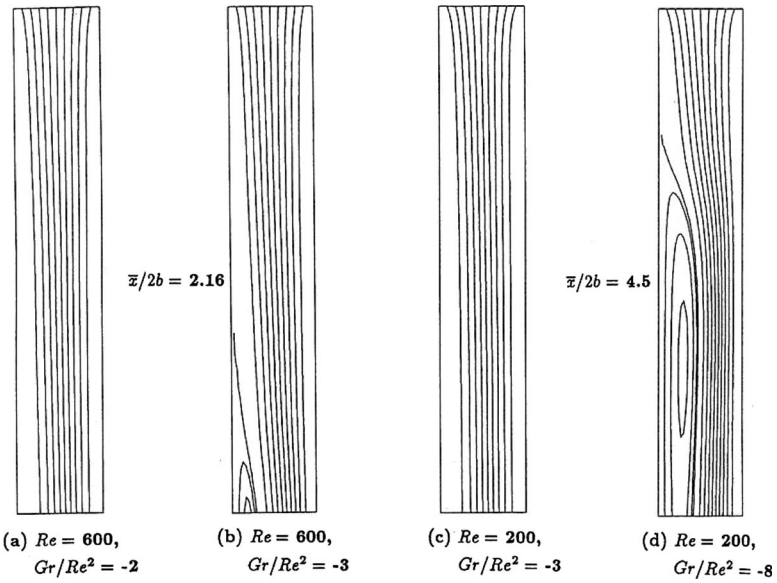

Fig. 3 Streamline plots for opposed convection with (*a*) Re=600, Gr/Re^2 =−2, (*b*) Re=600, Gr/Re^2=−3, (*c*) Re=200, Gr/Re^2=−3, and (*d*) Re=200, Gr/Re^2=−8

imposed in the experiment in Ref. [14] are relatively large, the numerical calculation at large values of Gr/Re^2 and Re could not be performed due to the rapid growth of mass residual, which causes divergence of solution. However, the general trends obtained from the prediction and the data agree very well.

The thermal boundary layer for assisted convection is thinner than for opposed convection, as shown in Figs. 2 and 4. For assisted convection, the increase in either Gr/Re^2 or Re tends to decrease the thermal layer thickness, which leads to an increase in heat transfer. In addition, the reversed flow along the insulated wall has a significant effect on the temperature profile near the edge of the thermal layer. Nevertheless, the occurrence of reversed flow does not have a significant effect on the temperature gradient on the heated wall and hence has little effect on the heat transfer. For opposed convection, however, the increase in Gr/Re^2 or decrease in Re increases the thermal layer thickness, leading to a decrease in the heat transfer. In addition, the reversed flow reduces the temperature gradient at the heated wall in the region downstream of the separation point. Consequently, a reduction in heat transfer is expected in this region.

4.2 Reversed Flow Zone. The reversed flow zone in Gr/Re-Re regime maps, as shown in Figs. 5(*a*) and 5(*b*), for buoyancy assisted and opposed convection are derived from the present numerical results. The onset of flow reversal is determined by the condition $\partial u/\partial y|_{y=0.5}=0$ at the duct exit for assisted convection and $\partial u/\partial y|_{y=0}=0$ for opposed convection. It has been found that in an infinite long channel where fully developed con-

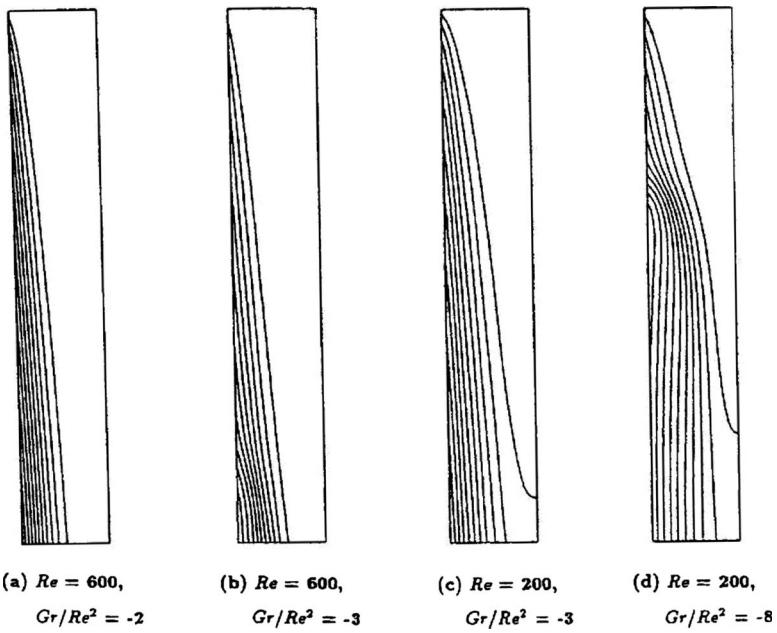

Fig. 4 Isotherms for opposed convection with (*a*) Re=600, Gr/Re^2=−2, (*b*) Re=600, Gr/Re^2=−3, (*c*) Re=200, Gr/Re^2=−3, and (*d*) Re=200, Gr/Re^2=−8

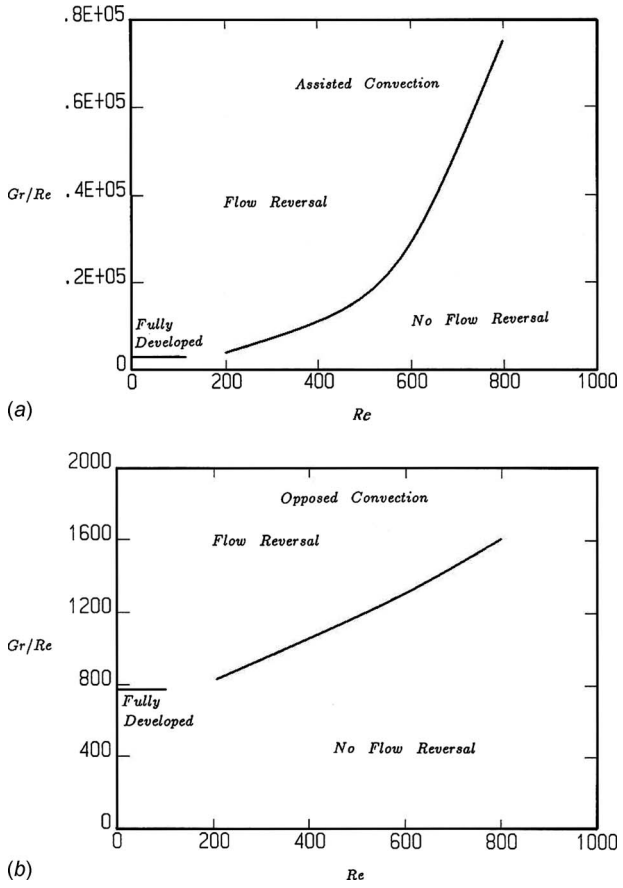

Fig. 5 (*a*) Onset of flow reversal for assisted convection and (*b*) onset of flow reversal for opposed convection

dition is reached, Gr/Re is the only parameter necessary to determine the onset of flow reversal. Therefore, to compare with the case of fully developed flow, the original parameters $\mathrm{Gr}/\mathrm{Re}^2$ and Re, which affect the occurrence of flow reversal, are replaced by Gr/Re and Re, as shown in Figs. 5(*a*) and 5(*b*). For an infinite duct where the flow is fully developed, the critical value of Gr/Re for the onset of flow reversal is 3050 for assisted convection and 786 for opposed convection. In a finite vertical channel, however, the critical value of Gr/Re for the onset of flow reversal increases with increasing Re for both assisted and opposed convection. This can be readily understood by the fact that in a finite channel, where fully developed flow with occurrence of flow reversal is reached in the downstream region, the penetration depth of the reversed flow increases with increasing Gr/Re but decreases with increasing Re for both assisted and opposed convection. To cut away the downstream region of the channel in which flow reversal has occurred, the reversed flow structure can be initiated again in the remaining region by increasing Gr/Re or decreasing Re. When both Gr/Re and Re are small, the critical value for the onset of flow reversal approaches the one for fully developed flow [28,29].

Correlations of the critical values of Gr/Re in terms of Re have been made and the results are written as follows. For assisted convection with $200 \le \mathrm{Re} \le 800$ and $18 \le \mathrm{Gr}/\mathrm{Re}^2 \le 95$

$$\mathrm{Gr}/\mathrm{Re}|_{\mathrm{cr}} = -6400.2 + 85.7\ \mathrm{Re} - 0.245\ \mathrm{Re}^2 + 0.000333\ \mathrm{Re}^3 \tag{8}$$

which has a standard deviation of 2.9%.

For opposed convection with $200 \le \mathrm{Re} \le 800$ and $-4.15 \le \mathrm{Gr}/\mathrm{Re}^2 \le -2$

$$\mathrm{Gr}/\mathrm{Re}|_{\mathrm{cr}} = 640.0 + 0.833\ \mathrm{Re} + 0.000625\ \mathrm{Re}^2 \tag{9}$$

which has a standard deviation of 0.15%.

The present results show that reversed flow can occur but at values of Gr/Re much higher than the range covered in Ref. [17]. The present finding is that the critical value increases with Re and depends on the height to wall spacing ratio. Let us examine this by using Eq. (8). The minimum Re for which the equation is valid is 200; hence, the minimum value of Gr/Re for which flow reversal can occur in the present specific case, which concerns a duct having a height to wall spacing ratio equal to 12, is 3603.8. As pointed out previously, for an infinitely long duct so that fully developed flow prevails in the duct, the critical value of Gr/Re is 3050.

5 Analytical Model for the Penetration Depth

The penetration depth for the reversed flow can be analyzed by means of a simple analytical model. The analysis is an approximation based on superficial physical similarity, which is carried out to extract useful physical insight, but this is not the actual analytical solution of this problem. Since the mechanism for the occurrence of reversed flow for assisted convection is different from that for opposed convection, we will consider the two cases separately.

5.1 Assisted Convection. It should be noted that the lowest point of the V-shaped recirculation flow region is the point of flow separation beyond or downstream of which the transport process is dominated by natural convection. This is the point where all the air flow supplied by the outside blower, situated at the bottom of the duct, is used completely to furnish the air required for the occurrence of pure natural convection flow in the downstream reaches of the channel. In addition, the flow and transport processes in the entire channel are in the developing region. It has been found [13,28] that the local heat transfer in the region downstream of the separation point agrees well with the prediction of natural convection heat transfer along a single vertical plate. This is the condition when the parameter $\mathrm{Gr}/\mathrm{Re}^2$ is greater. One can also obtain a similar conclusion that the natural convection heat transfer approaches the mixed convection, as discussed in Sec. 5. Therefore, the natural convection process in the channel at and beyond the separation point can be viewed as natural convection along a single heated vertical plate, which starts to develop from the entrance of the channel. Accordingly, the following equation can be written and used to predict the penetration depth

$$u_o b = \int_0^{\delta} u_n dy|_{\text{at separation point}} \tag{10}$$

where u_o is the uniform entrance velocity and u_n is the boundary layer velocity distribution of a natural convection flow along a vertical flat plate. By using the integral method and assuming third order polynomials for the velocity and the temperature distributions, the coupled momentum and energy equations for natural convection along a vertical plate can be readily solved [30]. The velocity distribution is obtained as follows

$$u_n = u_r \eta (1 - \eta)^2 \tag{11a}$$

where

$$u_r = (\nu/x)[6000\ \ \mathrm{Gr}_x^2/\mathrm{Pr}(\mathrm{Pr} + 0.8)^2]^{1/5} \tag{11b}$$

$$\eta = y/\delta \tag{11c}$$

$$\delta = x[360(\mathrm{Pr} + 0.8)/\mathrm{Pr}^2\ \ \mathrm{Gr}_x]^{1/5} \tag{11d}$$

By substituting Eq. (11) into Eq. (10), the equation used for predicting the location of the separation point can be readily obtained as follows

$$x/D_h = E(\mathrm{Re}^5/\mathrm{Gr})^{1/4} \tag{12}$$

where

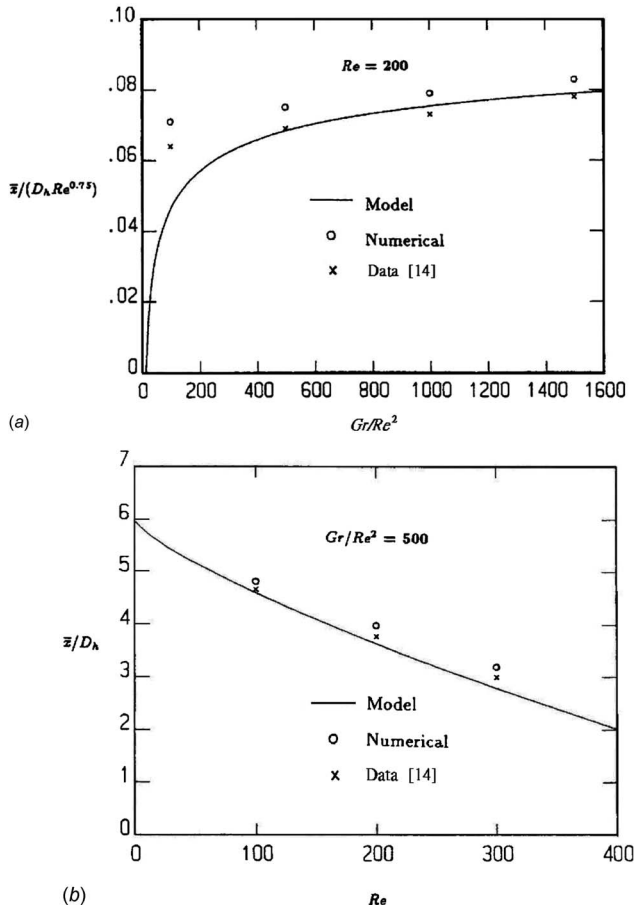

Fig. 6 (*a*) Comparison of the penetration depths calculated using analytical model and the numerical results for assisted convection with Re=200 and (*b*) comparison of the penetration depths calculated using analytical model and the numerical results for assisted convection with $Gr/Re^2=500$

$$E = [36\ \ Pr^3(Pr + 0.8)/10^4]^{1/4}$$

Rearranging Eq. (12), the model prediction for the penetration depth can be written as

$$\bar{x}/(D_h\ Re^{0.75}) = L/(D_h\ \ Re^{0.75}) - E(Gr/Re^2)^{-0.25} \tag{13}$$

This equation is shown and plotted graphically in Figs. 6(*a*), 6(*b*), and 7.

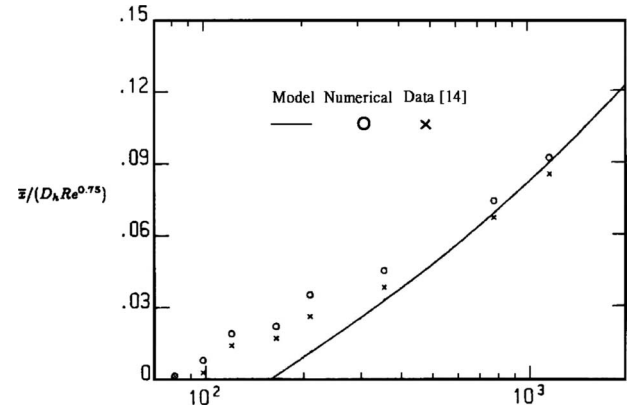

Fig. 7 Comparison of the penetration depths given by the analytical model, the numerical results, and the experimental data for assisted convection

The above analytical model can be used only for the case when Gr/Re^2 is relatively large so that natural convection dominates the transport processes inside the channel. Comparison of the penetration depth of the reversed flow given, respectively, by the model prediction, the numerical results, and the experimental data [14] is made for Re=200 at various Gr/Re^2, as shown in Fig. 6(*a*). Note that, in the experiment, the V-shaped recirculation flow is not steady and the penetration depth oscillates up and down. Therefore, only the average values of the penetration depth are used and presented for comparison. In general, the data are slightly lower than the numerical results. This may be due to the freestream turbulence intensity of the entrance air in the experiments that can enhance the mixing between the heated buoyant flow and the V-shaped recirculation region and reduce the penetration depth. In spite of this, the agreement among these three sets of results is very good, especially when Gr/Re^2 is large. At a lower value of Gr/Re^2, however, the analytical model deviates significantly from the numerical results. This fact suggests that the model fails to predict the penetration depth, as the buoyancy force inside the channel is relatively weak when compared with the inertia force. Comparison is also made for $Gr/Re^2=500$ at various Re, as shown in Fig. 6(*b*). Similar conclusions can be made. As the Reynolds number increases and the forced convection effect becomes significant, the model cannot accurately predict the penetration depth. It is found that for analytical model to give results within 10% of the data, the value of Re should be less than 300 and Gr/Re^2 should be greater than 350.

5.2 Opposed Convection. For opposed convection, the reversed flow is the heated buoyant flow itself, with the velocity directly proportional to the buoyancy force. The location of the separation point defines the penetration depth. To identify the separation point, one needs to find the streamwise velocity profile along the heated wall. Since the duct considered is of finite length, the entire duct flow is, in general, in the developing region. The velocity profile near the heated wall can be considered as a mixed convection boundary layer profile along a single heated vertical plate. One can thus readily find the velocity profile by using the integral method. To account for the effect of both forced and natural convection, one can assume that the velocity profile inside the duct is a summation of the boundary layer velocity profile of a pure forced convection and that of a pure natural convection along a vertical plate as follows

$$u = u_n + (-u_f) \tag{14}$$

where

$$u_f = u_o(3\eta_f/2 - \eta_f^3/2) \tag{15a}$$

$$\eta_f = y/\delta_f(x) \tag{15b}$$

$$\delta_f(x) = 4.64x/Re_x^{0.5} = 4.64(0.36 - \bar{x})/Re_{\bar{x}}^{0.5} \tag{15c}$$

The minus sign in front of u_f in Eq. (14) accounts for the opposed motion of the forced convection to the natural convection flow. Therefore, the location for the separation point can be predicted by the following equation

$$\partial(u_n - u_f)/\partial y|_{y=0} = 0 \tag{16}$$

By substituting Eqs. (11) and (15) into Eq. (16) and rearranging, the equation used to predict the penetration depth can be obtained as follows:

$$\bar{x}^{0.4}(0.36 - \bar{x})^{0.5} = 0.02\ \ Re^{0.3}(Gr/Re^2)^{-0.6} \tag{17}$$

Comparison of the penetration depths of the reversed flow given by the analytical model for opposed flow, the numerical results, and the experimental data is made at various Re and Gr/Re^2 in Fig. 8. The experimental data are slightly lower than the numerical results when Gr/Re^2 is small. This is attributed again to the freestream turbulence intensity effect in the experiments that can

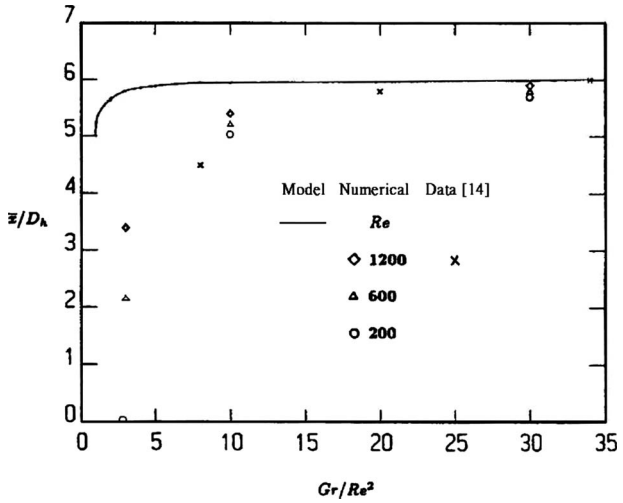

Fig. 8 Comparison of the penetration depths given by the analytical model, the numerical results, and the experimental data for opposed convection

enhance the mixing between the heated buoyant flow and the V-shaped recirculation region, thereby reducing the penetration depth. The analytical model is seen to vastly overpredict the penetration depth when $\mathrm{Gr}/\mathrm{Re}^2$ is small. The discrepancy among these three sets of results becomes small when $\mathrm{Gr}/\mathrm{Re}^2$ is large. This fact suggests that the model can predict the penetration depth, as the buoyancy force inside the channel is relatively large as compared with the inertia force. Comparison is also made for $\mathrm{Gr}/\mathrm{Re}^2=30$ at various Re, which can also be found in Fig. 8. As the Reynolds number increases, which causes a quadratic increase in the Grashof number, the model can accurately predict the penetration depth. However, as long as Re is greater than 200, the Re effect on the accuracy of model prediction is negligible. It is found that in order for the analytical model to be accurate to within 10 % of the numerical results, the applicable value of Re should be greater than 200 and that for $\mathrm{Gr}/\mathrm{Re}^2$ should be greater than 20.

6 Nusselt Number

In the previous governing equations one can find that the dimensionless temperature, θ, is actually a function of $\mathrm{Gr}/\mathrm{Re}^2$ and Re and x/L. From the definition the local Nusselt number is the inverse of θ. Therefore, one can conclude that the Nusselt number is a function of $\mathrm{Gr}/\mathrm{Re}^2$ and Re and x/L. Next, so that the Nusselt number results obtained at different Re can collapse into a single curve, the Nusselt number is divided by $\mathrm{Re}^{0.4}$ and the parameter $\mathrm{Nu}/\mathrm{Re}^{0.4}$ is plotted versus x/L, as shown in Figs. 9(*a*) and 9(*b*). The factor $\mathrm{Re}^{0.4}$ helps in collapsing the data in a self-similar form. The 0.4 power of the Reynolds number is first found from correlation of the experimental data in Ref. [15]. For pure forced convection, the Nusselt number results divided by $\mathrm{Re}^{0.4}$ can also collapse into a single curve, as shown in Fig. 8 in Ref. [15]. Therefore, in addition to x/L the parameter $\mathrm{Nu}/\mathrm{Re}^{0.4}$ is a function of $\mathrm{Gr}/\mathrm{Re}^2$. Comparison was also made only with the experimental data found in Ref. [15] for the case of parallel plate channel where the freestream turbulence intensity has been significantly minimized in the channel. The prediction for the Nusselt number agrees very well with the data within the region studied. This result indicates that the freestream turbulence intensity in the channel is so small that it does not have a significant effect on the wall heat transfer. Figure 9(*a*) shows that for assisting flow, buoyancy can increase the Nusselt number, while in opposed flow buoyancy can reduce the heat transfer. Flow reversal occurs only for the case of $\mathrm{Gr}/\mathrm{Re}^2=-3$ and $\mathrm{Re}=600$, as shown in Fig. 3(*b*). However, the heat transfer in the downstream region is only slightly affected and no heat transfer enhancement by the reversed flow is noticeable. It appears that the reversed flow, which is adjacent to the adiabatic wall, is too weak to influence the thermal energy transport from the heated wall. The separation point identified from the streamline plot is located at approximately $x/L=0.64$, which cannot be discerned from the local Nusselt number distribution along the heated wall.

Figure 9(*b*) presents the cases for $\mathrm{Re}=200$. Flow reversal occurs when $\mathrm{Gr}/\mathrm{Re}^2=500$, 100, and -8. Again, for assisted convection, there is no discernible effect on the heat transfer by the reversed flow. In other words, the heat transfer process along the heated wall does not know if flow reversal would occur along the opposite wall. At a higher buoyancy parameter, however, the strong mixing process between the reversed flow and the mainstream may render the flow in its vicinity unstable and give rise to transition to turbulent flow [14]. This can significantly increase the heat transfer rate. However, the current calculation could not be extended to such a high buoyancy parameter. For opposed convection, however, one can clearly conclude that the reversed flow has a significant effect on the heat transfer. The reversed flow can make the local heat transfer in the downstream near the exit higher than in the upstream. A similar phenomenon is also found in the experiments [15]. In the latter work, however, turbulent

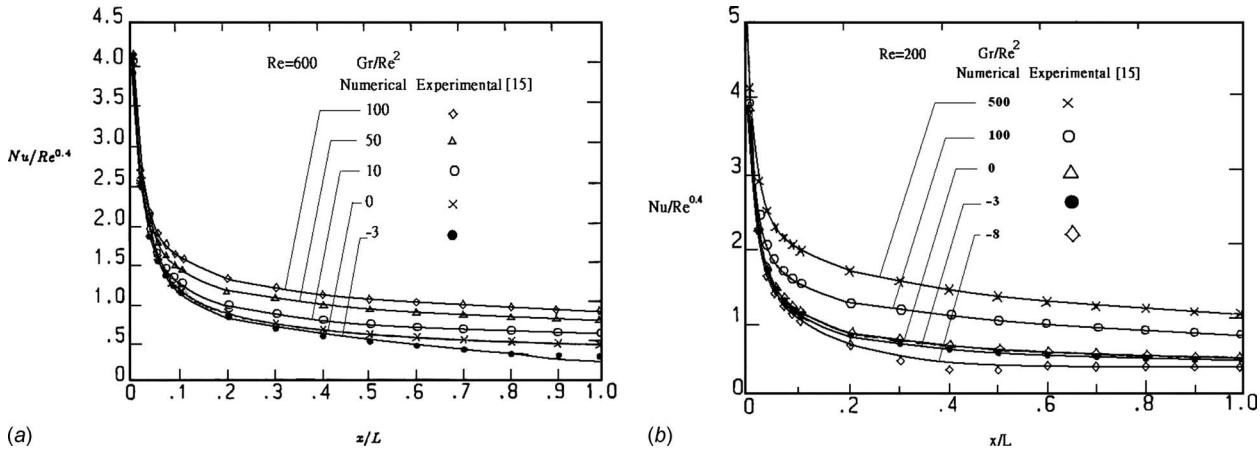

Fig. 9 (*a*) Effect of $\mathrm{Gr}/\mathrm{Re}^2$ on the local Nusselt number distribution on the heated wall at $\mathrm{Re}=600$ for both assisted and opposed convection and (*b*) effect of $\mathrm{Gr}/\mathrm{Re}^2$ on the local Nusselt number distribution on the heated wall at $\mathrm{Re}=200$ for both assisted and opposed convection

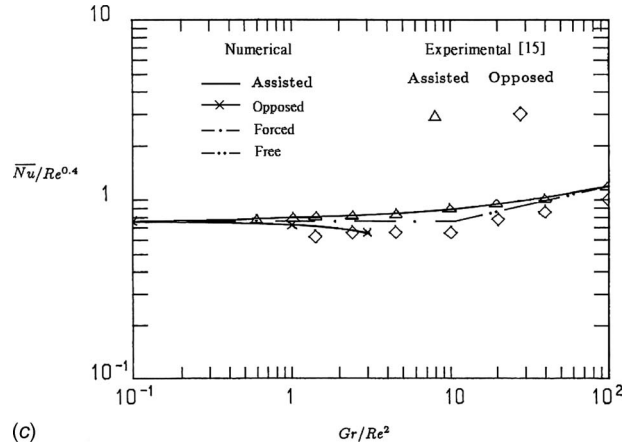

Fig. 10 Effect of Gr/Re^2 on the average Nusselt number for both assisted and opposed convection

convection is triggered by the reversed flow, and the heat transfer is significantly enhanced. In the present study, the separation point is found from the streamline plot to be at approximately $x/L = 0.25$. On the other hand, a significant reduction in heat transfer is found at approximately $x/L = 0.3$. The minimum in heat transfer is located at $x/L = 0.4$. It appears that the separation point is far upstream of the minimum in heat transfer.

The average heat transfer coefficient over the entire heated plate is calculated by dividing the average heat flux by the mean temperature difference between the heated wall and the entrance air. The average Nusselt number, which is defined as $\bar{h}D_h/k$, is also normalized with $Re^{0.4}$ and the results are presented in Fig. 10. Since the local Nusselt number, $Nu/Re^{0.4}$, is a function of both x/L and Gr/Re^2, the averaged Nusselt number, $\overline{Nu}/Re^{0.4}$ is then a function of Gr/Re^2 only. This has also been confirmed in the final correlations in the following.

For the purpose of comparison, numerical results of pure forced convection [31] and pure natural convection in a finite vertical duct [32] are also presented. Correlation for the pure forced convection for $600 \le Re \le 1800$ is written as follows:

$$\overline{Nu}/Re^{0.4} = 0.76 \tag{18}$$

The correlation for pure natural convection in a finite vertical duct is written as

$$\overline{Nu}/Gr^{0.2} = 0.476 \tag{19}$$

Equation (19) can be rearranged and rewritten as follows

$$\overline{Nu}/Re^{0.4} = 0.476(Gr/Re^2)^{0.2} \tag{20}$$

Equation (20) is valid only for $Gr < 10^3$ and in absence of flow reversal.

In Fig. 10, Eqs. (18) and (20) have been plotted as the pure forced and pure natural convection asymptotes, respectively. It is seen that the numerical result for assisted convection approaches the pure forced convection result for small values of Gr/Re^2 and approaches the pure natural convection result for large values of Gr/Re^2. The correlation of natural convection heat transfer for a single vertical plate has the same form as Eq. (19) except that the constant 0.476 should be changed to 0.434. The addition of an insulated wall near a single heated plate, therefore, does not have a significant effect on the heat transfer. Therefore, at a higher buoyancy parameter, the heat transfer for assisted convection inside a vertical channel approaches the natural convection results along a single vertical plate. This argument can be confirmed by comparison of heat transfer prediction with the experimental results, as shown in Fig. 10, for assisted convection. For opposed convection, no prediction for the regime studied in the experiments is available for comparison, except in a very low buoyancy parameter condition where agreement with the data is very good. However, the heat transfer for opposed convection is smaller than for assisted convection, not even in small buoyancy parameter region, but also in large buoyancy parameter region, as shown in Fig. 10.

To facilitate practical application of the present results, correlation for the average heat transfer in the entire channel based on the numerical results is developed and summarized in the following. The correlation gives the average heat transfer parameter $\overline{Nu}/Re^{0.4}$ in terms of Gr/Re^2. For buoyancy assisted convection with $0 \le Gr/Re^2 \le 100$ and $200 \le Re \le 1800$, the result is

$$\log \overline{Nu}/Re^{0.4} = -0.12 + 0.023 \log(1 + Gr/Re^2) + 0.037[\log(1 + Gr/Re^2)]^2 \tag{21}$$

which has a standard deviation of 0.1%. For buoyancy opposed convection with $0 \le Gr/Re^2 \le 3$ and $200 \le Re \le 600$, the corresponding equation is

$$\log \overline{Nu}/Re^{0.4} = -0.12 + 0.05 \log(1 + Gr/Re^2) - 0.208[\log(1 + Gr/Re^2)]^2 \tag{22}$$

which has a standard deviation of 0.1%. The above correlation has been confirmed by comparison with the experimental data.

7 Conclusions

For both assisted and opposed convection, a reversed flow structure can be initiated in the downstream region of the duct, and the reversed flow extends gradually upstream as the buoyancy parameter Gr/Re^2 increases. However, the increase in Re has an opposite effect as it pushes the reversed flow downstream. Simple analytical models developed in the present study to predict the penetration depths of the reversed flow have been shown to give acceptable results for situation where the transport process inside the channel is dominated by natural convection. In addition, the criterion for the onset of flow reversal has been determined, and the critical value of Gr/Re for the occurrence of flow reversal is shown to be well correlated with the Reynolds number.

The effects of the reversed flow and the buoyancy parameter on the heat transfer have also been studied. For opposed convection, the reversed flow can cause a slight increase in heat transfer in the downstream region; however, the increase in the average Nusselt number is hardly discernible. For assisted convection, the occurrence of flow reversal does not have any significant effect on the heat transfer. The increase in Gr/Re^2 makes the average Nusselt number to approach the results of a pure natural convection along a vertical plate. The average heat transfer parameter $\overline{Nu}/Re^{0.4}$ predicted for both assisted and opposed convection has been well correlated in terms of Gr/Re^2.

The present numerical results have been compared with the experimental data published in the literature, and the trend predicted is in good agreement with the data. Since the numerical calculation does not account for the turbulent transport (due to turbulence intensity in the freestream), which can occur in the experiments, the prediction for the penetration depth of the reversed flow is slightly on the high side, as to be expected. However, the agreement for the heat transfer prediction with the experimental data suggests that this turbulent transport in the reversal flow does not have a significant effect on the heat transfer.

Nomenclature

b = channel width
D_h = channel hydraulic diameter, $2b$
g = gravitational acceleration
Gr = Grashof number, $g\beta q D_h^4/(k\nu^2)$
Gr_x = Grashof number, $g\beta q x^4/(k\nu^2)$

h = local heat transfer coefficient based on inlet temperature
$\bar{h}$ = average heat transfer coefficient
k = thermal conductivity of air
L = height of the heated section in the duct
Nu = local Nusselt number, hD_h/k
$\overline{\mathrm{Nu}}$ = average Nusselt number, $\bar{h}D_h/k$
p = pressure
Pr = Prandtl number, ν/α
q = heat flux
Re = Reynolds number, u_oD_h/ν
T = temperature
u = axial velocity
v = transverse velocity
x = streamwise coordinate, pointing upward for assisted flow and downward for opposed flow
$\bar{x}$ = penetration depth, L-x
$x^\dagger$ = reduced coordinate, $x/(D_h\ \mathrm{Re}\ \mathrm{Pr})$
y = transverse coordinate from the heated wall

Greek Symbols

β = coefficient of expansion
δ = thermal or momentum boundary layer thickness
η = dimensionless distance, γ/δ
θ = dimensionless temperature, $(T-T_o)/(qD_h/k)$
ν = kinematic viscosity
ρ = density
τ = dimensionless time

Subscripts

f = refers to pure forced convection
n = refers to pure natural convection
o = refers to inlet
r = refers to reference

References

[1] Wilkinson, G. T., Tsang, B. K.-H., and Hoffman, T. W., 1982, "Flow Reversal in Turbulent Mixed Convection," *Proceedings of the Seventh IHTC*, Munich, Germany, pp. 501–505.
[2] Swanson, L. W., and Catton, I., 1987, "Enhanced Heat Transfer Due to Secondary Flows in Mixed Turbulent Convection," ASME J. Heat Transfer, **109**(4), pp. 943–946.
[3] Jackson, J. D., Cotton, M. A., and Axcell, B. P., 1989, "Studies of Mixed Convection in Vertical Tubes," Int. J. Heat Fluid Flow, **10**(1), pp. 2–15.
[4] Scheele, G. F., and Hanratty, T. J., 1962, "Effect of Natural Convection on Stability of Flow in a Vertical Pipe," J. Fluid Mech., **14**, pp. 244–255.
[5] Brown, C. K., and Gauvin, W. H., 1965, "Combined Free and Forced Convection, I. Heat Transfer in Aiding Flow," Can. J. Chem. Eng., **43**, pp. 306–312.
[6] Zeldin, B., and Schmidt, F. W., 1972, "Developing Flow With Combined Forced-Free Convection in an Isothermal Vertical Tube," ASME J. Heat Transfer, **94**, pp. 211–223.
[7] Mori, Y., and Ohbuchi, M., 1989, "A Fundamental Study of Flow and Heat Transfer Performances of Downward Water Flow at Low Reynolds Numbers in a Vertical Heated Straight Tube," Int. J. Heat Mass Transfer, **32**, pp. 1231–1238.
[8] Lavine, A. S., Kim, M. K., and Shores, C. N., 1989, "Flow Reversal in Opposing Mixed Convection in Inclined Pipes," ASME J. Heat Transfer, **111**, pp. 114–120.
[9] Morton, B. R., Ingham, D. B., Keen, D. J., and Heggs, P. J., 1989, "Recirculating Combined Convection in Laminar Pipe Flow," ASME J. Heat Transfer, **111**, pp. 106–113.
[10] Ingham, D. B., Keen, D. J., Heggs, P. J., and Morton, B. R., 1990, "Recirculating Pipe Flows," J. Fluid Mech., **213**, pp. 443–464.
[11] Wirtz, R. A., and Mckinley, P., 1985, "Buoyancy Effects on Downward Laminar Convection Between Parallel Plates," *Proceedings of the ASME Heat Transfer Division*, ASME, New York, Vol. HTD-42, pp. 105–112.
[12] Wirtz, R. A., and Hamadah, T., 1987, "Transitional Reynolds Number Convection in a Vertical Channel With Opposing Buoyancy Effects," ASME-JSME Thermal Engineering Joint Conference, pp. 1443–1448.
[13] Gau, C., Yih, K. A., and Aung, W., 1992, "Measurement of Heat Transfer and Flow Reversal in Heated Vertical Channels With Buoyancy Assisted and Opposed Flows," AIAA J., **6**(4), pp. 707–712.
[14] Gau, C., Yih, K. A., and Aung, W., 1992, "Reversed Flow Structure and Heat Transfer Measurements for Buoyancy Assisted Convection in a Heated Vertical Duct," ASME J. Heat Transfer, **114**(4), pp. 928–935.
[15] Huang, T. M., Gau, C., and Aung, W., 1995, "Mixed Convection Flow and Heat Transfer in a Heated Vertical Convergent Channel," Int. J. Heat Mass Transfer, **38**, pp. 2445–2456.
[16] Aung, W., and Worku, G., 1986, "Developing Flow and Flow Reversal in a Vertical Channel With Asymmetric Wall Temperatures," ASME J. Heat Transfer, **108**, pp. 299–304.
[17] Aung, W., and Worku, G., 1987, "Mixed Convection in Ducts With Asymmetric Wall Heat Fluxes," ASME J. Heat Transfer, **109**, pp. 947–951.
[18] Ingham, D. B., Keen, D. J., and Heggs, P. J., 1988, "Two Dimensional Combined Convection in Vertical Parallel Plate Ducts, Including Situations of Flow Reversal," Int. J. Numer. Methods Eng., **26**, pp. 1645–1664.
[19] Ingham, D. B., Keen, D. J., and Heggs, P. J., 1988, "Flows in Vertical Channels With Asymmetric Wall Temperatures and Including Situations Where Reverse Flows Occur," ASME J. Heat Transfer, **110**, pp. 910–917.
[20] Williams, P. G., 1975, "A Reversed Flow Computation in the Theory of Self-Induced Separation," Lect. Notes Phys., **35**, pp. 445–451.
[21] Cheng, C.-H., Weng, C.-J., and Aung, W., 1995, "Buoyancy Effect on the Flow Reversal of Three-Dimensional Developing Flow in a Vertical Rectangular Duct—A Parabolic Model Solution," ASME J. Heat Transfer, **117**(1), pp. 238–241.
[22] Naito, E., and Nagano, Y., 1989, "Combined Forced and Free Upward-Flow Convection in the Entrance Region Between Inclined Parallel Plates," ASME J. Heat Transfer, **111**, pp. 675–682.
[23] Naito, E., and Nagano, Y., 1989, "The Effect of Buoyancy on Downward and Upward Laminar-Flow Convection in the Entrance Region Between Inclined Parallel Plates," Int. J. Heat Mass Transfer, **32**, pp. 811–823.
[24] Fimeira da Silva, E., and Cotta, R. M., 1998, "Mixed Convection Within Vertical Parallel Plates: Hybrid Solution by Integral Transforms," Numer. Heat Transfer, Part A, **33**, pp. 85–106.
[25] Barletta, A., 2001, "Analysis of Flow Reversal for Laminar Mixed Convection in Vertical Rectangular Duct With One or More Isothermal Walls," Int. J. Heat Mass Transfer, **44**, pp. 3481–3497.
[26] Chen, Y. C., and Chung, J. N., 1998, "Stability of Mixed Convection in a Differentially Heated Vertical Channel," ASME J. Heat Transfer, **120**(1), pp. 127–132.
[27] Patankar, S. V., 1980, *Numerical Heat Transfer and Fluid Flow*, Hemisphere, Washington, DC.
[28] Yih, K. A., 1992, "Experimental and Numerical Study of Flow and Heat Transfer in Vertical Channels," Ph.D. thesis, Institute of Aeronautics and Astronautics, NCKU, Tainan, Taiwan, R.O.C.
[29] Cheng, C. H., Kou, H. S., and Huang, W. H., 1990, "Flow Reversal and Heat Transfer of Fully Developed Mixed Convection in Vertical Channel," AIAA J., **4**, pp. 375–383.
[30] Burmeister, L. C., 1993, *Convective Heat Transfer*, 2nd ed., Wiley, New York, pp. 393–454.
[31] Heaton, H. S., Reynolds, W. C., and Kays, W. M., 1964, "Heat Transfer in Annular Passages. Simultaneous Development of Velocity and Temperature Fields in Laminar Flow," Int. J. Heat Mass Transfer, **7**, pp. 763–781.
[32] Yan, W. M., and Lin, T. F., 1987, "Natural Convection Heat Transfer in Vertical Open Channel Flows With Discrete Heating," Int. Commun. Heat Mass Transfer, **14**(2), pp. 187–200.

Heat Transfer and Fluid Flow Characteristics in Supercritical Pressure Water

Jeremy Licht
e-mail: jeremyrlicht@gmail.com

Mark Anderson
e-mail: manderson@engr.wisc.edu

Michael Corradini
e-mail: corradini@engr.wisc.edu

Nuclear Engineering and Engineering Physics,
College of Engineering,
University of Wisconsin-Madison,
1500 Engineering Drive,
Madison, WI 53706

A series of integral heat transfer measurements in a square annular flow passage was performed for bulk water temperatures of 175–400°C with upward mass velocities of 300 kg/m² s and 1000 kg/m² s and heat fluxes of 0, 200 kW/m², and 440 kW/m², all at a pressure of 25 MPa. Mean and turbulent velocities measured with a two-component laser Doppler velocimetry system along with simulations using the computational fluid dynamics (CFD) code FLUENT were used to explain the deterioration and enhancement of heat transfer in supercritical pressure water. At low mass velocities, the integral heat transfer measurements exhibited large localized wall temperature spikes that could not be accurately predicted with Nusselt correlations. Detailed mean and turbulent velocities along with FLUENT simulations show that buoyancy effects cause a significant reduction in turbulent quantities at a radial location similar to what is the law of the wall region for isothermal flow. At bulk temperatures near the pseudocritical temperature, high mass velocity integral heat transfer measurements exhibited an enhanced heat transfer with a magnitude dependent on the applied heat flux. Measured mean and turbulent velocities showed no noticeable changes under these conditions. FLUENT simulations show that the integrated effects of specific heat can be used to explain the observed effects. The experimentally measured heat transfer and local velocity data also serve as a database to compare existing CFD models, such as Reynolds-averaged Navier-Stokes (RANS) equations and possibly even large Eddy simulations (LES) and direct numerical simulations (DNS). Ultimately, these measurements will aid in the development of models that can accurately predict heat transfer to supercritical pressure water.
[DOI: 10.1115/1.3090817]

Keywords: supercritical water, heat transfer, buoyancy, turbulence

1 Introduction

The supercritical water reactor (SCWR) has been selected as one of the next steps in nuclear reactor designs [1]. The SCWR is essentially a light water reactor (LWR) operating at higher pressure (25 MPa) and higher exit temperature (510°C) with the goal of increasing the thermal efficiency from 33% to 44% while building upon the well established LWR's and supercritical fossil plants. The coolant enthalpy passes above and beyond the two-phase dome remaining single phase but undergoing large changes in its thermophysical properties. A significant amount of research on heat transfer to supercritical fluids has been carried out over the past 50 years and has been summarized by Pioro et al. [2]. Experiments have shown that variable property fluids can cause an enhancement or deterioration in heat transfer. Hall [3] suggested that deterioration was caused by changes in the shear stress and derived an expression for the wall shear stress for a variable property fluid. From this, criteria were developed to identify significant changes in the shear stress due to the axial gradients in density (acceleration effects) and/or the radial gradients in density (buoyancy effects).

At relatively high mass velocities, buoyancy effects are unimportant and the flow is considered to be in the forced convection region [4]. For this type of flow, previous experiments have shown that an enhancement in heat transfer occurs for bulk temperatures (T_b) near the pseudocritical temperature[1] (T_{pc}) at low heat fluxes and, in general, its magnitude is reduced with increasing heat flux [5]. This heat transfer effect is thought to be due to the varying specific heat (c_p) of the fluid [6]. Many Nusselt correlations have been developed to model enhanced heat transfer but the correlations including property ratios between the wall and the bulk have proven most successful [2]. Computational fluid dynamics (CFD) simulations using turbulence models developed for constant property applications have also shown good agreement [7]. In small hydraulic diameters ($d \lesssim 1$ mm) with strong heating, a deterioration in heat transfer due to acceleration effects, represented by broad increases in wall temperature (T_w) with T_b's near the T_{pc}, occurs in both upward and downward flows [8]. This type of heat transfer is not well studied but has been the focus of some ongoing research [9].

At relatively low mass velocities, buoyancy effects are important because of radial gradients in density. This mixed convection heat transfer can result in an enhancement or deterioration depending on the flow direction [10]. Downward flow experiments have shown an enhancement in heat transfer. In upward flow, the deterioration in heat transfer is represented by large localized spikes in the T_w and has been studied extensively [11]. Current Nusselt correlations are not able to predict this type of heat transfer. CFD simulations using turbulence models developed for constant property application are also not able to capture this heat transfer effect [7]. The inability to predict heat transfer deterioration in variable property fluids has led to a more detailed research with the measurement of the fluid flow characteristics, i.e., mean and turbulent properties.

At supercritical pressures, Wood and Smith [12], Bourke and Pulling [13], Miropl'skii and Baigulov [14], and Kurganov et al. [15] used Pitot tubes and microthermocouples to measure mean axial velocities in circular tubes with upward flowing CO2 used as

[1]The pseudocritical temperature is defined as the temperature at which, for a given pressure, the fluid exhibits a maximum in its specific heat.

Contributed by the Heat Transfer Division of ASME publication in the JOURNAL OF HEAT TRANSFER DIVISION. Manuscript received June 3, 2008; final manuscript received December 19, 2008; published online May 13, 2009. Review conducted by Frank Cunha.

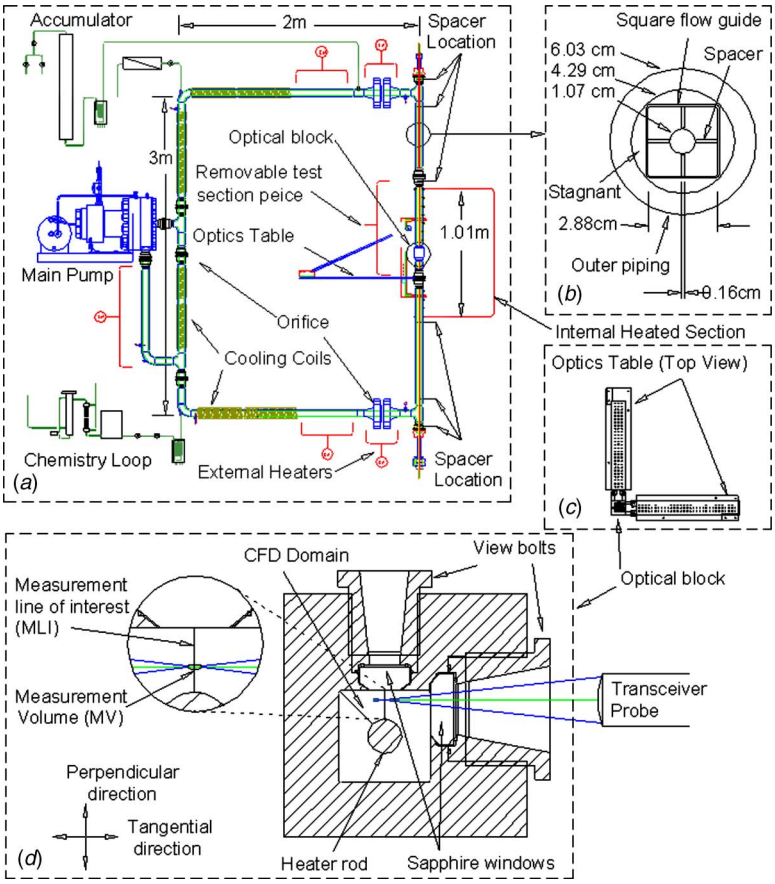

Fig. 1 Schematic of the important experimental components: (*a*) the heat transfer loop, (*b*) cross section of the flow geometry, (*c*) top view of the optics table, and (*d*) cross section of the optical block with an exploded view of the optical measurement region

a coolant. The results of these experiments indicated an "M-shaped" velocity profile. Bourke and Pulling [13] found that the M-shaped velocity profile occurred after the spike in wall temperature, where as Kurganov et al. [15] found that the M-shaped velocity profile occurred at the spike in wall temperature.

Buoyancy effected heat transfer is not unique to supercritical fluids and can occur at subcritical pressures. A significant amount of subcritical mixed convection heat transfer research was done in Russia and summarized by Petukhov et al. [16]. However, there has recently been an increasing amount of work in this area as summarized by Jackson [17] where they used the laser Doppler velocimetry (LDV) technique to measure local instantaneous velocities under conditions of deterioration. Additional velocity measurements were done by Kang et al. [18] using R-113 as a coolant, while similar measurements were done by Wardana et al. [19] using air.

While there has been a significant amount of research in the area of variable property heat transfer, there has not been a significant improvement in the methods used to predict the deterioration in heat transfer. It is likely that the only success will come with the use of CFD due to the importance of local conditions within the flow. Current turbulence models developed from constant property experiments have had only limited success in predicting variable property heat transfer effects. In order to improve and develop turbulence models, local fluid flow characteristics coupled with heat transfer data are needed.

In an effort to further study heat transfer at supercritical pressures, a SCW heat transfer facility was built at the University of Wisconsin-Madison with the capabilities of optical access for local measurements of turbulent velocities and density [20]. Due to the lack of methods to accurately predict variable property heat transfer, it was necessary to perform experiments over a wide range of conditions to identify which heat transfer effects, such as enhancement and deterioration, occur within the facility. An initial set of heat transfer experiments in a circular annular geometry was previously published [21]. The accuracy and validity of selected heat transfer correlations and buoyancy criterion were compared with heat transfer measurements and used to identify conditions that require further investigation.

Currently it is believed that no detailed velocity measurements have been made in supercritical pressure water under conditions of deterioration nor have there been similar measurements for enhanced heat transfer under forced convection for any supercritical pressure fluid. While Nusselt correlations that include property ratios do a reasonable job in predicting enhanced heat transfer, it is not clear that property variations are the only reason for the measured heat transfer effects (as opposed to changes in turbulence). The work presented in this paper investigates, both experimentally and computationally, the fluid flow characteristics (properties, velocities, and turbulence) that cause an enhancement (forced convection) and a deterioration (mixed convection) in heat transfer.

2 Experimental Facility

2.1 Heat Transfer Loop. A SCW heat transfer facility was built at the University of Wisconsin-Madison to study heat transfer in a circular and square annular geometry [20]. The loop (Fig. 1) has dimensions of approximately 2 m wide by 3 m tall and is made of 4.29 cm inner diameter Inconel 625 piping and is capable

of operating up to 600°C at 25 MPa. A Chempump™ (model GCT-5k 36I) capable of operating at SCW conditions can produce mass velocities up to 2000 kg/m^2 s through the test section. The circular annular test section geometry is a 1.07 cm diameter heater rod within a 4.29 cm diameter flow channel. The square annular test section geometry is a 1.07 cm diameter heater rod within a 2.88 cm wide flow channel. The 3.3 m long heater rod spans the entire right leg of the loop and protrudes out both ends. This design permits the use of 16 thermocouples evenly spaced along the inner cladding of the 1.01 m heated length. The center portion of the right leg of the loop serves as the internally heated test section, allowing a 76 cm entrance length for both upward and downward flow studies. The heater is centered within the flow channel with six spacers; four of which are located on either side of the tees and two that are 5 cm from either end of the heated section. For the upward flow, square annular geometry experiments presented in this paper, the original removable test section piece (circular) is replaced with a new test section piece with optical access [22]. The optical block has optical access through two sapphire windows: one centered to view the heater rod and the other is offset to view a portion of the flow field. While the optical block was machined to have an inner square flow path, the remaining vertical test section piping (circular) is fitted with square flow guides that cleanly mate with the optical block, effectively making the ~3 m test section a square annular geometry. The facility is capable of operating at any steady state condition by using a variable heat removal system made up of copper cooling coils. Eight copper coils of various contact areas are tightly wrapped to the Inconel piping. Heat removal by the cooling coils can be set to match that supplied by the heater by simply controlling the number of coils receiving cooling water and controlling their respective flow rates.

2.2 System Measurements. The data acquisition system for the loop is currently a National Instrument system along with a LABVIEW™ 7.1 software interface. This system consists of a 16 bit 300 kHz A/D converter (PCI-6052E) connected to an SCXI 1001 chassis that can hold up to 12 SCXI modules. Currently there are four 32 channel 1102 high accuracy thermocouple modules used for temperature and voltage measurements around the loop and four 1160 general-purpose switching modules consisting of 16 independent relays to control valves and external heating on the loop.

The inlet fluid temperature is measured with an E-type thermocouple (model GEMQIN-0625-12) with an uncertainty of ±1°C or 0.4%, which ever is greater. The pressure in the loop was measured with a Siemens Sitrans P pressure gauge (model 7MF4032-1GA10-1NC1-Z) with an uncertainty of 0.1%. Mass velocities were determined by measuring the pressure drop across the test section orifice plate with a Siemens Sitrans P differential pressure gauge (model 7MF4032-1GA10-1NC1-Z). Mass flux uncertainties conservatively varied from 5% to 11%. Heater power was determined from voltage measurements of the dc power supply and current determined from voltage measurements across a shunt. Heat flux uncertainties varied from 1% to 3.5%. Heat transfer coefficients and T_w's were determined from inner-cladding temperatures measured with K-type thermocouples (model XL-K-MO-020), which have uncertainties of ±1.1°C or 0.4%, whichever is greater. Heat transfer coefficient uncertainties are described in Ref. [20] and vary depending on the operating conditions. Uncertainties are typically 1.5–13% but can be as high as 27% for cases exhibiting a significant enhancement in heat transfer.

2.3 The Laser Doppler Velocimeter. The two-component LDV system from TSI Inc. consisted of a transceiver probe (model TR260) with a 50 mm beam spacing. A 135 mm focal length lens (model TLN06-120) forms an ellipsoid shaped measuring volume (MV) with a major axis of 200 μm long and a minor axis of 33 μm in diameter. A 10 W argon-ion Lexel (model 95) operated at 4 W was used as the light source. The fluid was seeded with 1–2 μm diameter aluminum oxide particles following the particle selection criterion described by Menon and Lai [23]. Light is collected in backscatter mode with the transceiver probe and transmitted to a photodetector (model PDM1000-2) and analyzed with a multibit digital burst correlator (model FSA4000-2) and FLOWSIZER software (Version 1.1.1). When the beam pairs were operated in coincidence mode, the coincidence window was set to 200 μs based on the recommendations of Kang et al. [24]. Two PCI-7342 National Instrument motion control cards controlled a pair of two-axis National Instrument NuDrive power amplifiers (model 2SX-411). These amplifiers powered two Newport translation stages (model UTMPP.1) with a positional resolution of 0.1 μm.

3 Methods

3.1 LDV Alignment and Data Collection. Accurate positioning of the MV was needed in both the tangential and radial (perpendicular) directions (see Fig. 1). With the MV positioned near the heater rod, the probe was translated 4 mm in the tangential direction so that the measured mean axial velocity profile spanned the measurement line of interest (MLI). When the MV was furthest from the MLI, it was also furthest from the inner wall, resulting in a larger velocity measurement. When the MV was located on the MLI, it is closest to the wall and will give the minimum measured velocity. The MV was considered positioned on the MLI when it measured the lowest velocity. The estimated uncertainty of this location was ±50 μm.

One of the significant measurement uncertainties when using a LDV system is knowing the absolute distance between the MV and the wall (perpendicular direction). Durst et al. [25] developed a method that allows for finding the wall shear stress and the bias in the MV's distance from the wall for channel and pipe flow, thus allowing one to accurately know the location of the MV relative to the wall. A similar method was developed here for an annular geometry.

Integrating the differential equation of momentum for an incompressible, steady, fully developed axial flow of a Newtonian fluid with constant properties in an annular geometry gives [20]

$$\frac{U_\tau^2}{R}\left(\frac{XR_oR^2 - XR_oR_i^2 - R^2R_i + R_o^2R_i}{(R_o^2 - R_i^2)}\right) = \nu\frac{\partial U_m}{\partial R} - \overline{uv} \tag{1}$$

where X is the ratio of the outer and inner wall shear stresses.

By expanding u, v, and w in a Taylor series about R_i and employing the continuity equation, the following can be found to be valid for the turbulent shear stress in the inner near wall region:

$$\overline{uv} = a(R - R_i)^3 + b(R - R_i)^4 + c(R - R_i)^5 + \ldots$$

Inserting this into Eq. (1) and solving for U_m gives

$$U_m = \frac{U_\tau^2}{\nu(R_o^2 - R_i^2)}\left(\frac{XR_o(R-e)^2}{2} - XR_oR_i^2\ln(R-e) - \frac{(R-e)^2R_i}{2} + R_o^2R_i\ln(R-e)\right) + A(R - R_i - e)^4 + B(R - R_i - e)^5 - \frac{U_\tau^2}{\nu(R_o^2 - R_i^2)}\left(\frac{XR_oR_i^2}{2} - XR_oR_i^2\ln(R_i) - \frac{R_i^3}{2} + R_o^2R_i\ln(R_i)\right) \tag{2}$$

The radial position (R) is replaced with ($R-e$), where e is the systematic error in the MV position. There are now five unknowns (X, U_τ, e, A, and B) which can be determined by fitting Eq. (2) to the measured data. In the analysis by Durst et al. [25], the wall shear stress was found to be accurate to within 1% provided a minimum of 20 points are taken within a range of $y^+ < 12$. A similar approach was employed here.

To implement this method, the MV is positioned so that it par-

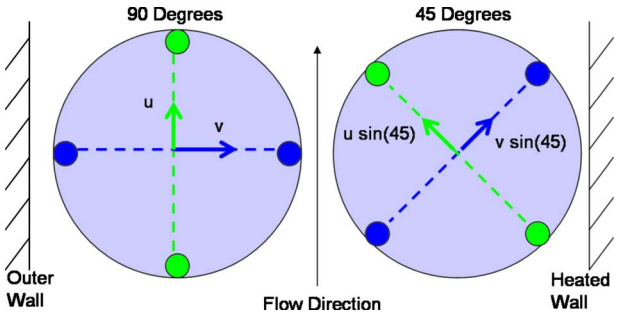

Fig. 2 The two different orientations of the beam pairs used in velocity measurements

tially intersects at the inner wall, causing the LDV system to detect a zero velocity. The MV is then traversed radially away from the wall, in 5 μm increments, until the zero velocity is no longer detected. This position is temporarily assumed to be the location of the wall while collecting data. Approximately 20 velocity measurements are then recorded in 5 μm increments perpendicular from the wall. These initial measurements were used along with Eq. (2) to determine the absolute distance between the wall and the MV. The value of e was typically found to be about 50–100 μm.

The transceiver probe can be orientated at any rotation about its axis. Two different probe rotation angles were used in an effort to identify methods to improve the range of near wall velocity measurements affected by gradients in fluid density. Figure 2 illustrates the probe rotations used relative to the flow direction. For example, in the 90 deg rotation, each beam pair independently measures a component of the flow velocity. In the 45 deg rotation, each beam pair measures a portion of each of the components of the flow velocity, requiring both beam pair measurements to determine a component of the flow velocity. Each method offered both improvements and compromises in the spatial range of turbulence measurements. The 90 deg rotation allowed axial velocity measurements to be made across the entire channel width, while the 45 deg rotation improved the ability to maintain beam coincidence near the heated wall.

After a sufficient number of near wall measurements were collected, the MV was traversed in the perpendicular direction until the outer wall was reached (90 deg rotation) or the beams were cut off due to an obstruction (45 deg rotation).

After velocity data were collected at isothermal conditions for a given inlet temperature and mass flux, velocity data were collected for the different heat flux cases while utilizing the radial position scaling determined at isothermal conditions. When operating at a $T_b > 300\,^{\circ}C$, it was not possible to maintain steady state isothermal conditions due to the external heating power limitations. When the probe was oriented at 45 deg, radial scaling was based on previous setups, and thus the positional uncertainty was high. When the probe was rotated 90 deg, the MV was located based on the mean axial velocity profile near the outer wall. However, minor disturbances caused by the window located at the outer wall prevented accurate measurements, resulting in a positional uncertainty estimated to be less than 200 μm.

At each radial position, 5000 data points were attempted in low mass velocity flows while 20,000 data points were attempted in high mass velocity flows. The number of actual data points collected depended on the local velocity and severity of the density gradients. At isothermal conditions, the time to acquire data points at one radial position was on the order of 1–5 min. When a heat flux was applied, data rates could be significantly reduced near the heated wall so data collection was either terminated at 30 min or the number of data points collected was reduced. Data collection for a particular experimental set of conditions was terminated when it took longer than 30 min to collect 512 data points for the axial velocity component.

3.2 Computational Method. The computational fluid dynamics software used was FLUENT 6.3.26. The geometry used for modeling the fluid dynamics is a 1/8 section (Fig. 1) 2.1 m in length. The first meter was used to develop the inlet velocity profile and the last 1.1 m was designated as the test section. The inlet and outlet boundary conditions were mass flux and outflow, respectively. Nonwall edges were designated as symmetry boundaries. The turbulence model chosen was the Reynolds stress model to simulate the anisotropy in the Reynolds stress, accounting for the stress induced secondary flows present in the square annular geometry.

Two wall function methods were used and are described in the FLUENT user's guide [26]. The standard wall function requires the closest wall node to be in the law of the wall region (node nearest the wall located at $y+ \approx 30$). While the bulk of the flow is solved with the Reynolds stress model, this method uses a wall function to bridge the gap between the closest node and the wall. The enhanced wall function requires fully meshing the near wall region to resolve the viscous sublayer (node nearest to wall located at $y+ \approx 1$). Again, while the bulk of the flow is solved with the Reynolds stress model, this method uses a combination of a two layer model with enhanced wall functions in the near wall region. The method was used for the low mass velocity simulations while the standard wall function was used for high mass velocity experiments.

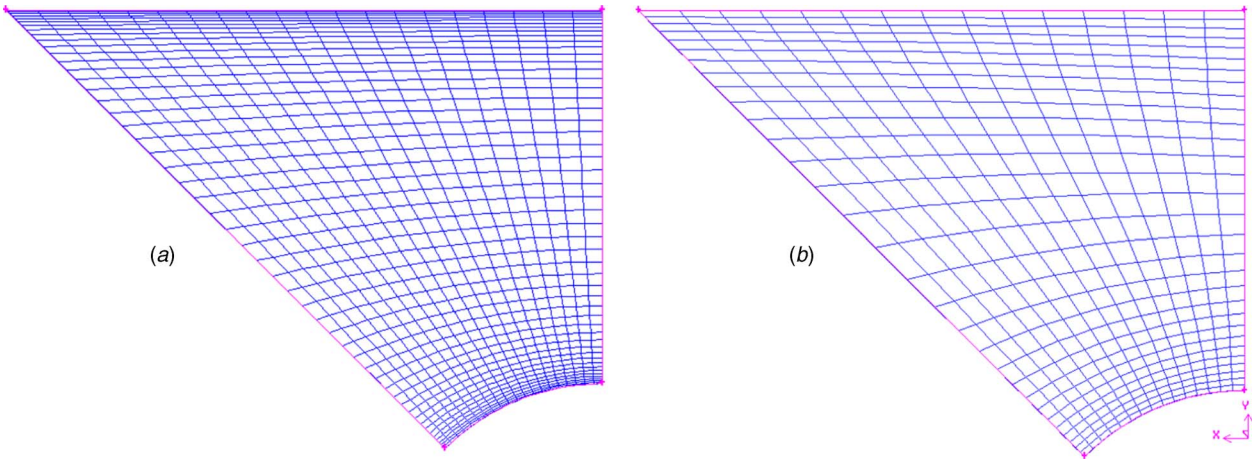

Fig. 3 Cross-sectional view of the meshing scheme: (*a*) enhanced wall function and (*b*) standard wall function

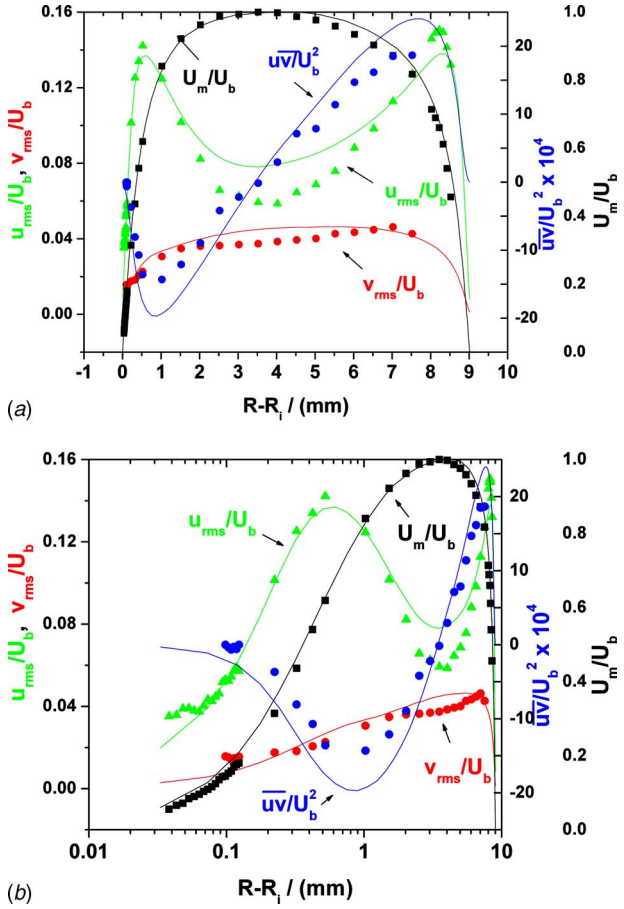

Fig. 4 FLUENT **simulations using the enhanced wall function are compared with LDV measurements: (*a*) linear scaling for view of the bulk and (*b*) logarithmic scaling for view of the near wall. The solid lines represent simulation; the symbols represent measured data.**

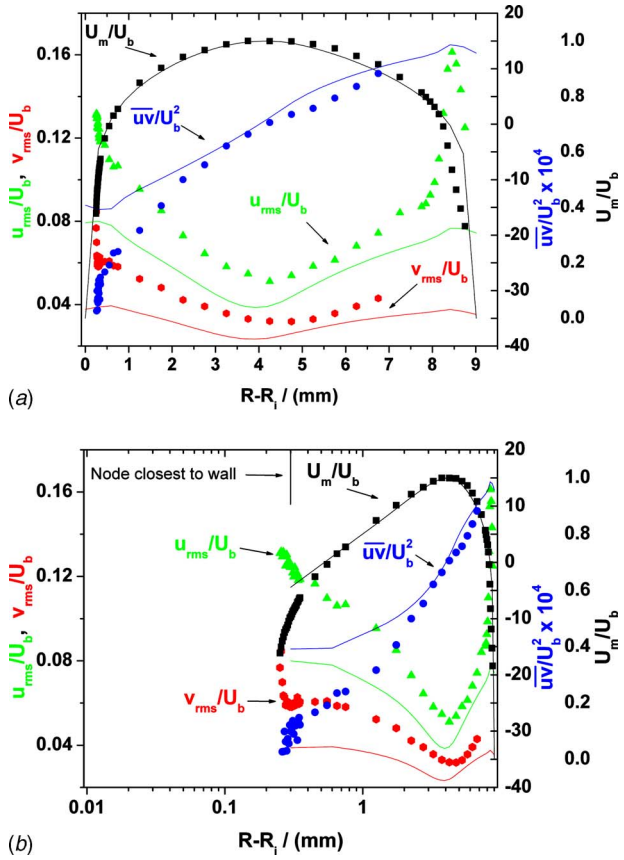

Fig. 5 FLUENT **simulations using the standard wall function are compared with LDV measurements: (*a*) linear scaling for view of the bulk and (*b*) logarithmic scaling for view of the near wall. The solid lines represent simulation; the symbols represent measured data.**

Figure 3 illustrates the cross sectional view of the meshing scheme used for each wall function method. For the low mass velocity case, a total of 1.5×10^6 cells were used. 500 and 1000 divisions were used in the axial direction for the developing and test section regions, respectively. 50 divisions were used in the radial direction (bell-shaped distribution) and 20 divisions were used in the circumferential direction. For the high mass velocity case, a total of 1.26×10^6 mesh cells were used. 2800 divisions were used in the axial direction. 30 divisions were used in the radial direction (bell-shaped distribution) and 15 divisions were used in the circumferential direction.

3.3 Measurement and Computational Validation. Because the nondimensional variables used in meshing are dependent on the varying properties of the fluid, changes in meshing were needed for a given set of boundary conditions to meet the requirements of the near wall model. The following validation of measurement and simulation techniques is used to demonstrate their proper application at high and low mass velocities for isothermal conditions.

Figure 4 shows a comparison of normalized velocity and turbulence versus radial position along the MLI for measurement and simulation performed at a pressure of 10 MPa, an inlet temperature of 25°C, and a mass velocity of 310 $\mathrm{kg/m^2\,s}$, with no heat flux. The enhanced wall function was used for simulating this relatively low mass flux condition. In general, there is very good agreement. The measured mean axial velocity (U_m) normalized with the bulk axial velocity (U_b) matches FLUENT well in both the bulk of the flow and the inner near wall region. The radial positioning of the data followed the description given in Sec. 3.1. The agreement between FLUENT and the measured results in the near wall region suggest the assumptions used in the development of Eq. (2) are adequate. The root mean square of the axial turbulence (u_{rms}) shows a slight discrepancy in the magnitudes at the bulk and outer wall, while good agreement is found near the heater wall. The root mean square of the radial turbulence (v_{rms}) matches well near the walls but there is a slight difference in the core. The measured and simulated turbulent shear stress ($\overline{uv}$) show similar trends; however, there are slight differences in magnitude. In the bulk of the flow, each crosses zero within 200 μm of each other. The difference seen between simulations and the measurements is likely due to the factors that are not modeled in FLUENT. These effects could include asymmetries, turbulence generated by the main pump, spacers, imperfect union of the square flow guides, and so on. However, the measurement and simulation results show excellent similarity.

Figure 5 shows a comparison of the normalized velocity and turbulence versus the radial position along the MLI for measurement and simulation performed at a pressure of 25 MPa, an inlet temperature of 200°C, and a mass velocity of 1050 $\mathrm{kg/m^2\,s}$, with no heat flux. The standard wall function was used for simulating this relatively high mass flux condition. Good agreement is found for the U_m in the bulk and near wall regions. Measurement and simulation show similar trends for the u_{rms}, v_{rms}, and $\overline{uv}$; however, the simulated results are lower in magnitude. Similar results were found when applying the standard wall function

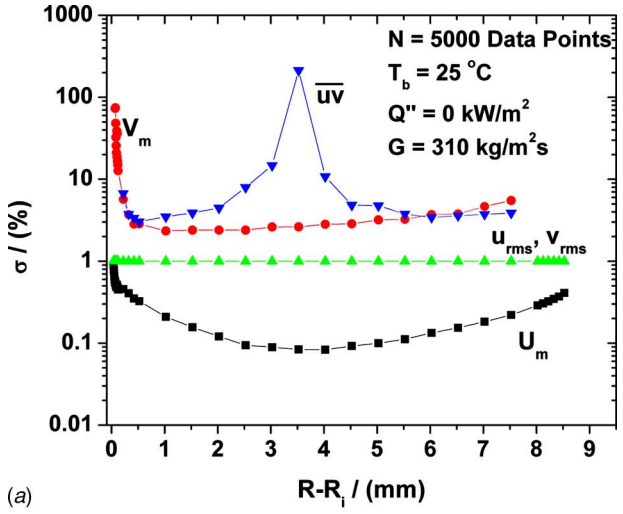

(*a*)

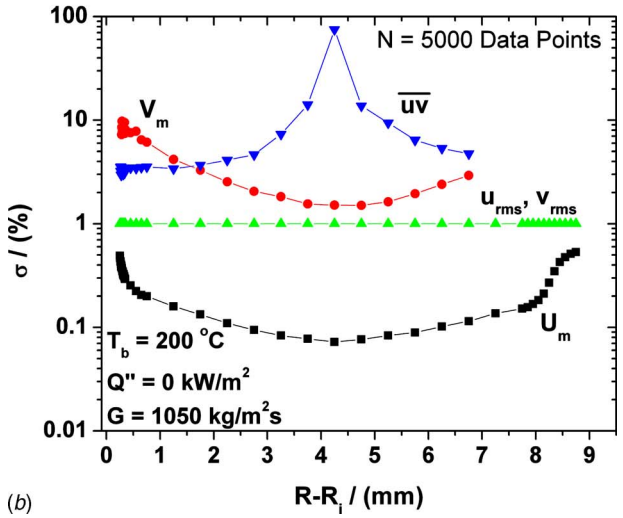

(*b*)

Fig. 6 Uncertainties of the LDV measurements shown in Figs. 4 and 5

method to the conditions shown in Fig. 4. The standard wall function requires less computational power but compromises the accuracy of near wall turbulence.

Uncertainties for the LDV measurements were estimated as described by Benedict and Gould [27]. The percent error versus radial position along the MLI for the data measured in Figs. 4 and 5 are shown in Fig. 6. The percent error in U_m is kept below 1% due to the number of data points collected. Similarly, the errors in u_{rms} and v_{rms} are as low as 1%. The percent error in the mean radial velocity (V_m) is fairly large; however, the magnitude of V_m is approximately zero resulting in a large percent error. A similar effect is seen for the $\overline{uv}$ error in the bulk of the flow where it crosses through zero.

4 Results and Discussion

An initial set of upward flow integral heat transfer experiments was performed in a circular annular geometry and reported in Ref. [21]. The results showed that two types of heat transfer could occur within our facility. At high mass velocities, an enhancement in the heat transfer coefficient occurred at T_b's near the T_{pc}. In general, the enhancement was reduced with increasing heat flux. At relatively low mass velocities, a deterioration in heat transfer represented by large localized spikes in T_w occurred. Several buoyancy criteria applied to the data suggested that buoyancy effects due to the radial gradients of fluid density caused the deterioration in heat transfer. Selected Nusselt correlations were found to adequately reproduce heat transfer in the absence of buoyancy effects. Based on these results, a similar set of integral heat transfer experiments were performed in a square annular geometry along with turbulence measurements and FLUENT simulations to better understand the mechanisms causing an enhancement and deterioration in heat transfer.

Table 1 Experimental conditions at which LDV experiments were performed

Run No.				
Probe rotation (90 deg)	Probe rotation (45 deg)	T_b (°C)	G (kg/m² s)	Q'' (kW/m²)
-	194	25	315	0
179, 182, 183	203, 204	175	315	0, 220, 440
188–190	195–197	200	315	0, 220, 440
191–193	198–200	250	315	0, 220, 440
229, 230	212, 213	300	315	0, 220, 440
232, 233	219, 220	340	315	220, 440
240, 242	221, 223	370	315	220,440
243, 244	227, 228	393	315	220, 440
235, 236	-	200	1000	0, 220, 440
246–248	-	300	1000	0, 220, 440
249, 250	-	340	1000	220, 440
251, 252	-	370	1000	220, 440
253, 254	-	383	1000	220, 440
255, 256	-	397	1000	220, 440

4.1 Integral Heat Transfer. A series of integral heat transfer measurements in a square annular flow passage was performed for bulk water temperatures of 175–400 °C with upward mass velocities of 300 kg/m² s and 1000 kg/m² s and heat fluxes of 0, 220 kW/m², and 440 kW/m², all at a pressure of 25 MPa (Table 1).

Figure 7 shows the measured Nusselt number (Nu_{exp}) divided by the forced convection Nusselt number evaluated with the Jackson correlation (Nu_{Ja}) versus the $\text{Gr}/\text{Re}^{2.7}$ buoyancy criterion. This analysis method developed by Jackson et al. [10] provides a method to identify heat transfer data influenced by buoyancy effects. They developed several empirical lines that bound measured data. At $\text{Gr}/\text{Re}^{2.7}$ less than 10^{-5}, the experimental data are in the forced convection region and Nu_{Ja} should equal experimental data. At $\text{Gr}/\text{Re}^{2.7}$ values greater than 10^{-5}, the data are in the

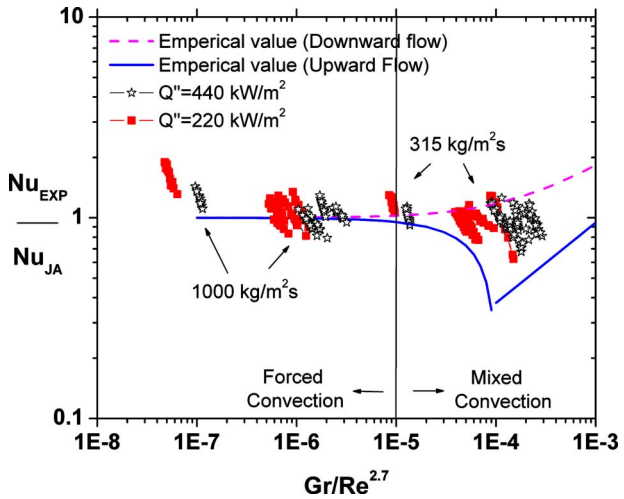

Fig. 7 Experimental data from conditions shown in Table 1 are plotted with empirical lines determined by Jackson and Hall [10] to relate the data to the convection regions

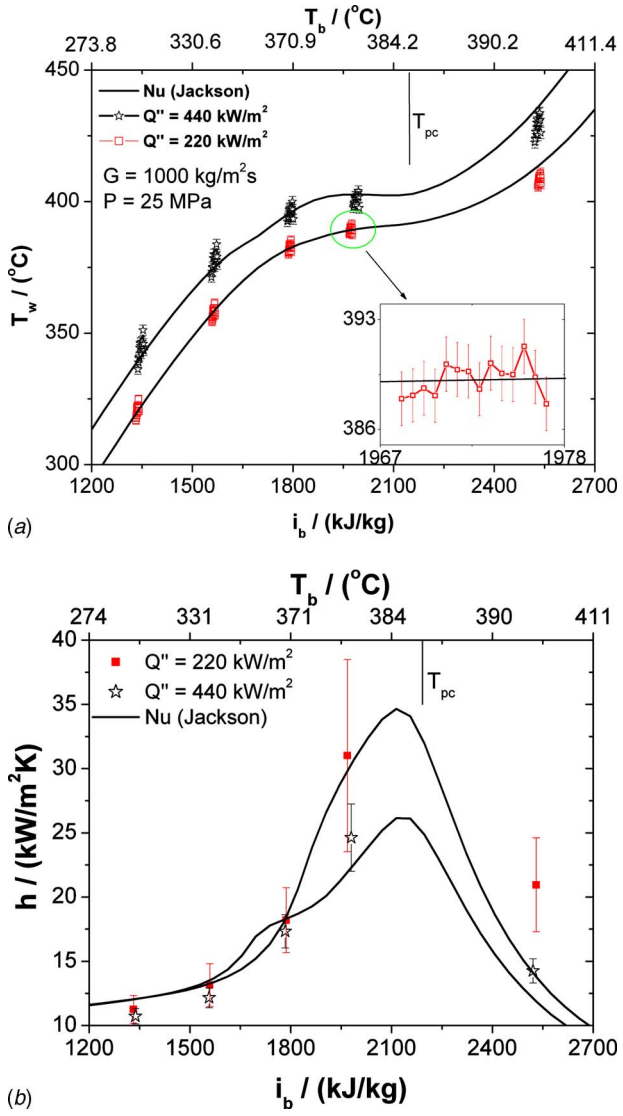

Fig. 8 Comparison of high mass velocity data with Nusselt correlation of Jackson et al. [33]: (*a*) wall temperature; (*b*) heat transfer coefficient

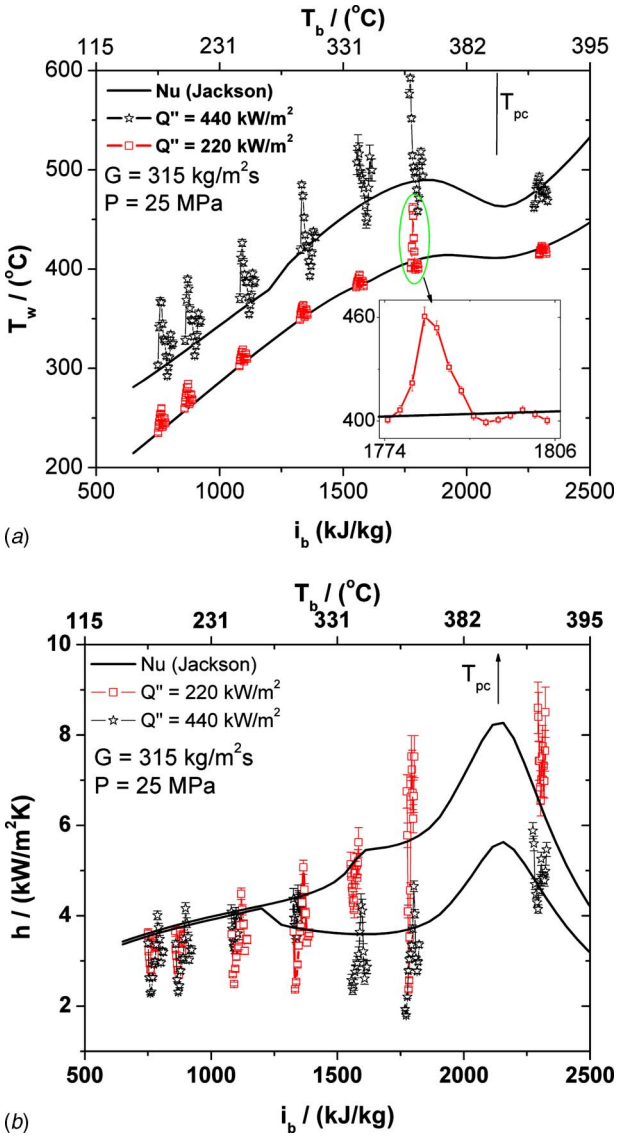

Fig. 9 Comparison of low mass velocity data with the Nusselt correlation of Jackson et al. [33]: (*a*) wall temperature and (*b*) heat transfer coefficient

mixed convection region. The heat transfer is now susceptible to buoyancy effects and is dependent on flow direction. In upward flow, the experimental heat transfer initially falls below that predicted by Nu_{Ja}. Further increasing the $Gr/Re^{2.7}$ leads to conditions where the heat transfer is greater than that predicted by Nu_{Ja}. In downward flow, the heat transfer is better than that predicted by Nu_{Ja}. The 10^{-5} criterion limit suggested by Hall [3] was found to successfully identify the boundary between forced and mixed convection heat transfer for the circular annular geometry data. For the square annular geometry, Fig. 7 shows that all high mass velocity experiments are in the forced convection region and should be free of buoyancy effects. The low mass velocity experiments are mostly in the mixed convection region suggesting that buoyancy effects should be present, even at a low heat flux. Based on these results, the heat transfer experiments can be classified as forced convection (high mass velocity) and mixed convection data (low mass velocity).

For the high mass velocity data, the T_w and average heat transfer coefficient versus bulk enthalpy and temperature along with T_w predictions using Nu_{Ja} are plotted in Fig. 8. The large hydraulic diameter in combination with the mass flux and heat flux results in a small enthalpy rise for a given inlet temperature. This results in a similar T_b and enthalpy along the heated section for a given set of experimental conditions. In forced convection heat transfer (Fig. 8(*a*)), good agreement is found between the measured data and that predicted by Nu_{Ja} for T_b's spanning the T_{pc}. The inserted figure shows that there is a normal T_w distribution successfully predicted by Nu_{Ja}. Due to the similarity in the axial heat transfer coefficient, an average value is used to represent each T_b and heat flux experiment (Fig. 8(*b*)). The heat transfer coefficient exhibits an enhancement in heat transfer at T_b's near the T_{pc} and its magnitude depends on the heat flux.

The T_w and heat transfer coefficient versus bulk enthalpy and temperature along with T_w predictions using Nu_{Ja} for a low mass velocity are plotted in Fig. 9. For a heat flux of 440 kW/m^2, severe deterioration represented by large spikes in T_w occurs for all T_b's below the T_{pc}. At a low heat flux, severe deterioration occurs at a T_b of 370 °C; however, based on the buoyancy criterion shown in Fig. 7, deterioration is likely occurring at all but the highest T_b (393 °C). The data show that deterioration in heat transfer is most severe for T_b's slightly below the T_{pc} and the range over which it occurs increases with heat flux. The inserted figure exemplifies the fact that standard Nusselt correlations are

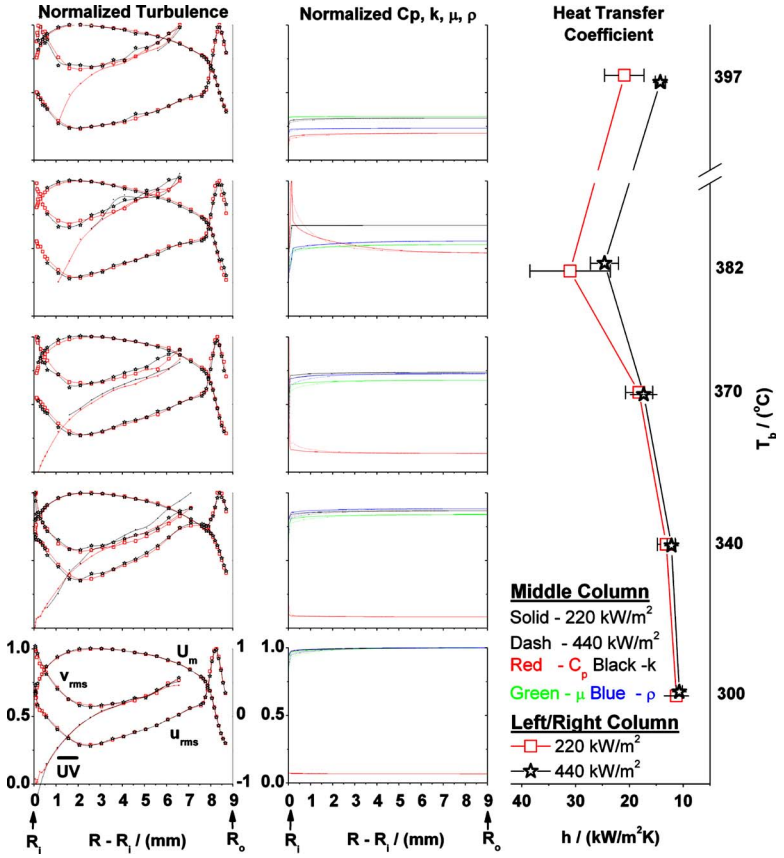

Fig. 10 Forced convection results on a linear scale for view of bulk flow. Left figures: Normalized LDV data. Middle figures: Normalized properties simulated with FLUENT. Right figure: Average of measured integral heat transfer coefficient.

not able to capture the large localized T_w spikes seen in buoyancy-affected flows. Figure 9(*b*) shows that, in addition to the localized reduction in heat transfer, the heat transfer coefficient is dependent on the heat flux, similar to the high mass velocity data.

For the data presented in Table 1, the water was seeded with 1 μm diameter aluminum oxide particles as required for the LDV measurements. The effect of seeded particles on deteriorated heat transfer was investigated at a pressure of 25 MPa, a mass flux of 290 kg/m^2 s, a bulk inlet temperature of 175°C, and a heat flux of 440 kW/m^2. The particle concentration was altered from approximately 0 to 4×10^{-3}% resulting in data rates up to 1 kHz. There was no measurable difference in heat transfer at these conditions. No seeding particle effects were measured until much later, when an experiment was performed at a similar set of conditions, but at a T_b=300°C.

It was found that at T_b's >300°C, a noticeable but very thin coating of particles would build up on the heated section of the heater rod over a time period of approximately 6 h. In addition, close inspection of the heater rod revealed several spots of small but visible particle agglomerations with coating patterns, indicating induced turbulence several centimeters in length along the downstream side of their location. Based on the observed effects, there does not appear to be an enhancement in heat transfer similar to that seen in fluids seeded with nanometer-sized particles [28]. Ultimately, it was found that for T_b's >300°C, small amounts of particles resulting in data rates less than ~300 Hz could be added to the water without altering the heat transfer. Additionally, the heater rod was routinely wiped down to remove any particle buildup.

Regardless of the addition of particles to the water, the heat transfer data presented here are consistent with the results found in the circular annular geometry data presented in Ref. [21]. What follows is the results and discussion of this heat transfer data coupled with CFD simulations and mean and turbulent velocity measurements.

4.2 Forced Convection Heat Transfer. The experimentally measured heat transfer coefficients and mean and turbulent velocities, along with fluid properties simulated with the CFD code FLUENT, are shown in Figs. 10 and 11 for the high mass velocity data. For each T_b (vertical axis of rightmost plot), the average *axial* heat transfer coefficient (right plot) is shown along with the *radial* plots of the normalized physical properties (middle column) and normalized mean and turbulent velocities (left column) at an axial position of 0.5 m downstream from the beginning of the heated section. The simulated properties use the assumption that the temperature varies linearly between the wall and the first mesh node from the wall. For each heat flux and T_b case, the properties (C_p, ρ, k, and μ) are normalized with their maximum value in the temperature range investigated (300–430°C). For both heat flux cases, the mean and turbulent velocities are normalized with their maximum value found in the low heat flux case. The scalings for the U_m, $u_{\rm rms}$, and $v_{\rm rms}$ occupy the left axis while the $\overline{uv}$ scale occupies the right axis. The radial scaling of the fluid properties and turbulence in Fig. 10 allows for visualization of the bulk flow, while Fig. 11 shows the same data with a log scale to emphasize the near wall region.

For a T_b=300°C, the heat transfer coefficient is independent of heat flux. This is a typical characteristic of constant property heat transfer data. From the radial fluid property plots, it is evident that at this T_b the properties are not varying significantly in the bulk or near wall region. Additionally, there are no measurable differences

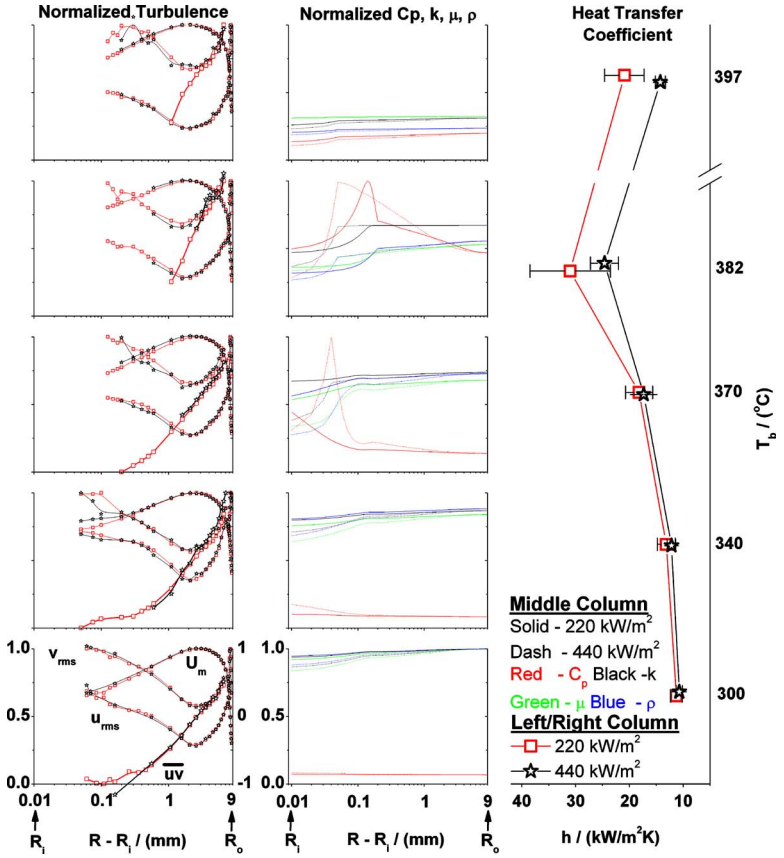

Fig. 11 Forced convection results on a log scale for view of near wall region. Left figures: Normalized LDV data. Middle figures: Normalized properties simulated with FLUENT. Right figure: Average of measured integral heat transfer coefficient.

in the bulk or near wall region for the measured quantities U_m, u_{rms}, v_{rms}, or $\overline{uv}$. At a T_b=340°C, the heat transfer coefficient is still independent of heat flux, but changes in the near wall properties are beginning to develop.

For a T_b=370°C, there is no difference in the average heat transfer coefficient for the heat flux cases shown even though the radial profile of the c_p varies differently for each. Jackson [6] suggested that the viscosity and conductivity likely only play a small role in the heat transfer. While a reduction in μ reduces the thickness of the conduction layer, this is associated with a reduction in k increasing the thermal resistance. In the circular annular data presented earlier in Ref. [21], there was a significant dependence of the heat transfer coefficient at higher heat fluxes. It is commonly stated that increasing the heat flux reduces the enhancement, but this is not always true for when the $T_b < T_{\mathrm{pc}}$. For example, at a T_b=370°C and a low heat flux, the T_w is still well below the T_{pc}. As the heat flux is increased, the near wall fluid temperature increases toward the T_{pc}, causing the c_p of the near wall fluid to increase. This allows the near wall fluid to absorb more energy for a given temperature increase. This results in a reduction in the temperature difference between the wall and the bulk, and hence an increased heat transfer coefficient. For the experimental conditions investigated here, the range of heat flux for which this occurs is small. Further increasing the heat flux produces enough energy input to overcome the large values of c_p, resulting in a temperature gradient that spans the T_{pc}. As a result the c_p peak becomes localized within the fluid, causing a reduction in the integrated effect of the c_p and hence the heat transfer coefficient. Upon close inspection, these effects can be seen in previous integral heat transfer experiments [5]. The two heat flux cases studied here produce a similar integrated effect of the c_p. Based on this description, a reduction below 220 kW/m^2 or increase above 440 kW/m^2 would cause a reduction in heat transfer at a T_b of 370°C. Despite the significant changes in the properties, there are again no measurable changes in the mean velocity or turbulence profiles. This suggests that the radial changes in density do not play a significant role in the velocity and turbulence in forced convection heat transfer. This also suggests that the changes in the specific heat do not play a role in the velocity and turbulence, even though it does affect the overall heat transfer. It can also be seen that as the T_b increases there is a reduction in the range in which turbulence measurements can be made near the heated wall region. This inability to acquire data in the near heated wall region is likely due to the changes in the fluid density. This could result in a reduction in the seeding density and/or index of refraction changes causing the beam crossing to be decoupled.

The reduction in enhancement with an increase in heat flux is always true for cases where the $T_b > T_{\mathrm{pc}}$. The reason for this can be seen in the property plot shown for the 397°C case. Since the T_b of the fluid has passed beyond the T_{pc}, the highest c_p will always be in coolant away from the heated wall, since any increase in heat flux will reduce the c_p in the near wall region. The integrated effect of the c_p can be estimated to be about 20% higher for the low heat flux case. Again, there are no measurable differences in velocity or turbulence.

The T_b at which the largest enhancement occurs will be dependent on the Reynolds number and heat flux and be located at a T_b slightly below the T_{pc}. Of the T_b's investigated, the largest heat transfer coefficient was located at 382°C. The large values of c_p

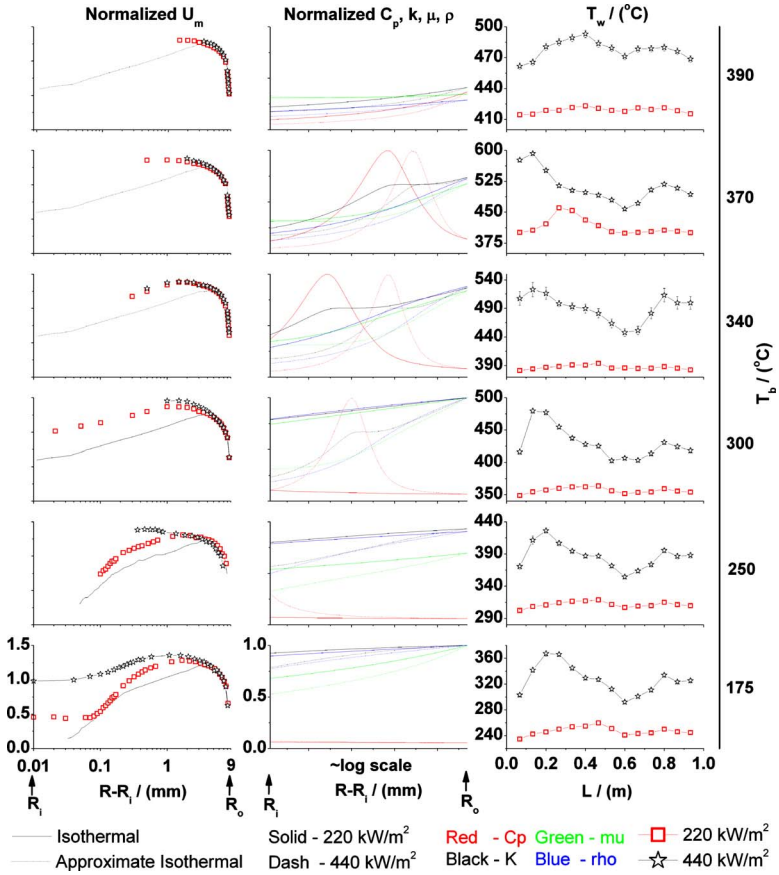

Fig. 12 Mixed convection results on a log scale for view of near wall region. Left column: Normalized LDV data. Middle column: Estimation of normalized property profiles based on measured T_b and T_w. Right column: Axial wall temperature distribution.

in the near wall and bulk regions are well depicted in the property plots. Despite the variability in the properties, there are again no measurable changes in mean and turbulent velocities. The results presented here strongly support that it is the c_p that influences the heat transfer coefficient at high mass velocities.

4.3 Mixed Convection Heat Transfer. Plots similar to Fig. 11 were created for the low mass velocity data (Fig. 12). For each T_b (far right scale) a plot of the axial T_w profile (right column) is displayed along with the radial plots of the normalized physical properties (middle column) and normalized $\bar{U}$ (left column) at an axial position of 0.5 m. The mean axial velocities are normalized with the mean isothermal bulk velocity. At temperatures above 300°C, the isothermal velocity measurements were not possible so the normalized isothermal case measured at 300°C is plotted for higher temperature cases as an estimate. Because CFD simulations are not capable of accurately simulating the mixed convection experiments performed here, the radial property information was based on the measured bulk and T_w. The scaling from the inner wall to the outer wall was approximated with a linear scaling of constant increments of enthalpy. This scaling gives an approximate log scaling of the properties. Comparing this method with the FLUENT simulations for the high mass velocity data suggests that this is a reasonable approximation. For each heat flux and T_b case, the properties (C_p, ρ, k, and μ) are normalized with their maximum value in the temperature range investigated (175–600°C).

The deterioration in heat transfer is easily recognized for the high heat flux case for a T_b=175°C. The T_w increases up to ~376°C at 0.2 m and then begins to decrease to a minimum of ~300°C at 0.6 m. Following this, the T_w begins to increase again. The low heat flux case exhibits a similar but less pronounced T_w profile with the peak reaching 256°C at an axial location slightly less than 0.5 m. Based on Jackson's criterion, buoyancy effects due to radial gradients in density are present for both heat flux cases. The estimated radial density profiles show that this is true at the location of the LDV measurements. The buoyancy forces acting on density profile cause an increase in the velocity in the near wall region. This causes the peak velocity to shift toward the heated wall and increase in magnitude relative to the isothermal profile.

At a T_b=250°C, a similar T_w profile is seen for both heat fluxes compared with the case where the T_b=175°C. This is especially interesting for the higher heat flux case since the maximum T_w reaches 426°C, exceeding the T_{pc}. This means that the fluid temperature radially spans the T_{pc} for some portions of the axial heated length. For a T_b=175°C, the T_w never exceeded ~376°C. In fact, a very similar profile in heat transfer is seen at all T_b's, with the only difference being the severity. For mild cases of deterioration, the peak in T_w occurs further downstream. An increase in severity causes the peak to increase and shift upstream. This effect has been seen in previous experiments by Watts [29].

Trends in the axial T_w and U_m (especially for the T_b=175 and 250°C) suggest that a similar deterioration process occurs regardless of whether or not the T_w exceeds the T_{pc}. To understand this, it is again assumed that the conductivity and viscosity effects cancel. While a radial density gradient is seen for both T_b=175 and 250°C, the 250°C case sees a large variation in the c_p in some portions of the flow. The reason the c_p may not play an

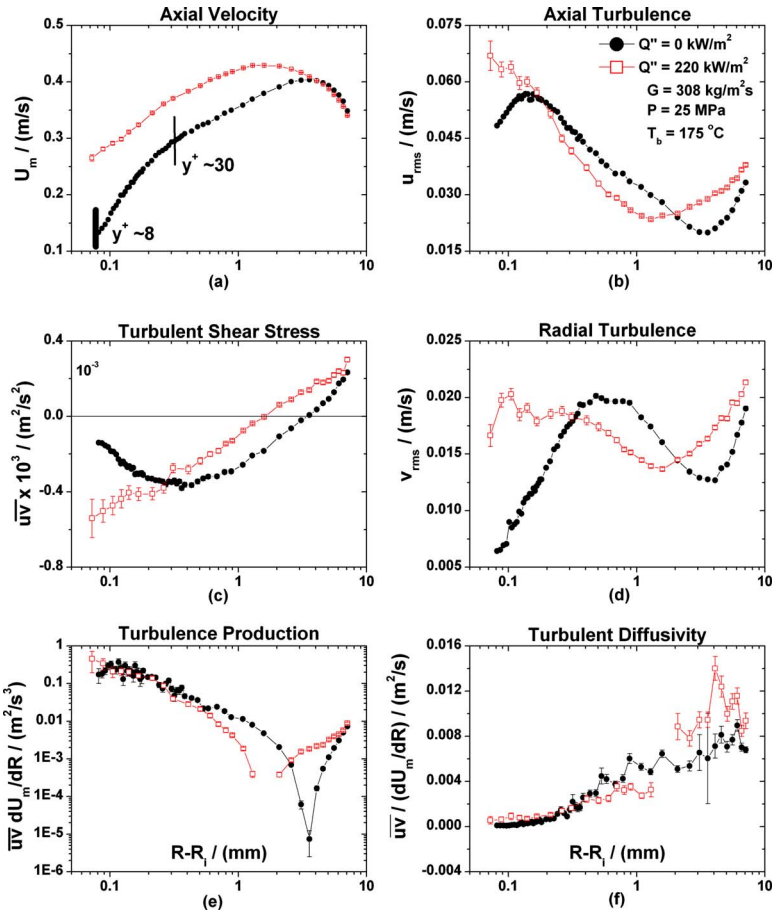

Fig. 13 Detailed LDV measurements comparing isothermal and low heat flux conditions at an axial location of 0.5 m for conditions of 175°C, 25 MPa, and 308 kg/m^2 s

important role in deterioration is that the temperature gradient is large between the bulk of the flow and the wall; thus the integrated effects of the c_p are small.

The axial velocity data in Fig. 12 show that both an increase in heat flux and an increase in the T_b decreases the range in which LDV measurements can be acquired. Because of this, a detailed analysis is given for the isothermal and 220 kW/m^2 case when the T_b=175°C so that changes in the turbulence causing deterioration can be understood. While only this case is shown here, detailed data are available for all T_b's. Figure 13 shows the measured U_m, u_{rms}, v_{rms}, and $\overline{uv}$ profiles radially from the heater rod to the outer window at an axial location of 0.5 m. From these data, the turbulence production $[\overline{uv}\cdot(dU_m/dR)]$ and the turbulent diffusivity $[\overline{uv}/(dU_m/dR)]$ profiles can also be calculated. These data were collected at the same conditions as the data plotted in Fig. 12 with the exception that an extra effort was given to increase the number of radial measurements and data collection times were extended to reduce measurement uncertainty in the near wall region. Additionally, a FLUENT simulation was used to estimate a radial temperature profile for a similar T_b and T_w when a heat flux is present. From this, a beam-tracing program was used to correct the radial scaling of the data, which is effected by radial changes in the index of refraction.

Because water has constant properties for the isothermal case, the shape of the U_m profile on a log scale indicates the important regions defined in nondimensional scaling [30] (Fig. 13(*a*)). The boundary between the law of the wall region and the buffer layer is at $y^+\approx 30$ while the nearest wall measurement is at $y^+\approx 8$, very near the boundary between the buffer layer and viscous sublayer. When deterioration is present, buoyancy effects have increased the U_m in the near wall region relative to the isothermal case. Very similar changes in turbulent velocities occur, as seen in Figs. 13(*b*)–13(*d*). Turbulence values in the bulk of the flow are increased above the isothermal case. Moving toward the inner wall, turbulence values become lower than the isothermal case. In the very near wall region, the turbulence values again increase above the isothermal values.

To better understand the physical importance of these trends, the turbulent production and turbulent diffusivity of momentum are shown in Figs. 13(*e*) and 13(*f*). In the very near wall region ($0\approx 0.5$ mm), the turbulent production and diffusivity are equal to or greater than the isothermal case. In nondimensional units, this occurs out to a distance of $y^+\approx 50$. Further out into the flow, the values are less than the isothermal case. Each figure is missing a data point at ~2 mm from the inner wall. This is due the fact that the $\overline{uv}$ and velocity gradient used in the calculation are essentially zero; this in addition to the associated uncertainties results in an erroneous data point. Progressing further into the bulk of the flow, the values are again larger than in the isothermal case. The effects on the diffusion of momentum are also likely happening to the diffusion of heat. The turbulent Prandtl number is defined as the ratio of the diffusivity of momentum and heat and is typically assumed to be about 1. Recent measurements by Kang et al. [24] suggest that this assumption holds true for variable property heat transfer. This means that both the diffusivity of momentum and heat are reduced during deterioration at radial position equivalent to what is the law of the wall region for isothermal flow. This means the energy in the very near wall region cannot be diffused

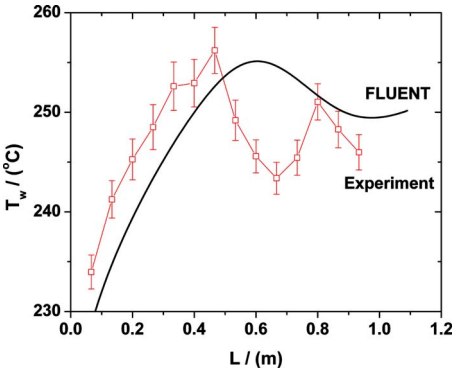

Fig. 14 Comparison of the measured and simulated wall temperature profile exhibiting a relatively small spike in wall temperature

out to the bulk of the flow. While the difference between the deteriorated and isothermal case is not large, it must be remembered that the measurements are made at an axial location where the heat transfer is beginning to improve and the T_w is starting to decrease.

While it is possible to make measurements at different axial locations, this work has not yet been carried out. However, for this "simple" case of deterioration where the property variations are small, FLUENT can be used to better understand the LDV measurements and the deterioration process. At this time, simulations with an enhanced wall treatment were not successful so the simpler standard wall function method was used with the Reynolds stress model. Figure 14 compares the experimental T_w profile with the FLUENT results for a similar set of conditions ($G=290$ kg/m^2 s, $T_b=175°$C, and $Q''=220$ kW/m^2). FLUENT comes close to predicting the T_w variation; however, the location of the maximum T_w is shifted downstream from the measured results and the recovery of heat transfer after the temperature peak is not as dramatic in the simulation. The simulation also shows the start of a second increase in T_w.

The mean and turbulent velocity data were measured at an axial location of 0.5 m, which is slightly downstream of the measured peak in T_w. Thus the experimental data approximately correspond to the FLUENT results at an axial location 0.7 m, which is a similar location with respect to the T_w profile. It turns out that there is very good qualitative agreement in trends when comparing FLUENT results with velocities and turbulence shown in Fig. 13. The experimental data and the simulations show that buoyancy effects cause a significant reduction in turbulence values at a radial location similar to what is the law of the wall region for isothermal flow. This causes a reduction in the diffusivity of momentum and heat, preventing the transport of thermal energy from the near wall region to the bulk of the flow.

Further insight of the deterioration process can be gained by investigating the evolution of the turbulence along the heated section. Figure 15(*a*) shows the axial T_w as predicted by FLUENT. In increments of 0.2 m, the vertical lines represent the location where radial plots of fluid temperature, U_m, $\overline{uv}$, and turbulent diffusivity are shown.

The fact that deterioration occurs in mixed convection heat transfer is quite clear when considering simulations of the turbulence evolution along the heated wall in Fig. 15. The process can be broken up into three parts.

First part. As the fluid enters the heated section, the near wall fluid begins to increase in temperature. This increase in temperature is associated with a decrease in density. Because the near wall density is lower than the density of the fluid in the bulk of the flow, the near wall velocity begins to increase due to buoyancy forces. This initially forms a flatter velocity profile, meaning that the velocity gradient is moved to the very near wall region where molecular viscosity effects dominate. The lack of velocity gradient in the typical law of the wall region drastically reduces the diffusion of momentum and heat to the bulk of the flow, causing the wall and near wall fluid to further increase in temperature, further increasing the density difference. The axial evolution of the fluid temperature profile (from 0.2 m to 0.4 m) indicates that as the turbulent diffusion is reduced, the temperature within ~1.1 mm increases while the bulk fluid remains a similar temperature. The evolution of the axial T_w is initially a self-induced growth in deterioration.

Second part. As the wall and near wall fluid temperatures increase and buoyant forces further act on the fluid, the peak velocity increases and shifts toward the heated wall. The velocity gradient between ~1 mm and 4 mm goes from a flattened profile at axial position of 0.2 m to a profile with a significant increase in velocity gradient at 0.6 m. This transition causes the diffusion in the bulk of the flow to increase and expand into the near wall region. The increased diffusion allows the energy to be removed from the near wall region causing the wall and near wall fluid temperatures to decrease and the bulk fluid temperature to increase (temperature profile at 0.6 mm and 0.8 mm). As a consequence, the density difference between the inner and outer walls decreases, reducing the buoyancy force. As the peak velocity decreases and shifts away from the inner wall, the diffusivity will begin to decrease again, although its changes lag behind the changes in the velocity gradient. This decrease in diffusivity will again cause the T_w to increase, explaining the oscillatory shape of the T_w for both simulation and experiment. For large hydraulic diameter experiments, the T_b is not increasing significantly so these oscillatory changes in velocity gradient and diffusivity could continue in the axial direction. This type of T_w profile can be seen in experiments by Kenning et al. [31].

Third part. The radial gradient in density is lost as the bulk fluid temperature passes through the T_{pc}. The loss of density difference forces the velocity gradient to pass through a flattened profile to reach a velocity profile similar to that seen in isothermal flow. Thus it would be expected to see a T_w increase due to this effect. In an experiment performed by Hall et al. [32], a large localized spike in T_w occurred near the beginning of the heated section. Following this, as the bulk carbon dioxide temperature approached the T_{pc}, a more broadly shaped T_w increase was seen. Burke and Pulling [13] measured a similar T_w profile but also measured radial U_m profiles at several axial locations. The initial increase in T_w was caused by a flattening in the U_m gradient (first part) followed by a recovery in the heat transfer as the peak in the U_m increased and shifted toward the heated wall (second part). As the bulk fluid temperature increased toward the T_{pc}, a more gradual decrease in the heat transfer coefficient was observed and is associated with a transition of the U_m back to the typical profile seen in isothermal flow (third part).

Jackson et al. [33] used the LDV technique to measure turbulence characteristics in low-pressure water flowing through an annular geometry in which heat transfer on the inner wall exhibited deterioration. The trends found in the study of Jackson et al. [33] are very similar to the results presented in this paper, with the exception that when a heat flux was imposed on the fluid, their measured turbulence values decreased relative to the isothermal case in the entire near wall region. Wang et al. [34] performed CFD simulations of mixed convection heat transfer to air in a vertical plane passage and found results similar to that of Jackson et al. [33]. However, because of the properties of the fluids used in both of these studies, much lower Reynolds numbers were needed to cause deterioration. The Reynolds number of Jackson et al. [33] ranged from 2000 up to 12,000 compared with a Reynolds number of 35,000 presented in Fig. 13. This small discrepancy in turbulence trends may be simply due to the Reynolds number. While the molecular viscosity dominates in the near wall region, it appears that at higher Reynolds numbers the turbulent transport may be of some importance.

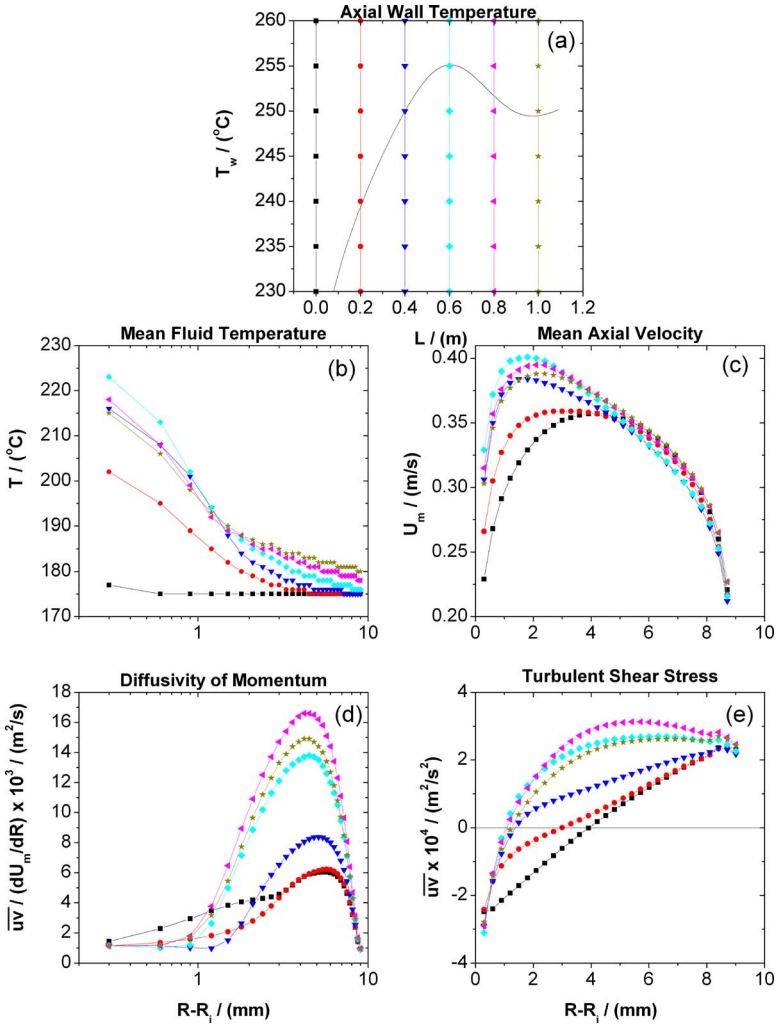

Fig. 15 Simulated evolution of the wall temperature and turbulence parameters at different axial positions; spanning the evolution of the deterioration process

5 Conclusions

Forced convection heat transfer occurs at relatively high mass velocities where the $\mathrm{Gr}/\mathrm{Re}^{2.7} < 10^{-5}$. At these conditions, the Nu correlation of Jackson et al. [33] is capable of adequately predicating the measured wall temperatures.

The heat transfer coefficient exhibits an enhancement in heat transfer for bulk temperatures near the pseudocritical temperature. The magnitude of the enhancement is dependent on the heat flux.

No significant changes in the mean or turbulent velocity profiles were measured with changes in the applied heat flux.

FLUENT simulations were used to produce radial profiles of the fluid properties. Changes in the integrated effect of the specific heat were used to explain changes in the heat transfer coefficient due to changes in the applied heat flux.

Mixed convection heat transfer occurs at relatively low mass velocities where the $\mathrm{Gr}/\mathrm{Re}^{2.7} > 10^{-5}$. At these conditions, standard Nu correlations are not able to predict localized spikes in wall temperature seen in experimental measurements.

Measurements of mean axial velocity profiles and axial wall temperature distributions show similar deterioration profiles regardless of whether the wall temperature exceeds the pseudocritical temperature or not.

Detailed mean and turbulent velocity measurements show that the turbulence, diffusivity of momentum, and likely the diffusivity of heat are reduced during deterioration at a radial position equivalent to what is the law of the wall region for isothermal flow.

For the simple case of deterioration investigated in detail, FLUENT simulations offered qualitative insight into changes in fluid temperature and turbulent velocities responsible for the axial evolution of the wall temperature.

Acknowledgment

This work was performed under the DOE NEER Grant No. DEFC07-04ID14602 and DOE Contract No. 00037404. The authors would also like to acknowledge the help of Mr. Paul Brooks, Mr. Roch Kendrick, and Dr. Carl Martin.

Nomenclature

A = fitting parameter (m^{-4})
B = fitting parameter (m^{-5})
c_p = specific heat (J/kg K)
d = hydraulic diameter (m)
e = bias in MV location (m)
G = mass flux (kg/m^2 s)
g = gravity (m/s^2)
Gr = Grashof number, $(\rho_b - \bar{\rho}) d^3 g / \rho \nu^2$

h = heat transfer coefficient ($W/m^2\,K$)
i = enthalpy (J/kg)
k = thermal conductivity ($W/m\,K$)
L = heated length (m)
N = number
Nu = Nusselt number
$\overline{\mathrm{Pr}}$ = average Prandtl number, $(i_w - i_b/T_w - T_b)(\mu_b/k_b)$
Q'' = heat flux (W/m^2)
R = radius (m)
Re = Reynolds number
T = temperature (°C)
U, V = velocity, axial, radial (m/s)
U_τ = friction velocity (m/s)
u, v, w = fluctuating velocity; axial, radial, azimuthal (m/s)
$\overline{uv}$ = turbulent shear stress (m^2/s^2)
X = τ_{wo}/τ_{wi}
y^+ = nondimensional distance, $U_\tau(R-R_i)/\nu$

Greek Symbols

μ = dynamic viscosity ($kg/m\,s$)
ρ = density (kg/m^3)
$\overline{\rho}$ = average density, $(1/(T_w - T_b))\int_{T_b}^{T_w}\rho dT$ (kg/m^3)
σ = percent error, uncertainty divided by the mean $\times 100$ (%)
τ = shear stress ($kg/m\,s^2$)
ν = kinematic viscosity (m^2/s)

Subscripts

b = bulk
exp = experiment
i = inner wall
Ja = Jackson
m = mean
o = outer wall
pc = pseudocritical temperature
rms = root mean square
w = wall

References

[1] U.S. Department of Energy, Nuclear Energy Research Advisory Committee, Generation IV International Forum, 2002, "A Technology Roadmap for the Generation IV Nuclear Energy Systems," GIF-002-00, http://gif.inel.gov/roadmap/pdfs/gen_iv_roadmap.pdf.

[2] Pioro, I. L., 2006, *Heat Transfer and Hydraulic Resistance at Supercritical Pressure in Power-Engineering Applications*, ASME, New York.

[3] Hall, W. B., 1975, "Forced Convective Heat Transfer to Supercritical Pressure Fluids," Archiwum Termodynamiki i Spalania, **6**(3), pp. 341–352.

[4] Jackson, J. D., and Hall, W. B., 1979, "Forced Convection Heat Transfer to Fluids at Supercritical Pressure," *Turbulent Forced Convection in Channels and Bundles*, Vol. 2, Hemisphere, New York, pp. 563–611.

[5] Yamagata, K., Nishikawa, K., Hasegawa, S., and Fujii, T., 1972, "Forced Convective Heat Transfer to Supercritical Water Flowing in Tubes," Int. J. Heat Mass Transfer, **15**(12), pp. 2575–2593.

[6] Jackson, J. D., 2001, "Some Striking Features of Heat Transfer With Fluids at Pressures and Temperatures Near the Critical Point," *Proceedings of the International Conference on Energy Conversion and Application*, Wuhan, China, pp. 50–61.

[7] Seo, K. W., 2005, "Heat Transfer Mechanism in Supercritical Fluids: Analysis and Model Developments," Ph.D. thesis, Pohang University, Pohang.

[8] Shiralkar, B., and Griffith, P., 1970, "The Effect of Swirl, Inlet Conditions, Flow Direction and Tube Diameter on the Heat Transfer to Fluids at Supercritical Pressure," ASME J. Heat Transfer, **92**, pp. 465–474, ASME Paper No. 69-WA/HT-1.

[9] Jackson, J. D., 2007, "A Semi-Empirical Model of Forced Convection Heat Transfer to Fluids at Supercritical Pressure," The Third International Symposium on Supercritical Water-Cooled Reactors—Design and Technology, Shanghai, China, Paper No. SCR2007-1010.

[10] Jackson, J. D., and Hall, W. B., 1979, "Influence of Buoyancy on Heat Transfer to Fluids Flowing in Vertical Tubes Under Turbulent Conditions," *Turbulent Forced Convection in Channels and Bundles*, Vol. 2, Hemisphere, New York, pp. 613–640.

[11] Shitsman, M. E., 1963, "Impairment of the Heat Transmission at Supercritical Pressures," High Temp., **1**(2), pp. 237–244.

[12] Wood, R. D., and Smith, J. M., 1964, "Heat Transfer in the Critical Region—Temperature and Velocity Profiles in Turbulent Flow," AIChE J., **10**(2), pp. 180–186.

[13] Bourke, P.J., Pulling, D.J., 1971, "Experimental Explanation of Deterioration in Heat Transfer to Supercritical Carbon Dioxide," ASME Paper No. 71-HT-24.

[14] Miropol'skii, Z. L., and Baugulov, V. I., 1974, "Investigation in Heat Transfer, Velocity and Temperature Profiles With Carbon Dioxide Flow in a Tube Over the Nearly Critical Region of Parameters," Tribune du CEBEDEAU (FC4. 12), pp. 177–181.

[15] Kurganov, V. A., Ankudinov, V. B., and Kaptil'nyi, A. G., 1986, "Experimental Study of Velocity and Temperature Fields in an Ascending Flow of Carbon Dioxide at Supercritical Pressure in a Heated Vertical Tube," High Temp., **24**(6), pp. 811–818.

[16] Petukhov, B. S., and Polyakov, A. F., 1988, *Heat Transfer in Turbulent Mixed Convection*, Hemisphere, New York.

[17] Jackson, J. D., 2006, "Studies of Buoyancy-Influenced Turbulent Flow and Heat Transfer in Vertical Passages," *Proceedings of the 13th International Heat Transfer Conference*, Sydney, Australia, Paper No. KN-24.

[18] Kang, S., Patil, B., Zarate, J. A., and Roy, R. P., 2001, "Isothermal and Heated Turbulent Upflow in a Vertical Annular Channel—Part I. Experimental Measurements," Int. J. Heat Mass Transfer, **44**(6), pp. 1171–1184.

[19] Wardana, I. N. G., Ueda, T., Kurihara, S., and Mizomoto, M., 1999, "Turbulence Structure in an Annuli With Strongly Heated Inner Cylinder," Exp. Fluids, **27**(2), pp. 137–144.

[20] Licht, J. R., 2008, "Heat Transfer and Fluid Flow Characteristics in Supercritical Water," Ph.D. thesis, University of Wisconsin-Madison, Madison.

[21] Licht, J., Anderson, M., and Corradini, M., 2008, "Heat Transfer to Water at Supercritical Pressures in Circular and Square Annular Flow Geometry," Int. J. Heat Fluid Flow, **29**(1), pp. 156–166.

[22] Allex, P., 2006, "Density Measurements Using Raman Scattering Photometry in Supercritical Water, MS thesis," University of Wisconsin-Madison, Madison.

[23] Menon, R., and Lai, W. T., 1991, "Key Considerations in the Selection of Seed Particles for LDV Measurements," *Proceedings of the Fourth International Conference on Laser Anemometry*, Cleveland, OH, pp. 719–730.

[24] Kang, S., Patil, B., and Roy, R. P., 2001, "Effects of Coincidence Window and Measuring Volume Size on Laser Doppler Velocimetry Measurements of Turbulence," Exp. Fluids, **30**(4), pp. 365–370.

[25] Durst, F., Kikura, H., Lekakis, I., Jovanovic, J., and Ye, Q., 1996, "Wall Shear Stress Determination From Near-Wall Mean Velocity Data in Turbulent Pipe and Channel Flows," Exp. Fluids, **20**(6), pp. 417–428.

[26] 2006, FLUENT 6.3 User's Guide, Sec. 12.10.1.

[27] Benedict, L. H., and Gould, R. D., 1996, "Towards Better Uncertainty Estimates for Turbulence Statistics," Exp. Fluids, **22**(2), pp. 129–136.

[28] Keblinski, P., Eastman, J. A., and Cahill, D. G., 2005, "Nanofluids for Thermal Transport," Mater. Today, **8**(6), pp. 36–44.

[29] Watts, M. J., and Chou, C. T., 1982, "Mixed Convection Heat Transfer to Supercritical Pressure Water," *Proceedings of the Seventh International Heat Transfer Conference*, Munich, Germany, pp. 495–500.

[30] Kays, W. M., 1980, *Convective Heat and Mass Transfer*, McGraw-Hill, New York.

[31] Kenning, D. B. R., Shock, R. A. W., and Poon, J. Y. M., 1974, "Local Reductions in Heat Transfer Due to Buoyancy Effects in Upward Turbulent Flow," *Proceedings of the Fifth International Heat Transfer Conference*, Tokyo, Japan, pp. 139–143.

[32] Hall, W. B., and Jackson, J. D., 1969, "Laminarization of Turbulent Pipe Flow by Buoyancy Forces," ASME Paper No. 69-HT-55.

[33] Jackson, J. D., Xu, Z., and Wu, T., 2003, "On the Influence of Buoyancy on Turbulence Production and Effectiveness of Heat Transfer in Vertical Flows," *Turbulence, Heat and Mass Transfer 4*, K. Hanjalić, Y. Nagano, and M. Tummers, eds., Begell House, New York, pp. 837–844.

[34] Wang, J., Li, J., He, S., and Jackson, J. D., 2004, "Computational Simulations of Buoyancy-Influenced Turbulent Flow and Heat Transfer in a Vertical Plane Passage," Proc. Inst. Mech. Eng., Part C: J. Mech. Eng. Sci., **218**(11), pp. 1385–1397.

Natural Convection in an Anisotropic Porous Enclosure Due to Nonuniform Heating From the Bottom Wall

Ashok Kumar

P. Bera[1]
e-mail: pberafma@iitr.ernet.in

Department of Mathematics,
Indian Institute of Technology,
Roorkee 247667, India

A comprehensive numerical investigation on the natural convection in a hydrodynamically anisotropic porous enclosure is presented. The flow is due to nonuniformly heated bottom wall and maintenance of constant temperature at cold vertical walls along with adiabatic top wall. Brinkman-extended non-Darcy model, including material derivative, is considered. The principal direction of the permeability tensor has been taken oblique to the gravity vector. The spectral element method has been adopted to solve numerically the governing conservative equations of mass, momentum, and energy by using a stream-function vorticity formulation. Special attention is given to understand the effect of anisotropic parameters on the heat transfer rate as well as flow configurations. The numerical experiments show that in the case of isotropic porous enclosure, the maximum rates of bottom as well as side heat transfers (Nu_b and Nu_s) take place at the aspect ratio, A, of the enclosure equal to 1, which is, in general, not true in the case of anisotropic porous enclosures. The flow in the enclosure is governed by two different types of convective cells: rotating (i) clockwise and (ii) anticlockwise. Based on the value of media permeability as well as orientation angle, in the anisotropic case, one of the cells will dominate the other. In contrast to isotropic porous media, enhancement of flow convection in the anisotropic porous enclosure does not mean increasing the side heat transfer rate always. Furthermore, the results show that anisotropy causes significant changes in the bottom as well as side average Nusselt numbers. In particular, the present analysis shows that permeability orientation angle has a significant effect on the flow dynamics and temperature profile and consequently on the heat transfer rates.
[DOI: 10.1115/1.3089545]

Keywords: anisotropic porous medium, non-Darcy model, nonuniform heating, spectral element method

1 Introduction

A great deal of research activity in physics has recently been focused on transport in porous media [1,2] because the theory of porous media [3] includes several unsolved problems in the engineering and applied sciences ranging from contaminant transport [4], paper manufacturing [5], geophysics, and petroleum engineering [6] to marine science [7]. Understanding the dynamical evolution of fluid through porous media, due to natural convection, has received a considerable attention from many researchers and is amply documented in the review work of Nield and Bejan [8].

In the framework of the present paper, we refer to the literature pertinent to free convection in a cavity filled with a porous medium, whose four walls have different temperatures or heat fluxes [9–11]. In the broad sense, the above class of problem can be split into two major categories: (i) with uniform boundary conditions and (ii) with nonuniform boundary conditions. The former type of problems has been studied extensively by many researchers [12,13] in isotropic porous media. Except in few papers [14–19], in spite of wide applications in transport of contaminant in saturated soils, migration of moisture in fibrous insulation, and nutrient transfer in sea-bed, natural convection in anisotropic porous medium has not received much attention.

Degan et al. [16] summarized an analytical and numerical study of natural convection in a rectangular cavity filled with a porous medium, where the medium was assumed to be both hydrodynamically and thermally anisotropic. They reported that the heat transfer rate is maximum (minimum) when the porous matrix is oriented with principal axis and with higher permeability parallel (perpendicular) to the vertical direction and also found that large thermal conductivity ratio causes a higher flow intensity but a lower heat transfer. A more detailed investigation on the effect of anisotropy (hydrodynamically as well as thermally) on the natural convection was given by Degan and Vasseur [16] while studying the heat transfer and fluid flow in a vertical slot. It has been found that both permeability ratio and inclination angle of principal axes have a strong influence on the flow structure and the heat transfer rate. Similar results are also reported by Dhanasekaran et al. [17], while studying the natural convection in a cylindrical enclosure. However, the effect of anisotropy on the thermosolutal natural convection in the cavity was investigated by Bera et al. [18]. They found the significant influence of media anisotropy on the flow rate and, consequently, on the heat and mass transfer mechanisms for both buoyancy assisted and opposed cases. Further extensive study on double-diffusive buoyancy opposed natural convection in the cavity by Bera and Khalili [19] reports the existence of multiple steady solutions as well as oscillating unsteady solution in certain range of controlling parameters.

The comprehensive literature review on the above defined second category of natural convection in the enclosure shows that in fluid environments, a good number of papers [20–22] are avail-

[1]Corresponding author.

Contributed by the Heat Transfer Division of ASME for publication in the JOURNAL OF HEAT TRANSFER. Manuscript received March 26, 2008; final manuscript received December 3, 2008; published online May 4, 2009. Review conducted by Jamal Seyed-Yagoobi.

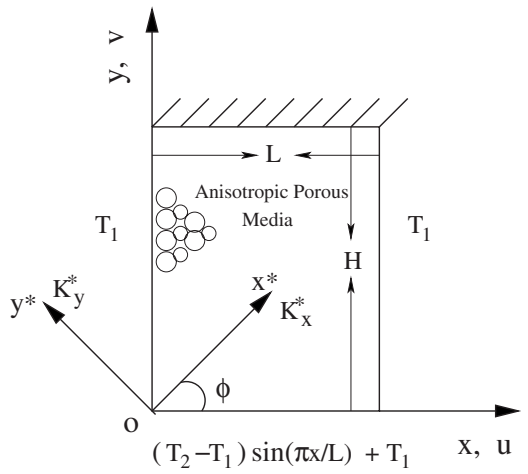

Fig. 1 Schematic of the dimensional physical problem considered

able. However, in porous media very few investigations on natural convection with nonuniform boundary conditions have been reported (e.g., Refs. [23–25]).

Using Darcy model, Saeid [23] studied the natural convection in a porous cavity, in which one of the vertical walls is heated nonuniformly (spatial sinusoidal) and the other is cooled uniformly. He investigated the effect of amplitude on the bottom wall temperature variation and the heat source strength for Ra in the range [20, 500] and found that the average Nusselt number (Nu) increases when the length of the heat source or amplitude of the temperature variation increases.

Basak et al. considered the similar problem in the square cavity with the different boundary conditions: uniformly and nonuniformly heated bottom walls and adiabatic top wall along with uniformly cooling vertical walls. They used the non-Darcy model. Their comparative study revealed that nonuniform heating of the bottom wall produces higher heat transfer rate at the center of the bottom wall than the uniform heating case for the entire range of Rayleigh number mentioned in Ref. [24]. Also the overall heat transfer rate for nonuniform heating case is lower than the uniform one. In the same geometry, Zahmatkesh [25] reported the importance of thermal boundary conditions of the heated/cooled walls in heat transfer and entropy generation characteristics in the isotropic porous medium.

The present paper extends the work of Basak et al. [24] by introducing anisotropy of the porous media. The non-Darcy–Brinkman-extended model has been adopted to simulate the momentum transfer in the porous medium. The spectral element method (SEM) [26,27] has been used to solve the governing mass conservation, momentum, and energy equations by using the vorticity-stream-function approach.

2 Mathematical Formulation

We consider a two dimensional fluid saturated porous medium enclosed in a rectangular cavity of length L and height H, as shown schematically in Fig. 1. It is assumed that the bottom wall is heated nonuniformly, while the top wall is insulated and vertical walls are cooled at constant temperature. The medium is anisotropic in permeability, which may be the consequence of a preferential orientation or asymmetric geometry of the grain in the geothermal system [28–31]. The second order permeability tensor, $\bar{\bar{K}}$, is diagonal in the (ox^*, oy^*) coordinate system with the diagonal components, K_{x^*} and K_{y^*}, respectively. Since the medium is anisotropic, diffusion properties are also anisotropic in nature [28,32]. However, because our main focus is on the influence of anisotropic media permeability on the heat transfer rates in the cavity in order to reduce the number of influencing parameters, isotropic effective thermal diffusivity is considered. We assume that the physical situation is described by local equilibrium model equations. The thermophysical properties of the fluid are assumed to be constant except for the density dependence of the buoyancy body-force term in the momentum equation, which is satisfied by the Boussinesq approximation. Also internal radiation in the porous media is neglected due to low absolute temperature in the cavity. The governing equations for the steady-state flow as well as heat transfer in the Cartesian coordinate system (x,y) are given by

$$\nabla \cdot \mathbf{V} = 0 \tag{1}$$

$$(\mathbf{V} \cdot \nabla)\mathbf{V} = -\frac{1}{\rho}\nabla p + \nu\nabla^2\mathbf{V} - \frac{\nu}{\bar{\bar{K}}}\mathbf{V} - \rho g\mathbf{Q} \tag{2}$$

$$\mathbf{V} \cdot \nabla T = \alpha_e \nabla^2 T \tag{3}$$

$$\rho = \rho_0[1 - \beta_T(T - T_1)] \tag{4}$$

with the boundary conditions

$$u(0,y) = u(L,y) = u(x,0) = u(x,H) = 0$$

$$v(0,y) = v(L,y) = v(x,0) = v(x,H) = 0$$

$$T(x,0) = (T_2 - T_1)\sin\left(\frac{\pi x}{L}\right) + T_1$$

$$T(0,y) = T(L,y) = T_1$$

$$\frac{\partial T}{\partial x} = 0 \quad \text{at} \quad y = H$$

In the above equations, $\mathbf{V}(\mathbf{u},\mathbf{v})$, p, T, α_e, and ρ are the flow velocity, pressure, temperature, effective thermal diffusivity, and fluid density, respectively. The permeability tensor, $\bar{\bar{K}}$, is defined as

$$\bar{\bar{K}} = K_{x^*}\begin{bmatrix} a & c \\ c & b \end{bmatrix}$$

with

$$a = K^* \sin^2\phi + \cos^2\phi, \quad b = K^* \cos^2\phi + \sin^2\phi,$$
$$c = (1 - K^*)\sin\phi\cos\phi$$

where ϕ is the orientation angle. Using nondimensional quantities $X = x/L$, $Y = y/L$, $U = Lu/\alpha_e$, $V = Lv/\alpha_e$, $P = pL^2/\rho\alpha_e^2$, and $\theta = (T - T_1)/(T_2 - T_1)$, the above differential equations can be written as

$$\frac{\partial U}{\partial X} + \frac{\partial V}{\partial Y} = 0 \tag{5}$$

$$U\frac{\partial U}{\partial X} + V\frac{\partial U}{\partial Y} = -\frac{\partial P}{\partial X} + \mathrm{Pr}[\nabla^2 U] - \frac{\mathrm{Pr}}{\mathrm{Da}}(bU - cV) \tag{6}$$

$$U\frac{\partial V}{\partial X} + V\frac{\partial V}{\partial Y} = -\frac{\partial P}{\partial Y} + \mathrm{Pr}[\nabla^2 V] - \frac{\mathrm{Pr}}{\mathrm{Da}}(-cU + aV) + \mathrm{Ra}\ \mathrm{Pr}\ \theta \tag{7}$$

$$U\frac{\partial \theta}{\partial X} + V\frac{\partial \theta}{\partial Y} = \frac{\partial^2 \theta}{\partial X^2} + \frac{\partial^2 \theta}{\partial Y^2} \tag{8}$$

where Ra, Da, K^*, A, and Pr are the Rayleigh number, Darcy number, permeability ratio, aspect ratio, and Prandtl number, respectively.

The momentum equations (6) and (7) may be rewritten in terms of dimensionless vorticity, (ω), and stream function, ψ, as

$$U\frac{\partial \omega}{\partial X}+V\frac{\partial \omega}{\partial Y}=\Pr[\nabla^2\omega]+\frac{\Pr}{\mathrm{Da}}\left[b\frac{\partial^2\psi}{\partial Y^2}+2c\frac{\partial^2\psi}{\partial X\,\partial Y}+a\frac{\partial^2\psi}{\partial X^2}\right]-\mathrm{Ra}\ \Pr\frac{\partial\theta}{\partial X} \tag{9}$$

where

$$\omega\equiv\frac{\partial U}{\partial Y}-\frac{\partial V}{\partial X}=-\frac{\partial^2\psi}{\partial Y^2}-\frac{\partial^2\psi}{\partial X^2}$$

We can obtain ψ from ω by solving the Poisson equation

$$\nabla^2\psi=-\omega \tag{10}$$

The nondimensional boundary conditions over the walls of enclosure are

$$\psi=0,\quad \theta=0,\quad \text{and}\quad \omega=-\frac{\partial^2\psi}{\partial X^2}\quad \text{at}\ X=0$$

$$\psi=0,\quad \theta=0,\quad \text{and}\quad \omega=-\frac{\partial^2\psi}{\partial X^2}\quad \text{at}\ X=1$$

$$\psi=0,\quad \theta=\sin(\pi X),\quad \text{and}\quad \omega=-\frac{\partial^2\psi}{\partial Y^2}\quad \text{at}\ Y=0$$

$$\psi=0,\quad \frac{\partial\theta}{\partial Y}=0,\quad \text{and}\quad \omega=-\frac{\partial^2\psi}{\partial Y^2}\quad \text{at}\ Y=A$$

The rates of heat transfer (Nusselt number (Nu)) along the side as well as bottom walls are determined from the temperature field. The average side and bottom Nusselt numbers, respectively, Nu_s and Nu_b, are defined as follows:

$$\mathrm{Nu}_s=\frac{1}{A}\int_0^A\left[-\frac{\partial\theta}{\partial X}\right]_{X=0}dY \tag{11}$$

$$\mathrm{Nu}_b=\int_0^1\left[-\frac{\partial\theta}{\partial Y}\right]_{Y=0}dX \tag{12}$$

We compute the above integrals in Eqs. (11) and (12) by using Chebyshev–Gauss–Lobatto integration.

2.1 Numerical Solution. The governing partial differential equations (8)–(10), along with hydrodynamic and thermal boundary conditions, are solved by the SEM. In the spectral element method, the computational domain is broken into a number of elements, and within each element the dependent variable is represented as a high-order Lagrangian interpolant in terms of Chebyshev polynomials; the coefficients of which are related to the function values at the Gauss–Lobatto–Chebyshev collocation points. The main advantages of this method are (i) great precision; actually, the approximation error size is only limited by the regularity of the exact solution, and (ii) flexibility in handling complex geometry. The details of this technique and its implication can be found elsewhere [18]. To solve the above governing equations (8)–(10), using spectral element method, a pseudotransient term $(\partial\zeta/\partial t)$ of the corresponding field variable is added in each equation. Then this pseudotransient Cauchy–Kowalewski form of vorticity, stream, and energy equations is discretized by a semi-implicit discretization in which a first-order finite-difference approximation, with time step Δt, is used for the time derivative, the Laplacian term is treated implicitly (using unknown values at time step $n+1$), and all other terms are treated explicitly (using known values at time step n). The time discretized form of the resulting equations is given by a Helmholtz equation of the form

$$\nabla^2\zeta^{(n+1)}-\lambda_\zeta^2\zeta^{(n+1)}=f_\zeta^{(n)} \tag{13}$$

where ζ may represent any one of the fundamental field variables (ω,ψ,θ). Both terms on the left side of Eq. (13) contain unknown values of ζ at the new time step $(n+1)$, while the forcing function f_ζ on the right hand side is evaluated using previous values.

The solution procedure is given as follows.

1. Specify the initial guess for the temperature, vorticity, stream-function, and velocities, $n=0$.
2. Solve the energy equation for $(n+1)$th time step.
3. Solve the vorticity equation for $(n+1)$th time step.
4. Solve the stream-function for $(n+1)$th time step.
5. Compute the velocity field and velocity gradient in the solution domain and vorticities at the boundaries.
6. Check the convergence by the criterion

$$\Delta_{\mathrm{rms}}=\sqrt{\frac{\sum_{i=1}^{N_{\mathrm{total}}}[\zeta_i^{n+1}-\zeta_i^n]^2}{N_{\mathrm{total}}}}<\epsilon\Delta\tau \tag{14}$$

update the variables, i.e., $\zeta^n\leftarrow\zeta^{n+1}$, for all variables.

Steps 2–6 are repeated until this convergence condition is satisfied by all variables, ζ.

It has been found that for a single iteration (from Steps 1–6) the real and user times by Hp-Compaq (dx 2280 MT) are 0 m:24.002 s and 0 m:23.057 s, respectively, when the order of Chebyshev polynomials (N,M) is (10,10) and the number of elements (N_X,M_Y) is (3,3). As the order of polynomials (N,M) is changed from (10,10) to (9,9) and the number of elements in the domain is fixed as above, the real as well as user times are reduced to 0 m:10.652 s and 0 m:10.233 s, respectively.

2.2 Validation of Numerical Solution. The validation of our numerical simulation was shown in two ways. First, the independence of the solution was examined for variation in grid size by changing order of polynomials (N,M) in the X and Y directions in each element. We have also made a rigorous numerical experiment on the number of elements (N_X,M_Y) along X and Y directions and chosen the best possible one. Second, results of our special case are compared with the published one.

For the grid independency we have taken different orders of polynomial ranging from 7 to 12 in spectral approximation to find the average Nusselt number at $\mathrm{Ra}=10^6$, $\mathrm{Da}=10^{-4}$, $K^*=1$ and 5, $A=1.5$, and $\phi=45^*$, which is depicted in Table 1. It can be seen that by changing the order of polynomial from 7 to 9, the average Nusselt numbers (Nu_b as well as Nu_s) change from second decimal onward. As the order of polynomial in the approximation is increased from 10 to 12, the results remain consistent, and the accuracy also improved for both isotropic $(K^*=1)$ and anisotropic $(K^*=5)$ cases. Therefore, for the entire numerical computation presented here, (10,10) is considered as the order of polynomials (N,M) in the X and Y directions in each element. From the same table it can also be observed that (3,2) is the best choice of the number of elements (N_X,M_Y) for $A=1.5$. In comparison with published results of Lauriat and Prasad [33] in which they also used the same Brinkman-extended non-Darcy model without Forchheimer term, we have modified our problem by changing boundary conditions suitably. As can be seen from Table 2, the agreement is good. These tests provide a strong validation of our numerical results.

3 Results and Discussions

When media anisotropy is taken into account, the number of governing flow parameters increases drastically compared to an isotropic medium. In the present case, the parameters are K^*, ϕ, and Da. In addition, the problem depends on parameters such as aspect ratio A, Prandtl number Pr, and Rayleigh number Ra.

A rigorous numerical experiment is made to study the effect of different controlling parameters on the average side as well as bottom wall heat transfer rates of the cavity filled with an aniso-

Table 1 Dependence of the heat transfer rate (Nu_b as well as Nu_s) on the number of grid points as well as elements ($Ra=10^6$, $Da=10^{-4}$, $Pr=0.71$, and $\phi=45$ deg)

K^*	A	$N_X \times M_Y$	$N \times M$	Nu_b	Nu_s
5	1.5	3×2	7×7	2.252	0.967
5	1.5	3×2	8×8	2.275	0.965
5	1.5	3×2	9×9	2.299	0.943
5	1.5	3×2	10×10	2.305	0.942
5	1.5	3×2	11×11	2.305	0.941
5	1.5	3×2	12×12	2.306	0.941
5	1.5	1×1	10×10	2.189	0.815
5	1.5	2×2	10×10	2.272	0.887
5	1.5	3×2	10×10	2.305	0.942
5	1.5	3×3	10×10	2.286	0.890
5	1.5	4×2	10×10	2.289	0.947
1	1.5	3×2	7×7	3.912	1.436
1	1.5	3×2	8×8	3.948	1.439
1	1.5	3×2	9×9	4.009	1.438
1	1.5	3×2	10×10	4.013	1.440
1	1.5	3×2	11×11	4.065	1.439
1	1.5	3×2	12×12	4.104	1.440
1	1.5	1×1	10×10	3.844	1.440
1	1.5	2×2	10×10	3.963	1.440
1	1.5	3×2	10×10	4.013	1.440
1	1.5	3×3	10×10	4.013	1.440
1	1.5	4×2	10×10	4.089	1.431

Table 2 Comparison between present and published results

Da	Ra	Lauriat and Prasad [33] (Brinkman-extended)	Present
10^{-6}	10^7	1.07	1.0755
10^{-6}	10^8	3.09	3.0808
10^{-4}	10^5	1.07	1.0752
10^{-4}	10^6	3.09	3.0664

tropic porous medium in terms of Nusselt number. From our numerical experiments it has been found that the effect of Prandtl number, Pr, is negligible when $Ra\,Da \leq 100$ (results are not shown here), which in turn says that the role of nonlinear $(\mathbf{V}\cdot\nabla)\mathbf{V}$ term in the model equation (2) is not significant for the set of parameters chosen here. That is why, in this study, we have fixed

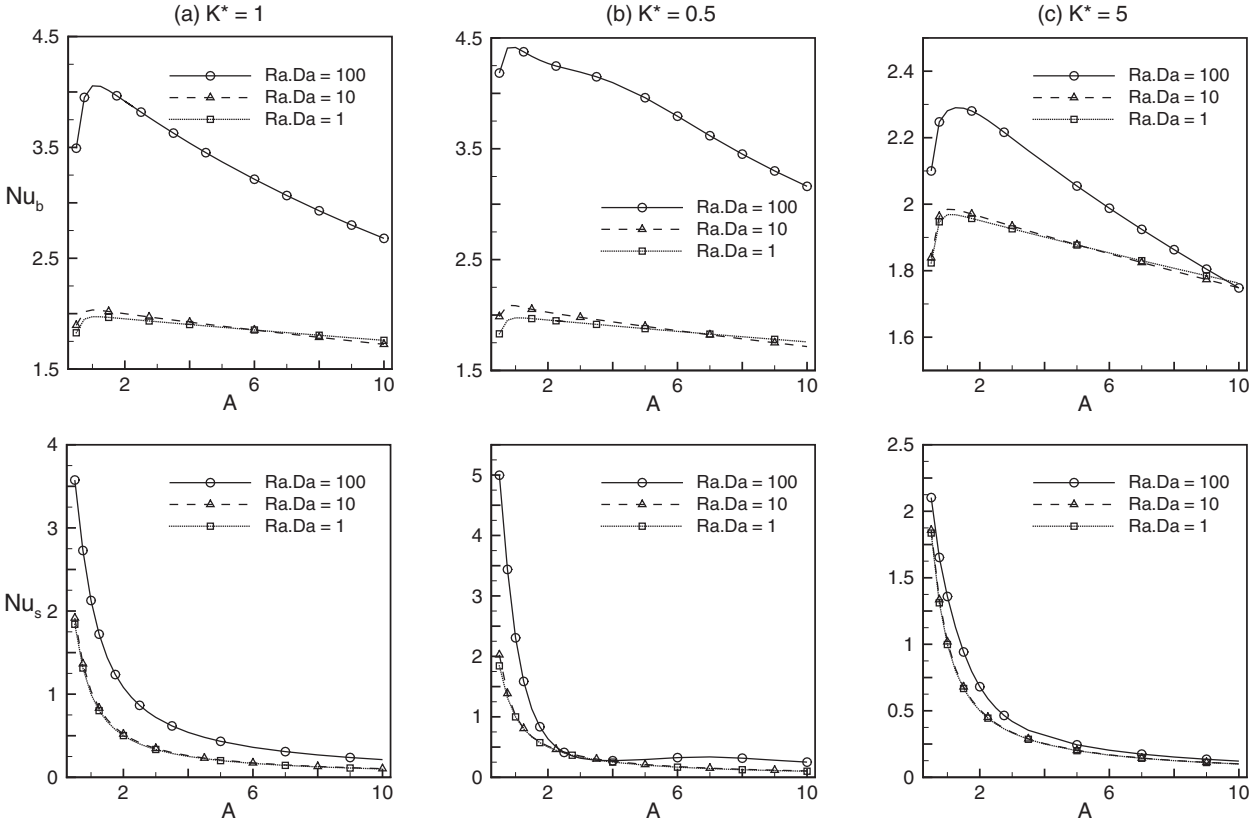

Fig. 2 Variation in average Nusselt numbers (Nu_b as well as Nu_s) as a function of aspect ratio for different values of Ra: (*a*) $K^*=1$, (*b*) $K^*=0.5$, and (*c*) $K^*=5$ when $Da=10^{-4}$ and $\phi=45$ deg

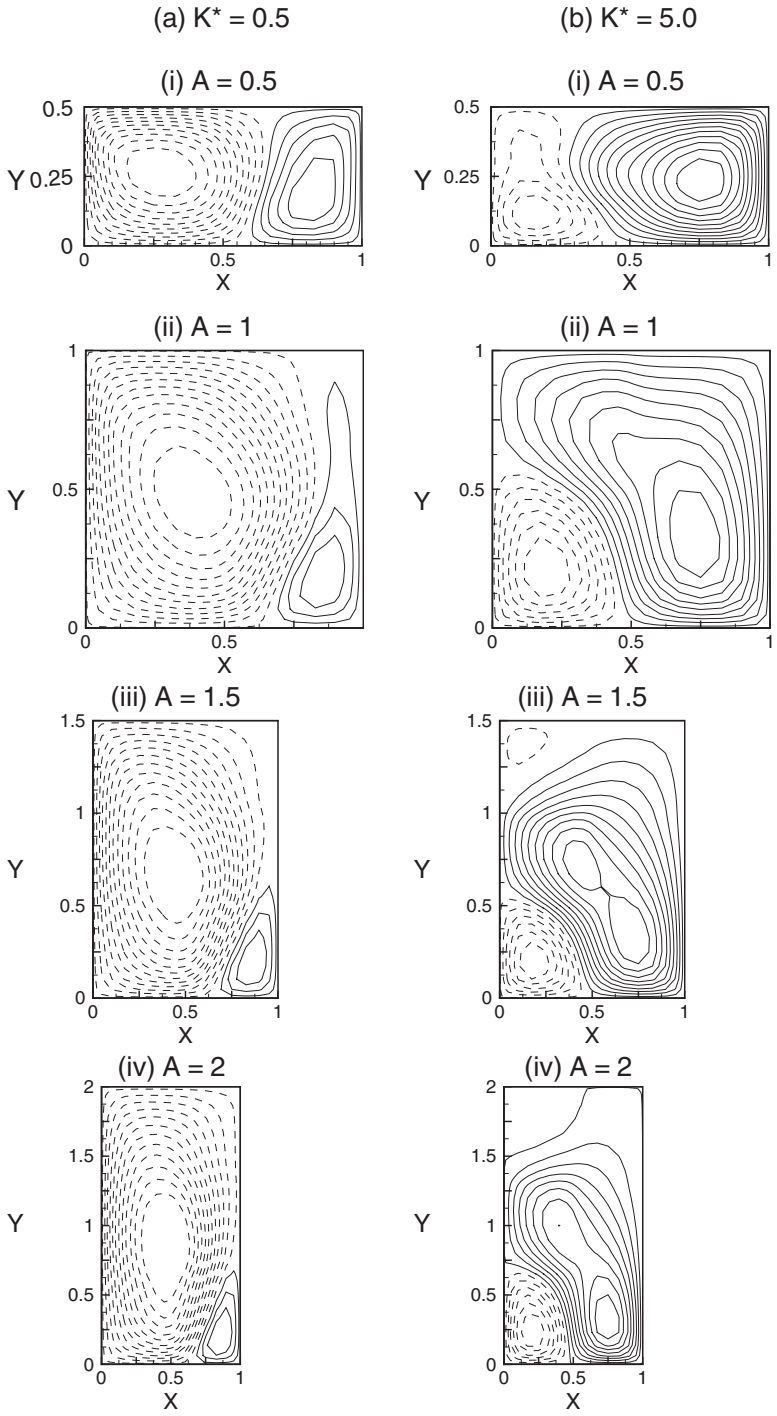

Fig. 3 Effect of aspect ratio on streamlines: (*a*) $K^*=0.5$ and (*b*) $K^*=5$ for $Ra=10^6$, $Da=10^{-4}$, and $\phi=45$ deg

Pr at 0.71 by considering fluid as air. The main emphasis is given on the influence of anisotropy of the media on flow dynamics as well as heat transfer mechanism. In all contour plots, dashed lines denote negative values whereas solid lines denote positive values. In addition, for stream function, solid and dashed lines are associated with anticlockwise and clockwise rotations, respectively.

3.1 Effect of Aspect Ratio. The influence of aspect ratio on the overall bottom as well as side heat transfer rates, i.e., Nu_b and Nu_s, is considered for isotropic as well as anisotropic systems, which is shown in Figs. 2(*a*)–2(*c*), respectively. As can be observed from Fig. 2(*a*) for all three values of Ra Da (1, 10, 100), when the aspect ratio (A) increases from 0.5 to 1, the average bottom heat transfer rate (Nu_b) increases but as the value of A increases beyond unity, Nu_b decreases smoothly. The maximum heat transfer rate takes place at the unit value of A. A similar result was also reported by other researchers [18]. From the same figure, it can also be seen that the corresponding side heat transfer rate, Nu_s, decreases with increasing A for all above Ra Da. It is to be noted that Nu_s changes drastically as A varies from 0.5 to 1 and beyond this it changes slowly. Another important observation is that both Nu_b and Nu_s are increased with increasing value of Ra Da. To understand the possible similar phenomena in hydrody-

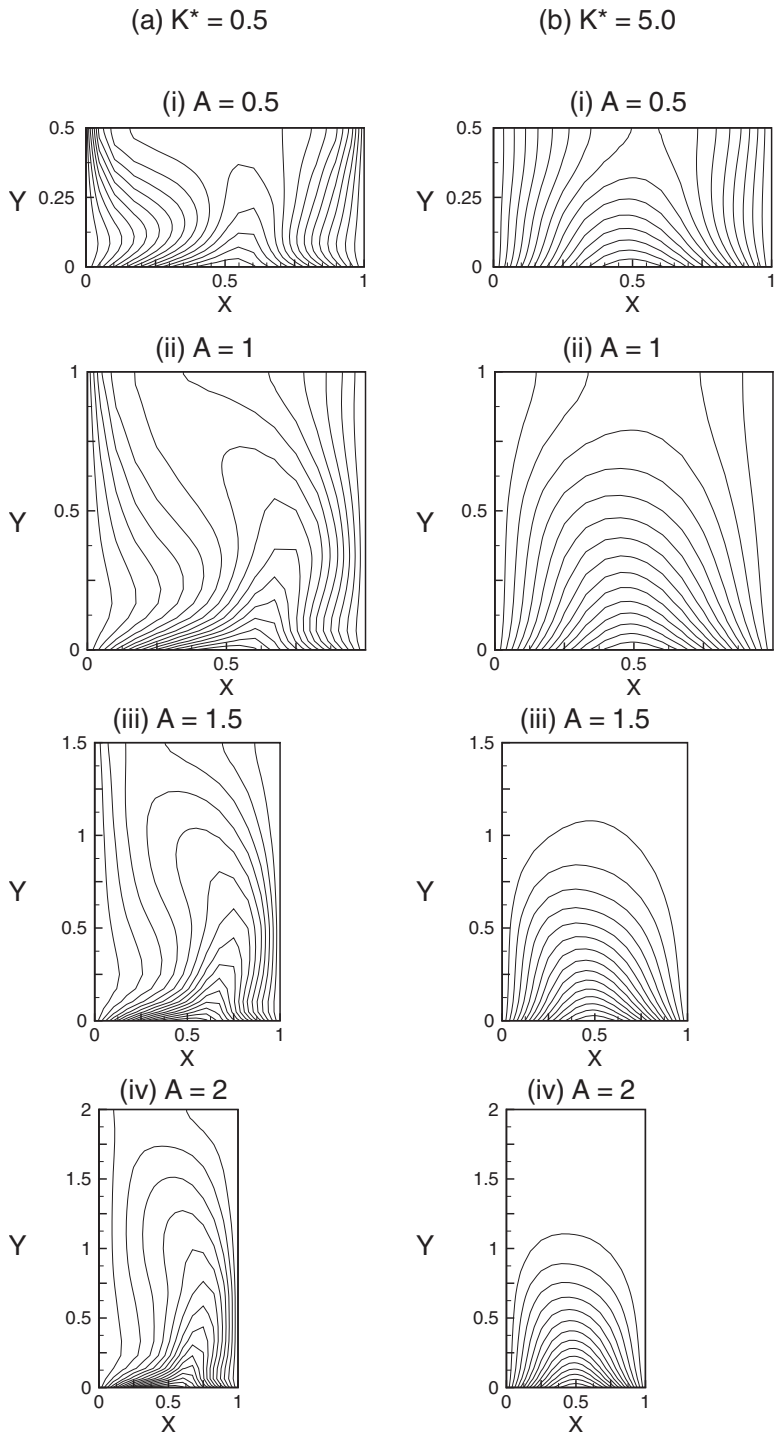

Fig. 4 Effect of aspect ratio on temperature: (*a*) $K^*=0.5$ and (*b*) $K^*=5$ for $Ra=10^6$, $Da=10^{-4}$, and $\phi=45$ deg

namically anisotropic porous media the influences of A on Nu_b as well as Nu_s are plotted in Figs. 2(*b*) and 2(*c*), respectively, for two different values of 0.5 and 5.0 with permeability ratio K^* at $\phi = 45$ deg. It is to be noted that when all other parameters are kept at constant values, the change in K^* is due to the change in K_{y^*} only, i.e., permeability along the horizontal direction only.

As can be seen from Figs. 2(*b*) and 2(*c*), depending on Ra Da and K^*, an increase in A up to a certain value reduces the value of Nu_s drastically and beyond that it converges slowly and smoothly to a constant value. Furthermore, for Ra Da=100 and $K^*=0.5$, initially Nu_s decreases with increasing A beyond 0.5 but it starts to increase as A is moved beyond a certain value around 4 (see Fig. 2(*b*)) in the domain [0.5, 10] of A, which is may be due to the complex flow mechanism in the anisotropic porous media. Similar to the isotropic results in Fig. 2(*a*), for $K^*=0.5$ the maximum Nu_b is attained at A equal to 1, whereas the same is attained around A equal to 1.25 when $K^*=5.0$ (see Figs. 2(*b*) and 2(*c*)).

In order to understand the physics behind this, the contour plot of stream function is plotted in Figs. 3(*a*) and 3(*b*) for four different values (0.5, 1, 1.5, and 2) of A at (a) $K^*=0.5$ and (b) $K^*=5$ when Ra Da=100. It may be pointed out from these figures that, first, in all the situations, there are two different types of convec-

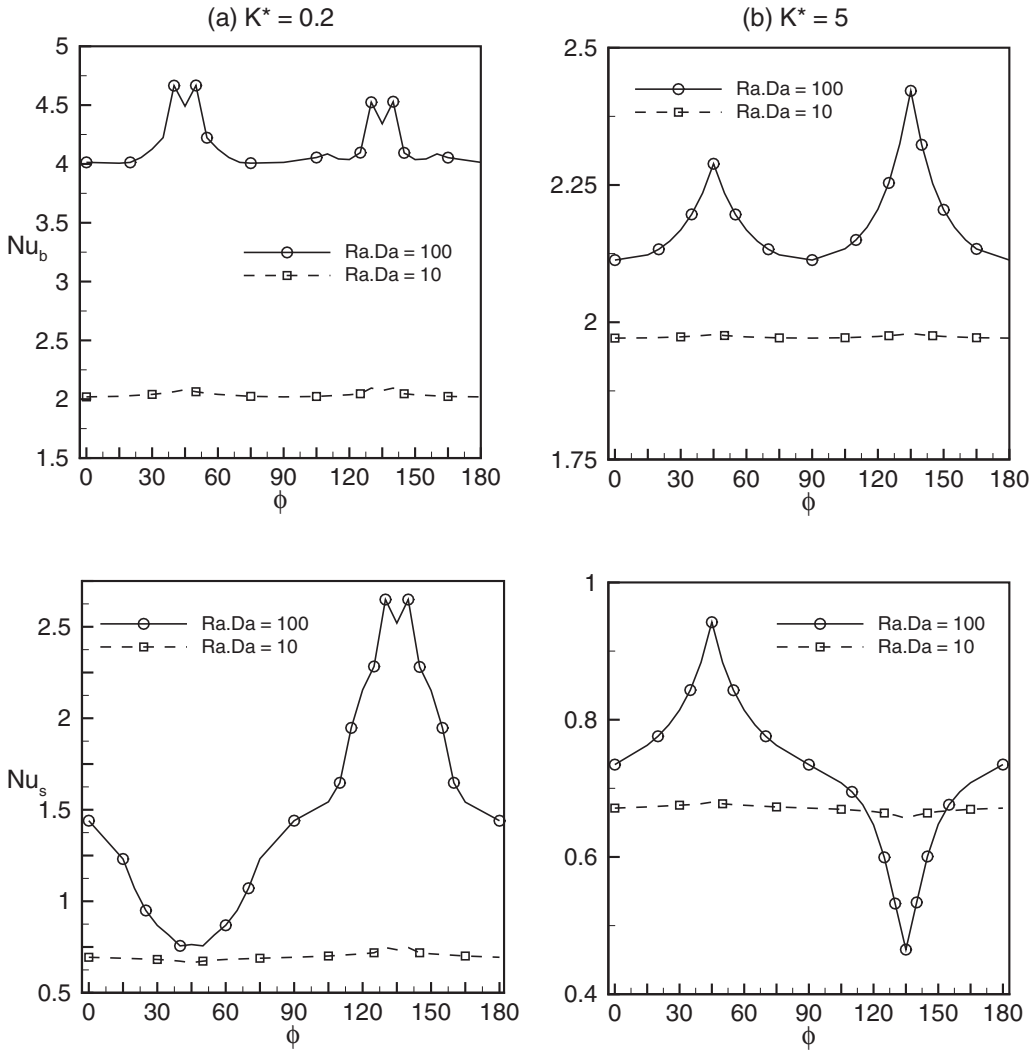

Fig. 5 Variation in average Nusselt numbers (Nu_b as well as Nu_s) as a function of orientation angle (ϕ) for different values of Ra: (*a*) $K^*=0.2$ and (*b*) $K^*=5$ when $Da=10^{-4}$ and $A=1.5$

tive cells, rotating anticlockwise (solid lines) and rotating clockwise (dotted lines), that appear on the streamline contour plots, which may be due to nonuniform heating of the bottom wall by the sine function, $\sin \pi x$. Depending on the media permeability one of the cells dominates the other; here the dominating cell is referred to as the primary cell, whereas the other will be called as the secondary cell. Second, for each case ($K^*=0.5$ or 5), there exists a threshold value of aspect ratio in $1 \le A < 1.5$, at which the secondary cell has a minimum height (approximately one-third of the cavity height).

Third, the primary cells are stretched upward with an angle of 45 deg for $A>1$ and K^* equal to 5, which may be the consequence of equality of the permeabilities (K_{xx}, K_{yy}), in both the directions at ϕ equal to 45 deg. As a result, the primary and secondary convective cells are not uniform. Apart from these, at A equal to 1.5 another secondary vorticity appears in the left side upper corner of the cavity. Due to buoyancy force, it is natural that the streamline will evolve upward with increasing A. But the maximum stretching of the primary cells in general is attained in the domain of $1 \le A < 1.5$, which may be the cause of attaining maximum bottom heat transfer rate at this value of A. Therefore, for the rest of the discussion presented here $A=1.5$ is considered.

In order to understand the change in temperature profile under these circumstances, temperature profile was also observed meticulously from Figs. 4(*a*) and 4(*b*), and the following conclusion is made. An increase in A reduces the top boundary effect on the temperature profile by reducing the conduction zone in the cavity.

3.2 Effect of Orientation Angle. Before discussing the effect of orientation angle ϕ, a note must be made regarding the periodicity of the permeability tensor. Since each entry of the tensor $\bar{\bar{K}}$ is periodic with period π, heat transfer rate will also be a periodic function of the same period. Therefore, to understand the influence of orientation angle on the heat transfer rate [0 deg, 180 deg] is considered as the range of ϕ. Figures 5(*a*) and 5(*b*) show the influence of orientation angle, ϕ, of the permeability tensor on the heat transfer rate in (ϕ,Nu_b)- and (ϕ,Nu_s)-planes for different values of Ra as well as K^* at $Da=10^{-4}$. As can be observed from Fig. 5, first, for $K^*=0.2$ Nu_b attains its maximum value around ϕ equal to 45 deg, where the corresponding Nu_s is minimum. But Nu_s is maximum around $\phi \approx 135$ deg. Second, for $K^*=5$, Nu_b (Nu_s) is maximum (minimum) at ϕ equal to 135 deg, whereas Nu_s is maximum at $\phi=45$ deg. Third, both bottom and side wall heat transfer profiles are symmetric about the lines $\phi=45$ deg and $\phi=135$ deg in the domains [0 deg, 90 deg] and [90 deg, 180 deg], respectively. Apart from these, the overall heat transfer rate from the bottom as well as side increases with increasing value of Ra. It is to be noted that at $K^*=5$, increasing ϕ from 0 deg to 45 deg of the overall media permeability, ($K_{yy}=K_{x*}[(\sin^2 \phi + K^* \cos^2 \phi)$

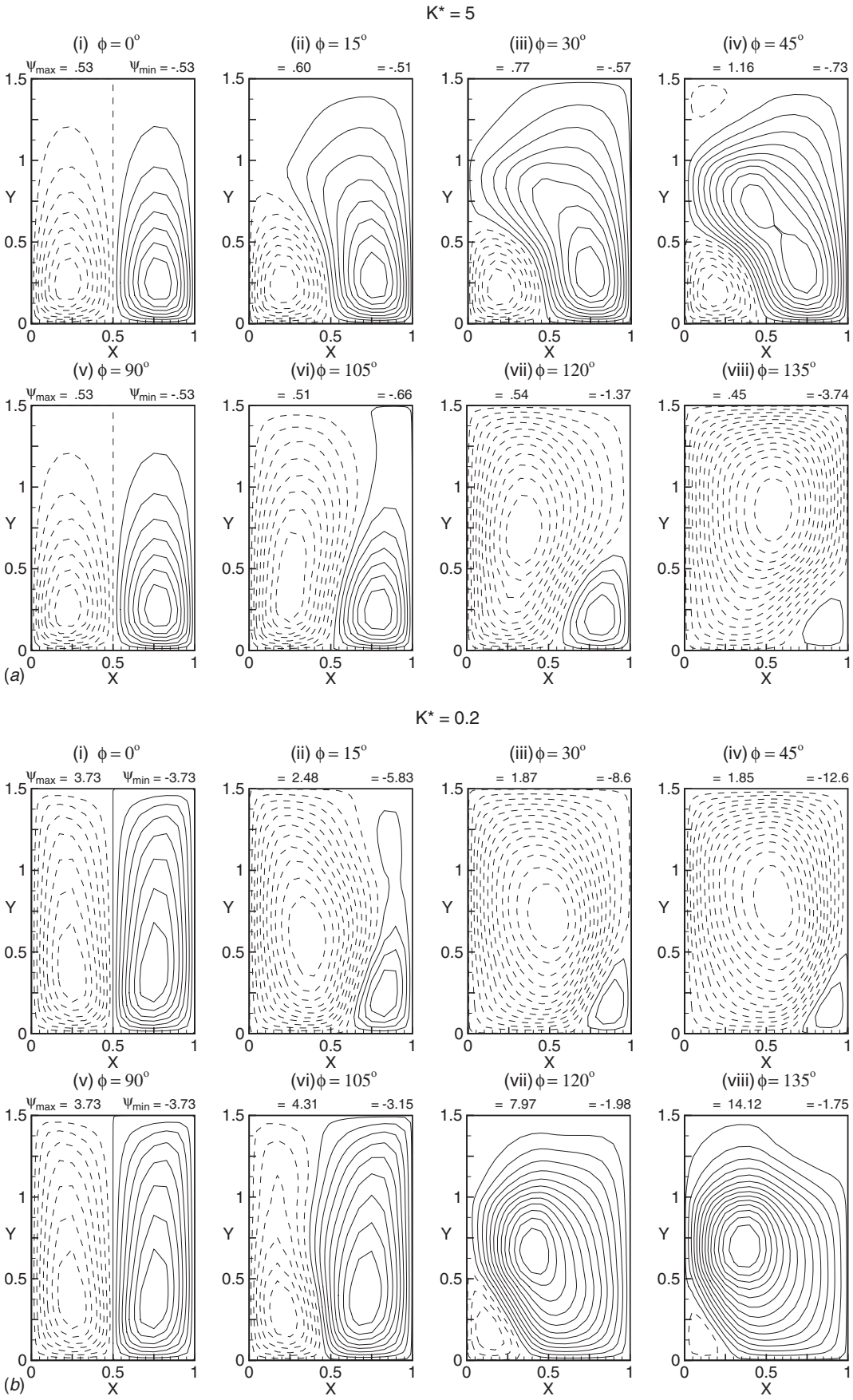

Fig. 6 Effect of orientation angle on streamlines: (*a*) $K^*=5$ and (*b*) $K^*=0.2$ for $Ra=10^6$, $Da=10^{-4}$, and $A=1.5$

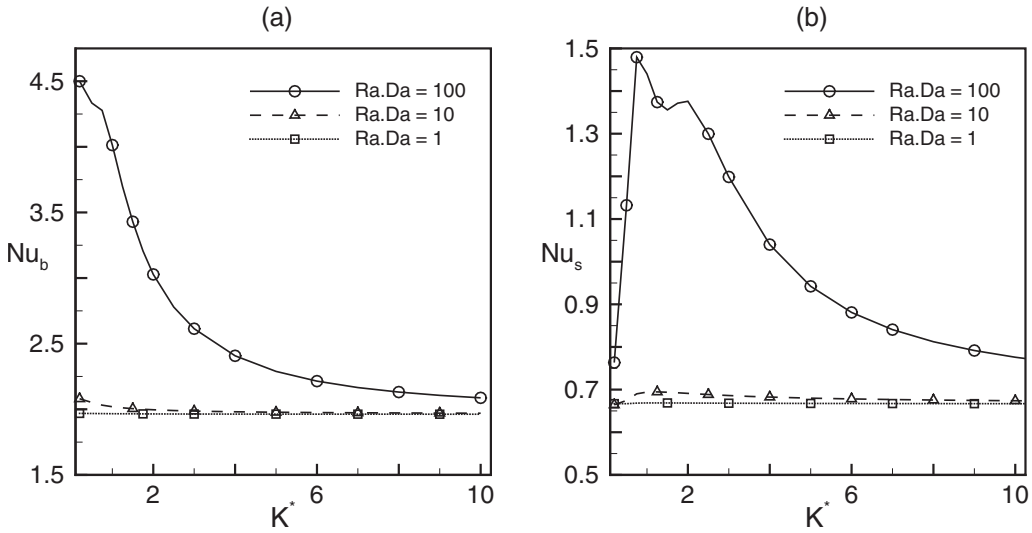

Fig. 7 Dependence of the (*a*) average bottom Nusselt number and (*b*) side Nusselt number on the permeability ratio for different values of Ra when Da=10^{-4}, ϕ=45 deg, and A=1.5

$+(1-K^*)\sin\phi\cos\phi]$), along the vertical direction is reduced, whereas the same is changed in reverse way for $K^*=0.2$. This implies that with decreasing media permeability in the main flow direction, it is not necessary that the bottom heat transfer rate will be reduced always.

To shed more light on the mechanism of the above observations the streamline contours for eight different values of ϕ (0 deg, 15 deg, 30 deg, 45 deg, 90 deg, 105 deg, 120 deg, and 135 deg) at $K^*=5, 0.2$ are plotted in Figs. 6(*a*) and 6(*b*). It can be observed from Fig. 6(*a*) that changing ϕ from 0 deg to 45 deg when $K^*=5$, the maximum values of primary cells (anticlockwise rotating streamlines) are increased. A similar trend can also be seen as ϕ varies from 90 deg to 135 deg (although the primary cells are clockwise rotating streamlines). But the strength of the primary cells is maximum at ϕ equal to 135 deg. As a consequence the maximum bottom heat transfer at this value of ϕ is expected. At the same time, a closed view on the streamline variation as a function of ϕ in the range of [0 deg, 45 deg] as well as [90 deg, 135 deg] indicates that as ϕ moves from 0 deg to 45 deg the convection region from the left side of the cavity increases, whereas the same decreases as ϕ varies from [90 deg, 135 deg] and becomes minimum at ϕ=135 deg. As a consequence Nu_s is minimum for this value of ϕ.

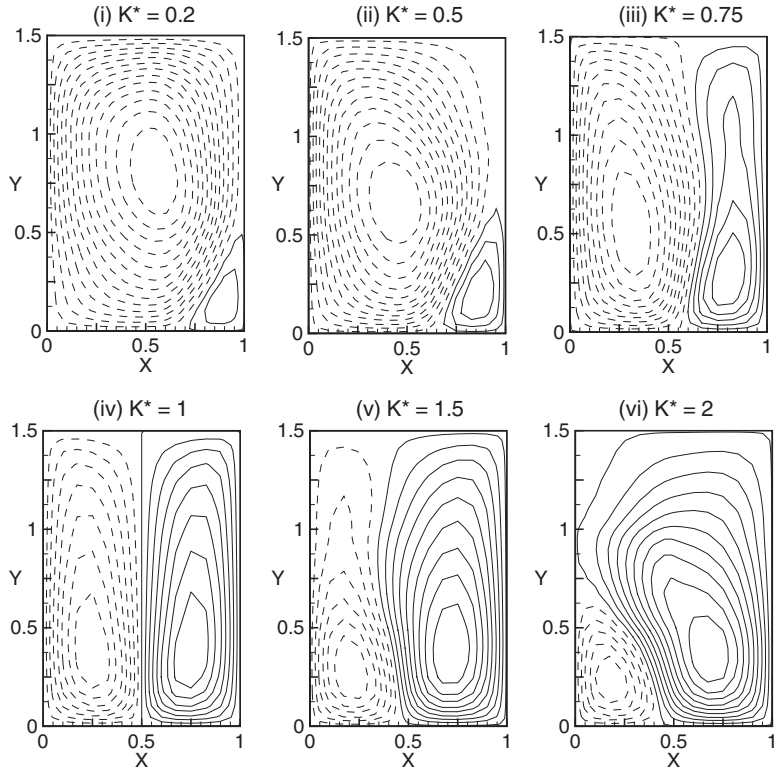

Fig. 8 Effect of permeability ratio (K^*) on streamlines at Da=10^{-4}, A=1.5, and ϕ=45 deg

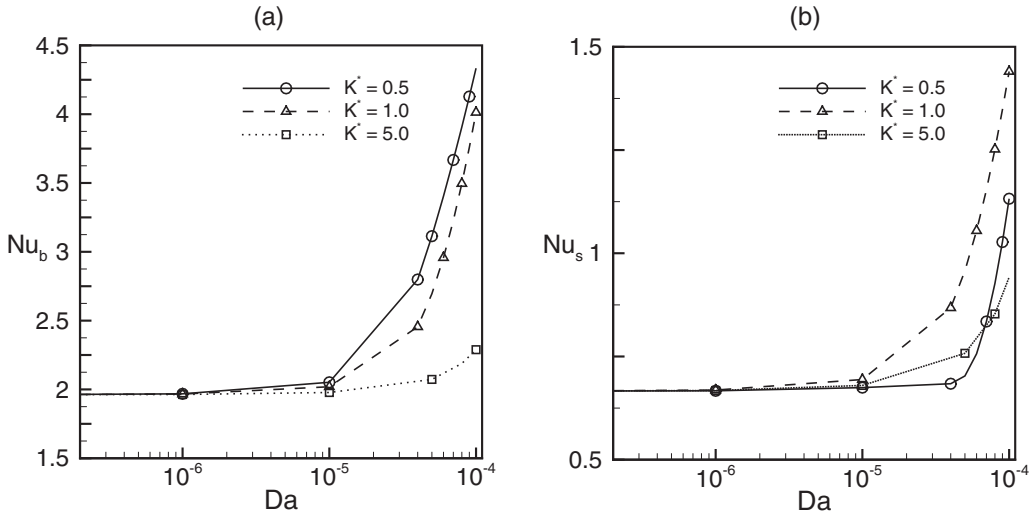

Fig. 9 Dependence of the (*a*) average bottom Nusselt number and (*b*) side Nusselt number on the Darcy number for different values of K^* when Ra=10^6, ϕ=45 deg, and A=1.5

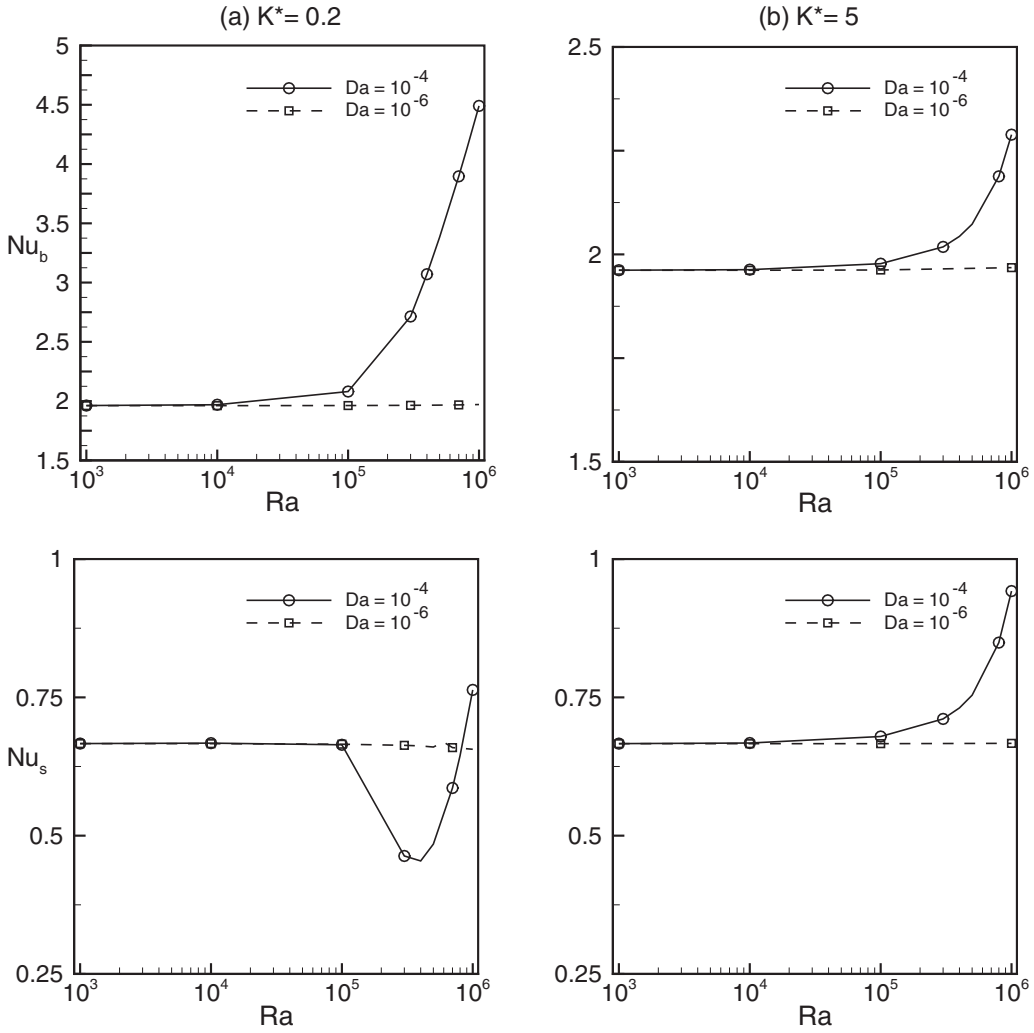

Fig. 10 Variation in average Nusselt numbers (Nu_b as well as Nu_s) as a function of Rayleigh number for different values of Da: (*a*) K^*=0.2 and (*b*) K^*=5 when ϕ=45 deg and A=1.5

From Fig. 6(*b*) it can be observed that for $K^*=0.2$, the maximum magnitude of primary cells increases (from 3.73 to 12.6 as well as from 3.73 to 14.12) on varying ϕ from 0 deg to 45 deg as well as from 90 deg to 135 deg, but the side region of convective flow is minimum (maximum) at ϕ equal to 45 deg (135 deg). Therefore, the above results are expected.

Furthermore, it is worthwhile to mention here that the most complicated flow in the anisotropic system is observed when the permeability tensor is oblique with the usual (X,Y) coordinate system by 45 deg. That is why, for the entire discussion presented in this section, excluding this subsection, ϕ is fixed at 45 deg.

3.3 Effect of Media Permeability. The permeability is a measure of material's ability to transmit the fluids, i.e., it measures the flow strength of the medium and also acts as a conductivity of the fluid flows. In general, high permeability produces the strong flow, whereas low permeability produces the weak flow. In this study, the effect of media permeability is considered by studying separately the following: (a) effect of horizontal permeability through K^* and (b) effect of vertical permeability via Da. From the definition of Da, when other parameters are kept at constant values, variation in Da indicates the variation in vertical permeability only. The influence of (K^*) is depicted in Figs. 7(*a*) and 7(*b*) for three values of Ra Da (100, 10, and 1) at $\mathrm{Da}=10^{-4}$.

It can be observed from Figs. 7(*a*) and 7(*b*) that for all the cases, with an increase in K^*, the bottom heat transfer rate decreases, whereas the side heat transfer rate fluctuates in the subdomain [0.2, 2] of K^*, and beyond it the same decreases smoothly with increasing media permeability ratio. The fluctuation can be seen clearly as Ra increases from 10^4 to 10^6, and the length of the subdomain in which fluctuation takes place is increased with the enhancement of Ra. It is natural that the reduction in flow by reducing the media permeability causes less overall heat transfer rate, which can be observed from Fig. 7(*a*). Therefore the fluctuation of Nu_s is generally unexpected. To shed some light on this anomaly, stream-function contours are plotted at K^* equal to 0.2, 0.75, 1, 1.5, and 2 in Fig. 8 for Ra Da=100, where Nu_s is calculated as 0.76, 1.48, 1.44, 1.36, and 1.37. A closer look at the streamline contours showed that with increasing K^* from 0.2 to 1, the height of the secondary cells is increased and becomes the mirror image of the primary cell at $K^*=1$. The appearance of counter-rotations at the same height leads to a mutual excess of heat from the side walls [34]. That is why the side wall heat transfer rate increases with increasing K^* from 0.2 to 1. However, in anisotropic cases the flow rate does not have a straightforward relationship with K^*. Attaining a maximum value of Nu_s at $K^*=0.75$ is an example.

In order to understand the effect of Da, a comparative study is made. As can be seen from Figs. 9(*a*) and 9(*b*), first, in general, increasing Da from 10^{-7} to 10^{-4} increases both average heat transfer rates, Nu_b as well as Nu_s, which is based on the fact that enhancing Da is due to an increase in permeability along both the directions. As a consequence, the flow strength increases, and more heat transfer takes place. Second, when Da moves from 10^{-7} to 10^{-6} Nu_b is changed from 1.962 to 1.968, whereas the same is changed from 2.05 to 4.33 with the variation in Da from 10^{-5} to 10^{-4} at $K^*=0.5$. Simultaneously, Nu_s is also increased by two times at $\mathrm{Da}=10^{-5}$, which is maybe due to the increase in driving parameter Ra Da. Overall, it can be pointed out that at $\mathrm{Ra}=10^6$, the impact of the enhancement of the media permeability along the vertical direction by changing Da from 10^{-7} to 10^{-5} on the heat transfer rates is negligible. But a significant influence on Nu_b as well as Nu_s can be observed when Da is increased from 10^{-5} to 10^{-4}.

3.4 Effect of Rayleigh Numbers. The effect of increasing heat source intensity, i.e., Rayleigh number, on the heat transfer process in an anisotropic porous medium has been analyzed by varying both bottom and side heat transfer rates as a function of Ra and is depicted in Figs. 10(*a*) and 10(*b*). As can be seen from Fig. 10, for isotropic as well as anisotropic media, the effect of Rayleigh number on the average heat transfer rates becomes significant when the Rayleigh–Darcy number, Ra Da, is greater than 10. Apart from this, increasing Ra enhances the heat transfer rates for both isotropic [24] and anisotropic media except in the case of side heat transfer rate at Da equal to 10^{-4} and $K^*=0.2$.

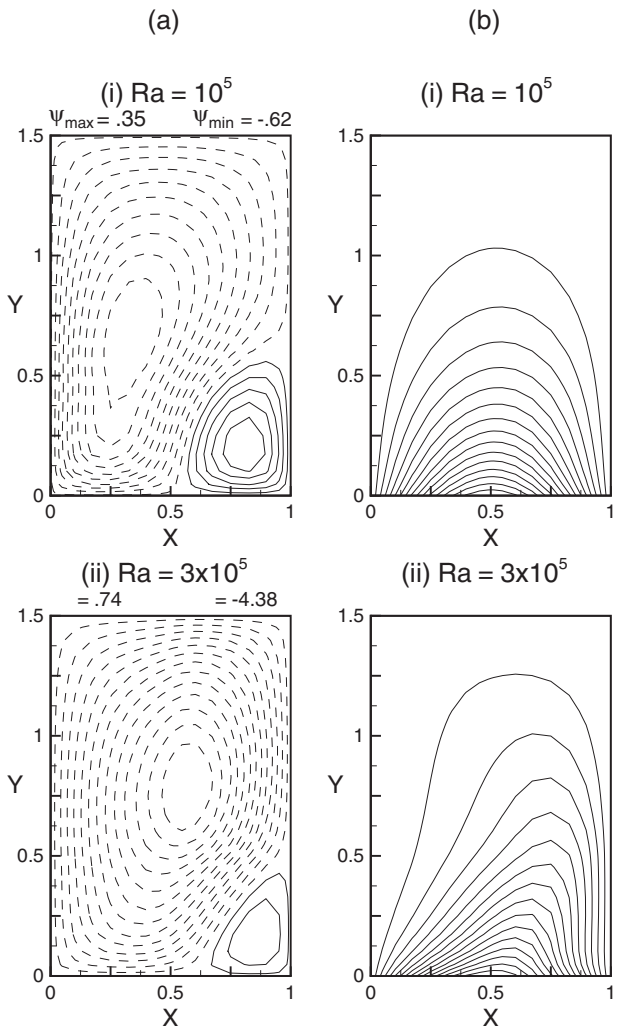

Fig. 11 Contour plots of streamlines and temperature: (*a*) Ra $=10^5$ and (*b*) Ra $=3\times10^5$ when $K^*=0.2$, $\phi=45$ deg, and $A=1.5$

From the definition of Ra, when other parameters are fixed, increasing Ra implies the enhancement of thermal buoyancy force, which in turn increases the thermal convection in the cavity. As a result, the average heat transfer rate is expected to increase. But the result in Fig. 10(*a*) at $\mathrm{Da}=10^{-4}$ is anticipated. To reveal the physics behind this anticipating result, contour plots of streamlines and temperature profiles are plotted at Ra equal to 10^5 and 3×10^5 (see Figs. 11(*a*) and 10(*b*)). Important finding is that although the maximum magnitude of the contour lines increases from 0.62 to 4.4, the left side of the convective flow region is reduced. That is why, the average side heat transfer rate falls down at $\mathrm{Ra}=3\times10^5$, which is also the consequence of flow complexity in hydrodynamically anisotropic porous media.

4 Conclusions

We have attempted to understand the impact of hydrodynamic anisotropy on the natural convection in a porous cavity, where flow is induced by nonuniform heating of the bottom wall and uniform cooling of side walls when the top wall is in the adiabatic

state. To this end, we have adopted the Brinkman-extended non-Darcy model. By means of rigorous numerical experiments, we are able to extract detailed information on the flow and heat transfer mechanisms in anisotropic porous media. The main objective in this study is to investigate the effect of anisotropic parameters: (i) orientation angle of media permeability tensor and (ii) permeability of the media via Darcy number (Da) as well as permeability ratio on the flow mechanism and consequently on the average bottom as well as side heat transfer rates. The following conclusions can be drawn from this study.

- For isotropic as well as anisotropic cases, the maximum heat transfer in the enclosure takes place when $1 \leq A < 1.5$.
- Two types of convective cells, (i) rotating anticlockwise way and (ii) rotating clockwise way, are observed in the entire flow mechanism. Depending on the media permeability one dominates the other.
- Furthermore, the results indicate that for $K^*=5$ and $\mathrm{Da}=10^{-4}$, the bottom heat transfer profiles (side heat transfer profiles), as a function of orientation angle, experience a maximum (minimum) value at an orientation angle equal to 135 deg.
- In contrast to isotropic porous media, enhancement of the strength of flow convection in the anisotropic porous enclosure does not increase the heat transfer rate always. It depends on the flow dynamics in the medium. In particular, the present investigation shows the significant impact of the orientation angle of the media permeability tensor on the flow mechanisms and temperature profile and consequently on the average heat transfer rates.

Acknowledgment

One of the authors (A.K.) is grateful to the Council of Scientific and Industrial Research (CSIR), India for providing financial support during the preparation of this manuscript.

Nomenclature

A = aspect ratio $= H/L$
L = width of cavity
H = height of cavity
Pr = Prandtl number $= \nu/\alpha_e$
Da = Darcy number $= K_y^*/L^2$
Ra = Rayleigh number $= g\beta L^3(T_2-T_1)/[\alpha_e \nu]$
$\bar{\bar{K}}$ = permeability tensor
K_{x^*} = permeability along the x^* axis of the tilted coordinate system
K_{xx} = $K_{x^*}[a+c]$, permeability along the X axis
K_{y^*} = permeability along the y^* axis of the tilted coordinate system
K_{yy} = $K_{x^*}[b+c]$, permeability along the Y axis
K^* = ratio of principal components of $\bar{\bar{K}} = K_{y^*}/K_{x^*}$
Nu_b = average bottom Nusselt number
Nu_s = average side Nusselt number
N_X = number of elements along the X-direction
N = order of approximation along the X-direction
M_Y = number of elements along the y-direction
M = order of approximation along the Y-direction
p = pressure
P = nondimensional pressure
$\mathbf{Q}$ = gravitational direction vector
t = time
T = temperature
T_2 = temperature at the hot bottom wall
T_1 = temperature at cold vertical walls
u,v = velocity components
U,V = nondimensional velocity components
x,y = dimensional space coordinates
X,Y = nondimensional space coordinates
x^*,y^* = dimensional tilted space coordinates
g = gravitational acceleration

Greek Symbols

α_e = effective thermal diffusivity
β_T = coefficient of thermal expansion
ν = kinematic viscosity
ω = vorticity
Δt = nondimensional time step
Ψ = stream function
ρ = density of the fluid
ρ_0 = initial density
ϕ = anisotropy orientation angle

References

[1] Holm, N. G., Cairns-Smith, A. G., Daniel, R. M., Ferris, J. P., Hennet, R. J. C., Shock, E. L., Simoneit, B. R. T., and Yanagawa, H., 1992, "Future Research," *Marine Hydrothermal Systems and the Origin of Life*, N. G. Holm, ed., Kluwer Academic, Dordrecht.
[2] Kaviany, M., 1995, *Principles of Heat Transfer in Porous Media*, Springer, New York.
[3] Sahimi, M., 1995, *Flow and Transport in Porous Media and Fractured Rock*, VCH, Weinheim.
[4] Helmig, R., 1997, *Multiphase Flow and Transport Processes in the Subsurfaces*, Springer-Verlag, Berlin.
[5] Koponen, A., Kandhai, D., Hellen, E., Alava, M., Hoekstra, A., Kataja, M., Niskanen, K., Sloot, P., and Timonen, J., 1998, "Permeability of Three Dimensional Random Fiber Webs," Phys. Rev. Lett., **80**, pp. 716–719.
[6] King, P. R., Buldyrev, S. V., Dokholyan, N. V., Havlin, S., Lee, Y., Paul, G., and Stanley, H. E., 1999, "Applications of Statistical Physics to the Oil Industry: Predicting Oil Recovery Using Percolation Theory," Physica A, **274**, pp. 60–66.
[7] Dando, P. R., Stuben, D., and Varnavas, S. P., 1999, "Hydrothermalism in the Mediterranean Sea," Prog. Oceanogr., **44**, pp. 333–367.
[8] Nield, D. A., and Bejan, A., 2006, *Convection in Porous Media*, Springer, New York.
[9] Poulikakos, D., 1985, "A Departure From Darcy Model in Boundary Layer Natural Convection in a Vertical Porous Layer With Uniform Heat Flux from the Side," J. Heat Transfer, **107**, pp. 716–720.
[10] Nithiarasu, P., Seetharamu, K. N., and Sundararajan, T., 1997, "Natural Convective Heat Transfer in the Fluid Saturated Variable Porosity Medium," Int. J. Heat Mass Transfer, **40**, pp. 3955–3967.
[11] Baytas, A. C., and Pop, I., 2002, "Free Convection in a Square Porous Cavity Using a Thermal Non-Equilibrium Model," Int. J. Therm. Sci., **41**, pp. 861–870.
[12] Walker, K. L., and Homsy, G. M., 1978, "Convection in Porous Cavity," J. Fluid Mech., **87**, pp. 449–474.
[13] Saeid, N. F., and Pop, I., 2004, "Transient Free Convection in a Square Porous Cavity Filled With Porous Medium," Int. J. Heat Mass Transfer, **47**, pp. 1917–1924.
[14] Ni, J., and Beckermann, C., 1991, "Natural Convection in a Vertical Enclosure Filled With Anisotropic Porous Media," ASME J. Heat Transfer, **113**, pp. 1033–1037.
[15] Degan, G., Vasseur, P., and Bilgen, E., 1995, "Convective Heat Transfer in a Vertical Anisotropic Porous Layer," Int. J. Heat Mass Transfer, **38**, pp. 1975–1987.
[16] Degan, G., and Vasseur, P., 1996, "Natural Convection in a Vertical Slot Filled With an Anisotropic Porous Medium With Oblique Principal Axes," Numer. Heat Transfer, Part A, **30**, pp. 397–412.
[17] Dhanasekaran, M. R., Das, S. K., and Venkateshan, S. P., 2002, "Natural Convection in a Cylindrical Enclosure Filled With Heat Generating Anisotropic Porous Medium," ASME J. Heat Transfer, **124**, pp. 203–207.
[18] Bera, P., Eswaran, V., and Singh, P., 1998, "Numerical Study of Heat and Mass Transfer in an Anisotropic Porous Enclosure Due to Constant Heating and Cooling," Numer. Heat Transfer, Part A, **34**, pp. 887–905.
[19] Bera, P., and Khalili, A., 2002, "Double-Diffusive Natural Convection in an Anisotropic Porous Cavity With Opposing Buoyancy Forces: Multi-Solutions and Oscillations," Int. J. Heat Mass Transfer, **45**, pp. 3205–3222.
[20] Lage, J. I., and Bejan, A., 1993, "The Resonance of Natural Convection in an Enclosure Heated Periodically From the Side," Int. J. Heat Mass Transfer, **36**, pp. 2027–2038.
[21] Sarris, I. E., Lekakis, I., and Vlachos, N. S., 2002, "Natural Convection in a 2D Enclosure With Sinusoidal Upper Wall Temperature," Numer. Heat Transfer, Part A, **42**, pp. 513–520.
[22] Bilgen, E., and Yedder, R. B., 2007, "Natural Convection in Enclosure With Heating and Cooling by Sinusoidal Temperature Profiles on One Side," Int. J. Heat Mass Transfer, **50**, pp. 139–150.
[23] Saeid, N. F., 2005, "Natural Convection in Porous Cavity With Sinusoidal Bottom Wall Temperature Variation," Int. Commun. Heat Mass Transfer, **32**, pp. 454–463.
[24] Basak, T., Roy, S., Poul, T., and Pop, I., 2006, "Natural Convection in a Square

Cavity Filled With a Porous Medium: Effect of Various Thermal Boundary Conditions," Int. J. Heat Mass Transfer, **49**, pp. 1430–1441.
[25] Zahmatkesh, I., 2008, "On the Importance of Thermal Boundary Conditions in Heat Transfer and Entropy Generation for Natural Convection Inside a Porous Enclosure," Int. J. Therm. Sci., **47**, pp. 339–346.
[26] Patera, A. T., 1984, "A Spectral Element Method for Fluid Dynamics: Laminar Flow in a Channel Expansion," J. Comput. Phys., **54**, pp. 468–488.
[27] Canuto, C., Hussaine, M. Y., Quarteroni, A., and Zang, T. A., 1986, *Spectral Method in Fluid Dynamics*, Springer, New York.
[28] Neale, G., 1977, "Degrees of Anisotropy for Fluid Flow and Diffusion (Electrical Conduction) Through Anisotropic Porous Media," AIChE J., **23**, pp. 56–62.
[29] Wooding, R. A., 1976, "Large-Scale Geothermal Field Parameters and Convection Theory," Second Workshop Geothermal Reservoir Engineering, December 1–3, Stanford University, Stanford, pp. 339–345.
[30] Tyvand, P. A., and Storesletten, L., 1991, "Onset of Convection in an Anisotropic Porous Medium With Oblique Principal Axes," J. Fluid Mech., **226**, pp. 371–382.
[31] Storesletten, L., 1998, "Effects of Anisotropy on Convective Flow Through Porous Media," *Transport Phenomena in Porous Media*, D. B. Ingham and I. Pop, eds., Pergamon, Oxford, pp. 261–283.
[32] Tyvand, P. A., 1980, "Thermohaline Instability in Anisotropic Porous Media," Water Resour. Res., **16**, pp. 325–330.
[33] Lauriat, A., and Prasad, V., 1989, "Non-Darcian Effects on Natural Convection in a Vertical Porous Enclosure," Int. J. Heat Mass Transfer, **32**, pp. 2135–2148.
[34] Bera, P., and Khalili, A., 2007, "Stability of Buoyancy Opposed Mixed Convection in a Vertical Channel and Its Dependency on Permeability," Adv. Water Resour., **30**, pp. 2296–2308.

Darcy–Forchheimer Flow With Viscous Dissipation in a Horizontal Porous Layer: Onset of Convective Instabilities

A. Barletta
e-mail: antonio.barletta@mail.ing.unibo.it

M. Celli
e-mail: michele.celli@mail.ing.unibo.it

Dipartimento di Ingegneria Energetica, Nucleare e del Controllo Ambientale (DIENCA),
Università di Bologna,
Via dei Colli 16,
I-40136 Bologna, Italy

D. A. S. Rees
Department of Mechanical Engineering,
University of Bath,
Bath BA2 7AY, UK
e-mail: d.a.s.rees@bath.ac.uk

Parallel Darcy–Forchheimer flow in a horizontal porous layer with an isothermal top boundary and a bottom boundary, which is subject to a third kind boundary condition, is discussed by taking into account the effect of viscous dissipation. This effect causes a nonlinear temperature profile within the layer. The linear stability of this nonisothermal base flow is then investigated with respect to the onset of convective rolls. The third kind boundary condition on the bottom boundary plane may imply adiabatic/isothermal conditions on this plane when the Biot number is either zero (adiabatic) or infinite (isothermal). The solution of the linear equations for the perturbation waves is determined by using a fourth order Runge–Kutta scheme in conjunction with a shooting technique. The neutral stability curve and the critical value of the governing parameter $R=GePe^2$ are obtained, where Ge is the Gebhart number and Pe is the Péclet number. Different values of the orientation angle between the direction of the basic flow and the propagation axis of the disturbances are also considered. [DOI: 10.1115/1.3090815]

Keywords: laminar flow, mixed convection, Darcy–Forchheimer model, porous medium, linear stability, viscous dissipation

1 Introduction

Convective instabilities in porous layers have been the subject of very many investigations in the past decades. A cornerstone in this field is the so-called Horton–Rogers–Lapwood (HRL) problem [1,2]. This problem consists of the linear stability analysis of a fluid at rest in a porous plane layer where the bottom isothermal boundary is held at a relatively high temperature while the top isothermal boundary is at a lower temperature. Physically, the HRL problem is the porous medium analog of the classical Bénard problem for a clear fluid and is often called the Darcy–Bénard problem. The HRL problem admits a very simple analytical solution for the basic state, which is compatible with both the Darcy and the Darcy–Forchheimer models. Several other variants of the original HRL problem have been investigated in the past years. Reviews of the wide literature on this subject may be found in Refs. [3–5]. An important problem closely related to the HRL problem is the much less well-known Prats problem [6]. This latter problem is the linear stability analysis, according to the Darcy model, of the HRL configuration in the presence of a uniform horizontal flow.

The present paper investigates the onset of linear instabilities in a horizontal porous layer induced by the viscous heating effect, a topic on which very few papers have been published (see Refs. [7–9]). Unlike in the Prats problem [6], the vertical temperature gradient causing the onset of convective rolls is not imposed externally through the boundary conditions. Rather, it is the internally generated heat due to viscous friction that causes the vertical temperature gradient and thus gives rise to the possibility of convective instability. In this paper, the top boundary surface is considered to be isothermal, while the bottom boundary is subject to a thermal boundary condition of the third kind for which a Biot number, Bi, may be defined. This latter boundary condition is studied including the two limiting cases, $\mathrm{Bi}\to 0$ (adiabatic boundary) and $\mathrm{Bi}\to\infty$ (isothermal boundary). A linear stability analysis of oblique rolls, which are inclined arbitrarily with respect to the uniform base flow direction, is performed. The disturbance equations are solved numerically by a fourth order Runge–Kutta method. The governing parameter for the onset of convective instabilities is defined as $R=\mathrm{GePe}^2$, where Ge is the Gebhart number and Pe is the Péclet number.

2 Mathematical Model

A laminar buoyant flow in a horizontal parallel channel with height L is considered (see Fig. 1). Both the Darcy–Forchheimer model and the Boussinesq approximation are invoked. The horizontal boundary walls, $\bar{y}=0,L$, exchange heat with an external environment at temperature T_w: the top surface is taken to be perfectly isothermal at temperature T_w (infinite Biot number), while the bottom surface is taken to be imperfectly isothermal (finite Biot number).

The governing mass, momentum, and energy balance equations may be expressed as

$$\overline{\boldsymbol{\nabla}}\cdot\overline{\mathbf{u}}=0 \tag{1}$$

$$\frac{\nu}{K}\left(1+\frac{C_f\sqrt{K}}{\nu}\sqrt{\overline{\mathbf{u}}\cdot\overline{\mathbf{u}}}\right)\overline{u}=-\frac{1}{\rho}\frac{\partial\overline{P}}{\partial\overline{x}} \tag{2}$$

$$\frac{\nu}{K}\left(1+\frac{C_f\sqrt{K}}{\nu}\sqrt{\overline{\mathbf{u}}\cdot\overline{\mathbf{u}}}\right)\overline{v}=-\frac{1}{\rho}\frac{\partial\overline{P}}{\partial\overline{y}}+\beta g(\overline{T}-\overline{T}_w) \tag{3}$$

$$\frac{\nu}{K}\left(1+\frac{C_f\sqrt{K}}{\nu}\sqrt{\overline{\mathbf{u}}\cdot\overline{\mathbf{u}}}\right)\overline{w}=-\frac{1}{\rho}\frac{\partial\overline{P}}{\partial\overline{z}} \tag{4}$$

Contributed by the Heat Transfer Division of ASME for publication in the JOURNAL OF HEAT TRANSFER. Manuscript received July 17, 2008; final manuscript received October 22, 2008; published online May 14, 2009. Review conducted by Peter Vadasz.

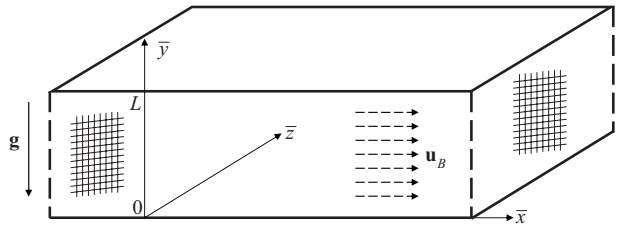

Fig. 1 Sketch of the horizontal porous channel

$$\sigma\frac{\partial\bar{T}}{\partial\bar{t}}+\bar{\mathbf{u}}\cdot\bar{\boldsymbol{\nabla}}\bar{T}=\alpha\bar{\nabla}^2\bar{T}+\frac{\nu}{Kc_p}\left(1+\frac{C_f\sqrt{K}}{\nu}\sqrt{\bar{\mathbf{u}}\cdot\bar{\mathbf{u}}}\right)\bar{\mathbf{u}}\cdot\bar{\mathbf{u}} \tag{5}$$

where σ is the ratio between the average volumetric heat capacity $(\rho c_p)_m$ of the porous medium and the volumetric heat capacity $(\rho c_p)_f$ of the fluid. In Eqs. (1)–(5), the x, y, and z components of velocity are denoted as $\bar{\mathbf{u}}=(\bar{u},\bar{v},\bar{w})$; then the velocity and temperature boundary conditions are expressed as

$$\bar{y}=0:\quad \bar{v}=0=\frac{\partial\bar{T}}{\partial\bar{y}}-\frac{h}{k}(\bar{T}-\bar{T}_w)$$

$$\bar{y}=L:\quad \bar{v}=0=\bar{T}-\bar{T}_w \tag{6}$$

2.1 Nondimensionalization. Let us introduce nondimensional variables such that

$$(\bar{x},\bar{y},\bar{z})=(x,y,z)L,\quad \bar{t}=t\frac{\sigma L^2}{\alpha},\quad (\bar{u},\bar{v},\bar{w})=(u,v,w)\frac{\alpha}{L}$$

$$\bar{T}=\bar{T}_w+T\frac{\nu\alpha}{Kc_p},\quad \bar{p}=p\frac{\mu\alpha}{K} \tag{7}$$

Then, Eqs. (1)–(5) may be rewritten in the form

$$\frac{\partial u}{\partial x}+\frac{\partial v}{\partial y}+\frac{\partial w}{\partial z}=0 \tag{8}$$

$$(1+\eta\sqrt{\mathbf{u}\cdot\mathbf{u}})u=-\frac{\partial p}{\partial x} \tag{9}$$

$$(1+\eta\sqrt{\mathbf{u}\cdot\mathbf{u}})v=-\frac{\partial p}{\partial y}+\mathrm{Ge}T \tag{10}$$

$$(1+\eta\sqrt{\mathbf{u}\cdot\mathbf{u}})w=-\frac{\partial p}{\partial z} \tag{11}$$

$$\frac{\partial T}{\partial t}+u\frac{\partial T}{\partial x}+v\frac{\partial T}{\partial y}+w\frac{\partial T}{\partial z}=\frac{\partial^2 T}{\partial x^2}+\frac{\partial^2 T}{\partial y^2}+\frac{\partial^2 T}{\partial z^2}+(u^2+v^2+w^2)(1+\eta\sqrt{\mathbf{u}\cdot\mathbf{u}}) \tag{12}$$

where $\mathbf{u}=(u,v,w)$ and Ge is the Gebhart number, namely,

$$\mathrm{Ge}=\frac{g\beta L}{c_p} \tag{13}$$

and η is a nondimensional Forchheimer coefficient,

$$\eta=\frac{C_f\sqrt{\mathrm{Da}}}{\mathrm{Pr}}\quad \text{where}\quad \mathrm{Da}=\frac{K}{L^2}\quad \text{and}\quad \mathrm{Pr}=\frac{\nu}{\alpha} \tag{14}$$

The boundary condition (6) may be expressed in dimensionless form,

$$y=0:\quad v=0=\frac{\partial T}{\partial y}-\mathrm{Bi}T$$

$$y=1:\quad v=0=T \tag{15}$$

where Bi is the Biot number, which is defined as

$$\mathrm{Bi}=\frac{hL}{k} \tag{16}$$

2.2 Basic Flow. For the basic solution, we assume a horizontal steady parallel flow in the x-direction and a purely vertical heat flux. Then, the basic state, which has to be analyzed for stability, is given by

$$u_B=\mathrm{Pe}>0,\quad v_B=0,\quad w_B=0$$

$$\frac{\partial p_B}{\partial x}=-\mathrm{Pe}(1+\eta\mathrm{Pe})$$

$$\frac{\partial p_B}{\partial y}=\mathrm{Ge}T_B$$

$$\frac{\partial p_B}{\partial z}=0$$

$$T_B=-\mathrm{Pe}^2(\mathrm{Pe}\,\eta+1)\frac{y^2(\mathrm{Bi}+1)-\mathrm{Bi}y-1}{2(\mathrm{Bi}+1)} \tag{17}$$

where

$$\mathrm{Pe}=\frac{\bar{u}_B L}{\alpha} \tag{18}$$

defines the Péclet number referred to the dimensional uniform base flow velocity $\bar{u}_B$.

2.3 Linearization. Perturbations of the base flow given by Eq. (17) are defined as

$$u=u_B+\varepsilon U,\quad v=v_B+\varepsilon V,\quad w=w_B+\varepsilon W,\quad T=T_B+\varepsilon\theta,$$

$$p=p_B+\varepsilon\mathcal{P} \tag{19}$$

where ε is an asymptotically small perturbation parameter. On substituting Eq. (19) into Eqs. (8)–(12) and neglecting nonlinear terms in the perturbations, i.e., terms of $O(\varepsilon^2)$, one obtains the linearized stability equations, namely,

$$\frac{\partial U}{\partial x}+\frac{\partial V}{\partial y}+\frac{\partial W}{\partial z}=0 \tag{20}$$

$$U(1+2\eta\mathrm{Pe})=-\frac{\partial\mathcal{P}}{\partial x} \tag{21}$$

$$V(1+\eta\mathrm{Pe})=-\frac{\partial\mathcal{P}}{\partial y}+\mathrm{Ge}\theta \tag{22}$$

$$W(1+\eta\mathrm{Pe})=-\frac{\partial\mathcal{P}}{\partial z} \tag{23}$$

$$\frac{\partial\theta}{\partial t}+\mathrm{Pe}\frac{\partial\theta}{\partial x}-\mathrm{Pe}^2(1+\mathrm{Pe}\,\eta)VB(y)=\frac{\partial^2\theta}{\partial x^2}+\frac{\partial^2\theta}{\partial y^2}+\frac{\partial^2\theta}{\partial z^2}+\mathrm{Pe}U(2+3\mathrm{Pe}\,\eta) \tag{24}$$

where B is a function of both Bi and y and is defined as

$$B(y)=y-\frac{\mathrm{Bi}}{2(\mathrm{Bi}+1)} \tag{25}$$

3 Instability With Respect to Rolls

Now, one may differentiate Eqs. (21)–(23) and substitute the results into Eq. (20). Then one may also substitute the velocity components in Eqs. (21) and (22) into Eq. (24) in order to obtain the following pressure/temperature formulation:

$$\left(\frac{1+\mathrm{Pe}\,\eta}{1+2\mathrm{Pe}\,\eta}\right)\frac{\partial^2\mathcal{P}}{\partial x^2}+\frac{\partial^2\mathcal{P}}{\partial y^2}+\frac{\partial^2\mathcal{P}}{\partial z^2}=\mathrm{Ge}\frac{\partial\theta}{\partial y} \tag{26}$$

$$\frac{\partial\theta}{\partial t}+\mathrm{Pe}\frac{\partial\theta}{\partial x}+\mathrm{Pe}^2\left(\frac{\partial\mathcal{P}}{\partial y}-\mathrm{Ge}\,\theta\right)B(y)=\frac{\partial^2\theta}{\partial x^2}+\frac{\partial^2\theta}{\partial y^2}+\frac{\partial^2\theta}{\partial z^2}-\mathrm{Pe}\left(\frac{2+3\mathrm{Pe}\,\eta}{1+2\mathrm{Pe}\,\eta}\right)\frac{\partial\mathcal{P}}{\partial x} \tag{27}$$

Let us assume that the disturbances are given by

$$\mathcal{P}(x,y,z,t)=\Re\{P(y)e^{\lambda t}e^{ia(x\cos\chi+z\sin\chi)}\}$$

$$\theta(x,y,z,t)=\Re\{\Theta(y)e^{\lambda t}e^{ia(x\cos\chi+z\sin\chi)}\} \tag{28}$$

where $\lambda=\lambda_1+i\lambda_2$ is a complex coefficient and χ is the angle between the base flow direction and the propagation direction of the disturbance. The system of Eqs. (26) and (27) now reduces to

$$P''-a^2\left[\left(\frac{1+\mathrm{Pe}\,\eta}{1+2\mathrm{Pe}\,\eta}\right)\cos^2\chi+\sin^2\chi\right]P-\mathrm{Ge}\Theta'=0 \tag{29}$$

$$\Theta''-[\lambda+a^2+ia\mathrm{Pe}\cos\chi-\mathrm{GePe}^2B(y)]\Theta-\mathrm{Pe}^2B(y)P'-ia\mathrm{Pe}\cos\chi\left(\frac{2+3\mathrm{Pe}\,\eta}{1+2\mathrm{Pe}\,\eta}\right)P=0 \tag{30}$$

where primes denote differentiation with respect to y. The boundary condition (15) may be expressed in terms of pressure and temperature as

$$y=0:\quad P'=\mathrm{Ge}\Theta,\quad \Theta'-\mathrm{Bi}\Theta=0;\quad y=1:\quad P'=0=\Theta \tag{31}$$

We will set $\Re(\lambda)=\lambda_1=0$ in order to investigate neutral stability. Moreover, for numerical convenience, we shall also set

$$\gamma=\lambda_2+a\mathrm{Pe}\cos\chi \tag{32}$$

so that Eq. (30) may be rewritten as

$$\Theta''-[a^2+i\gamma-\mathrm{GePe}^2B(y)]\Theta-\mathrm{Pe}^2B(y)P'-ia\mathrm{Pe}\cos\chi\left(\frac{2+3\mathrm{Pe}\,\eta}{1+2\mathrm{Pe}\,\eta}\right)P=0 \tag{33}$$

3.1 Transverse Rolls ($\chi=0$). The condition $\chi=0$ identifies the transverse roll case. Equations (29), (31), and (33) become

$$P''-a^2\left(\frac{1+\mathrm{Pe}\,\eta}{1+2\mathrm{Pe}\,\eta}\right)P-\mathrm{Ge}\Theta'=0 \tag{34}$$

$$\Theta''-[a^2+i\gamma-\mathrm{GePe}^2B(y)]\Theta-\mathrm{Pe}^2B(y)P'-ia\mathrm{Pe}\left(\frac{2+3\mathrm{Pe}\,\eta}{1+2\mathrm{Pe}\,\eta}\right)P=0 \tag{35}$$

$$y=0:\quad P'=\mathrm{Ge}\Theta,\quad \Theta'-\mathrm{Bi}\Theta=0;\quad y=1:\quad P'=0=\Theta \tag{36}$$

3.2 Longitudinal Rolls ($\chi=\pi/2$). In the case $\chi=\pi/2$, Eqs. (29), (31), and (33) become

$$P''-a^2P-\mathrm{Ge}\Theta'=0 \tag{37}$$

$$\Theta''-[a^2+i\gamma-\mathrm{GePe}^2B(y)]\Theta-\mathrm{Pe}^2B(y)P'=0 \tag{38}$$

$$y=0:\quad P'=\mathrm{Ge}\Theta,\quad \Theta'-\mathrm{Bi}\Theta=0;\quad y=1:\quad P'=0=\Theta \tag{39}$$

It is important to note the absence of the parameter η in Eqs. (37)–(39). Thus, longitudinal rolls are not affected by the dependence on the Forchheimer term in the momentum equation. Moreover, the problem becomes self-adjoint as one may now set $\gamma=0$ and determine the solution $\{P,\Theta\}$ in terms of real-valued functions.

4 Eigenvalue Problem

Equations (29) and (33) are a pair of coupled homogeneous complex second order ODEs and are subject to the four homogeneous boundary conditions (Eq. (31)). The system always admits a null solution, but it may also be interpreted as an eigenvalue problem for λ where values for λ depend on Ge, Pe, η, χ, and a. Alternatively, incipient instability is given by $\lambda_1=0$; therefore the system may now be regarded as a double eigenvalue problem for Pe and γ, for example, as functions of the remaining parameters. The computation of these eigenvalues requires a further normalization condition to force the solutions for P and Θ to be nonzero; we choose the following:

$$\mathrm{Bi}\Theta'(0)+\Theta(0)=\mathrm{Bi}+1 \tag{40}$$

It also proves convenient to work with the parameter

$$R=\mathrm{GePe}^2 \tag{41}$$

rather than Ge. The critical value of R, which is denoted by R_{cr}, is now determined by seeking the minimum of R as a function of a in the neutral stability curve. In practice this is done by extending the system, Eqs. (29) and (33), by differentiating it with respect to a and by setting $\partial R/\partial a=0$.

4.1 Stability Analysis. In order to solve Eqs. (29), (31), (33), and (40), a numerical solver based on the classical fourth order Runge–Kutta method coupled with the shooting method has been used. In all cases we used 100 intervals, and this, coupled with the fourth order accuracy of the method, yields highly accurate results. The change in R_{cr} as a function of three parameters has been studied. These parameters are the Biot parameter Bi, the angle χ, and the parameter η_+, which is defined as

$$\eta_+=\frac{\eta}{\sqrt{\mathrm{Ge}}} \tag{42}$$

and allows one to remove the explicit dependence on Ge in the physically reasonable range of very small Ge. Indeed, if one substitutes Eq. (42) and the relationship

$$P_+(y)=\frac{P(y)}{\mathrm{Ge}} \tag{43}$$

in Eqs. (29), (31), (33), and (40), one obtains

$$P_+''-a^2\left[\left(\frac{1+\sqrt{R}\eta_+}{1+2\sqrt{R}\eta_+}\right)\cos^2\chi+\sin^2\chi\right]P_+-\Theta'=0 \tag{44}$$

$$\Theta''-[a^2+i\gamma-RB(y)]\Theta-RB(y)P_+'-ia\sqrt{\mathrm{Ge}R}\cos\chi\left(\frac{2+3\sqrt{R}\eta_+}{1+2\sqrt{R}\eta_+}\right)P_+=0 \tag{45}$$

$$y=0:\quad P_+'=\Theta,\quad \Theta'-\mathrm{Bi}\Theta=0,\quad \mathrm{Bi}\Theta'+\Theta=\mathrm{Bi}+1;\qquad y=1:\quad P_+'=0=\Theta \tag{46}$$

It must be mentioned that, on account of Eq. (42), the limit $\eta_+\to 0$ can be interpreted as the limit of the negligible form-drag effect, i.e., the limit of validity of Darcy's law. On the other hand, the limit $\eta_+\to\infty$ is the limit of a very small Gebhart number.

Under the physically realistic assumption of $\mathrm{Ge}\ll 1$, if R is of

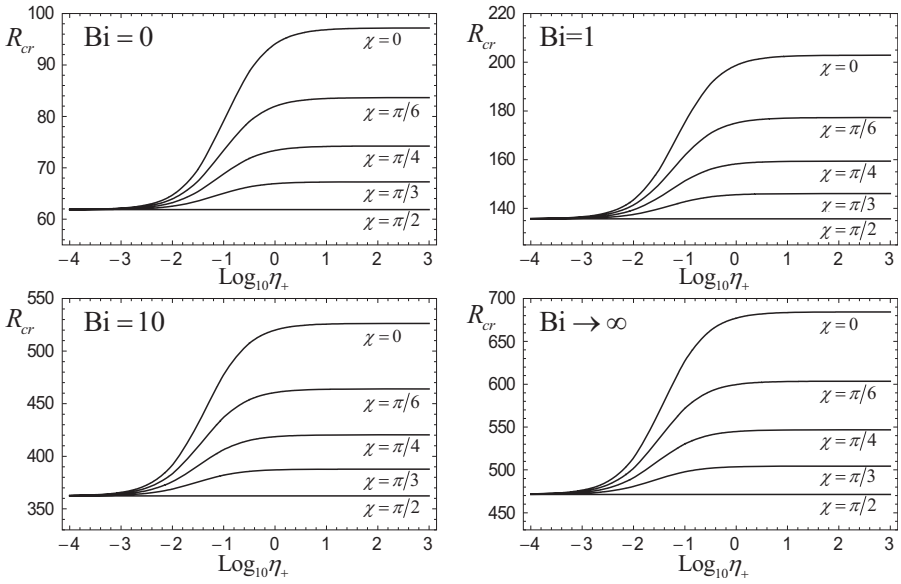

Fig. 2 R_{cr} **as a function of** η_+ **for different values of** χ **for** $\mathrm{Bi}=0,1,10,\infty$

$O(1)$, then the last term on the left hand side of Eq. (45) is of $O(\mathrm{Ge}^{1/2})$. As a consequence, this term is significantly smaller than the other terms. Thus, one can easily infer that neglecting this term allows one to set $\gamma=0$, so that the problem becomes self-adjoint and only admits real solutions for (P,Θ). The Biot number Bi affects the bottom boundary condition. On account of Eq. (25), in the limit of an adiabatic boundary, one has

$$\mathrm{Bi}\to 0 \Rightarrow B(y)=y \tag{47}$$

while, in the limit of a perfectly isothermal boundary, one has

$$\mathrm{Bi}\to\infty \Rightarrow B(y)=y-\tfrac{1}{2} \tag{48}$$

From Fig. 2 one can see that, for any chosen parameter set, the values of R_{cr} are higher in the case of an isothermal bottom boundary than in the case of an adiabatic bottom boundary. This feature could have been expected. In fact, when examining the basic flow in the case of isothermal bottom boundary ($\mathrm{Bi}\to\infty$), one can see from Eq. (48) that the midplane $y=1/2$ is adiabatic, i.e., $B(1/2)=0$. In other words, in the analysis of the basic flow, the layer with adiabatic bottom boundary is coincident with the upper half of the layer with isothermal bottom boundary, except for the thickness. One sees that R is proportional to L^3. Therefore, one would expect that the critical value of R in the case of a layer with isothermal bottom boundary is eight times that in the case of a layer with adiabatic bottom boundary. The factor of 8 would be exact if in the perturbed flow of the layer with isothermal bottom boundary, the midplane $y=1/2$ is both adiabatic and impermeable. In fact, these conditions are perfectly fulfilled by the basic flow but not by the disturbances. It should be mentioned, however, that the lower half of the layer with isothermal bottom boundary is expected to be affected only marginally by roll disturbances as the midplane $y=1/2$ is, in the basic state, hotter than the bottom boundary $y=0$.

In Fig. 2 one may also notice that R_{cr}, for every Biot number Bi, is not affected by the orientation angle χ in the limit of validity of Darcy's law, $\eta_+\to 0$. On the contrary, in the limit of important form-drag effects with $\mathrm{Ge}\ll 1$ ($\eta_+\to\infty$), one finds an important dependence of R_{cr} on the orientation of the oblique rolls. In particular, longitudinal rolls ($\chi=\pi/2$) appear to be the most unstable. For longitudinal rolls, R_{cr} is independent of η_+. This feature is evident from Eqs. (44)–(46) as the parameter η_+ disappears from the equations when $\chi=\pi/2$. For $\eta_+\to 0$ there appears an asymptotic behavior described in Table 1. For $\eta_+\to\infty$, a different asymptotic value of either R_{cr} or a_{cr} is reached for every χ. The highest asymptotic values of R_{cr} or a_{cr} refer to transverse rolls ($\chi=0$). These values are reported in Table 1.

Figure 3 shows the plots of the critical wavenumber a_{cr} versus η_+ for different orientation angles χ and Biot numbers Bi. The qualitative behavior of a_{cr} is similar to that of R_{cr}. The curves display the asymptotic behavior for $\eta_+\to 0$ as for $\eta_+\to\infty$. Both the lower and the upper asymptotic values are specified in Table 1.

The plots reported in Figs. 4–7 suggest a not too strong dependence of $\Theta_{cr}(y)$ on both η_+ and χ. In particular, for $\eta_+=10^{-5}$, the solid and dashed lines corresponding, respectively, to $\chi=0$ and $\chi=\pi/4$ are perfectly coincident. Indeed, the eigenvalue problem (44)–(46) becomes independent of χ in the limit $\eta_+\to 0$ (i.e., in the limit of validity of Darcy's law). The temperature profiles $\Theta_{cr}(y)$ represented in Fig. 4 refer to an adiabatic bottom boundary, while those reported in Figs. 5–7 refer to an imperfectly isothermal boundary ($\mathrm{Bi}=1,10$) and to a perfectly isothermal boundary ($\mathrm{Bi}\to\infty$). Due to Eq. (46), all the profiles reported in Figs. 4–7 display at $y=0$ a fixed temperature, $\Theta(0)=(\mathrm{Bi}+1)/(\mathrm{Bi}^2+1)$, and a fixed heat flux, $\Theta'(0)=\mathrm{Bi}(\mathrm{Bi}+1)/(\mathrm{Bi}^2+1)$.

Figures 8–11 refer to critical conditions and show the isotherms, $\theta=\mathrm{const}$, and the streamlines of the two-dimensional velocity disturbance field (U,V), respectively, for the orientation angle $\chi=0$ and $\eta_+=10^3$. In fact, from Eq. (23), one has $W=0$ as Eq. (28) predicts for $\chi=0$ that $\mathcal{P}$ is independent of z. For the adiabatic case, $\mathrm{Bi}=0$ (Figs. 8 and 9), one may see that the velocity rolls are spread over the whole channel width and are almost symmetric with respect to the horizontal midplane. When the bottom boundary is isothermal, $\mathrm{Bi}\to\infty$ (Figs. 10 and 11), the velocity rolls are placed predominantly within the upper part of the chan-

Table 1 Asymptotic values of a_{cr} **and** R_{cr} **for different Biot numbers**

	$\eta_+\to 0$		$\eta_+\to\infty;\ \chi=0$	
Bi	a_{cr}	R_{cr}	a_{cr}	R_{cr}
0	2.4483	61.867	3.0342	97.184
1	2.9697	135.71	3.6482	202.88
10	4.2573	362.32	5.0722	526.30
∞	4.6752	471.38	5.5616	684.36

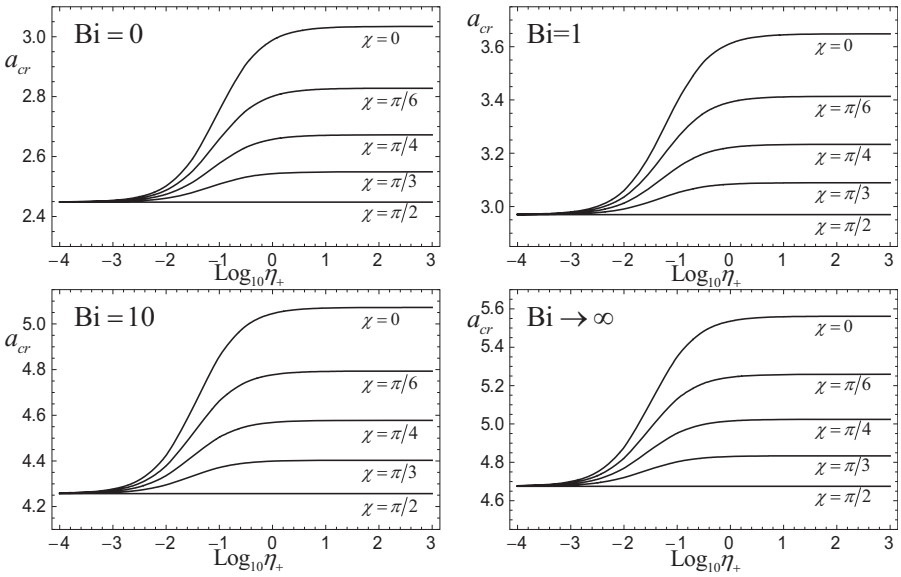

Fig. 3 a_{cr} as a function of η_+ for different values of χ for Bi=0,1,10,∞

nel. This upward displacement is justified since the fluid is unstably stratified only in the upper part of the porous layer. In fact, in the basic flow solution Eq. (17) for Bi→∞, the horizontal midplane is hotter than the boundary planes.

5 Conclusion

A stability analysis of the basic parallel uniform flow in a horizontal porous layer with impermeable boundaries has been per-

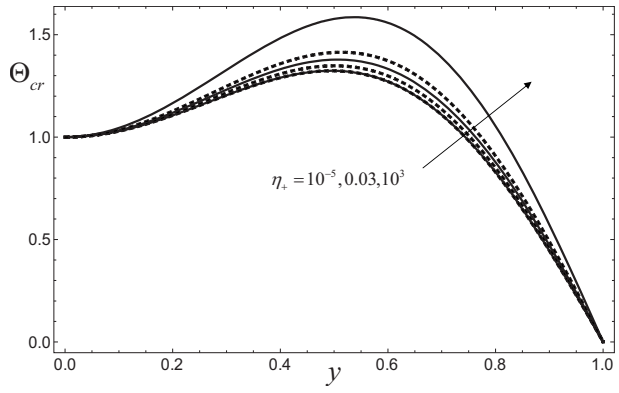

Fig. 4 Plots of Θ_{cr} as a function of y for Bi=0 and $\eta_+ = 10^{-5}, 0.03, 10^3$. Solid lines refer to $\chi=0$, while dashed lines refer to $\chi=\pi/4$.

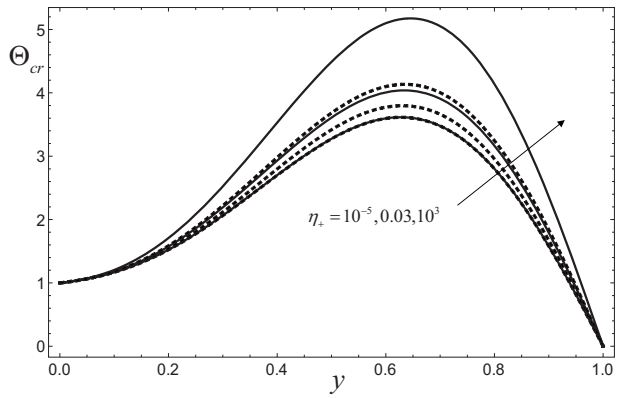

Fig. 5 Plots of Θ_{cr} as a function of y for Bi=1 and $\eta_+ = 10^{-5}, 0.03, 10^3$. Solid lines refer to $\chi=0$, while dashed lines refer to $\chi=\pi/4$.

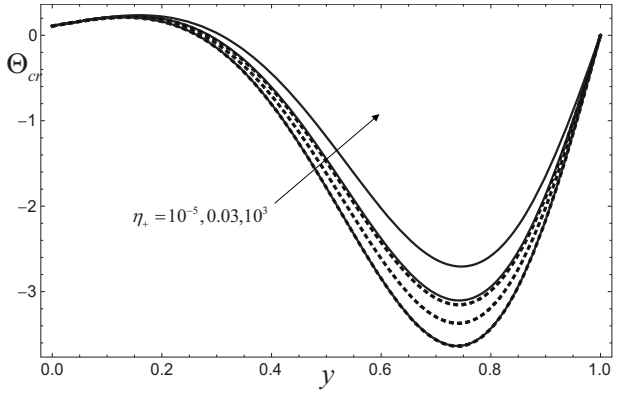

Fig. 6 Plots of Θ_{cr} as a function of y for Bi=10 and $\eta_+ = 10^{-5}, 0.03, 10^3$. Solid lines refer to $\chi=0$, while dashed lines refer to $\chi=\pi/4$.

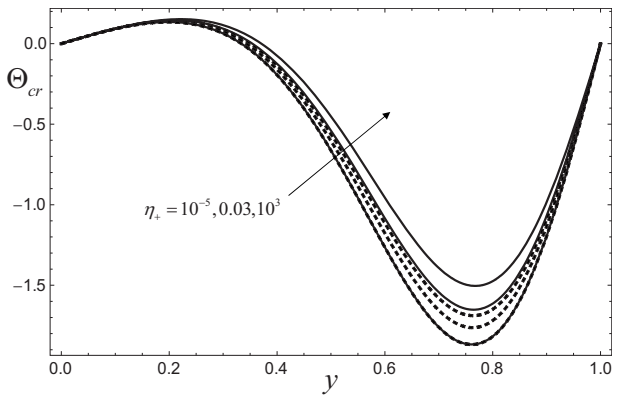

Fig. 7 Plots of Θ_{cr} as a function of y for Bi→∞ and $\eta_+ = 10^{-5}, 0.03, 10^3$. Solid lines refer to $\chi=0$, while dashed lines refer to $\chi=\pi/4$.

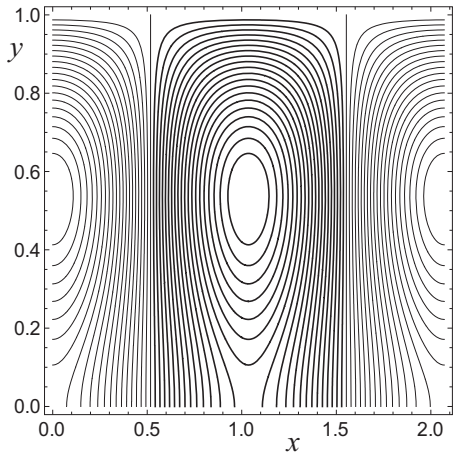

Fig. 8 Disturbance isotherms for Bi=0, $\eta_+=10^3$, and $\chi=0$

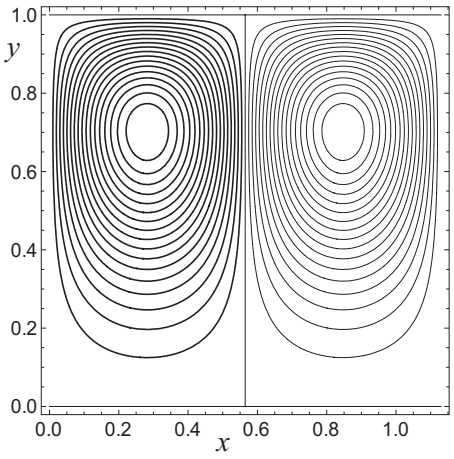

Fig. 11 Streamlines for Bi$\to\infty$, $\eta_+=10^3$, and $\chi=0$

formed. The Darcy–Forchheimer model, together with the Oberbeck–Boussinesq approximation, has been adopted. The basic temperature profile is nonlinear due to the effect of viscous dissipation. The top boundary plane has been taken to be isothermal. The bottom boundary has been assumed to be subject to a third kind boundary condition described in the dimensionless equations through the Biot number, Bi. The conditions of vanishing heat flux and of uniform temperature at the bottom boundary are mathematically expressed as two limiting cases Bi$\to$0 (adiabatic boundary) Bi$\to\infty$ (isothermal boundary). Arbitrarily orientated roll disturbances have been studied by adopting a pressure-temperature formulation. The resulting eigenvalue ODE problem has been solved numerically by means of a fourth order Runge–Kutta method coupled with the shooting method.

The main results obtained are the following:

1. The governing parameter describing the onset of convective instabilities is $R=\mathrm{GePe}^2$, where Ge is the Gebhart number and Pe is the Péclet number.
2. Under the physically reasonable assumption Ge$\ll$1, the eigenvalue ODE problem becomes self-adjoint, thus admitting real solutions.
3. The most unstable rolls are the longitudinal ones.
4. The critical wavenumber and the critical value of R for the onset of longitudinal rolls are independent of the form-drag coefficient.
5. The critical wavenumber and the critical value of R for the onset of transverse or oblique rolls other than longitudinal ones depend on the form-drag coefficient.
6. The layer with an isothermal bottom boundary is more stable than the layer with an adiabatic bottom boundary.

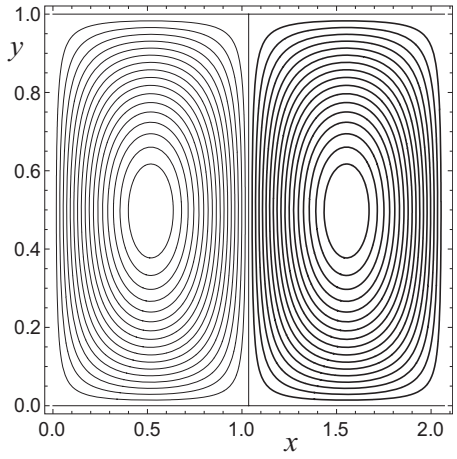

Fig. 9 Streamlines for Bi=0, $\eta_+=10^3$, and $\chi=0$

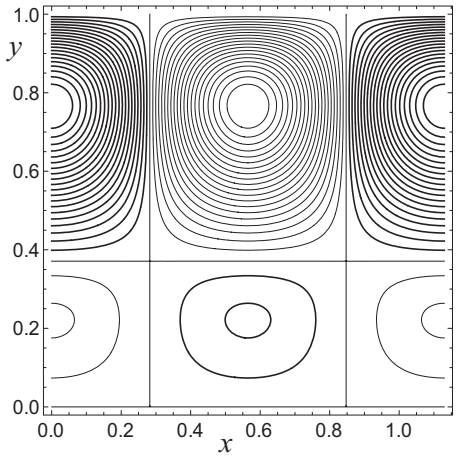

Fig. 10 Disturbance isotherms for Bi$\to\infty$, $\eta_+=10^3$, and $\chi=0$

Nomenclature

a = nondimensional wavenumber, Eq. (28)
Bi = Biot number, Eq. (16)
$B(y)$ = nondimensional function, Eq. (25)
c_p = specific heat at constant pressure
C_f = Forchheimer parameter
Da = Darcy number, Eq. (14)
g = modulus of gravitational acceleration
$\mathbf{g}$ = gravitational acceleration
Ge = Gebhart number, Eq. (13)
h = external heat transfer coefficient
K = permeability
k = effective thermal conductivity
L = channel height
n = integer number
p = nondimensional pressure, Eq. (7)
$\mathcal{P}$ = nondimensional pressure disturbance, Eq. (19)
$P(y)$ = nondimensional function, Eq. (28)
$P_+(y)$ = nondimensional function, Eq. (43)
Pe = Péclet number, Eq. (18)
Pr = Prandtl number, Eq. (14)
R = nondimensional parameter, Eq. (41)
$\Re$ = real part
t = nondimensional time, Eq. (7)

T = nondimensional temperature, Eq. (7)
$\bar{T}_w$ = boundary temperature or external temperature
u,v,w = nondimensional velocity components, Eq. (7)
U,V,W = nondimensional velocity disturbances, Eq. (19)
x,y,z = nondimensional coordinates, Eq. (7)

Greek Symbols

α = effective thermal diffusivity
β = volumetric coefficient of thermal expansion
γ = reduced exponential coefficient, Eq. (32)
η = nondimensional Forchheimer parameter, Eq. (14)
η_+ = nondimensional modified Forchheimer parameter, Eq. (42)
ε = perturbation parameter, Eq. (19)
θ = nondimensional temperature disturbance, Eq. (19)
$\Theta(y)$ = nondimensional function, Eq. (28)
λ = exponential coefficient, Eq. (28)
λ_1,λ_2 = real and imaginary parts of λ
ν = kinematic viscosity
ρ = mass density
σ = heat capacity ratio
χ = angle between the propagation direction of the disturbance and the x-axis

Superscript and Subscripts

$-$ = dimensional quantity
B = base flow
cr = critical value

References

[1] Horton, C. W., and Rogers, F. T., Jr., 1945, "Convection Currents in a Porous Medium," J. Appl. Phys., **16**, pp. 367–370.
[2] Lapwood, E. R., 1948, "Convection of a Fluid in a Porous Medium," Proc. Cambridge Philos. Soc., **44**, pp. 508–521.
[3] Nield, D. A., and Bejan, A., 2006, *Convection in Porous Media*, 3rd ed., Springer, New York.
[4] Rees, D. A. S., 2000, "Stability of Darcy-Bénard Convection," *Handbook of Porous Media*, K. Vafai, ed., Dekker, New York, pp. 521–558.
[5] Tyvand, P. A., 2002, "Onset of Rayleigh-Bénard Convection in Porous Bodies," *Transport Phenomena in Porous Media II*, D. B. Ingham and I. Pop, eds., Elsevier, New York, pp. 82–112.
[6] Prats, M., 1966, "The Effect of Horizontal Fluid Flow on Thermally Induced Convection Currents in Porous Mediums," J. Geophys. Res., **71**, pp. 4835–4838.
[7] Rees, D. A. S., Magyari, E., and Keller, B., 2005, "Vortex Instability of the Asymptotic Dissipation Profile in a Porous Medium," Transp. Porous Media, **61**, pp. 1–14.
[8] Barletta, A., Celli, M., and Rees, D. A. S., 2009, "The Onset of Convection in a Porous Layer Induced by Viscous Dissipation: A Linear Stability Analysis," Int. J. Heat Mass Transfer, **52**, pp. 337–344.
[9] Storesletten, L., and Barletta, A., 2009, "Linear Instability of Mixed Convection of Cold Water in a Porous Layer Induced by Viscous Dissipation," Int. J. Therm. Sci., **48**, pp. 655–664.

S. Haussener
Department of Mechanical and Process Engineering,
ETH Zurich,
8092 Zurich, Switzerland

W. Lipiński
Department of Mechanical Engineering,
University of Minnesota,
Minneapolis, MN 55455

J. Petrasch
Department of Mechanical and Process Engineering,
ETH Zurich,
8092 Zurich, Switzerland

P. Wyss
Department of Electronics/Metrology,
EMPA Material Science and Technology,
Überlandstrasse 129,
8600 Dübendorf, Switzerland

A. Steinfeld[1]
Department of Mechanical and Process Engineering,
ETH Zurich,
8092 Zurich, Switzerland;
Solar Technology Laboratory,
Paul Scherrer Institute,
5232 Villigen, Switzerland
e-mail: aldo.steinfeld@eth.ch

Tomographic Characterization of a Semitransparent-Particle Packed Bed and Determination of its Thermal Radiative Properties

A two-phase medium consisting of densely packed large nonspherical semitransparent particles in a transparent fluid is considered. Its 3D digital geometry is obtained by computer tomography and employed to numerically calculate its porosity, specific surface, pore and particle size distributions, and the representative elementary volume for continuum domain. The collision-based Monte Carlo method is applied to calculate the probability distribution functions for attenuation path length and direction of incidence at the fluid-solid interface for each phase, which, in turn, are used to derive the extinction and scattering coefficients and the scattering phase functions. The methodology is applied to a packed bed of $CaCO_3$ particles, used in industrially relevant high-temperature processes. Spectral and directional dependencies of the radiative properties are analyzed. [DOI: 10.1115/1.3109261]

Keywords: packed bed, radiation, semitransparent, solar energy, chemical reactors

1 Introduction

Packed-bed reactors are commonly used in chemical processing because of their relatively high contacting area. Of special interest are packed beds for solar-driven thermochemical processes, e.g., the thermal and carbothermic reductions of ZnO [1,2] and the gasification of coal [3,4], which proceed above 1500 K using concentrated solar radiation as the energy source of high-temperature process heat. At these temperatures, thermal radiative transport becomes the dominant heat transfer mode. Thus, knowledge of the radiative properties of packed beds is crucial for the engineering design and optimization of these chemical reactors and processes. Experimental investigations of transmittance and extinction coefficients of porous media have been performed for foams and packed beds of opaque, transparent, and semitransparent phases [5–8]. Numerical simulation were carried out for artificially generated [9–16] and real [17,18] porous media by applying the radiative distribution function identification (RDFI) [9,17,18], Monte Carlo (MC) [15,16], two-flux [10–12], and discrete ordinate [13] methods.

In this paper, the RDFI method, calculated by MC, is applied to determine the radiative properties of a packed bed containing large nonspherical semitransparent particles. $CaCO_3$ particles (source: Carrara marble; Ferret's diameter=3 mm) have been selected for modeling because of their relevance in the high-temperature processing of lime, cement, and other material commodities, and in the capture of CO_2 from combustion flue gases [19].

Radiative characteristics of packed beds containing complex morphological structures may significantly deviate from those obtained when applying simplifying approximations, e.g., spherical particles. In this paper, computer tomography (CT) is applied to obtain the exact 3D geometrical representation of complex porous media composed of semitransparent phases. CT allows for nondestructive scanning of the structure in a single experimental run. In contrast to previous investigations [9–16], the CT-based methodology enables the determination of accurate effective radiative properties in the limit of geometric optics with negligible diffraction, which, in turn, can serve as reference values to those obtained by approximate methods.

2 Governing Equations

Radiative transfer in a quasicontinuous two-phase medium containing semitransparent phases can be described by two coupled equations of radiative transfer equations (RTEs) for phases i and j[2][18].

$$f_{v,i}\left[\frac{dI_i(s,\hat{\mathbf{s}})}{ds}+\beta_i I_i(s,\hat{\mathbf{s}})\right] = f_{v,i}\left[n_i^2\kappa_i I_{ib}(s,\hat{\mathbf{s}})+\frac{\sigma_{s,ii}}{4\pi}\int_{4\pi} I_i(s,\hat{\mathbf{s}}_{in})\Phi_{ii}(\hat{\mathbf{s}},\hat{\mathbf{s}}_{in})d\Omega_{in}\right] + f_{v,j}\frac{\sigma_{s,ji}}{4\pi}\int_{4\pi} I_j(s,\hat{\mathbf{s}}_{in})\Phi_{ji}(\hat{\mathbf{s}},\hat{\mathbf{s}}_{in})d\Omega_{in}, \quad i,j=1,2;\ i\neq j \tag{1}$$

[1]Corresponding author.

Manuscript received May 7, 2008; final manuscript received February 11, 2009; published online May 4, 2009. Review conducted by Ofodika A. Ezekoye.

[2]The spectral subscript λ is omitted for brevity.

where $\sigma_{s,i}$ and Φ_i are the internal scattering coefficient and internal scattering phase function of the bulk material forming phase i, $\sigma_{s,ii}$ and Φ_{ii} are those associated with internal reflections and internal scattering within phase i, and $\sigma_{s,ij}$ and Φ_{ij}, $i \neq j$, are those associated with radiation leaving phase i and entering phase j. Thus,

$$\sigma_{s,ii} = \sigma_{s,\mathrm{refl},i} + \sigma_{s,i} \tag{2}$$

$$\Phi_{ii} = \sigma_{s,ii}^{-1}(\Phi_{\mathrm{refl},i}\sigma_{s,\mathrm{refl},i} + \Phi_i\sigma_{s,i}) \tag{3}$$

$$\beta_i = \kappa_i + \sigma_{s,ii} + \sigma_{s,ij} \tag{4}$$

where $\sigma_{s,i}$, k_i, and Φ_i are determined by applying an appropriate theory, e.g., Mie. The two-phase medium morphology-associated properties $\sigma_{s,\mathrm{refl},i}$, $\sigma_{s,ij}$, $\Phi_{\mathrm{refl},i}$, and Φ_{ij} are determined by applying the MC methodology outlined below.

3 Methodology

The collision-based Monte Carlo ray-tracing method is used [20]. Characteristic size parameters $\xi = \pi d_h/\lambda \gg 1$ for both phases are assumed; thus, geometric optics is valid [21]. A large number of stochastic rays are launched within a representative elementary volume (REV). The rays are emitted isotropically and are uniformly distributed over REV. They undergo scattering/absorption internally and reflection/refraction at the fluid-solid interface. The distance between emission and collision points, and the direction of incidence at the interface are recorded for each ray. The following probability density and cumulative distribution functions, and the corresponding medium properties are then computed.

For the attenuation (extinction) path length within phase i,

$$F_{e,i} = \frac{1}{N_{\mathrm{ray},i}} \sum_{k=1}^{N_{\mathrm{ray},i}} \delta(s - s_k), \quad i = 1,2 \tag{5}$$

$$G_{e,i}(s) = \int_0^s F_{e,i}(s^*)ds^* \approx 1 - \exp(-\beta_i s), \quad i = 1,2 \tag{6}$$

For the absorption path length within phase i,

$$F_{a,i} = \frac{1}{N_{\mathrm{ray},i}} \sum_{k=1}^{N_{\mathrm{ray},i}} \delta(s - s_{a,k}), \quad i = 1,2 \tag{7}$$

$$G_{a,i}(s) = \int_0^s F_{a,i}(s^*)ds^* \approx \frac{\kappa_i}{\beta_i}[1 - \exp(-\beta_i s)], \quad i = 1,2 \tag{8}$$

For the scattering path length associated with refraction from phases i to j, and reflection and internal scattering within phase i,

$$F_{s,ij}(s) = \frac{1}{N_{\mathrm{ray},i}} \sum_{k=1}^{N_{\mathrm{ray},i}} \delta(s - s_{s,k}), \quad i,j = 1,2 \tag{9}$$

$$G_{s,ij}(s) = \int_0^s F_{s,ij}(s^*)\mathrm{d}s^* \approx \frac{\sigma_{ij}}{\beta_i}[1 - \exp(-\beta_i s)], \quad i,j = 1,2 \tag{10}$$

For the direction of incidence at the phase interface within phase i,

$$F_{\mu_{\mathrm{in}},i} = \frac{1}{N_{\mathrm{att},i}} \sum_{k=1}^{N_{\mathrm{att},i}} \delta(\mu_{\mathrm{in},i} - \mu_{\mathrm{in},i,k}), \quad i = 1,2 \tag{11}$$

$$\Phi_{ij}(\mu_s) = \frac{2\int_{\mu_{\mathrm{in}}=0}^{1}\int_{\varphi_d=0}^{\pi}\int_{\mu_{\mathrm{refl}}=0}^{1} \delta(\mu_s - \sqrt{(1-\mu_{\mathrm{in}}^2)(1-\mu_{\mathrm{refl}}^2)}\cdot\cos\varphi_d - \mu_{\mathrm{in}}\mu_{\mathrm{refl}})\cdot\rho''(\mu_{\mathrm{in}},\mu_{\mathrm{refl}},\varphi_d)F_{\mu_{\mathrm{in}},i}\mu_{\mathrm{refl}}d\mu_{\mathrm{refl}}d\varphi_d d\mu_{\mathrm{in}}}{\int_{\mu_{\mathrm{in}}=0}^{1}\int_{\varphi_d=0}^{\pi}\int_{\mu_{\mathrm{refl}}=0}^{1}\rho''(\mu_{\mathrm{in}},\mu_{\mathrm{refl}},\varphi_d)F_{\mu_{\mathrm{in}},i}\mu_{\mathrm{refl}}d\mu_{\mathrm{refl}}d\varphi_d d\mu_{\mathrm{in}}}, \quad i = j = 1,2 \tag{12}$$

$$\Phi_{ij}(\mu_s) = \frac{2\int_{\mu_{\mathrm{in}}=0}^{1}\int_{\varphi_d=0}^{\pi}\int_{\mu_t=0}^{1} \delta(\mu_s - \sqrt{(1-\mu_{\mathrm{in}}^2)(1-\mu_t^2)}\cdot\cos\varphi_d - \mu_{\mathrm{in}}\mu_t)\cdot(1-\rho''(\mu_{\mathrm{in}},\mu_t,\varphi_d))F_{\mu_{\mathrm{in}},i}\mu_t d\mu_t d\varphi_d d\mu_{\mathrm{in}}}{\int_{\mu_{\mathrm{in}}=0}^{1}\int_{\varphi_d=0}^{\pi}\int_{\mu_t=0}^{1}(1-\rho''(\mu_{\mathrm{in}},\mu_t,\varphi_d))F_{\mu_{\mathrm{in}},i}\mu_t d\mu_t d\varphi_d d\mu_{\mathrm{in}}}, \quad i \neq j = 1,2 \tag{13}$$

In Eqs. (5)–(13), $N_{\mathrm{ray},i}$ is the number of rays launched in phase i within REV, and $N_{\mathrm{att},i}$ is the number of rays attenuated in phase i at the phase interface.

4 Application to a Packed Bed of $CaCO_3$ Particles

4.1 Morphology Characterization. *Computer tomography.* The sample consists of a packed bed of nonspherical $CaCO_3$ particles randomly placed in a 4.5 cm-diameter rubber tube, as seen in Fig. 1(*a*). The sample is exposed to a polychromatic X-ray beam, generated by electrons incident on a wolfram target and filtered by a 0.0025 mm Re filter. The generator is operated at an acceleration voltage of 140 keV and a current of 0.11 mA. A Hamamatsu flatpanel C7942 CA-02 protected by a 0.1 mm brass filter is used to detect the transmitted X-rays. The sample is scanned at 600 angles (projections). Each projection is an average over 8 scans with exposure time of 0.25 s, leading to a voxel size of 45 μm. Figures 1(*b*) and 1(*c*) show the 2D tomographic image and the 3D surface rendering of the sample, respectively.

The histogram of the normalized absorption values $\alpha/\alpha_{\max}$, shown in Fig. 2, reveals two distinct peaks that account for the solid and fluid (void) phases. The calculated and nearly identical width of the two peaks supports the assumption of homogeneity. The calculated minimum between the two peaks ($\alpha/\alpha_{\max} = 0.43$) is used as threshold value for phase identification. Phase boundaries between two $CaCO_3$ particles are neglected, as they cannot be distinguished in the tomography images.

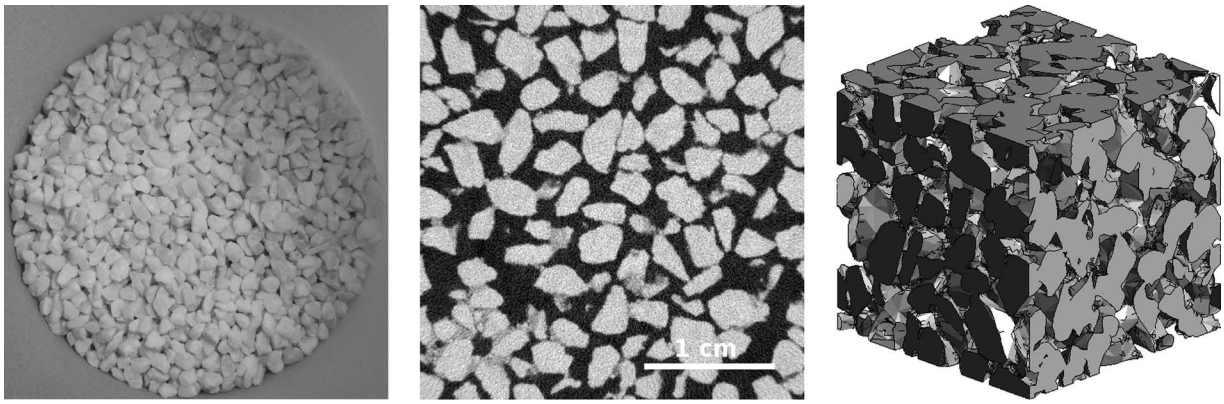

Fig. 1 Sample of the packed bed of $CaCO_3$ particles: (*a*) top view photograph, (*b*) 2D tomographic image, and (*c*) 3D surface rendering

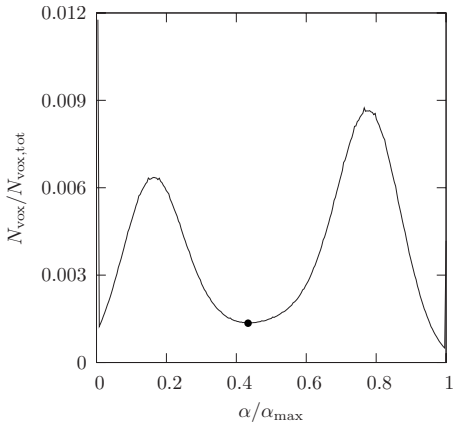

Fig. 2 Normalized histogram of the sample's absorption values obtained by CT for the void phase (left peak) and for the solid phase (right peak). The bullet indicates the threshold value $\alpha/\alpha_{max}=0.43$ used for phase identification.

Porosity and specific surface. The two-point correlation function indicates the probability of two points separated by a distance r to be in the void phase, given by [22,23]

$$s_2(r) = \frac{\int_V \int_{4\pi} \psi(\mathbf{r})\psi(\mathbf{r}+r\hat{\mathbf{s}})d\hat{\mathbf{s}}d\mathbf{r}}{4\pi V} \tag{14}$$

where ψ is the pore-space indicator function (=1 if the point lies within the void space; =0 if it lies within the solid phase). The specific surface area and porosity are calculated from [22]

$$\left.\frac{ds}{dr}\right|_{r=0} = -\frac{A_0}{4} \tag{15}$$

$$\lim_{r\to\infty} s_2(r) = \varepsilon^2 \tag{16}$$

$$s_2(0) = \varepsilon \tag{17}$$

Figure 3(*a*) shows the two-point correlation function for the $CaCO_3$ packed bed. The calculated porosity is 0.39, which compares well with the porosity determined experimentally from the sample weight 0.40 ± 0.02. This value is close to the one for a

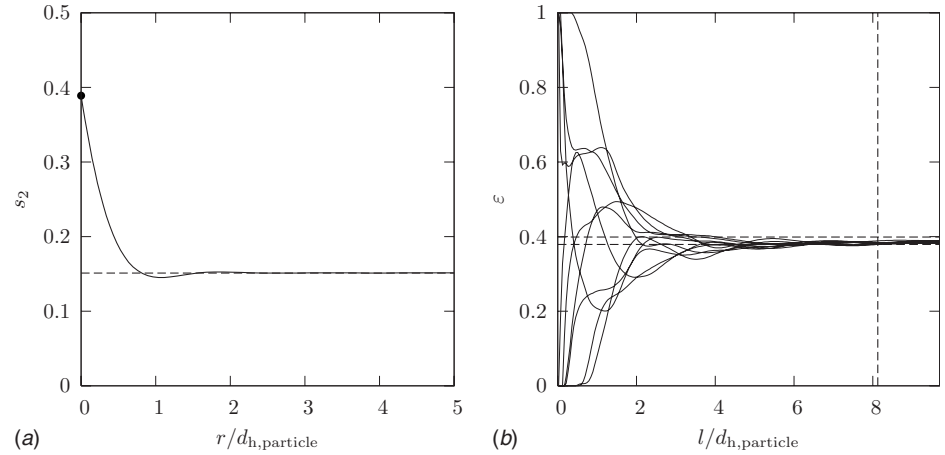

Fig. 3 (*a*) Two-point correlation function for the $CaCO_3$ packed bed. The value at $r=0$ corresponds to the bed porosity. The dashed line indicates the asymptotic value of the function, which corresponds to ε^2. (*b*) Determination of the REV edge length (indicated by the vertical dashed line) by calculating the porosity of ten subvolumes with varying edge lengths l at random locations. The tolerance band for conversion and determination of the REV volume at $\varepsilon \pm 0.01$ is indicated by the two horizontal dashed lines.

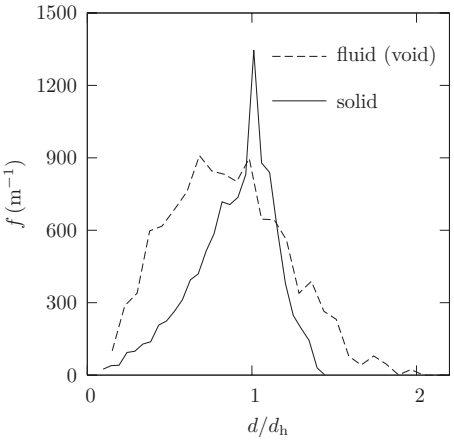

Fig. 4 Opening size distribution functions, $f=-d\varepsilon_{\mathrm{op}}(d)/(\varepsilon_\infty dd)$ of the solid and fluid phases of the $CaCO_3$ packed bed ($d_h \equiv d_{\mathrm{h,pore}}$ for fluid and $d_h \equiv d_{\mathrm{h,particle}}$ for solid)

dense random or orthorhombic packed bed made of uniform monodispersed spheres [24]. The calculated specific surface area is 1.31×10^3 m^{-1}, which corresponds to an analytically calculated particle diameter of 2.8 mm for uniform monodispersed spheres. As will be shown later, the hydraulic particle diameter for the randomly shaped $CaCO_3$ particles lies around 1.9 mm.

Table 1 Arithmetic mean diameter, mode, median, and hydraulic diameter calculated from the pore and particle size distributions

	Pore	Solid
Arithmetic mean (mm)	1.00	1.66
Mode (mm)	0.81	1.89
Median (mm)	0.98	1.75
Hydraulic diameter (mm)	1.19	1.87

Representative elementary volume. REV indicates the minimum volume for which the continuum assumption is still valid. REV is determined based on the porosity for subvolume sizes at ten random locations in the sample, as indicated in Fig. 3(*b*). Note that for an edge length l approaching zero, the porosity is either 0 or 1, depending whether the point lies in the void or the solid phase. Assuming a tolerance band of ±0.01, $l_{\mathrm{REV}}=0.0152$ m (for ±0.02, $l_{\mathrm{REV}}=0.0105$ m; for ±0.05 $l_{\mathrm{REV}}=0.0054$ m) and is used as the minimum sample size in the following analysis.

Pore and particle size distributions. Opening, a mathematical morphology operation consisting of erosion followed by dilation using the same structuring element, is applied to calculate the pore and particle size distributions, i.e., the size distribution defined by the sphere that fits completely within the pore or particle space, respectively. Figure 4 shows the distribution functions of the pore and particle sizes. The median, mode, mean, and hydraulic diameters $d_{\mathrm{h,particle}}=4\varepsilon/A_0$ and $d_{\mathrm{h,pore}}=4(1-\varepsilon)/A_0$ are listed in Table 1. Thus, the assumption of geometrical optics is valid for $\lambda < 3500$ μm.

4.2 Radiative Properties. In this section, the void phase and the $CaCO_3$ particles of the packed bed are referred to as fluid and solid phases, respectively. The corresponding phase indices i,j used in Eqs. (5)–(13) are 1 for the fluid phase and 2 for the solid phase. Spectral calculations of the radiative properties are performed for 150 distinct points between 0.1 μm and 100 μm. Reflection and refraction at the specularly reflecting and diffusely reflecting interfaces are modeled by Fresnel's equations and diffuse reflection/refraction, respectively.

Single-phase internal radiative properties. The fluid phase is assumed to be transparent, i.e., its internal absorption and scattering coefficients $\sigma_{s,1}$ and κ_1, respectively, are equal to zero, and its refractive index is equal to 1. The bulk properties of $CaCO_3$ are determined based on the properties of $CaCO_3$ grains (monocrystals). They are randomly shaped and oriented, as seen in the scanning electron microscope (SEM) photograph of Fig. 5. Their characteristic size is 160 μm. Figure 6 shows the complex refractive index $m_2=n_2-ik_2$ of $CaCO_3$ [25]. In the spectral range 0.2–6 μm, the imaginary part was obtained by applying the Lorentz theory [26].

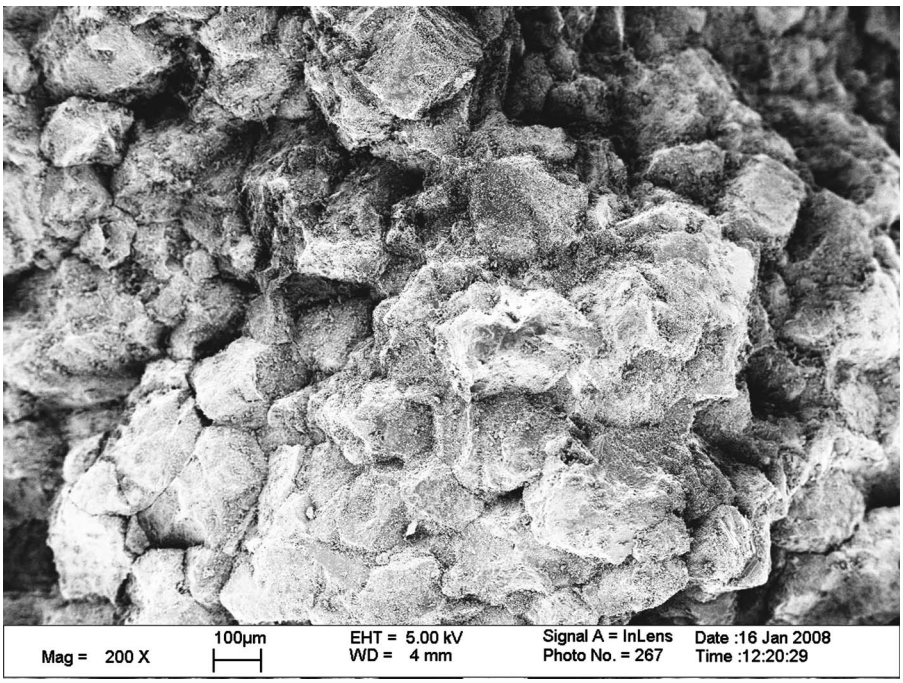

Fig. 5 SEM picture of a single $CaCO_3$ particle

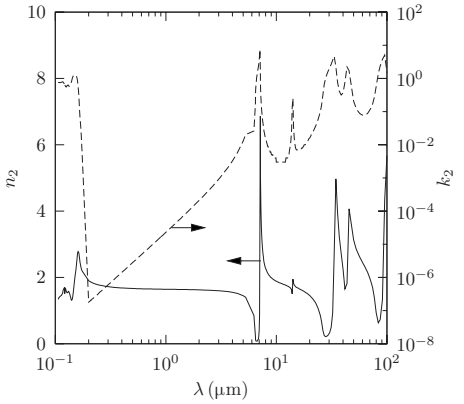

Fig. 6 Complex refractive index of $CaCO_3$: (solid line) real part obtained experimentally [25], and (dashed line) imaginary part obtained by the Lorentz theory in the spectral range 0.2–6 μm [26] and experimentally in the remaining range [25]

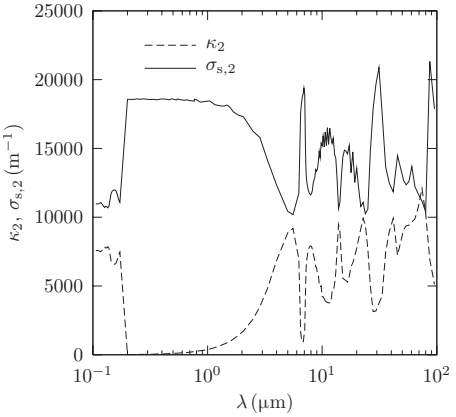

Fig. 8 Internal absorption and scattering coefficients of $CaCO_3$ particles

The directional-hemispherical reflectivities at the specular fluid-solid interface for radiation incident from the fluid phase $\rho_{sp,12}$ and for radiation incident from the solid phase $\rho_{sp,21}$ are calculated using Fresnel's equations [21]. The hemispherical reflectivities of both sides of a diffuse fluid-solid interface ρ_d are equal to that for a diffuse $CaCO_3$ surface [27]. For $\lambda<0.8$ μm and $\lambda>2.5$ μm, the hemispherical reflectivity is extrapolated with constant values 0.85 and 0.87, respectively. $\rho_{sp,12}$, $\rho_{sp,21}$, and ρ_d are shown in Fig. 7 as a function of wavelength.

The internal radiative coefficients of $CaCO_3$, $\sigma_{s,2}$, and κ_2, obtained by applying the Mie theory, are shown in Fig. 8 [28]. The spectral oscillations, particularly for $\lambda>6$ μm, result from oscillations in the complex refractive index (see Fig. 6). The internal scattering within $CaCO_3$ is assumed isotropic ($\Phi_2=1$). Figure 9 shows the ratio of the scattering efficiency factor for dependent scattering, calculated by gas, packed-sphere, liquid, or modified-liquid model [29], to that for independent scattering calculated by Mie theory (assumed $f_v=1$). Dependent scattering effects are thus neglected in this study since the maximal reduction in the scattering efficiency factor for 100 μm$>\lambda>$0.1 μm is only about 10%.

Two-phase medium radiative coefficients. The scattering coefficients of the $CaCO_3$ packed-bed two-phase medium are shown in Fig. 10 as a function of wavelength for the fluid phase (Figs. 10(*a*) and 10(*b*)) and the solid phase (Figs. 10(*c*) and 10(*d*)), assuming specularly reflecting particles (Figs. 10(*a*) and 10(*c*)) and diffusely reflecting particles (Figs. 10(*b*) and 10(*d*)). The reflection behavior of the fluid-solid interface significantly influences $\sigma_{s,ij}$ and $\sigma_{s,\mathrm{refl},i}$. For the fluid phase and specular interface, $\sigma_{s,\mathrm{refl},i}<\sigma_{s,ij}$ for $\lambda<6$ μm, while for the diffuse interface $\sigma_{s,\mathrm{refl},i}>\sigma_{s,ij}$. For the solid phase, $\sigma_{s,\mathrm{refl},i}>\sigma_{s,ij}$, and this trend is independent of the reflection interface type. $\sigma_{s,\mathrm{refl},1}$, obtained for the specular and diffuse interfaces, clearly follows the shape of ρ_{sp} and ρ_d, respectively (see Fig. 7). $\sigma_{s,\mathrm{refl},2}$ and $\sigma_{s,21}$ are additionally influenced by the presence of the total reflection phenomenon in the particle. Obviously, for any phase, $\sigma_{s,ij}$ is complementary to $\sigma_{s,\mathrm{refl},i}$ since it refers to the transmitted portions of radiation across the interface.

The extinction coefficients β_i are shown in Fig. 11. They are independent of the interface reflection type (specular/diffuse). In addition, β_1 is independent of λ as it is a function of the interface geometry only. β_2 increases with λ because of the increasing $\kappa_2+\sigma_{s,2}$. The spectral oscillations in β_1 result from the statistical MC oscillations. The spectral oscillations in β_2 are mostly the result of the spectral oscillations of κ_2 and $\sigma_{s,2}$ (see Fig. 8).

Two-phase medium scattering phase functions. The probability density functions of the directional cosine of the incidence angle at the fluid-solid interface, determined by MC, are plotted in Fig. 12 for both phases. Assuming $\kappa_2=\sigma_{s,2}=0$, $F_{\mu_{in},1}$ and $F_{\mu_{in},2}$ compare well to $F_{\mu_{in}}$, computed for identical overlapping opaque spheres (IOOS) and for identical overlapping transparent spheres

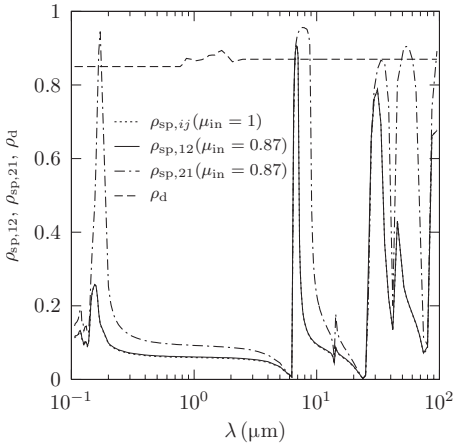

Fig. 7 Spectral directional-hemispherical reflectivities at the specular fluid-solid interface for selected incidence directions, and spectral hemispherical reflectivity of the diffuse fluid-solid interface

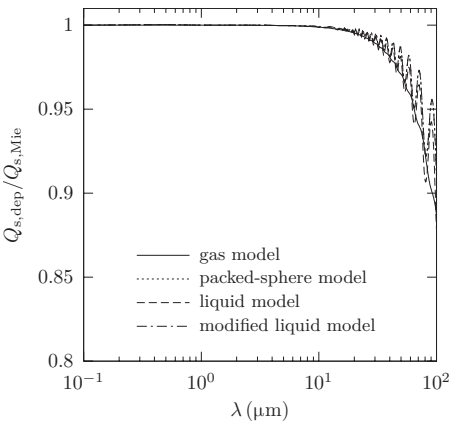

Fig. 9 Ratio of the scattering efficiency factor obtained for dependent scattering calculated by gas, packed-sphere, liquid, and modified-liquid models to that obtained for independently scattering calculated by the Mie theory

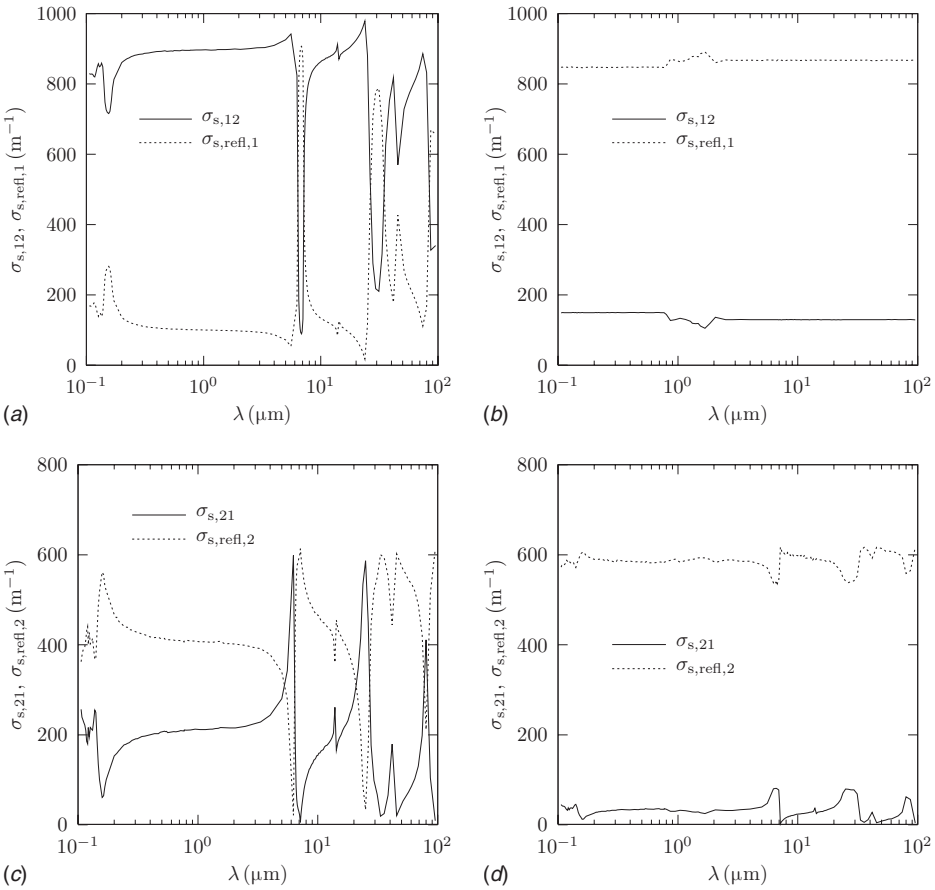

Fig. 10 Spectral scattering coefficients of the $CaCO_3$ packed bed for ((*a*) and (*b*)) the fluid phase and ((*c*) and (*d*)) the solid phase, assuming ((*a*) and (*c*)) specularly reflecting particles and ((*b*) and (*d*)) diffusely reflecting particles

(IOTS), respectively [9,17]. For the real values of κ_2 and $\sigma_{s,2}$, $F_{\mu_{in},2}$ depends weakly on β_2 and hence on λ. The dependency of $F_{\mu_{in},2}$ on β_2 is explained by the fact that, for increasing β_2, the incidence angles corresponding to longer paths occur less frequently. Functions $F_{\mu_{in},i}$ are then used to calculate the scattering phase functions by applying Eqs. (12) and (13).

Figures 13 and 14 show the scattering phase functions for spectral and diffuse interfaces, respectively, as a function of the cosine of the scattering angle at selected wavelengths λ = 0.1 μm, 1 μm, 10 μm, and 100 μm. Φ_{12} and Φ_{21} are identical for the specularly reflecting solid-fluid interface because the Fresnel's equation gives the same results when the angle of incidence and transmission are interchanged [21]. The forward scattering peak decreases with λ due to increasing normal-hemispherical reflectivity of the interface, which in turn is the result of the increasing n_2 and k_2. Since total reflection is assumed for the diffuse interface, $\Phi_{21}=0$ for $\mu_s < -\sqrt{1-\mu_{refl,tot}^2}$. For the specular interface, $\Phi_{refl,1}$ and $\Phi_{refl,2}$ are clearly functions of λ due to the spectral variation of ρ_{sp}, while

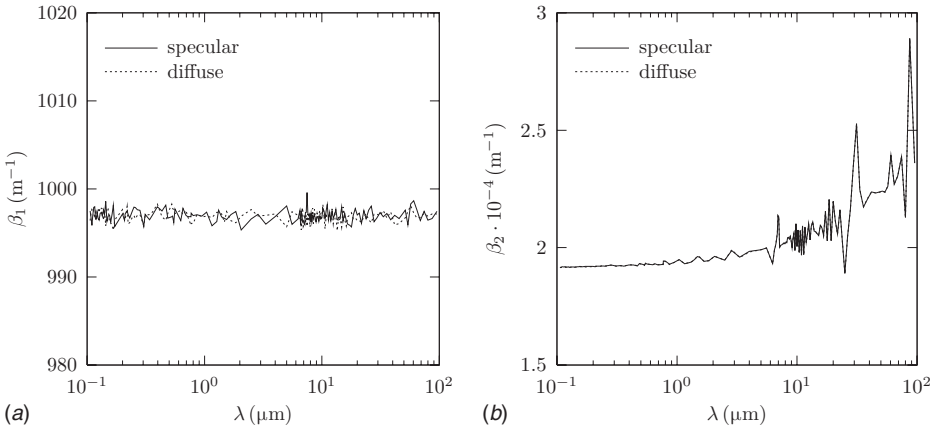

Fig. 11 Spectral extinction coefficients of the packed bed: (*a*) fluid phase and (*b*) solid phase

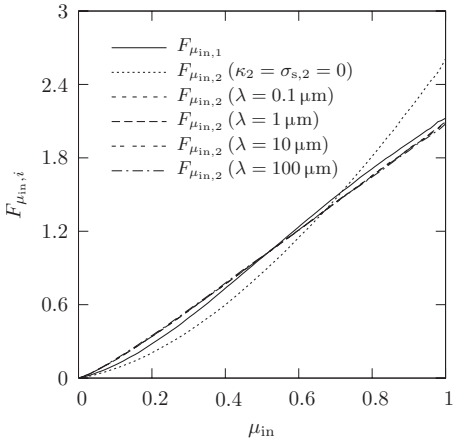

Fig. 12 Probability density functions of the directional cosine of the incident angle at the fluid-solid interface for selected wavelengths

this cannot be observed for the diffuse interface. The jump of $\Phi_{\text{refl},2}$ is explained by enhanced interface reflections for $\mu_s > \sqrt{1-\mu_{\text{refl,tot}}^2} - \mu_{\text{refl,tot}}$. Obviously, Φ_{11} is equal to $\Phi_{\text{refl},1}$ because of the absence of internal scattering in the fluid phase. In contrast, Φ_{22} is mostly influenced by Φ_2 because of the large internal scattering in the solid phase (see Eq. (3)).

Sensitivity analysis. A MC parametric study is carried out to elucidate the influence of the uncertainties in n_2, k_2, and ρ_d on the radiative properties by varying by $\pm 20\%$ their reference values $n_2 = 1.64$, $k_2 = 2.3 \times 10^{-5}$, and $\rho_d = 0.87$ at $\lambda = 1$ μm. These variations do not affect β_i ($<1\%$ change). κ_2 is influenced by variations of k_2 (up to 20%) and n_2 (6%) for specular and diffuse fluid-solid interfaces. For the specular interface, variation of n_2 leads to remarkable effect on $\sigma_{s,\text{refl},1}$, $\sigma_{s,\text{refl},2}$, $\sigma_{s,12}$, and $\sigma_{s,21}$ (up to 66% change), because ρ_{sp} depends on n_2. For diffusely reflecting particles, variation of n_2 and k_2 leads to only small variations in $\sigma_{s,\text{refl},1}$, $\sigma_{s,\text{refl},2}$, and $\sigma_{s,12}$ (up to 5% change) due to the varying particle optical thicknesses and the total reflection angles. The change in $\sigma_{s,21}$ is up to 55%. The variation of ρ_d has a more pronounced effect on the scattering coefficients. For example, for $\rho_d = 1.0$ (no refraction), $\sigma_{s,ij} = 0$, while reduction in ρ_d by 20% nearly doubles $\sigma_{s,ij}$. Decreasing values of n_2 augments the forward scattering peaks of Φ_{12} and Φ_{21} for both specular and diffuse interfaces, as seen in Fig. 15. This is due to smaller relative angles between the incident and refracted rays for both specular and diffuse interfaces, according to Fresnel's equations. Variations of k_2 and ρ_d by $\pm 20\%$ do not affect the scattering phase functions. Variation of n_2 has an effect on $\Phi_{\text{refl},1}$ and $\Phi_{\text{refl},2}$ for the specular interface because the shape of $\rho_{sp}(\mu_{in})$ depends on n_2. Specular reflection generally leads to more pronounced forward scattering

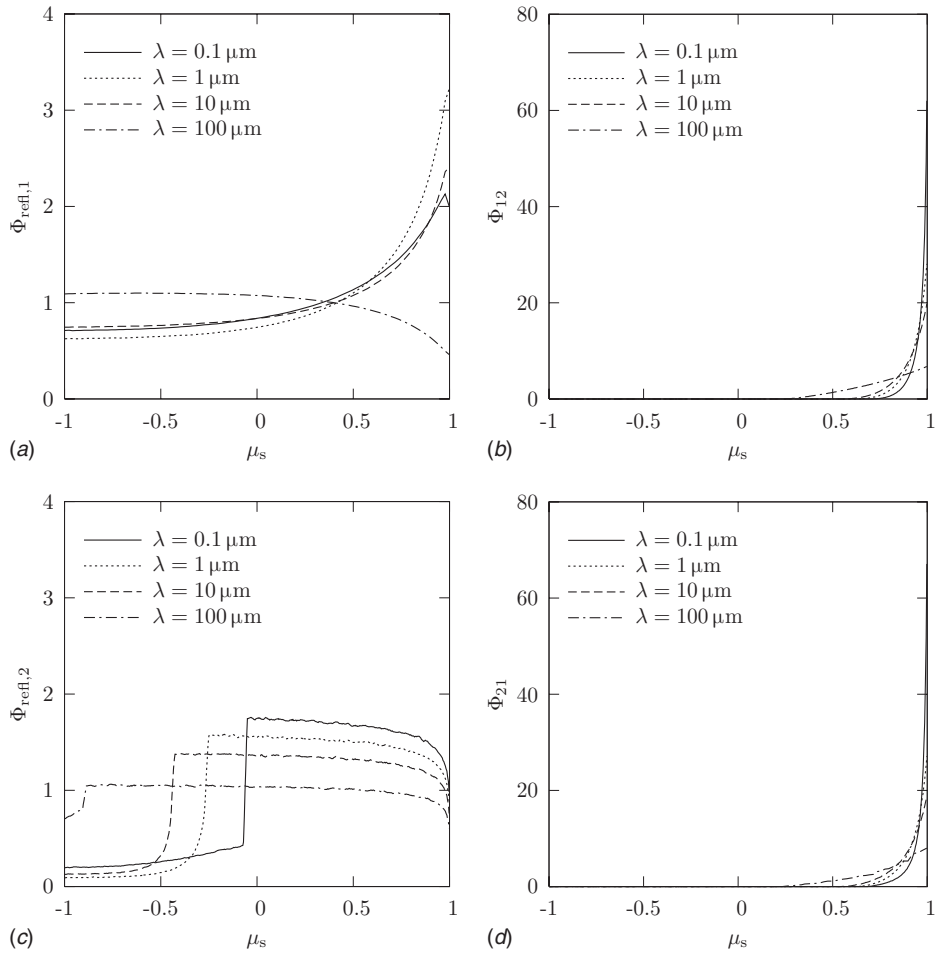

Fig. 13 Scattering phase functions of the $CaCO_3$ packed bed versus cosine of the scattering angle for a specularly reflecting solid-fluid interface, at selected wavelengths $\lambda = 0.1$ μm, 1 μm, 10 μm, and 100 μm

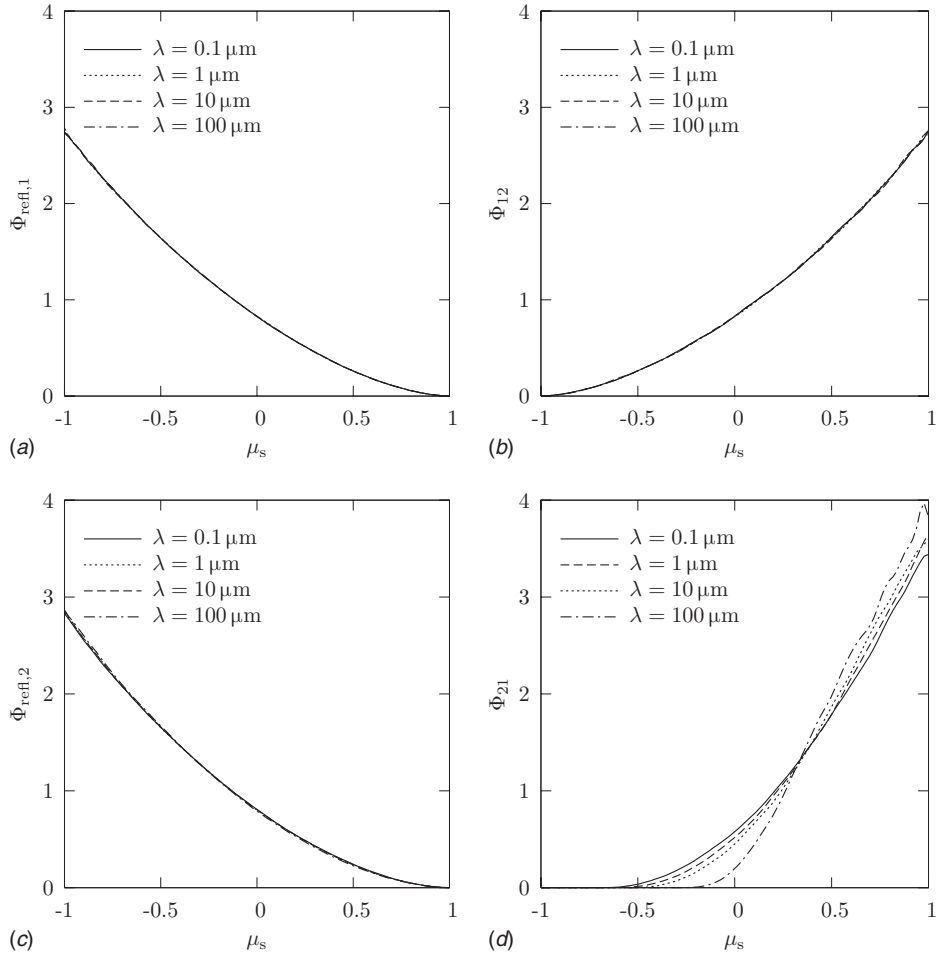

Fig. 14 Scattering phase functions of the $CaCO_3$ packed bed versus cosine of the scattering angle for a diffusely reflecting solid-fluid interface, at selected wavelengths $\lambda = 0.1$ μm, 1 μm, 10 μm, and 100 μm

in $\Phi_{\text{refl},1}$ and $\Phi_{\text{refl},2}$, mainly as a result of the enhanced reflective behavior of the interface at larger incidence angles, while backward scattering is favored for diffusely reflecting particles. This behavior is less evident for materials with higher β_2 and $\sigma_{s,2}$, respectively, since the fraction of internal (isotropic) scattering is larger. Sensitivity analysis of the statistically determined characteristic size of the grains indicates that reduced grain size enhances the variations in the extinction behavior for wavelengths above 10 μm, while the opposite is true for larger grain sizes. Changing the characteristic size by $\pm 20\%$ leads to variations in the extinction efficiency of up to 13%, scattering efficiency of up to 25%, and absorption efficiency of up to 19%.

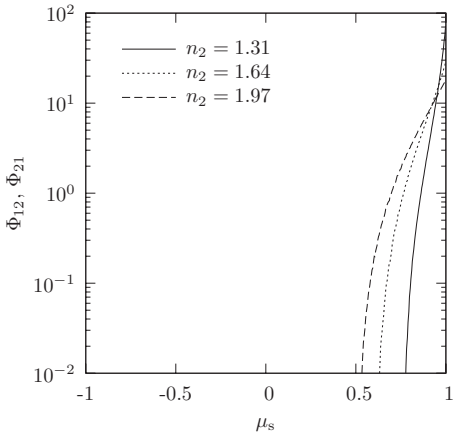

Fig. 15 Scattering phase function Φ_{12} and Φ_{21} for specular and diffuse fluid-solid interfaces, as a function of the scattering angle cosine, for selected refractive indices $n_2 = 1.31$, 1.64, and 1.97

Accuracy and validation of the MC algorithm. MC convergence is examined for 2-norms of $F_{\mu_{\text{in}},i}$, $G_{\text{e},i}$, $G_{\text{a},i}$, and $G_{\text{s},ij}$ for 10^4, 10^5, 10^6, 10^7, and 10^8 stochastic rays, normalized with respect to the reference solution for 10^9 rays, $\epsilon = \|\bar{y} - \bar{y}_{\text{ref}}\|_2 / \|\bar{y}_{\text{ref}}\|_2$, with $\bar{y}$ being the computed vector of the corresponding cumulative distribution function for the corresponding number of rays. The results are shown for the selected functions in Fig. 16. ϵ decrease exponentially with N_{ray}. The maximum $\epsilon = 1.3$, obtained for $F_{\mu_{\text{in}},2}$ using $N_{\text{ray}} = 10^4$, decreases to 1.2×10^{-2} using $N_{\text{ray}} = 10^8$. ϵ is relatively high for $F_{\mu_{\text{in}},2}$ because of the large values of the optical thickness inside the particles, which leads to a small number of rays reaching particle boundaries and, consequently, high uncertainties in $F_{\mu_{\text{in}},2}$.

The MC algorithm was used to calculate the radiative characteristics of an independently scattering particle cloud of large opaque spheres for $f_v = 1.6 \times 10^{-3}$, $d = 2$ μm, $n = 1.64$, and $k = 2.6 \times 10^{-5}$ at $\lambda = 1$ μm. The scattering phase functions for diffusely reflecting and specularly reflecting particle surfaces are plotted in Fig. 17. Also shown are the corresponding phase functions obtained analytically [21].

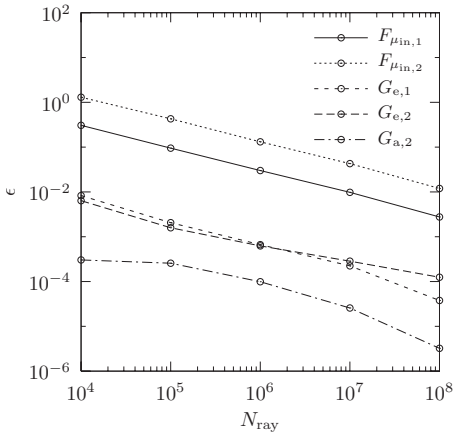

Fig. 16 Normalized two-norm of the cumulative distribution functions

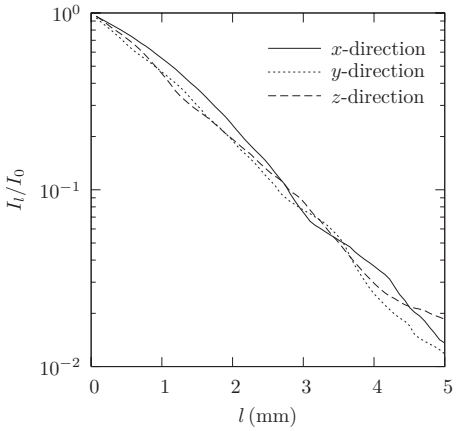

Fig. 18 Normalized mean intensity along three orthogonal directions as a function of sample length

$$\Phi_{\text{refl,1,d,an}}(\mu_s) = \frac{8}{3\pi}(\sqrt{1-\mu_s} - \mu_s \arccos(\mu_s)) \tag{18}$$

$$\Phi_{\text{refl,1,sp,an}}(\mu_s) = \frac{\rho_{sp}(1/2(\pi - \arccos(\mu_s)))}{2\int_0^1 \rho_{sp}(\mu_{in})\mu_{in} d\mu_{in}} \tag{19}$$

The scattering and extinction coefficients can be calculated analytically [21] as follows:

$$\sigma_{s,an} = \frac{3}{2}\frac{f_v}{d}Q_s \tag{20}$$

$$\beta_{an} = \frac{3}{2}\frac{f_v}{d}Q_e \tag{21}$$

where $Q_{s,d}=\rho_d$, $Q_{s,sp}=\rho_{sp}$, and $Q_e=1$ for large spheres without diffraction [21]. The MC-computed scattering coefficients for diffuse and specular particles, and the extinction coefficients are 1071 m^{-1}, 126 m^{-1}, and 1237 m^{-1}, respectively; the analytically calculated ones are 1032 m^{-1}, 121 m^{-1}, and 1200 m^{-1}, respectively. Furthermore, the code was validated for IOOS and IOTS [17].

The anisotropy of the sample was examined by subdividing the volume domain in eight subvolumes and calculating β_i along each coordinate axis for each subvolume [17], assuming opaque particles. The results are presented in Fig. 18 and indicate the negligible role of the sample's anisotropy.

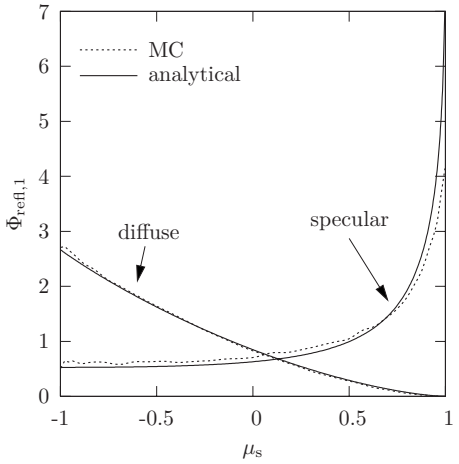

Fig. 17 MC (dashed line) and analytically (solid line) calculated phase functions of a particle cloud for $f_v=1.6\times10^{-3}$, $d=2$ μm, $n=1.64$, and $k=2.6\times10^{-5}$ at $\lambda=1$ μm, $\rho_d=0.866$, and for specularly and diffusively reflecting particles

The MC algorithm was further used to compute the radiative characteristics of a cubic ($\varepsilon=0.48$) and orthorhombic ($\varepsilon=0.40$) packed bed of glass spheres ($n=1.5$, $k=0$ at $\lambda=0.6328$ μm) with diameter 1.269 mm. Since the glass particles are transparent at $\lambda=0.6328$ μm, $I_1(\hat{s})=I_2(\hat{s})$ [18] and $\beta_{MC}=\beta_1\varepsilon+\beta_2(1-\varepsilon)$. β_{MC} was calculated to be 1775 m^{-1} and 1952 m^{-1} for the cubic and orthorhombic bed configurations, respectively. The experimentally determined value for a randomly packed bed ($\varepsilon=0.42$) was $\beta_{EX}=2326\pm416$ m^{-1} [6]. The strength of the CT-based methodology is that it can utilize the exact 3D geometry of porous media in the limit of the geometric optics with negligible diffraction. Once the accurate spectral bulk (microscale) radiative properties of the material and interface are known, the macroscale radiative properties can be determined with good accuracy.

5 Conclusions

A computational technique has been developed to study the thermal radiative properties of two-phase media containing densely packed large nonspherical semitransparent particles. The 3D digital geometry of a packed bed of $CaCO_3$ particles was obtained by employing CT and was used to directly determine medium morphological characteristics such as porosity, specific surface, pore and particle size distributions, and the REV for continuum domain. The collision-based MC method was applied to calculate the probability distribution functions of the attenuation path length and the direction of incidence at the fluid-solid interface for the fluid and solid phases, which, in turn, were used to obtain the radiative properties of the two-phase medium.

Spectral extinction coefficients were found to be independent on the reflectivity type (specular/diffuse) of the fluid-solid interface. In contrast, they depend strongly on the packed-bed geometry and the internal extinction coefficient $\sigma_{s,2}+\kappa_2$, which increases with wavelength due to the increasing complex refractive index. The scattering coefficients associated with refraction and reflection at the fluid-solid interface $\sigma_{s,ij}$ $(i\neq j)$ and $\sigma_{s,refl,i}$, respectively, depend on its morphology and reflective characteristics and on the internal radiative properties of the solid phase. $\sigma_{s,ij}$ and $\sigma_{s,refl,i}$ behave complementary. Scattering functions related to the diffraction phenomenon Φ_{ij} $(i\neq j)$ are restricted by total reflection. $\Phi_{refl,i}$ strongly depends on wavelength for specularly reflecting interfaces, while the opposite is true for diffuse-reflecting interfaces. Forward scattering was found to be predominant for specular-reflecting particles, while backscattering is typical for

diffusely reflecting particles. Large internal extinction coefficient with isotropic internal scattering lead to less pronounced directional behavior of Φ_{ii}.

Directional determination of the extinction coefficient elucidated the negligible anisotropy of the sample. The MC algorithm was validated by computing the radiative properties of semitransparent porous media reported in the literature.

The methodology presented here can be generally applied for the determination of the radiative properties of porous materials of complex geometry, especially for low porosity media where measurements become difficult.

Acknowledgment

This work has been financially supported by the Swiss National Science Foundation under C No. 200021-115888 and by the European Commission under Contract No. 212470 (Project HYCYCLES). We thank M. F. Modest for fruitful discussions and M. Huber for the SEM images.

Nomenclature

A_0 = specific surface, m^{-1}
d = particle diameter, m
d_h = hydraulic diameter, m
f = size distribution function, m^{-1}
f_v = volumetric fraction
F = probability density function
G = cumulative distribution function
I = radiative intensity, W m^{-3} sr^{-1}
k = imaginary part of complex refractive index
l = length, m
m = complex refractive index
n = real part of complex refractive index
N_{ray} = number of rays
N_{att} = number of attenuated rays
N_{vox} = number of voxels
Q = efficiency factor
r = distance between two points in the sample, m
$\mathbf{r}$ = position vector for spatial coordinates in the sample, m
s = path length, m
$\hat{\mathbf{s}}$ = unit vector of path direction
s_2 = two-point correlation function
V = total sample volume, m^3

Greek

α = absorption values of tomographic scans, m^{-1}
β = extinction coefficient, m^{-1}
δ = Dirac delta function
ε = porosity
κ = absorption coefficient, m^{-1}
λ = radiation wavelength, m
μ_{in} = cosine of incidence angle
μ_{refl} = cosine of reflection angle
μ_s = cosine of scattering angle
μ_t = cosine of transmission angle
ξ = size parameter
ϵ = normalized two-norm of relative error
ρ'' = bidirectional reflectivity, sr^{-1}
ρ' = directional-hemispherical reflectivity
σ = scattering coefficient, m^{-1}
φ_d = difference azimuthal angle $\varphi_d = \varphi_{in} - \varphi_r$, rad
φ_{in} = azimuthal angle of incidence, rad
φ_r = azimuthal angle of reflection, rad
Φ = scattering phase function
ψ = pore-space indicator function
ω = scattering albedo
Ω = solid angle, sr

Subscripts

a = absorption
an = analytical
b = blackbody
boundary = medium's boundary
d = diffuse
dep = dependent
e = extinction
EX = experiment
i, j = phase indices (1 = void, 2 = solid)
in = incoming
int = internal
max = maximum
op = opening
ref = reference
refl = reflection
refr = refraction
s = scattering
sp = specular
tot = total
λ = spectral
∞ = initial

References

[1] Schunk, L., Haeberling, P., Wepf, S., Wuillemin, D., Meier, A., and Steinfeld, A., 2008, "A Receiver-Reactor for the Solar Thermal Dissociation of Zinc Oxide," ASME J. Sol. Energy Eng., **130**, p. 021009.
[2] Wieckert, C., Frommherz, U., Kräupl, S., Guillot, E., Olalde, G., Epstein, M., Santen, S., Osinga, T., and Steinfeld, A., 2007, "A 300 kW Solar Chemical Pilot Plant for the Carbothermic Production of Zinc," ASME J. Sol. Energy Eng., **129**, pp. 190–196.
[3] von Zedtwitz, P., and Steinfeld, A., 2005, "Steam-Gasification of Coal in a Fluidized-Bed/Packed-Bed Reactor Exposed to Concentrated Thermal Radiation-Modeling and Experimental Validation," Ind. Eng. Chem. Res., **44**, pp. 3852–3861.
[4] Piatkowski, N., and Steinfeld, A., 2008, "Solar-Driven Coal Gasification in a Thermally Irradiated Packed-Bed Reactor," Energy Fuels, **22**, pp. 2043–2052.
[5] Osinga, T., Lipiński, W., Guillot, E., Olalde, G., and Steinfeld, A., 2006, "Experimental Determination of the Extinction Coefficient for a Packed-Bed Particulate Medium," Exp. Heat Transfer, **19**, pp. 69–79.
[6] Zhao, C. Y., Lu, T. J., and Hodson, H. P., 2004, "Thermal Radiation in Ultralight Metal Foams With Open Cells," Int. J. Heat Mass Transfer, **47**, pp. 2927–2939.
[7] Kamiuto, K., Iwamoto, M., Nishimura, T., and Sato, M., 1991, "Radiation-Extinction Coefficients of Packed-Sphere Systems," J. Quant. Spectrosc. Radiat. Transf., **45**, pp. 93–96.
[8] Chen, J., and Churchill, S., 1963, "Radiant Heat Transfer in Packed Beds," AIChE J., **9**, pp. 35–41.
[9] Tancrez, M., and Taine, J., 2004, "Direct Identification of Absorption and Scattering Coefficients and Phase Function of a Porous Medium by a Monte Carlo Technique," Int. J. Heat Mass Transfer, **47**, pp. 373–383.
[10] Yang, Y., Howell, J., and Klein, D., 1983, "Radiative Heat Transfer Through a Randomly Packed Bed of Spheres by the Monte Carlo Method," ASME J. Heat Transfer, **105**, pp. 325–332.
[11] Argento, C., and Bouvard, D., 1996, "A Ray Tracing Method for Evaluating the Radiative Heat Transfer in Porous Media," Int. J. Heat Mass Transfer, **39**, pp. 3175–3180.
[12] Chan, C., and Tien, C., 1974, "Radiative Transfer in Packed Spheres," ASME J. Heat Transfer, **96**, pp. 52–58.
[13] Brewster, M., and Tien, C., 1982, "Radiative Transfer in Packed Fluidized Beds—Dependent Versus Independent Scattering," ASME J. Heat Transfer, **104**, pp. 573–579.
[14] Tien, C., 1988, "Thermal Radiation in Packed and Fluidized Beds," ASME J. Heat Transfer, **110**, pp. 1230–1242.
[15] Coquard, R., and Baillis, D., 2004, "Radiative Characteristics of Opaque Spherical Particles Beds: A New Method of Prediction," J. Thermophys. Heat Transfer, **18**, pp. 178–186.
[16] Coquard, R., and Baillis, D., 2005, "Radiative Characteristics of Beds of Spheres Containing an Absorbing and Scattering Medium," J. Thermophys. Heat Transfer, **19**, pp. 226–234.
[17] Petrasch, J., Wyss, P., and Steinfeld, A., 2007, "Tomography-Based Monte Carlo Determination of Radiative Properties of Reticulate Porous Ceramics," J. Quant. Spectrosc. Radiat. Transf., **105**, pp. 180–197.
[18] Zeghondy, B., Iacona, E., and Taine, J., 2006, "Determination of the Anisotropic Radiative Properties of a Porous Material by Radiative Distribution Function Identification (RDFI)," Int. J. Heat Mass Transfer, **49**, pp. 2810–2819.
[19] Stanmore, B., 2005, "Review—Calcination and Carbonation of Limestone

During Thermal Cycling for CO_2 Sequestration," Fuel Process. Technol., **86**, pp. 1707–1743.
[20] Farmer, J. T., and Howell, J. R., 1998, "Comparison of Monte Carlo Strategies for Radiative Transfer in Participating Media," Adv. Heat Transfer, **31**, pp. 333–429.
[21] Modest, M., 2003, *Radiative Heat Transfer*, 2nd ed., Academic, San Diego.
[22] Berryman, J., and Blair, S., 1986, "Use of Digital Image Analysis to Estimate Fluid Permeability of Porous Material: Application of Two-Point Correlation Functions," J. Appl. Phys., **60**, pp. 1930–1938.
[23] Petrasch, J., Wyss, P., Stämpfli, R., and Steinfeld, A., 2008, "Tomography-Based Multiscale Analyses of the 3D Geometrical Morphology of Reticulated Porous Ceramics," J. Am. Ceram. Soc., **91**, pp. 2659–2665.
[24] 2003, *Handbook of Fluidization and Fluid-Particle Systems*, W. C. Yang, ed., Marcel Dekker, New York.
[25] Palik, E., 2003, *Handbook of Optical Constants of Solids*, Academic, San Diego.
[26] Querry, M., Osborne, G., Lies, K., Jordon, R., and Coveney, R., 1978, "Complex Refractive Index of Limestone in the Visible and Infrared," Appl. Opt., **17**, pp. 353–356.
[27] Rodriguez-Navarro, C., Rodriguez-Navarro, A., Elert, K., and Sebastian, E., 2004, "Role of Marble Microstructure in Near-Infrared Laser-Induced Damage During Laser Cleaning," J. Appl. Phys., **95**(7), pp. 3350–3357.
[28] Bohren, C., and Huffman, D., 2004, *Absorption and Scattering of Light by Small Particles*, 3rd ed., Wiley, New York.
[29] Tien, C. L., and Drolen, B. L., 1987, "Thermal Radiation in Particulate Media With Dependent and Independent Scattering," Annu. Rev. Numer. Fluid Mech. Heat Transfer, **1**, pp. 1–32.

Experimental Investigations on the Thermal Conductivity of Silica Aerogels by a Guarded Thin-Film-Heater Method

Sandra Spagnol[1]
e-mail: spagnol@cict.fr

Bérangère Lartigue

Alain Trombe

Laboratoire PHASE,
Université de Toulouse,
Bâtiment 3R1,
118 Route de Narbonne,
31062 Toulouse Cedex 9, France

Florence Despetis
Groupe d'Etude des Semiconducteurs,
Université Montpellier II,
Place Eugène Bataillon,
34095 Montpellier Cedex 5, France
e-mail: despetis@univ-montp2.fr

A thin-film-heater method is setup to measure the thermal conductivity of super insulating materials such as silica aerogels. The experimental setup is purposely designed for insulating materials and allows direct measurement of the thermal conductivity. Few experimental data are available in the literature concerning thermal conductivity of aerogels even though these materials are of major interest in thermal insulation. More data are necessary in order to understand thermal transport and to validate existing models. Monolithic and granular silica aerogels are investigated. Our experimental technique enables to quantify the influence of important parameters, such as air pressure and distribution of grain sizes, on the insulating performance of this material.
[DOI: 10.1115/1.3089547]

Keywords: thermal conductivity, silica aerogel, guarded hot plate, nanoporous media

1 Introduction

Silica aerogel is a nanoporous medium with remarkable physical properties, which enables various applications [1]. An application in the building sector such as super insulating material can be of great interest as traditional insulation has reached its performance limit. Indeed, silica aerogel is one of the most insulating synthetic materials. As reported in literature, experimental heat transfer through aerogels has been studied since 1985 [2,3]. Models describing heat transfer in these materials have been proposed. The analytical model proposed by Fricke et al. [4] and improved by Hrubesh and Pekala [5] is based on the addition of three components due to the contribution of coupled heat transfer: conduction in the silica skeleton, conduction in the air-filled nanopores, and radiation through nanopores. Recent numerical models have studied in detail the solid and gaseous conductions in such nanoporous media [6,7]. However, experimental studies are necessary to validate these models. At the moment, few data can be found in literature, particularly for monolithic samples.

The steady state method of the guarded hot plate is the most appropriate and widespread method to obtain direct measurements of thermal conductivities with low uncertainties. The first articles dealing with this method applied to silica aerogels came from Germany [2,3]. In 1989, LOLA III has been described as the most complete setup to measure thermal conductivities of cylindrical aerogel samples [8]. The method has been improved by the Lawrence Berkeley National Laboratory. In 1996, a setup called VICTOR is built where the hot plate is replaced by a thin hot film [9]. Likewise, our experimental setup is based on a thin-film-heater method that is convenient in order to decrease the lateral heat losses, which are the first cause of error and which are increased by super insulating samples. Moreover, our film is also guarded as a second protection against heat losses.

In this paper, we first describe an entire experimental method to measure variations in the thermal conductivity of super insulating materials such as monolithic and granular silica aerogels, both described here. New data on thermal conductivities of silica aerogels are then given in order to enrich a quite light literature in this topic.

2 Experimental Design

The guarded thin-film-heater method is based on the guarded hot plate method in steady state. The hot plate is replaced by a thin film in order to avoid lateral heat losses. Our apparatus is composed of a central cell placed in a vacuum chamber and the required instrumentation.

2.1 Central Cell. Figure 1(*a*) shows the constitution of the central cell. The thin-film-heater is placed between two identical samples of the same thickness (e), and each of them is in contact with a cold plate on the other side. The electrical power is integrally dissipated by the Joule effect and is divided into two equal heat fluxes (q).

The film is 0.185 mm thick and is composed of two layers. The first one has two concentric resistances engraved on a kapton support (see Fig. 1(*b*)). The central resistance is 55 mm in diameter, which determines the measurement surface (s). The peripheral resistance is called the guarded zone and has an external diameter of 70 mm. The second layer of the film consists of two thermocouples of type T (copper-constantan) also engraved on a kapton support. The central thermocouple gives the hot temperature (T_{hot}), and the intermediate thermocouple gives the guard temperature (T_{guard}).

The two cold plates are cylinders made of brass 70 mm in diameter and 8 mm in thickness. They are excavated in a spiral form for the circulation of the cooled water. The water temperature is maintained constant using a thermostatic-controlled bath. A thermocouple engraved on a kapton layer is attached on each surface in contact with the samples and measures the cold temperature (T_{cold1} and T_{cold2} must be equal to assume symmetrical conditions, see Fig. 1(*a*)).

2.2 Instrumentation. All temperatures and voltage are registered by a data acquisition device connected with a computer. When the power supply is fixed in order to obtain $T_{hot}=T_{guard}$ and when steady state is reached, data are registered within 2 h. Registered signals are filtered and averaged. Values are used to calculate the thermal conductivity according to the following expression:

$$k_{app} = \frac{q \times e}{(T_{hot} - T_{cold}) \times s} \quad (1)$$

[1]Corresponding author.

Contributed by the Heat Transfer Division of ASME for publication in the JOURNAL OF HEAT TRANSFER. Manuscript received March 6, 2008; final manuscript received January 26, 2009; published online April 30, 2009. Review conducted by Jamal Seyed-Yagoobi.

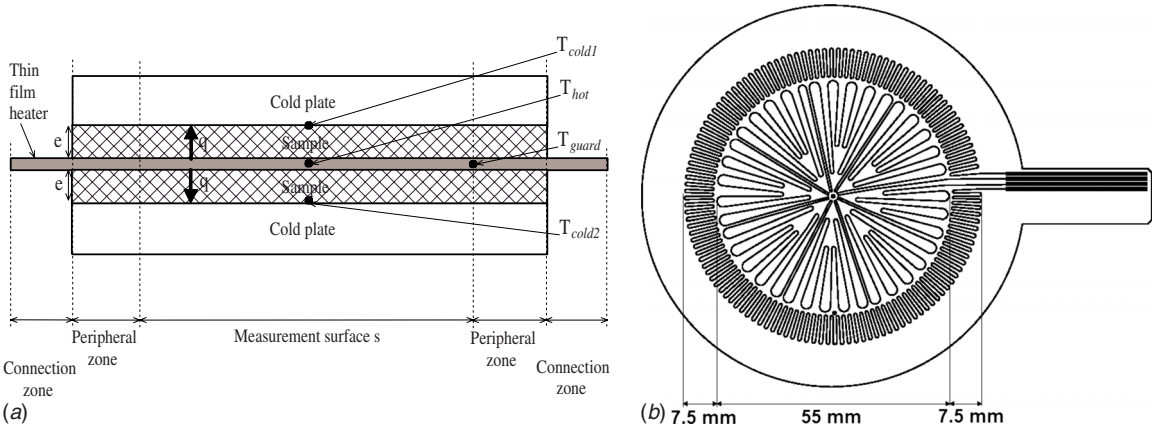

Fig. 1 (*a*) **Central cell of the thin-film-heater setup;** (*b*) **scheme of the resistance layer composing the hot film**

The thickness (e) of samples is measured before and after each experimental session with a caliper.

The central cell described earlier is placed in a vacuum chamber. The chamber can be evacuated with a rotary pump (from 10^3 to 10^{-2} mbar) and a diffusion pump (down to around 10^{-5} mbar). A combined pressure gauge monitors the primary and secondary vacuums.

The vacuum chamber is placed in a temperature-controlled room in order to obtain steady state during the experiment.

2.3 Uncertainty Analysis. Uncertainty from the measurement is quantifiable. From Eq. (1), the relative error on the thermal conductivity can be written as

$$\frac{\Delta k}{|k|} = \frac{\Delta U}{|U|} + \frac{\Delta I}{|I|} + \frac{\Delta e}{|e|} + \frac{2 \times \Delta T}{|T_{\text{hot}} - T_{\text{cold}}|} + \frac{2 \times \Delta r}{|r|} \simeq 5 - 9\% \quad (2)$$

according to the experiments. The absolute error of each component is given by the apparatus.

Uncertainties linked to the experimental method are difficult to quantify. First, the lateral heat losses are limited by using a guarded thin film and by investigating thin samples. A contact resistance can also exist between samples and plates. Surfaces in contact have to be as parallel and smooth as possible. A precision screw enables precise positioning of the surfaces to bring them all in contact with one another. Finally, the symmetry of the central cell is assumed to justify the hypothesis of the heat flux division into two equal parts.

3 Sample Characteristics

3.1 Monolithic Aerogels. Monolithic samples are made at the Groupe d'Etude des Semiconducteurs, Montpellier, France. The dimensions of the supercritical drying system have determined the dimensions of the samples. Cylinders of 72 mm in diameter and 6 mm in thickness are synthesized. The samples have slightly larger dimensions than the ones of the setup in order to take into account shrinkage during aging and drying.

The experimental protocol consists of mixing the organometallic precursor called tetramethooxysilane (TMOS) and the associated alcohol (ethanol) for 15 min at ambient temperature. The hydrolysis solution is then slowly added. Ammoniac is chosen to make basic aerogels. The gelling mixture is introduced into containers at the chosen dimensions for samples. Gels are preserved at ambient conditions during a number of days corresponding to the aging period. Gels are then supercritically dried in their own containers. The temperature is increased to 623 K with a heating speed of $0.2\,^{\circ}\text{C min}^{-1}$. The pressure is decreased to 0.1 bar min^{-1}. The maximum pressure is equal to 125 bars. Two pairs of samples are successfully synthesized with an apparent density of 110 ± 4 kg m^{-3} and a specific surface of 547 ± 22 m^2 g^{-1}.

3.2 Granular Aerogels. Granular samples are synthesized by Cabot Corporation from a silicate solution sprayed in the presence of an alcohol solution. Three different samples are studied in function of their grain size. The grains of each sample have a mean diameter of 1 mm, 3 mm, or 5 mm. The mean diameter of the pores, porosity, and density of the three samples are investigated using a nitrogen absorption-desorption technique according to a Brunauer Emmett Teller (BET) method. The three samples presented densities of about 225 kg m^{-3} and porosities of about 90% with nanopores of about 15 nm.

The granular samples have to be packaged in containers to be placed in the experimental setup. They are enclosed in containers made of thin polyvinyl chloride (PVC) ring (internal diameter of 70 mm) covered by a plastic clingfilm (about 0.01 mm thick) on the two surfaces in contact with the film heater and the cold plate. Three thicknesses are chosen for the rings: 6 mm, 9 mm, and 12 mm. Rings are perforated to allow the evacuation of air during the sample depressurization. For each sample and each ring thickness, two identical containers are prepared with identical masses of material.

4 Results

4.1 Monolithic Aerogels. Figure 2 shows that the apparent thermal conductivity decreases rapidly as the air pressure decreases. From 10^{-2} mbar, thermal conductivity does not decrease anymore, as gaseous conduction is then inexistent. For vacuumed samples, the thermal conductivity is almost one-third of its value under atmospheric conditions. Same trends are found in literature [2,10].

The results on monolithic samples are synthesized in Table 1. The apparent and effective thermal conductivities are defined as follows:

$$k_{\text{app}} = k_{\text{eff}} + k_r \quad (3)$$

where k_{eff} represents the part of the conduction in the silica skeleton and in the air-filled nanopores, and k_r represents the part of the radiative transport that can be quantified from the following relation [4,5]:

$$k_r = \frac{16 n^2 \sigma T_r^3}{3 \rho_{\text{app}} \frac{K_{\text{sol}}}{\rho_{\text{sol}}}} \quad (4)$$

Under atmospheric conditions, thermal conductivity is lower than the one of air at same conditions. Under vacuum conditions, the

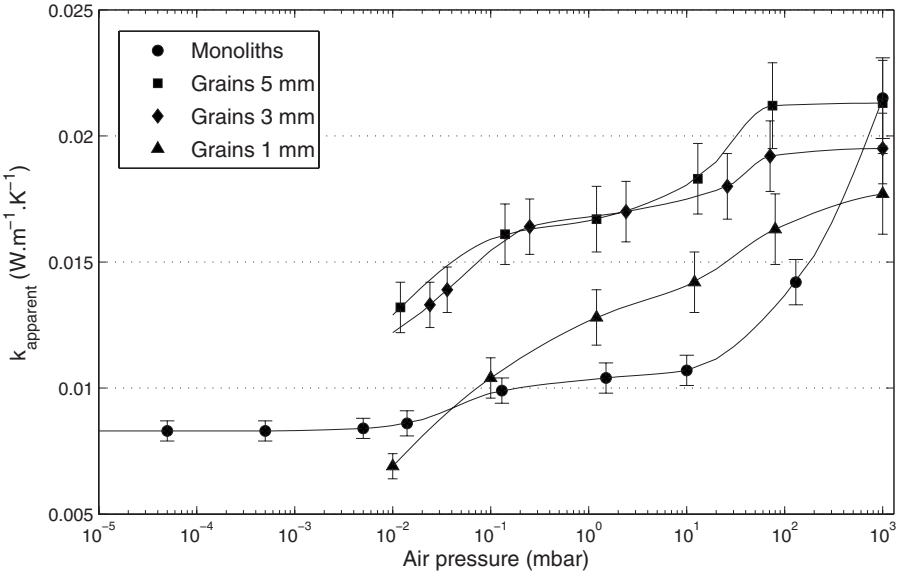

Fig. 2 Apparent thermal conductivity versus air pressure for monolithic and granular samples

thermal conductivity is extremely low (only 8 mW m^{-1} K^{-1}). The part of gaseous conduction $(=(k_{\text{eff}})_{P=10^3 \text{ mbars}}-(k_{\text{eff}})_{P=5\times10^{-5} \text{ mbar}})$ is the most important. It is then interesting to use these materials in a vacuumed way. At ambient temperature, the radiation part is low in comparison with the two others.

4.2 Granular Aerogels. For each grain size, all samples with different thicknesses (6 mm, 9 mm, or 12 mm) are tested several times to verify reproducibility. The sample thickness does not influence the apparent thermal conductivity. Lateral heat losses, which might be due to a large thickness of samples, can then be neglected.

Figure 2 shows thermal conductivities depending on air pressure for the 9 mm thick granular samples with three different diameters. When the grain size decreases, the apparent thermal conductivity decreases too. As the grain size decreases, the size of intergranular voids decreases too and radiation is reduced. This trend is in good agreement with other results published in Ref. [10] from measurements made by a hot wire method.

Moreover, the apparent thermal conductivity decreases significantly while air pressure decreases. Thermal conductivities are obtained starting from vacuum conditions to atmospheric pressure. All experimental curves present two distinct steps expected for porous materials with two different pore sizes. According to Fig. 2, the first stage occurs between 10^{-2} mbar and 0.5 mbar and corresponds to the filling of pores between grains. The second one starts at about 50 mbars and is the consequence of the filling of nanopores within grains. For samples with grains of 1 mm in diameter, the first stage tends to merge with the second one. The smaller the grains, the higher the gas pressure where the first stage of gaseous conduction occurs. A mixture of granulates with a powder, which can fill the intergranular voids, should be then even better to obtain lower thermal conductivities. Our results are in good agreement with those of the literature [4,10].

Table 1 Summary of the measurements at atmospheric pressure and at 5×10^{-5} mbar for monolithic samples (values are presented in mW m^{-1} K^{-1} and for the mean temperature comprised between 300 K and 315 K)

	Atmospheric air pressure	Vacuum conditions
	10^3 mbars	5×10^{-5} mbar
k_{app} (measurements)	21 ± 2	8 ± 1
k_r (calculations, see Eq. (4))	3 (radiative part)	
k_{eff} (calculations, see Eq. (3))	18 ± 2	5 ± 1 (solid part)
Gaseous part	13 ± 3	

5 Conclusions

An experimental characterization of the thermal conductivity of monolithic and granular silica aerogels is proposed in this paper. The guarded thin-film-heater method under steady state, derived from the hot plate method, gives the possibility to directly measure the thermal conductivity of super insulating materials in restraining lateral heat losses and in obtaining low uncertainties.

Several parameters are tested to analyze the variation in thermal conductivity. Experimental results are in good agreement with the results from the literature obtained by the hot plate or hot wire method. For monolithic and granular samples, air pressure is a crucial element. Their insulating performance can be largely improved under vacuum conditions. The distribution of grain sizes is also important for granular samples and can be optimized by reducing sizes or mixing several sizes.

Nomenclature

e = thickness (m)
I = current intensity (A)
k = thermal conductivity (W m^{-1} K^{-1})
K = Rosseland mean extinction coefficient (m^2 kg^{-1})
n = refraction index
q = heat flux (W)
Q = heat flux density (W m^{-2})
r = radius (m)
s = measurement surface (m^2)
T = temperature (K)
U = voltage (V)
Δ = absolute uncertainty
ρ = density (kg m^{-3})
σ = Stefan–Boltzmann constant (W m^{-2} K^{-4})

Subscripts

app = apparent

eff = effective
r = radiative
sol = solid phase

References

[1] Hrubesh, L., 1998, "Aerogel Applications," J. Non-Cryst. Solids, **225**, pp. 335–342.

[2] Büttner, D., Caps, R., Heinemann, U., Hümmer, E., Kadur, A., Sheuerpflug, P., and Fricke, J., 1986, "Thermal Conductivity of SiO_2-Aerogel Tiles," First International Symposium on Aerogels, pp. 104–109.

[3] Büttner, D., Hümmer, E., and Fricke, J., 1986, "Thermal Conductivity of Granular SiO_2 Aerogel," First International Symposium on Aerogels, pp. 116–120.

[4] Fricke, J., Hümmer, E., Morper, H., and Sheuerpflug, P., 1989, "Thermal Properties of Silica Aerogels," Second International Symposium on Aerogels, pp. 87–97.

[5] Hrubesh, L., and Pekala, W., 1994, "Thermal Properties of Organic and Inorganic Aerogels," J. Mater. Res., **9**, pp. 731–738.

[6] Rochais, D., Domingues, G., and Enguehard, F., 2005, "Numerical Simulation of Thermal Conduction and Diffusion Through Nanoporous Superinsulating Materials," European Conference on Thermophysical Properties, Bratislava.

[7] Spagnol, S., Lartigue, B., Trombe, A., and Gibiat, V., 2007, "Thermal Modeling of Two Dimensional Periodic Fractal Patterns, an Application to Nanoporous Media," Europhys. Lett., **78**(46005), pp. 1–5.

[8] Caps, R., Döll, G., Fricke, J., Heinemann, U., and Hetfleisch, J., 1989, "Thermal Transport in Monolithic Silica Aerogel," Rev. Phys. Appl., **24**, pp. 113–118.

[9] Zeng, J. S. Q., Stevens, P. C., and Hunt, A. J., 1996, "Thin-Film-Heater Thermal Conductivity Apparatus and Measurement of Thermal Conductivity of Silica Aerogel," Int. J. Heat Mass Transfer, **39**, pp. 2311–2317.

[10] Bisson, A., Rigacci, A., Lecomte, D., and Achard, P., 2004, "Effective Thermal Conductivity of Divided Silica Xerogel Beds," J. Non-Cryst. Solids, **350**, pp. 379–384.

Novel Hub Fins for Axial Flow Fans for the Enhancement of Impingement Heat Transfer on a Flat Plate

D. Sui
School of Energy and Power Engineering,
Xi'an Jiaotong University,
Xi'an 710049, P.R. China

T. Kim[1]
e-mail: tongbeum@gmail.com

M. L. Xu

T. J. Lu

MOE Key Laboratory for Strength and Vibration,
School of Aerospace,
Xi'an Jiaotong University,
Xi'an 710049, P.R. China

The thermal characteristics of exit flow issued from an axial fan widely used for impingement cooling of power electronics are experimentally studied. A new fan configuration is proposed to improve the impingement cooling performance at the center of a uniformly heated flat plate. Results demonstrate that the addition of fin attachments to the fan hub housing the driving motor intensifies reverse flow from the plate, leading to enhanced local heat transfer (up to 12%) relative to that of a reference fan. The effectiveness of hub fin attachments is limited to relatively short impinging distances ($H/D<0.6$). [DOI: 10.1115/1.3109244]

Keywords: axial fan flow, hub fins, reverse flow, impingement, heat transfer

1 Introduction

Among a variety of different cooling schemes, impinging jets are known to be an effective means for achieving desirable high levels of heat dissipation and have been widely used in various industrial processes including electronics cooling [1–4]. In some applications, the impinging jet flow is forced to swirl when exiting a jet orifice/nozzle, resulting in the commonly known swirling jet [5]. In this case, the axial, tangential, and radial velocity components of the exit flow coexist. Typically, the swirling jet provides a more uniform distribution of local heat transfer than that achievable with a conventional jet. Furthermore, such swirling jet is usually considered to be "steady."

In comparison, flow in a conventional heat sink for electronics cooling driven by an axial fan is "annular" and "periodically unsteady swirling." The former is attributable to the existence of a fan hub housing the dc motor, which displaces approximately 25% of the total flow area, leading to a "reverse flow region" at the central portion of the base plate, coinciding with the fan axis [6,7]. The importance of the reverse flow region for electronics cooling is attributed to the fact that a heat source (e.g., central processing unit (CPU)) is typically located in this region. The latter is due to the presence of periodic tangential and radial flow motions in fan exit flow, in addition to axial flow, generated by rotating blades.

Despite numerous efforts made, a further study on heat transfer enhancement in the reverse flow region is necessary, as impinging heat transfer characteristics under such flow conditions are yet fully explored. The present study aims to experimentally investigate the pressure and heat transfer characteristics on a heated plate subjected to impinging cooling from axial fan flow. Particularly, the focus is placed upon how to improve heat transfer efficiency in the reverse flow region. To this end, a novel axial flow fan with hub fin attachments is designed, fabricated, and tested, and its performance is compared with that of a conventional fan.

2 Design Considerations

The generic design of a conventional axial fan widely used in electronics cooling is shown in Fig. 1. The hub of the fan housing the motor displaces about 25% of the total flow area. As a result, a high momentum flow driven by the fan exists radially off from the fan axis [6]. Consequently, when the exit flow impinges on a heated flat plate, intensified heat transfer takes place on the plate off from the fan axis [7]. In electronics cooling, the heat source is typically attached to the central portion of the base plate and is posed in a flow region formed as a result of interacting reverse flows. Heat transfer in this region is relatively low and hence undesirable.

To improve impinging heat transfer in the reverse flow region, a new design of the fan is proposed. The design uses additional fins attached normally to the end of the hub to promote "flow interaction" in the reverse flow region, while maintaining the original shape of the fan blades (Fig. 1). The straight fins have a length (a) equal to the blade span (S) and a height (b) equal to $0.55S$ with a thickness of 1 mm. The attached fins lead to about 15% increase in the total weight of the fan and 7.7% reduction in rotation speed from 2544 ± 12 rpm to 2347 ± 15 rpm when powered with 12 V in the free exit. On the other hand, it is expected that the flow in the reverse flow region is perturbed by the additional hub fins, leading to enhanced heat transfer.

3 Experimental Details

The purpose-built test rig for measuring the exit flow from an axial fan of diameter D is shown schematically in Fig. 2. An acrylic plate, $0.3 \times 0.6 \times 0.01$ m^3 in size, was mounted on a linear traverse system to vary the fan exit-to-plate spacing. Both the reference fan and the new fan have seven forward-swept fan blades and are ducted with a gap (tip clearance, $\delta/S \sim 0.03$). Except for the additional hub fins, the new fan is identical to the reference fan (Table 1).

The inlet velocity (c_x) was traversed upstream of the fan using a Pitot tube, which was then used to calculate the volume flow rate. With the dc fan motor powered at 12 V, the nominal volume flow rate is approximately 0.00871 m^3/s (or 18.5 ft^3/m). For wall pressure measurements, a total of 14 flush mounted static pressure tappings were laterally distributed on the base plate, all connected to a differential pressure transducer.

An etched-foil heating pad, 151×254 mm^2 in size, was used to impose a constant heat flux ($q''_{net} = 1400$ W/m^2) through the plate. The other side of the heating pad was attached to a 0.01 m thick Perspex™ plate. A T-type foil thermocouple, 13 μm in thickness, was placed at the center of the heating pad, coinciding with the fan axis, to monitor the plate surface temperature, T_s. The plate was linearly traversed along the y-axis to measure the lateral distribution of Nusselt number using the same foil thermocouple. Prior to the measurements, the imposed heat flux (q''_{net}) was measured by a foil heat flux gauge attached to the plate. A bead T-type

[1]Corresponding author.

Contributed by the Heat Transfer Division of ASME for publication in the JOURNAL OF HEAT TRANSFER. Manuscript received February 23, 2008; final manuscript received February 7, 2009; published online April 30, 2009. Review conducted by Minking Chyu.

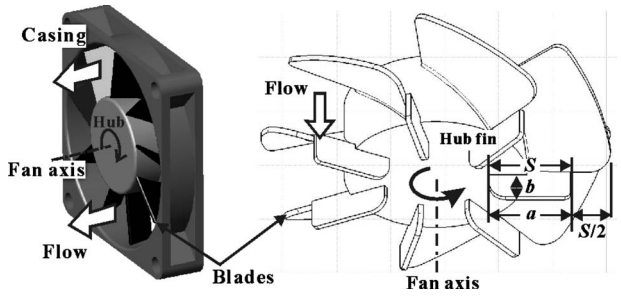

Fig. 1 Conceptual design of axial flow fan with hub fins to promote flow perturbation below the fan hub

thermocouple was used at the inlet of the fan to measure the inlet flow temperature, T_i, which was used as reference.

4 Discussion of Results

Wall static pressure distribution. Figure 3 plots the wall pressure coefficient Cp as a function of lateral position y/D for $H/D=0.2$ and 0.4 defined as

$$Cp = \frac{p_s - p_{\text{in}}}{\rho V_{\text{tip}}^2/2} \tag{1}$$

where p_s is the static pressure on the plate, p_{in} is the reference static pressure, and V_{tip} is the blade tip speed. The uncertainties associated with static pressure and pressure coefficient were estimated (based on 20:1 odds [8]) to be within 2.9% and 4.1%, respectively.

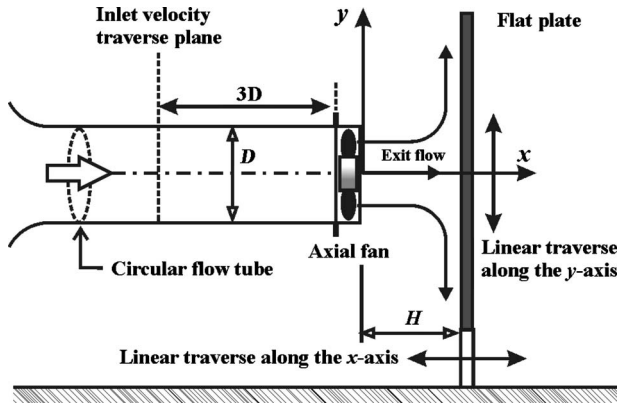

Fig. 2 Schematic of axial fan test setup

Table 1 Parameters of blades and axial flow fan units tested in the current study

		Fan type	
		Reference fan	Fan with hub fins
Fan unit	Fan diameter, D	67 mm	
	Hub diameter, D_{hub}	34 mm	
	Number of blades	7	
Blades	Blade span, S	16.5 mm	
	Chord at hub (tip)	17 mm (24 mm)	
	Forward swept angle	30 deg	
	Pitch angle at hub (tip)	+50 deg (+30 deg)	
	Twist angle	−20 deg	
	Hub fin span,a	N/A	16.5 mm
	Hub fin height, b	N/A	9 mm

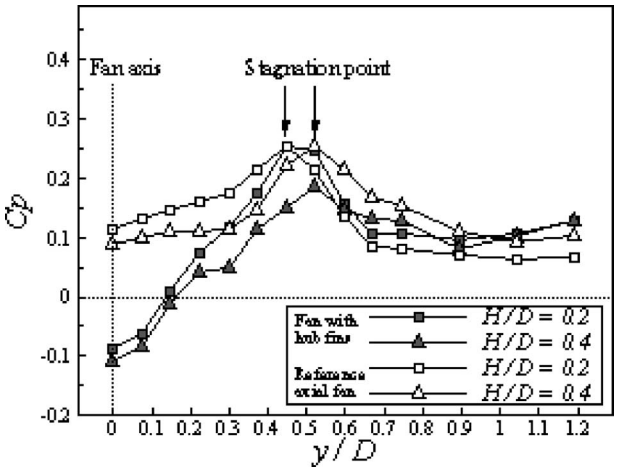

Fig. 3 Comparison of radial distributions of wall static pressure coefficient (*Cp*) at *H*/*D*=0.2 and 0.4

For $H/D=0.2$, the static pressure is low in the reverse flow region but high in the region after the peak at $y/D\sim\pm0.45$ (although not as high as that in the stagnation region). As the plate is moved away from the fan exit, e.g., from $H/D=0.2$ to 0.4, the location of the peak pressure is moved outward to about $y/D=0.5$. When convecting downstream, the exit flow is affected by centrifugal force caused by tangential flow, leading to the lateral shift of the peak pressure [6,7].

The difference in wall pressure distribution between the two fan types is remarkable. Figure 3 indicates that, for the new fan, while the pressure in the flow region after the peak is little affected, it is pronouncedly lower in the reverse flow region than that of the reference fan. For both fan types, as the separation distance is increased, the pressure at $y/D=0$ is slightly increased while that at the stagnation point is decreased. Correspondingly, the location of the stagnation point is moved from $y/D=0.45$ to 0.6. It is inferred that flow interaction in the reverse flow region is intensified, reducing the wall static pressure in this region. By increasing the separation distance, the reverse flow is weakened.

Characteristics of impinging heat transfer. Local Nusselt number on the plate surface is defined as

$$\text{Nu} = \left(\frac{q''_{\text{net}}}{(T_s(y/D) - T_i)}\right)\frac{D}{k_f} \tag{2}$$

where k_f is the thermal conductivity of air. The uncertainty associated with the Nusselt number was estimated to be within 5.8%.

Figure 4(*a*) presents the distribution of Nusselt number on the uniformly heated plate. At small separation distances (e.g., $H/D=0.2$, 0.4) for the reference fan, the Nusselt number increases monotonically when moving laterally outward from the plate center, peaking approximately at $y/D=0.5$, and then decreases (Fig. 4(*a*)). For larger separation distances (e.g., $H/D=0.6$, 1.0, 2.0), the peak value moves outward from the fan axis, e.g., $y/D=1.1$ for $H/D=2.0$. This lateral shifting is, as in the case of wall pressure, caused by the centrifugal force due to tangential exit flow.

With flow perturbation by fin attachments, the stagnation point is moved closer to the fan axis for a given separation distance. Furthermore, the overall trend of the Nusselt number distribution is maintained while its magnitude is increased. In comparison, for relatively small separation distances (e.g., $H/D=0.2$ and 0.4), a distinct feature of heat transfer associated with the new fan is that the Nusselt number in the reverse flow region becomes comparable or even higher than that in the outer flow region. However, no heat transfer enhancement due to fin attachments is observed in

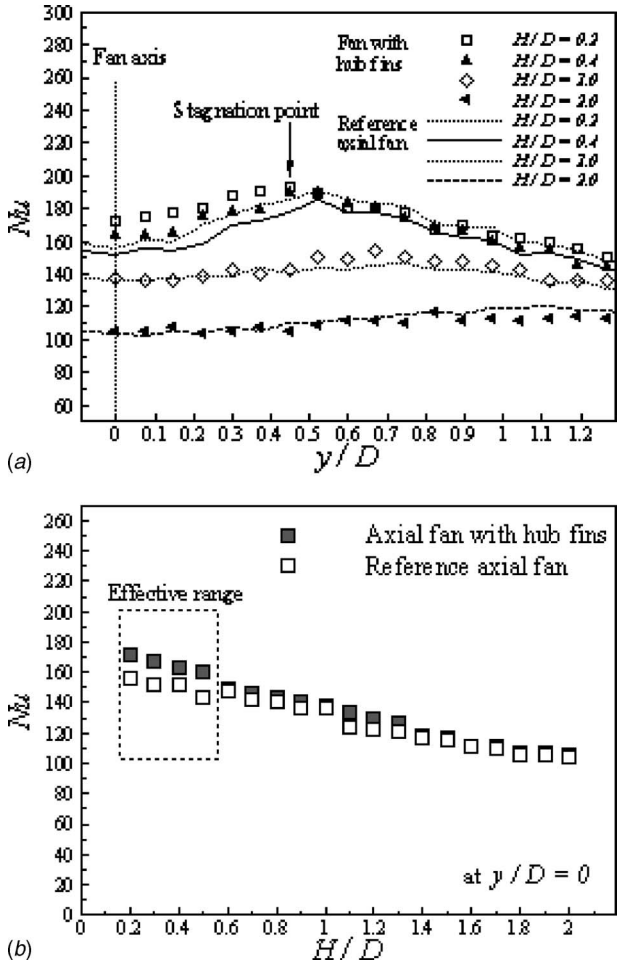

Fig. 4 Radial distributions of Nusselt number at $H/D=0.2$, 0.4, 1.0, and 2.0 and effectiveness of hub fins at the reverse flow region: (*a*) y/D versus Nu and (*b*) H/D versus Nu at $y/D=0$

the outer flow region. In other words, only heat transfer in the reverse flow region for relatively short separation distances is enhanced by flow perturbation due to hub fins.

Figure 4(*b*) plots the Nusselt number at $y/D=0$ as a function of separation distance for both fan types. At relatively large separation distances ($H/D \geq 0.6$), the use of hub fins has negligible influence on the Nusselt number. As the separation distance is reduced, the influence of the hub fins increases, leading to, for example, about 12% enhancement of the Nusselt number at $H/D=0.5$.

5 Summary

The cooling performance of an impinging axial fan flow has been experimentally characterized. To enhance local heat transfer in a particular region on a uniformly heated flat plate coinciding with the axial fan axis, a new axial fan with hub fin attachment has been designed and its cooling performance is compared with that of a reference axial fan. The following conclusions are drawn.

(1) The hub fins are shown to intensify flow interaction (reverse flow) in a region on the flat plate coinciding with the axial fan axis (reverse flow region), resulting in up to 12% enhancement of local heat transfer.
(2) The effectiveness of hub fins for local heat transfer enhancement in the reverse flow region is restricted to relatively short separation distances ($H/D<0.6$).

Acknowledgment

This work was supported by the National Basic Research Program of China (Contract No. 2006CB601203) and the National Natural Science Foundation of China (Contract No. 50676075).

Nomenclature

Cp = static pressure coefficient (Eq. (1))
D = fan diameter, m
H = fan exit-to-flat plate spacing (separation distance), m
Nu = Nusselt number (Eq. (2))
Re = Reynolds number based on fan diameter
rpm = revolution per minute
v = velocity component of exit flow, m/s
x,y,z = coordinates corresponding to axial, radial, and tangential components

References

[1] Saini, M., and Webb, R., 2003, "Heat Rejection Limits of Air Cooled Plane Fin Heat Sinks for Computer Cooling," IEEE Trans. Compon. Packag. Technol., **26**, pp. 71–79.
[2] Chu, R. C., Simons, R. E., Ellsworth, M. J., Schmidt, R. R., and Cozzolino, V., 2004, "Review of Cooling Technologies for Computer Products," IEEE Trans. Device Mater. Reliab., **4**, pp. 568–585.
[3] El-Sheikh, H. A., and Garimella, S. V., 2000, "Enhancement of Air Jet Impingement Heat Transfer Using Pin-Fin Heat Sink," IEEE Trans. Compon. Packag. Technol., **23**, pp. 300–308.
[4] Brignoni, L. A., and Garimella, S. V., 1999, "Experimental Optimization of Confined Air Jet Impingement on a Pin Fin Heat Sink," IEEE Trans. Compon. Packag. Technol., **22**, pp. 399–404.
[5] Huang, L., and El-Genk, M. S., 1998, "Heat Transfer and Flow Visualization Experiments of Swirling, Multi-Channel, and Conventional Impinging Jets," Int. J. Heat Mass Transfer, **41**, pp. 583–600.
[6] Sui, D., Wang, S. S., Kim, T., Mao, J. R., and Lu, T. J., "Exit Flow Structures of Axial Fan Flows With/Without Impingement," ASME J. Fluids Eng., in press.
[7] Sui, D., Kim, T., Xu, M. L., and Lu, T. J., 2008, "Flow and Heat Transfer Characteristics of Impinging Axial Fan Flows on a Uniformly Heated Flat Plate," Int. J. Transp. Phenom., **10**, pp. 353–363.
[8] Coleman, H. W., and Steele, W. G., 1999, *Experimentation and Uncertainty Analysis for Engineers*, 2nd ed., Wiley, New York.

Heat Transfer Enhancement in Channel Flow Using an Inclined Square Cylinder

Dong-Hyeog Yoon

Kyung-Soo Yang[1]
e-mail: ksyang@inha.ac.kr

Choon-Bum Choi

Department of Mechanical Engineering,
Inha University,
Incheon 402-751, Republic of Korea

Heat transfer enhancement in channel flow by using an inclined vortex generator has been numerically investigated. A square cylinder is located on the centerline of laminar channel flow, which is subject to a constant heat flux on the lower channel wall. As the cylinder is inclined with some angle of attack with respect to the main flow direction, flow characteristics change downstream of the cylinder, and significantly affect heat transfer on the channel wall. A parametric study has been conducted to identify the cause, and to possibly find the optimal inclination angle. It turns out that the increased periodic fluctuation of the vertical velocity component in the vicinity of the channel walls is responsible for the heat transfer enhancement. The large fluctuation is believed to be induced by the large-scale vortices shed from the inclined square cylinder, as well as by the secondary vortices formed near the channel walls. [DOI: 10.1115/1.3090808]

Keywords: heat transfer enhancement, inclined square cylinder, immersed boundary method, channel flow, vortex shedding

1 Introduction

Periodic vortex shedding from a cylindrical object immersed in cross-flow has been one of the classical research subjects for decades because it induces periodic force loading on the object, which could significantly damage the cylindrical structure. Thus most of research on the vortex shedding has been focused on how to control it in order to minimize its damage [1]. On the other hand, the large-scale vortices shed from a cylindrical object as a vortex generator can be used to enhance heat transfer in a heat exchanger [2]. Furthermore, the large-scale vortices induce secondary vortices on the walls of a heat exchanger, which also play a positive role in heat transfer enhancement [3].

A rectangular cylinder has been popular in the research of vortex shedding [4,5], especially with emphasis on periodic vortex shedding and its application to heat transfer. In most of the studies, channel flow with a square cylinder aligned with the direction of the main flow has been extensively considered. Valencia [6] reported that heat transfer on the channel walls is enhanced in the presence of a square cylinder, and that heat transfer becomes more effective as the blockage ratio and Reynolds number increase. Nakagawa et al. [2] experimentally studied heat transfer characteristics on the channel wall with a constant heat flux in a turbulent flow regime using rectangular cylinders of different aspect ratios. They reported that the large-scale vortices generated by a cylinder enhance heat transfer on the channel wall downstream of the cylinder, and that the aspect ratio of the cylinder significantly affects the heat transfer characteristics.

When a square cylinder is inclined with respect to the direction of the main flow, flow separation may occur at various pairs of the edges of the square, resulting in drastic change of the key flow parameters such as force coefficients and the Strouhal number (St) [7]. In the current numerical investigation, it is attempted to enhance heat transfer capacity in laminar channel flow (Fig. 1) by taking advantage of the diverse flow characteristics of the vortices generated by an inclined square cylinder. Heat transfer characteristics vary with the inclination angle of the cylinder with respect to the main flow direction. Further attempt has been made to find the optimal inclination angle, which yields the maximum heat transfer enhancement. A possible physical mechanism for the enhancement is also proposed. The current laminar result would be the first step toward understanding the heat transfer enhancement, which had been obtained in turbulent channel flow with a square cylinder aligned with the main flow direction [2], and also sheds light on how to improve performance of heat exchangers by using diverse large-scale vortices due to inclination of a vortex generator.

2 Formulation and Numerical Methodology

The current investigation requires a parametric study where numerous numerical simulations must be performed with various inclination angles. This kind of parametric study demands considerable amount of computing resources; the computing efforts can be significantly reduced by employing an immersed boundary method, which facilitates implementing the solid surfaces of the inclined cylinder on a Cartesian grid system.

The governing equations for two-dimensional incompressible flow, modified for the immersed boundary method [8], are as follows:

$$\frac{\partial u_j}{\partial x_j} - q = 0 \tag{1}$$

$$\frac{\partial u_i}{\partial t} + \frac{\partial u_i u_j}{\partial x_j} = -\frac{\partial p}{\partial x_i} + \frac{1}{\mathrm{Re}}\frac{\partial^2 u_i}{\partial x_j \partial x_j} + f_i, \quad i = 1,2 \tag{2}$$

$$\frac{\partial \Theta}{\partial t} + \frac{\partial u_j \Theta}{\partial x_j} = \frac{1}{\mathrm{Re}\ \mathrm{Pr}}\frac{\partial^2 \Theta}{\partial x_j \partial x_j} + F \tag{3}$$

where u_i (or u, v), p, q, f_i, F, and Θ represent the velocity component in the x_i (or x, y) direction, pressure, mass source/sink, momentum forcing, heat source/sink, and temperature, respectively. Re and Pr denote the Reynolds number and Prandtl number, respectively. All the physical variables were nondimensionalized by inlet uniform velocity (U_0) and a proper length scale (l). It should be noted that for the dimensionless quantities associated with the cylinder, such as force coefficients and the Strouhal number, we used $l=h$ and $\mathrm{Re}=\mathrm{Re}_h$. For those associated with the channel wall, such as the Nusselt number and friction coefficient, $l=H$ and $\mathrm{Re}=\mathrm{Re}_H$ were used. Here, H represents channel height, and h denotes the projected length of the square cylinder (Fig. 1). $\Theta=k(T-T_0)/q_w H$, where T_0, k, and q_w represent inlet uniform temperature, thermal conductivity of the fluid, and constant heat flux on the channel wall, respectively. The governing equations were discretized using a finite-volume method in a nonuniform staggered Cartesian grid system. Spatial discretization is second-order accurate. A hybrid scheme is used for time advancement; nonlinear terms are explicitly advanced by a third-order Runge–Kutta scheme, and the other terms are implicitly advanced by the Crank–Nicolson method. A fractional step method was employed to decouple the continuity and momentum equations. For detailed description of the numerical method used in the current investigation, see Ref. [9].

[1]Corresponding author.

Contributed by the Heat Transfer Division of ASME for publication in the JOURNAL OF HEAT TRANSFER. Manuscript received May 10, 2008; final manuscript received December 13, 2008; published online May 6, 2009. Review conducted by Gautam Biswas.

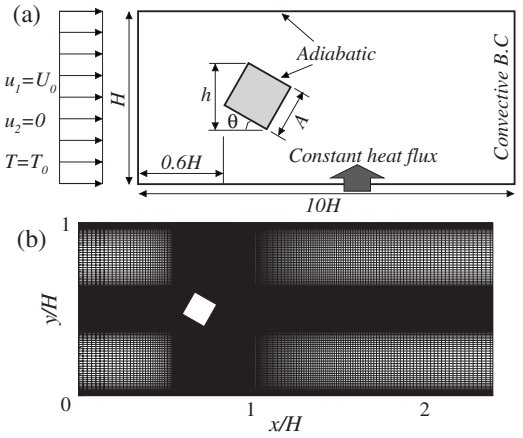

Fig. 1 Flow configuration; (*a*) boundary conditions, (*b*) grid system

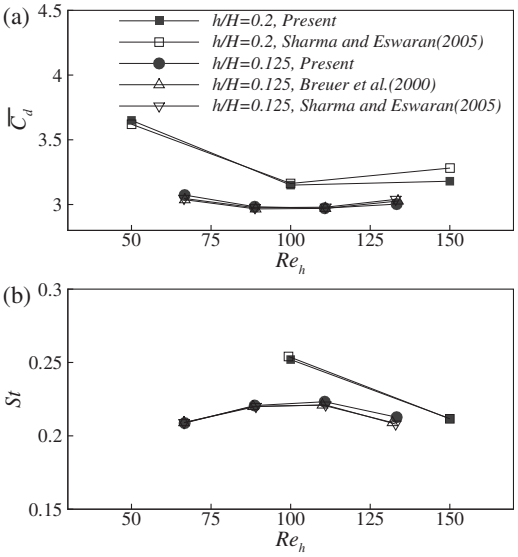

Fig. 2 Comparison of (*a*) mean drag coefficient and (*b*) Strouhal number, over a range of Reynolds number for $h/H=0.125$ and $h/H=0.2$, $\theta=0$ deg

3 Boundary Conditions and Numerical Parameters

The square cylinder of fixed size ($A/H=0.2$, where A is side length of the cylinder) is located on the channel centerline (Fig. 1) with an inclination angle (θ). The Prandtl number is fixed as Pr $=0.71$, and the Reynolds number as $\mathrm{Re}_H=500$ and 750. The streamwise length of the computational domain is $L=10H$, and the cylinder is placed $0.6H$ downstream of the inlet (Fig. 1). At the inlet, uniform velocity and temperature were specified, while a convective boundary condition [10] was employed at the outlet for both velocity and temperature fields. No-slip condition was imposed on all the solid walls. For thermal boundary conditions on the solid surfaces, a constant heat flux was specified on the lower wall of the channel, while the other solid walls were assumed adiabatic. Grid cells were clustered near the solid walls (Fig. 1(*b*)) for better numerical resolution, and the number of grid cells was determined by a grid refinement study as 2968×216 in x and y, respectively. The smallest grid cells of $0.0083h$ were allocated near the channel walls and around the cylinder. We used the tanh function for grid stretching; typical ranges of the stretching ratio are 1.001–1.057 in x direction, 1.01–1.15 in y direction. Twelve cases ($\theta=0,5,10,15,20,30,45,60,70,75,80,85$ deg) were computed for each Re_H.

4 Verification of the Code

For verifying our numerical methodology and resolution, our results with $\theta=0$ deg and $h/H=0.125$ and 0.2 are compared with those of other authors [4,5] in Fig. 2, where variations in mean drag coefficient ($\overline{C_d}=\overline{\mathrm{drag}}/\frac{1}{2}\rho U_0^2 h$) and the Strouhal number with Re_h are presented. In this computation for code validation, fully developed flow was imposed at the inlet as the other authors did. Our results are in good agreement with theirs, verifying that the numerical scheme and resolution used in the current simulation are adequate and reliable.

5 Results and Discussion

It would be more realistic to control heat transfer in practical applications by varying the inclination angle of a given square cylinder. As θ increases to 45 deg, the blockage ratio also increases due to the fixed cylinder size. Thus for a given Re_H, the fluid velocity between the cylinder and the channel wall accordingly increases, affecting convective heat transfer on the channel wall in a positive manner. In Fig. 3, instantaneous streamlines (solid lines) together with instantaneous isothermal lines (dotted lines) near the lower wall are presented depending on θ for Re_H $=500$. Figure 3(*a*) corresponds to the channel flow without the square cylinder. It is seen that a thermal boundary layer develops on the lower wall (Fig. 3(*a*)). In the presence of the square cylinder (Figs. 3(*b*)–3(*e*)), the vortex shedding downstream of the cylinder significantly affects fluid temperature in the vicinity of the channel walls. One can notice that fluctuation magnitude of near-wall streamlines increases with θ up to 45 deg (Figs. 3(*b*)–3(*e*)), implying the increase in v'_{rms} near the lower wall, as seen in Fig. 4. Figure 4 presents the distribution of the rms of periodic fluctuation of the normal velocity component (v'_{rms}) in the vicinity of the lower wall ($y/H=0.1$). In addition, the secondary vortices near the wall (indicated by arrows in Fig. 3(*e*)) tend to intensify v'_{rms} leading to more efficient heat transfer on the wall.

Figure 5 presents variations in the normalized $\langle\overline{\mathrm{Nu}}\rangle$ on the lower wall, revealing a significant enhancement of heat transfer. The corresponding value for the pure channel flow was used for the normalization. The Nusselt number is defined as follows:

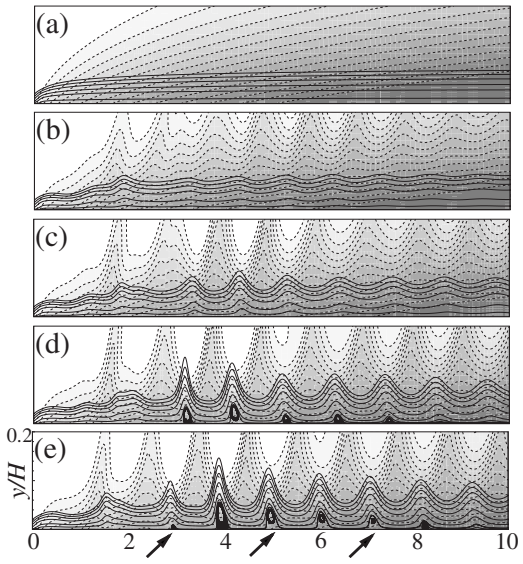

Fig. 3 Instantaneous streamlines and temperature contours, $\mathrm{Re}_H=500$; (*a*) channel flow without a cylinder, (*b*) $\theta=0$ deg, (*c*) $\theta=15$ deg, (*d*) $\theta=30$ deg, and (*e*) $\theta=45$ deg

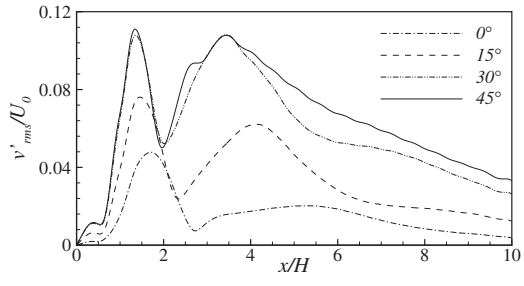

Fig. 4 Distribution of v'_{rms}; $Re_H=500$, $y/H=0.1$

$$\mathrm{Nu}=\frac{h_{\mathrm{conv}}H}{k}=\frac{1}{\Theta_s} \tag{4}$$

Here, h_{conv} and Θ_s represent convective heat transfer coefficient and local temperature of the lower wall, respectively. The mean Nusselt number averaged on the entire lower wall was defined as

$$\langle\overline{\mathrm{Nu}}\rangle=\frac{\int_0^L \overline{\mathrm{Nu}}\ dx}{L} \tag{5}$$

where the overbar indicates time averaging, and $\langle\ \rangle$ denotes spatial averaging on the lower channel wall. When $\theta=0$ deg, $\langle\overline{\mathrm{Nu}}\rangle$ increases approximately by 5.5% compared with that of the corresponding channel flow without the square cylinder ($\langle\overline{\mathrm{Nu}_{\mathrm{ch}}}\rangle$). In particular, the maximum enhancement is obtained at $\theta=45$ deg, approximately by 21% compared with the corresponding channel flow without the cylinder. This is consistent with Valencia's result [6], which says that heat transfer on the wall is enhanced as the blockage ratio increases. Nakagawa et al. [2] performed experimental measurement of $\langle\overline{\mathrm{Nu}}\rangle$ on the wall with a constant heat flux in turbulent channel flow at $\mathrm{Re}_H=15{,}000$ and reported that the large-scale periodic and alternating rollup motion of the vortices shed downstream of the rectangular cylinder significantly contributes to the extensive enhancement of heat transfer at the channel wall, which is consistent with our results.

To quantify the mean pressure drop caused by the inclusion of cylinder, we define friction factor as $f=((\Delta p/L)H)/(1/2\rho U_0^2)$ and reveal its value for some cases reported in the present study in Table 1. Here, Δp and ρ represent mean pressure drop between inlet and outlet, and fluid density, respectively. Thermal performance [11] is accordingly defined as $(\langle\overline{\mathrm{Nu}}\rangle/\langle\overline{\mathrm{Nu}_{\mathrm{ch}}}\rangle)/(f/f_{\mathrm{ch}})^{1/3}$ and computed, as seen in Table 1. Friction factor reaches its maximum at $\theta=45$ deg, while thermal performance is rather flat.

Figure 6(*a*) shows the distribution of time-averaged friction coefficient ($\overline{C_f}$) defined as

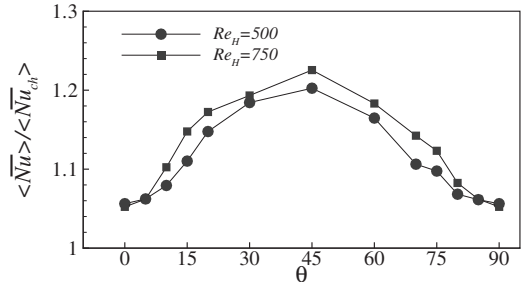

Fig. 5 Normalized mean Nusselt number for various inclination angles

Table 1 Friction factor and thermal performance

Inclination angle (deg)	Friction factor		Thermal performance	
	$\mathrm{Re}_H=500$	$\mathrm{Re}_H=750$	$\mathrm{Re}_H=500$	$\mathrm{Re}_H=750$
0	0.172	0.147	0.921	0.894
10	0.182	0.165	0.924	0.901
20	0.205	0.194	0.944	0.907
30	0.225	0.214	0.945	0.895
45	0.238	0.225	0.942	0.903
60	0.225	0.214	0.930	0.887
70	0.205	0.194	0.910	0.884
80	0.182	0.165	0.914	0.885

$$\overline{C_f}=\frac{\overline{\tau_w}}{\frac{1}{2}\rho U_0^2} \tag{6}$$

where $\overline{\tau_w}$ is time-averaged shear stress on the lower wall. Compared with the pure channel flow, $\overline{C_f}$ greatly increases in the near-wake region ($0.6<x/H<3.5$) due to the blockage effect of the cylinder. Although very little difference in $\overline{C_f}$ is identified among the cases in the far downstream region ($x/H>3.5$), that is not the case for rms of C_f fluctuation ($C'_{f,\mathrm{rms}}$), as seen in Fig. 6(*b*). Figure 6 confirms that heat transfer on the channel wall is strongly correlated with wall-shear-stress fluctuation rather than mean wall-shear stress. This observation is consistent with the previous finding that the amplified vertical periodic fluctuation of velocity (Fig. 4) enhances convective heat transfer on the channel walls because vertical velocity fluctuation necessarily induces horizontal velocity fluctuation via continuity. Yang et al. [12] also reported that mass transfer has a close correlation with wall-shear-stress fluctuation in their corrosion study.

6 Conclusion

A numerical parametric study was carried out to investigate the feasibility of utilizing large-scale vortices to enhance heat transfer on a channel wall with constant heat flux. As a vortex generator, an inclined square cylinder of fixed size ($A/H=0.2$) was employed, and its effectiveness was estimated depending on its inclination angle. Laminar flows at $\mathrm{Re}_H=500$ and 750 were considered.

The large-scale vortices shed from the cylinder induce periodic vertical fluctuation of velocity, which enhances heat transfer on

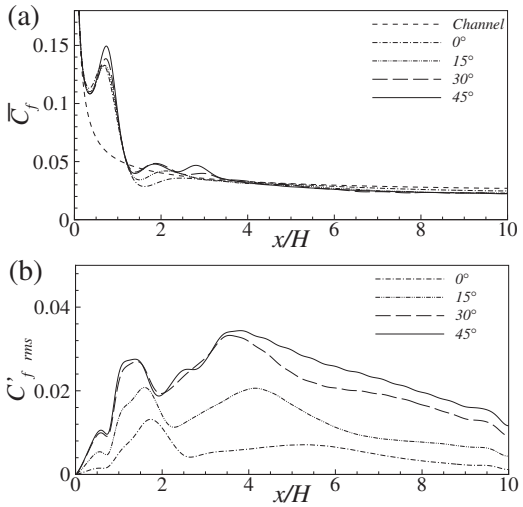

Fig. 6 Distribution of (*a*) mean friction coefficient and (*b*) rms of friction-coefficient fluctuation for $\mathrm{Re}_H=500$

the channel wall. The maximum enhancement was obtained at $\theta = 45$ deg approximately by 21%. In particular, secondary vortices generated on the channel walls also amplify the vertical fluctuation of velocity, thus contribute to heat transfer enhancement. It was also shown that heat transfer on the channel wall is closely correlated with wall-shear-stress fluctuation. Since vertical velocity fluctuation induces horizontal velocity fluctuation via continuity, leading to wall-shear-stress fluctuation, the close correlation supports our finding that vertical velocity fluctuation plays a key role in convective heat transfer on the channel wall, and an inclined square cylinder is an effective tool to control heat transfer in channel flows by varying its inclination angle to generate desirable levels of vertical velocity fluctuation via vortex shedding.

Acknowledgment

This work was financially supported by UVRC, Korea.

References

[1] Hwang, J.-Y., Yang, K.-S., and Sun, S.-H., 2003, "Reduction of Flow-Induced Forces on a Circular Cylinder Using a Detached Splitter Plate," Phys. Fluids, **15**(8), pp. 2433–2436.

[2] Nakagawa, S., Senda, M., Hiraide, A., and Kikkawa, S., 1999, "Heat Transfer Characteristics in a Channel Flow With a Rectangular Cylinder," JSME Int. J., Ser. B, **42**(2), pp. 188–196.

[3] Suzuki, K., and Suzuki, H., 1994, "Unsteady Heat Transfer in a Channel Obstructed by an Immersed Body," Annu. Rev. Heat Transfer, **5**, pp. 177–206.

[4] Sharma, A., and Eswaran, V., 2005, "Effect of Channel Confinement on the Two-Dimensional Laminar Flow and Heat Transfer Across a Square Cylinder," Numer. Heat Transfer, Part A, **47**(1), pp. 79–107.

[5] Breuer, M., Bernsdorf, J., Zeiser, T., and Durst, F., 2000, "Accurate Computations of the Laminar Flow Past a Square Cylinder Based on Two Different Methods: Lattice-Boltzmann and Finite-Volume," Int. J. Heat Fluid Flow, **21**(2), pp. 186–196.

[6] Valencia, A., 1995, "Heat Transfer Enhancement in a Channel With a Built-In Square Cylinder," Int. Commun. Heat Mass Transfer, **22**(1), pp. 47–58.

[7] Sohankar, A., Norberg, C., and Davidson, L., 1998, "Low-Reynolds-Number Flow Around a Square Cylinder at Incidence: Study of Blockage, Onset of Vortex Shedding and Outlet Boundary Condition," Int. J. Numer. Methods Fluids, **26**(1), pp. 39–56.

[8] Kim, J., Kim, D., and Choi, H., 2001, "An Immersed-Boundary Finite-Volume Method for Simulations of Flow in Complex Geometries," J. Comput. Phys., **171**(1), pp. 132–150.

[9] Yang, K.-S., and Ferziger, J. H., 1993, "Large Eddy Simulation of a Turbulent Obstacle Flow Using a Dynamic Subgrid-Scale Model," AIAA J., **31**(8), pp. 1406–1413.

[10] Kim, D.-H., Yang, K.-S., and Senda, M., 2004, "Large-Eddy Simulation of Turbulent Flow Past a Square Cylinder Confined in a Channel," Comput. Fluids, **33**(1), pp. 81–96.

[11] Fu, W. S., and Tong, B. H., 2003, "Numerical Investigation of Heat Transfer of a Heated Channel With an Oscillating Cylinder," Numer. Heat Transfer, Part A, **43**(6), pp. 639–658.

[12] Yang, K.-S., Hwang, J.-Y., Bremhorst, K., and Nesic, S., 2003, "Numerical Investigation of Turbulent Flow Around a Rotating Stepped Cylinder for Corrosion Study," Can. J. Chem. Eng., **81**(1), pp. 26–36.

Transient Heat Transfer in a Partially Cooled Cylindrical Rod

Lawrence Agbezuge
Visiting Associate Professor
Rochester Institute of Technology,
Rochester, NY 14623
e-mail: lxaeme@rit.edu

Finite element and finite difference solutions are obtained for transient temperature distribution in a partially cooled cylindrical rod that generates heat at a uniform rate. A portion of the rod is immersed in a coolant reservoir that is maintained at constant temperature, and the exposed portion of the rod is cooled by convective heat transfer. Because thermal conductivity of the rod is temperature dependent, the governing partial differential equation is nonlinear. The analytical techniques utilized in solving the problem could be applied to analyzing the cooling of spent nuclear fuel rods. The finite difference method used to solve the problem utilizes an implicit formulation of the governing equation, and a numerical technique for handling the nonlinear terms. Validation of the numerical solution is obtained by comparing the results at a specified time against those generated by a commercial finite element software package. The computer model for the problem was used to estimate heat generation rates that could initiate meltdown of a fuel rod. [DOI: 10.1115/1.3090816]

Keywords: nonlinear equation, conduction, convection, fuel rods, coolant, numerical methods, finite difference, finite element

1 Introduction

The purpose of this paper is to present a finite element and an implicit finite difference method for solving a nonlinear transient heat transfer problem that involves mixed boundary conditions. The problem that is solved has practical significance related to the cooling of spent nuclear fuel rods. The technique of using an implicit, unconditionally stable method for solving differential equations is well known [1,2]. Nonlinearity of the governing equation arises because the thermal conductivity of the rod is temperature dependent.

The nonlinearity is handled by using partial derivatives at successive time steps, and by using time steps that will make the derivatives vary slowly. This strategy is implemented in a software by using small time steps at the beginning stages of the solution, when temperature gradients are high. As the solution proceeds, temperature gradients become lower, and larger time steps are used. This same strategy is utilized in a commercial finite element software.

The problem solved is that of a heated cylindrical rod partially immersed in a coolant and partially cooled by convective heat transfer. Because of axial and rotational symmetries, the problem is solved as a rectangular slice of the cylinder taken from its center to its outer radius. A computer program written in MATLAB® was used to obtain transient state temperature distribution in the cylindrical rod.

As a test of reasonableness, temperature distribution along the cylindrical axis of the rod was compared with results obtained from the commercial finite element program ANSYS®.

Contributed by the Heat Transfer Division of ASME for publication in the JOURNAL OF HEAT TRANSFER. Manuscript received June 3, 2008; final manuscript received January 11, 2009; published online May 12, 2009. Review conducted by Gautam Biswas.

Although this problem was solved primarily as an academic exercise, the techniques and principles utilized in solving the problem could be applicable in solving certain types of industrial problems related to the cooling of spent nuclear fuel rods [3–5]. It is a known fact that a major problem arose when cooling effectiveness was compromised in nuclear fuel rods for the 3 mile island nuclear emergency [6]. Solutions for problems related to the cooling of fuel rods are essential for establishing guidelines for cooling nuclear reactor fuels [7,8]. Recent work by Laursen et al. [3] analyzed the cooling of spent nuclear rod fuels in a large water pool, followed by convective cooling in concrete casks. Wang et al. [9] performed studies on forced convection and boiling heat transfer curves for clean rod surfaces in order to understand crud formation on fuel pin clad surfaces, as observed in pressurized water reactors. Gomez and Greiner [10] performed two-dimensional simulations of steady natural convection and radiation heat transfer for a 14×14 pressurized water reactor (PWR) spent nuclear fuel assembly. More recent work related to the cooling of nuclear fuel rods may be found in the cited references [4,5,11,12].

2 Problem Description

A cylinder rod of radius, a, and length, $2b$, is submerged in coolant to half its length (Fig. 1). The rod generates heat at a constant rate, f. The top surface of the cylinder is thermally insulted. The cylindrical exposed surface of the cylinder exchanges heat by convection with ambient air with film coefficient, h, and ambient temperature, T_∞.

The objectives are (a) to create a finite difference model for determining transient temperature distribution in the rod, and (b) to validate the results obtained at a specified time against those obtained from a commercial finite element software package. The general form of the governing equation for the problem is

$$\nabla\cdot(k\,\nabla\,T)+q=\rho c_p\frac{\partial T}{\partial t} \tag{1}$$

where $T(r,\theta,z,t)$ = temperature variation in the cylindrical coordinate system (r,θ,z), k = thermal conductivity, ρ = density, c_p = specific heat, t = time, and q = heat generation rate.

Because of rotational symmetry, variation with respect to the θ-coordinate is ignored. Because thermal conductivity is temperature dependent, $\nabla k=(dk/dT)\nabla T$, and the governing equation in cylindrical coordinates is

$$\frac{dk}{dT}\left[\left(\frac{\partial T}{\partial r}\right)^2+\left(\frac{\partial T}{\partial z}\right)^2\right]+k\left(\frac{\partial^2T}{\partial r^2}+\frac{1}{r}\frac{\partial T}{\partial r}+\frac{\partial^2T}{\partial z^2}\right)+q(r,z)=\rho c_p\frac{\partial T}{\partial t} \tag{2}$$

Because of axial and rotational symmetries, the problem will be solved as a rectangular slice of the cylinder taken from its center to its outer radius.

The boundary conditions are

$$T(r,0,t)=T_C,\quad r\in[0,a]$$

for specified coolant temperature at $z=0$

$$T(a,z,t)=T_C,\quad z\in[0,b]$$

for specified coolant temperature at $r=a$

$$k(T)\frac{\partial T}{\partial r}\bigg]_{r=a}+h[T(a,z,t)-T_\infty]=0,\quad z\in[b,2b]$$

for convective heat flux at $r=a$

$$\frac{\partial T}{\partial z}\bigg]_{z=2b}=0,\quad r\in[0,a]$$

for thermal insulation at $z=2b$

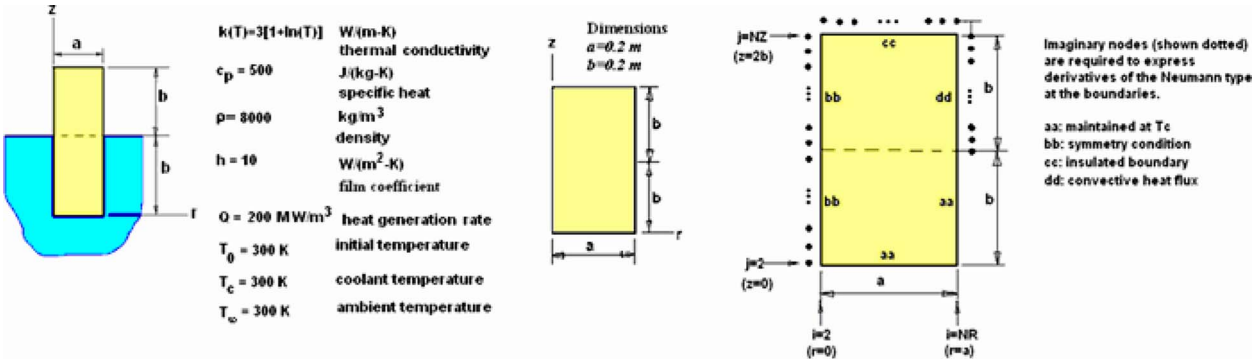

Fig. 1 Problem definition and FD grid set up

$$\left.\frac{\partial T}{\partial r}\right]_{r=0} = 0, \quad z \in [0,2b] \quad \text{as symmetry condition}$$

The initial condition is $T(r,z,0)=T_0, r \in [0,a], z \in [0,2b]$.

The problem is formulated as an implicit finite difference problem and solved numerically for 10,000 s. Temperature distribution is generated in the form of contour plots. To validate the solution, results obtained along the central axis of the rod are plotted together with the solution obtained from ANSYS®, a commercial finite element software package.

3 Implicit FD Formulation of the Governing Equations

Finite difference (FD) discretization of the governing equation is formulated by defining the dependent variable

$$T_{i,j}^{(k)} \equiv T(r_i, z_j, t_k) \quad \text{where} \quad r_i = i\Delta r, \quad z_j = j\Delta z, \quad t_k = k\Delta t$$
$$\text{for} \quad \Delta r = a/N_r, \quad \Delta z = (2b)/N_z; \quad i = 0,1,2,\ldots,N_r \qquad (3)$$
$$j = 0,1,2,\ldots,N_z, \quad k = 0,1,2,\ldots$$

As an approximation, the nonlinear terms in the governing equation that involve partial derivatives will be split into partial derivatives at successive time steps. At time step $t+\Delta t$, we shall use these approximations

$$\left[\left(\frac{\partial T}{\partial r}\right)^2\right]^{(t+\Delta t)} \cong \left(\frac{\partial T}{\partial r}\right)^{(t)}\left(\frac{\partial T}{\partial r}\right)^{(t+\Delta t)} \quad \text{and}$$
$$\left[\left(\frac{\partial T}{\partial z}\right)^2\right]^{(t+\Delta t)} \cong \left(\frac{\partial T}{\partial z}\right)^{(t)}\left(\frac{\partial T}{\partial z}\right)^{(t+\Delta t)} \qquad (4)$$

The approximations are reasonable and acceptable, provided that small time steps are taken when temperature gradients are high (at the beginning of the solution). As the solution proceeds, temperature gradients become lower and larger time steps may be taken. Another approximation is to use integrated average values for $k(T)$ and its derivative with respect to T. That is, over the temperature range of $[T_1, T_2] \equiv [300,800]$, the integrated average values are computed as

$$\bar{k} = \frac{1}{T_2 - T_1}\int_{T_1}^{T_2} 3[1+\ln(T)]dT = 21.8$$
$$\bar{\eta} = \frac{1}{T_2 - T_1}\int_{T_1}^{T_2} \frac{3}{T}dT = 0.0059 \qquad (5)$$

Because the solution will be obtained at discrete time steps $t = 0, \Delta t, 2\Delta t, \ldots$, the governing equation is written as

$$\left[\bar{\eta}\left(\frac{\partial T}{\partial r}\right)^{(t)} + \frac{\bar{k}}{r}\right]\left[\frac{\partial T}{\partial r}\right]^{(t+\Delta t)} + \bar{\eta}\left(\frac{\partial T}{\partial z}\right)^{(t)}\left(\frac{\partial T}{\partial z}\right)^{(t+\Delta t)} + \bar{k}\left[\frac{\partial^2 T}{\partial r^2} + \frac{\partial^2 T}{\partial z^2}\right]^{(t+\Delta t)} + q(r,z) = \rho c_p \frac{[T^{(t+\Delta t)} - T^{(t)}]}{\Delta t}$$

After applying centered finite differencing on spatial coordinates, the governing equation, in discretized form is

$$\left(\beta_r C_r^k + \frac{\eta_r}{r_i}\right)[T_{i+1,j} - T_{i-1,j}]^{(k+1)} + \beta_z C_z^k [T_{i,j+1} - T_{i,j-1}]^{(k+1)} + \gamma_r [T_{i+1,j} + T_{i-1,j} - 2T_{i,j}]^{(k+1)} + \gamma_z [T_{i,j+1} + T_{i,j-1} - 2T_{i,j}]^{(k+1)} + Q_{ij}^k = T_{i,j}^{(k+1)} - T_{i,j}^{(k)}$$
$$\text{for} \quad k = 0,1,\ldots; \quad i = 0,1,\ldots,N_r; \quad j = 0,1,\ldots,N_z. \qquad (6)$$

$$\text{where} \quad \beta_r = \frac{\bar{\eta}\Delta t}{4\rho c_p (\Delta r)^2}, \quad \beta_z = \frac{\bar{\eta}\Delta t}{4\rho c_p (\Delta z)^2}, \quad \eta_r = \frac{\bar{k}\Delta t}{2\rho c_p \Delta r} \qquad (7)$$

$$\gamma_r = \frac{\bar{k}\Delta t}{\rho c_p (\Delta r)^2}, \quad \gamma_z = \frac{\bar{k}\Delta t}{\rho c_p (\Delta z)^2} \qquad (8)$$

$$C_r^{(k)} = [T_{i+1,j} - T_{i-1,j}]^{(k)}, \quad C_z^{(k)} = [T_{i,j+1} - T_{i,j-1}]^{(k)}, \quad Q_{ij}^{(k)} = \frac{q\Delta t}{\rho c_p} \qquad (9)$$

Limits for nodal indices i and j should be modified to handle mixed boundary conditions for the problem. Because the method of solution that is utilized for computer implementation is iterative, the discretized equation should be written in a form that is suitable for methods such the Jacobi, Gauss–Seidel, or successive over-relaxation methods [13]. The implicit finite difference method is stable and unconditionally convergent as opposed to the explicit method. Enhancements to the implicit method such as Crank–Nicholson or Galerkin [14] that use weighting or the alternating direction implicit (ADI) method [15] could also be used. The enhancements are not used for this problem, but they may be necessary for improving stability and convergence for certain types of boundary value problems. The iterative form of the discretized equation is

$$T_{i,j}^{(k+1)} = \frac{1}{D}\left[T_{i,j}^{(k)} + \left(\beta_r C_r^k + \frac{\eta_r}{r_i}\right)E_{i,j}^{(k+1)} + \beta_z C_z^k F_{i,j}^{(k+1)} + \gamma_r G_{i,j}^{(k+1)} + \gamma_z H_{i,j}^{(k+1)} + Q_{ij}^{(k)}\right] \qquad (10)$$

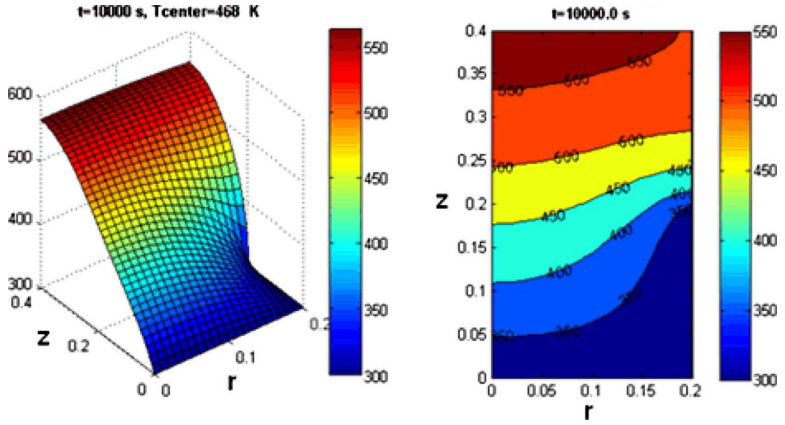

Fig. 2 Contour plot for temperature after 10,000 s

where $E_{i,j}^{(k+1)} = [T_{i+1,j} - T_{i-1,j}]^{(k+1)}$, $F_{i,j}^{(k+1)} = [T_{i,j+1} - T_{i,j-1}]^{(k+1)}$

$$G_{i,j}^{(k+1)} = [T_{i+1,j} + T_{i-1,j}]^{(k+1)}, \quad H_{i,j}^{(k+1)} = [T_{i,j+1} + T_{i,j-1}]^{(k+1)} \tag{11}$$

$$D = 1 + 2(\gamma_r + \gamma_z)$$

The boundary conditions are recast in discretized form for computer implementation.

4 Numerical Solution of the FD Equations

In the computer implementation of the FD solution, a grid or mesh was set up as shown in Fig. 1.

The solution was obtained by assigning an initial temperature of T_c to all nodes in the solution domain, and by selecting a small time step for the beginning of the solution. At each time step, the discretized equation is solved iteratively at all nodes within the domain, while satisfying the mixed boundary conditions. Convergence at a time step is obtained when the residual error becomes less than a specified residual error tolerance. The residual error is computed as the sum of relative errors between computed nodal values between successive iterations within the solution domain. When the residual error satisfies the specified criterion, another time step is taken.

As the solution proceeds, the number of iterations required for convergence at a specified time step decreases because temperature gradients decrease. This provides the opportunity to increase the size of the time step in order to reduce computational time. This same technique is used by commercial finite element programs.

For the example presented in this paper, input data used for the FD solution are given in Fig. 1.

Contour plots for temperature after 10,000 s from the FD solution are shown in Fig. 2.

Comparison of transient temperature along the axis of the cylinder at two locations is shown in Fig. 3. The good agreement validates the finite element solution, and confirms that the approximations that were made to the nonlinear governing equation are reasonable.

Of interest is the rate of heat generation that could initiate meltdown of the fuel rod. Variation of the temperature at the top of the cylinder axis was obtained by running several simulations of the computer model at varying values of heat generation rate. Temperature in the cylinder after 10,000 s was considered as the steady state value because it asymptotically approaches steady state, as is typical of parabolic partial differential equations. For typical stainless steel 316, the melting temperature [16,17] of about 1700 K will be initiated by heat generation rates of 10 MW/m^3 or above.

5 Finite Element Solution and Computer Implementation

Because of axial and rotational symmetries, only a two-dimensional slice of the cylinder was modeled.

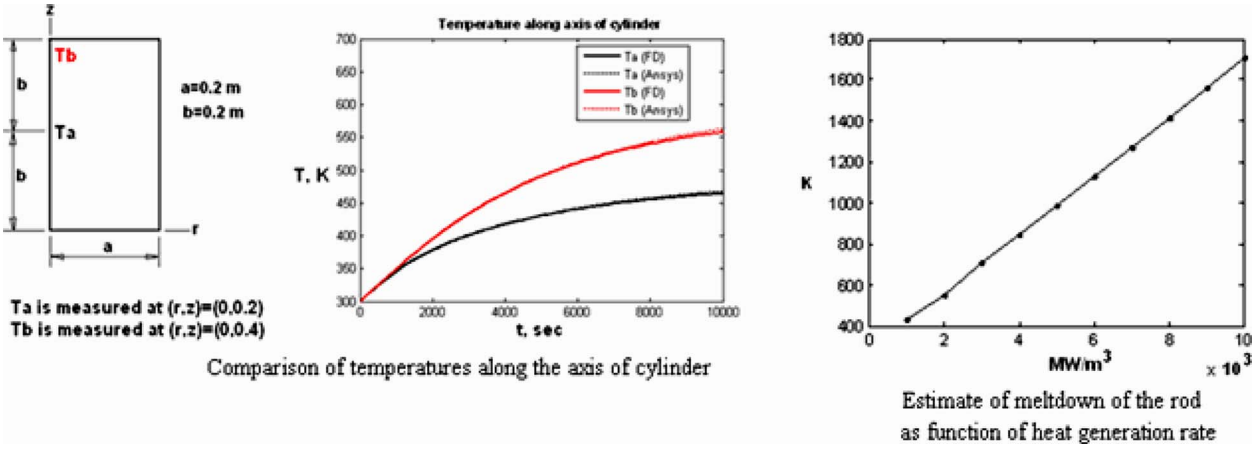

Fig. 3 Summary and comparison between FE and FD results

Table 1 Comparison of temperature at two selected locations

t (s)	T_A (K)			T_B (K)			T_C (K)		
	FD	Slice	Wedge	FD	Slice	Wedge	FD	Slice	Wedge
0	300	300	300	300	300	300	300	300	300
100	305	305	305	305	305	305	305	305	305
200	310	310	310	310	310	310	310	310	310
500	325	325	325	325	325	325	324	324	324
1,000	346	347	347	350	350	350	348	348	348
2,000	378	379	379	395	395	395	391	391	391
5,000	431	431	430	492	491	490	481	480	479
10,000	468	465	463	563	558	556	549	544	541

Finite element solution for the problem in ANSYS® was obtained by following these main steps.

- An eight-node PLANE77 thermal element was selected. Material properties (see Fig. 1) were assigned and temperature-dependent thermal conductivity was specified in tabular form.
- The rectangular geometry was created and map meshed with 20 divisions per line boundary. The boundary conditions and initial condition were specified. The solution was obtained to within 2% relative error accuracy by using *h-mesh refinement*.
- Because the governing equation is nonlinear, three time steps were specified: $\Delta t_{\min}=5$, $\Delta t_{\max}=100$, and $\Delta t=50$. The solution was printed at every load step.
- Contour plot for temperature distribution was generated at the end of the simulation time of 10,000 s in the postprocessor.
- Time history data at two locations: $r=0$ and $z=0.2,0.4$ were obtained in the time history postprocessor.

Table 1 lists temperature at three locations *A*, *B*, and *C* with coordinate $(r,z)=(0,0.2)$, (0.0.4), and (0.2,0.4), respectively. The agreement between the finite element and finite difference solutions is excellent, with relative error less than 1%.

6 Results and Discussion

Comparison of temperature distribution at three locations in the solution domain indicates that the finite element and FD solutions are in excellent agreement.

Because of axial and rotational symmetries, a two-dimensional slice of the problem was modeled in cylindrical coordinates in order to save computational resources. The entire cylindrical rod, or an angular wedge taken from the cylinder, should yield the same results as obtained from the slice. This was demonstrated by excellent agreement between the solution obtained with a two-dimensional slice taken from the cylindrical rod, and the solution obtained with a 20-deg wedge taken from the rod.

This paper has demonstrated the use of a numerical method for solving a transient nonlinear heat transfer problem typical of that found in fuel rods. The method requires that reasonable approximations be made to handle nonlinearity in the governing partial differential equation. Application of the method could be used for solving practical problems that are necessary for establishing safety criteria for shutting down operation of fuel rods, should the cooling system should become compromised or ineffective.

The ability of the commercial finite element method to handle nonlinear problems has also been demonstrated, because material property variations (such as temperature-dependent thermal conductivity) are easily handled at the element level.

The computer model was used to project that heat generation rates of about 10 MW/m^3 and above will initiate meltdown of typical stainless steel 316, with melting temperature of about 1700 K.

References

[1] Carnahan, B., 1969, *Applied Numerical Methods*, Wiley, New York.
[2] Larssom, S., and Thomee, V., 2003, *Partial Differential Equations With Numerical Methods*, Springer-Verlag.
[3] Laursen, A. L., Moody, F. J., and Law, J. C., 2006, "Air Cooling Temperature Analysis of Spent Fuel," 14th International Conference on Nuclear Engineering (ICONE14), Miami, FL, Jul. 17–20, pp. 275–282, Paper No. ICONE14–89261.
[4] Lele, H. G., Srivastava, A., Chatterjee, B., Gaikwad, A. J., Kumar, R., and Gupta, S. K., 2004, "Transient Analysis for the Case of Changes in Coolant Inventory for Advanced Heavy Water Reactor," 12th International Conference on Nuclear Engineering (ICONE12), Arlington, VA, Apr. 25–29, pp. 321–328, Paper No. ICONE12–49148.
[5] Stevanovic, V., Stosic, Z., and Stoll, U., 2004, "Analytical and CFD Investigation of Ex-Core Cooling of the Nuclear Fuel Rod Bundle in a Water Pool," 12th International Conference on Nuclear Engineering (ICONE12), Vol. 2.
[6] Craddock, A., 1994, "Faulty Rods," *Mother Jones*.
[7] Edmond, V., 1977, "Emergency Cooling Device for a Nuclear Reactor," U.S. Patent No. 4035231.
[8] Olov, N., 1992, "Fuel Assembly for a Boling Reactor," U.S. Patent No. 5089220.
[9] Wang, G., Byers, W. A., Karoutas, Z. E., Hochreiter, L. E., Young, M. Y., and Jacko, R. J., 2006, "Single Rod Heat Transfer Tests to Study the Effects of Crud Deposition," 14th International Conference on Nuclear Engineering (ICONE14), Miami, FL, Jul. 17–20, pp. 275–282, Paper No. ICONE14–89261.
[10] Gomez, P. E. A., and Greiner, M., 2006, "2D Natural Convection and Radiation Heat Transfer Simulations of a PWR Fuel Assembly Within a Constant Temperature Support Structure," ASME Paper No. PVP2006-ICPVT-11–93332.
[11] Khushnood, S., Malik, M. A., Khan, Z. M., Khan, A., Iqbal, Q., Khalil, M. S., Rashid, B., and Hussain, S. Z., 2006, "Modeling and Analysis of Thermal Damping in Heat Exchanger Tube Bundles," ASME Conference Proceedings (ICONE14), Vol. 3, p. 147.
[12] Wenfeng, L., and Mujid, S. K., 2006, "Modeling Cladding-Coolant Heat Transfer of High-Burnup Fuel During RIA," ASME Conference Proceedings (ICONE14), Vol. 2, p. 855.
[13] Faires, J. D., and Burden, R., 2003, *Numerical Methods*, 3rd ed., Thomson, Pacific Grove, CA, pp. 306–314.
[14] Crank, J., and Nicolson, P., 1947, "A Practical Method for Numerical Evaluation of Solutions of Partial Differential Equations of the Heat Conduction Type," Proc. Cambridge Philos. Soc., **43**, pp. 50–64.
[15] Chang, M. J., Chow, L. C., and Chang, W. S., 1991, "Improved Alternating-Direction Implicit Method for Solving Transient Three-Dimensional Heat Diffusion Problems," Numer. Heat Transfer, Part B, **19**, pp. 69–84.
[16] Engineer's Edge, "Properties of Metals–Thermal," http://www.engineersedge.com/properties_of_metals.htm.
[17] British Stainless Steel Association, "Making the Most of Stainless Steel," http://www.bssa.org.uk/topics.php?article=103.

Erratum: "Nanofluids: Synthesis, Heat Conduction, and Extension" [Journal of Heat Transfer, 2009, 131(3), p. 033102]

Liqiu Wang and Xiaohao Wei

There was a symbol mix-up in Sec. 3. Therefore corrections are needed in the paper, as follows.

1. Page 033102-4: Eqs. (9)–(14), (16), and (18) should read

$$\gamma_\beta \frac{\partial \langle T_\beta \rangle^\beta}{\partial t} = k_{\beta\beta}\Delta\langle T_\beta\rangle^\beta + k_{\beta\sigma}\Delta\langle T_\sigma\rangle^\sigma + ha_v(\langle T_\sigma\rangle^\sigma - \langle T_\beta\rangle^\beta) \tag{9}$$

$$\gamma_\sigma \frac{\partial \langle T_\sigma \rangle^\sigma}{\partial t} = k_{\sigma\sigma}\Delta\langle T_\sigma\rangle^\sigma + k_{\sigma\beta}\Delta\langle T_\beta\rangle^\beta + ha_v(\langle T_\beta\rangle^\beta - \langle T_\sigma\rangle^\sigma) \tag{10}$$

$$\begin{bmatrix} \gamma_\beta \frac{\partial}{\partial t} - k_{\beta\beta}\Delta + ha_v & -k_{\beta\sigma}\Delta - ha_v \\ -k_{\sigma\beta}\Delta - ha_v & \gamma_\sigma \frac{\partial}{\partial t} - k_{\sigma\sigma}\Delta + ha_v \end{bmatrix} \begin{bmatrix} \langle T_\beta\rangle^\beta \\ \langle T_\sigma\rangle^\sigma \end{bmatrix} = 0 \tag{11}$$

$$\left[\left(\gamma_\beta \frac{\partial}{\partial t} - k_{\beta\beta}\Delta + ha_v\right)\left(\gamma_\sigma \frac{\partial}{\partial t} - k_{\sigma\sigma}\Delta + ha_v\right) - (k_{\beta\sigma}\Delta + ha_v)^2\right]\langle T_i\rangle^i = 0 \tag{12}$$

$$\frac{\partial \langle T_i\rangle^i}{\partial t} + \tau_q \frac{\partial^2 \langle T_i\rangle^i}{\partial t^2} = \alpha\Delta\langle T_i\rangle^i + \alpha\tau_T \frac{\partial}{\partial t}(\Delta\langle T_i\rangle^i) + \frac{\alpha}{k}\left[F(\mathbf{r},t) + \tau_q \frac{\partial F(\mathbf{r},t)}{\partial t}\right] \tag{13}$$

$$\tau_q = \frac{\gamma_\beta\gamma_\sigma}{ha_v(\gamma_\beta + \gamma_\sigma)}, \quad \tau_T = \frac{\gamma_\beta k_{\sigma\sigma} + \gamma_\sigma k_{\beta\beta}}{ha_v(k_{\beta\beta} + k_{\sigma\sigma} + 2k_{\beta\sigma})}$$

$$k = k_{\beta\beta} + k_{\sigma\sigma} + 2k_{\beta\sigma}, \quad \alpha = \frac{k_{\beta\beta} + k_{\sigma\sigma} + 2k_{\beta\sigma}}{\gamma_\beta + \gamma_\sigma}$$

$$F(\mathbf{r},t) + \tau_q \frac{\partial F(\mathbf{r},t)}{\partial t} = \frac{k_{\beta\sigma}^2 - k_{\beta\beta}k_{\sigma\sigma}}{ha_v}\Delta^2\langle T_i\rangle^i \tag{14}$$

$$\frac{k}{k_\beta} = \frac{k_{\beta\beta} + k_{\sigma\sigma} + 2k_{\beta\sigma}}{k_\beta} \tag{16}$$

$$\frac{\tau_T}{\tau_q} = 1 + \frac{\gamma_\beta^2 k_{\sigma\sigma} + \gamma_\sigma^2 k_{\beta\beta} - 2\gamma_\beta\gamma_\sigma k_{\beta\sigma}}{\gamma_\beta\gamma_\sigma(k_{\beta\beta} + k_{\sigma\sigma} + 2k_{\beta\sigma})} \tag{18}$$

2. Page 033102-4: The line below Eq. (10) should read "where $k_{\beta\beta}$ and $k_{\sigma\sigma}$ are the effective thermal conductivities of the β-."
3. Page 033102-4: The second line below Eq. (14) should read "conduction equation with $((k_{\beta\sigma}^2 - k_{\beta\beta}k_{\sigma\sigma})/(ha_v))\Delta^2\langle T_i\rangle^i$ as the DPL."
4. Page 033102-4: The fourth line below Eq. (17) should read "nanoparticle-fluid interface due to the term $k_{\beta\beta}+k_{\sigma\sigma}+2k_{\beta\sigma}$."
5. Page 033102-4: The seventh line below Eq. (17) should read "thus focus on $k_{\beta\beta}+k_{\sigma\sigma}+2k_{\beta\sigma}$ to develop predicting models of thermo-."
6. Page 033102-4: The paragraph above Eq. (18) should read "To show the possibility of conductivity enhancement, consider."
7. Page 033102-4: The second line below Eq. (18) should read "of $\gamma_\beta^2 k_{\sigma\sigma} + \gamma_\sigma^2 k_{\beta\beta} - 2\gamma_\beta\gamma_\sigma k_{\beta\sigma}$. Therefore, by the condition for the ex-."
8. Page 033102-5: The first equation should read
$$\gamma_\beta^2 k_{\sigma\sigma} + \gamma_\sigma^2 k_{\beta\beta} - 2\gamma_\beta\gamma_\sigma k_{\beta\sigma} < 0$$
9. Page 033102-5: The eighth line in the second paragraph in Sec. 4 should read "k_β-enhancement can occur for all cases with $k_{\beta\beta}+k_{\sigma\sigma}+2k_{\beta\sigma} > k_\beta$ (Eq."
10. Page 033102-6: In the Nomenclature list the symbols k_β and k_σ should be changed into $k_{\beta\beta}$ and $k_{\sigma\sigma}$, respectively.

